GENESIS OF BARITE ASSOCIATED WITH THE LEMARCHANT Zn-Pb-Cu-Ag-Au-RICH VOLCANOGENIC MASSIVE SULFIDE (VMS) DEPOSIT: IMPLICATIONS FOR THE GENESIS OF VMS-RELATED BARITE, CAMBRIAN SEAWATER CHEMISTRY, AND THE ORIGIN OF BARITE-RICH VMS DEPOSITS

By

© Marie-Ève Lajoie

A Thesis submitted

to the School of Graduate Studies in partial fulfillment of the

requirements for the degree of

Master of Science

Department of Earth Sciences

Memorial University of Newfoundland

September 2017

St. John's Newfoundland and Labrador

ABSTRACT

The Cambrian Tally Pond group hosts the Zn-Pb-Cu-Ag-Au-Ba Lemarchant VMS deposit. Despite the presence of barite in the deposit, the detailed relationships to mineralization, textural variations, and genesis are not well understood.

Barite in the Lemarchant deposit is generally massive and locally bladed. Trace element as well as stable and radiogenic isotopic signatures of barite crystals are remarkably homogeneous regardless of texture. The results presented herein reveal a complex origin for the barite indicating input from Cambrian seawater and mixing with VMS-related hydrothermal fluids. Fluid inclusion studies of bladed barite show three types of fluid inclusions. Low-salinity carbonic-rich inclusions are the most abundant, but these inclusions are interpreted to be secondary in origin.

These results illustrate that barite in VMS deposits is useful for recording physical and chemical processes associated with the formation of VMS deposits. In addition, the study of barite is useful for identifying potential sources of hydrothermal fluids responsible for the formation of barite and associated mineralization in the Lemarchant deposit and in other barite-rich VMS globally.

ACKNOWLEGEMENTS

The writing of this thesis would not have been possible without the help of many individuals. I learned a great deal during my graduate studies from a professional and scientific perspective and I owe my gratitude to all the people who have made my graduate experience one that I will value forever. First and foremost, I would like to extend my sincere thanks to my supervisor Dr. Stephen J. Piercey for giving me the opportunity to work on a topic that was of great interest to me. He gave me the freedom to do my own research and interpretations; from this I learned to be independent, hard-working, and disciplined. His enthusiasm and devotion towards research and teaching has guided and encouraged me throughout my graduate studies. I am forever grateful for the time and effort he invested in me and my research.

I would like to thank my committee member, Dr. Luke Beranek, for his constructive reviews and comments during committee meetings and also for his thoughtful input and editing during the revision of my thesis.

I would like to acknowledge the valuable input of Dr. James Conliffe from the Department of Natural Resources (Newfoundland and Labrador branch) for his help with the analysis of fluid inclusions. I am deeply appreciative of the time spent conducting analyses and guiding me through the process of writing and interpretation of the fluid inclusion data.

I wish to express my sincere thanks to Faculty Staff Dr. Wanda Aylward, Sherri Strong, and Dr. Alison Pye for their help with geochemical analyses.

I would like to extend my sincere gratitude to Dr. Daniel Layton-Matthews and Evelyne Leduc of Queen's University for their help in doing laser ablation trace element analysis. A special thanks to Nicholas Joyce and Dr. Stefanie Brueckner for help with laser ablation analyses and laser ablation data reduction. The time spent helping me was greatly appreciated.

Funding from this project comes primarily from the Natural Sciences and Engineering Research Council Canada Graduate Scholarship-Master's Program (NSERC-CGS-M). Additional funding comes from grants to Dr. Stephen J. Piercey, including a Natural Sciences and Engineering Research Council (NSERC) Discovery Grant and the NSERC-Altius Industrial Research Chair in Mineral Deposits supported by NSERC, Altius Resources Inc., and the Research and Development Corporation of Newfoundland and Labrador. Many thanks to Canadian Zinc Inc. for access to the Lemarchant drill core and for the use of their core logging facility. I would also like to extend my thanks to the Canadian Zinc Inc. exploration and management team for all their help and great company during my time in the field.

Finally, I would not be here without the help and support of my family, friends, and colleagues. I wish to express my sincere gratitude to them for their support, encouragements, motivation, patience, and kindness. To my father for teaching me to live fully and to not miss an opportunity. To my eldest brother, Justin, for sparking my passion for science at a young age and for his support and encouragements throughout my post-secondary studies; to my brother, Simon-Pierre, for guiding me my whole life and teaching me how to be a leader and a hard-working person; to Jean-Luc, my colleague, my friend, my mentor, and my partner, I thank you for guiding, supporting, encouraging, and inspiring me throughout my time here at Memorial University. Your passion and love for geology inspires and will continue to inspire me. To my loving grand-parents who have been my “rocks” my whole life and who have thought me to be a strong, independent woman. And finally, to my mother. For all the times that you have helped me get back up on my feet, and for all the encouraging phone calls and conversations, I cannot thank you enough. You are always there for me and have encouraged me throughout all my adventures. You are my role-model and my closest friend.

Table of Contents

List of Tables

List of Figures

List of Symbols, Nomenclature or Abbreviations

Table 0-1. List of mineral phases and associated mineral abbreviations.

Mineral Phases	Mineral Abbreviation
Barite	Brt
Sphalerite	Sp
Pyrite	Py
Galena	Gn
Chalcopyrite	Ccp
Bornite	Bn
Bournonite	Brn
Chalcocite	Cc
Covellite	Cv
Cubanite	Cub
Digenite	Dg
Gold	Au
Marcasite	Mar
Tetrahedrite	Tet
Calcite	Cal
Dolomite	Dol
Albite	Ab
Muscovite	Ms
Celsian	Cel
Fluorite	Fl

Table 0-2. Analytical instrumentation abbreviation and associated nomenclature.

Analytical instrumentation abbreviation	Nomenclature
EMPA	Electron Microprobe Analyser
HR-ICP-MS	High-resolution inductively coupled plasma-mass spectrometer
IRMS	Isotope ratio mass spectrometer
LA-ICP-MS	Laser ablation inductively couple plasma-mass spectrometer
Quad-ICP-MS	Quadrupole inductively coupled plasma-mass spectrometer
SEM	Secondary Electron Microscope
TIMS	Thermal ionization mass spectrometer

Table 0-3. Unit abbreviations and associated nomenclature.

Unit abbrevations	Nomenclature
BDL (or "-")	Below detection limit
n.d.	Not detected
cps	Counts per second
g/t	Grams per tonne
per mil (or "‰")	Parts per thousand
ppm	Parts per million
wt. %	Weight percent
°C	Degree Celsius

Table 0-4. In-text abbreviations and associated nomenclature.

In-text abbreviations	Nomenclature
e.g.	For example
Fig (s)	Figure(s)
i.e.	That is

Table 0-5. Miscellaneous abbreviations and associated nomenclature.

Miscellaneous abbreviations	Nomenclature
LFB	Lower Felsic Block
VMS	Volcanogenic massive sulfide
NSERC	Natural Sciences and Engineering Research

List of Appendices

Chapter 1 - Introduction: Geology, mineralogy, geochemistry, and genesis of barite associated with volcanogenic massive sulfide (VMS) mineralization

1.1 - Introduction

Volcanogenic massive sulfide (VMS) deposits are important global sources of base and precious metals, with total global past production, current reserves, and geological resources measuring ~14 billion tonnes (Hannington, 2014). These deposits have accounted for more than half of global Zn and Pb production, 7% of the Cu production, 18% of the Ag, and a significant amount of Au and other by-product metals, such as Cd, Se, Sn and Bi (Singer, 1995).

Canada is well endowed with VMS deposits, including the Central Mobile Belt of the Newfoundland Appalachians (Swinden, 1988, 1991; Swinden and Thorpe, 1984; Pollock and Wilton, 2001; Kean and Evans, 2002; Squires and Moore, 2004; Rogers et al., 2006; Hinchey, 2008; Copeland et al., 2009; McNicoll et al., 2010; van Staal and Barr, 2011; Piercey and Hinchey, 2012). This thesis project is focused on the Tally Pond VMS belt in the Central Mobile Belt and centered on the bimodal felsic Zn-Pb-Cu-Ag-Au Lemarchant VMS deposit. The Lemarchant deposit is spatially proximal, but distinct from the past-producing Cu-Zn-rich Duck Pond and Boundary deposits (Squires et al., 2001; Piercey and Hinchey, 2012). The geological setting and genesis of the Lemarchant deposit is the subject of ongoing studies, and previous work has examined the geological environment, hydrothermal mudstones, and mineralogy of the ores (e.g., Lode et al., 2012, 2015, 2016; Gill and Piercey, 2014; Gill, 2015; Gill et al., 2015, 2017). However, numerous questions remain unanswered about its genesis.

Mineralization in the Lemarchant deposit is spatially associated and intergrown with stratiform baritic zones containing both massive to locally bladed barite, in which the latter is frequently enriched in sulfosalts and anomalous precious metal concentrations. The association of massive sulfide mineralization with barite provide a mean to evaluate the genesis of mineralization fluids. Despite this intimate association, very little is known about the barite genesis and its relationship to mineralization. The general aim of this study is to understand the geochemistry, mineralogy, and textural variations of the baritic lens and to determine its relationship to deposit genesis. Furthermore, this study will provide critical constraints on the relative roles that mixing with seawater vs. hydrothermal and/or magmatic fluid input play in the genesis of barite and mineralization at Lemarchant using sulfur and strontium isotope geochemistry, mineral and whole-rock geochemistry, and fluid inclusion microthermometric data.

This introduction is divided into four parts: (1) general geology and property geology; (2) research questions; (3) methodology; and (4) potential results. Through this, the background information, objectives, and methodology will be provided. In addition, potential implications of this project will also be discussed.

1.2 - Regional geological setting

The Canadian Appalachians consist of intra-oceanic, peri-continental, and continental blocks that were assembled into the Appalachian orogen between the Cambrian and Permian (e.g. Wilson, 1966; Williams, 1979, 1995; Williams et al., 1988; van Staal et al., 1998, 2009; Nance et al., 2008; Hibbard et al., 2010). The Canadian Appalachians are divided into tectono-stratigraphic zones and subzones, each separated by major faults

(Williams, 1979, 1995; Williams et al., 1988). From west to east, these are the Humber, Dunnage, Gander, Avalon, and Meguma zones (Fig. 1-1a).

The majority of the VMS deposits in Newfoundland occur within the Dunnage Zone of the Central Mobile Belt (Williams, 1979; Swinden, 1991; Evans and Kean, 2002; Squires and Moore, 2004; Hinchey, 2008; Piercey and Hinchey, 2012). The Dunnage Zone is mainly composed of Cambro-Ordovician rocks of ophiolitic, island to continental arc, and back-arc affinity that formed within the Iapetus Ocean (Dean, 1978; Swinden, 1989; Williams, 1995). The Dunnage Zone is further divided into two distinct tectonostratigraphic subzones: the Notre Dame subzone and the Exploits subzone (Williams et al., 1988). These subzones are differentiated by their stratigraphic, structural and isotopic characteristics (Williams et al., 1988; Williams, 1995). These two subzones are separated by the Red Indian Line, which is the suture zone that separates the peri-Laurentian Notre Dame subzone from the peri-Gondwanan Exploits subzone (Williams, 1995; Williams et al., 1988; Neuman, 1984; Colman-Sadd et al., 1992; van Staal et al., 1998; Evans and Kean, 2002; Rogers et al., 2006, 2007; van Staal, 2007). Peri-Laurentian and peri-Gondwanan crustal blocks were accreted to the Laurentian and Gondwanan margins during the late Cambrian-early Ordovician Taconic and Penobscot orogenies, respectively, which were both associated with the closure of the Iapetus Ocean (Colman-Sadd et al. 1992; Zagorevski et al. 2007, 2010). The subzones were later accreted to one other along the Red Indian Line during the Silurian Salinic orogeny (Dunning et al., 1990; van Staal, 2007; Zagorevski et al., 2007; van Staal and Barr, 2012).

The Lemarchant deposit is situated within the Exploits subzone and hosted within the Victoria Lake supergroup, a series of belts composed of bimodal Neoproterozoic to

Ordovician arc-related magmatic and sedimentary rocks (Kean, 1977; Swinden and Dunsworth, 1995; Williams, 1995; Evans and Kean, 2002; Rogers and van Staal, 2002; Fig. 1-1b). Previously, the Victoria Lake supergroup was divided into two main volcanic belts: the Tulks Hill and the Tally Pond volcanic belts (Dunning et al., 1991; Evans and Kean, 2002; Zagorevski et al., 2007; Hinchey and McNicoll, 2009; McNicoll et al., 2010). More recently, the Victoria Lake supergroup has been subdivided into six fault-bounded packages, which include from east to west: the Tally Pond group (~513-509 Ma; Dunning et al., 1991; McNicoll et al., 2010), Long Lake group (~511-506 Ma; Zagorevski et al., 2007; Hinchey, 2014), Tulks group (~498 to 491 Ma; Evans et al., 1990; Evans and Kean, 2002), Sutherlands Pond group (~462 Ma; Dunning et al., 1987), and Pats Pond and Wigwam Brook groups (~488 and ~453 Ma, respectively; Zagorevski et al., 2007). Lithogeochemical studies demonstrated that the mafic volcanic rocks have island-arc tholeiite to calc-alkaline basalt affinities (Dunning et al., 1991; Swinden et al., 1989; Squires and Moore, 2004; Zagorevski et al., 2010; Piercey et al., 2014).

The Tally Pond group is host to the Lemarchant deposit as well as the Duck Pond and Boundary deposits, and is the easternmost and oldest of the belts composing the Victoria Lake supergroup (Evans & Kean, 2002; Rogers et al., 2006; Squires et al., 2006). The Neoproterozoic (ca. 565 Ma) arc-related Crippleback Lake plutonic suite, located southeast of the Tally Pond group, represents the Ganderian basement on which the Tally Pond group was deposited (Fig. 1-1c; van Staal et al., 2002; Rogers et al., 2006; Gill et al., 2015; Lode et al., 2015, 2016).

The Cambrian Tally Pond group consists of volcanic, volcaniclastic, and sedimentary rocks that constitute two main volcanic sequences: the lower, mafic-dominated Lake Ambrose formation and the upper, felsic-dominated Bindons Pond formation (Rogers and van Staal, 2002; Rogers et al., 2006; McNicoll et al., 2010). The Lake Ambrose is composed of pillow basalt intercalated with felsic pyroclastic rocks, whereas the Bindons Pond formation consists of dominantly felsic volcanic rocks (rhyolitic flows and volcaniclastic rocks) and minor subvolcanic intrusive and sedimentary rocks (Dunning et al., 1991, Evans and Kean, 2002; Rogers and van Staal, 2002; Rogers et al., 2006). The unmineralized Lake Ambrose formation occurs stratigraphically below the Bindons Pond formation based on map interpretations and regional structure; however, the formation is likely thrusted on top of the younger Bindons Pond formation (Rogers et al., 2006). Younger mafic sills and dykes crosscut the Tally Pond group units and are probably related to the Ordovician Harpoon Hill Gabbro (~465 Ma, Pollock, 2004; Squires and Moore, 2004; Piercey and Hinchey, 2012). The entire belt is overprinted by Silurian-Devonian greenschist metamorphism and east-northeast striking faults and minor regional folds (Dunning, 1991; Evans and Kean, 2002; Rogers et al., 2006; Fraser et al., 2012).

1.3 - Deposit geology

The Lemarchant deposit is hosted within north-south striking, shallow moderate east- to weakly west-dipping mafic and felsic volcanic units (Fig. 1-2; Fraser et al., 2012). The geological contacts (projected to surface) trend approximately north-south with a gentle to moderate east-dip (25 to 60°) (Fig. 1-2; Fraser et al., 2012). An upright anticline is delineated in the northwest zone where the units become sub-horizontal to gently westerly-dipping (Fraser et al., 2012).

1.3.1 Deposit sequence

The deposit sequence at the Lemarchant deposit consists of volcano-sedimentary sequences, one mineralized sequence, and several intrusive phases. Cloutier et al. (2017) recognized four volcaniclastic lithofacies based on lithogeochemistry and volcanic textures. A general description of the volcanoclastic sequences will be discussed here; however, the reader is referred to Cloutier et al. (2017) for a detailed description of the stratigraphic sequence of the Lemarchant deposit.

Sequence 1, 2, and 3 form the footwall sequences of the Lemarchant deposit. Sequence 1 is found at the base of the Lemarchant stratigraphy and is described as a basaltic/andesite unit of tuff, breccia, and minor lapilli tuff. Sequence 2 conformably overlies sequence 1 and consists primarily of polymictic breccia and chemically falls in the basalt/andesite field of Pearce (1996) (Cloutier et al., 2017). Rocks from sequence 3 are bimodal in composition, where the base of the sequence is dominated by andesite, and dacite dominates the top of the sequence. The sequence consists of poorly sorted monomictic breccia, a texture and lithofacies typically associated with vent proximal depositional setting (McPhie et al., 1993; Allen, 1996; Gibson et al., 1999). Veinlets of sphalerite, chalcopyrite, quartz, carbonate, and chlorite cross-cut the monomictic breccia units and the whole sequence is overprinted by a weak to strong sericite alteration (Cloutier et al., 2017).

The barite and sulfide mineralization are hosted in the dacitic breccia and lapilli tuff of sequence 3 (Cloutier et al., 2017). Mineralization is composed of massive to semi-massive sulfide lenses up to 25 m thick associated with medium-grained, granular to bladed barite (Gill and Piercey, 2014; Gill et al., 2015, 2017).

A pyrite- and pyrrhotite-rich exhalative mudstone unit (<5 m) overlies the rocks of sequence 3 and mineralization is locally interlayered with the overlying basaltic rocks of the hanging wall (Lode et al., 2012, 2015, 2016). The mudstone unit is well laminated and locally contains carbonate, chlorite, barite, quartz, and apatite (Lode et al., 2012, 2015, 2016). Jasper and chert exhalite units are also locally present at the Lemarchant deposit and generally located beneath semi-massive sulfide and barite lenses. Jasper is also present in the hanging wall mafic volcanic rocks as either clasts or Fe-rich sedimentary material between pillow basalts (Copeland, 2008; Copeland et al., 2009; Fraser et al., 2012).

The hanging wall (sequence 4) consists of gently east-dipping, aphyric, pillowed, amygdaloidal, and massive to brecciated basalt up to 150-200 m-thick. Alteration in the hanging wall basalt is generally weak, but the unit is locally weakly chlorite and quartz altered. The hanging wall basalt contains very rare barite-filled veins that are associated with chalcopyrite (Cloutier et al., 2017).

In summary, the deposit footwall consists of moderate to strongly altered andesite-dacite that hosts stringer-style mineralization. The altered andesite/dacite unit ranges up to 30-50 m below the mineralized zone and gradually grades into a less altered volcanic unit at depth (Fraser et al., 2012; Cloutier et al., 2017). Monomictic andesite/dacite breccia units hosts the mineralization at the Lemarchant deposit. The mudstones vary in thickness between 0.1-10 m and are found stratigraphically above the mineralization. The hangingwall is dominated by basaltic flows and barren of mineralization. The dominant alteration consists of quartz-sericite ± chlorite (Fraser et al., 2012; Cloutier et al., 2017).

However, chlorite alteration is locally dominant within a tabular lens immediately underlying barite-rich mineralization, particularly in the northwest zone of mineralization (Fraser et al., 2012).

1.3.2 Intrusive rocks

The footwall felsic volcanic rocks are cut by green to brown mafic dykes and sills and by white, aphyric felsic dykes (Pollock, 2004; Squires and Moore, 2004; Copeland et al., 2008). The mafic dykes are aphyric, fine grained, with chlorite and quartz alteration. As mentioned before, these dykes are likely related to the Harpoon Hill gabbro.

The Lemarchant microgranite is a large (6 km^2) granodioritic intrusive body located 500 m northwest of the mineralized zones (Fig. 1-2). The Lemarchant microgranite has similar lithogeochemical signatures to the felsic volcanic rocks of the Lemarchant deposit suggesting that it is a synvolcanic intrusion and may be related to the formation of VMS alteration and mineralization (Squires and Moore, 2004).

1.3.3 Mineralization

The Lemarchant deposit is composed of stratabound, semi-massive to massive sulfide, usually underlying a massive mineralized barite unit. Most of the mineralization occurs between section 101N and 104N and is referred to as the “Main Zone” (Fig. 1-2). The “Northwest Zone” comprises two smaller mineralized zones located between sections 105N and 106N. The “Northwest Zone” mineralized lense lies 300 m below the surface (Fig. 1-2; Copeland et al., 2008, 2009; Fraser et al., 2012). Both zones are separated by a complex structural corridor and represent mineralized lenses that were superimposed during post-VMS deformation (Cloutier et al., 2017). Mineralization in the Lemarchant deposit consists of polymetallic massive sulfides, sulfosalts and barite with locally elevated precious metal contents (Gill and Piercey, 2014; Gill, 2015; Gill et al., 2015, 2017). Visible gold is present in core from numerous drillholes. The indicated mineral resource of the Lemarchant deposit is 1.24 Mt grading 5.38% Zn, 1.19% Pb, 0.58% Cu, 59.17 g/t Ag, and 1.01 g/t Au (Fraser et al., 2012).

The mineralization at the Lemarchant deposit consists of a Zn-Pb-rich stratiform sulfide zone and an underlying Cu-rich stringer sulfide zone. The mineralization is subsequently divided into four sulfide-mineral assemblages (Gill and Piercey, 2014; Gill, 2015; Gill et al., 2015, 2017): 1) semi-massive white (low-Fe) sphalerite, granular barite, recrystallized pyrite, galena, minor tetrahedrite; 2A) bornite-galena-stromeyerite ± chalcopyrite; 2B) bladed barite, coarse-grained tetrahedrite, galena, electrum, colusite ± bournonite-polybasite-miargyrite; 3) massive red (high-Fe) sphalerite, fine-to medium-grained pyrite-chalcopyrite-galena; and 4) chalcopyrite-pyrite ± orange sphalerite stringers. The stratiform zone contains type 1 assemblage, which is crosscut by type 2A and 2B assemblage and overprinted by type 3 mineral assemblages. The basal stringer zone is host to the type 4 assemblage and represents minor zone refinement of the stratiform and stringer zones (Gill and Piercey, 2014; Gill, 2015; Gill et al., 2015, 2017).

1.3.4 Structure

The Lemarchant deposit contains numerous faults that locally offset the mineralization and host rock sequences (Fraser et al., 2012; Cloutier et al., 2017). Deformation occurred following the deposition of volcanic sequences 1-4 (Cloutier et al., 2017). Three shear zones are recognized at the Lemarchant deposit: LJ, KJ, and the

Lemarchant shear zones. The LJ and KJ shear zones are interpreted to be syn-volcanic. These high-angle, syn-volcanic shear zones thrusted older rocks of sequences 1 and 2 on top of the younger rocks sequence 3. The LJ and KJ shear zones were later cross-cut by the Lemarchant shear zone, creating stacking of the Main zone lens on top of the Northwest zone lens. The timing of the main thrusting phase is interpreted to be coincident with the Penobscot orogeny (486-478 Ma: Colman-Sadd et al., 1992; van Staal, 1994; Zagorevski et al., 2010; Cloutier et al., 2017). Late extensional deformation created a set of NW-SE striking normal faults (i.e. Bam fault) (Cloutier et al., 2017).

1.4 - Volcanogenic massive sulfide (VMS) deposits

1.4.1 Genetic model for Zn-Pb-Ba-Cu-Ag-Au bimodal felsic deposits

Volcanogenic massive sulfide (VMS) deposits are major sources of Zn, Pb, Cu, Ag, and Au. These deposits form tabular polymetallic massive sulfide lenses at or near the seafloor in volcanically active oceanic spreading centers and in rifted arc and back-arc environments (Herzig and Hannington, 1995; Hannington et al., 2005; de Ronde et al., 2005). On modern seafloor, sulfide deposits have been documented at water depths of between ~80 and 5000 m at water (Herzig and Hannington, 1995; Franklin et al., 1998; Allen and Weihed, 2002; Connelly et al., 2012; Ligi et al., 2014; Monecke et al., 2014; Petersen et al., 2014). Due to a greater preservation potential, ancient VMS deposits are typically found in paleo-oceanic and continental nascent-arc, rifted arc, and back-arc settings (Fig. 1-3; Franklin et al. 1998; Allen and Weihed, 2002; Piercey, 2011; Cawood et al., 2013, 2015).

Typical volcanogenic massive sulfide systems form in rifted oceanic and/or continental crust that contains faults and fissures, with heat provided by deep-seated magma chambers and/or subvolcanic intrusions (Campbell et al., 1981; Barrie and Hannington, 1999; Large et al., 2001; Cathles et al., 1997; Galley, 2003; Hart et al., 2004; Piercey, 2010, 2011). The underlying heat results in the circulation of evolved seawater deep into the crust where it strips metals from the host substrate (Spooner and Fyfe, 1973; Franklin et al., 1981; Lydon, 1988; Large, 1992; Ohmoto, 1996; Cathles et al., 1997; Barrie et al., 1999; Cathles and Adams, 2005; Franklin et al., 2005). The hot modified seawater/hydrothermal fluid, contains metals and buoyantly rises towards the seafloor and discharges from black and/or white smoker chimneys (Haymon, 1983; Lydon, 1988; Large, 1992; Hannington, 2014). The fluids range from low temperature (~200-250°C) and can reach maximum temperatures of ~400°C (Eldridge et al., 1983; Pisutha-Arnond and Ohmoto, 1983; Lydon, 1988; Hannington, 2014; German and von Damm, 2006). As the metal-enriched fluids approach the seafloor, the fluids conductively cool due to interaction with wall rocks and from the extensive mixing with seawater, ultimately changing the pH and the oxidation state of the hydrothermal fluids. These processes results in the precipitation of both sulfide and gangue minerals (Large, 1977; Urabe and Sato, 1978; Spiess et al., 1980; Haymon, 1983; Galley et al., 2007; Hannington, 2014). The polymetallic lenses are typically underlain by a discordant sulfide-rich stockwork zone with a pipe-like structure with distinct alteration halo (Riverin and Hodgson, 1980; Franklin et al., 1981; Lydon. 1984, 1988; Gemmell and Large, 1992; Galley, 1993; Gibson, 2005; Galley et al., 2007). Mineralization in the stockwork zone is generally in the form of stringer and replacement-type sulfides (Fig. 1-4, and 1-5; Lydon, 1984, 1988; Galley et al., 2007; Hannington, 2014).

The process of massive sulfide lens formation is generally synchronous with volcanism and results in well-developed metal and mineralogical zonation. The sequence of metal precipitation and the growth mechanism of the typical VMS mounds reflect the varying metal solubilities during fluid evolution of the hydrothermal system. The zone refining model of mound growth of Eldridge et al. (1983), Large (1992), and Ohmoto (1996) suggests that the first minerals to precipitate are Zn-Pb-(Ba)-rich black ore minerals (sphalerite, galena, tetrahedrite, barite, pyrite) at temperatures of ~150-250°C. Such fluids transport metals as chloride complexes along with reduced sulfur (H_2S) and precipitate primitive black ore when mixed with seawater at the top of the ore mound (Stage 1, Fig. 1-4). In this early, low temperature stage, Au is most likely transported as a bisulfide complex ($Au(HS)_2^-$) and precipitates with low-temperature ore minerals (Large, 1977; Eldridge et al., 1983; Pisutha-Arnond and Ohmoto, 1983; Hannington and Scott, 1989; Huston and Large, 1989). During the growth of the ore mound, the hydrothermal fluids become hotter (250-300°C) and are capable of carrying Cu as a chloride complex ($CuCl_2$) resulting in the precipitation of massive chalcopyrite (Stage 2, Fig. 1-4; Large, 1977; Eldridge et al., 1983; Pisutha-Arnond and Ohmoto, 1983). The stage-1 "primitive ore" reacts with the hotter hydrothermal fluids and the former low temperature minerals (sphalerite, galena) are dissolved and re-precipitated further closer to the mound-seawater interface near the top of the ore body (Eldridge et al., 1983; Ohmoto, 1996). This process is responsible for the formation of high-grade ore found at the top of numerous VMS deposits. As fluids evolve to higher temperature (300-350°C), Cu is continuously added to the interior, further precipitating chalcopyrite and Cu-bearing minerals. The final stage of VMS mineralization occurs when chalcopyrite is dissolved by later fluids and pyrite replaces Cu-bearing phases

(Stage 3, Fig. 1-4). Therefore, mineral zonation in VMS deposits is defined by a predictable mineralization sequence going from low-temperature to high temperature mineral assemblages (Ba-Zn-Pb-Cu-Fe) (Ohmoto, 1996). High temperature VMS deposits can also be overprinted by lower temperature minerals during the cooling of the system and create overlapping alteration halos with characteristic mineralogy and geochemistry but with little change in ore minerals (Barrett et al., 1999; Large et al., 2001).

The sulfide mineralization is often overlain by a thin, bedded, sulfide or oxide bearing sediment layer, which is commonly referred to as an exhalite (Haymon and Kastner, 1981; Gurvich, 2006). This sedimentary unit is a product of hydrothermal seafloor venting and is often found in Kuroko-type VMS deposits (Kalogeropolous and Scott, 1983; Lydon, 1984; Kalogeropolous and Scott, 1989; Liaghat and MacLean, 1992; Peter, 2003; Gibson, 2005), including the Lemarchant deposit (Lode et al., 2015, 2016).

Volcanogenic massive sulfide (VMS) deposits are delineated into five classes based on lithostratigraphic associations (Barrie and Hannington, 1999): (1) bimodal-mafic, (2) bimodal-felsic; (3) mafic; (4) pelitic-mafic; and (5) siliciclastic-felsic. Added to this is a sixth group of hybrid bimodal felsic (Galley et al., 2007). The Lemarchant deposit is a bimodal felsic-type VMS deposit and dominated by felsic rocks with minor mafic volcanic rocks (Barrie & Hannington, 1999; Franklin et al., 2005; Galley et al., 2007; Huston et al., 2010). The Lemarchant deposit is also a classic example of a Zn-Pb-Ba-rich Kuroko-type VMS deposit that is interpreted to have formed in an arc-rift to back-arc environment (Rogers et al., 2006). The deposit contains abundant barite, precious metals and sulfosalts, similar to other deposits globally (e.g., Eskay Creek – Sherlock et al., 1999; Jade Field, Okinawa Trough - Lüders et al., 2001; Wetar Island – Scotney et al., 2005; La Plata – Chiaradia et al., 2008).

Most barite-rich VMS systems form from low temperature fluids (~ <250°C) and generally at shallow water depths (~ <2000-1500 m) (Sillitoe et al., 1996; Leistel et al., 1998; Hannington et al., 1999; Sherlock et al., 1999; Scotney et al., 2005; de Ronde et al., 2011); although some barite-bearing VMS systems are much deeper (e.g. ~2050 m depth; Endeavour Segment; Delaney et al., 1992). The precipitation of precious metals and abundant sulfosalts within the barite lenses are thought to be associated with the low-temperature hydrothermal fluids (Hannington et al., 1999; Mercier-Langevin, 2011). Barite is interpreted to represent mixing between Ba-rich hydrothermal fluid and ambient seawater (SO_4^{2-}) (Watanabe and Sakai, 1983; Ohmoto, 1996; Sherlock et al., 1999; Lüders et al., 2001; Scotney et al., 2005; Chiaradia et al., 2008; Griffith and Paytan, 2012).

1.4.2 Growth processes of barite lenses

Barite is a common gangue mineral in massive sulfide deposits and can form during the entire growth process of the massive sulfide mound. Due to its low solubility in seawater (Averyt and Paytan, 2003), barite can affect the morphology of massive sulfide edifice and preserve geochemical signatures associated with primary ore-forming processes during VMS formation (Hannington et al., 1995a). The Lemarchant deposit contains abundant barite mineralization and understanding the genesis and geochemical signatures of barite can provide insight into the physicochemical conditions of the different stages of VMS formation.

In modern oceans, barite is undersaturated and precipitation requires fluids containing elevated Ba^+ and SO_4^{2-} (Griffith and Paytan, 2012). Barite in the marine environment is formed by five different processes (Paytan et al., 2002; Hein et al., 2007): 1) hydrogenetic precipitation/pelagic barite (Goldberg and Arrhenius, 1958); 2) authigenic barite precipitated from pore fluids within the sediments during diagenesis; 3) cold-seep barite; 4) hydrothermal barite precipitated in seafloor plumes and chimneys; and 5) hydrothermal barite precipitated at warm-springs. Massive sulfide-related barite forms when seafloor hydrothermal fluids are generally enriched in metals and Ba derived from leaching of footwall rocks during convective hydrothermal circulation (Murchey et al., 1987; Lydon, 1988; Large, 1992). When Ba-bearing hydrothermal fluid buoyantly rises towards the seafloor it mixes with oxidized seawater, the primary source of SO_4, and results in barite precipitation (Blount, 1977; Ohmoto et al., 1983; von Damm, 1990; Ohmoto, 1996; Griffith & Paytan, 2012). However, other potential sources of sulfate exist and include magmatic sulfate, pore water sulfate, sulfate by calcium sulfate minerals, and sulfate produced by oxidation of reduced sulfur species (Griffith and Paytan, 2012). Most studies show that sulfur isotope compositions of barite reflect that of seawater, further suggesting that barite precipitates from mixtures of hydrothermal fluids and local seawater (e.g., Ohmoto et al., 1983; Seal et al., 2000; Huston et al., 1999).

The solubility of barite decreases with decreasing pressure and temperature (Holland and Malinin, 1979; Hanor, 2000). Therefore, barite can precipitate from low-temperature (< 250°C) hydrothermal fluids that are discharged near or on the seafloor usually through low-temperature white smoker chimneys (Ohmoto, 1996; Franklin, 2005). Barite also forms a solid-solution series with celestine ($SrSO_4^{2-}$) (Hanor, 2000).

1.4.3 Precipitation of precious metals in low-temperature VMS deposits

Many modern and ancient gold-rich polymetallic sulfide deposits have a strong gold-barite correlation (e.g. southern Lau basin; Herzig et al., 1993; eastern Manus basin; Binns et al., 1993; Scott and Binns, 1995; Eskay Creek; Sherlock et al., 1999; Wetar Island; Scotney et al., 2005). This mineralogical association is also observed in the Lemarchant deposit, where gold occurs in the baritic top of the sulfide lens, and reflects the behaviour of these metals in hydrothermal fluids during transportation. Therefore, understanding the genesis of barite can provide insight into the introduction of gold in the VMS system.

Gold can be found in variable amounts in VMS deposits, and generally occurs with two main associations (Hannington and Scott, 1989; Huston and Large, 1989): 1) in low-temperature Au-Zn-Pb-Ag-Ba association found in the upper portion of the massive sulfide mound (e.g. Rosebery, Hellyer, Eskay Creek, Wetar); and 2) in higher-temperature Au-Cu association commonly found in the deeper stockwork zone of the VMS deposit (e.g. LaRonde deposit, Mt. Chalmers, Millenbach, Mt. Lyell). Gold is typically associated in low-temperature Zn-Pb-Ba-rich assemblages found at the top of massive sulfide mounds with sulfosalts (Fig. 1-4 and 1-5; Huston and Large, 1989; Hannington and Scott, 1989; Hannington and Gorton; 1991; Hannington et al., 1995b, 1999). In high-temperature Cu-rich assemblages, Au is less common but can be associated with Cu-As and high sulfidation assemblages (Hannington et al., 1995b). These associations suggest that gold transport is strongly temperature-dependent (Hannington et al., 1995).

Numerous factors can influence the transport and deposition of Au in volcanogenic massive sulfide deposits such as changes in pH, fO_2, and temperature (Huston and Large, 1989; Seward, 1973, 1984). In low temperature systems (i.e., <300^{o}C) gold is transported as Au bisulfide ($Au(HS)_2^-$), whereas in high temperature systems gold is transported as a $AuCl_2$ complex (Seward, 1973, 1984; Williams-Jones et al., 2009). In most low temperature Zn-Pb-Ba-rich volcanogenic massive sulfide deposits, such as the Lemarchant deposit, Au is transported as $Au(HS)_2^-$ and tends to be deposited in the overlying barite cap and associated with elements such as Ag, Pb, Zn, As, Sb, and Hg (Hannington et al., 1999).

Mixing of fluids at the seawater interface results in a temperature decrease and the oxidation of fluids, initiating the precipitation of low-temperature minerals (e.g. Ag-Pb-Zn) (Large, 1977; Urabe and Sato, 1978; Spiess et al., 1980; Hayman, 1983; Hannington et al., 2005; Galley et al., 2007; Hannington, 2014). In this case, the precipitation and transport of gold is favoured by the oxidation of $Au(HS)_2^-$ during mixing with seawater and in neutral pH conditions. Furthermore, the precipitation of sulfides decreases the redox buffering capacity of the fluids. During sulfide precipitation, the seawater composition will approach the H_2S-HSO_4^- buffer, which will also promote the precipitation of Au (Hannington, 1995b). In shallow water environments, phase separation of the hydrothermal fluid (also referred as boiling) is an effective mechanism to favour precious metal precipitation due the decrease in temperature and rapid change in pH (Poulsen and Hannington, 1996). Moreoever, discharging hydrothermal chimneys are porous and can contain dendritic sphalerite (Hannington et al., 1995b). The porous nature of white smoker chimneys, coupled with the large surface area that the dendritic texture of the sulfides, allows for both efficient mixing between seawater and hydrothermal fluids, and acts as a mechanical/physical trap, both assisting in enhancing precious metal precipitation (Hannington, 1995b).

As the sulfide mound grows, the input of higher temperature Cu-rich fluids from below results in the remobilization of Au as $Au(HS)_2^-$. Gold can thus reprecipitate near the top of the sulfide mound into barite mineralization (Hekinian et al., 1985; Hekinian and Fouquet; 1985; Hannington et al., 1986, 1995b). Therefore, Au-enrichment may be caused by the constant reworking and transport of Au towards the upper parts of the mound during hydrothermal circulation (i.e., zone refining; Hannington, 1995b).

In the higher temperature portions of the VMS hydrothermal system (>300°C), Au is transported as a chloride complex ($AuCl^-$). At this stage, pyrite and chalcopyrite start replacing sphalerite-galena-pyrite ore. These replacement reactions are associated with a pH increase and a temperature and fO_2 decrease, thus facilitating Au precipitation. Since the solubility of Au increases with high fO_2, higher Au grades can be associated with pyrite-chalcopyrite assemblages (Huston & Large, 1989; Hannington, 1995b).

Silver occurs predominantly as sulfosalts (tetrahedrite-tennantite-polybasite), electrum, and within galena in bimodal felsic (Kuroko)-type deposits (Huston et al., 1992; Herzig and Hannington, 1995; Ohmoto, 1996). Additionally, Ag/Zn ratios are uniform in VMS deposits suggesting that Ag^+ and Zn^{2+} behave similarly in hydrothermal fluids (Ohmoto, 1996).

1.4.4 VMS-epithermal hybrid deposits – the link between VMS and precious metal enrichment

Some VMS deposits contain evidence for input from magmatic-hydrothermal fluids/volatiles (i.e., epithermal signatures) (Horikoshi and Shikazono, 1978; Urabe, 1987; Hannington and Scott, 1989; Stanton, 1991; Sillitoe, 1994, 1996; Yang and Scott, 2002, 1996; Moss and Scott, 2001; Galley et al., 2007). Epithermal mineralization, including that in the subaqueous environment, is classified by some workers as a function of sulfidation state of the ore assemblages, which reflects the pH of the fluids that formed the mineralization (e.g., Hedenquist et al., 2000; Simmons et al., 2005). The two main subdivisions include high-sulfidation and low-sulfidation (Table 1-1). Low-sulfidation deposits have sericite (± adularia) and/or intermediate argillic alteration, and low to intermediate sulfidation state minerals (Table 1-1). In some cases, low-sulfidation deposits contain bladed quartz, calcite, and/or barite (Simmons and Christensen, 1994; Etoh et al., 2002). The fluids that formed low-sulfidation deposits are near-neutral, relatively reduced, and sulfur-poor suggesting the mixing of magmatic fluids with meteoric water (and/or seawater). Conversely, high-sulfidation deposits have alunite-bearing advanced argillic alteration and high-sulfidation state ore minerals, such as bornite, tennantite, covellite, and low-Fe sphalerite (Table 1-1). The fluids are magmatic in origin with minimal dilution from groundwater or seawater. The ore forming fluids are interpreted to be acidic, relatively oxidized, and sulfur-rich (Sillitoe et al., 1996; Hedenquist et al., 1998, 2000; Simmons et al., 2005).

Most VMS deposits have low-sulfidation minerals; however, Sillitoe et al. (1996) suggested that some low-sulfidation deposits have localized zones of high-sulfidation minerals, which reflect variations in fluid chemistry during VMS formation. For example, in most cases, high-sulfidation mineral assemblages occur in the upper parts of the deposits (Sillitoe et al., 1996). This localized increase in sulfidation state in the upper portion of the mound may result from the boiling or oxidation of sulfur in the solution or the condensation of gases exsolved from the hydrothermal fluids (Hannington and Scott, 1989). VMS and epithermal Au deposits that contain both low- and high-sulfidation mineral assemblages are known as intermediate-sulfidation VMS deposits and the fluid is interpreted to have had both intermediate pH and sulfidation state (Sillitoe et al., 1996; Simmons et al., 2005).

A link has also been made between Au grades and S activity of sulfides in VMS deposits (Seward, 1973; Hannington and Scott, 1989; Huston and Large, 1989; Williams-Jones et al., 2009). As mentioned in the previous section (section 1.4.3), the transport of Au in solution is not only dependent on temperature, but also on the sulfidation state of the hydrothermal fluids (Hannington and Scott, 1989). Numerous workers have shown that the solubility of gold as $Au(HS)_2^-$ is highest in low-temperature fluids and at elevated oxygen and sulfur activities; consequently, there is a strong correlation between significant Au grades and accessory sulfide minerals and Fe-poor sphalerite (Hannington et al., 1986; Hannington and Scott, 1989; Huston and Large, 1989; Large et al., 1989). The sulfidation states of sulfides that co-precipitate with Au generally reflect the same physicochemical conditions of Au transport and deposition (Fig. 1-6) (Hannington and Scott, 1989).

1.4.5 Isotopic and chemical compositions of barite

Stable and radiogenic isotopes provide critical information about the sources of metals and fluids in ore deposits and the physiochemical conditions of ore formation (Ohmoto and Goldhaber, 1997). Sulfur isotopes are particularly useful for determining the sources of sulfur in both sulfides and sulfates. For example, the $\delta^{34}S$ of barite can be used to delineate the relative roles of seawater SO_4, seawater sulfate modified by microbial reduction (i.e., H_2S), magmatic sulfate, pore water sulfate, or sulfate produced by the oxidation of reduced sulfur species (Hanor, 2000; Griffith and Paytan, 2012; Sangster, 1968; Ishihara and Sasaki, 1978; Solomon et al., 1988). The latter information can provide insights into the environment of deposition and into depositional processes (Paytan et al., 2002; Griffith and Paytan, 2012; Huston, 1999).

In general, barite in VMS deposits reflects the $\delta^{34}S$ of seawater at the time of formation (e.g., Ohmoto and Rye, 1979; Herzig et al., 1998; Ohmoto and Goldhaber, 1998; Lüders et al., 2001; Hein et al., 2014). However, barite can have variable signatures depending on the contributions from these sources (Lüders et al., 2001).

Strontium isotopes can be used to understand the sources of Sr in barite because of the high concentration of Sr in the crystal structure of barite (up to 3 mol%; Monnin & Cividini, 2006). Strontium isotopes are particularly useful since barite contains high concentrations of Sr and little Rb; therefore, it contains negligible $^{87}Sr/^{86}Sr$ formed via the in-situ radiogenic decay of ^{87}Rb over time. The Sr-isotopic composition of barite indicates the source of Sr in the fluids that formed barite (Paytan et al., 2002). Strontium can have multiple origins, such as seawater, mantle-derived hydrothermal fluids, or older crustal basement (McArthur et al., 2001). Strontium signatures in marine rocks (i.e., barite, carbonate minerals) are potential records of the secular changes of weathering and hydrothermal activity within the ocean (Burke et al., 1982; McArthur et al., 2001).

Both the S isotopes of seawater sulfate and the $^{87}Sr/^{86}Sr$ signature of seawater have changed through geological time (e.g., Claypool et al., 1980; Veizer, 1989; Veizer et al., 1999; Seal and Wandless, 2003). The sulfur isotope composition of seawater has varied greatly (Claypool et al., 1980; Huston, 1999), particularly in the Phanerozoic, and correspondingly $\delta^{34}S$ of VMS-associated barite has also mirrored this pattern (Sangster, 1968; Ohmoto and Rye, 1979; Huston, 1999; Seal and Wandless, 2003). Similarly, Sr isotopes in barite (and carbonate) have varied as a function of the relative contributions of juvenile mantle-derived magmatic strontium (low $^{87}Sr/^{86}Sr$) and continentally derived strontium (high $^{87}Sr/^{86}Sr$) present in the water column at the time of barite precipitation (Albarède et al., 1981; Veizer, 1989).

Fluid inclusions within barite can also give information about the temperature of fluid entrapment, salinity, and chemistry (Roedder, 1984; Hanor, 2000; Bodnar, 2003). The salinity of primary fluid inclusions in barite is close to that of seawater, suggesting that Kuroko ore-forming fluids are derived from modified seawater (Pisutha-Arnond & Ohmoto, 1983). Fluid inclusion studies demonstrate that barite is generally formed at temperatures between 150°C and 200°C and the salinity resembles that of seawater (e.g. 3.2% $NaCl^-$; Bischoff & Rosenbauer, 1985), again suggesting that modified seawater is the main source of fluid in VMS hydrothermal fluids (Lüders et al., 2001).

1.5 - Objectives and fundamental research questions to be tested

This project is aimed at understanding the genesis of barite associated with VMS mineralization using modern geochemical techniques and new field relationships. Despite its common occurrence, there has been few in-depth modern studies of barite in VMS deposits. This study will provide one of the most integrated field, mineralogical, and geochemical studies of barite associated with VMS deposits. In addition, barite layers are often precious metal enriched (Hannington and Scott, 1989; Huston and Large, 1989). The Lemarchant deposit contains both granular barite and bladed barite, the latter akin to that found in some epithermal deposits. Therefore, understanding the genesis of barite at Lemarchant will not only provide insight into VMS formation processes, but also potentially insight into precious metal enrichment associated with barite. The following thesis objectives are aimed at testing the above and include:

1) to document the mineralogical and textural relationships between barite and massive sulfides, including the types of sulfide assemblages associated with various barite types;
2) utilize geochemical, mineralogical, and isotopic tools to define the physicochemical properties of barite genesis, fluid compositions, and ligand sources;
3) evaluate the potential contributions of seawater vs. magmatic hydrothermal fluids in the genesis VMS-related barite;
4) provide insight into the composition of Cambrian seawater using barite as a proxy;
5) understand the relationship of precious metals in barite lenses and relationships to barite textures;
6) compare the barite mineralization of the Lemarchant deposit and its isotopic and geochemical signatures with global analogues to understand barite formation associated with VMS deposits.

1.6 - Proposed methods

This project is a combination of field observations and analytical work. Fieldwork was undertaken in 2014.

1.6.1 Fieldwork

Eighteen drill holes containing barite were logged in 2014 to document textural and mineralogical relationships of barite to both host rock and mineralization, and this was used as the basis of sampling for thin sections and subsequent analytical work. Core logging was undertaken on NQ-sized core from drill holes within the dominant mineralized zones (e.g. Main Zone, Northwest Zone, and 24 Zone) to obtain a good spatial coverage of the Lemarchant deposit (Fig. 1-2). Logging was centered around the mineralized horizon(s) and approximately 30 meters above and below the mineralized zone. A total of 111 halved core samples were taken and ranged between 10 and 20 cm in length. The depths, photos, and detailed description of samples were carefully documented. Detailed digitized graphic logs of selected boreholes are found in Appendix 1.

1.6.2 Petrography and scanning electron microscopy

Standard transmitted and reflected light microscopy of 52 polished thin sections was utilized to understand paragenesis, micro-textures, and mineralogical relationships between barite and ore minerals. This work will be compared to previous studies by Gill and Piercey (2014), Gill et al. (2015), Gill (2015) and Gill et al. (2017). A subset of sections was further studied using scanning electron microscopy (SEM) for micro-textural documentation, identification of microscopic phases, and for semi-quantitative elemental maps and mineral spectra. These methods were both utilized for pre-screening samples for microanalysis.

1.6.3 Microanalytical methods

Quantitative analyses of barite were undertaken using electron microprobe (EMPA) and laser ablation-inductively coupled plasma-mass spectrometry (LA-ICP-MS). Major element and minor elements in minerals, mineral compositions and mineral formulae were undertaken using EMPA at Memorial University of Newfoundland. Some samples were analyzed by LA-ICP-MS (Queen's Facility for Isotope Research (QFIR)) to understand ultra low-level trace elements in barite and complement EMPA data. Both methods were utilized to understand spatial distributions of elements, compositional patterns in barite crystals, and compositional differences of various barite crystals as a function of texture and paragenesis. These collective results were utilized to determine the geochemical processes responsible for barite compositional variations.

1.6.4 Fluid inclusions, stable and radiogenic isotopes

Fluid inclusion microanalysis was undertaken to understand the chemistry and physiochemical conditions of barite deposition. Petrographic analysis of doubly polished fluid inclusion wafers was used to identify fluid inclusion assemblages and determine a paragenetic scheme for mineralizing fluids. Fluid inclusion microthermometry was performed using a Linkam THMSG600 heating-freezing stage at Memorial University of Newfoundland to obtain homogenization temperatures and salinities of fluid inclusions, which were used to characterize the fluids present in barite and conditions of formation.

Sulfur isotopes were determined on barite samples using micro-drilled portions of barite crystals followed by analysis using MAT252 isotope ratio mass spectrometry (IR-MS) at Memorial University of Newfoundland. Strontium isotopes in barite samples were determined by leaching the samples in HCl^- (e.g., Marchev et al., 2002; Jamieson et al., 2016), followed by cation exchange column chemistry to isolate the Sr from the solutions; Sr isotope were measured on a Finnigan MAT 262 thermal ionization mass spectrometer (TIMS) at Memorial University of Newfoundland.

1.7 - Potential results

Barite is an important component of the Lemarchant deposit and is interbedded and associated with massive sulfide mineralization, including Au-Ag- and sulfosalt-rich assemblages (Gill and Piercey, 2014; Gill et al., 2015, 2017). The integrated field and laboratory approach taken within this study will assist in identifying how barite forms in the massive sulfide environment, sources of S (e.g., seawater, leached igneous, or magmatic fluids) and Sr (e.g., seawater, leached basement) in the mineralization, and the precious metal enrichment processes in massive sulfides. In addition, this study will contribute to the general model of bimodal felsic (Kuroko)-type VMS deposits and improve our understanding of hydrothermal processes that led to their formation.

1.8 - References

Albarède, F., Michard, A., Minster, J., and Michard, G. (1981). $^{87}Sr/^{86}Sr$ ratios in hydrothermal waters and deposits from the east pacific rise at 21 N. Earth and Planetary Science Letters, 55: 229-236.

Allen, R. L., and Weihed, P. (2002). Global comparisons of volcanic-associated massive sulphide districts. Geological Society, London, Special Publications, 204: 13-37.

Averyt, K. B., and Paytan, A. (2003). Empirical partition coefficients for Sr and Ca in marine barite: Implications for reconstructing seawater Sr and Ca concentrations. Geochemistry, Geophysics, Geosystems, 4: 1043.

Barrett, T. J., and MacLean, W. H., (1999). Volcanic sequences, lithogeochemistry, and hydrothermal alteration in some bimodal volcanic-associated massive sulfide systems: Reviews in Economic Geology, 8: 101-131.

Barrie, C. T., Cathles, L. M., and Erendi, A. (1999). Finite element heat and fluid-flow computer simulations of a deep ultramafic sill model for the giant Kidd Creek volcanic-associated massive sulfide deposit. Economic Geology Monograph, 10: 529-540.

Barrie, C., and Hannington, M. (1999). Classification of volcanic-associated massive sulfide deposits based on host-rock composition. Reviews in Economic Geology, 8: 1-11.

Binns, R. A., Scott, S. D., Bogdanov, Y. A., Lisitzin, A. P., Gordeev, V. V., Gurvich, E. G., Finlayson, E. J., Dotter, L. E., Wheller, G. E., and Muravyev, K. G. (1993). Hydrothermal oxide and gold-rich sulfate deposits of Franklin Seamount, western Woodlark Basin, Papua New Guinea. Economic Geology, 88: 2122-2153.

Bischoff, J. L., and Rosenbauer, R. J. (1985). An empirical equation of state for hydrothermal seawater (3.2 percent $NaCl^-$). American Journal of Science, 285: 725-763.

Blount, C. (1977). Barite solubilities and thermodynamic quantities up to 300/sup 0/C and 1400 bars. American Mineralogist, 62: 9-10.

Bodnar, R. J. (2003). Introduction to aqueous-electrolyte fluid inclusions. Fluid Inclusions: Analysis and Interpretation, 32: 81-100.

Burke, W., Denison, R., Hetherington, E., Koepnick, R., Nelson, H., and Otto, J. (1982). Variation of seawater $^{87}Sr/^{86}Sr$ throughout Phanerozoic time. Geology, 10: 516-519.

Campbell, I. H., Franklin, J. M., Gorton, M. P., Hart, T. R., and Scott, S. D. (1981). The role of subvolcanic sills in the generation of massive sulfide deposits. Economic Geology, 76: 2248-2253.

Campbell, I. H., McDougall, T. J., and Turner, J. S. (1984). A note on fluid dynamic processes which can influence the deposition of massive sulfides. Economic Geology, 79: 1905-1913.

Cathles, L. M., and Adams, J. J. (2005). Fluid flow and petroleum and mineral resources in the upper (< 20 km) continental crust. Economic Geology 100th Anniversary Volume: 77-110.

Cathles, L.M., Erendi, A.H.J., Theyer, J.B., and Barrie, C.T., (1997). How long can a hydrothermal system be sustained by a single intrusion event? Economic Geology, 92: 766-771.

Cawood, P. A., Hawkesworth, C. J., and Dhuime, B. (2013). The continental record and the generation of continental crust. Geological Society of America Bulletin, 125: 14-32.

Cawood, P. A., and Hawkesworth, C. J. (2015). Temporal relations between mineral deposits and global tectonic cycles. Geological Society, London, Special Publications, 393: 9-21.

Chiaradia, M., Tripodi, D., Fontboté, L., and Reza, B. (2008). Geologic setting, mineralogy, and geochemistry of the early Tertiary Au-rich volcanic-hosted massive sulfide deposit of La Plata, western Cordillera, Ecuador. Economic Geology, 103: 161-183.

Claypool, G. E., Holser, W. T., Kaplan, I. R., Sakai, H., and Zak, I. (1980). The age curves of sulfur and oxygen isotopes in marine sulfate and their mutual interpretation. Chemical Geology, 28: 199-260.

Cloutier, J., Piercey, S. J., Lode, S., Guchte, M. V., and Copeland, D. A. (2017). Lithostratigraphic and structural reconstruction of the Zn-Pb-Cu-Ag-Au Lemarchant volcanogenic massive sulphide (VMS) deposit, Tally Pond group, central Newfoundland, Canada. Ore Geology Reviews, 84: 154-173.

Colman-Sadd, S. P., Dunning, G., and Dec, T. (1992). Dunnage-Gander relationships and Ordovician orogeny in central Newfoundland; a sediment provenance and U-Pb age study. American Journal of Science, 292: 317-355.

Connelly, D. P., Copley, J. T., Murton, B. J., Stansfield, K., Tyler, P. A., German, C. R., ... & Hayman, N. (2012). Hydrothermal vent fields and chemosynthetic biota on the world's deepest seafloor spreading centre. Nature Communications, 3; 620.

Copeland, D. A., Toole, R.M.S., and Piercey, S.J. (2008). Assessment report on diamond drilling and soil sampling, Licence 8183M (10th year) and 9569M (5th year) South Tally Pond property, Rogerson Lake area, Newfoundland and Labrador, NTS 12A/10 and 12A/07; Newfoundland and Labrador Geological Survey, Assessment Report: p. 956.

Copeland, D. A. (2009). Assessment Report 012/1486 on Prospecting, Lithogeochemical Sampling and Data Interpretation on the Harpoon Property (Licenses 7695M, 10461M, 10464M, 10465M, 10607M, 12357M, 12885M, 13583M, 13448M, 13449M and 13667M) and the South Tally Pond Property (Licences 8183M, 9569M and 14158M) Lake Ambrose Area, Newfoundland and Labrador. NTS 12A/10 and 12A/07. Paragon Minerals Corporation.

Czamanske, G. K. (1974). The FeS content of sphalerite along the chalcopyrite-pyrite-bornite sulfur fugacity buffer. Economic Geology, 69: 1328-1334.

Dean, P. L. (1978). The Volcanic Stratigraphy and Metallogeny of Notre Dame Bay, Newfoundland, Unpublished M.Sc. Thesis, Memorial University of Newfoundland, Newfoundland.

Delaney, J. R., Robigou, V., McDuff, R. E., and Tivey, M. K. (1992). Geology of a vigorous hydrothermal system on the Endeavour Segment, Juan de Fuca Ridge. Journal of Geophysical Research: Solid Earth, 97: 19663-19682.

de Ronde, C. E., Hannington, M., Stoffers, P., Wright, I., Ditchburn, R., Reyes, A., Walker, S. (2005). Evolution of a submarine magmatic-hydrothermal system: Brothers volcano, southern Kermadec arc, New Zealand. Economic Geology, 100: 1097-1133.

de Ronde, C. E., Massoth, G. J., Butterfield, D. A., Christenson, B. W., Ishibashi, J., Ditchburn, R. G., and Takai, K. (2011). Submarine hydrothermal activity and gold-rich mineralization at Brothers Volcano, Kermadec Arc, New Zealand. Mineralium Deposita, 46: 541-584.

Dunning, G. R., Kean, B. F., Thurlow, J. G., and Swinden, H. S. (1987). Geochronology of the Buchans, Roberts Arm, and Victoria Lake groups and Mansfield Cove Complex, Newfoundland. Canadian Journal of Earth Sciences, 24: 1175-1184.

Dunning, G. R., O'Brien, S. J., Colman-Sadd, S. P., Blackwood, R. F., Dickson, W. L., O'Neill, P. P., and Krogh, T. E. (1990). Silurian orogeny in the Newfoundland Appalachians. The Journal of Geology: 895-913.

Dunning, G. R., Swinden, H. S., Kean, B. F., Evans, D. T. W., and Jenner, G. A. (1991). A Cambrian island arc in Iapetus: geochronology and geochemistry of the Lake

Ambrose volcanic belt, Newfoundland Appalachians. Geological Magazine, 128: 1-17.

Eldridge, C. S., Barton Jr, P. B., and Ohmoto, H. (1983). Mineral textures and their bearing on formation of the Kuroko orebodies. Economic Geology Monograph, 5: 241-281.

Etoh, J., Izawa, E., Watanabe, K., Taguchi, S., and Sekine, R. (2002). Bladed quartz and its relationship to gold mineralization in the Hishikari low-sulfidation epithermal gold deposit, Japan. Economic Geology, 97: 1841-1851.

Evans, D. T. W., and Kean, B. (2002). The Victoria Lake supergroup, central Newfoundland-its definition, setting and volcanogenic massive sulfide mineralization. Newfoundland and Labrador Department of Mines and Energy, Geological Survey, Open File NFLD/2790, p. 68.

Evans, D. T. W., Kean, B., and Dunning, G. (1990). Geological studies, Victoria Lake Group, central Newfoundland. Current Research. Newfoundland Department of Mines and Energy, Geological Survey Branch, Report, 90-91.

Franklin, J. M., Gibson, H. L., Jonasson, I. R., and Galley, A. G. (2005). Volcanogenic massive sulfide deposits. Economic Geology 100th Anniversary Volume, 98: 523-560.

Franklin, J., Hannington, M., Jonasson, I., and Barrie, C. (1998). Arc-related volcanogenic massive sulfide deposits: Proceedings of short course on metallogeny of volcanic arcs, January 24-25, Vancouver: British Columbia Geological Survey Open-File, p.8.

Franklin, J. M., Lydon, J. W., and Sangster, D. F. (1981). Volcanic-associated massive sulfide deposits. Economic Geology, 75: 485-627.

Fraser, D., Giroux, G.H., Copeland, D.A., Devine, C.A. (2012). NI-43-101 technical report and mineral resource estimate on the Lemarchant deposit, South Tally Pond VMS project, central Newfoundland, Canada. Paragon Minerals Corporation.

Galley, A. G. (1993). Characteristics of semi-conformable alteration zones associated with volcanogenic massive sulphide districts. Journal of Geochemical Exploration, 48 : 175-200.

Galley, A. G. (2003). Composite synvolcanic intrusions associated with Precambrian VMS-related hydrothermal systems. Mineralium Deposita, 38: 443-473.

Galley, A. G., Hannington, M., and Jonasson, I. (2007). Volcanogenic massive sulfide deposits. Mineral Deposits of Canada: A Synthesis of Major Deposit-Types, District Metallogeny, the Evolution of Geological Provinces, and Exploration Methods:

Geological Association of Canada, Mineral Deposits Division, Special Publication, 5: 141-161.

German, C., and Von Damm, K. (2006). Hydrothermal processes. The Oceans and Marine Geochemistry. Treatise on Geochemistry Series, Vol.6, Elsevier: 181-222.

Gibson, H. L. (2005). Volcano-hosted ore deposits. In: Marti, J. and Emst, G.J. (eds) Volcanoes and the environment. Cambridge: Cambridge University Press: 333-386.

Gill. S. (2015). Mineralogy, metal zoning, and genesis of the Cambrian Zn-Pb-Cu-Ag-Au Lemarchant volcanogenic massive sulfide deposit. Masters thesis, Memorial University of Newfoundland, 153 pages.

Gill, S.B. and Piercey, S. J. (2014). Preliminary observations on styles of mineralization and sulfide-mineral zonation in the Cambrian Zn-Pb-Cu-Ag-Au Lemarchant volcanogenic massive-sulfide deposit, Newfoundland and Labrador; Geological Survey of Canada, Current Research 2014-5, p. 17.

Gill, S., Piercey, S., Layton-Matthews, D., Layne, G., and Piercey, G. (2015). Mineralogical, sulphur, and lead isotopic study of the Lemarchant Zn-Pb-Cu-Ag-Au-VMS deposit: Implications for precious-metal enrichment processes in the VMS environment. Targeted Geoscience Initiative, 4: 183-195.

Gemmell, J. B., and Large, R. R. (1992). Stringer system and alteration zones underlying the Hellyer volcanogenic massive sulfide deposit, Tasmania, Australia. Economic Geology, 87: 620-649.

Goldberg, E.D. and Arrhenius, G. (1958) Chemistry of pelagic sediments. Geochim. Cosmochim. Acta, 13: 153–212.

Gurvich, E. G. (2006). Metalliferous sediments of the World Ocean-fundamental theory of deep sea hydrothermal sedimentation. Berlin-Heidelberg, Springer: 1-416.

Griffith, E. M., and Paytan, A. (2012). Barite in the ocean–occurrence, geochemistry and palaeoceanographic applications. Sedimentology, 59: 1817-1835.

Groves, D.I., Goldfarb, R.J., Gebre-Mariam, M., Hagemann, S.G., and Robert, E. (1998). Orogenic gold deposits - a proposed classification in the context of their crustal distribution and relationship to other gold deposit types. Ore Geology Reviews, 13: 7-27.

Halbach, P., Nakamura, K. I., Wahsner, M., Lange, J., Sakai, H., Käselitz, L., ... and Seifert, R. (1989). Probable modern analogue of Kuroko-type massive sulphide deposits in the Okinawa Trough back-arc basin. Nature, 338: 496-499.

Hannington, M.D. (2014). Volcanogenic massive sulfide deposits, In H.D.H.K. Turekian, ed., Treatise on geochemistry, 2nd ed.: Oxford, Elsevier: 463-488.

Hannington M.D., de Ronde C.E.J., and Petersen, S. (2005). Sea-floor tectonics and submarine hydrothermal systems. In: Hedenquist, J.W., Thompson, J.F.H., Goldfarb, R.J., and Richards, J.P. (eds.) 100th Anniversary Volume of Economic Geology: 111–142.

Hannington, M. D., Galley, A. G., Herzig, P. M., and Petersen, S. (1998). Comparison of the Tag mound and stockwork complex with Cyprus-type massive sulfide deposits. Paper presented at the Proceedings of the Ocean Drilling Program, Scientific Results, 158: 389-415.

Hannington, M. D., and Gorton, M. (1991). Analysis of sulfides for gold and associated trace metals by direct neutron activation with a Low‐Flux reactor. Geostandards Newsletter, 15: 145-154.

Hannington, M., Jonasson, I., Herzig, P., and Petersen, S. (1995a). Physical and chemical processes of seafloor mineralization at the mid-ocean ridges. Seafloor hydrothermal systems: Physical, chemical, biological, and geological interactions, Monograph 11: 115-157.

Hannington, M. D., Larocque, A. C., Petersen, S., and Rona, P. A. (1995b). The occurrence of gold in sulfide deposits of the TAG hydrothermal field, Mid-Atlantic Ridge. The Canadian Mineralogist, 33: 1285-1310.

Hannington, M. D, Peter, J., and Scott, S. (1986). Gold in sea-floor polymetallic sulfide deposits. Economic Geology, 81: 1867-1883.

Hannington, M. D., Poulsen, K. H., and Thomsen, J. F. (1999). Volcanogenic gold in the massive sulfide environment. Reviews in Economic Geology, 8: 325-356.

Hannington, M. D., and Scott, S. D. (1989). Sulfidation equilibria as guides to gold mineralization in volcanogenic massive sulfides; evidence from sulfide mineralogy and the composition of sphalerite. Economic Geology, 84: 1978-1995.

Hanor, J. S. (2000). Barite–celestine geochemistry and environments of formation. Reviews in Mineralogy and Geochemistry, 40: 193-275.

Hart, T. R., Gibson, H. L., and Lesher, C. M. (2004). Trace element geochemistry and petrogenesis of felsic volcanic rocks associated with volcanogenic massive Cu-Zn-Pb sulfide deposits. Economic Geology, 99: 1003-1013.

Haymon, R. M. (1983). Growth history of hydrothermal black smoker chimneys. Nature, 301: 695-698.

Haymon, R. M., and Kastner, M. (1981). Hot spring deposits on the East Pacific Rise 21°N: Preliminary description of mineralogy and genesis. Earth and Planetary Science Letters, 53: 363-381.

Hedenquist, J. W., Arribas, A., and Gonzalez-Urien, E. (2000). Exploration for epithermal gold deposits. Reviews in Economic Geology, 13: 245-277.

Hedenquist, J. W., Arribas, A., and Reynolds, T. J. (1998). Evolution of an intrusion-centered hydrothermal system; Far Southeast-Lepanto porphyry and epithermal Cu-Au deposits, Philippines. Economic Geology, 93: 373-404.

Hein, J. R., de Ronde, C. E., Koski, R. A., Ditchburn, R. G., Mizell, K., Tamura, Y., et al. (2014). Layered hydrothermal barite-sulfide mound field, East Diamante caldera, Mariana volcanic arc. Economic Geology, 109: 2179-2206.

Hein, J. R., Zierenberg, R. A., Maynard, J. B., and Hannington, M. D. (2007). Barite-forming environments along a rifted continental margin, Southern California Borderland. Deep Sea Research Part II: Topical Studies in Oceanography, 54: 1327-1349.

Hekinian, R., Francheteau, J., and Ballard, R. (1985). Morphology and evolution of hydrothermal deposits at the axis of the East Pacific Rise. Oceanologica Acta, 8: 147-155.

Hekinian, R., and Fouquet, Y. (1985). Volcanism and metallogenesis of axial and off-axial structures on the East Pacific Rise near 13 degrees N. Economic Geology, 80: 221-249.

Herzig, P. M., and Hannington, M. D. (1995). Polymetallic massive sulfides at the modern seafloor. A review. Ore Geology Reviews, 10: 95-115.

Herzig, P. M., Hannington, M. D., Fouquet, Y., von Stackelberg, U., and Petersen, S. (1993). Gold-rich polymetallic sulfides from the Lau back arc and implications for the geochemistry of gold in sea-floor hydrothermal systems of the southwest Pacific. Economic Geology, 88: 2182-2209.

Herzig, P., Hannington, M., and Arribas Jr, A. (1998). Sulfur isotopic composition of hydrothermal precipitates from the Lau back-arc: Implications for magmatic contributions to seafloor hydrothermal systems. Mineralium Deposita, 33: 226-237.

Hibbard, J. P., van Staal, C. R., and Rankin, D. W. (2010). Comparative analysis of the geological evolution of the northern and southern Appalachian Orogen: Late Ordovician-Permian. Geological Society of America Memoirs, 206: 51-69.

Hinchey, J. G. (2008). Volcanogenic massive sulphides of the northern Tulks volcanic belt, central Newfoundland: Preliminary findings, overview of deposit reclassifications and mineralizing environments. Newfoundland and Labrador Department of Natural Resources, Geological Survey, Report, 08-1: 151-172.

Hinchey, J. G. (2014). The Long Lake group: Preliminary U-Pb geochronology and lithogeochemistry, and implications for tectonostratigraphic architecture and VMS mineralization. Current Research. Newfoundland and Labrador Department of Natural Resources, Report, 14-1: 15-44.

Hinchey, J. G, and McNicoll, V. (2009). Tectonostratigraphic architecture and VMS mineralization of the southern Tulks volcanic belt: New insights from U–Pb geochronology and lithogeochemistry. Newfoundland and Labrador Department of Natural Resources, Geological Survey, Report, 09-1: 13-42.

Holland, H. D., and Malinin, S. D. (1979). The solubility and occurrence of non-ore minerals. In: H. L. Barnes (Editor), Geochemistry of Hydrothermal Ore Deposits, 2nd ed. Wiley, New York, NY, pp. 461-508.

Horikoshi, E., and Shikazano, N., (1978). Sub-types and their characteristics of Kuroko-type deposits. Mining Geology, 28: 267-276.

Huston, D. L. (1999). Stable isotopes and their significance for understanding the genesis of volcanic-hosted massive sulfide deposits: A review. Reviews in Economic Geology, 8: 157-179.

Huston, D. L., Bottrill, R. S., Creelman, R. A., Zaw, K., Ramsden, T. R., Rand, S. W., ... and Large, R. R. (1992). Geologic and geochemical controls on the mineralogy and grain size of gold-bearing phases, eastern Australian volcanic-hosted massive sulfide deposits. Economic Geology, 87: 542-563.

Huston, D. L., and Large, R. R. (1989). A chemical model for the concentration of gold in volcanogenic massive sulfide deposits. Ore Geology Reviews, 4: 171-200.

Huston, D. L., Pehrsson, S., Eglington, B. M., and Zaw, K. (2010). The geology and metallogeny of volcanic-hosted massive sulfide deposits: Variations through geologic time and with tectonic setting. Economic Geology, 105: 571-591.

Ishihara, S., & Sasaki, A. (1978). Sulfur of Kuroko deposits-a deep seated origin?. Mining Geology, 28: 361-367.

Jamieson, J. W., Hannington, M. D., Tivey, M. K., Hansteen, T., Williamson, N. M. B., Stewart, M., Fietzke, J., Butterfield, D., Frische, M., Allen, L., Cousens, B., and Langer, J. (2016). Precipitation and growth of barite within hydrothermal vent deposits from the Endeavour Segment, Juan de Fuca Ridge. Geochimica et Cosmochimica Acta, 173: 64-85.

Kalogeropoulos, S. I., and Scott, S. D. (1983). Mineralogy and geochemistry of tuffaceous exhalites (Tetsusekiei) of the Fukazawa mine, Hokuroku district, Japan. Economic Geology Monograph, 5: 412-432.

Kalogeropoulos, S. I., and Scott, S. D. (1989). Mineralogy and geochemistry of an Archean tuffaceous exhalite: The main contact tuff, Millenbach mine area, Noranda, Quebec. Canadian Journal of Earth Sciences, 26: 88-105.

Kean, B.F. (1977). Geology of the Victoria Lake area (12-A/06), Newfoundland: Newfoundland and Labrador Department of Mines and Energy, Mineral Development Division, Report N. 77-4, 11

Large, R. R. (1977). Chemical evolution and zonation of massive sulfide deposits in volcanic terrains. Economic Geology, 72: 549-572.

Large, R.R. (1992). Australian volcanic-hosted massive sulfide deposits: Features, styles, and genetic models. Economic Geology, 87: 549–572.

Large, R. R., Allen, R. L., Blake, M. D., and Herrmann, W. (2001). Hydrothermal alteration and volatile element halos for the Rosebery K Lens volcanic-hosted massive sulfide deposit, western Tasmania. Economic Geology, 96: 1055-1072.

Large, R.R., Huston, D.L., McGoldrick, P. J., and Ruxton, P. A. (1989). Gold distribution and genesis in Australian volcanogenic massive sulfide deposits and their significance for gold transport models. Economic Geology Monologue, 6: 520-536.

Leistel, J., Marcoux, E., Thiéblemont, D., Quesada, C., Sánchez, A., Almodóvar, G., Pascual, E., and Sev, R. (1998). The volcanic-hosted massive sulfide deposits of the Iberian Pyrite Belt. Review and preface to the thematic issue. Mineralium Deposita, 33: 2-30.

Liaghat, S., and MacLean, W. (1992). The Key Tuffite, Matagami mining district; origin of the tuff components and mass changes. Exploration and Mining Geology, 1: 197-207.

Ligi, M., Cocchi, L., Bortoluzzi, G., D'Oriano, F., Muccini, F., Tontini, F. C., ... & Carmisciano, C. (2014). Mapping of seafloor hydrothermally altered rocks using geophysical methods: Marsili and Palinuro seamounts, southern Tyrrhenian Sea. Economic Geology, 109: 2103-2117.

Lode, S., Piercey, S. J. P., Copeland, D. A., Devine, C. A., and Sparrow, B. (2012). Setting and styles of hydrothermal mudstones near the Lemarchant volcanogenic massive sulfide (VMS) deposit, Central Mobile Belt, Newfoundland. In Abstracts, Geological Survey of Canada Joint Annual Meeting, St. John's, Newfoundland, 35: 27-29.

Lode, S., Piercey, S. J., and Devine, C. A. (2015). Geology, mineralogy, and lithogeochemistry of metalliferous mudstones associated with the Lemarchant volcanogenic massive sulfide deposit, Tally Pond group, central Newfoundland. Economic Geology, 110: 1835-1859.

Lode, S., Piercey, S. J., Layne, G. D., Piercey, G., and Cloutier, J. (2016). Multiple sulphur and lead sources recorded in hydrothermal exhalites associated with the Lemarchant volcanogenic massive sulphide deposit, central Newfoundland, Canada. Mineralium Deposita: 1-24.

Lüders, V., Pracejus, B., and Halbach, P. (2001). Fluid inclusion and sulfur isotope studies in probable modern analogue Kuroko-type ores from the JADE hydrothermal field (Central Okinawa Trough, Japan). Chemical Geology, 173: 45-58.

Lydon, J.W. (1984). Volcanogenic massive sulfide deposits Part I: A descriptive model. Geoscience Canada, 11: 195–202.

Lydon J.W. (1988). Volcanogenic massive sulfide deposits Part 2: Genetic Models. Geoscience Canada, 15: 43–65.

MacLachlan, K., and Dunning, G. (1998)a. U-Pb ages and tectono-magmatic evolution of Middle Ordovician volcanic rocks of the Wild Bight Group, Newfoundland Appalachians. Canadian Journal of Earth Sciences, 35: 998-1017.

MacLachlan, K., and Dunning, G. (1998)b. U-Pb ages and tectonomagmatic relationships of Early Ordovician low-ti tholeiites, boninites and related plutonic rocks in central Newfoundland, Canada. Contributions to Mineralogy and Petrology, 133: 235-258.

Marchev, P., Downes, H., Thirlwall, M. F., and Moritz, R. (2002). Small-scale variations of $^{87}Sr/^{86}Sr$ isotope composition of barite in the Madjarovo low-sulphidation epithermal system, SE Bulgaria: implications for sources of Sr, fluid fluxes and pathways of the ore-forming fluids. Mineralium Deposita, 37: 669-677.

McArthur, J., Howarth, R., and Bailey, T. (2001). Strontium isotope stratigraphy: LOWESS version 3: Best fit to the marine Sr - isotope curve for 0–509 Ma and accompanying look‐up table for deriving numerical age. The Journal of Geology, 109: 155-170.

McNicoll, V., Squires, G., Kerr, A. and Moore, P. (2010). The Duck Pond and Boundary Cu-Zn deposits, Newfoundland: new insights into the ages of host rocks and the timing of VHMS mineralization. Canadian Journal of Earth Sciences, 47: 1481-1506.

Monacke, T., Petersen, S., Hannington, M.D. (2014). Constraints on water depth of massive sulfide formation: Evidence from modern seafloor hydrothermal systems in arc-related settings. Economic Geology, 109: 2079-2101.

Mercier-Langevin, P., Hannington, M. D., Dubé, B., and Bécu, V. (2011). The gold content of volcanogenic massive sulfide deposits. Mineralium Deposita, 46: 509-539.

Monnin, C., and Cividini, D. (2006). The saturation state of the world's ocean with respect to (Ba, Sr)SO_4 solid solutions. Geochimica Et Cosmochimica Acta, 70: 3290-3298.

Moss, R., Scott, S. D., and Binns, R. A. (2001). Gold content of eastern Manus basin volcanic rocks: implications for enrichment in associated hydrothermal precipitates. Economic Geology, 96: 91-107.

Murchey, B. L., Madrid, R. J., and Poole, F. G. (1987). Paleozoic bedded barite associated with chert in western North America. Siliceous Sedimentary Rock-Hosted Ores and Petroleum. J.R. Hein (Ed.) Van Nostrand: 269-283.

Nance, R. D., Murphy, J. B., Strachan, R. A., Keppie, J. D., Gutiérrez-Alonso, G., Fernández-Suárez, J., Pisarevsky, S. A. (2008). Neoproterozoic-early Palaeozoic tectonostratigraphy and palaeogeography of the peri-Gondwanan terranes: Amazonian v. West African connections. Geological Society, London, Special Publications, 297: 345-383.

Neoproterozoic-Early Palaeozoic tectonostratigraphy and palaeogeography of the peri-Gondwanan terranes: Amazonian v. west African connections. Geological Society, London, Special Publications, 297: 345-383.

Neuman, R. B. (1984). Geology and paleobiology of islands in the Ordovician Iapetus ocean: Review and implications. Geological Society of America Bulletin, 95: 1188-1201.

Ohmoto, H. (1996). Formation of volcanogenic massive sulfide deposits: the Kuroko perspective. Ore geology reviews, 10: 135-177.

Ohmoto, H., and Goldhaber, M. B. (1997). Sulfur and carbon isotopes. Geochemistry of hydrothermal ore deposits, 3: 517-611.

Ohmoto, H., and Rye, R.O. (1979) Isotopes of sulfur and carbon. In: H.L. Barnes (Editor). Geochemistry of Hydrothermal Ore Deposits, 2nd e. Wiley, New York: 509-567.

Ohmoto, H., Mizukami, M., Drummond, S. E., Eldridge, C. S., Pisutha-Arnond, V., and Lenagh, T. C. (1983). Chemical processes of Kuroko formation. Economic Geology Monographs, 5: 570-604.

Paytan, A., Kastner, M., Martin, E. E., Macdougall, J. D., and Herbert, T. (1993). Marine barite as a monitor of seawater strontium isotope composition. Nature, 366: 445-449.

Paytan, A., Mearon, S., Cobb, K., and Kastner, M. (2002). Origin of marine barite deposits: Sr and S isotope characterization. Geology, 30: 747-750.

Pearce, J. A. (1996). A user's guide to basalt discrimination diagrams. Trace element geochemistry of volcanic rocks: applications for massive sulphide exploration. Geological Association of Canada, Short Course Notes, 12: 113.

Peter, J., and Lentz, D. (2003). Ancient iron formations: Their genesis and use in the exploration for stratiform base metal sulfide deposits, with examples from the Bathurst mining camp. Geotext, 4: 145-176.

Petersen, S., Monecke, T., Westhues, A., Hannington, M. D., Gemmell, J. B., Sharpe, R., ... & Gibson, H. (2014). Drilling shallow-water massive sulfides at the Palinuro volcanic complex, Aeolian island arc, Italy. Economic Geology, 109: 2129-2158.

Piercey, S. J. (2010). An overview of petrochemistry in the regional exploration for volcanogenic massive sulphide (VMS) deposits. Geochemistry: Exploration, Environment, Analysis, 10: 119-136.

Piercey, S. J. (2011). The setting, style, and role of magmatism in the formation of volcanogenic massive sulfide deposits. Mineralium Deposita, 46: 449-471.

Piercey, S.J., and Hinchey, J. G. (2012). Volcanogenic massive sulfide (VMS) deposits of the Central Mineral Belt, Newfoundland. Geological Association of Canada Mineralogical Association of Canada Joint Annual Meeting, Field Trip Guidebook B4. Newfoundland and Labrador Department of Natural Resources, Geological Survey, Open File NFLD/3173, 56 pages.

Piercey, S. J., Squires, G. C., and Brace, T. D. (2014). Lithostratigraphic, hydrothermal, and tectonic setting of the Boundary volcanogenic massive sulfide deposit, Newfoundland Appalachians, Canada: formation by subseafloor replacement in a Cambrian rifted arc. Economic Geology, 109: 661-687.

Pisutha-Arnond, V., and Ohmoto. J. (1983). Thermal History, and chemical and isotopic compositions of the ore-forming fluids responsible for the Kuroko massive sulfide deposits in the Hokuroko District of Japan. Economic Geology, 5: 523-558.

Pollock, J., (2004). Geology and paleotectonic history of the Tally Pond Group, Dunnage zone, Newfoundland Appalachians: an integrated geochemical, geochronological, metallogenic and isotopic study of Cambrian island arc along the Peri-Gondwanan margin of Iapetus. MSc. Thesis, Memorial University, St. John's, Newfoundland, p. 420.

Poulsen, K. H., & Hannington, M. D. (1996). Volcanic-associated massive sulphide gold. Geology of Canadian Mineral Deposit Types, Geological Survey of Canada, Geology of Canada, 8: 183-196.

Robb, L. (2005). Introduction to ore-forming processes. Blackwell Publishing company.

Riverin, G., and Hodgson, C. J. (1980). Wall-rock alteration at the Millenbach Cu-Zn mine, Noranda, Quebec. Economic Geology, 75: 424-444.

Roedder, E. (1984). Fluid inclusions. Mineralogical Society of America. Reviews in Mineralogy, 12. p. 644.

Rogers, N., and van Staal, C. (2002). Toward a Victoria Lake supergroup: A provisional stratigraphic revision of the Red Indian to Victoria Lakes area, central Newfoundland. Newfoundland and Labrador Department of Natural Resources, Geological Survey, Report, 02-01: 185-195.

Rogers, N., van Staal, C., McNicoll, V., Pollock, J., Zagorevski, A., and Whalen, J. (2006). Neoproterozoic and Cambrian arc magmatism along the eastern margin of the Victoria Lake supergroup: A remnant of Ganderian basement in central Newfoundland? Precambrian Research, 147: 320-341.

Rogers, N., van Staal, C., Zagorevski, A., Skulski, T., Piercey, S., and McNicoll, V. (2007). Timing and tectonic setting of volcanogenic massive sulfide bearing terranes within the Central Mobile Belt of the Canadian Appalachians. Paper presented at the Proceedings of Exploration, 7: 1199-1205.

Sangster, D. (1968). Relative sulfur isotope abundances of ancient seas and strata-bound sulfide deposits. Paper presented at the Proceedings of the Geological Association of Canada, 19: p. 79.

Scotney, P. M., Roberts, S., Herrington, R. J., Boyce, A. J., and Burgess, R. (2005). The development of volcanic hosted massive sulfide and barite–gold orebodies on Wetar Island, Indonesia. Mineralium Deposita, 40: 76-99.

Scott, S. D., and Barnes, H. L. (1971). Sphalerite geothermometry and geobarometry. Economic Geology, 66: 653-669.

Seal, R. R., Alpers, C. N., and Rye, R. O. (2000). Stable isotope systematics of sulfate minerals. Reviews in Mineralogy and Geochemistry, 40: 541-602.

Seal, R.R. II., and Wandless, G.A. (2003). Sulfur isotope evidence for sea-floor mineralizing processes at the Bald Mountain and Mount Chase massive sulfide deposits, northern Maine. Economic Geology Monograph, 11: 567-587. .

Seward, T. M. (1973). Thio complexes of gold and the transport of gold in hydrothermal ore solutions. Geochimica et Cosmochimica Acta, 37: 379-399.

Seward, T. (1984). The transport and deposition of gold in hydrothermal systems. Paper presented at the Gold, 8: 165-181.

Sherlock, R., Roth, T., Spooner, E., and Bray, C. (1999). Origin of the Eskay Creek precious metal-rich volcanogenic massive sulfide deposit; fluid inclusion and stable isotope evidence. Economic Geology, 94: 803-824.

Sillitoe, R. H. (1994). Indonesian mineral deposits—introductory comments, comparisons and speculations. Journal of Geochemical Exploration, 50: 1-11.

Sillitoe, R. H., Hannington, M. D., and Thompson, J. F. (1996). High sulfidation deposits in the volcanogenic massive sulfide environment. Economic Geology, 91: 204-212.

Simmons, S.F., and Christenson, B.W. (1994), Origins of calcite in boiling geothermal system. American Journal of Science, 294: 361–400.

Simmons, S. F., White, N. C., and John, D. A. (2005). Geological characteristics of epithermal precious and base metal deposits. Economic Geology One Hundredth Anniversary Volume: 1905-2005: 485-522.

Singer, D. A. (1995). World class base and precious metal deposits; a quantitative analysis. Economic Geology, 90: 88-104.

Solomon, M., Eastoe, C. J., Walshe, J. L., & Green, G. R. (1988). Mineral deposits and sulfur isotope abundances in the Mount Read Volcanics between Que River and Mount Darwin, Tasmania. Economic Geology, 83: 1307-1328.

Spiess, F., Macdonald, K. C., Atwater, T., Bal, R., Francheteau, J., Guerrero, J., Juteau, M. K. (1980). East Pacific Rise: Hot spring and geophysical experiment. Science, 207: p. 28.

Spooner, E. T. and Fyfe, W. S. (1973). Sub-seafloor metamorphism of F/S “Meteor” near 40°N. Earth and Planetary Science Letters 23: 91-9.

Squires, G., Brace, T., and Hussey, A. (2001). Newfoundland’s polymetallic Duck Pond deposit: Earliest Iapetan VMS mineralization, formed within a sub-seafloor, carbonate-rich alteration system. Paper presented at the Geology and Mineral Deposits of the Northern Dunnage Zone, Newfoundland Appalachians. Edited by D.T.W. Evans and A. Kerr. Geological Association of Canada–Mineralogical Association of Canada (GAC–MAC) Annual Meeting, St. John’s, Nfld, pp. 167-187.

Squires, G.C., and Hinchey, J.G. (2006). Geology of the Tally Pond Volcanic Belt and adjacent areas (parts of NTS 12A/09 and 12A/10. Government of Newfoundland and Labrador, Department of Natural Resources, Geological Survey, Map 2006-01, Open File 012A/1202.

Squires, G. C., and Moore, P. J. (2004). Volcanogenic massive sulfide environments of the Tally Pond volcanics and adjacent area: Geological, lithogeochemical and geochronological results. Geological Survey, Report, 04-1: 63-91.

Stanton, R. L. (1991). Understanding volcanic massive sulfides; past, present, and future: Economic Geology Monograph, 8: 82-95.

Swinden, H. S. (1988). Introduction to volcanogenic sulphide deposits in Newfoundland In: Swinden HS, Kean BF (eds) The volcanogenic sulphide districts of central Newfoundland, Geological Association of Canada: 1-26.

Swinden, H. S. (1991). Paleotectonic settings of volcanogenic massive sulphide deposits in the Dunnage Zone, Newfoundland Appalachians CIM bulletin, 84: 59-69.

Swinden, H. S., Jenner, G., Kean, B., and Evans, D. (1989). Volcanic rock geochemistry as a guide for massive sulfide exploration in central Newfoundland. Newfoundland Department of Mines and Energy, Geological Survey Branch, Report, 89: 201-219.

Swinden, H.S., and Dunsworth, S.M., (1995). Metallogeny; Chapter 9, in Williams, H., ed., The Appalachian/Caledonian Orogen: Canada and Greenland, Geology of Canada, No. 6: Geological Survey of Canada: 681-814.

Swinden, H. S., and Thorpe, R. I. (1984). Variations in style of volcanism and massive sulfide deposition in Early to Middle Ordovician island-arc sequences of the Newfoundland Central Mobile Belt. Economic Geology, 79: 1596-1619.

Tufar, W. (1991). Paragenesis of complex massive sulfide ores from the Tyrrhenian Sea. Mitteilungen Der Österreichischen Geologischen Gesellschaft, 84: 265-300.

Urabe, T. (1987). The effect of pressure on the partitioning ratios of lead and zinc between vapor and rhyolite melts. Economic Geology, 82: 1049-1052.

Urabe, T., and Sato, T. (1978). Kuroko deposits of the Kosaka mine, northeast Honshu, Japan; products of submarine hot springs on Miocene sea floor. Economic Geology, 73: 161-179.

van Staal, C. R. (1994). Brunswick subduction complex in the Canadian Appalachians: Record of the Late Ordovician to Late Silurian collision between Laurentia and the Gander margin of Avalon. Tectonics, 13: 946-962.

van Staal, C. R. (2007). Pre-Carboniferous tectonic evolution and metallogeny of the Canadian Appalachians. *Mineral Resources of Canada:* A Synthesis of Major Deposit Types, District Metallogeny, the Evolution of Geological Provinces, and Exploration Methods. Edited by W.D. Goodfellow. Geological Association of Canada, Mineral Deposits Division, Special Publication, 5: 793-818.

van Staal, C. R., and Barr, S. M. (2012). Lithospheric architecture and tectonic evolution of the Canadian Appalachians and associated Atlantic margin. Tectonic Styles in Canada: The Lithoprobe Perspective: Geological Association of Canada Special Paper, 49: 55.

van Staal, C., Dewey, J., Mac Niocaill, C., and McKerrow, W. (1998). The Cambrian-Silurian tectonic evolution of the northern Appalachians and British Caledonides: History of a complex, west and southwest Pacific-type segment of Iapetus. Geological Society, London, Special Publications, 143: 197-242.

van Staal, C. R., Whalen, J. B., Valverde-Vaquero, P., Zagorevski, A., and Rogers, N. (2009). Pre-Carboniferous, episodic accretion-related, orogenesis along the Laurentian margin of the northern Appalachians. Geological Society, London, Special Publications, 327: 271-316.

Veizer, J. (1989). Strontium isotopes in seawater through time. Annual Review of Earth and Planetary Sciences, 17: 141.

Veizer, J., Ala, D., Azmy, K., Bruckschen, P., Buhl, D., Bruhn, F., ... and Jasper, T. (1999). $^{87}Sr/^{86}Sr$, $\delta^{13}C$ and $\delta^{18}O$ evolution of Phanerozoic seawater. Chemical geology, 161: 59-88.

Von Damm, K. L. (1990). Seafloor hydrothermal activity: black smoker chemistry and chimneys. Annual Review of Earth and Planetary Sciences, 18: 173.

Watanabe, M., and Sakai, H. (1983). Stable isotope geochemistry of sulfates from the Neogene ore deposits in the Green Tuff region, Japan. Economic Geology Monograph, 5: 282-291.

Williams, H. (1979). Appalachian orogen in Canada. Canadian Journal of Earth Sciences, 16: 792-807.

Williams, H. (1995). Geology of the Appalachian-Caledonian Orogen in Canada and Greenland. Geological Survey of Canada: Minister of Energy, Mines and Resources Canada, p. 944.

Williams, H., Colman-Sadd, S., and Swinden, H. (1988). Tectonic-stratigraphic subdivisions of central Newfoundland. Current Research, Part B. Geological Survey of Canada, Paper, 88: 91-98.

Williams-Jones, A. E., Bowell, R. J., and Migdisov, A. A. (2009). Gold in solution. Elements, 5: 281-287.

Wilson, J. T. (1966). Did the Atlantic close and then re-open? Nature, 211: 676-681.

Yang, K. H., and Scott, S. D. (1996). Possible contribution of a metal-rich magmatic fluid to a sea-floor hydrothermal system. Nature, 383: 420-423.

Yang, K., and Scott, S. D. (2002). Magmatic degassing of volatiles and ore metals into a hydrothermal system on the modern sea floor of the eastern Manus back-arc basin, western Pacific. Economic Geology, 97: 1079-1100.

Zagorevski, A., Van Staal, C., McNicoll, V., and Rogers, N. (2007). Upper Cambrian to upper Ordovician peri-Gondwanan island arc activity in the Victoria Lake supergroup, central Newfoundland: Tectonic development of the northern Ganderian margin. American Journal of Science, 307: 339-370.

Zagorevski, A., van Staal, C.R., Rogers, N., McNicoll, V., Dunning, G.R., and Pollock, J.C. (2010). Middle Cambrian to Ordovician arc-backarc development on the leading edge of Ganderia, Newfoundland Appalachians. *In* From Rodinia to Pangea: The Lithotectonic Record of the Appalachian Region. *Edited by* R.P. Tollo, M.J. Batholomew, J.P. Hibbard, and P.M. Karabinos. Geological Society of America, Memoir 206, pp.367–396.

Table 1-1. Defining characteristics of high-sulfidation and low-sulfidation volcanogenic massive sulfide deposits according to Sillitoe et al. (1996).

	High-sulfidation	Low-sulfidation
Fluids	Acidic pH, probably saline initially, dominantly magmatic	Near-neutral pH, low salinity, gas-rich (CO_2, H_2S), dominantly meteoric
Alteration assemblage	Advanced argillic (zonation: quartz-alunite-kaolinite-illite-montmorillonite-chlorite) barite, native sulfur	Quartz, sericite, chlorite, carbonate ± kaolinite
Metal associations	Au-Cu (lesser Ag, Bi, Te), bornite, enargite, luzonite, tennantite, covellite, low-Fe sphalerite, orpiment, realgar	Au-Ag (lesser As, Sb, Se, Hg), bornite-pyrite and/or enargite-tennantite

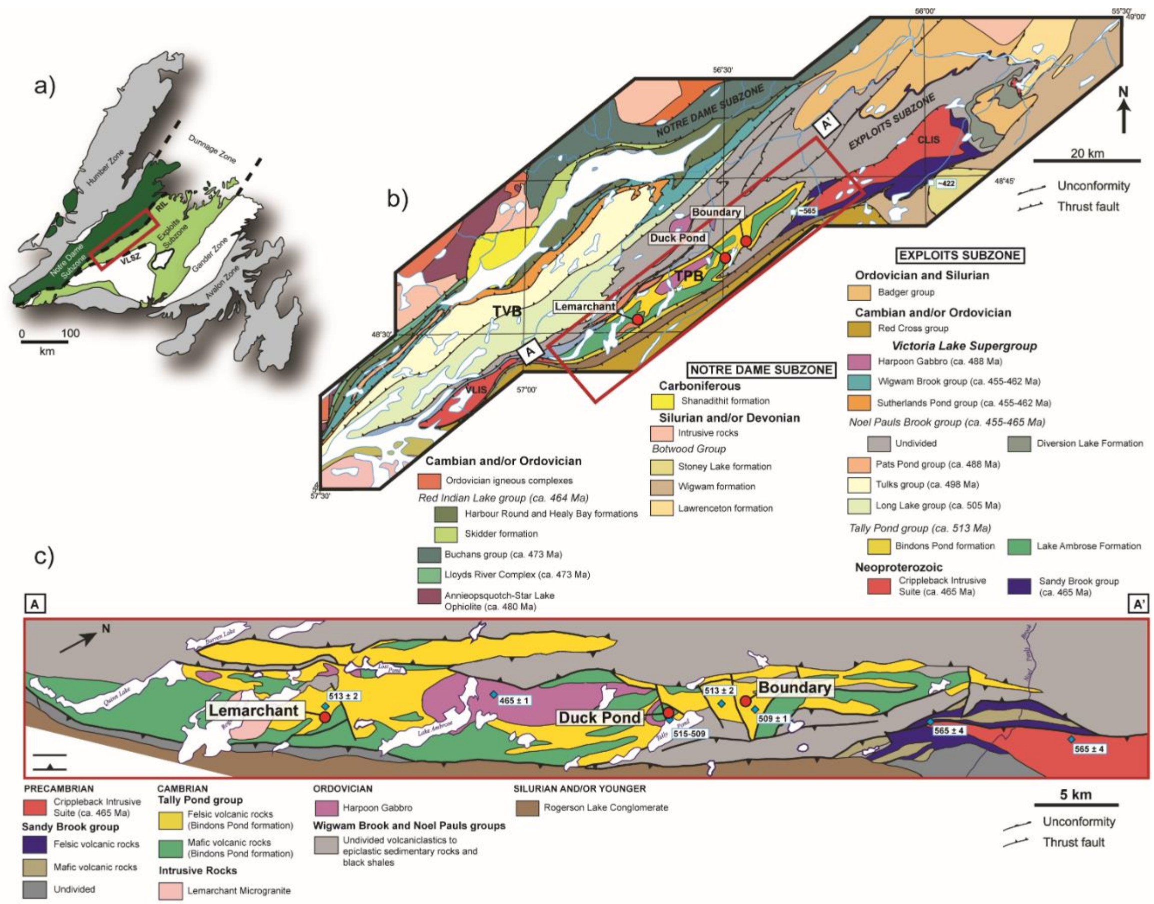

Figure 1-1. A) Simplified tectonostratigraphic zones of the Newfoundland Appalachians. The red square indicates the location of the study area located in the Exploits subzone of the Dunnage zone, east of the Red Indian Line. B) Geologic map of the Victoria Lake supergroup and adjacent areas, including the Tulks volcanic belt, the Tally Pond group, and the Crippleback Intrusive Suite. The Tally Pond group hosts the Lemarchant deposit as well as the Duck Pond and Boundary deposits. C) Detailed geologic map of the Tally Pond group with deposit locations and existing U-Pb ages. TVB = Tulks volcanic belt; TPB = Tally Pond; CLIS = Crippleback Intrusive Suite. Figure modified from McNicoll et al. (2010).

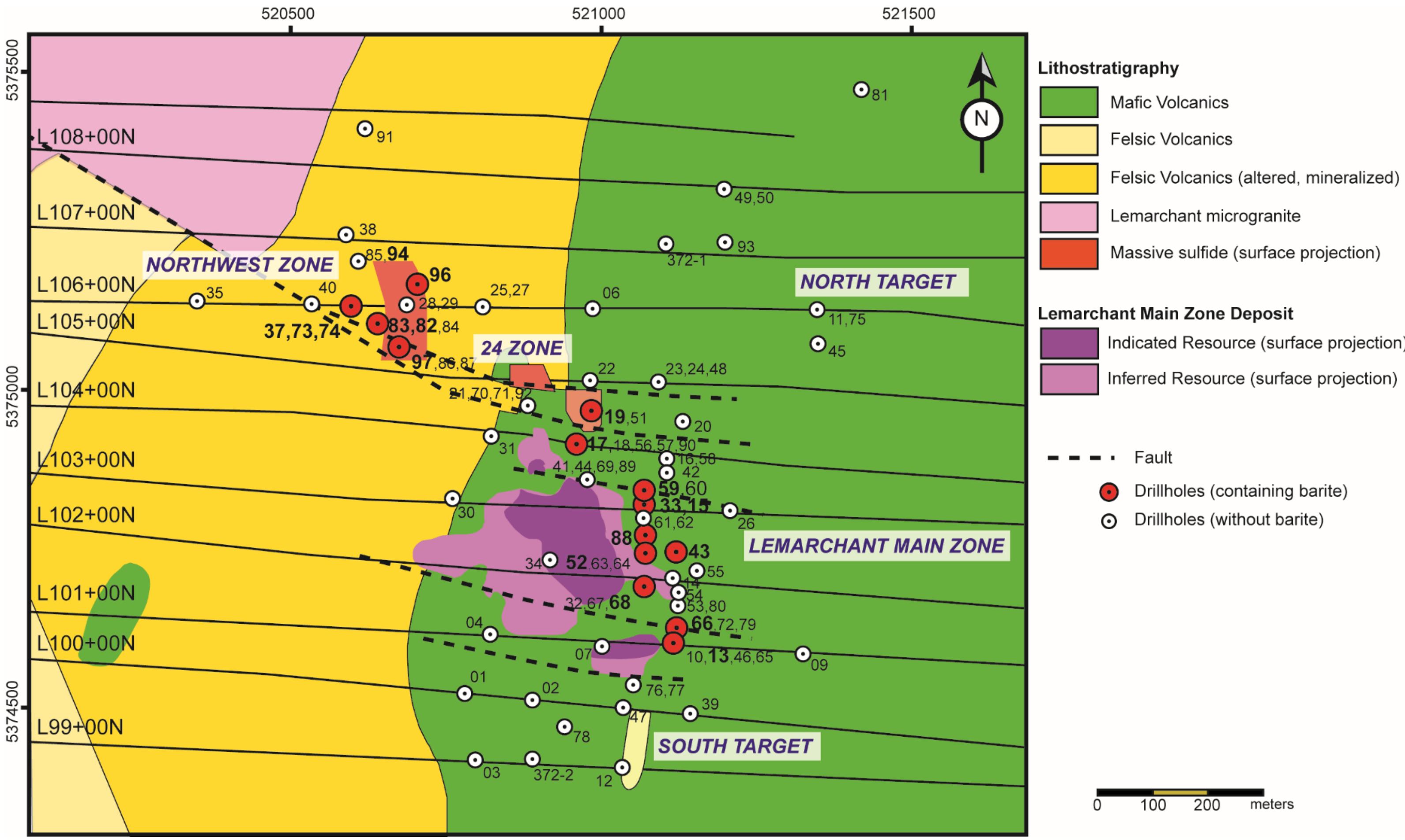

Figure 1-2. Simplified geologic map of the Lemarchant deposit with drill hole locations. The bimodal nature of the Lemarchant deposit is illustrated by the felsic volcanic footwall and the mafic volcanic hangingwall. The Lemarchant microgranite is located 500m northwest of the mineralized zone. The Lemarchant fault strikes north-south and is indicated by the black line. Surface projection of indicated and inferred resources are shown and are represented by the dark and light purple colors (Main zone). The surface projection of the indicated resources in the northwest zone is represented by the red rectangle. Modified after Fraser et al. (2012).

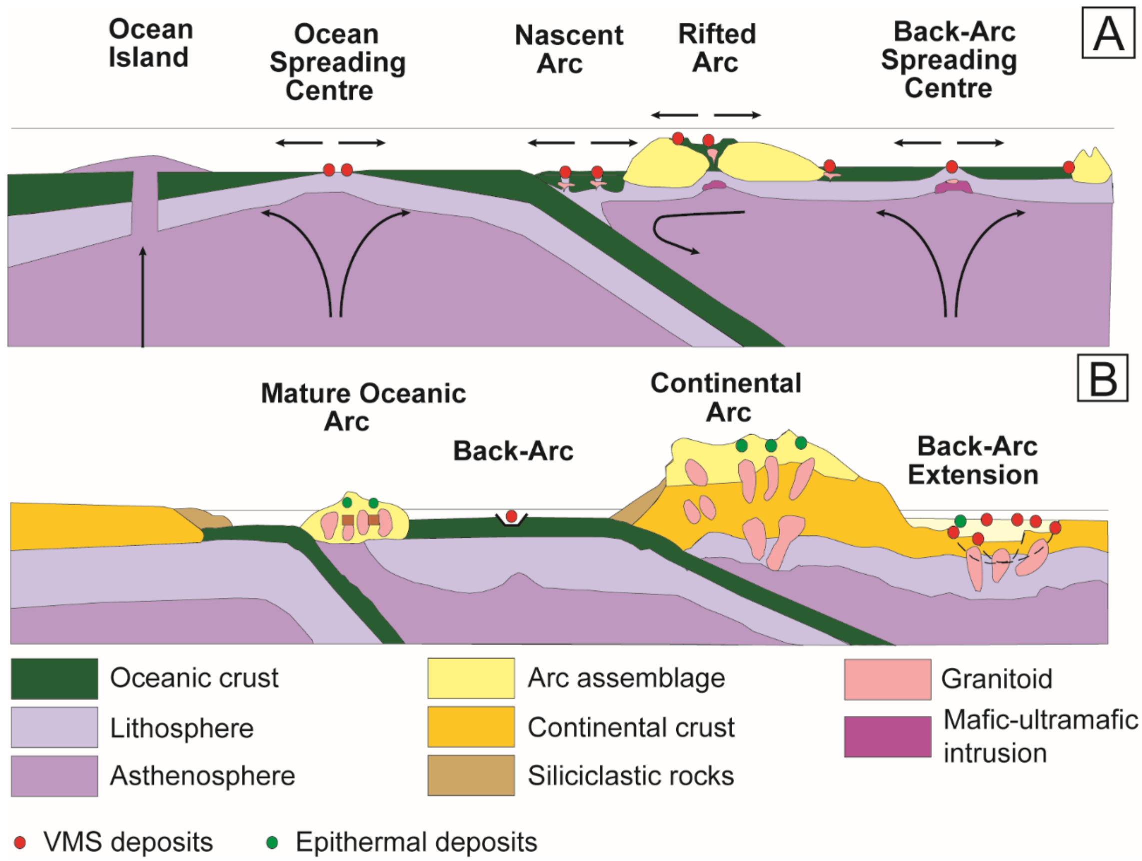

Figure 1-3. Main tectonic environments where VMS deposits can form: A) Mafic-dominated VMS deposits associated with the formation of ocean basins and development of spreading centers. B) Felsic-dominated and bimodal siliciclastic deposits formed in mature arc settings and ocean-continent subduction zones. Figure from Galley et al. (2007); modified from Groves et al. (1998).

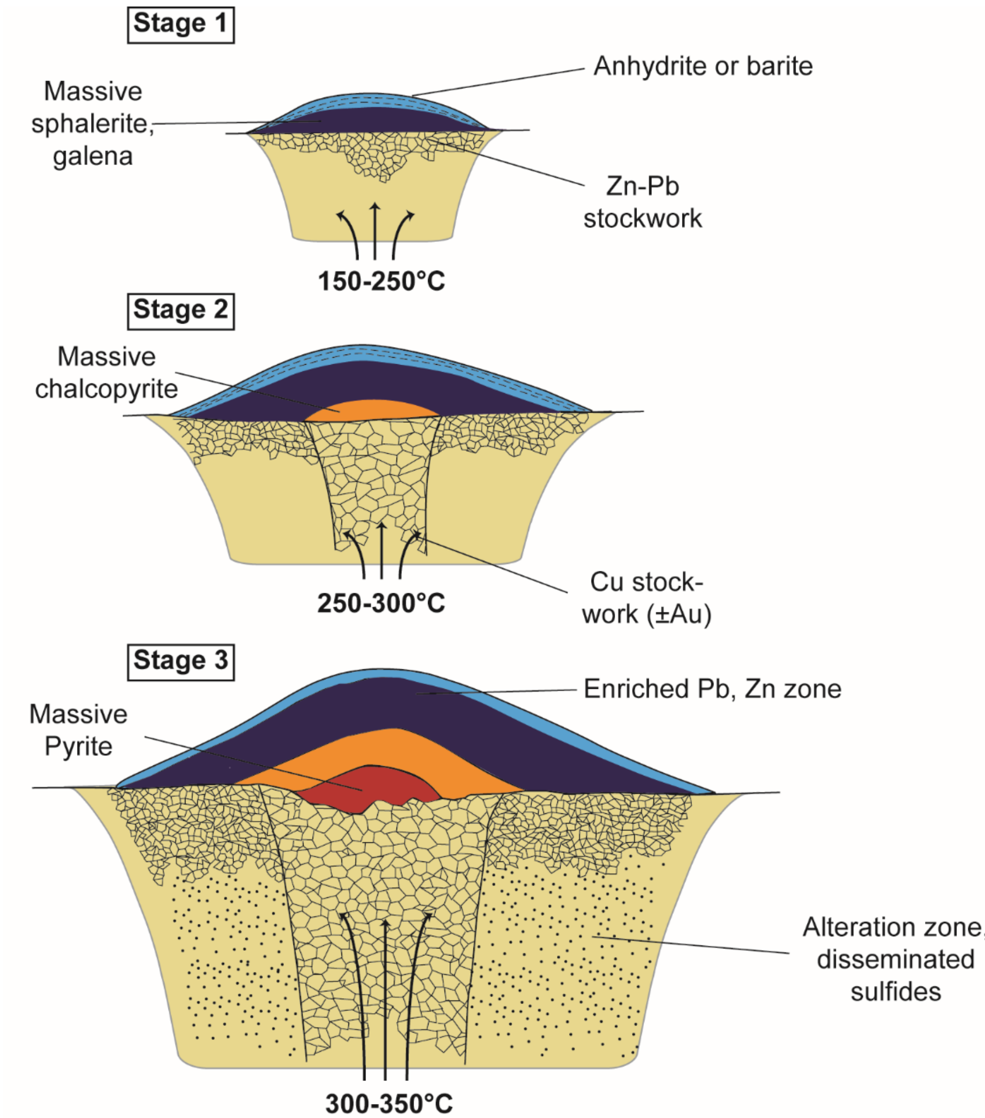

Figure 1-4. Evolution of ore minerals during growth of massive sulfide mound in VMS deposits. Stage 1- Anhydrite-barite-sphalerite-galena precipitate during the early stage of hydrothermal circulation at low-temperatures (150-250°C). Stage 2- Hotter temperature fluids (250-300°C) precipitate chalcopyrite in the interior of the mound and dissolves stage-1 ore. Stage 3- Massive pyrite is precipitated in the interior of the mound during circulation of higher temperatures (300-350°C) and chalcopyrite can be replaced by pyrite. Figure after the model from Eldridge et al. (1983). Figure modified from Large (1992) with genetic models based on the work of Eldridge et al. (1983) and Campbell et al. (1984).

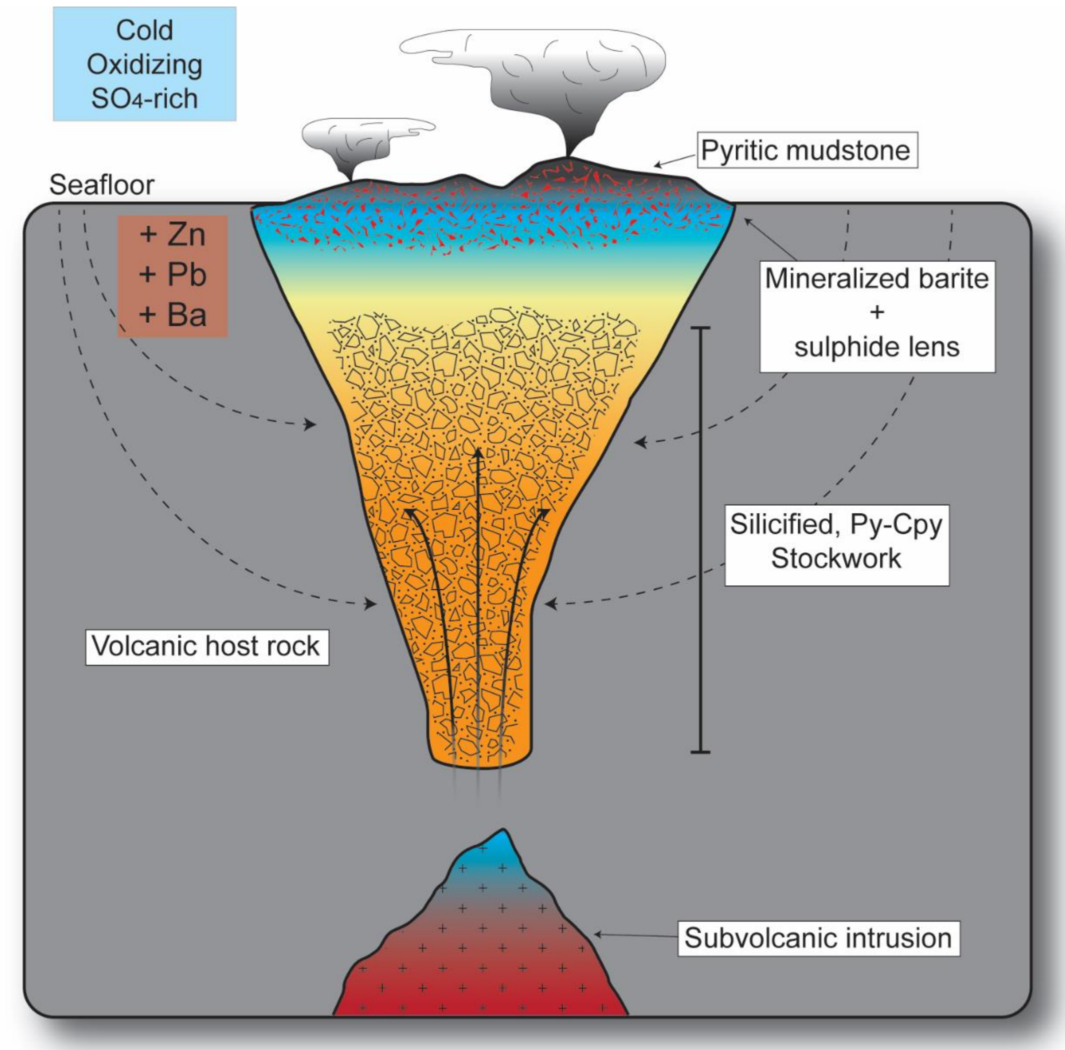

Figure 1-5. Schematic cross-section of a typical modern day Kuroko-type VMS model. The top of the section is characterized by a semi to massive sulfide lens underlain by a stockwork "pipe" that is characterized by a distinct alteration halo. Figure modified from Hannington et al. (1998).

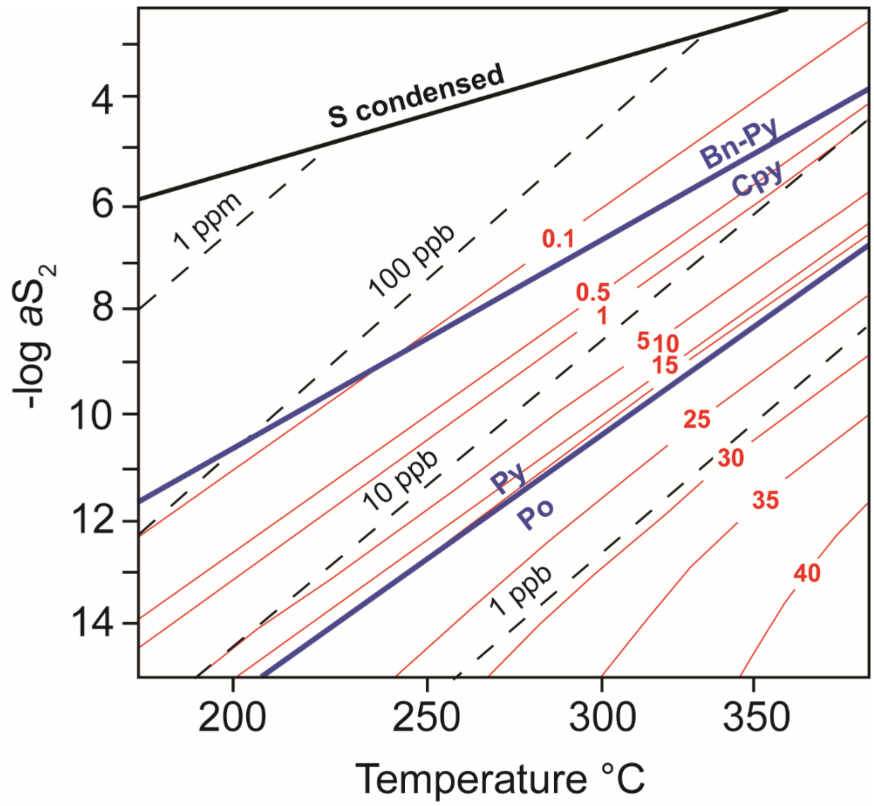

Figure 1-6. Log aS_2 vs. temperature phase diagram (Fig. 4; Hannington and Scott, 1989) showing the contours of $Au(HS)_2^-$ concentration (dashed black lines) and the contours of mole percent FeS in sphalerite (red lines) at pH=5 and 250 ppm H_2S. The sulfidation boundaries for pyrite-pyrrhotite and bornite-pyrite-chalcopyrite are represented by the dark blue solid lines. This diagram shows that at higher H_2S, $Au(HS)_2^-$ concentrations is the dominant Au species in solution. Sulfidation boundaries are taken from Scott and Barnes (1971) and Czamanske (1974).

Chapter 2 - Genesis of barite associated with the Lemarchant Zn-Pb-Cu-Ag-Au-rich volcanogenic massive sulfide (VMS) deposit, Newfoundland, Canada: implications for the genesis of VMS-related barite, Cambrian seawater chemistry, and the origin of barite-rich VMS deposits

2.1 - Abstract

The Central Mobile Belt in Newfoundland, Canada, hosts numerous volcanogenic massive sulfide (VMS) deposits, including the bimodal felsic, Zn-Pb-Cu-Ag-Au-Ba Lemarchant VMS deposit in the Tally Pond group. The Lemarchant deposit contains a complex assemblage of sulfides, sulfosalts, and precious metal phases that are intergrown with barite. Despite the presence of barite in the deposit, the detailed relationships of barite to mineralization, its textural variations, and genesis are not well understood.

Barite in the Lemarchant deposit is massive and locally bladed. Massive barite is associated with sphalerite, galena, pyrite and minor chalcopyrite, whereas bladed barite is associated with intermediate- to high-sulfidation mineral assemblages (e.g. sulfosalts, bornite, covellite, and precious metals). Microscopic sulfides and sulfosalts (± electrum) are found within secondary and pseudo-secondary fluid inclusions in bladed barite, although they occur in primary growth zones; these microscopic inclusions contain minerals with elevated concentrations of Au-Ag-As-Sb and Ga-Mo-Hg-Tl-V. Electron microprobe (EMPA) and high-resolution and quadrupole laser ablation-inductively coupled plasma-mass spectrometry (HR- and Q-LA-ICP-MS) analyses indicate that barite geochemistry is remarkably homogeneous regardless of texture and contains only Ba, S, and Sr with minor Na and Ca; little to no other trace elements are present in barite crystals, except for when associated with microscopic sulfide/sulfosalt inclusions. Sulfur isotope

($\delta^{34}S$) results on bladed and massive barite are similar (24.7-28.1‰) and have a mean value of 27‰, which is similar to Cambrian seawater sulfate. Whole-rock strontium isotope ratios ($^{87}Sr/^{86}Sr$) of barite range from 0.706993 to 0.707510.

Fluid inclusions in bladed barite are of three types: 1) type-I aqueous carbonic; 2) type-II aqueous two-phase (± CO_2); and 3) type-III vapor-rich inclusions (± CO_2?). Type-I is the most abundant fluid inclusion type. Homogenization temperatures (T_h) determined on type-I inclusions range from 211°C to 276°C, with most of the temperatures measured between 245°C and 250°C with an average calculated salinity of 1.6 wt.% NaCl equivalent. Fluid inclusion pressure determinations were calculated based on volumetric properties and homogenization temperatures of the type-I fluid inclusions. The estimated minimum trapping pressures range between 1711-2007 bars.

The results indicate a complex origin for the Lemarchant barites. Sulfur isotope data suggests derivation of sulfur from the mixing of VMS-hydrothermal fluids with Cambrian seawater sulfate. However, the Sr isotope values are lower than mid-Cambrian seawater $^{87}Sr/^{86}Sr$, which suggests that some of the Sr was derived from underlying Neoproterozoic basement. Calculated isochores from homogenization temperatures and pressures recorded by fluid inclusions in the bladed barite are consistent with regional metamorphic conditions that are recorded for the Tally Pond group. These results illustrate that the fluid inclusions represent regional metamorphic conditions and reequilibration, rather than primary signatures. Moreover, fluid inclusion analyses illustrate that while barite may preserve original textures akin to modern barite, the fluid inclusion results are reset and do not reflect primary conditions of formation.

2.2 - Introduction

Barite is a common gangue mineral in both ancient and modern volcanogenic massive sulfide (VMS) deposits (e.g. Hannington and Scott, 1988; Hannington et al., 1991, 1995; Sharpe, 1991; Sherlock et al., 1999; Scotney et al., 2005). Despite the significant number of barite-bearing VMS deposits, multidisciplinary field and micro-analytical studies of hydrothermal barite have only recently been undertaken (e.g. Safina et al., 2015; Jamieson et al., 2016). The current model for the formation of hydrothermal sulfate-sulfide mounds involves mixing of ascending hot hydrothermal fluids with cold ambient seawater (Eldridge et al., 1983; Goldfarb et al., 1983; Ohmoto et al., 1983; Ohmoto, 1996). Barite ($BaSO_4$) in VMS deposits typically precipitates during the early low-temperature growth stage of a hydrothermal mound when Ba-rich hydrothermal fluids mix with seawater - the primary source of SO_4^{2+}, usually forming the outer carapace of the ore mound (Blount, 1977; Hanor, 2000; Hannington and Scott, 1988; Griffith and Paytan, 2012) but can also occur in high temperature venting zones within chimneys, where extensive mixing with seawater occurs (Hannington and Scott, 1988; Hannington et al., 1991). Due to the extremely low solubility of barite in seawater, barite preserves the geochemical signatures associated with the ore-forming conditions during VMS formation (Eldridge et al., 1983; Kusakabe and Chiba, 1983; Ohmoto et al., 1983; Watanabe and Sakai, 1983; Paytan et al., 1993; Averyt and Paytan, 2003). Thus, geochemical and isotopic signatures can provide insights into the origin and formation of barite and help broaden our understanding of the genesis of barite-rich VMS deposits. The lack of penetrative deformation and low grade metamorphism associated with the Lemarchant deposit also makes it a relatively pristine setting to study barite since primary mineralogical textures are well preserved (e.g., Gill et al., 2017).

The polymetallic Zn-Pb-Cu-Ag-Au-Ba Lemarchant deposit occurs within the Tally Pond group (~513-509 Ma; Evans et al., 1990; Dunning et al., 1991; Evans and Kean, 2002; Pollock et al., 2002), part of the Victoria Lake supergroup (informal) in central Newfoundland, Canada. The Tally Pond group comprises Cambrian island-arc volcanic rocks predominantly composed of felsic volcaniclastic rocks intercalated with mafic volcanic and sedimentary rocks that formed in the Iapetus Ocean (Evans et al., 1990; Dunning et al., 1991; Evans and Kean, 2002; Pollock et al., 2002; Pollock, 2004; Rogers et al., 2006). The Tally Pond group represents vestiges of Cambrian arc in the Exploits subzone in the Canadian Appalachians and is host to several other VMS deposits such as the past-producing Duck Pond and Boundary deposits (combined resources of 4.08 Mt @ 3.29% Cu, 5.68% Zn, 0.9% Pb, 59.3 g/t Ag, 0.9 g/t Au; Wagner, 1993; Squires et al., 2001; Evans and Kean, 2002; Squires and Moore, 2004; Piercey et al., 2014; Buschette and Piercey, 2016).

The Lemarchant deposit is hosted primarily in felsic to intermediate flows and volcaniclastic rocks like other deposits in the Tally Pond group, but has a complex mineral assemblage consisting of sulfides, sulfosalts, and precious metal phases, all intimately associated with barite, features not common in the Duck Pond or Boundary deposits (Copeland et al., 2008; Fraser et al., 2012; Gill and Piercey, 2014; Gill, 2015; Gill et al., 2015, 2017). The mineralization is similar to Kuroko-type VMS deposits; however, the deposit contains mineral assemblages typically belonging to an intermediate sulfidation epithermal suite of minerals (e.g. tetrahedrite, electrum, colusite, bornite, and covellite).

The latter minerals and elements likely reflect potential magmatic fluid contributions to the Lemarchant VMS deposits (Gill and Piercey, 2014; Gill et al., 2013, 2014, 2015, 2017; Gill, 2015).

Given the intimate relationship between barite and the mineralization at Lemarchant, the investigation of its genesis is critical for obtaining a full understanding of the mineralizing conditions. Despite the presence of barite in the Lemarchant deposit, the detailed relationships to mineralization, textural variations, and genesis are not well understood. Herein, results of integrated deposit-scale study of barite that included drill core logging, petrography, mineral chemistry, stable ($\delta^{34}S$) and radiogenic ($^{87}Sr/^{86}Sr$) isotope geochemistry, and fluid inclusion thermometry will be discussed and interpreted. These data provide new insight into the conditions of formation and the sources of fluids and metals in the Lemarchant deposit. These results will not only have an impact on understanding of the genesis of the Lemarchant deposit, but other barite-associated VMS deposits globally.

2.3 - Regional geology and metallogenic framework

The Newfoundland Appalachians consist of a collage of intra-oceanic, peri-continental, and continental blocks that were assembled together between the Cambrian and Permian (van Staal, 2007; Zagorevski et al., 2007; van Staal and Barr, 2012). The Newfoundland Appalachians are divided into four tectonostratigraphic zones (Williams, 1979; Swinden, 1988, 1991; Williams et al., 1988; Hibbard et al., 2004; van Staal, 2007;

van Staal and Barr, 2012) and from west to east comprise the Humber, Dunnage, Gander, and Avalon zones (Fig. 2-1a).

The Dunnage zone, also termed the Central Mobile Belt, is host to most of the VMS deposits in the Appalachians and some of the largest and highest grade VMS deposits in the world, including the past producing Bathurst mining camp in New Brunswick (Goodfellow et al., 2003) and Buchans mining camp in Newfoundland (Thurlow, 2010). The Dunnage zone represents vestiges of Cambro-Ordovician arc, back-arc, and ophiolitic rocks that formed in the Iapetus Ocean and is further subdivided into peri-Laurentian and peri-Gondwanan subzones; the Notre Dame and Exploits subzone, respectively (Swinden et al., 1989; Swinden, 1991; Evans and Kean, 2002; Rogers and van Staal, 2002; Rogers et al., 2006, 2007; van Staal, 2007; van Staal and Barr, 2012). The Red Indian Line is a major suture zone that separates these two subzones (Williams et al., 1988; Williams, 1995; Colman-Sadd et al., 1992; van Staal et al., 1998; Evans and Kean, 2002; Rogers et al., 2006, 2007; van Staal, 2007). The Exploits subzone, located east of the Red Indian Line, is composed primarily of bimodal Cambro-Ordovician volcanic and sedimentary rocks that formed along the margin of western Gondwana (Neuman, 1984; Colman-Sadd et al., 1992; van Staal, 1998; Zagorevski et al., 2007). The Lemarchant deposit is located within the peri-Gondwana Exploits subzone.

The Victoria Lake Group (Kean, 1977) constitutes part of the Exploits subzone and was later informally renamed the Victoria Lake supergroup (Evans et al., 1990; Evan and Kean, 2002; Rogers and van Staal, 2002) to better characterize the composite nature of the rock packages. The Victoria Lake supergroup includes all pre-Caradocian volcanic and sedimentary rocks located between the Red Indian Line to the northwest and the Noel Pauls

Line to the southeast (Kean, 1977; Evans and Kean, 2002; Rogers and van Staal, 2002; Fig. 2-1b). The Victoria Lake supergroup has been subdivided into six fault-bounding packages based on detailed bedrock mapping, stratigraphy, geochronology, and geochemistry (van Staal et al., 2005; Rogers et al., 2006; Zagorevski et al., 2007; Zagorevski et al., 2010; Piercey et al., 2014). From east to west, these are: the Tally Pond group (~513–509 Ma; Dunning et al., 1991; Pollock, 2004); the Long Lake Group (~511-506 Ma; Zagorevski et al., 2007; Hinchey, 2014); the Tulks Group (~498–487 Ma; Evans et al., 1990; Evans and Kean, 2002); the Sutherlands Pond Group (~462 Ma; Dunning et al., 1987); and the Pats Pond and Wigwam Brook groups (~488 and ~453 Ma, respectively; Zagorevski et al., 2007).

The Tally Pond group is host to the Lemarchant VMS deposit and the past producing Boundary and Duck Pond deposits (Fig. 2-1b, c). The group consists of a linear belt dominated by submarine felsic volcanic rocks and lesser amounts of mafic volcanic and sedimentary rocks (Swinden and Thorpe, 1984; Pollock and Wilton, 2001; Kean and Evans, 2002; Squires and Moore, 2004; Rogers et al., 2006; Piercey and Hinchey, 2012). The Lake Ambrose and the Bindons Pond formations are two informal units that comprise the Tally Pond group (Rogers et al., 2006).

The Lake Ambrose formation is dominantly mafic and composed of massive to pillowed basalt, volcaniclastic rocks (andesite and minor tuff), and minor sedimentary rocks (Kean and Evans, 1986; Evans and Kean, 2002; Rogers and van Staal, 2002; Rogers et al., 2006). In contrast, the Bindons Pond formation is felsic-dominated (dacite to rhyolite) and constitutes aphyric to massive or flow banded dacite and rhyolite, felsic tuff and breccia, volcaniclastic and clastic sedimentary rocks, and minor mafic flows (Kean and

Evans, 1986; Evans and Kean, 2002; Rogers and van Staal, 2002; Rogers et al., 2006). Regionally, the Lake Ambrose formation (~513 Ma; McNicoll et al., 2010) is stratigraphically below the Bindons formation (~509 Ma; McNicoll et al., 2010); however, at the Lemarchant deposit, the rocks of the Lake Ambrose formation are tectonically overlying the rocks of the Bindons formation (Copeland, 2008).

Previous lithogeochemical studies (Swinden et al., 1989; Dunning et al., 1991; Pollock and Wilton, 2001; Evans and Kean, 2002) have determined that the Tally Pond volcanic rocks in the area of Duck Pond and Lemarchant deposits are bimodal and exhibit arc-like affinities. Lithogeochemical data of Bindons formation rocks near the Boundary deposit have immobile element signatures that agree with the model of Zagorevski et al. (2010) in which the felsic rocks formed within an extensional peri-continental rift due to melting of the base of arc crust during rifting (Piercey et al., 2014; Buschette and Piercey, 2016; Cloutier et al., 2017).

Post-mineralization deformation created a series of east-west trending faults and a major north-trending, gently west dipping thrust fault (the Lemarchant fault) that offset sections of the Lemarchant deposit, creating repeated volcanic and mineralized sequences (e.g. Northwest zone) (Cloutier et al., 2017). The similarity between the massive sulfide horizons in the Northwest and the Main zones, as well as evidence of stratigraphic continuity in many drill holes, may indicate that these deposit-scale faults, mainly the Lemarchant fault, caused stacking of mineralized and barren volcanic strata (Squires and Moore, 2004; Copeland et al., 2008; Fraser et al., 2012; Cloutier et al., 2017).

Crosscutting felsic intrusions are also present in the Tally Pond group. The Lemarchant microgranite, a poorly exposed quartz-monzonite to granite, is located approximately 500 m northeast of the Lemarchant alteration zone. Geochemical similarities suggest that the Lemarchant microgranite is a co-genetic subvolcanic intrusion related to the Tally Pond group volcanic rocks that host the Lemarchant deposit (Squires and Moore, 2004). Quartz-feldspar porphyry dykes and sills are also regionally abundant (McNicoll et al., 2010). Younger mafic intrusive rocks, ranging from diabase to coarse-grained gabbro, are abundant in the Tally Pond group and likely coeval with the Harpoon Hill Gabbro (~465 ± 1 Ma; Pollock, 2004).

The entire belt is overprinted with Silurian-Devonian age greenschist metamorphism and east-northeast striking faults and minor regional folds (Dunning et al., 1991; Evans and Kean, 2002; Rogers et al., 2006).

2.4 - Deposit geology

The Lemarchant deposit is hosted within a tectonically juxtaposed bimodal volcanic sequence now exposed in an eroded upright anticline (Squires et al., 2001; Pollock and Wilton, 2001; Fraser et al., 2012; Cloutier et al., 2017; Fig. 2-2). In the Lemarchant area, the deposit footwall consists of moderate to strongly altered andesite-dacite volcanic rocks that hosts stringer-style mineralization. The altered andesite/dacite unit ranges up to 30-50 m below the mineralized zone and gradually grades into a less altered volcanic unit at depth; this entire unit is up to 250 m-thick (*sequence 1 and 2*) (Cloutier et al., 2017). Rocks immediately below mineralization are bimodal in composition, where the base of the sequence is dominated by andesite sequences grading into dacitic sequences towards the top (*sequence 3*) (Cloutier et al., 2017). The sequence consists of poorly sorted monomictic breccia, a texture and lithofacies commonly associated with a vent proximal depositional setting (McPhie et al., 1993; Allen, 1996; Gibson et al., 1999). Veinlets of sphalerite, chalcopyrite, quartz, carbonate, and chlorite cross-cut the monomictic breccia. The hanging wall is predominantly comprised of massive to pillowed submarine mafic rocks and basaltic andesite (*sequence 4*) (Cloutier et al., 2017). The basalt and mafic rocks are fine grained, green to grey in colour, and locally contain hyaloclastic flow-top breccia. Euhedral pyrite and carbonate/chlorite filled amygdales are common within these mafic rocks. The hangingwall mafic rocks are relatively unaltered and barren of mineralization. The mineralized horizon occurs at the contact between the unaltered hanging wall (*sequence 4*) and the altered footwall (*sequence 3*) and consists massive sulfide mineralization immediately overlain by a pyritic to graphitic mudstone layer (Fig. 2-3, 2-4, and 2-5).

Two main mineralized sections exist at the Lemarchant deposit (Lemarchant Main Zone and the Northwest Zone), and three other target zones (North, South, and the 24 Zones) (Fig. 2-2). The Lemarchant fault repeats the host-rock and displaced part of the main sulfide lens (Copeland et al., 2008; Fraser et al., 2012; Cloutier et al., 2017). The Main and Northwest zones are both hosted in the Bindon Ponds formation felsic volcanics and separated by a complex structural zone. Structural investigations led Cloutier et al. (2017) to suggest that the Main and Northwest zones represent two separate mineralized lens that were superimposed during post-deformation events, likely during the Penobscot orogeny (486-487 Ma), and not a single massive sulfide lens that was displaced by the Lemarchant fault as first proposed by Fraser et al. (2012). Despite post-mineralization deformation, the stratigraphy is well preserved and contains abundant primary volcanic textures (Cloutier et al., 2017). In general, mineralization within the Lemarchant Main Zone consists of a precious metal-rich barite outer zone grading into a Pb-Zn semi-massive to massive sulfide-rich zone and a stringer zone composed predominantly of chalcopyrite and pyrite with decreased base and precious-metal grades below the massive sulfides (Gill et al., 2013, 2014, 2015; Gill and Piercey, 2014; Gill, 2015; Gill et al., 2017) The Main Zone of the Lemarchant deposit contains indicated resources of 1.24 Mt at 5.38% Zn, 0.58% Cu, 1.19% Pb, 1.01 g/t Au, and 59.17 g/t Ag with inferred resources of 1.34 Mt at 3.70% Zn, 0.41% Cu, 0.86% Pb, 1.00 g/t Au, and 50.41 g/t Ag (Fraser et al., 2012). The Northwest Zone, discovered in 2013, does not have a documented resource. Mineral zonation at the Lemarchant deposit is archetypal of bimodal felsic Kuroko style mineralization (Eldridge et al., 1983; Ohmoto, 1996; Fraser et al., 2012, Gill and Piercey, 2014; Gill et al., 2015).

The mineralization has a complex paragenesis (Fig. 2-6) that reflects varying contributions from leaching of metals from the substrate and a potential magmatic fluid contribution of metals to the deposit (Gill et al., 2017). Gill et al. (2017) showed that the mineralization has five distinct sulfide mineral assemblages that precipitated in three stages. The barite in the upper stratiform zone is intergrown with low-Fe sphalerite, galena, and trace chalcopyrite (*stage 1*). The metals precipitated in *stage 1* were interpreted to be transported by low temperature (200-300°C), oxidized hydrothermal fluids (Gill et al., 2015, 2017). The deposit also contains abundant sulfosalts and Cu-rich phases (i.e., bornite, tetrahedrite, covellite, colusite, and electrum) and enrichments in epithermal suite elements (i.e., As, Bi, Cr, Co, In, Mo, Ni, Sb, Se, Te, Au), particularly in the upper parts of the mineralized lens associated with bladed barite (*stage 2*) (Gill et al., 2015, 2017). Precious metal enrichment and the presence of epithermal-suite elements observed at the Lemarchant deposit formed at relatively low temperatures (150-250°C) and shallow water depths (< 1500 mbsl). Intermittent boiling events contributed to the enrichment of precious metals during *stage 2* mineralization (Gill et al., 2015, 2017). Mineral assemblages associated with stages 1 and 2 are crosscut by higher temperature mineral assemblages (> 300°C) that include Fe-rich sphalerite, chalcopyrite and pyrite and form the basal stringer sulfide zone (*stage 3*) (Gill et al., 2015, 2017).

A thin, exhalative mudstone layer immediately overlies the mineralization at the Lemarchant deposit and is typically interlayered with hanging wall mafic volcanic flows (Fraser et al., 2012; Lode et al., 2015, 2016). Pyrite, pyrrhotite are the main sulfide minerals in this exhalative unit; however, chalcopyrite, sphalerite, galena, arsenopyrite, marcasite, and graphite are also present. The sulfides within the mudstone are also spatially associated with barite and barium-bearing minerals (Lode et al., 2015). Sulfides occur parallel to bedding or in cross-cutting late stage veins and associated with euhedral pyrite, white to bladed barite, and precious-metals (Lode et al., 2015).

Both felsic and mafic dykes cross-cut the Lemarchant deposit. There are two types of mafic dykes. The first type is light beige-brown, fine-grained to aphanitic synvolcanic dykes with carbonate and/or chlorite filled amygdales, whereas the second type is a medium-grained gabbro that cross-cuts the first intrusive type. The second type of mafic dykes are geochemical equivalents of the Harpoon Hill Gabbro (Pollock, 2004; Squires and Moore, 2004). The felsic dykes are white to pink and generally aphyric with small (~1-2mm) carbonate-filled amygdales.

Alteration in the Lemarchant deposit is consistent with typical Kuroko-type alteration (Eldridge et al., 1983; Ohmoto et al., 1983; Ohmoto, 1996). Quartz and sericite alteration are widespread in the felsic-dominated footwall and within the mineralized zone and chlorite alteration occurs locally. A zone of intense black chlorite alteration is regularly found below the massive sulfide lenses. The alteration in the mafic-dominated hangingwall consists of silica-epidote-Mn-carbonate. Quartz-carbonate vein networks are abundant throughout the deposit and often contain Fe-carbonate, and surrounding wall rocks are locally altered to Fe-carbonate.

2.5 - Petrographic and microtextural features of barite

Boreholes containing barite units were logged to document textural and mineralogical relationships (see Appendix 1 for full log descriptions and sample locations). Samples were selected based on texture and mineralogical relationships for thin sections (43) and subsequent analytical work. Thin sections were studied using standard reflected and transmitted light microscopy and scanning electron microscopy (SEM); SEM was utilized for documentation of unknown mineral phases and precious-metal phases. An FEI Quanta 650 SEM equipped with a field emission gun and silicon drift detectors was utilized for collection of both back-scatter electron images, and semi-quantitative elemental maps derived from energy dispersive X-ray spectra (EDS) were processed using Bruker Espirit software (v. 1.9).

2.5.1 Barite mineralization

Barite is spatially associated with massive sulfides at Lemarchant and barite-rich layers range between 1.7 - 30.4 meters thick (Fraser et al., 2012). Various generations of barite were difficult to distinguish because no geochemical divisions (e.g. major element composition, REE geochemistry, S and Sr isotope) can be made between barite textures associated with distinct mineral assemblages (e.g. Fig. 2-9 and 2-13). Additionally, trace element geochemistry (REE) of barite textures are comparable between both types of barite, making the geochemical distinction of barite phases difficult. Therefore, barite types were separated according to their texture (granular and bladed barite) and their association with mineralization type.

Barite is generally granular, medium- to fine-grained and dark grey-blue in colour. Granular barite is commonly associated with white to honey sphalerite, pyrite, galena, and minor chalcopyrite and tetrahedrite-tennantite (i.e, type 1 mineralization- *stage 1* of Gill et al., 2015) (Fig. 2-7a, b). Bladed/tabular barite occurs as euhedral blades (up to 0.5 cm in size) that are associated with a fine grained, granular baritic matrix and bornite, chalcopyrite, tetrahedrite-tennantite, galena, pyrite, and electrum (i.e., type 2A and type 2B-*stage 2* of Gill et al., 2015) (Fig. 2-7c, d, e). The contacts between the granular and bladed barite section are typically sharp and irregular to locally gradational (Fig. 2-7e). Barite also occurs in thin (~1 cm) veins that crosscut the granular barite in the upper mineralized lens (Fig. 2-7a). Both granular and bladed barite are cross-cut by honey brown to red sphalerite, pyrite, galena and chalcopyrite of type 3 mineralization (*stage 3*-Gill et al., 2015) (Fig. 2-7f). Barite-rich veins are generally composed of large interlocking euhedral to subhedral grains with chalcopyrite, galena, and pyrite of type 3 mineralization often accompanying these late stage veins. Semi-continuous layers and secondary barite veinlets are also within mudstone above the massive sulfides (Fig. 2-7g) (Lode et al., 2015). Barite also occurs in fractures and interstitial spaces in the quartz altered footwall volcanic rocks associated with chalcopyrite, pyrite, honey brown to orange sphalerite, and galena stringers (type 4 mineralization- *stage 3* of Gill et al., 2015; Fig. 2-7h). Barite and carbonate nodules (up to 3 cm in size) are rare but occur locally within massive sulfide units.

Barite is also associated with other Ba-rich phases in the baritic-massive sulfide lens. Celsian ($BaAl_2Si_2O_8$) is commonly associated with alteration minerals such as albite and phlogopite usually near barite crystals in the mineralized lens. Hyalophane ($(K,Ba)Al(Si,Al)_3O_8$) and witherite ($BaCO_3$) are also present with barite in the mudstones above mineralization (Lode et al., 2015).

In thin section, barite textures range from small granular (1-50 µm) crystals to large (up to 0.5 cm in size) tabular barite laths. Radial aggregates ("rosettes") of barite and plumose textured barite are also present (Fig. 2-8a, b). Large tabular barite crystals are generally hosted in granular barite or in a dolomitic matrix (Fig. 2-8c). Small, rounded barite crystals in interstitial spaces between tabular barite laths are common (Fig. 2-8d).

In zones of well-formed crystalline tabular barite, sulfides are present in minor amounts and generally occur along barite grain boundaries or in interstitial spaces (Fig. 2-8e and f). Growth zones are locally visible in tabular barite and are usually denoted by abundant fluid inclusions that often contain sulfide micro-inclusions (<10 µm) (Fig. 2-8g); fluid inclusions are absent in granular barite. In zones of high sulfide content, barite generally occurs as small (~1-100 µm), rounded and fractured grains (i.e. groundmass) (Fig. 2-8h).

Paragenetically, massive granular barite was the first barite to crystallize and is associated with precipitation of pyrite, sphalerite, galena, and minor chalcopyrite (i.e. type 1 mineralization; Gill et al., 2015). This was immediately followed by the bladed/tabular barite associated with tetrahedrite-tennantite, pyrite, galena, and electrum of type 2A and 2B mineral assemblage. Small, rounded barite crystals that fill interstitial spaces between larger tabular barite appear later than the tabular laths and granular massive barite.

Nevertheless, the interstitial barite crystals may also represent recrystallized phases of earlier granular barite. All the above barite types are cut by barite-rich veins associated with type 3 mineralization. Finally, granular barite associated with high temperature type 4 mineralization in the footwall stringer zone is the youngest phase paragenetically.

2.6 - Mineral chemistry

2.6.1 Analytical methods

Electron microprobe analyser (EMPA): Major element concentrations of individual barite crystals were determined by electron microprobe analysis (EMPA). Twenty one thin sections were analyzed for ten elements (Ba, S, Sr, Na, Si, Ca, K, Fe, Zn, Pb, F) on different barite textures using a five-spectrometer JEOL JXA-8230 electron microprobe at Memorial University of Newfoundland. The analyses were conducted at an accelerating voltage of 15 kV and intensity of 20 nA using a spot size of 1 µm. The X-ray takeoff angle was 40 degrees. Count times for elements varied between 10-30 seconds with off-peak count times set to equal half the peak count times. Element concentrations were determined using LIF, PET, and TAP crystals. Natural and synthetic mineral phases were used as calibration standards. The following standards and lines were used: SPI synthetic compound group $BaSO_4$ (BaLα on LIF), and then the Astimex mineral suite, including: pyrite (SKα on PET), celestite (SrKα on PET), albite (NaKα, SiKα on TAP), bustamite (CaKα on PET), orthoclase (KKα on PET), almandine garnet (FeKα on LIF), willemite (ZnKα on LIF), and galena (PbKα on PET). Quality control was maintained by using a secondary standard (BaF_2; obtained from SPI Supplies®). The secondary standard was measured at the beginning and end of each round and the measured values were in compliance with the accepted concentrations in this standard. Major element precision was generally better than 1% (1σ); however, precision was reduced for minor elements. The analytical totals were accepted if they fell within a range of 100 ± 1.5 wt. %.

Laser ablation quadrupole ICP-MS: 14 of the 21 barite samples analyzed by EMPA were analyzed for trace elements using a ThermoFisher™ X-series 2 quadrupole ICP-MS coupled to a ESI™ NWR-193nm Excimer laser system at Queen's Facility for Isotope Research (QFIR), Kingston, Ontario, Canada. Thin section samples containing different barite textures and standards were affixed in the laser chamber using mounting putty. Barite crystals were ablated at 100% power using a repetition rate of 20 Hz and focused laser beam of 50 µm. Gas blanks were analysed for 30s between each sample analysis. The ablation speed was 5 µm/s with a fluence of ~5 J/cm^2. USGS glass standards (GSC-1G, GSD-1G, and GSE-1G; Jochum et al., 2005) were used as external calibration at the beginning and end of every round and the measured values were in compliance with the accepted concentrations in this standard. The K-0253 standard glass (SPI Supplies®) was used as a reference material for Ba at the beginning and end of each run and the BHVO-2G standard (Jochum et al., 2005) was used as an unknown once every ten sample analysis to monitor instrument drift, correct for changes in element ionization, and assess data quality. Quantitative results were obtained through external calibration and normalisation of each analysis to Sr contents of the barites as determined by electron-probe analysis. The whole suite of trace elements was measured using the quadrupole-ICP-MS.

High-resolution ICP-MS: To eliminate or reduce the effect of interferences due to mass overlap, trace element data were also collected using a Finnigan MAT Element ICP-MS and Thermo Scientfic 2 XR high-resolution instrument coupled to a ESI™ NWR-

193nm Excimer laser system at QFIR. High resolution ICP-MS was used following quadrupole ICP-MS analyses. Laser parameters for HR-ICP-MS analyses were identical to the parameters used for quadrupole-ICP-MS analysis. The ablated material was carried to the high-resolution mass spectrometer using ultra-high purity helium at a daily optimized flow rate of approximately 1 L/min. The sample gas flow rate (~0.9 L/min) was optimized daily for sensitivity and reduction of oxide generation. Similar to quadrupole ICP-MS analysis, a standard bracketing approach was used to monitor instrument drift and correct for changes in element ionization. USGS glass standards (GSC-1G, GSD-1G, and GSE-1G) as well as the NIST 612 glass and NIST 610 standard glass were used for external calibration at the beginning and end of every run and BHVO-2G was analysed as an unknown every ~10 samples.

Measured isotopes by HR-ICP-MS were: ^{134}Ba, ^{135}Ba, ^{138}Ba, ^{139}La, ^{140}Ce, ^{141}Pr, ^{143}Nd, ^{145}Nd, ^{147}Sm, ^{149}Sm, ^{151}Eu, ^{153}Eu, ^{155}Gd, ^{157}Gd, ^{159}Tb, ^{161}Dy, ^{163}Dy, ^{165}Ho, ^{166}Er, ^{167}Er, ^{169}Tm, ^{172}Yb, ^{173}Yb, ^{175}Lu, ^{197}Au, and ^{209}Bi.

2.6.2 Results

Major element (Ba, Sr, Na, and Ca) concentrations for the 21 analyzed samples (n = 514) are shown in Fig. 2-9 (see appendix 3.4 for complete results) with average concentrations listed in Table 2-1. Barite shows little variations in major element composition ($Ba_{0.95-0.99}$, $Sr_{0.01-0.04}$, $Na_{0.01}$, $Ca_{0.00-0.01}$)SO_4 and is stoichiometric regardless of texture. Barium and S contents in barite vary from 59.66-67.97 wt.% (avg. 64.49 wt.%) and 33.50-36.05 wt.% (avg. 34.77 wt.%), respectively. Strontium is the most abundant minor element in barite and averages 0.96 wt.%, but varies between 0.02 wt.% and 4.78 wt.%, and exhibits a negative, moderate correlation (R^2=0.5388) with Ba. This negative trend suggests that Sr^{2+} substitutes for Ba^{2+} in barite, and corresponds to the solid solution between barite and celestine ($SrSO_4$) (Hanor, 2000; Zhu, 2004; Monnin and Cividini, 2006). Barite contains trace amounts of Na and Ca, averaging 0.16 wt.% and 0.02 wt.%, respectively, but shows very poor correlations with Ba content.

Average trace element concentrations analyzed by laser ablation on bladed and granular barite samples are reported in Table 2-2 (see Appendix 4.1 for results for all analyzed elements). Plots of selected elements concentrations, including epithermal-suite elements, for both bladed and granular barite are illustrated in Fig. 2-10. In general, the results from laser ablation analyses indicate that barite contains low amounts of trace elements that are at or below detection (e.g., Sc, Co, Ni, Ge, In, Bi, and Te). However, some elements are well correlated (Fig. 2-11). For example, Sb, As, Ag, and Au are well correlated in bladed barite (r=0.77-0.93) (Fig. 2-11a, b, c, d, e). Granular barite also exhibits strong positive correlation between As, Sb, and Ag (r=0.9) (Fig. 2-11d, e) and locally contains enrichments of Mo, As, Ag, and Sb (Fig. 2-10). However, concentrations of these elements in granular barite are much lower compared to bladed barite. Additionally, Ga, Mo, Hg, Tl, and V are moderately well correlated in bladed barite (r=0.71-0.85) compared to granular barite ($r \leq 0.5$) (Fig. 2-11f, g, h, i, j, k). It is likely that these enrichments and correlations do not reflect trace elements within the lattice of barite, but represent sulfide/sulfosalt inclusions as detected by SEM (e.g., Fig. 2-12 and Fig. 2-14 e, f, g, h).

2.7 - Bulk rock analyses

2.7.1 Sampling and analytical methods

Whole-rock geochemistry: Whole-rock lithogeochemistry was measured on ten barite samples that contain a mixture of barite textures (bladed and granular). The samples were selected to represent a good spatial coverage of the Lemarchant deposit. These same barite samples were used for Sr isotope analyses. The selected core samples containing barite were crushed and sieved to < 80µm. Bulk samples were analysed for major, trace, and rare earth elements (REE) at Activation Laboratories in Ancaster, Ontario, Canada. Samples were fused using lithium metaborate/tetraborate and subsequently dissolved in HNO_3 and then analyzed by ICP-MS. Lithogeochemistry on these samples was measured prior to Sr isotope analyses to determine Sr and Rb concentrations.

Whole-rock Sr isotopes ($^{87}Sr/^{86}Sr$): Whole-rock Sr isotope ($^{87}Sr/^{86}Sr$) compositions of crushed barite samples that contained mixed textures (bladed and granular) were acquired using a standard step leaching process to eliminate impurities. Approximately 50 mg of crushed barite was placed in 15 mL beakers and 7N HNO_3 was added to cover each sample. The beakers were taken off the hot plate after a couple of hours and left covered for two days to allow the samples to settle to the bottom. The acid was pipetted from each beaker and this process was repeated three times. The samples were left on a hot plate to ensure that barite samples were dry and no more HNO_3 remained. Each sample was then submersed in 6N HCl^-, covered, and subsequently placed on hot plates at 100°C for three days. The 6N HCl^- was pipetted from the beakers and the barite samples were left to dry overnight. Approximately 1.5 mL of 2.5N HCl^- was added to each beaker and the samples were left covered for two days. After leaching procedures, the samples were run through Sr resin columns to isolate the strontium from the barite.

Whole-rock strontium isotope ($^{87}Sr/^{86}Sr$) compositions were determined on the samples using a Finningan MAT 262V thermal ionization mass spectrometer (TIMS) in dynamic mode at Memorial University of Newfoundland, Canada. Instrumental mass fractionation of Sr isotopes was corrected using a Rayleigh law relative to $^{88}Sr/^{86}Sr$ = 8.375209. The reported $^{87}Sr/^{86}Sr$ ratios are corrected for the deviation from repeated duplicates of NBS 987 standard ($^{87}Sr/^{86}Sr$ = 0.710240, Veizer et al., 1999). Replicates of the standard give an average of $^{87}Sr/^{86}Sr$ = 0.710245 ± 11 (n=23).

Sulfur isotopes. 23 barite samples were analyzed for sulfur isotope geochemistry: (1) granular purple-grey barite (associated with *stage 1* mineralization; n=5), and (2) bladed white barite (associated with *stage 2* mineralization; n=18) from the various zones of the deposit (see above). For each sample, barite was drilled out using a hand-held micro-drill. The micro-drill was cleaned with acetone between each sample to eliminate sample contamination. Approximately 0.35 mg of drilled mineral separate was used for analysis, with analyses undertaken on a Finnigan MAT252 isotope ratio mass spectrometer (IRMS) at Memorial University of Newfoundland, Canada. Stable isotope results are reported in standard (δ) notation as per mil (‰) relative to the Vienna Canyon Diablo Troilite (V-CDT), with an analytical uncertainty of ± 0.4 ‰ (1σ) (*Alison Pye, pers comm, 2016*). Duplicate analyses during the course of the study illustrated that samples have maximum internal variations of <0.85‰.

2.7.2 Results

Lemarchant barite samples have abundant Sr, and minimal Rb (Table 2-3 and Appendix 2). The high Sr, coupled with low Rb, indicates that the Sr measured isotope ratios are similar to those at the time of formation and do not require age correction for decay of ^{87}Rb. The barite exhibits a narrow range of $^{87}Sr/^{86}Sr$ ratios ranging from 0.706993 ± 10 to 0.707510 ± 16 (Table 2-4 and Fig. 2-13).

Measured ($\delta^{34}S$) compositions of 5 granular barite and 18 bladed barite samples within different mineralized zones from the Lemarchant deposit are listed in Table 2-5. Sulfur isotopic compositions are reported in Fig. 2-13 and display a relatively narrow range from 24.7 to 28.7‰, with an average isotope composition of 27.1‰. The measured $\delta^{34}S$ compositions of bladed barite samples show a slightly higher range (25.7 to 28.7‰) than for massive/granular barite (24.7 to 27.8‰). Despite these differences, the average measured $\delta^{34}S$ composition for barite within the Northwest zone, Main zone, and 24 zone are very similar and within error (27‰, 27.1‰, and 27.3‰, respectively).

2.8 - Fluid inclusion microthermometry

2.8.1 Analytical methods

Four samples were analyzed for fluid inclusion microthermometry. The selected samples covered both the Main zone and Northwest zone of the Lemarchant deposit. All the studied fluid inclusions are in bladed barite hosted within the massive sulfide lenses, including one barite vein, and were selected based on their well-preserved fluid inclusions assemblages (FIAs) and their abundance. Samples were prepared as ~100 μm doubly-polished thin sections mounted with acetone-soluble glue (cyanoacrylate). Prior to microthermometric measurements, a detailed petrographic examination of the samples was completed to determine FIAs and the types of fluid inclusions. Samples were examined using a petrographic microscope, starting at low magnification to document their distribution, size, and origin, and then proceeding to higher magnification to identify phase relations. The polished thick sections were removed from the glass backing prior to heating and freezing experiments by immersing the samples overnight in acetone. The general method for heating/freezing experiments is described elsewhere (e.g. Roedder, 1984; Shepherd et al., 1985). Measurements were completed at Memorial University of Newfoundland, Canada, using a Linkam THMSG600 heating freezing stage mounted on an Olympus BX51 microscope equipped for use with reflected, transmitted, and infrared light. Fluid inclusion images were captured using an Olympus BX51 camera. The accuracy and precision of measurements was insured by calibration against the triple point of CO_2 (-56.6 ± 0.1 °C), freezing point of water (0.0 ± 0.1 °C), and critical point of water (374.6 ± 0.5 °C) using SYNFLINC® synthetic fluid inclusions. Barite is particularly susceptible to leakage and necking-down processes (Ulrich and Bodnar, 1988); therefore, fluid inclusions near cracks or showing necking-down or leakage were not analyzed.

Salinities of aqueous-carbonic fluid inclusions were calculated using the *Q2* program within the software package CLATHRATES (Bakker et al., 1996; Bakker, 1997, 1998). Salinities were calculated for all inclusions that contain a coexisting liquid and vapor gas phase (CO_2) using the temperature of clathrate melting. Pressure (bars) for fluid inclusion assemblages were calculated using the *Q2* program within the software package Loner15 and calculated from homogenization temperatures of aqueous carbonic inclusion assemblages (Bakker, 1997, 2003; Bakker and Brown, 2003). Isochores for type-I fluid inclusion assemblages were calculated using the FLUIDS software package and the equation of state reported by Anderko and Pitzer (1993) and Duan et al. (1995). Bulk fluid compositions calculated from the Loner15 software and homogenization temperatures of the FIA were used to calculate the isochores on a P-T diagram.

2.8.2 Results

2.8.2.1 Petrography

Fluid inclusion assemblages were analysed in bladed barite from samples CNF31723, CNF31860, CNF31865, and CNF31874 (drill holes: LM13-73, LM11-68, LM14-96, and LM13-82, respectively) and within a vein composed entirely of barite from sample CNF31723.

Three types of fluid inclusion assemblages that appear to be in primary growth zones in barite (type-I, -II, and -III) are recognized at room temperature including (in order of decreasing abundance):

I. three-phase immiscible liquid inclusions (L_1+L_2 ± V) characterized by the presence of two immiscible liquids, one aqueous and the other liquid CO_2 occurring as a thin meniscus surrounding the vapour bubble (~20-40 vol. %) (Fig. 2-14a, b). The inclusions are <1 µm to ~30 µm and are equant to oblate. The term aqueous-carbonic is typically used to describe these immiscible liquid inclusions (Roedder and Coombs, 1967; Roedder, 1984; Van den Kerkhof and Thiery, 2001);

II. two-phase, liquid (L)-rich, containing liquid water plus a water (± CO_2) vapor bubble of approximately 40-60 vol.%. The inclusions are irregular to equant in shape; and

III. vapor (V)-rich (80-100 vol. %) (±CO_2).

Abundant fluid inclusion assemblages in bladed barite occur as clouds away from crystal edges and within primary growth zones of the host crystal (Fig. 2-14c, d). Pseudosecondary inclusions, while less common than primary inclusions, cross-cut growth zones; however, the inclusion trails do not cut across all growth zones of the host mineral. Captured sulfide inclusions (i.e. tetrahedrite-tennantite, pyrite, galena, electrum) of type 2B mineralization (e.g. Gill, 2015) are found within what appears to be in primary and pseudo-secondary fluid inclusion trails in bladed barite crystals (Fig. 2-14e, f, respectively). Secondary fluid inclusion assemblages are less common than primary inclusions and occur as trails cross-cutting all growth zones of the host mineral. Only fluid inclusions belonging to primary assemblages were analyzed.

Type-I inclusions are by far the most abundant (i.e. 75-95% of the inclusions observed) and present in both bladed barite and the barite vein. Type-II inclusions comprise 5-25% of the observed fluid inclusion assemblages and are present in bladed barite and occur together with aqueous-carbonic inclusions (type-I). Type-III inclusions are very rare (< 2%) and most are decrepitated inclusions.

2.8.2.2 Thermometric measurements

Microthermometric measurements of fluid inclusions in bladed barite from the Lemarchant deposit are listed in Table 2-6. The aqueous carbonic inclusions (type-I) were cooled to below -100 °C to trigger solidification and slowly heated until melting of the carbonic phase occurred. Upon heating, the initial melting temperatures of the carbonic phase ($T_m(CO_2)$) (n = 11) occurred between -56.0 and -59.2 °C (average: -56.6 °C), which is close to the experimental CO_2 melting point (-56.6 °C). Final melting temperatures

(T_m(clath)) of the clathrates of type-I inclusions range from 7.1 °C to 10.5 °C (n = 27). The average salinity of the aqueous carbonic inclusions within both the bladed and vein barite is 1.6 wt.% NaCl equivalent (Fig. 2-15a), which is lower than seawater values (3.2 wt. % NaCl equivalent: Bischoff and Rosenbauer, 1985; Bodnar and Vityk, 1994). Upon further heating, the temperature of homogenization of CO_2 into the liquid state (T_hCO_2) (n = 8) for aqueous carbonic inclusions occurred between 27.7°C and 31°C (average: 30.04°C), comparable to the critical point of pure CO_2 at +31.1°C (Fig. 2-15b).

Final homogenization temperatures (T_h(total)) of type-I inclusions in both bladed and vein barite (n = 23) occurred at temperatures between 211°C and 276°C, with most of the temperatures measured between 245°C and 250°C (Fig. 2-15c).

First ice melting temperatures (Tm(ice)) measured for type-II inclusions occurred between -4°C to 1°C (n = 4). Although measurements of final homogenization temperatures (T_h(total)) of type-II inclusions are less abundant than measurements on type-I inclusions, the final homogenization temperatures are lower and range from 198°C to 216°C (n=3) (Fig. 2-15c).

Final homogenization temperatures (T_h(total)) for type-III inclusions could not be determined since all the inclusions were decrepitated. Although type-III inclusions are difficult to distinguish from decrepitated or leaked inclusions, CO_2 was detected in a small number of vapour-rich inclusions from initial melting temperatures (T_{mi}) (-56°C; n = 1) and final melting temperatures (T_m) of the clathrate (7.8°C - 10.3°C; n = 3).

2.8.2.3 Pressure trapping conditions

Pressure calculations were constrained to aqueous-carbonic inclusions of type-I inclusions and calculated for each fluid inclusion assemblage (calculated using the program CLATHRATES). The results are listed in Table 2-7. Microthermometric data were used to calculate fluid densities of 22.14 to 24.17 cc/ml and xCO_2 of 0.08 to 0.13 for type-I inclusions. These data were used to estimate minimum trapping pressures and the results range between 1711.2 bars to 2006.9 bars, which corresponds to depths of ~6 to 7.5 km. Thus, the calculated minimum trapping pressures and depths of type-I inclusions are much higher than would be expected for typical VMS formation environments (i.e. >1500 m below sea-level for Kuroko-type VMS deposits; Monecke et al., 2014).

2.9 - Discussion

2.9.1 Mineral chemical variations

Barite crystals show little geochemical variations in both granular and bladed barite, and most trace element contents are near the limits of detection for both EMPA and LA-ICP-MS. Strontium is the most abundant trace element in barite and concentrations can reach up to 4.78 wt.% SrO, although bulk chemical analyses with minor sulfides indicate much lower Sr contents (<1 wt.% Sr; Table 2-3); however, bulk rock Sr is likely diluted by sulfides and trapped silicate minerals. The SrO contents of Lemarchant barite are similar to those found in modern hydrothermal deposits. For example, SrO contents vary from 0.6-3.5 wt.% in barite from the Franklin Seamount, Papua New Guinea (Binns et al., 1993); 0-17.8 wt.% (av. 7 wt.%) in barite from the Endeavour Segment, Juan de Fuca Ridge (Jamieson et al. 2016); and up to 4.4 wt.% in barite Axial Seamount, Juan de Fuca Ridge

(Hannington and Scott, 1988). The Sr contents of barite in ancient VMS deposits are also variable (i.e., 0-2 wt.%, Hellyer deposit, Australia - Sharpe, 1991; up to 4.73 wt.%, Saf'yanovka, Central Urals - Safina et al., 2015). Similarities in ionic radii, charge, and electronegativity between Ba^{2+} and Sr^{2+} create a complete solid solution between barite ($BaSO_4$) and celestite ($SrSO_4$) (Sabine and Young, 1954; Boström et al., 1967). The variation in SrO is attributed to this solid-solution series and varying Sr substitution for Ba in the barite structure. The range of SrO contents for barite was initially thought to represent fluctuations in fluid chemistry during genesis or the high degree of mixing between ambient seawater and hydrothermal fluids (Farrell, 1978; Kalogeropoulos and Scott, 1983, 1989; Farrell and Holland, 1983; Hannington and Scott, 1988). However, Jamieson et al. (2016) suggested that the Sr-partitioning in barite is attributed to temperature fluctuations and that Sr substitution is independent of fluid mixing.

The substitution of other cations such as Ca^{2+} and Na^{+} is controlled by the degree of similarities in charge, ionic radius, and electronegativity to Ba^{2+} and Sr^{2+}. The incorporation of Ca^{2+} in barite is influenced by many kinetic parameters such as temperature, pressure, growth rate, competing complexation reactions, and saturation state (Jones et al., 2004; Griffith et al., 2008). Barite from the Lemarchant deposit contains trace amounts of CaO, with concentrations up to 0.73 wt.% (av. 0.02 wt. %). Due to the instability of anhydrite ($CaSO_4$) at ambient seafloor conditions, barite may replace anhydrite in hydrothermal systems and forms a more restricted or incomplete solid solution between barite and anhydrite ($BaSO_4$-$CaSO_4$) (Hanor, 2000; Griffith and Paytan, 2012). Despite this incomplete solid-solution, the low concentrations of CaO, the lack of correlation between BaO *vs* CaO wt.%, and the absence of anhydrite in the Lemarchant deposit suggests that the dominant source of Ca in Lemarchant barite was not derived from the partial replacement of anhydrite.

Calcium isotope studies of Holocene marine samples show that modern barite are isotopically homogeneous across all major ocean basins, which suggests that the likely source of Ca is seawater (Griffith et al., 2008). However, the Ca isotopic compositions of barite from hydrothermal chimneys on the Juan de Fuca Ridge are more depleted and isotopically distinct from marine barite. The Ca sources during barite precipitation can include several potential endmembers, such as hydrothermal fluids (Amini et al., 2008), seawater (Hippler et al., 2003), and cold seep fluids (Teichert et al., 2005). Calcium substitution is influenced by partitioning processes (e.g. temperature, saturation state, ionic strength, and other factors), despite an incomplete understanding of how such processes influence Ca^{2+} substitution (Griffith et al., 2008). It is highly unlikely that cold seep fluids are a source of Ca in the Lemarchant barite given its association with hydrothermal fluid activity. Furthermore, current models for VMS-associated barite, and the results herein, suggest that mixing of seawater and hydrothermal fluids are the main mechanism for barite precipitation and that these two reservoirs were the likely source of Ca in the Lemarchant barite. At this point it is not possible to discriminate between these two sources of Ca.

The incorporation of Na^+ in hydrothermal barite is still not fully understood, particularly in ancient massive sulfide deposits. However, measured Na^+ compositions of vent fluids from the PACMANUS hydrothermal field (av. 417 mmol/kg) are similar to the measured concentration of Na^+ of the ambient bottom seawater (471 mmol/kg) (Reeves et al., 2011). Similarly, the measured Na compositions of seafloor hydrothermal solutions from the Galapagos Spreading Center (av. 378 mmol/kg), 21°N East Spreading Ridge (av.

456 mmol/kg), Guaymas Basin (av. 487 mmol/kg), Southern Juan de Fuca Ridge (747 mmol/kg), 11-13°N East Spreading Ridge (av. 519 mmol/kg), Mid-Atlantic Ridge (av. 534 mmol/kg), and Axial Volcano (av. 358 mmol/kg) are also similar to the measured Na^+ concentrations of seawater (464 mmol/kg) (von Damm, 1990). Therefore, akin to Ca^{2+}, the substitution of Na^+ in the barite lattice may also be derived from the mixture of seawater and hydrothermal fluids. Nevertheless, Na concentrations in hydrothermal fluids can vary significantly in individual deposits, or in different vents within a single hydrothermal system (e.g. Axial Seamount; Butterfield et al., 1990) by the process of boiling or supercritical phase separation.

In contrast to the uncertain provenance of Ca and Na, the enrichment of Ag, Sb, and Au in bladed barite compared to granular barite is directly related to micro-inclusions of electrum, galena, sphalerite, and tetrahedrite-tennantite. Although electrum inclusions were not observed via reflected light petrography and SEM, the high content of Au (up to ~400 ppm) in some bladed barite suggests the presence of electrum micro-inclusions in selected samples (i.e. CNF31860). The strong correlation and localized peaks of Ga-Mo-Hg-Tl-V are attributed to pyrite inclusions within bladed barite as these elements are enriched in pyrite grains from the stage 2 mineralization (Gill, 2015; Gill et al., 2017).

Petrographic observations of these bladed barite samples show that the sulfide inclusions are found within fluid inclusions, usually along growth zones or in pseudo-secondary fluid inclusion trails (Fig. 2-14f, g, h). It is suggested that the sulfide inclusions were "captured" mineral phases, and were solid phases suspended in the ore-forming fluid that were trapped in the inclusions, rather than daughter minerals. This is attributed to the fact that only selected samples have these features, rather than uniformly present in all bladed barite.

2.9.2 *Sulfur sources*

Sulfur in VMS deposits can come from a variety of sources, including leaching of basement rocks, seawater sulfate, and in some cases, magmatic fluids (Ohmoto and Rye, 1979; Sakai et al., 1984; Janecky and Shanks, 1988; Halbach et al., 1989; Rye, 1993; de Ronde, 1995; Hannington et al., 1995; Herzig et al., 1998; Shanks, 2001; de Ronde et al., 2005; Seal, 2006). To determine the source of sulfur in barite in VMS deposits, the isotopic composition of sulfate in hydrothermal fluids and seawater must be determined. Using analyses of $\delta^{34}S$ values of barite from the Kuroko deposit, Ohmoto et al. (1983) used chemical modeling to estimate the proportion of sulfate (ΣSO_4^{-2}) in ore-forming fluids relative to modern seawater. Their calculations for hydrothermal fluids ($T_{hydrothermal\ fluid}$ = 250 °C) suggested that the concentration of sulfate in hydrothermal fluids was much lower than the concentration of sulfate (ΣSO_4^{-2}) in modern seawater. Negligible sulfate concentrations in hydrothermal fluids have been observed in many modern hydrothermal vent systems (e.g. Butterfield et al. 1990, 1997; Reeves et al. 2011). Many authors have shown that when plotted against dissolved Mg, SO_4 concentrations approach a value of zero for end-member hydrothermal fluids (von Damm, 1985; Seyfried and Ding, 1995). The low concentration of sulfate in the exolved hydrothermal fluids is attributed to the removal of sulfate in the downwelling fluids from the precipitation of anhydrite in and around the subseafloor reaction zone (Bischoff and Seyfried, 1978). Anhydrite is not directly observed in the Lemarchant deposit due to the retrograde solubility of the mineral.

Assuming that the Lemarchant deposit formed under similar hydrothermal fluid conditions as modern seafloor systems (e.g., Gill et al., 2017), it can be presumed that the hydrothermal fluids also contained low concentrations of sulfate. Moreover, while there were variations in seawater sulfate concentrations in the Phanerozoic (Berner, 2004), the concentration of seawater sulfate is much higher than sulfate in hydrothermal fluids as explained above (e.g. von Damm, 1985). Correspondingly, it is likely that hydrothermal sulfate was not an important contributor to the sulfate budget of barite in the Lemarchant deposit.

Most workers argue that seawater sulfate is the main source of sulfate in VMS-associated sulfate minerals (Huston et al., 1999; Seal et al., 2000), while in some relatively rare instances sulfate from magmatic fluids, often from condensed SO_2, can result in sulfate minerals (e.g., Rye, 1993; Huston et al., 2011). The $\delta^{34}S$ isotope data for both granular and bladed barite in the Lemarchant deposit are very consistent (Table 2.5; Fig. 2-13), overlapping the values for Cambrian seawater sulfate (Sangster, 1968; Claypool et al., 1980; Ohmoto and Goldhaber, 1997; Huston, 1999; Seal, 2006), and similar to the sulfur isotope values in barite from other Cambro-Ordovician VMS deposits globally (e.g. 25-28 ‰, Barite Hill deposit, South Carolina - Seal et al., 2001; 22.5-24.8 ‰, Buchans deposit, Newfoundland - Kowalik et al., 1981; and 27.6-32.4 ‰, Mt. Windsor deposit, Australia - Hill, 1996). In contrast, sulfates formed from magmatic SO_2, can result in complex sulfate-sulfide relationships with highly variable $\delta^{34}S$ in sulfates due to sulfur partitioning between H_2S-bearing phases and SO_4-bearing phases during SO_2 disproportionation (e.g., Rye, 1993; Seal, 2006). Whereas more positive $\delta^{34}S$ sulfate can form during this process (e.g., Rye, 1993, 2005; Seal, 2006), the homogeneity of the $\delta^{34}S$ signature in the Lemarchant barite, coincident with the remarkably similar $\delta^{34}S$ for Cambrian seawater, all argue that seawater sulfate was the main source of S in the Lemarchant barites. Existing models for barite formation also support that they formed via the mixing of Ba-rich hydrothermal fluids with SO_4-rich seawater.

Despite a lack of magmatic sulfur contributions, it is important to note that the barite crystals are intimately associated with epithermal suite element-enriched sulfide mineral assemblages, which may reflect a magmatic fluid addition to the hydrothermal system (e.g., Gill et al., 2017). The coincidence of epithermal suite minerals, accompanied by a lack of a magmatic S isotope signature, suggests that any magmatic contribution was likely swamped by seawater SO_4 due to the size of this reservoir relative to the magmatic S reservoir. Extensive mixing between seawater and rising hydrothermal fluids may have also masked any magmatic S isotope signature (Herzig et al., 1998).

Given that these barites represent mid-Cambrian seawater sulfate, and that barite has a low solubility, these values also provide a pin for the composition of seawater sulfate within the Iapetus Ocean at this time, and are similar to global Cambrian seawater sulfate $\delta^{34}S$ values (e.g., Sangster, 1968; Claypool et al., 1980; Ohmoto and Goldhaber, 1997, Huston et al., 1999; Seal et al., 2000; Seal, 2006).

2.9.3 Strontium sources

The Sr isotopic composition of barite is used to constrain the source of ore-forming fluids that formed the barite, given that Sr substitutes for Ba (Paytan et al., 1993). Whole-rock lithogeochemical data (Table 2-3) show that barite is enriched in Sr with minimal Rb, eliminating the requirement for age correction of $^{87}Sr/^{86}Sr$ ratios; therefore, current day $^{87}Sr/^{86}Sr$ ratios represent the fluid from which the barite precipitated.

In VMS deposits, the potential sources of Sr include seawater, crustal basement (i.e. high $^{87}Sr/^{86}Sr$ sources), and mantle-derived mafic crust (i.e. low $^{87}Sr/^{86}Sr$ sources) (Griffith and Paytan, 2012). Strontium isotopic studies of carbonate rocks have shown that the $^{87}Sr/^{86}Sr$ of Cambrian seawater is ≈ 0.7090 (Burke et al., 1982; Derry et al., 1989, 1994; Asmerom et al., 1991; Montañez et al., 1996; Denison et al., 1998). While Cambrian seawater $^{87}Sr/^{86}Sr$ is well known, deciphering hydrothermal to magmatic/hydrothermal signatures is more problematic. In modern systems, ridge-dominated hydrothermal signatures have Sr isotopic signatures similar to underlying basaltic crust ($^{87}Sr/^{86}Sr$ ~0.7030-0.7035; Albarède et al., 1981; Ayuso and Schulz, 2003; Griffith and Paytan, 2012), and fluids in the Cambrian that equilibrated with Sr from such sources would inherit similar signatures (i.e., like mid-Cambrian mantle; $^{87}Sr/^{86}Sr$ ≈ 0.7025-0.7030; Ayuso and Schulz, 2003; see calculations in Appendix 6.3). In contrast, fluids that equilibrated with more crustal material would have higher $^{87}Sr/^{86}Sr$ values, similar to the isotopic signatures of the underlying crust (e.g., $^{87}Sr/^{86}Sr$ of upper crust at 510 Ma ≈ 0.7104; see calculations in Appendix 6.3).

The Sr isotopic compositions of Lemarchant barite are consistent with $^{87}Sr/^{86}Sr$ = 0.7069-0.7075, which itself is much lower than the $^{87}Sr/^{86}Sr$ values (~0.7090) of Cambrian seawater (Burke et al., 1982; Derry et al., 1989, 1994; Asmerom et al., 1991; Montañez et al., 1996; Denison et al., 1998), thus requiring a more juvenile Sr source with lower $^{87}Sr/^{86}Sr$ values. While there are no direct Sr isotopic constraints on the basement beneath the Tally Pond group, the Nd isotopic compositions of Tally Pond group and underlying

Neoproterozoic basement rocks (Rogers et al., 2006), Pb isotopic compositions of sulfides (Gill et al., 2015), and inherited zircon U-Pb ages (McNicoll et al., 2010), are consistent with the Cambrian Tally Pond arc being built on young continental crust. An estimation of the initial $^{87}Sr/^{86}Sr$ ratios of mid-Cambrian upper continental crust (~0.7104) provides a representation of the isotopic characteristics of the continental component; however, this value is too high to explain the low $^{87}Sr/^{86}Sr$ in the barite and thus the low Sr values cannot be derived from continental crust. In contrast, given the abundance of mantle-derived basaltic materials within the underlying Sandy Brook group with only weakly evolved Nd isotopic signatures, it would be reasonable to assume that the Sr isotope signature of this unit was somewhere between mantle-like values (i.e., $^{87}Sr/^{86}Sr$ ~ 0.7025-0.7030; Albarède et al., 1981; Ayuso and Schulz, 2003; Griffith and Paytan, 2012) and normal upper crust ($^{87}Sr/^{86}Sr$ ~0.7100; Griffith and Paytan, 2012). Thus, the $^{87}Sr/^{86}Sr$ values lower than Cambrian seawater suggest that at least some of the Sr present in the barite was derived from the basalt-rich, Neoproterozoic crust of the Sandy Brook group.

The interpretation of Sr isotopic data herein is consistent with existing models for Sr sources in barite in modern and ancient VMS deposits, where numerous workers have illustrated that much of the Sr in barite was derived from older crustal basement (e.g. Whitford et al., 1992; Marchev et al., 2002; Ayuso and Schulz, 2003). These results also illustrate the decoupling of isotopic systems in barite, where some materials are derived predominantly from basement sources (i.e., Sr), whereas others are derived predominantly from seawater (i.e., S), consistent with seawater-hydrothermal fluid mixing models for barite genesis (von Damm, 1990; Hannington et al., 2005; Griffith and Paytan, 2012). In particular, the Sr and S isotopic data are consistent with a mixing model where hydrothermal fluids leached Ba and Sr from the underlying basement and were mixed with SO_4 derived from Cambrian seawater.

Since seawater contains high concentrations of Sr and very low to no Ba, and that hydrothermal fluids contain high concentrations of both Sr and Ba, many studies of modern massive sulfide systems have used Sr/Ba ratio to determine the degree of mixing between seawater and the ore-forming fluids to form barite (Farrell, 1978; Kalogeropoulos and Scott, 1983, 1989; Farrell and Holland, 1983; Hannington and Scott, 1988). Shikazono et al. (2012) and Sasaki and Minato (1983) link Sr partitioning in barite to higher degrees of supersaturation and rapid crystal growth. However, the lack of correlation between Sr/Ba ratios and apparent partition coefficients in modern barite samples from the Endeavour Segment in the Juan de Fuca Ridge show that fluid mixing, hence fluctuations in fluid composition, is not a primary control on Sr partitioning (Jamieson et al., 2016). Additionally, the lack of variations in $^{87}Sr/^{86}Sr$ values across Sr-rich zones and Sr-poor zones from the Endeavour Segment further supports the interpretation that Sr partitioning is not controlled by fluid mixing, but is controlled by changes in conductive cooling in the vent chimney walls and higher degrees of supersaturation (Jamieson et al., 2016).

To further test the thermal control on Sr concentration hypothesis, the relative contribution of hydrothermal fluids to the Sr budget of the Lemarchant barite during mixing with seawater was calculated using geochemical data of a modern massive sulfide system. The PACMANUS hydrothermal system was chosen as a modern analogue due to its similar geological setting (e.g., continental back-arc rift), host rocks (e.g., felsic volcanic rocks), mineral assemblages (e.g. precious metals and sulfosalt enrichments), and potential magmatic fluid influence (e.g., Yang and Scott, 1996; Reeves et al., 2011 vs. Cloutier et al., 2017, Gill et al., 2015, 2017). A two-component mixing model can be utilized using Sr isotopes to model the relative input of hydrothermal fluids: (Mills et al., 1998):

$$\% \, HF = 100 \times \frac{[\mathrm{Sr}]_{SW}\left[({}^{87}\mathrm{Sr}/{}^{86}\mathrm{Sr})_{SW} - ({}^{87}\mathrm{Sr}/{}^{86}\mathrm{Sr})_{M}\right]}{[\mathrm{Sr}]_{SW}[({}^{87}\mathrm{Sr}/{}^{86}\mathrm{Sr})_{SW} - ({}^{87}\mathrm{Sr}/{}^{86}\mathrm{Sr})_{M}] + [\mathrm{Sr}]_{HF}[({}^{87}\mathrm{Sr}/{}^{86}\mathrm{Sr})_{M} - ({}^{87}\mathrm{Sr}/{}^{86}\mathrm{Sr})_{HF}]} \quad (1)$$

where % HF is the proportion of hydrothermal fluid and the subscripts SW, M, and HF refer for Sr concentrations and $^{87}Sr/^{86}Sr$ ratios values of these in seawater, measured values (in barite), and hydrothermal fluids, respectively. Strontium concentrations $[Sr]_{HF}$ and Sr isotope compositions $(^{87}Sr/^{86}Sr)_{HF}$ of vent fluids were assumed to be similar to vent fluid samples from the modern PACMANUS hydrothermal field (Table 2-8; Reeves et al., 2011).

Using the equation above, relative hydrothermal fluid contribution for Lemarchant barite range between 37% to 51% (av. 45%) (Table 2-4). The consistency of Sr- and S-isotopic data in barite from Lemarchant, and the lack of correlation between Sr/Ba ratios and calculated relative contribution hydrothermal fluids (Fig. 2-16), support an interpretation that Sr substitution in barite was not controlled by fluctuations in fluid composition/mixing during precipitation. Rather, Sr substitution in barite was likely controlled by temperature variations caused by conductive cooling within chimney walls (Jamieson et al., 2016). Moreover, the paragenesis, the mineral assemblages, and the sulfide geochemistry that define the Lemarchant deposit reflect changes into the physicochemical conditions of metal transport (Gill et al., 2015, 2017), and further support the model that temperature fluctuations may have contributed to the variable substitution of Sr in barite.

2.9.4 *Nature and origin of CO_2-rich fluid inclusions*

Three types of fluid inclusions were identified in bladed barite from the massive sulfide lenses: 1) type-I aqueous carbonic; 2) type-II aqueous two-phase (± CO_2); and 3) type-III vapor-rich inclusions (± CO_2?). All inclusion assemblages appear to be in primary growth zones, with aqueous carbonic fluids being the most abundant type in bladed barite, with low salinities (avg. 1.6 wt.% $NaCl_{equiv}$) and homogenization temperatures ($T_{\underline{h}}$) between 198-280°C. Pressure estimates for the type-I fluid inclusion are between 1.7 to 2.0 kbars (~6.4 to 7.2 km depth). Most modern massive sulfides at ridges occur below 1500 m water depth and in backarc basins most VMS are at depths of ~1500 to 2000 m, at pressures of 150 to 200 bars (Monecke et al., 2014). Thus, the pressure estimates from the inclusions are inconsistent with the depths typical of seafloor VMS systems. Additionally, fluid inclusion studies in VMS deposits are commonly two-phase, with salinities near seawater values (2-6 wt.% $NaCl_{equiv}$), with low CO_2 (Bodnar, 2014). Although homogenization temperatures for fluid inclusions at Lemarchant are within the range of VMS mineralization (i.e. ~100 - 300°C), the extremely low salinity and high density of them are more like fluid inclusions found in deposits in metamorphic terranes (Bodnar, 2014).

The homogenization temperatures recorded in type-I fluid inclusions represent minimum trapping conditions. By using $T_{\underline{h}}$ and pressure data calculated from type-I inclusions, we can extrapolate the possible conditions of trapping through isochoric trajectories on a P-T plot in an H_2O-rich isopleth of the CO_2-H_2O system (Fig. 2-17) (Diamond, 2003). The calculated isochores based on our data show that the trapping conditions for aqueous-carbonic FI in bladed barite fall within the greenschist facies metamorphic field. Although the carbonic-rich fluid inclusions in barite from the Lemarchant deposit are well preserved and show no significant evidence of textural change from deformation and metamorphism, the anomalous calculated pressures suggest that fluid diffusion occurred during post-VMS (i.e., Silurian to Devonian) tectonism. The measured and calculated trapping conditions of the carbonic-rich inclusion are consistent with previous workers who have demonstrated that barite is particularly susceptible to stretching and leaking (Ulrich and Bodnar, 1988). The fluid inclusion assemblages in bladed barite in the Lemarchant deposit are therefore classified as secondary fluid inclusions. Hence, despite textural preservation, it is likely that the Lemarchant fluid inclusions leaked and/or may have been refilled by a younger metamorphism-related overprinting fluid event(s).

Regionally, three-phase carbonic-rich fluid inclusions similar to those observed in the Lemarchant deposit have been recorded in both the Midas Pond (Evans, 1990) and Valentine Lake deposits (*James Conliffe, unpublished data*) in the Victoria Lake supergroup. Boulanger et al. (2010) recorded similar carbonic-rich fluid inclusions in the primary ore in the Ming deposit in northeast Newfoundland, which they interpret to be secondary and related to the circulation of CO_2-rich fluids during regional metamorphism. These observations suggest that circulation of regional CO_2-rich metamorphic fluids did occur within the Victoria Lake supergroup and it is highly likely that they overprinted primary fluid inclusion assemblages.

The association of CO_2-rich fluids with later orogenic Au activity leads to the possibility that Au-enrichment in the Lemarchant deposit was due to a post-VMS orogenic overprint. This is unlikely for a number of reasons. Firstly, Au-enrichment is restricted to the Lemarchant deposit and not found in any rocks outside the immediate massive sulfide mineralization (i.e., Au does not extend along faults outside the massive sulfide horizon, nor is it present in quartz veins *vis-à-vis* orogenic Au regionally). Secondly, the mineralization has distinctive intermediate- to high-sulfidation epithermal suite minerals, including precious metals (tetrahedrite-group minerals, bornite, covellite, electrum, and sulfosalts) and enrichments of epithermal-suite elements in sulfosalt-rich assemblages, interpreted to be syngenetic and derived from magmatic fluids (Gill et al., 2017), features notably absent in orogenic Au deposits regionally (e.g., Evans, 1990). Finally, the alteration assemblages associated with Au in the Lemarchant deposit are generally Fe-carbonate poor, and are typical of global VMS deposits, and unlike those in orogenic Au deposits of the Newfoundland Appalachians and globally (Evans and Wilson, 1994; Groves et al., 1998; McCuaig and Kerrich, 1998; Ramezani et al., 2000; Goldfarb et al., 2001).

2.10 - Conclusion

Barite in the Lemarchant VMS deposit is intimately associated with mineralization, distinctive textures, and unique sulfide mineral assemblages. Granular barite is generally associated with all types of mineralization; however, bladed textured barite is associated with sulfosalt- and precious metal-enriched mineral assemblages with enrichments in Sb-Ag-As-Au and Ga-Mo-Hg-Tl-V. In certain samples of bladed barite there are micro-inclusions of sulfide minerals in pseudo-secondary fluid inclusion trails. It is suggested that the sulfide inclusions were “captured” mineral phases, and were solid phases suspended in the ore-forming fluid that were accidentally trapped in the inclusions, rather than daughter minerals. Barite geochemistry show little variations and is stoichiometric, although strontium concentrations vary in both granular and bladed barite showing a negative correlation with barium. The variable substitution of Sr in barite is likely controlled by temperature fluctuations within the paleo-chimney walls rather than fluid mixing. The contamination of Na and Ca is presumably from the mixing of seawater and hydrothermal fluids during barite precipitation. Barite generally contains low amounts of trace elements that are at or below detection limits by EMPA, LA-ICP-MS, and LA-HR-ICP-MS.

The S-isotope compositions of barite suggest that Cambrian seawater was the main source of sulfur, whereas Sr isotopes reflect mixing of seawater and ancient crustal sources, likely the underlying basement (Neoproterozoic Sandy Brook group). These data support a model where hydrothermal fluids leached Ba and Sr from the underlying basement and mixed with SO_4 in Cambrian seawater. Our results agree with other isotopic studies of host rocks and sulfides and the regional geology of the Tally Pond group.

Three types of fluid inclusions were identified in bladed barite: 1) type-I aqueous carbonic; 2) type-II aqueous two-phase (± CO_2); and 3) type-III vapor-rich inclusions (± CO_2?). All inclusions were observed in inclusion assemblages that appear to be in primary growth zones, with aqueous carbonic fluids being the most abundant type observed in bladed barite. Low salinities, high internal pressures, and high formation temperatures are characteristic of type-I inclusions in bladed barite. We suggest that the aqueous-carbonic inclusions in bladed barite are in fact secondary and are refilled primary inclusions with CO_2-rich metamorphic fluids during regional greenschist metamorphism.

2.11- Acknowledgments

This project was supported by an NSERC-Alexander Graham Bell Canada Graduate Scholarship. Additional funding was provided by the NSERC-Altius Industrial Research Chair in Mineral Deposits supported by NSERC, Altius Resources Inc., the Research and Development Corporation of Newfoundland and Labrador, and an NSERC Discovery Grant to S. J. Piercey. Access to the Lemarchant drill core, core logs, and assay database were provided by the Canadian Zinc Corporation. Many thanks to the following people for their help with analytical instruments: Evelyne Leduc (Queen’s University), Dr. Wanda Aylward, Sherri Strong, Matthew Crocker, and Dr. Dave Grant. A special thanks to Dr. Stefanie Brueckner for help with laser ablation data reduction.

2.12- References

Albarède, F., Michard, A., Minster, J., and Michard, G. (1981). $^{87}Sr/^{86}Sr$ ratios in hydrothermal waters and deposits from the East Pacific Rise at 21 N. Earth and Planetary Science Letters, 55: 229-236.

Allen, R. L., Lundstrom, I., Ripa, M., and Christofferson, H. (1996). Facies analysis of a 1.9 Ga, continental margin, back-arc, felsic caldera province with diverse Zn-Pb-Ag-(Cu-Au) sulfide and Fe-oxide deposits, Bergslagen region, Sweden. Economic Geology, 91: 979-1008.

Amini, M., Eisenhauer, A., Böhm, F., Fietzke, J., Bach, W., Garbe-Schönberg, D., ... and Hauff, F. (2008). Calcium isotope ($\delta^{44/40}Ca$) fractionation along hydrothermal pathways, Logatchev Field (Mid-Atlantic Ridge, 14 45′ N). Geochimica et Cosmochimica Acta, 72: 4107-4122.

Anderko, A., and Pitzer, K. S. (1993). Phase equilibria and volumetric properties of the systems KCl-H_2O and NaCl-KCl-H_2O above 573K: Equation of state representation. Geochimica et Cosmochimica Acta, 57: 4885-4897.

Anderson, A. (1975). Some basaltic and andesitic gases. Reviews of Geophysics, 13: 37-55.

Asmerom, Y., Jacobsen, S. B., Knoll, A. H., Butterfield, N. J., and Swett, K. (1991). Strontium isotopic variations of Neoproterozoic seawater: implications for crustal evolution. Geochimica et Cosmochimica Acta, 55: 2883-2894.

Averyt, K. B., and Paytan, A. (2003). Empirical partition coefficients for Sr and Ca in marine barite: Implications for reconstructing seawater Sr and Ca concentrations. Geochemistry, Geophysics, Geosystems, 4: 1043.

Ayuso, R. A., and Schulz, K. J. (2003). Nd-Pb-Sr isotope geochemistry and origin of the Ordovician Bald Mountain and Mount Chase massive sulfide deposits, northern Maine. Massive Sulfide Deposits of the Bathurst Mining Camp, New Brunswick, and Northern Maine. Economic Geology Monograph, 11: 611-630.

Bakker, R. J. (1997). Clathrates: Computer programs to calculate fluid inclusion V-X properties using clathrate melting temperatures. Computers and Geosciences, 23: 1-18.

Bakker, R. J. (1998). Improvements in clathrate modelling II: The H_2O-CO_2-CH_4-N_2-C_2H_6 fluid system. Geological Society, London, Special Publications, 137: 75-105.

Bakker, R. J., and Brown, P. E. (2003). Computer modelling in fluid inclusion research. Fluid inclusions*:* Analysis and interpretation, 32: 175-212.

Bakker, R. J., Dubessy, J., and Cathelineau, M. (1996). Improvements in clathrate modelling: I. the H_2O-CO_2 system with various salts. Geochimica Et Cosmochimica Acta, 60*:* 1657-1681.

Barbour, D., (1990). Valentine Lake Gold Deposit. *In* Swinden, H.S., Evans, D. T.W., and Kean, B. F., eds., Metallogenic framework of base and precious metal deposits, central and western Newfoundland. Geological Survey of Canada, Open File 2156: 73-77.

Barr, S., Raeside, R., and White, C. (1998). Geological correlations between Cape Breton Island and Newfoundland, northern Appalachian Orogen. Canadian Journal of Earth Sciences, 35: 1252-1270.

Berner, R. A. (2004). A model for calcium, magnesium and sulfate in seawater over Phanerozoic time. American Journal of Science, 304: 438-453.

Binns, R. A., Scott, S. D., Bogdanov, Y. A., Lisitzin, A. P., Gordeev, V. V., Gurvich, E. G., Finlayson, E. J., Dotter, L. E., Wheller, G. E., and Muravyev, K. G. (1993). Hydrothermal oxide and gold-rich sulfate deposits of Franklin Seamount, western Woodlark Basin, Papua New Guinea. Economic Geology, 88: 2122-2153.

Bischoff, J. L., and Rosenbauer, R. J. (1985). An empirical equation of state for hydrothermal seawater (3.2 percent $NaCl^-$). American Journal of Science, 285: 725-763.

Bischoff, J. L., & Seyfried, W. E. (1978). Hydrothermal chemistry of seawater from 25 degrees to 350 degrees C. American Journal of Science, 278: 838-860.

Blount, C. (1977). Barite solubilities and thermodynamic quantities up to 300/sup 0/C and 1400 bars. American Mineralogist, 62: 9-10.

Bodnar, R. J., and Vityk, M. O. (1994). Interpretation of microthermometric data for H_2O-NaCl fluid inclusions. Fluid inclusions in minerals: methods and applications, IMA Short Course: 117-130.

Bodnar, R. J., Lecumberri-Sanchez, P., Moncada, D., and Steele-MacInnis, M. (2014). 13.5—Fluid inclusions in hydrothermal ore deposits. Treatise on Geochemistry, Second Edition. Elsevier, Oxford: 119-142.

Boström, K., Frazer, J., and Blankenburg, J. (1967). Subsolidus phase relations and lattice constants in the system BaSO4-SrSO4-PbSO4. Arkiv Mineral Geol, 4: 477-485.

Buschette, M. J., and Piercey, S. J. (2016). Hydrothermal alteration and lithogeochemistry of the Boundary volcanogenic massive sulphide deposit, central Newfoundland, Canada. Canadian Journal of Earth Sciences, 53: 506-527.

Boulanger, R.A., Chi, G., Skulski, T., and Castonguay, S. (2010). Characterization and evolution of fluids associated with the Cu-Au deposit of the Ming Mine, Rambler area, northeast Newfoundland, Canada. GeoCanada 2010 – Working with the Earth: p. 5.

Burke, W., Denison, R., Hetherington, E., Koepnick, R., Nelson, H., and Otto, J. (1982). Variation of seawater $^{87}Sr/^{86}Sr$ throughout Phanerozoic time. Geology, 10: 516-519.

Butterfield, D. A., Jonasson, I. R., Massoth, G. J., Feely, R. A., Roe, K. K., Embley, R. E., ... & Delaney, J. R. (1997). Seafloor eruptions and evolution of hydrothermal fluid chemistry. Philosophical Transactions of the Royal Society of London A: Mathematical, Physical and Engineering Sciences, 355: 369-386.

Butterfield, D. A., Massoth, G. J., McDuff, R. E., Lupton, J. E., and Lilley, M. D. (1990). Geochemistry of hydrothermal fluids from Axial Seamount hydrothermal emissions study vent field, Juan de Fuca ridge: Subseafloor boiling and subsequent fluid-rock interaction. Journal of Geophysical Research: Solid Earth, 95: 12895-12921.

Carey, S., Nomikou, P., Bell, K. C., Lilley, M., Lupton, J., Roman, C., Stathopoulou, E., Bejelou, K., and Ballard, R. (2013). CO_2 degassing from hydrothermal vents at Kolumbo submarine volcano, Greece, and the accumulation of acidic crater water. Geology, 41: 1035-1038.

Claypool, G. E., Holser, W. T., Kaplan, I. R., Sakai, H., and Zak, I. (1980). The age curves of sulfur and oxygen isotopes in marine sulfate and their mutual interpretation. Chemical Geology, 28: 199-260.

Cloutier, J., Piercey, S. J., Lode, S., Guchte, M. V., and Copeland, D. A. (2017). Lithostratigraphic and structural reconstruction of the Zn-Pb-Cu-Ag-Au Lemarchant volcanogenic massive sulphide (VMS) deposit, Tally Pond group, central Newfoundland, Canada. Ore Geology Reviews, 84: 154-173.

Colman-Sadd, S. P., Dunning, G., and Dec, T. (1992). Dunnage-Gander relationships and Ordovician orogeny in central Newfoundland; a sediment provenance and U-Pb age study. American Journal of Science, 292: 317-355.

Copeland, D.A., Toole, R.M.S., and Piercey, S.J. (2008). Assessment report on diamond drilling and soil sampling, License 8183M (10^{th} year) and 9569M (5^{th} year) South Tally Pond property, Rogerson Lake area, Newfoundland and Labrador, NTS 12A/10 and 12A/07; Newfoundland and Labrador Geological Survey, Assessment Report, p. 956.

Denison, R. E., Koepnick, R. B., Burke, W. H., and Hetherington, E. A. (1998). Construction of the Cambrian and Ordovician seawater $^{87}Sr/^{86}Sr$ curve. Chemical Geology, 152: 325-340.

de Ronde, C. E. (1995). Fluid chemistry and isotopic characteristics of seafloor hydrothermal systems and associated VMS deposits: potential for magmatic contributions. Magmas, fluids, and ore deposits. Mineralogical Association of Canada, Short Course Series, 23: 479-509.

de Ronde, C. E., Massoth, G. J., Butterfield, D. A., Christenson, B. W., Ishibashi, J., Ditchburn, R. G., . . . and Kamenetsky, V. S. (2011). Submarine hydrothermal activity and gold-rich mineralization at Brothers volcano, Kermadec arc, New Zealand. Mineralium Deposita, 46: 541-584.

de Ronde, C. E., Hannington, M. D., Stoffers, P., Wright, I. C., Ditchburn, R. G., Reyes, A. G., ... and Greene, R. R. (2005). Evolution of a submarine magmatic-hydrothermal system: Brothers volcano, southern Kermadec arc, New Zealand. Economic Geology, 100: 1097-1133.

Derry, L. A., Brasier, M. D., Corfield, R. E. A., Rozanov, A. Y., and Zhuravlev, A. Y. (1994). Sr and C isotopes in Lower Cambrian carbonates from the Siberian craton: a paleoenvironmental record during the 'Cambrian explosion'. Earth and Planetary Science Letters, 128: 671-681.

Derry, L. A., Keto, L. S., Jacobsen, S. B., Knoll, A. H., and Swett, K. (1989). Sr isotopic variations in Upper Proterozoic carbonates from Svalbard and East Greenland. Geochimica et Cosmochimica Acta, 53: 2331-2339.

Diamond, L. W. (2003). Introduction to gas-bearing, aqueous fluid inclusions. Fluid Inclusions: Analysis and Interpretation, 32: 101-158.

Drummond, S., and Ohmoto, H. (1985). Chemical evolution and mineral deposition in boiling hydrothermal systems. Economic Geology, 80: 126-147.

Duan, Z., Møller, N., and Weare, J. H. (1995). Equation of state for the $NaCl-H_2O-CO_2$ system: prediction of phase equilibria and volumetric properties. Geochimica et Cosmochimica Acta, 59: 2869-2882.

Dunning, G. R., Kean, B. F., Thurlow, J. G., and Swinden, H. S. (1987). Geochronology of the Buchans, Roberts Arm, and Victoria Lake groups and Mansfield Cove Complex, Newfoundland. Canadian Journal of Earth Sciences, 24: 1175-1184.

Dunning, G. R., Swinden, H. S., Kean, B., Evans, D., and Jenner, G. (1991). A Cambrian island arc in Iapetus: Geochronology and geochemistry of the Lake Ambrose volcanic belt, Newfoundland Appalachians. Geological Magazine, 128: 1-17.

Eldridge, C. S., Barton, P., and Ohmoto, H. (1983). Mineral textures and their bearing on formation of the Kuroko orebodies. Economic Geology Monograph, 5: 241-281.

Elsgaard, L., Isaksen, M. F., Jørgensen, B. B., Alayse, A. M., and Jannasch, H. W. (1994). Microbial sulfate reduction in deep-sea sediments at the Guaymas Basin hydrothermal vent area: influence of temperature and substrates. Geochimica et Cosmochimica Acta, 58: 3335-3343.

Evans, D. T. W. (1993a). Gold mineralization of the eastern Dunnage Zone, central Newfoundland. Newfoundland Department of Mines, Mineral Development Division, Report, 93-1: 339-349.

Evans, D.T.W., (1993b). The Midas Pond gold prospect, Victoria Lake Group: geology, alteration and mineralization. Unpublished M.Sc. thesis. Memorial University of Newfoundland.

Evans, D.T.W., Kean, B.F., and Dunning, G.R. (1990). Geological studies, Victoria Lake supergroup, central Newfoundland. *In* Current Research. Newfoundland Department of Mines and Energy, Geological Survey Branch, Report 90-1, p. 131-144.

Evans, D., and Kean, B. (2002). The Victoria Lake supergroup, central Newfoundland-its definition, setting and volcanogenic massive sulphide mineralization. Newfoundland and Labrador Department of Mines and Energy, Geological Survey, Open File NFLD/2790, 68 pages.

Evans, D. T. W., and Wilson, M. R. (1994). Epigenetic gold occurrences in the eastern Dunnage Zone, Newfoundland: preliminary stable isotope results. Current Research. Newfoundland Department of Mines and Energy, Geological Survey, Report, 94-1.

Farrell, C. W., and Holland, H. D. (1983). Strontium isotope geochemistry of the Kuroko deposits. Economic Geology, Monograph, 5: 302-319.

Farrell, C., Holland, H., and Petersen, U. (1978). The isotopic composition of strontium in barites and anhydrites from Kuroko deposits. Mining Geology 28: 281-291.

Faure, G. (1986). Principles of isotope geochemistry. 2^{nd} ed. Wiley, New York, 589 pp.

Fouquet, Y., Von Stackelberg, U., Charlou, J. L., Donval, J. P., Erzinger, J., Foucher, J. P., ... and Whitechurch, H. (1991). Hydrothermal activity and metallogenesis in the Lau back-arc basin. Nature, 349: 778-781.

Fraser, D., Giroux, G.H., Copeland, D.A., and Devine, C.A. (2012). NI-43-101 technical report and mineral resource estimate on the Lemarchant deposit, South Tally Pond VMS project, central Newfoundland, Canada. Paragon Minerals Corporation.

Gamo, T., Sakai, H., Ishibashi, J., Nakayama, E., Isshiki, K., Matsuura, H., . . . and Ohta, S. (1993). Hydrothermal plumes in the eastern Manus Basin, Bismarck Sea: CH_4, Mn, Al and pH anomalies. Deep Sea Research Part I: Oceanographic Research Papers, 40*:* 2335-2349.

Gamo, T., Okamura, K., Charlou, J., Urabe, T., Auzende, J., Ishibashi, J., . . . and Chiba, H. (1997). Acidic and sulfate-rich hydrothermal fluids from the Manus back-arc Basin, Papua New Guinea. Geology, 25: 139-142.

Gibson, H.L., Morton, R.L., and Hudak, G.J. (1999), Submarine volcanic processes, deposits, and environments favorable for the location of volcanic-associated massive sulphide deposits. In: Barrie, C.T., Hannington, M.D. (Eds.), Volcanic-associated massive sulphide deposits: Progress and examples in modern and ancient settings. Reviews in Economic Geology 8: 13–51.

Gill, S.B. (2015). Mineralogy, metal zoning, and genesis of the Cambrian Zn-Pb-Cu-Ag-Au Lemarchant volcanogenic massive sulfide (VMS) deposit. Masters thesis, Memorial University of Newfoundland.

Gill, S.B. and Piercey, S. J. (2014). Preliminary observations on styles of mineralization and sulfide-mineral zonation in the Cambrian Zn-Pb-Cu-Ag-Au Lemarchant volcanogenic massive-sulfide deposit, Newfoundland and Labrador; Geological Survey of Canada, Current Research 2014-5, p. 17.

Gill, S.B., Piercey, S.J., and Devine, C.A. (2013). Preliminary mineralogy of barite associated sulphide mineralization in the Ordovician Zn-Pb-Cu-Ag-Au Lemarchant volcanogenic massive sulphide deposit, Newfoundland and Labrador. Geological Survey of Canada, Current Research, Report 2013–17, 15 p.

Gill, S.B., Piercey, S.J., and Layton-Matthews, D. (2017). Mineralogy and Metal Zoning of the Cambrian Zn-Pb-Cu-Ag-Au Lemarchant Volcanogenic Massive Sulfide (VMS) Deposit, Newfoundland. The Canadian Mineralogist; 54: 1307-1344.

Gill, S.B, Piercey, S., Layton-Matthews, D., Layne, G., and Piercey, G. (2015). Mineralogical, sulphur, and lead isotopic study of the Lemarchant Zn-Pb-Cu-Ag-Au-

VMS deposit: Implications for precious-metal enrichment processes in the VMS environment. Targeted Geoscience Initiative, 4: 183-195.

Goldfarb, M., Converse, D., Holland, H., and Edmond, J. (1983). The genesis of hot spring deposits on the East Pacific Rise, 21 N. Economic Geology, Monograph, 5, 184-197.

Goldfarb, R. J., Groves, D. I., and Gardoll, S. (2001). Orogenic gold and geologic time: a global synthesis. Ore geology reviews, 18: 1-75.

Goodfellow, W. D., Peter, J. M., Winchester, J. A., and van Staal, C. R. (2003). Ambient marine environment and sediment provenance during formation of massive sulfide deposits in the Bathurst Mining Camp: importance of reduced bottom waters to sulfide precipitation and preservation. Economic Geology Monograph, 11: 129-156.

Griffith, E. M., and Paytan, A. (2012). Barite in the ocean–occurrence, geochemistry and palaeoceanographic applications. Sedimentology, 59: 1817-1835.

Griffith, E. M., Schauble, E. A., Bullen, T. D., and Paytan, A. (2008). Characterization of calcium isotopes in natural and synthetic barite. Geochimica et Cosmochimica Acta, 72: 5641-5658.

Groves, D.I., Goldfarb, R.J., Gebre-Mariam, M., Hagemann, S.G., and Robert, E. (1998). Orogenic gold deposits - a proposed classification in the context of their crustal distribution and relationship to other gold deposit types. Ore Geology Reviews, 13: 7-27.

Habicht, K. S., and Canfield, D. E. (2001). Isotope fractionation by sulfate-reducing natural populations and the isotopic composition of sulfide in marine sediments. Geology, 29: 555-558.

Halbach, P., Nakamura, K. I., Wahsner, M., Lange, J., Sakai, H., Käselitz, L., ... and Seifert, R. (1989). Probable modern analogue of Kuroko-type massive sulphide deposits in the Okinawa Trough back-arc basin. Nature, 338: 496-499.

Hannington, M., Herzig, P., Scott, S., Thompson, G., and Rona, P. (1991). Comparative mineralogy and geochemistry of gold-bearing sulfide deposits on the mid-ocean ridges. Marine Geology, 101: 217-248.

Hannington, M. D., Jonasson, I. R., Herzig, P. M., and Petersen, S. (1995). Physical and chemical processes of seafloor mineralization at mid-ocean ridges. Seafloor Hydrothermal Systems: Physical, Chemical, Biological, and Geological Interactions, Geophysical Monograph, 91: 115-157.

Hannington, M. D., and Scott, S. D. (1988). Mineralogy and geochemistry of a hydrothermal silica-sulfide-sulfate spire in the caldera of Axial Seamount, Juan de Fuca Ridge. The Canadian Mineralogist, 26: 603-625.

Hanor, J. S. (2000). Barite–celestine geochemistry and environments of formation. Reviews in Mineralogy and Geochemistry, 40: 193-275.

Herzig, P. M., Hannington, M. D., and Arribas Jr, A. (1998). Sulfur isotopic composition of hydrothermal precipitates from the Lau back-arc: implications for magmatic contributions to seafloor hydrothermal systems. Mineralium Deposita, 33: 226-237.

Hibbard, J. P. (2004). The Appalachian Orogen—An essay by James P. Hibbard. Van der Pluijm, B. A., and Marshak, S., Earth structure: An introduction to structural geology and tectonics (2nd edition): New York, WW Norton, 582-592.

Hill, A. P. (1996). Structure, Volcanic Setting, Hydrothermal Alteration and Genesis of the Thalanga Massive Sulphide Deposit. PhD thesis, University of Tasmania, Tasmania.

Hinchey, J. G. (2014). The Long Lake group: Preliminary U-Pb geochronology and lithogeochemistry, and implications for tectonostratigraphic architecture and VMS mineralization. Current Research. Newfoundland and Labrador Department of Natural Resources, Report, 14-1: 15-44.

Hippler, D., Schmitt, A. D., Gussone, N., Heuser, A., Stille, P., Eisenhauer, A., and Nägler, T. F. (2003). Calcium isotopic composition of various reference materials and seawater. Geostandards and Geoanalytical Research, 27: 13-19.

Huston, D. L. (1999). Stable isotopes and their significance for understanding the genesis of volcanic-hosted massive sulfide deposits: A review. Reviews in Economic Geology, 8: 157-179.

Huston, D. L., Relvas, J. M., Gemmell, J. B., and Drieberg, S. (2011). The role of granites in volcanic-hosted massive sulphide ore-forming systems: an assessment of magmatic–hydrothermal contributions. Mineralium Deposita, 46: 473-507.

Ishibashi, J. I., and Urabe, T. (1995). Hydrothermal activity related to arc- back-arc magmatism in the western Pacific. In Backarc Basins, Springer US. pp. 451-495.

Ishihara, S., & Sasaki, A. (1978). Sulfur of Kuroko deposits-a deep seated origin?. Mining Geology, 28: 361-367.

Jamieson, J. W., Hannington, M. D., Tivey, M. K., Hansteen, T., Williamson, N. M. B., Stewart, M., Fietzke, J., Butterfield, D., Frische, M., Allen, L., Cousens, B., and Langer, J. (2016). Precipitation and growth of barite within hydrothermal vent deposits from the Endeavour Segment, Juan de Fuca Ridge. Geochimica et Cosmochimica Acta, 173: 64-85.

Janecky, D. R., and Shanks III, W. C. (1988). Computational modeling of chemical and sulfur isotopic reaction processes in seafloor hydrothermal systems: chimneys, massive sulfides, and subjacent alterations zones. The Canadian Mineralogist, 26: 805-825.

Jochum, K. P., Nohl, U., Herwig, K., Lammel, E., Stoll, B., and Hofmann, A. W. (2005). GeoReM: a new geochemical database for reference materials and isotopic standards. Geostandards and Geoanalytical Research, 29: 333-338.

Jones, F., Oliviera, A., Parkinson, G. M., Rohl, A. L., Stanley, A., and Upson, T. (2004). The effect of calcium ions on the precipitation of barium sulphate 1: calcium ions in the absence of organic additives. Journal of Crystal Growth, 262: 572-580.

Kalogeropoulos, S. I., and Scott, S. D. (1983). Mineralogy and geochemistry of tuffaceous exhalites (Tetsusekiei) of the Fukazawa mine, Hokuroku district, Japan. Economic Geology Monograph, 5: 412-432.

Kalogeropoulos, S. I., and Scott, S. D. (1989). Mineralogy and geochemistry of an Archean tuffaceous exhalite: The main contact tuff, Millenbach mine area, Noranda, Quebec. Canadian Journal of Earth Sciences, 26: 88-105.

Kean, B.F. (1977). Geology of the Victoria Lake area (12-A/06), Newfoundland: Newfoundland and Labrador Department of Mines and Energy, Mineral Development Division, Report N. 77-4, 11.

Kean, B. F., and Evans, D. T. W. (1986). Metallogeny of the Tulks Hill volcanics, Victoria Lake Group, central Newfoundland. Government of Newfoundland and Labrador Report, 86-1.

Kowalik, J., Rye, R. O., and Sawkins, F. J. (1981). Stable isotope study of the Buchans, Newfoundland, polymetallic sulphide deposits. Geological Association of Canada, Special Paper, 22: 229-254.

Koski, R. A., Jonasson, I. R., Kadko, D. C., Smith, V. K., and Wong, F. L. (1994). Compositions, growth mechanisms, and temporal relations of hydrothermal sulfide-sulfate-silica chimneys at the northern Cleft Segment, Juan de Fuca Ridge. Journal of Geophysical Research: Solid Earth, 99: 4813-4832.

Kramers, J. D., and Tolstikhin, I. N. (1997). Two terrestrial lead isotope paradoxes, forward transport modelling, core formation and the history of the continental crust. Chemical Geology, 139: 75-110.

Kusakabe, M., and Chiba, H. (1983). Oxygen and sulfur isotope composition of barite and anhydrite from the Fukazawa deposit, Japan. Economic Geology Monograph 5: 292-301.

Large, R.R. (1992). Australian volcanic-hosted massive sulfide deposits: Features, styles, and genetic models. Economic Geology, 87: 549–572.

Lode, S., Piercey, S. J., and Devine, C. A. (2015). Geology, mineralogy, and lithogeochemistry of metalliferous mudstones associated with the Lemarchant volcanogenic massive sulfide deposit, Tally Pond group, central Newfoundland. Economic Geology, 110: 1835-1859.

Lode, S., Piercey, S. J., Layne, G. D., Piercey, G., and Cloutier, J. (2016). Multiple sulphur and lead sources recorded in hydrothermal exhalites associated with the Lemarchant volcanogenic massive sulphide deposit, central Newfoundland, Canada. Mineralium Deposita: 1-24.

Marchev, P., Downes, H., Thirlwall, M. F., and Moritz, R. (2002). Small-scale variations of $^{87}Sr/^{86}Sr$ isotope composition of barite in the Madjarovo low-sulphidation epithermal system, SE Bulgaria: implications for sources of Sr, fluid fluxes and pathways of the ore-forming fluids. Mineralium Deposita, 37: 669-677.

McCuaig, T. C., and Kerrich, R. (1998). P-T-t-deformation-fluid characteristics of lode gold deposits: evidence from alteration systematics. Ore Geology Reviews, 12: 381-453.

McNicoll, V., Squires, G., Kerr, A., and Moore, P. (2010). The Duck pPond and Boundary Cu-Zn deposits, Newfoundland: New insights into the ages of host rocks and the timing of VHMS mineralization. Canadian Journal of Earth Sciences, 47: 1481-1506.

McPhie, J., Doyle, M., Allen, R. L. (1993). Volcanic textures: A Guide to the Interpretation of Textures in Volcanic Rocks. Hobart, Australia. Center for Ore Deposit and Exploration Studies, University of Tasmania, p. 198.

Mills R., Teagle D. and Tivey M. (1998) Fluid mixing and anhydrite precipitation within the TAG mound. In Proceedings of the Ocean Drilling Program, Scientific Results, 158 (eds. P. Herzig, S. Humphris, D. Miller and R. Zierenberg). Ocean Drilling Program, College Station, TX, pp. 119–127.

Monecke, T., Petersen, S., and Hannington, M. D. (2014). Constraints on water depth of massive sulfide formation: Evidence from modern seafloor hydrothermal systems in arc-related settings. Economic Geology, 109: 2079-2101.

Monnin, C., and Cividini, D. (2006). The saturation state of the world's ocean with respect to (Ba, Sr)SO_4 solid solutions. Geochimica Et Cosmochimica Acta, 70: 3290-3298.

Montañez, I. P., Banner, J. L., Osleger, D. A., Borg, L. E., and Bosserman, P. J. (1996). Integrated Sr isotope variations and sea-level history of Middle to Upper Cambrian platform carbonates: Implications for the evolution of Cambrian seawater $^{87}Sr/^{86}Sr$. Geology, 24: 917-920.

Neuman, R. B. (1984). Geology and paleobiology of islands in the Ordovician Iapetus ocean: Review and implications. Geological Society of America Bulletin, 95: 1188-1201.

Ohmoto, H. (1996). Formation of volcanogenic massive sulfide deposits: The Kuroko perspective. Ore Geology Reviews, 10: 135-177.

Ohmoto, H., and Goldhaber, M. B. (1997). Sulfur and carbon isotopes. Geochemistry of hydrothermal ore deposits, 3: 517-611.

Ohmoto, H., Mizukami, M., Drummond, S. E., Eldridge, C. S., Pisutha-Arnond, V., and Lenagh, T. C. (1983). Chemical processes of kuroko formation. Economic Geology, Monographs, 5: 570-604.

Ohmoto, H., and Rye, R. O. (1979). Isotopes of sulfur and carbon: *in* Barnes, H. L., ed., Geochemistry of Hydrothermal Ore Deposits, 2nd Edition: New York, Wiley: 509-567.

Paytan, A., Kastner, M., Martin, E., Macdougall, J., and Herbert, T. (1993). Marine barite as a monitor of seawater strontium isotope composition. Nature, 366: 445-449.

Piercey, S. J., and Hinchey, J. (2012). Volcanogenic massive sulphide (VMS) deposits of the Central Mineral Belt, Newfoundland. In Geological Association of Canada–Mineralogical Association of Canada Joint Annual Meeting, Field Trip Guidebook B, Newfoundland and Labrador Department of Natural Resources, Geological Survey, Open File NFLD/3173, 56 p.

Piercey, S. J., Squires, G. C., and Brace, T. D. (2014). Lithostratigraphic, hydrothermal, and tectonic setting of the Boundary volcanogenic massive sulfide deposit, Newfoundland Appalachians, Canada: formation by subseafloor replacement in a Cambrian rifted arc. Economic Geology, 109: 661-687.

Pisutha-Arnond, V., and Ohmoto. J. (1983). Thermal History, and chemical and isotopic compositions of the ore-forming fluids responsible for the Kuroko massive sulfide deposits in the Hokuroko District of Japan. Economic Geology, 5: 523-558.

Pollock, J.C. (2004). Geology of the Tally Pond Group, Victoria Lake Supergroup, Dunnage Zone, Newfoundland: an integrated geochemical, geochronological, isotopic and metallogenic study of a Cambrian ensimatic island arc. Unpublished M.Sc. thesis, Memorial University of Newfoundland, St. John’s, NL.

Pollock, J., and Wilton, D. (2001). Metallogenic studies of the Tally Pond group, Victoria Lake group: Trace element geochemistry and lead isotope data from the Exploits subzone, Newfoundland. Newfoundland and Labrador Department of Natural Resources, Geological Survey, Report, 2001-01, p. 247-266.

Pollock, J.C., Wilton, D.H.C., van Staal, C.R., and Tubrett, M.N. (2002). Laser ablation ICP-MS geochronology and provenance of detrital zircons from the Rogerson Lake Conglomerate, Botwood Belt, Newfoundland. *In* Current Research. Newfoundland Department of Mines and Energy, Geological Survey Branch, Report 02-1, p. 169-183.

Ramezani, J., Dunning, G. R., and Wilson, M. R. (2000). Geologic setting, geochemistry of alteration, and U-Pb age of hydrothermal zircon from the Silurian Stog’er Tight gold prospect, Newfoundland Appalachians, Canada. Exploration and Mining Geology, 9: 171-188.

Reeves, E. P., Seewald, J. S., Saccocia, P., Bach, W., Craddock, P. R., Shanks, W. C., . . . Rosner, M. (2011). Geochemistry of hydrothermal fluids from the PACMANUS, northeast Pual and Vienna Woods hydrothermal fields, Manus Basin, Papua New Guinea. Geochimica Et Cosmochimica Acta, 75: 1088-1123.

Roedder, E. (1984). Fluid inclusions. Mineralogical Society of America. Reviews in Mineralogy, 12. p. 644.

Roedder, E., and Coombs, D. S. (1967). Immiscibility in granitic melts, indicated by fluid inclusions in ejected granitic blocks from Ascension Island. Journal of Petrology, 8: 417-451.

Rogers, N., and van Staal, C. R. (2002). Toward a Victoria Lake Supergroup: a provisional stratigraphic revision of the Red Indian to Victoria Lakes area, central Newfoundland. Newfoundland and Labrador Department of Natural Resources, Geological Survey, Report, 02-1: 185-195.

Rogers, N., van Staal, C., McNicoll, V., Pollock, J., Zagorevski, A., and Whalen, J. (2006). Neoproterozoic and Cambrian arc magmatism along the eastern margin of the Victoria Lake supergroup: A remnant of Ganderian basement in central Newfoundland? Precambrian Research, 147: 320-341.

Rogers, N., van Staal, C., Zagorevski, A., Skulski, T., Piercey, S., and McNicoll, V. (2007). Timing and tectonic setting of volcanogenic massive sulfide bearing terranes within the Central Mobile Belt of the Canadian Appalachians. Paper presented at the Proceedings of Exploration, 7: 1199-1205.

Rye, R. O. (1993). The evolution of magmatic fluids in the epithermal environment; the stable isotope perspective. Economic Geology, 88: 733-752.

Sabine, P. A., Young, B. R. (1954). Cell size and composition of the baryte-celestine isomorphous series. Acta Crystallogr 7: 630 (abstract).

Safina, N. P., Melekestseva, I. Y., Nimis, P., Ankusheva, N. N., Yuminov, A. M., Kotlyarov, V. A., and Sadykov, S. A. (2016). Barite from the Saf'yanovka VMS deposit (central Urals) and Semenov-1 and Semenov-3 hydrothermal sulfide fields (Mid-Atlantic Ridge): A comparative analysis of formation conditions. Mineralium Deposita, 51: 491-507.

Sakai, H., Des Marais, D. J., Ueda, A., and Moore, J. G. (1984). Concentrations and isotope ratios of carbon, nitrogen and sulfur in ocean-floor basalts. Geochimica et Cosmochimica Acta, 48: 2433-2441.

Sakai, H., Gamo, T., Kim, E., Shitashima, K., Yanagisawa, F., Tsutsumi, M., . . . Tanaka, T. (1990). Unique chemistry of the hydrothermal solution in the Mid-Okinawa Trough backarc basin. Geophysical Research Letters, 17: 2133-2136.

Sangster, D. (1968). Relative sulphur isotope abundances of ancient seas and strata-bound sulphide deposits. Paper presented at the Proceedings of the Geological Association of Canada, 19, p. 79.

Sasaki, N., and Minato, H. (1983). Effect of the degree of supersaturation upon apparent partition coefficients of lead and strontium ions between $BaSO_4$ and aqueous solution. Mineralogical Journal, 1: 365-381.

Sato, T. (1977). Kuroko deposits: Their geology, geochemistry and origin. Geological Society, London, Special Publications, 7: 153-161.

Scotney, P. M., Roberts, S., Herrington, R. J., Boyce, A. J., and Burgess, R. (2005). The development of volcanic hosted massive sulfide and barite–gold orebodies on Wetar Island, Indonesia. Mineralium Deposita, 40: 76-99.

Scott, S. (1980). Geology and structural control of Kuroko-type massive sulphide deposits. Geological Association of Canada, Special Paper, 20: 705-721.

Seal, R. R. II (2006). Sulfur isotope geochemistry of sulfide minerals. Reviews in mineralogy and geochemistry, 61: 633-677.

Seal, R. R., Alpers, C. N., and Rye, R. O. (2000). Stable isotope systematics of sulfate minerals. Reviews in Mineralogy and Geochemistry, 40: 541-602.

Seal II, R. R., Ayuso, R. A., Foley, N. K., and Clark, S. H. (2001). Sulfur and lead isotope geochemistry of hypogene mineralization at the Barite Hill gold deposit, Carolina Slate Belt, southeastern United States: A window into and through regional metamorphism. Mineralium Deposita, 36: 137-148.

Seyfried, W. E., & Ding, K. (1995). Phase equilibria in subseafloor hydrothermal systems: A review of the role of redox, temperature, pH and dissolved Cl on the chemistry of hot spring fluids at mid-ocean ridges. Seafloor Hydrothermal Systems: Physical, Chemical, Biological, and Geological Interactions. Geophysical Monograph, 91: 248-272.

Shanks, W. C. (2001). Stable isotopes in seafloor hydrothermal systems: vent fluids, hydrothermal deposits, hydrothermal alteration, and microbial processes. Reviews in Mineralogy and Geochemistry, 43: 469-525.

Sharpe, R. (1991). The Hellyer baritic and siliceous caps: Unpublished B.Sc. dissertation, Honors thesis, University of Tasmania, Australia.

Shepherd, T. J., Rankin, A. H., and Alderton, D. (1985). A practical guide to fluid inclusion studies. Blackie, Glasgow, p. 239.

Sherlock, R., Roth, T., Spooner, E., and Bray, C. (1999). Origin of the Eskay Creek precious metal-rich volcanogenic massive sulfide deposit; fluid inclusion and stable isotope evidence. Economic Geology, 94: 803-824.

Shikazono, N., Kawabe, H., and Ogawa, Y. (2012). Interpretation of mineral zoning in submarine hydrothermal ore deposits in terms of coupled fluid flow-precipitation kinetics model. Resource Geology, 62: 352-368.

Squires, G., Brace, T., and Hussey, A. (2001). Newfoundland’s polymetallic Duck Pond deposit: Earliest Iapetan VMS mineralization, formed within a sub-seafloor, carbonate-rich alteration system. Paper presented at the Geology and Mineral Deposits of the Northern Dunnage Zone, Newfoundland Appalachians. Edited by D.T.W. Evans and A. Kerr. Geological Association of Canada–Mineralogical Association of Canada (GAC–MAC) Annual Meeting, St. John’s, Nfld: 167-187.

Squires, G., and Moore, P. (2004). Volcanogenic massive sulphide environments of the Tally Pond volcanics and adjacent area: Geological, lithogeochemical and geochronological results. Newfoundland and Labrador Department of Natural Resources, Geological Survey, Report, , 04-01: 63-91.

Swinden, H. S. (1988). Introduction to volcanogenic sulphide deposits in Newfoundland, in Swinden, H. S., and Kean, B. F., eds., The volcanogenic sulphide districts of central Newfoundland: Geological Association of Canada: 1-26.

Swinden, H. S., Jenner, G., Kean, B., and Evans, D. (1989). Volcanic rock geochemistry as a guide for massive sulfide exploration in central Newfoundland. Newfoundland Department of Mines and Energy, Geological Survey Branch, Report, 89: 201-219.

Swinden, H. S., and Thorpe, R. (1984). Variations in style of volcanism and massive sulfide deposition in early to middle Ordovician island-arc sequences of the Newfoundland central mobile belt. Economic Geology, 79: 1596-1619.

Swinden, H. S. (1991). Paleotectonic settings of volcanogenic massive sulphide deposits in the Dunnage Zone, Newfoundland Appalachians. CIM bulletin, 84: 59-69.

Teichert, B. M., Gussone, N., Eisenhauer, A., and Bohrmann, G. (2005). Clathrites: archives of near-seafloor pore-fluid evolution ($\delta^{44/40}$Ca, δ^{13}C, δ^{18}O) in gas hydrate environments. Geology, 33: 213-216.

Thurlow, J. G. (2010). Great Mining Camps of Canada 3. The history and geology of the Buchans mine, Newfoundland and Labrador. Geoscience Canada, 37: 145-173.

Ulrich, M. R., and Bodnar, R. J. (1988). Systematics of stretching of fluid inclusions; II, Barite at 1 atm confining pressure. Economic Geology, 83: 1037-1046.

Van den Kerkhof, A., and Thiery, R. (2001). Carbonic inclusions. Lithos, 55: 49-68.

van Staal, C. R. (2005). The Northern Appalachians. Encyclopedia of geology, 4: 81-91.

van Staal, C. R. (2007). Pre-Carboniferous tectonic evolution and metallogeny of the Canadian Appalachians. Mineral Resources of Canada: A Synthesis of Major Deposit Types, District Metallogeny, the Evolution of Geological Provinces, and Exploration Methods. Edited by W.D. Goodfellow. Geological Association of Canada, Mineral Deposits Division, Special Publication, 5: 793-818.

van Staal, C. R., and Barr, S. M. (2012). Lithospheric architecture and tectonic evolution of the Canadian Appalachians and associated Atlantic margin. Tectonic styles in Canada: The LITHOPROBE perspective: Geological Association of Canada Special Paper, 49: 55.

van Staal, C. R., Sullivan, R. W., and Whalen, J. B. (1996). Provenance and tectonic history of the Gander zone in the Caledonian/Appalachian orogen: Implications for the origin and assembly of Avalon. Special Papers-Geological Society of America, 304: 347-368.

van Staal, C., Dewey, J., Mac Niocaill, C., and McKerrow, W. (1998). The Cambrian-Silurian tectonic evolution of the northern Appalachians and British Caledonides: History of a complex, west and southwest Pacific-type segment of Iapetus. Geological Society, London, Special Publications, 143: 197-242.

van Staal, C. R., and Hatcher, R. D. (2010). Global setting of Ordovician orogenesis. Geological Society of America Special Papers, 466: 1-11.

Veizer, J., Ala, D., Azmy, K., Bruckschen, P., Buhl, D., Bruhn, F., ... and Jasper, T. (1999). $^{87}Sr/^{86}Sr$, $\delta^{13}C$ and $\delta^{18}O$ evolution of Phanerozoic seawater. Chemical geology, 161: 59-88.

Von Damm, K. L. (1990). Seafloor hydrothermal activity: black smoker chemistry and chimneys. Annual Review of Earth and Planetary Sciences, 18: 173-204.

Von Damm, K. L., Edmond, J. M., Grant, B., Measures, C. I., Walden, B., and Weiss, R. F. (1985). Chemistry of submarine hydrothermal solutions at 21° N, East Pacific Rise. Geochimica et Cosmochimica Acta, 49: 2197-2220.

Wagner, D. W., (1993). Volcanic stratigraphy and hydrothermal alteration associated with the Duck Pond and Boundary volcanogenic massive sulphide deposits, central Newfoundland. Unpublished dissertation. Carleton University, Ottawa.

Wallace, P. J. (2005). Volatiles in subduction zone magmas: Concentrations and fluxes based on melt inclusion and volcanic gas data. Journal of Volcanology and Geothermal Research, 140: 217-240.

Watanabe, M., and Sakai, H. (1983). Stable isotope geochemistry of sulfates from the Neogene ore deposits in the Green Tuff region, Japan. Economic Geology Monograph 5: 282-291.

Whitford, D. J., Korsch, M. J., and Solomon, M. (1992). Strontium isotope studies of barites; implications for the origin of base metal mineralization in Tasmania. Economic Geology, 87: 953-959.

Williams, H. (1979). Appalachian orogen in Canada. Canadian Journal of Earth Sciences, 16: 792-807.

Williams, H. (1995). Geology of the Appalachian-Caledonian Orogen in Canada and Greenland. Geological Survey of Canada: Minister of Energy, Mines and Resources Canada, p. 944.

Williams, H., Colman-Sadd, S. P., and Swinden, H. S. (1988). Tectonic-stratigraphic subdivisions of central Newfoundland. Current Research, Part B. Geological Survey of Canada, Paper, 88: 91-98.

Yang, K. H., and Scott, S. D. (1996). Possible contribution of a metal-rich magmatic fluid to a sea-floor hydrothermal system. Nature, 383: 420-423.

Zagorevski, A., Van Staal, C., McNicoll, V., and Rogers, N. (2007). Upper Cambrian to upper Ordovician peri-Gondwanan island arc activity in the Victoria Lake supergroup, central Newfoundland: Tectonic development of the northern Ganderian margin. American Journal of Science, 307: 339-370.

Zagorevski, A., van Staal, C.R., Rogers, N., McNicoll, V., Dunning, G.R., and Pollock, J.C. (2010). Middle Cambrian to Ordovician arc-backarc development on the leading edge of Ganderia, Newfoundland Appalachians. *In* From Rodinia to Pangea: The Lithotectonic Record of the Appalachian Region. *Edited by* R.P. Tollo, M.J. Batholomew, J.P. Hibbard, and P.M. Karabinos. Geological Society of America, Memoir 206: pp. 367–396.

Zaw, K., Hunns, S., Large, R., Gemmell, J., Ryan, C., and Mernagh, T. (2003). Microthermometry and chemical composition of fluid inclusions from the Mt Chalmers volcanic-hosted massive sulfide deposits, central Queensland, Australia: Implications for ore genesis. Chemical Geology, 194: 225-244.

Zhu, C. (2004). Coprecipitation in the barite isostructural family: 1. binary mixing properties. Geochimica Et Cosmochimica Acta, 68: 3327-3337.

Table 2-1. Electron microprobe results of average major element composition of barite from the Lemarchant deposit (n = 514); Av – average value; Min – minimum value; Max – maximum value.

BaO wt.%			SrO wt.%			Na_2O wt.%			CaO wt.%		
Av ± 1σ	Min	Max	Av ± 1σ	Min	Max	Av ± 1σ	Min	Max	Av ± 1σ	Min	Max
64.49 ± 0.04	59.66	67.97	0.96 ± 0.03	0.02	4.78	0.16 ± 0.00	0.02	0.28	0.02 ± 0.00	0.00	0.73

Table 2-2. Laser ablation results of trace elements for bladed and granular barite in the Lemarchant deposit. Complete micro-analytical analyses are found in Appendix 4.

	Bladed (n = 103)		Granular (n = 70)	
	Average (*ppm*)	2σ	Average (*ppm*)	2σ
Sc	2.49	1.38	0.59	0.92
Ti	108.00	29.42	49.40	23.54
V	8.71	2.31	12.84	10.48
Cr	48.27	10.95	36.76	19.23
Co	0.93	0.42	0.57	0.37
Ni	13.63	6.66	17.13	13.38
Ga	12.85	8.71	331.73	639.36
Ge	2.09	1.06	2.15	2.02
As	196.51	72.51	79.13	53.42
Se	32.19	10.76	29.21	13.68
Mo	248.65	291.96	71.66	76.82
Ag	2784.95	1458.83	932.68	1369.45
In	0.08	0.14	0.05	0.09
Sn	23.39	7.01	9.48	3.92
Sb	60.37	30.14	2.97	3.88
Te	-	-	0.09	0.18
Au	43.83	15.19	4.13	2.44
Hg	543.53	112.70	314.99	157.60
Tl	24.44	8.60	23.51	17.89
Bi	0.31	0.50	0.04	0.03

Table 2-3. Whole-rock lithogeochemical data of barite samples from the Lemarchant deposit.

Sample	CNF31816	CNF31861	CNF31733	CNF31810	CNF31730	CNF31721	CNF31874	CNF31865	CNF31868	CNF31855
Drill hole	LM08-19	LM11-68	LM13-94	LM10-43	LM13-94	LM13-73	LM13-82	LM14-96	LM14-96	LM11-52
Depth (m)	98.1	199.9	341.4	218.8	326.3	332.9	340.8	309.9	314.4	216.2
Mineralized zone	24 zone	Main zone	Northwest zone	Main zone	Northwest zone	Northwest zone	Northwest zone	Northwest zone	Northwest zone	Main zone
SiO_2 *wt.%*	0.83	0.53	1.46	0.5	1.47	0.42	4.63	0.03	0.23	1.18
Al_2O_3	0.63	0.08	0.12	0.06	0.77	0.14	0.19	< 0.01	0.1	0.43
Fe_2O_3	4.28	0.44	0.28	0.87	0.41	0.23	0.51	0.06	0.12	0.28
MnO	0.034	< 0.001	< 0.001	0.059	< 0.001	0.005	< 0.001	< 0.001	< 0.001	0.003
MgO	0.28	0.08	0.08	1.87	0.14	0.12	0.02	0.03	0.02	0.17
CaO	2.51	0.13	0.14	2.82	0.18	0.2	0.06	0.06	0.03	0.31
Na_2O	0.01	< 0.01	< 0.01	< 0.01	0.02	0.03	0.04	< 0.01	< 0.01	0.05
K_2O	0.07	< 0.01	0.02	< 0.01	0.1	< 0.01	0.03	< 0.01	< 0.01	0.04
TiO_2	0.01	0.001	0.001	< 0.001	0.001	< 0.001	0.004	< 0.001	0.001	0.001
P_2O_5	0.25	0.02	0.01	0.01	0.09	0.01	< 0.01	< 0.01	< 0.01	0.08
LOI	2.81	0.7	0.68	1.72	0.86	0.83	1.62	0.23	0.15	0.91
Total	11.71	1.99	2.8	7.94	4.04	1.99	7.12	0.4	0.65	3.47
Ba *ppm*	510000	551200	548300	505200	520300	547300	521400	568600	576500	543100
Cu	430	2780	3070	7090	2790	2000	1100	1390	240	1060
Zn	190	5040	5160	> 10000	> 10000	> 10000	> 10000	5260	510	> 10000
Pb	326	8640	4670	5320	> 10000	8460	6880	2910	401	3370
Ag	0.8	16.1	13.5	1.5	8.5	4.2	< 0.5	1.1	1	2.3
Cr	< 20	< 20	< 20	< 20	< 20	< 20	< 20	< 20	< 20	< 20
Co	< 1	< 1	< 1	< 1	< 1	< 1	< 1	< 1	< 1	< 1
Ni	30	< 20	< 20	< 20	< 20	< 20	< 20	< 20	< 20	< 20
Sc	< 1	< 1	< 1	< 1	< 1	< 1	< 1	< 1	< 1	< 1
Be	< 1	< 1	< 1	< 1	< 1	< 1	< 1	< 1	< 1	< 1
V	103	10	20	6	102	15	11	< 5	19	45
Ga	3	3	3	7	10	11	6	2	2	9
Ge	< 0.5	< 0.5	14.4	1.4	4.7	3.6	< 0.5	< 0.5	< 0.5	< 0.5
As	105	378	53	47	52	30	105	13	29	22
Rb	1	< 1	< 1	< 1	2	< 1	< 1	< 1	< 1	< 1
Sr	4889	5905	9348	4034	5419	4997	3604	7438	7233	5693
Y	12.1	4.2	4.9	3.8	6.8	4.8	4	3.6	3.8	8.7
Zr	6	2	3	2	4	2	3	2	3	2
Nb	< 0.2	< 0.2	< 0.2	< 0.2	< 0.2	< 0.2	< 0.2	< 0.2	< 0.2	< 0.2
Mo	3	33	59	> 100	68	81	> 100	7	3	76
In	< 0.1	< 0.1	< 0.1	< 0.1	< 0.1	< 0.1	< 0.1	< 0.1	< 0.1	< 0.1
Sn	< 1	< 1	< 1	< 1	< 1	< 1	< 1	< 1	< 1	< 1
Sb	30.4	103	56.1	64.6	119	87.1	46.3	12.6	23.8	48.7
Cs	< 0.1	< 0.1	< 0.1	< 0.1	< 0.1	< 0.1	< 0.1	< 0.1	< 0.1	< 0.1
La	7.12	12.8	11.4	7.22	10.9	8.8	7.4	11.1	7.72	8.47
Ce	4.09	9.23	8.05	2.57	7.3	4.38	5.12	7.29	3.26	5.16
Pr	0.64	0.63	0.71	0.19	0.65	0.3	0.39	0.52	0.21	0.57
Nd	3.06	1.62	2.12	0.55	1.98	0.8	1.48	1.22	0.56	2.29
Sm	1.47	0.73	0.97	0.67	0.79	0.71	1.05	0.71	0.64	1.27
Eu	1.88	0.188	0.07	< 0.005	1.05	0.622	< 0.005	1.68	0.648	2.45
Gd	1.99	1.14	1.28	0.91	1.2	1.06	1.63	1.01	0.92	1.84
Tb	0.18	0.04	0.08	0.04	0.07	0.04	0.12	0.05	0.04	0.15
Dy	0.82	0.1	0.22	0.11	0.31	0.12	0.36	0.08	0.1	0.66
Ho	0.16	0.02	0.03	0.02	0.06	0.02	0.05	0.01	0.02	0.11
Er	0.45	0.06	0.09	0.06	0.15	0.06	0.13	0.03	0.05	0.25
Tm	0.07	0.01	0.014	0.01	0.019	0.008	0.018	< 0.005	0.007	0.032
Yb	0.41	0.07	0.08	0.07	0.12	0.06	0.11	0.04	0.05	0.18
Lu	0.053	0.011	0.014	0.01	0.021	0.01	0.019	0.007	0.009	0.026
Hf	0.3	0.3	0.3	0.2	0.2	0.3	0.2	0.2	0.2	0.3
Ta	0.27	0.31	0.32	0.28	0.29	0.33	< 0.01	0.26	0.26	0.31
W	1.9	2.1	< 0.5	0.7	0.6	0.9	< 0.5	2.4	0.8	0.8
Tl	< 0.05	< 0.05	0.29	< 0.05	< 0.05	< 0.05	< 0.05	< 0.05	< 0.05	< 0.05
Bi	< 0.1	< 0.1	< 0.1	< 0.1	< 0.1	< 0.1	< 0.1	< 0.1	< 0.1	< 0.1
Th	0.12	< 0.05	0.44	< 0.05	< 0.05	< 0.05	< 0.05	< 0.05	< 0.05	< 0.05
U	8.81	0.5	1.53	3.23	3.05	0.4	3.15	0.08	0.57	10.6

Table 2-4. Whole-rock strontium isotope ratios ($^{87}Sr/^{86}Sr$), calculated % hydrothermal fluid, Sr and Rb concentrations (ppm), and calculated [Sr]/[Ba] ratios from barite whole-rock lithogeochemical analyses.

Sample Nº	Drill Hole	Depth (m)	$^{87}Sr/^{86}Sr \pm 2\sigma$	% hydrothermal fluid[a]	Sr (ppm)[b]	Rb (ppm)[b]	[Sr]/[Ba] (Whole rock)[c]
CNF31816	LM08-19	98.10	0.707485 ± 0.000010	37	4889	1	0.010
CNF31861	LM11-68	199.90	0.707320 ± 0.000010	41	5905	< 1	0.011
CNF31733	LM13-94	341.40	0.707053 ± 0.000010	47	9348	< 1	0.017
CNF31810	LM10-43	218.75	0.707049 ± 0.000010	47	4034	< 1	0.008
CNF31730	LM13-94	332.25	0.707283 ± 0.000010	42	5419	2	0.010
CNF31721	LM13-73	332.95	0.706993 ± 0.000010	48	4997	< 1	0.009
CNF31874	LM13-82	340.80	0.707192 ± 0.000010	44	3604	< 1	0.007
CNF31865	LM14-96	309.90	0.706905 ± 0.000010	51	7438	< 1	0.013
CNF31868	LM14-96	314.30	0.707031 ± 0.000010	48	7233	< 1	0.013
CNF31855	LM11-52	216.20	0.707305 ± 0.000010	41	5693	< 1	0.010

[a] % hydrothermal fluids are calculated using Eq. (1).

[b] Sr and Rb concentrations (ppm) from whole-rock lithogeochemical data.

[c] [Sr]/[Ba] ratios are calculated based on Sr and Rb from whole-rock lithogeochmical data.

Table 2-5. Sulfur isotopic compositions ($\delta^{34}S$ V-CDT) of granular and bladed barite samples from the Lemarchant deposit.

Sample Name	Drill Hole	Barite texture	Mineralized zone	$\delta^{34}S$ (‰ V-CDT)
CNF31715	LM13-73	Massive/granular	Northwest zone	27.8
CNF31721	LM13-73	Massive/granular	Northwest zone	27.0
CNF31723	LM13-73	Massive/granular	Northwest zone	24.7
CNF31730	LM13-94	Massive/granular	Northwest zone	27.1
CNF31861	LM11-68	Massive/granular	Main Zone	27.4
CNF31721	LM13-73	Bladed	Northwest zone	27.8
CNF31723	LM13-73	Bladed	Northwest zone	28.1
CNF31733	LM13-97	Bladed	Northwest zone	26.7
CNF31809	LM10-43	Bladed	Main Zone	27.9
CNF31810	LM10-43	Bladed	Main Zone	27.6
CNF31811	LM10-43	Bladed	Main Zone	26.1
CNF31811	LM10-43	Bladed	Main Zone	26.9
CNF31812	LM10-43	Bladed	Main Zone	26.6
CNF31812	LM10-43	Bladed	Main Zone	26.5
CNF31812	LM10-43	Bladed	Main Zone	26.1
CNF31816	LM08-19	Bladed	24 Zone	27.3
CNF31829	LM07-15	Bladed	Main Zone	27.8
CNF31855	LM11-52	Bladed	Main Zone	27.3
CNF31860	LM11-68	Bladed	Main Zone	28.7
CNF31861	LM11-68	Bladed	Main Zone	26.9
CNF31865	LM14-96	Bladed	Northwest zone	25.7
CNF31868	LM14-96	Bladed	Northwest zone	27.0
CNF31874	LM13-82	Bladed	Northwest zone	27.5

Table 2-6. Results of fluid inclusion microthermometry and salinity calculations for different fluid inclusion assemblages in bladed barite from the Lemarchant deposit.

Sample/assemblage	Assemblage	Type	Degree of Fill (F)	First melting temperature (T_{mCO2})	Final melting temperature ($T_{m\ ice\ clathrate}$ °C)	Final melting temperature ($T_{m\ ice}$ °C)	Temperature of homogenization (T_{hCO2})	Final homogenization temperature (T_h °C)	Salinity (wt. %)*
CNF31723 (vein)									
1	1	I	0.75	-56.1	8.90	-	-	248.1	1.8
2	1	I	0.75	-56.1	9.10	-	-	248.1	1.4
3	1	I	0.75	-	9.10	-	-	248.1	1.4
4	1	I	0.75	-	9.10	-	-	246	1.4
5	1	I	0.80	-56.0	7.80	-	-	246	3.9
6	1	I	0.80	-56.0	9.70	-	-	247.8	0.2
7	1	III	0.99	-56.0	-		-	-	
8	1	III	0.99	-	7.80		-	-	3.9
1	2	I	0.75	-56.0	9.70	-	-	236	0.2
2	2	I	0.75	-	-	-	-	236	
3	2	I	0.75	-	-	-	-	-	
4	2	I	0.75	-56.0	-	-	-	-	
CNF31723 (bladed barite)									
1	1	II	0.95	-	-	-	-	decrepitated	
2	1	II	0.95	-	-	-0.3	-	decrepitated	
3	1	II	0.95	-	-	1	-	198.3	
4	1	II	0.95	-	10.5	-	-	decrepitated	0.0
5	1	II	0.95	-	9.3	-	-	-	1.0
6	1	II	0.95	-	-	-	-	-	
1	2	II	0.75	-	-	-3.2	-	-	
2	2	II	0.75	-	-	-	-	214.4	
3	2	II	0.75	-	-	-2.9	-	216.2	
CNF31874 (bladed barite)									
1	1	II	0.75	-59.2	9.5	-4	-		0.6
2	1	II	0.95	-	9.5	-	27.7-29	211.7	0.6
3	1	III	1	-	7.1	-	-	-	5.2
4	1	II	0.75	-		-3.5	-	-	
5	1	II	0.9	-		-3	-	-	
6	1	II	0.95	-		-	-	-	
7	1	II	0.95	-		-	-	-	
8	1	II	0.95	-			-	-	
9	1	II	0.95	-			-	-	
10	1	II	0.95	-			-	-	
1	2	I	0.75	-56.3	-4.7	-4.7	31	-	
2	2	I	0.5	-56.3	-	-	-	decrepitated	
3	2	I	0.75	-56.3	-	-	-	261.3	
4	2	III	1	-	10.3	-	-	decrepitated	~0.0
5	2	I	0.75	-	-	-	-	256	
6	2	I	0.75	-	-	-	-	-	
7	2	I	0.75	-	9.9	-	-	276	~0.0
8	2	I	0.75	-	9.9	-	-	decrepitated	~0.0
9	2	I	0.75	-	9.9	-	-	decrepitated	~0.0
10	2	I	0.75	-	-	-	-	decrepitated	

*Salinities (wt.%) were calculated using the Q2 program within the software CLATHRATES.

Table 2-6. *Cont.'d*

Sample/assemblage	Assemblage	Type	Degree of Fill (F)	First melting temperature (T_{mCO2})	Final melting temperature ($T_{m\ ice\ clathrate}$ °C)	Final melting temperature ($T_{m\ ice}$ °C)	Temperature of homogenization (T_{hCO2})	Final homogenization temperature (T_h °C)	Salinity (wt. %)*
CNF31865 (bladed barite)									
1	1	I	0.75	-56.50	-	-	30.8	-	
2	1	I	0.75	-	9.5	-	-	-	0.6
3	1	I	0.95	-	7.6	-	-	-	4.2
4	1	I	0.75	-	-	-	-	-	
5	1	I	-	-	-	-	-	-	
6	1	I	-	-	-	-	-	-	
7	1	I	-	-	-	-	-	-	
8	1	I	0.75	-	9.5	-	-	-	
9	1	I	0.95	-	9.1	-	30.2	-	0.6
10	1	I	0.75	-	-	-	-	228	1.4
11	1	I	0.75	-	-	-	-	250	
12	1	I	0.75	-	-	-	-	250	
13	1	I	0.75	-	-	-	-	255	
1	2	I	0.75	-56.2	-	-	30.4	-	
2	2	I	0.75	-	-	-	30.4	-	
3	2	I	0.75	-	-	-	-	-	
4	2	I	0.95	-	9.4	-	-	-	
5	2	I	0.75	-	9.7	-	-	-	0.8
6	2	I	0.75	-	-	-	-	-	0.2
8	2	II	0.9	-	-	-	-	-	
9	2	II	0.95	-	-	-	-	-	
10	2	II	0.95	-	-	-	-	-	
11	2	II	0.75	-	-	-	-	-	
12	2	II	0.75	-	-	-	-	245	
CNF31860 (bladed barite)									
1	1	I	0.75	-	9.8	-	30.8	-	
2	1	I	0.75	-57.1	9.8	-	-	-	0.0
3	1	I	0.9	-	-	-	-	191	0.0
4	1	I	0.75	-	-	-	-	245.3	
5	1	I	0.9	-	-	-	-	245.3	

*Salinities (wt.%) were calculated using the Q2 program within the software CLATHRATES.

Table 2-7. Pressure trapping conditions (bars) of type-I fluid inclusion assemblages in bladed barite from the Lemarchant deposit.

Sample/inclusion #	xH_2O	xCO_2	xNa	xCl	Density (cc/mol)	Pressure (bars)*	Depth (km)
CNF31723 (vein)	-	-	-	-	-	-	-
CNF31723 (bladed barite)	-	-	-	-	-	-	-
CNF31874 (bladed barite)	0.87	0.13	0.00	0.00	23.99	1759.27	6.64
	0.88	0.12	0.00	0.00	24.17	1711.21	6.46
CNF31865 (bladed barite)	0.89	0.10	0.00	0.00	23.06	1955.96	7.38
CNF31860 (bladed barite)	0.92	0.08	0.00	0.00	22.14	2006.94	7.58

*Pressures (bars) were calculated using the *Q2* program within the software *Loner15*.

Table 2-8. Measured temperatures (ºC), Sr concentrations (μmmol/kg), and Sr isotopic ratios of hydrothermal fluids and seawater from the PACMANUS hydrothermal vent field. Values used in two-component fluid mixing calculations.

	PACMANUS vent fluid[a]	Seawater[a]
Temperature (ºC)	247	3
Sr (μmol/kg)	0.099	0.091
$^{87}Sr/^{86}Sr$	0.7049[b]	0.7092[c]

[a] PACMANUS vent fluid chemistry and seawater values are from Reeves et al. (2011).
[b] Average Sr-isotope ratios from vent fluids from the PACMANUS vent field (Reeves et al., 2011).
[c] From Reeves et al. (2011).

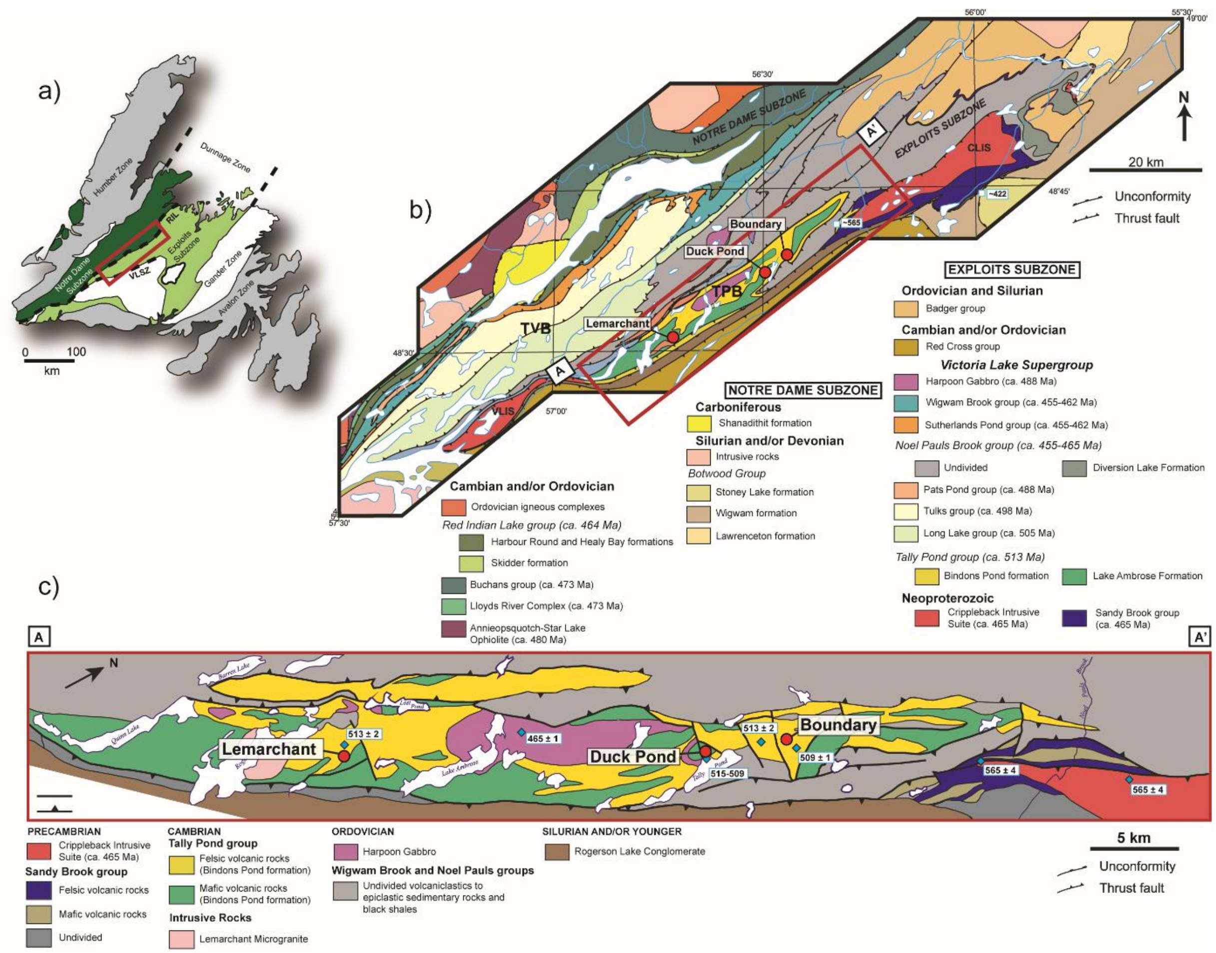

Figure 2-1. a) Simplified tectonostratigraphic zones of the Newfoundland Appalachians. The red square indicates the location of the study area located in the Exploits subzone of the Dunnage zone, east of the Red Indian Line. b) Geologic map of the Victoria Lake supergroup and adjacent areas, including the Tulks volcanic belt, the Tally Pond group, and the Crippleback Intrusive Suite/Sandy Brook formation. The Tally Pond group, in which Lemarchant deposit is located, is defined by the area within the red square. The Tally Pond group also hosts the Duck Pond and Boundary deposits. Their locations are marked by red circles. c) Detailed geologic map of the Tally Pond group and the locations U-Pb geochronological studies. TVB = Tulks volcanic belt; TPB = Tally Pond; CLIS = Crippleback Intrusive Suite. Diagram modified from McNicoll et al. (2010).

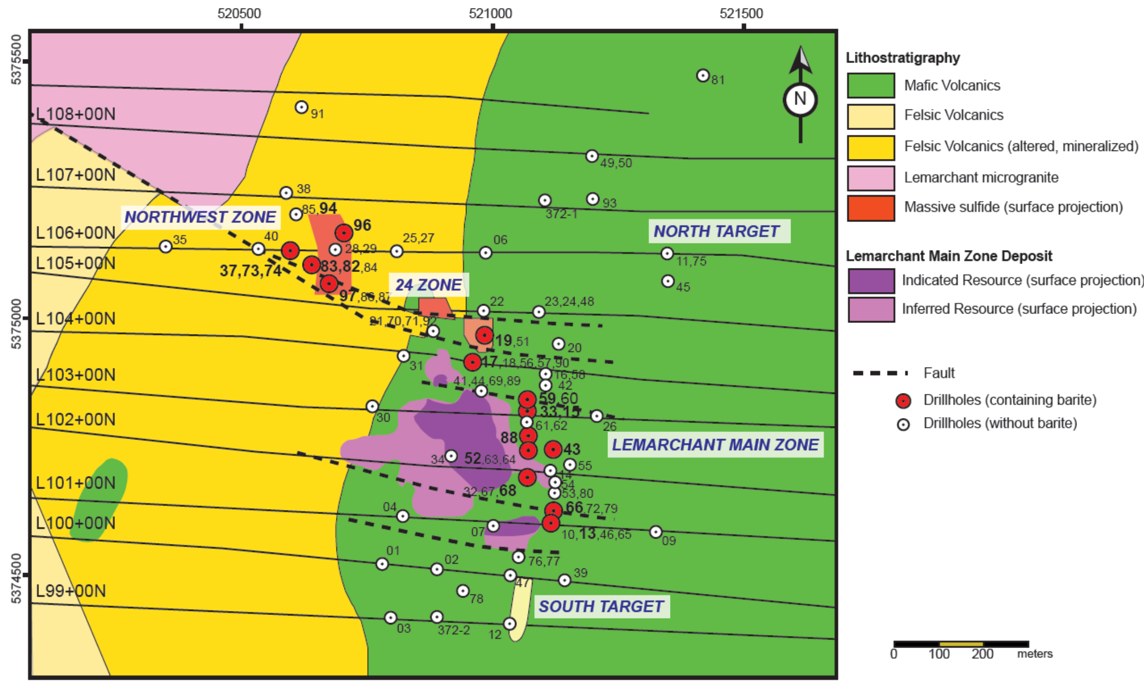

Figure 2-2. Simplified geologic map of the Lemarchant deposit with drill hole locations. Drill holes represented by a red circle are those that contain barite mineralization. The bimodal nature of the Lemarchant deposit is illustrated by the felsic volcanic footwall and the mafic volcanic hangingwall. The Lemarchant microgranite is located 500 m northwest of the mineralized zone. The Lemarchant fault strikes north-south and is indicated by the black line in the center. Surface projection of indicated and inferred resources are shown and are represented by the dark and light purple colors (Main zone). The surface projection of the indicated resources in the northwest zone is represented by the red rectangle. Modified after Fraser et al. (2012).

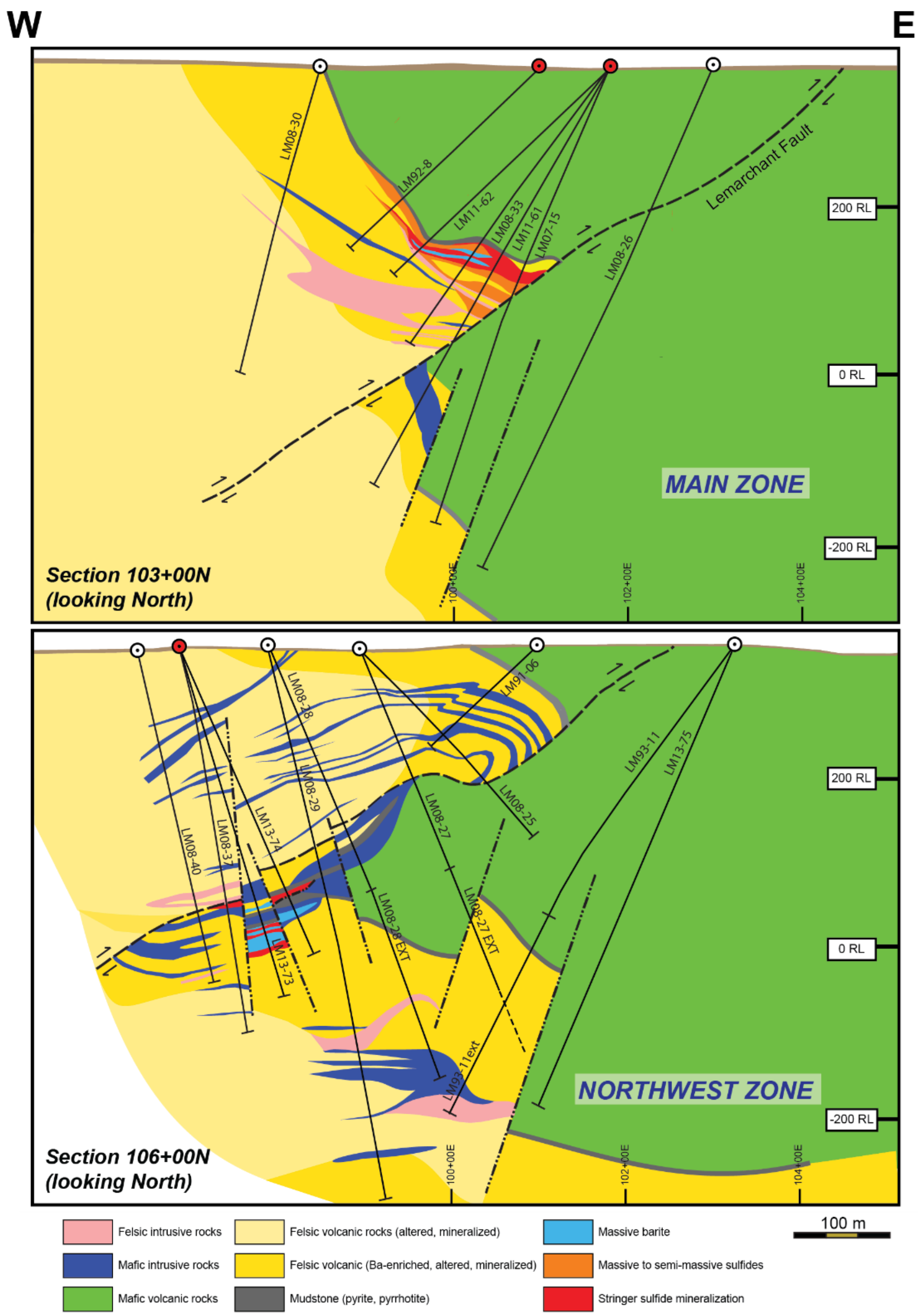

Figure 2-3. Schematic cross-section of section 103+00N (Main zone) and 106+00N (Northwest zone) of the Lemarchant deposit illustrating the mineralized zones and their relationship to the mafic-dominated hangingwall and the felsic-dominated footwall. Drill holes are represented by the thin solid black lines. Drill holes represented by a red circle are those that contain barite mineralization. Modified after Fraser et al. (2012).

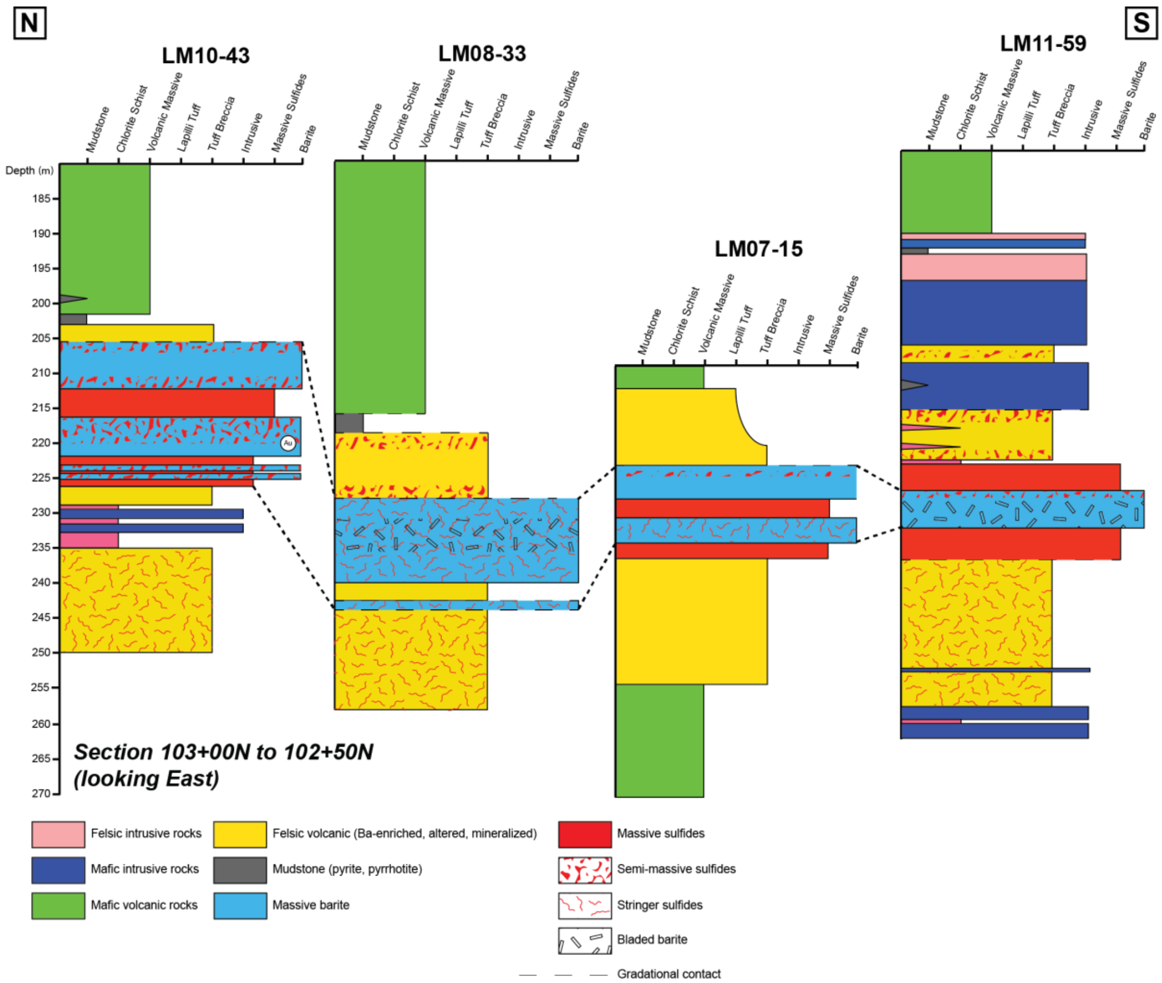

Figure 2-4. Graphic logs of section 103+00N to 102+50N intercepting the Main zone of the Lemarchant deposit. Barite units are interpolated between drill holes. Barite is intimately associated with mineralization and occurs between a metalliferous mudstone unit (above) and altered felsic volcanic rocks (below).

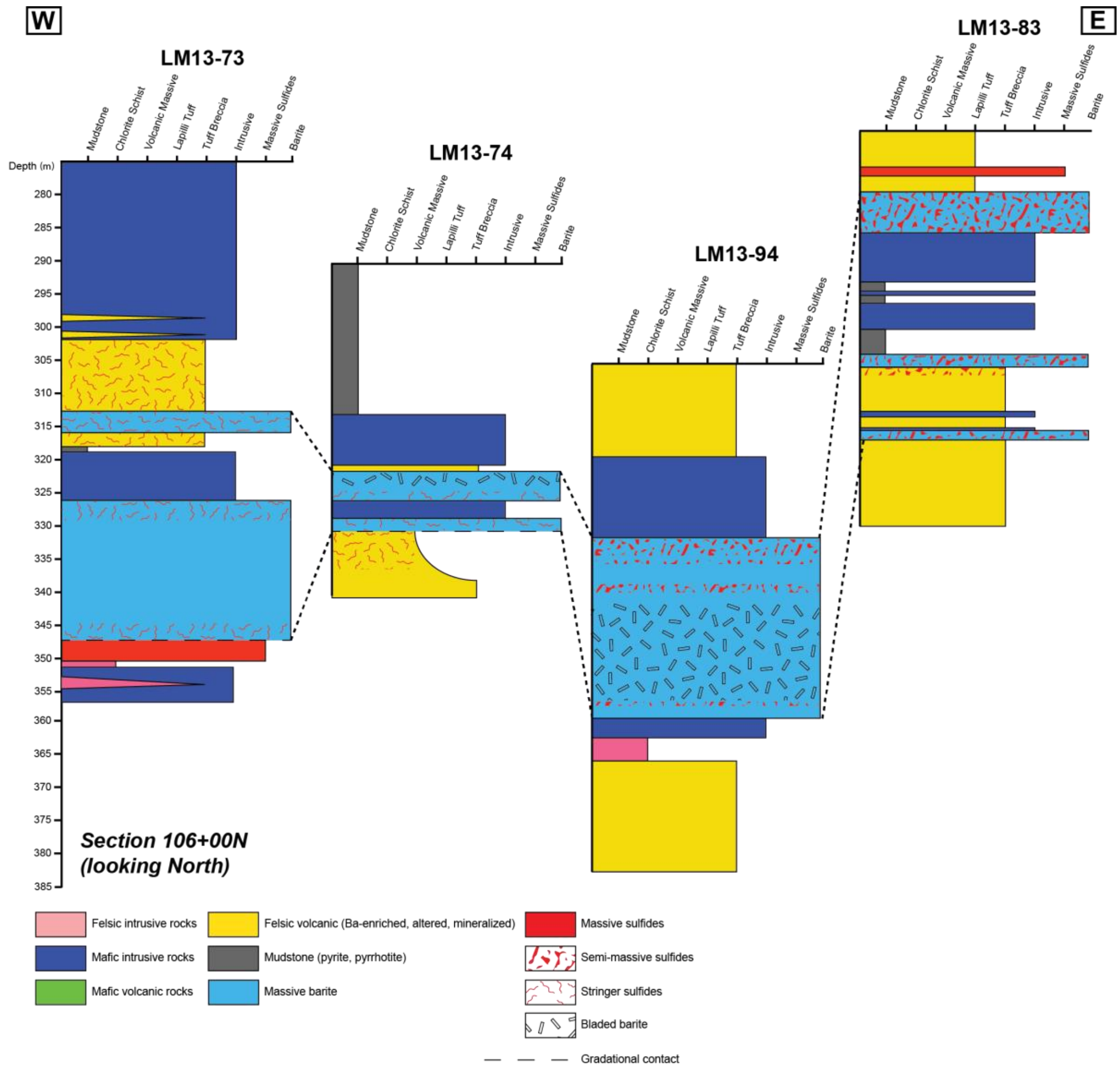

Figure 2-5. Graphic logs of section 106+00N intercepting the Northwest zone of the Lemarchant deposit. Barite units are interpolated between drill holes. Barite is intimately associated with mineralization and mafic dykes are abundant throughout the mineralized zone.

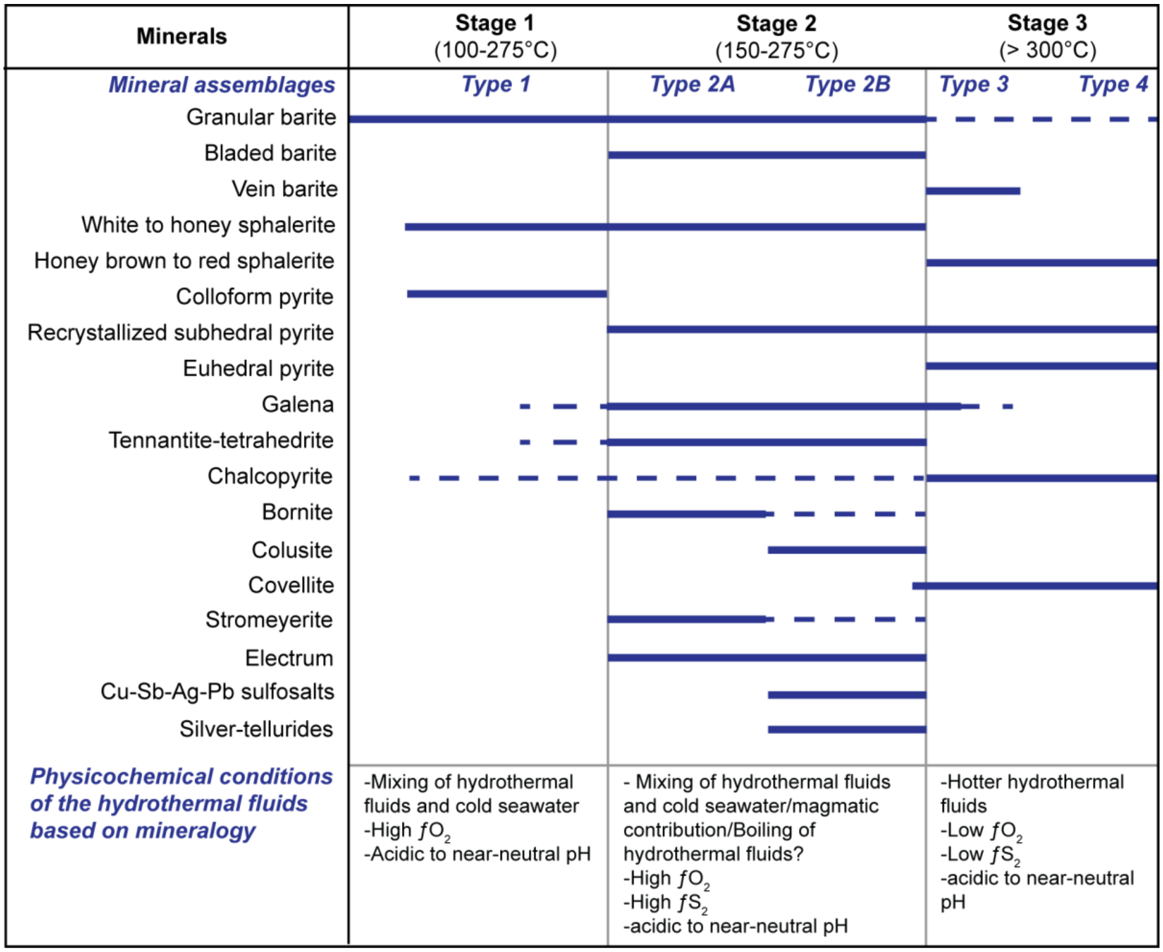

Figure 2-6. Simplified mineral paragenetic sequence diagram for the three main stages of mineralization of the Lemarchant deposit and the associated mineral assemblage types based on the work of Gill et al. (2015). Approximate temperature ranges for different minerals are based on temperature measurements from vent fluids, fluid inclusions, and thermodynamic equilibria (Hannington and Scott, 1988; Paradis et al., 1988; Koski et al., 1994; Drummond and Ohmoto, 1985). Modified from Gill et al. (2015).

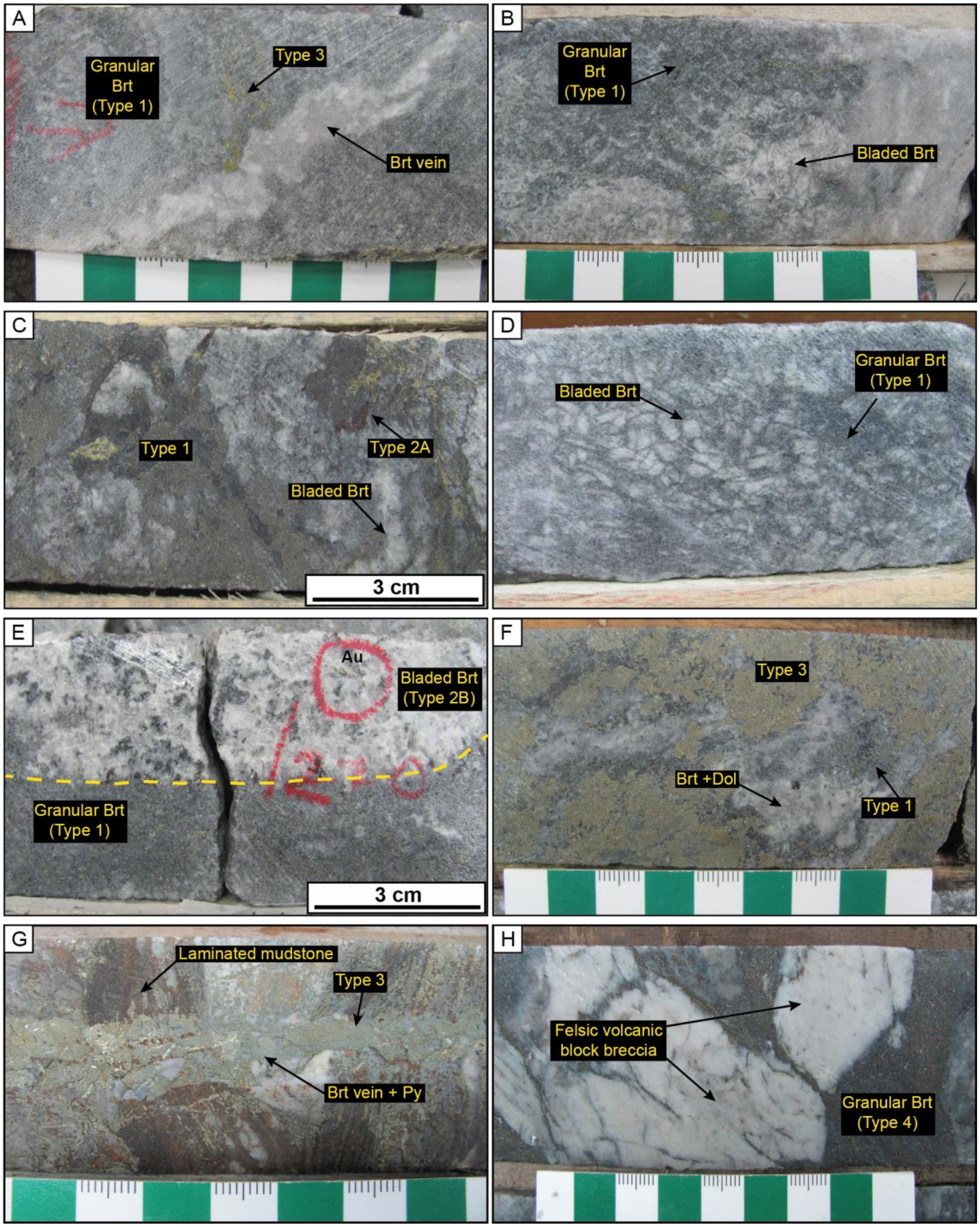
A
Granular Brt (Type 1)
Type 3
Brt vein
B
Granular Brt (Type 1)
Bladed Brt
C
Type 1
Type 2A
Bladed Brt
3 cm
D
Bladed Brt
Granular Brt (Type 1)
E
Au
Bladed Brt (Type 2B)
Granular Brt (Type 1)
3 cm
F
Type 3
Brt +Dol
Type 1
G
Laminated mudstone
Type 3
Brt vein + Py
H
Felsic volcanic block breccia
Granular Brt (Type 4)

Figure 2-7. Drill core images showing the different barite textures and associated mineral assemblage type. A) Granular barite associated with type 1 mineral assemblage (disseminated low-Fe sphalerite, galena, pyrite), crosscut by a white, euhedral barite vein associated with type 3 mineral assemblage (dominantly chalcopyrite) (sample CNF31830 from drill hole LM07-15, depth: 230 m). B) Granular barite associated with disseminated type 1 sulfide assemblage with localized areas of bladed barite, milky carbonate and wispy chalcopyrite blebs (sample CNF31830 from drill hole LM07-15, depth: 232 m). C) Type 2A mineral assemblages (bornite, covellite, chalcopyrite, galena) associated with localized areas of bladed barite overprinting disseminated sulfides from type 1 assemblage (sample CNF31809 from drill hole LM10-43, depth: 213.7 m). D) Bladed barite in a granular baritic matrix (sample CNF31804 from drill hole LM11-59, depth: 227.6 m). E) Sharp contact between bladed barite associated with type 2B mineralization and granular barite associated with type 1 mineralization. Visible electrum (type 2B) is present in bladed barite (sample CNF31811 from drill hole LM10-43, depth: 210 m). F) Type 3 mineralization composed dominantly of pyrite and minor chalcopyrite (zone refining) overprinting type 1 mineralization in a chaotic granular barite-dolomite matrix (sample). G) Type 3 pyrite-rich vein crosscutting the overlying laminated mudstone unit (sample CNF31847 from drill hole LM13-83, depth: 300.2 m). H) Type 4 mineralization (high-Fe sphalerite, pyrite, granular barite) within interstitial spaces of felsic volcanic blocks in the footwall stockwork zone (sample CNF31854 from drill hole LM13-88, depth: 214.5 m).

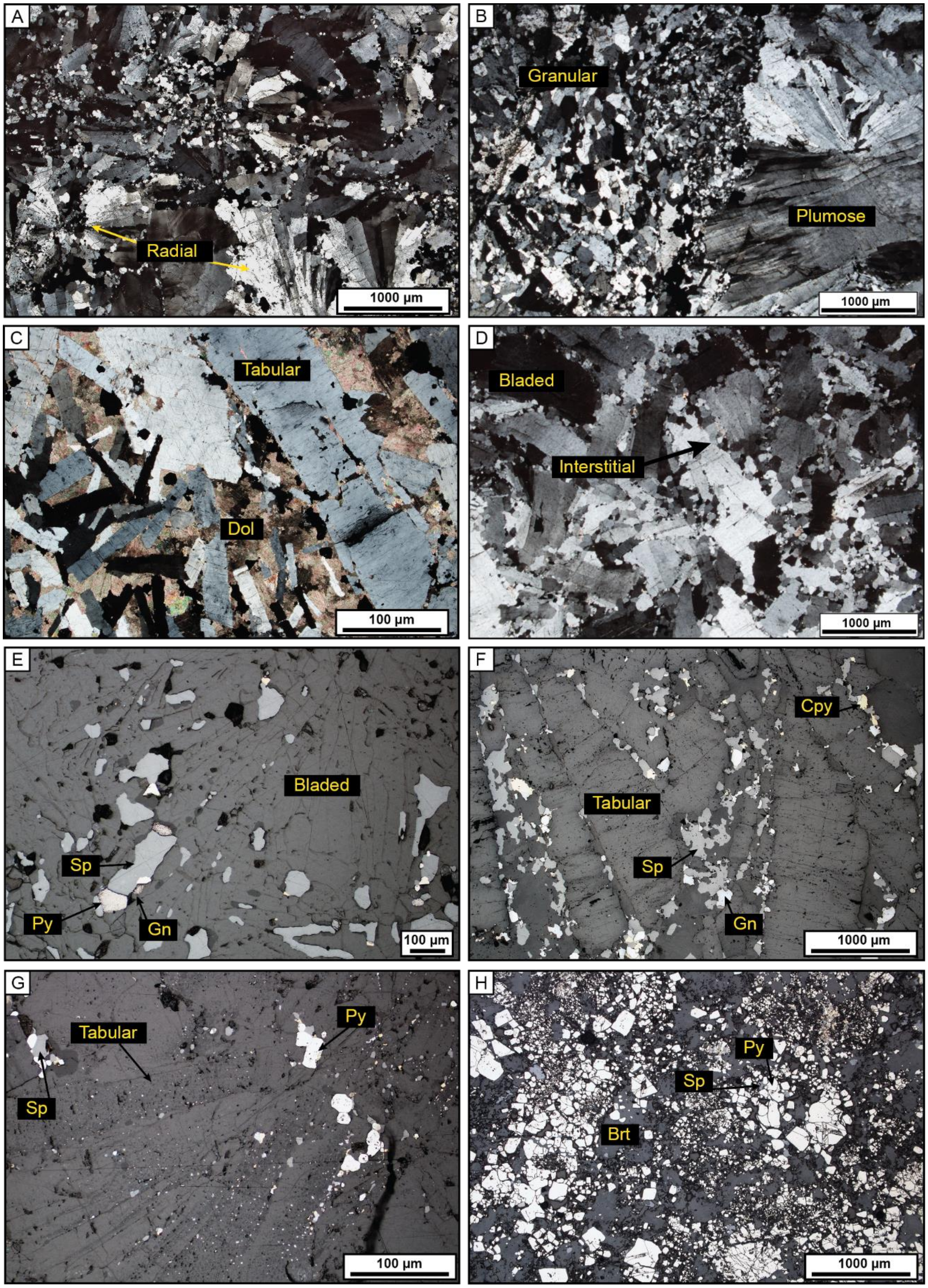
A
Radial
1000 µm
B
Granular
Plumose
1000 µm
C
Tabular
Dol
100 µm
D
Bladed
Interstitial
1000 µm
E
Bladed
Sp
Py
Gn
100 µm
F
Cpy
Tabular
Sp
Gn
1000 µm
G
Tabular
Py
Sp
100 µm
H
Py
Sp
Brt
1000 µm

Figure 2-8. Cross-polarized and reflected images of thin sections of the different barite textures found at the Lemarchant deposit. A) Cross-polarized image showing localized radiating barite laths from central subhedral, rounded barite clusters (sample CNF31803 from drill hole LM11-59, depth: 226.6 m). B) Cross-polarized image showing plumose barite crystal adjacent to small, subhedral, interlocking granular barite grains (sample CNF31860 from drill hole LM11-68, depth: 198 m). C) Cross-polarized image showing randomly oriented large tabular barite laths with carbonate filling interstitial spaces between barite crystals (sample CNF31863 from drill hole LM11-68, depth: 203.4 m). D) Cross-polarized image showing bladed barite with interstitial granular barite between barite blades (sample CNF31860 from drill hole LM11-68, depth: 198 m). E) Reflected image showing bladed crystals of barite. The matrix interstitial to the barite blades is composed of smaller, granular barite grains and sulfides such as sphalerite, galena, and pyrite (sample CNF31849 from drill hole LM13-83, depth: 304.4 m). F) Large tabular laths of barite with sulfides (sphalerite, galena, chalcopyrite) infilling the interstitial space between the laths (sample CNF31863 from drill hole LM11-68, depth: 203.4 m). G) Reflected image of micro-inclusions of sulfides in fluid inclusions in bladed/tabular barite (sample CNF31860 from drill hole LM11-68, depth: 198 m). H) Reflected image showing euhedral pyrite and disseminated sulfides associated with granular barite (sample CNF31877 from drill hole LM11-66, depth: 164.4 m).

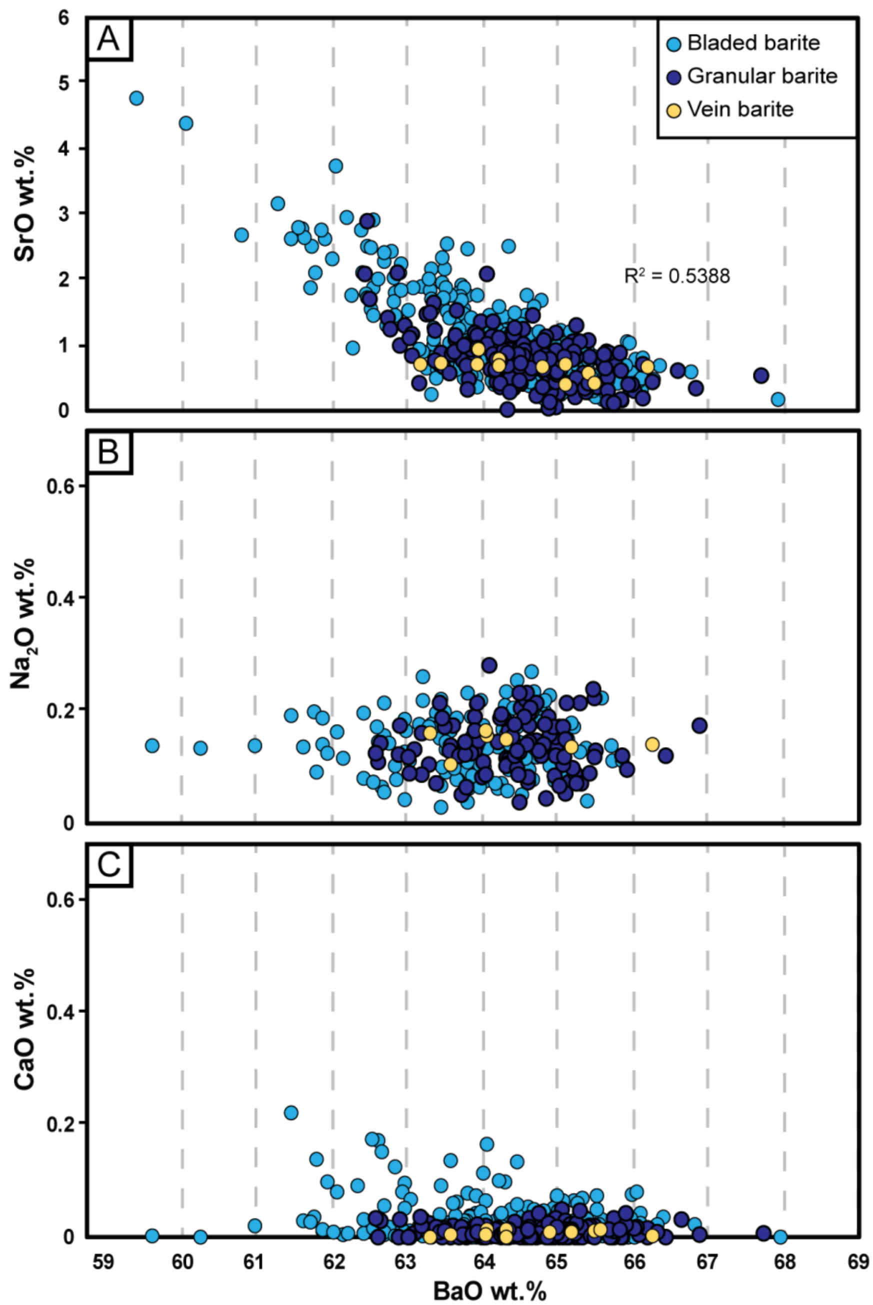

Figure 2-9. BaO versus a) strontium; b) sodium; c) calcium. A strong negative correlation exists between Sr and Ba, whereas no correlation exists between Na vs. Ba and Ca vs. Ba. The correlation between Sr and Ba is associated with the solid solution series between celestite ($SrSO_4$) and barite ($BaSO_4$).

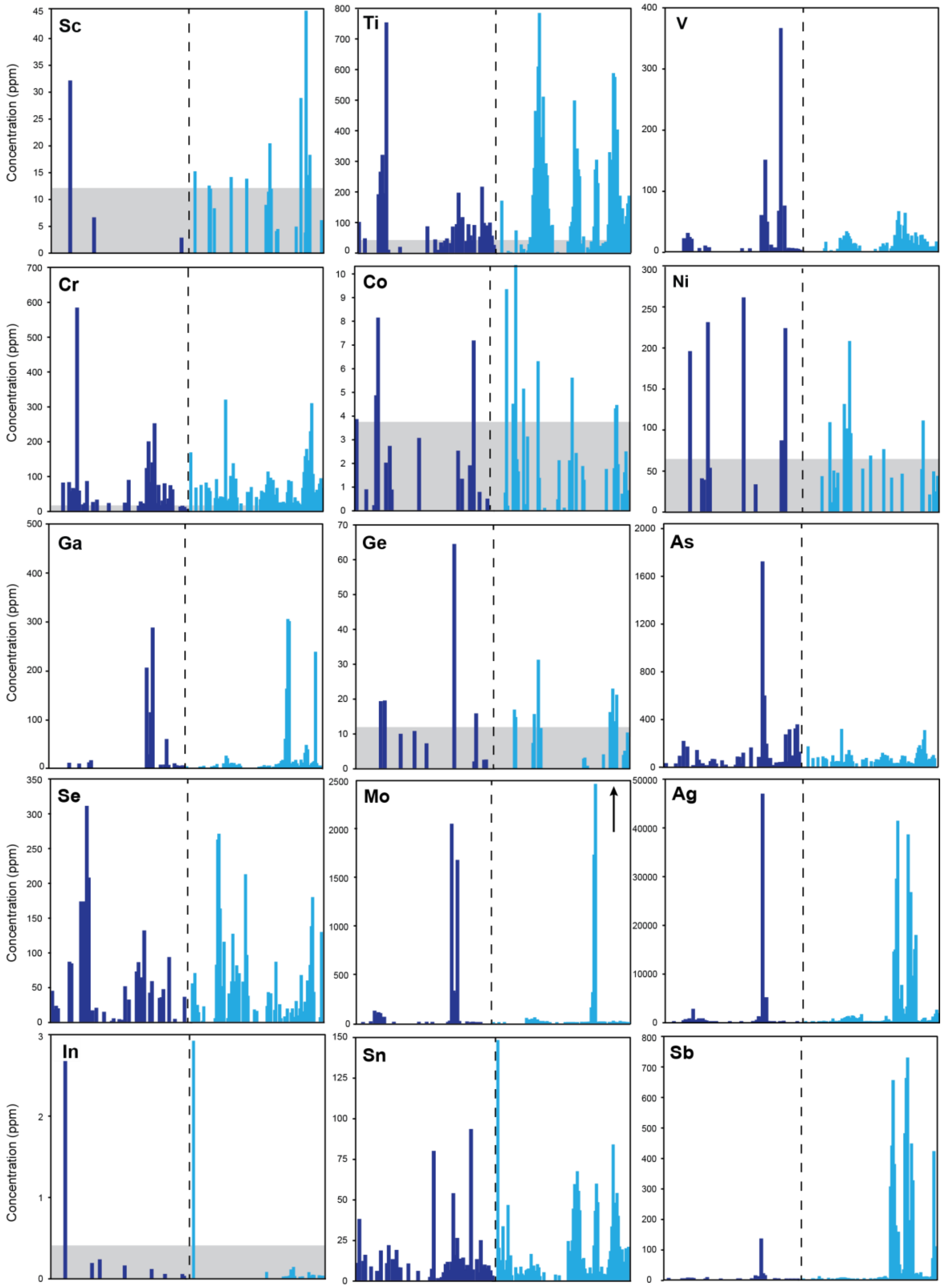
Sc
Ti
V
Cr
Co
Ni
Ga
Ge
As
Se
Mo
Ag
In
Sn
Sb
Concentration (ppm)

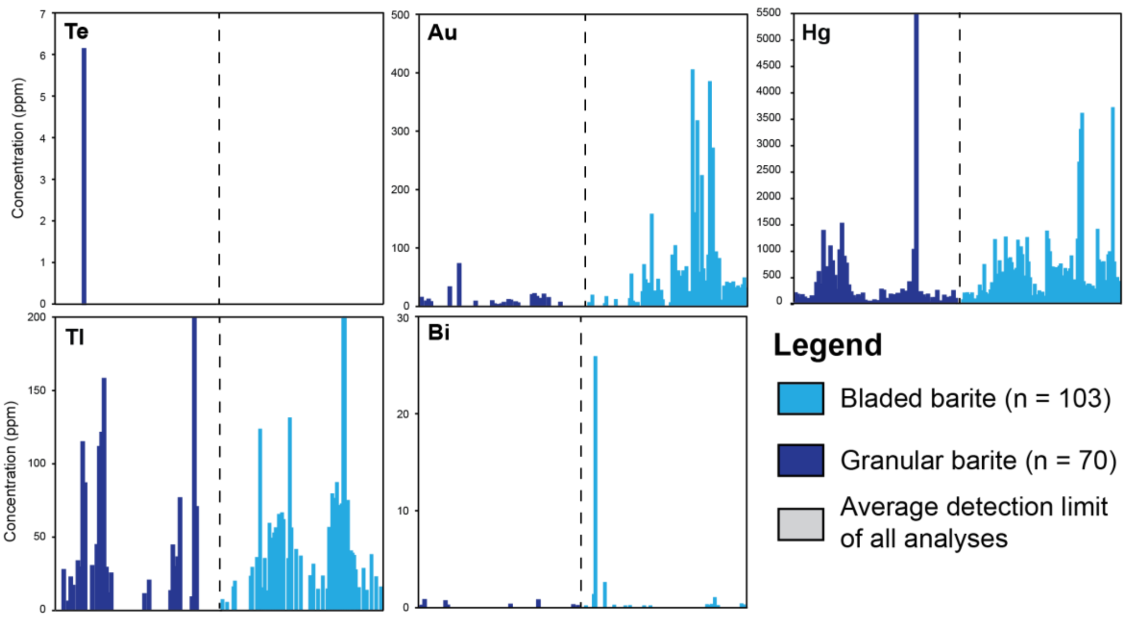

Figure 2-10. Trace element concentration (ppm) variations between bladed and granular barite. Bladed barite is represented by the light blue colour and granular barite by the dark blue colour. The average detection limit of all analyses for individual trace element is shown in light grey. The elements represented are: Sc, Ti, V, Cr, Co, Ni, Ga, Ge, As, Se, Mo, Ag, In, Sn, Sb, Te, Au, Hg, Tl, and Bi.

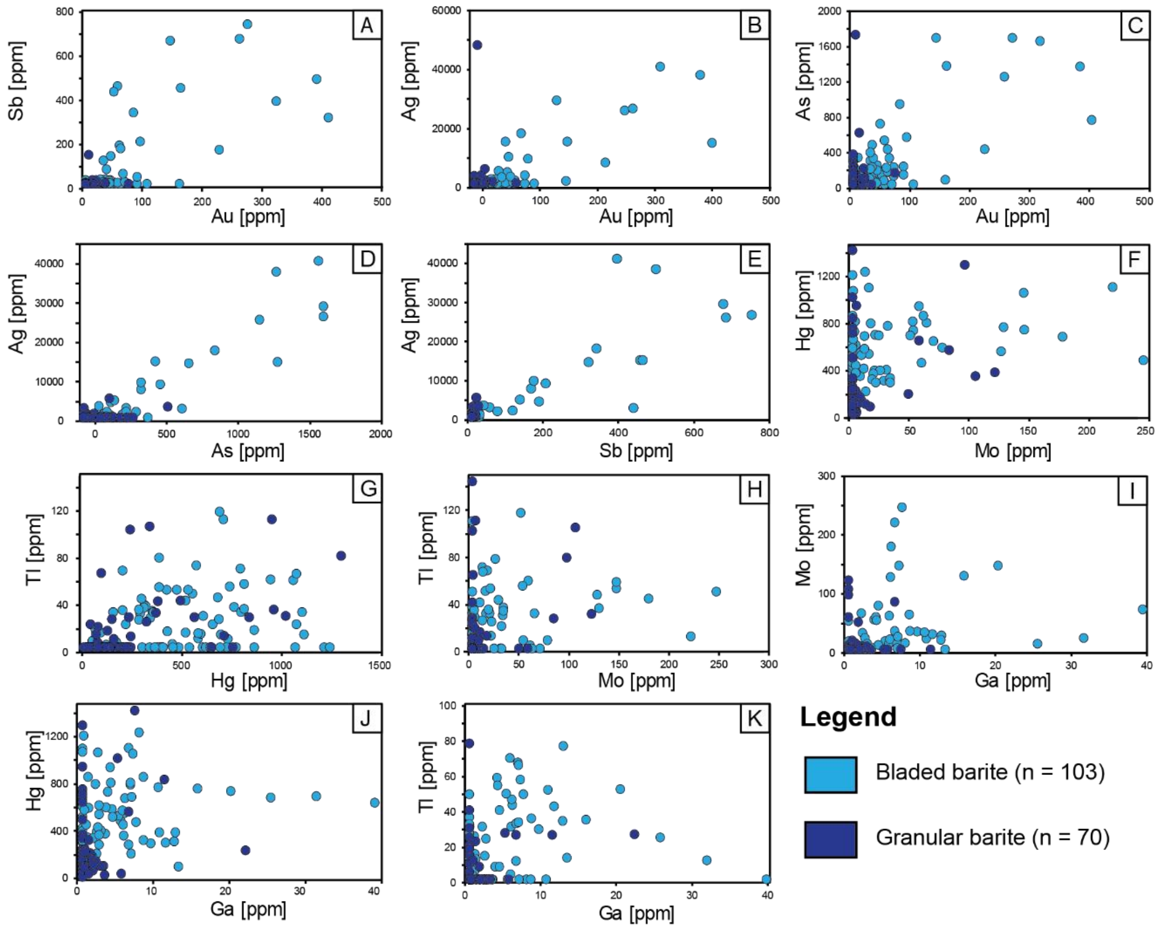

Figure 2-11. Compositional plots of selected trace elements from barite samples of the Lemarchant deposit: (A) Au vs Sb; (B) Au vs Ag; (C) Au vs As; (D) As vs Ag; (E) Sb vs Ag; (F) Mo vs Hg; (G) Hg vs Tl; (H) Mo vs Tl; (I) Ga vs Mo; (J) Ga vs Hg; (K) Ga vs Tl.

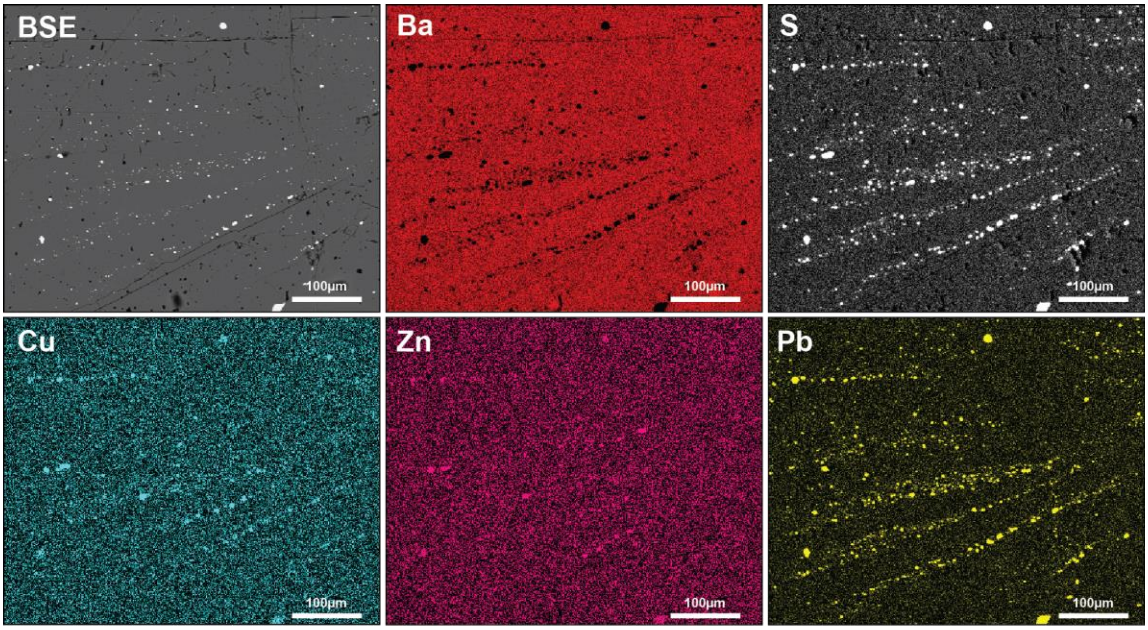

Figure 2-12. Back scattered electron (BSE) image and semi-quantitative elemental maps (Ba, S, Cu, Zn, and Pb) showing an example of captured sulfide phases in pseudo-secondary fluid inclusion trails in barite blades (sample CNF31860 from drill hole LM11-68, depth: 198 m).

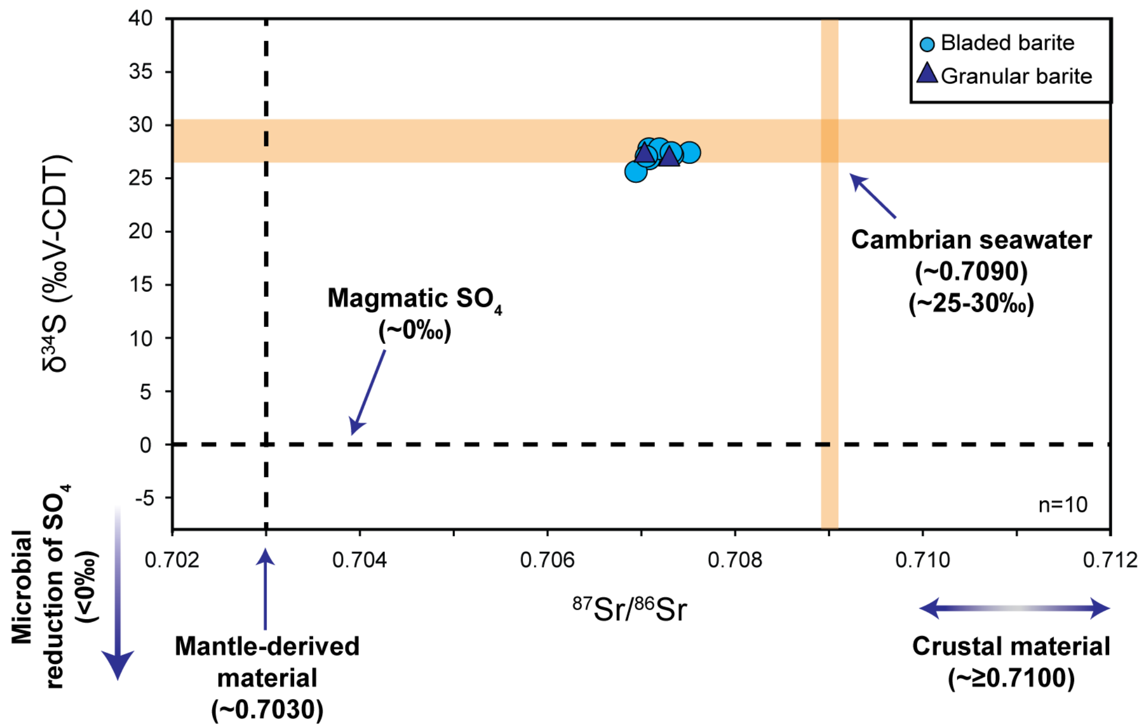

Figure 2-13. Plot of S isotopic composition of bladed and granular barite versus whole-rock Sr isotopic geochemistry of barite from the Lemarchant deposit and approximate endmember composition of different reservoirs. Light orange areas represent S and Sr isotopic composition of middle to late Cambrian seawater ($\delta^{34}S \approx 25\text{-}30‰$ and $^{87}Sr/^{86}Sr \approx 0.7090$, respectively; Sangster, 1968; Claypool et al., 1980; Ohmoto and Goldhaber, 1997; Huston, 1999; Seal, 2006; Burke et al., 1982; Derry et al., 1989, 1994; Asmerom et al., 1991; Montañez et al., 1996; Denison et al., 1998). Dotted black lines represent S isotope composition of magmatic sulfate ($\delta^{34}S$ ~0‰; Ohmoto and Rye, 1979; Janecky and Shanks, 1988, Huston, 1999, Shanks, 2001; Seal, 2006) and Sr isotope composition of Cambrian-Ordovician mantle-derived material ($^{87}Sr/^{86}Sr \approx 0.7030$; Ayuso and Schulz, 2003). Ranges of S isotope signatures of microbial reduction of sulfate ($\delta^{34}S$ <0‰; Elsgard et al., 1994; Habicht and Canfield, 2001; Shanks, 2001; Seal, 2006) and Sr isotope signatures of more radiogenic crustal material ($^{87}Sr/^{86}Sr$ > 0.7100; Griffith and Paytan, 2012) signatures are shown by the dark blue arrows.

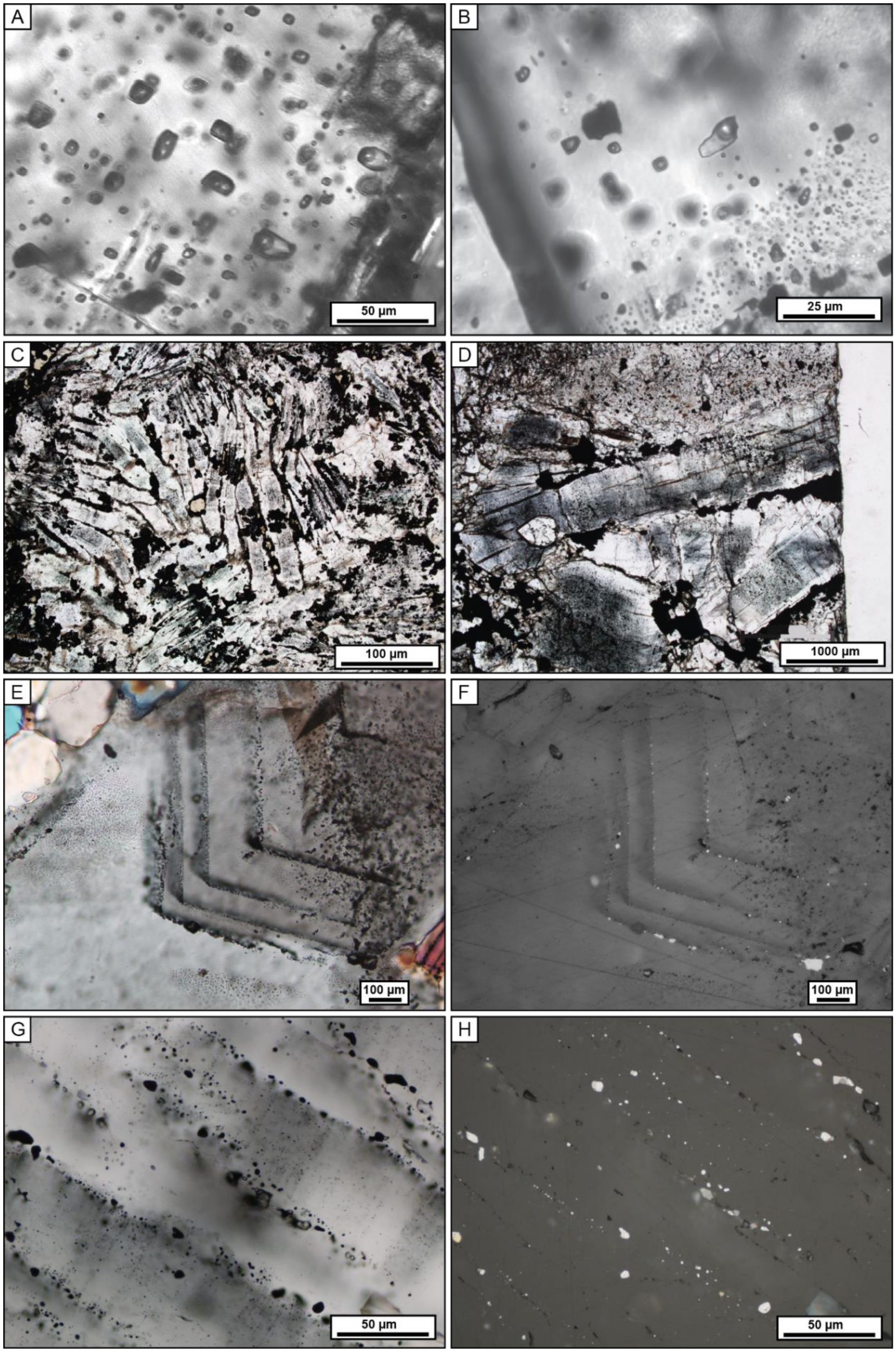
A
50 µm
B
25 µm
C
100 µm
D
1000 µm
E
100 µm
F
100 µm
G
50 µm
H
50 µm

Figure 2-14. Photomicrographs of fluid inclusions in bladed barite from the Lemarchant deposit. A) Transmitted light image showing secondary carbonic-rich fluid inclusion (L_1+L_2+V) population in primary growth zones in a late barite vein (sample CNF31723 from drill hole LM13-73, depth: 346.5 m). B) Transmitted light image showing secondary carbonic-rich fluid inclusion population clearly showing the immiscible three phases (L_1+L_2+V) (sample CNF31874 from drill hole LM13-82, depth: 340.8 m). C) Transmitted light image of bladed barite showing clusters of secondary fluid inclusions (L_1+L_2+V) in primary growth zones found in the center of blades (sample CNF31723 from drill hole LM13-73, depth: 346.5 m). D) Transmitted light image of bladed barite showing clusters of secondary fluid inclusions (L_1+L_2+V) in primary growth zones in the center of the blades (sample CNF31874 from drill hole LM13-82, depth: 340.8 m). E) Cross-polarized image showing growth zones in a single tabular barite crystal that are delineated by trails of secondary fluid inclusions that contain sulfides (black) (sample CNF31735 from drill hole LM13-94, depth: 346.7 m). F) Reflected image of the growth zones in E) supporting the presence of captured sulfides within the fluid inclusions. The sulfides are generally composed of sphalerite, galena, chalcopyrite, pyrite, and tetrahedrite (sample CNF31735 from drill hole LM13-94, depth: 346.7 m). G) Transmitted light image of pseudosecondary fluid inclusions that also contain micro-inclusions of captured sulfides (sample CNF31860 from drill hole LM11-68, depth: 198 m). H) Reflected image of pseudo-secondary fluid inclusions in G) clearly showing the abundance of micro-inclusions of sulfides within inclusion trails (sample CNF31860 from drill hole LM11-68, depth: 198 m).

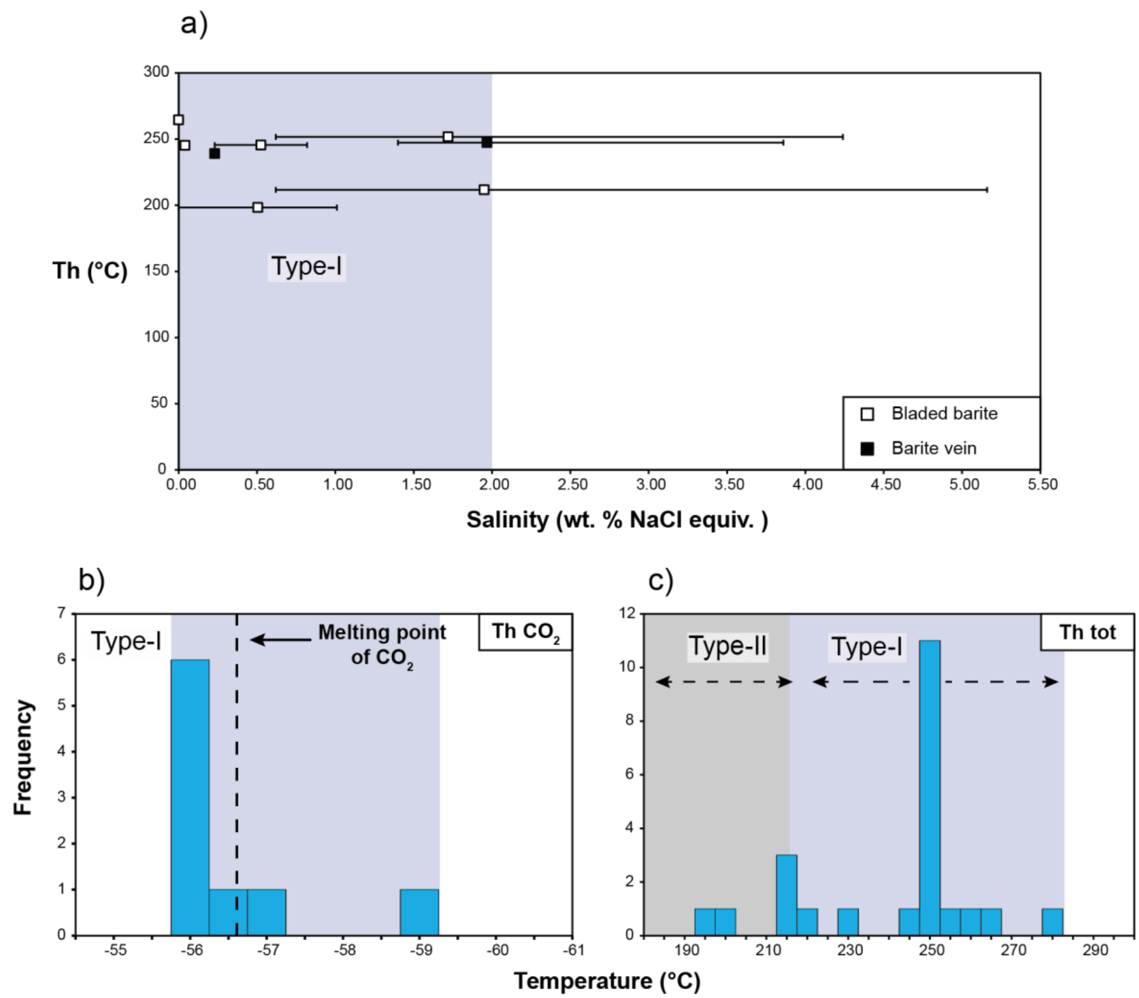

Figure 2-15. Fluid inclusion microthermometry results. A) Salinity (wt.% $NaCl_{equiv.}$) versus homogenization temperatures (T_h) of type-I (three-phase CO_2) inclusions. The squares represent the average salinity of individual fluid inclusion assemblages, whereas the solid black bars represent the range of salinities within individual fluid inclusion assemblages. The black squares represent salinity and homogenization temperatures of type-I inclusions from a barite vein (CNF31723). Note that the average salinities are below 2 wt.% $NaCl_{equiv}$. B) Range of temperature of homogenization of CO_2 ($ThCO_2$) (indicated by the shaded purple area) of all type-I inclusions in bladed barite. The theoretical melting point of CO_2 is indicated by the vertical dashed black line. C) Homogenization temperatures (T_h) of type-I and type-II (aqueous two-phase) fluid inclusions. T_h of type-I inclusions are represented by the shaded purple colour, whereas T_h for type-II inclusions are indicated by the shaded grey area. Notice that the T_h for type-I inclusions are generally higher than those of type-II inclusions.

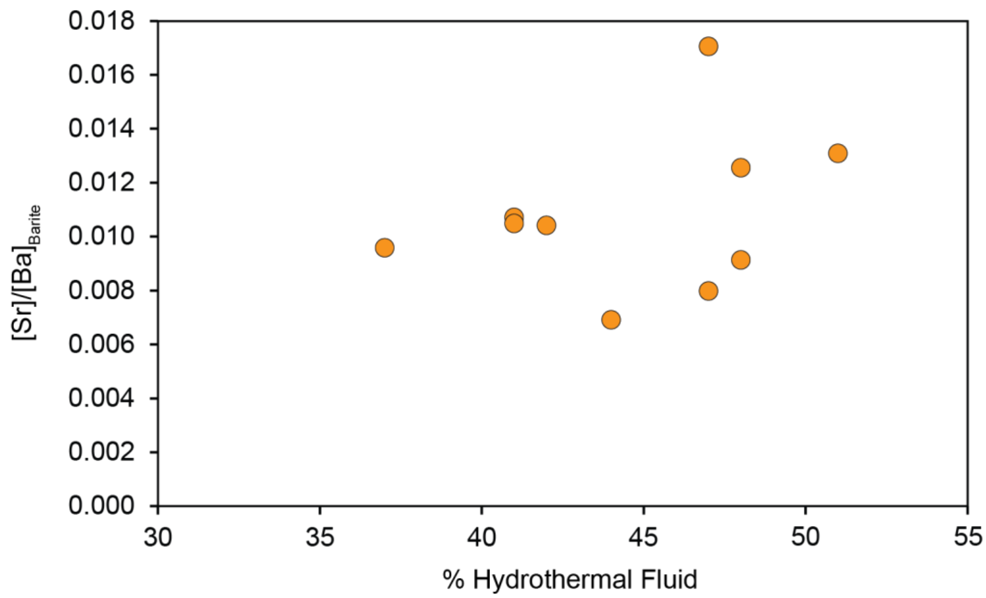

Figure 2-16. [Sr]/[Ba] ratio from whole-rock geochemistry results of barite versus %hydrothermal fluid for barite in the Lemarchant deposit.

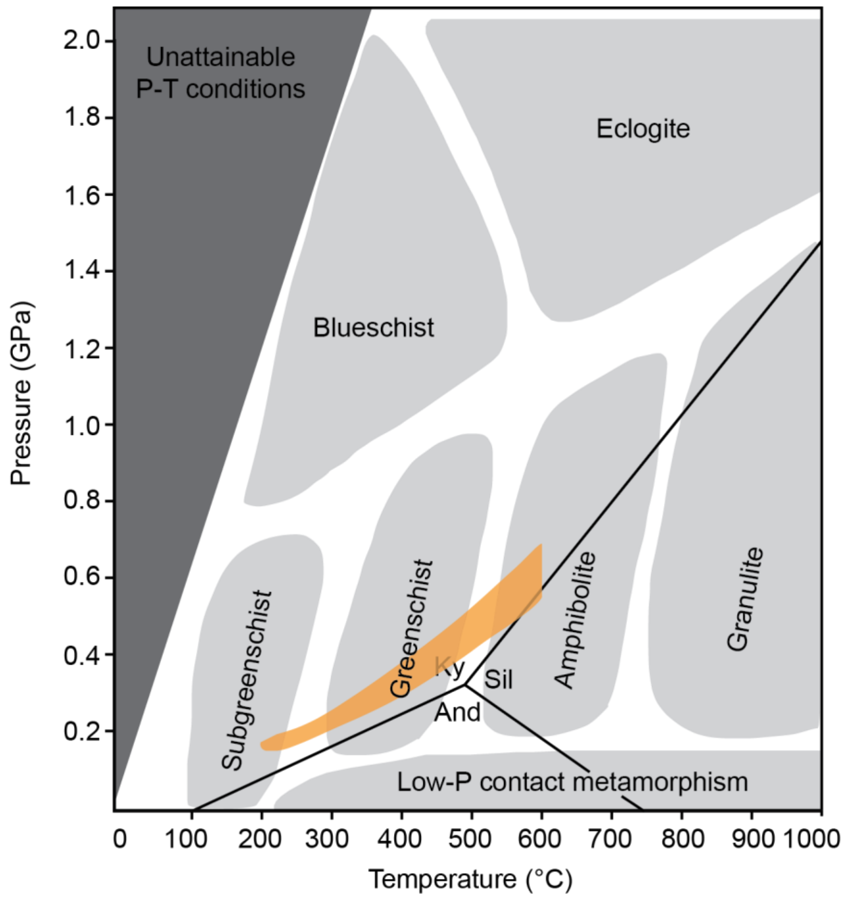

Figure 2-17. Schematic P-T projection of metamorphic facies. The orange field represents the range of isochores calculated for type-I aqueous-carbonic fluid inclusions in bladed barite. Our data suggests that type-I fluid inclusions are refilled primary fluid inclusions during circulation of greenschist facies metamorphic fluids. Our data is in agreement with the regional metamorphic grade of the Victoria Lake Supergroup. Isochores were calculated using the equation of states of Anderko and Pitzer (1993) and Duan et al. (1995). Metamorphic facies diagram from Bucher and Grapes (2011).

Chapter 3- Summary

The Zn-Pb-Cu-Ag-Au-Ba Lemarchant deposit is hosted within the bimodal Cambrian Tally Pond group in the Victoria Lake supergroup of the Exploits subzone, central Newfoundland. The Tally Pond group is host to numerous other VMS deposits including the past producing Duck Pond and Boundary deposits; all are hosted within the felsic volcanic rocks of the Bindons Pond formation. The mineralization style is broadly analogous to Kuroko-type VMS deposits, although the Lemarchant deposit had a significant contribution of magmatic volatiles to its metal budget.

Barite is preserved in most ancient VMS deposits due to its low solubility on the seafloor (Averyt and Paytan, 2003), and is an important marker horizon in many VMS deposits. Barite is often found in the uppermost portion of the deposits, and in some cases associated with precious-metal mineralization (Huston and Large, 1989; Hannington and Scott, 1989; Hannington and Gorton 1991, Hannington et al., 1995, 1999). A thorough study of barite using various techniques from the Lemarchant deposit has shown to be valuable for understanding the physicochemical conditions of barite formation and for identifying potential sources of hydrothermal fluids responsible for the formation of barite. In addition, preservation of geochemical characteristics in barite reveals a window into Cambrian seawater chemistry.

Despite being associated with intermediate- to high-sulfidation mineral assemblages, barite is remarkably homogeneous geochemically, regardless of texture. Major element geochemistry show that barite consists predominantly of Ba, S, Sr, with minor Na and Ca. Strontium partitioning is related to the solid solution between barite

($BaSO_4$) and celestine ($SrSO_4$) and may reflect temperature fluctuations during barite genesis (Jamieson et al., 2016). The presence of Na and Ca, albeit in low concentrations, is likely due to the mixing seawater and hydrothermal fluids during barite precipitation. Enrichments in trace elements (Ag-Au-As-Sb and Ga-Mo-Hg-Tl-V) in bladed barite, as found by LA-ICP-MS, likely reflect ablation of sulfide micro-inclusions. The sulfide micro-inclusions are probably captured solid phases rather than daughter minerals in fluid inclusions due to their localized appearance in selective samples.

Sulfur isotope signatures (avg. $\delta^{34}S$ = 27‰) of both granular and bladed barite indicate that Cambrian seawater was the main source of sulfur. Despite being intimately associated with sulfosalt-rich mineralization of potential magmatic-hydrothermal origin, sulfur isotope signatures do not show any evidence of magmatic input. Strontium isotope ratios measured in barite lay between those of Cambrian seawater values and crustal-derived reservoirs. We suggest that the $^{87}Sr/^{86}Sr$ ratios measured in barite may be attributed to the mixing of endmember seawater and crustal-derived Sr from underlying basement rocks (e.g. Sandy Brook group).

Three types of fluid inclusions are found in bladed barite: 1) type-I aqueous carbonic; 2) type-II aqueous two-phase (± CO_2); and 3) type-III vapor-rich inclusions (± CO_2?). The majority of the fluid inclusion assemblages in bladed barite from the Lemarchant deposit are refilled-primary aqueous carbonic fluid inclusions (type-I). We propose that CO_2-rich fluid inclusions from the Lemarchant deposit are in fact secondary and were originally two-phase fluid inclusions (similar to type-II) that subsequently refilled by later metamorphic fluids during regional greenschist metamorphism.

The geochemical data obtained during this study are comparable to present day barite-rich hydrothermal systems on the seafloor and complements the general Kuroko-style mineralization model initially discussed by Ohmoto et al. (1983). However, further research is required on barite in both ancient and modern VMS deposits to understand the controls on mineralization across geologic time.

3.1 Future research

While geochemical analyses from the Lemarchant deposit have demonstrated the implications for the genesis of VMS-related barite**,** many opportunities exist for future research that would add to the general model for barite in VMS-deposits and regional metallogenic framework of the Appalachians: 1) quantitatively determine the composition of fluid inclusions in barite using Raman spectroscopy. The use of Raman spectroscopy to quantitively identify other gaseous and solid phases in fluid inclusions in barite and sulfides such as sphalerite is a non-destructive method that has many geochemical applications such as understanding fluid (or phase) behaviour in hydrothermal systems. Using Raman spectroscopy in conjunction with microthermometric data of fluid inclusions can be a useful tool to understand mineralizing conditions at the Lemarchant deposit; 2) determine the temporal and spatial physicochemical properties of the hydrothermal fluids through deposit-scale fluid inclusion study of barite and/or metals from the stockwork zone to the overlying hydrothermal mudstone unit; 3) determine the source and thermal history of hydrothermal fluids (e.g. magmatic, metamorphic), and a more accurate model for the mineralization process responsible for the formation of barite using oxygen isotopes ($\delta^{18}O$) on barite and carbon isotopes ($\delta^{13}C$) on carbonate phases intergrown with barite; 4) determine fluid chemistry and temperature fluctuations during the growth of barite using *in situ* Sr- and S-isotopes of barite crystals; 5) in depth geochemical and petrological study of the Lemarchant microgranite to determine its relation with the Lemarchant deposit (source of metals from the Lemarchant microgranite (?); and 6) narrow the possible sources of Sr in Lemarchant barite through Sr isotope analyses of regional lithologies in the Tally Pond group. Our Sr isotope results suggests that the hydrothermal fluids responsible for the mineralization at the Lemarchant deposit and within the Tally Pond volcanic belt have encountered the underlying Neoproterozoic basement and implies that the Neoproterozoic basement is a source of metals. Additional Sr isotope studies of regional lithologies in the Tally Pond group could encourage exploration beyond the volcanic pile that hosts the Lemarchant deposit.

References

Albarède, F., Michard, A., Minster, J., and Michard, G. (1981). $^{87}Sr/^{86}Sr$ ratios in hydrothermal waters and deposits from the east pacific rise at 21 N. Earth and Planetary Science Letters, 55: 229-236.

Allen, R. L., Lundstrom, I., Ripa, M., and Christofferson, H. (1996). Facies analysis of a 1.9 Ga, continental margin, back-arc, felsic caldera province with diverse Zn-Pb-Ag-(Cu-Au) sulfide and Fe oxide deposits, Bergslagen region, Sweden. Economic Geology, 91: 979-1008.

Allen, R. L., and Weihed, P. (2002). Global comparisons of volcanic-associated massive sulphide districts. Geological Society, London, Special Publications, 204: 13-37.

Amini, M., Eisenhauer, A., Böhm, F., Fietzke, J., Bach, W., Garbe-Schönberg, D., ... and Hauff, F. (2008). Calcium isotope ($\delta^{44/40}Ca$) fractionation along hydrothermal pathways, Logatchev Field (Mid-Atlantic Ridge, 14 45′ N). Geochimica et Cosmochimica Acta, 72: 4107-4122.

Anderson, A. (1975). Some basaltic and andesitic gases. Reviews of Geophysics, 13: 37-55.

Anderko, A., and Pitzer, K. S. (1993). Phase equilibria and volumetric properties of the systems KCl-H_2O and NaCl-KCl-H_2O above 573K: Equation of state representation. Geochimica et Cosmochimica Acta, 57: 4885-4897.

Asmerom, Y., Jacobsen, S. B., Knoll, A. H., Butterfield, N. J., and Swett, K. (1991). Strontium isotopic variations of Neoproterozoic seawater: implications for crustal evolution. Geochimica et Cosmochimica Acta, 55: 2883-2894.

Averyt, K. B., and Paytan, A. (2003). Empirical partition coefficients for Sr and Ca in marine barite: Implications for reconstructing seawater Sr and Ca concentrations. Geochemistry, Geophysics, Geosystems, 4: 1043.

Ayuso, R. A., and Schulz, K. J. (2003). Nd-Pb-Sr isotope geochemistry and origin of the Ordovician Bald Mountain and Mount Chase massive sulfide deposits, northern Maine. Massive Sulfide Deposits of the Bathurst Mining Camp, New Brunswick, and Northern Maine. Economic Geology Monograph, 11: 611-630.

Bakker, R. J. (1997). Clathrates: Computer programs to calculate fluid inclusion V-X properties using clathrate melting temperatures. Computers and Geosciences, 23: 1-18.

Bakker, R. (1998). Improvements in clathrate modelling II: The H_2O-CO_2-CH_4-N_2-C_2H_6 fluid system. Geological Society, London, Special Publications, 137: 75-105.

Bakker, R. J., and Brown, P. E. (2003). Computer modelling in fluid inclusion research. Fluid inclusions*:* Analysis and interpretation, 32: 175-212.

Bakker, R. J., Dubessy, J., and Cathelineau, M. (1996). Improvements in clathrate modelling: I. the H_2O-CO_2 system with various salts. Geochimica Et Cosmochimica Acta, 60*:* 1657-1681.

Barbour, D., (1990). Valentine Lake Gold Deposit. *In* Swinden, H.S., Evans, D. T.W., and Kean, B. F., eds., Metallogenic framework of base and precious metal deposits, central and western Newfoundland. Geological Survey of Canada, Open File 2156: 73-77.

Barr, S., Raeside, R., and White, C. (1998). Geological correlations between Cape Breton Island and Newfoundland, northern Appalachian Orogen. Canadian Journal of Earth Sciences, 35: 1252-1270.

Barrett, T. J., and MacLean, W. H., (1999). Volcanic sequences, lithogeochemistry, and hydrothermal alteration in some bimodal volcanic-associated massive sulfide systems: Reviews in Economic Geology, 8: 101-131.

Barrie, C. T., Cathles, L. M., and Erendi, A. (1999). Finite element heat and fluid-flow computer simulations of a deep ultramafic sill model for the giant Kidd Creek volcanic-associated massive sulfide deposit. Economic Geology, Monograph, 10: 529-540.

Barrie, C., and Hannington, M. (1999). Classification of volcanic-associated massive sulfide deposits based on host-rock composition. Reviews in Economic Geology, 8: 1-11.

Berner, R. A. (2004). A model for calcium, magnesium and sulfate in seawater over Phanerozoic time. American Journal of Science, 304: 438-453.

Binns, R. A., Scott, S. D., Bogdanov, Y. A., Lisitzin, A. P., Gordeev, V. V., Gurvich, E. G., Finlayson, E. J., Dotter, L. E., Wheller, G. E., and Muravyev, K. G. (1993). Hydrothermal oxide and gold-rich sulfate deposits of Franklin Seamount, western Woodlark Basin, Papua New Guinea. Economic Geology, 88: 2122-2153.

Bischoff, J. L., & Seyfried, W. E. (1978). Hydrothermal chemistry of seawater from 25 degrees to 350 degrees C. American Journal of Science, 278: 838-860.

Bischoff, J. L., and Rosenbauer, R. J. (1985). An empirical equation of state for hydrothermal seawater (3.2 percent $NaCl^-$). American Journal of Science, 285: 725-763.

Blount, C. (1977). Barite solubilities and thermodynamic quantities up to 300/sup 0/C and 1400 bars. American Mineralogist, 62: 9-10.

Bodnar, R. J. (2003). Introduction to aqueous-electrolyte fluid inclusions. Fluid Inclusions: Analysis and Interpretation, 32: 81-100.

Bodnar, R. J., and Vityk, M. O. (1994). Interpretation of microthermometric data for H_2O-NaCl fluid inclusions. Fluid inclusions in minerals: methods and applications, IMA Short Course: 117-130.

Boström, K., Frazer, J., Blankenburg, J. (1967). Subsolidus phase relations and lattice constants in the system BaSO4-SrSO4-PbSO4. Arkiv Mineral Geol, 4: 477-485.

Buschette, M. J., and Piercey, S. J. (2016). Hydrothermal alteration and lithogeochemistry of the Boundary volcanogenic massive sulphide deposit, central Newfoundland, Canada. Canadian Journal of Earth Sciences, 53: 506-527.

Boulanger, R.A., Chi, G., Skulski, T., Castonguay, S. (2010). Characterization and evolution of fluids associated with the Cu-Au deposit of the Ming Mine, Rambler area, northeast Newfoundland, Canada. GeoCanada 2010 – Working with the Earth: p. 5.

Burke, W., Denison, R., Hetherington, E., Koepnick, R., Nelson, H., and Otto, J. (1982). Variation of seawater $^{87}Sr/^{86}Sr$ throughout Phanerozoic time. Geology, 10: 516-519.

Butterfield, D. A., Jonasson, I. R., Massoth, G. J., Feely, R. A., Roe, K. K., Embley, R. E., ... & Delaney, J. R. (1997). Seafloor eruptions and evolution of hydrothermal fluid chemistry. Philosophical Transactions of the Royal Society of London A: Mathematical, Physical and Engineering Sciences, 355: 369-386.

Butterfield, D. A., Massoth, G. J., McDuff, R. E., Lupton, J. E., and Lilley, M. D. (1990). Geochemistry of hydrothermal fluids from Axial Seamount hydrothermal emissions study vent field, Juan de Fuca ridge: Subseafloor boiling and subsequent fluid-rock interaction. Journal of Geophysical Research: Solid Earth, 95: 12895-12921.

Campbell, I. H., Franklin, J. M., Gorton, M. P., Hart, T. R., and Scott, S. D. (1981). The role of subvolcanic sills in the generation of massive sulfide deposits. Economic Geology, 76: 2248-2253.

Campbell, I. H., McDougall, T. J., and Turner, J. S. (1984). A note on fluid dynamic processes which can influence the deposition of massive sulfides. Economic Geology, 79: 1905-1913.

Carey, S., Nomikou, P., Bell, K. C., Lilley, M., Lupton, J., Roman, C., Stathopoulou, E., Bejelou, K., Ballard, R. (2013). CO_2 degassing from hydrothermal vents at Kolumbo submarine volcano, Greece, and the accumulation of acidic crater water. Geology, 41: 1035-1038.

Cathles, L. M., and Adams, J. J. (2005). Fluid flow and petroleum and mineral resources in the upper (< 20 km) continental crust. Economic Geology 100th Anniversary Volume: 77-110.

Cathles, L.M., Erendi, A.H.J., Theyer, J.B., and Barrie, C.T., (1997). How long can a hydrothermal system be sustained by a single intrusion event? Economic Geology, 92: 766-771.

Cawood, P. A., Hawkesworth, C. J., and Dhuime, B. (2013). The continental record and the generation of continental crust. Geological Society of America Bulletin, 125: 14-32.

Cawood, P. A., and Hawkesworth, C. J. (2015). Temporal relations between mineral deposits and global tectonic cycles. Geological Society, London, Special Publications, 393: 9-21.

Chiaradia, M., Tripodi, D., Fontboté, L., and Reza, B. (2008). Geologic setting, mineralogy, and geochemistry of the early Tertiary Au-rich volcanic-hosted massive sulfide deposit of La Plata, western Cordillera, Ecuador. Economic Geology, 103: 161-183.

Claypool, G. E., Holser, W. T., Kaplan, I. R., Sakai, H., and Zak, I. (1980). The age curves of sulfur and oxygen isotopes in marine sulfate and their mutual interpretation. Chemical Geology, 28: 199-260.

Cloutier, J., Piercey, S. J., Lode, S., Guchte, M. V., and Copeland, D. A. (2017). Lithostratigraphic and structural reconstruction of the Zn-Pb-Cu-Ag-Au Lemarchant volcanogenic massive sulphide (VMS) deposit, Tally Pond group, central Newfoundland, Canada. Ore Geology Reviews, 84: 154-173.

Colman-Sadd, S. P., Dunning, G., and Dec, T. (1992). Dunnage-Gander relationships and Ordovician orogeny in central Newfoundland; a sediment provenance and U-Pb age study. American Journal of Science, 292: 317-355.

Connelly, D. P., Copley, J. T., Murton, B. J., Stansfield, K., Tyler, P. A., German, C. R., ... & Hayman, N. (2012). Hydrothermal vent fields and chemosynthetic biota on the world's deepest seafloor spreading centre. Nature Communications, 3; 620.

Copeland, D. A. (2009). Assessment Report 012/1486 on Prospecting, Lithogeochemical Sampling and Data Interpretation on the Harpoon Property (Licenses 7695M, 10461M, 10464M, 10465M, 10607M, 12357M, 12885M, 13583M, 13448M, 13449M and 13667M) and the South Tally Pond Property (Licences 8183M, 9569M and 14158M) Lake Ambrose Area, Newfoundland and Labrador. NTS 12A/10 and 12A/07. Paragon Minerals Corporation.

Copeland, D. A., Toole, R.M.S., and Piercey, S.J. (2008). Assessment report on diamond drilling and soil sampling, Licence 8183M (10^{th} year) and 9569M (5^{th} year) South Tally Pond property, Rogerson Lake area, Newfoundland and Labrador, NTS 12A/10 and 12A/07; Newfoundland and Labrador Geological Survey, Assessment Report: p. 956.

Czamanske, G. K. (1974). The FeS content of sphalerite along the chalcopyrite-pyrite-bornite sulfur fugacity buffer. Economic Geology, 69: 1328-1334.

Dean, P. L. (1978). The Volcanic Stratigraphy and Metallogeny of Notre Dame Bay, Newfoundland, Unpublished M.Sc. Thesis, Memorial University of Newfoundland, Newfoundland.

Delaney, J. R., Robigou, V., McDuff, R. E., and Tivey, M. K. (1992). Geology of a vigorous hydrothermal system on the Endeavour Segment, Juan de Fuca Ridge. Journal of Geophysical Research: Solid Earth, 97: 19663-19682.

Denison, R. E., Koepnick, R. B., Burke, W. H., and Hetherington, E. A. (1998). Construction of the Cambrian and Ordovician seawater $^{87}Sr/^{86}Sr$ curve. Chemical Geology, 152: 325-340.

de Ronde, C. E. (1995). Fluid chemistry and isotopic characteristics of seafloor hydrothermal systems and associated VMS deposits: potential for magmatic contributions. Magmas, fluids, and ore deposits. Mineralogical Association of Canada, Short Course Series, 23: 479-509.

de Ronde, C. E., Hannington, M., Stoffers, P., Wright, I., Ditchburn, R., Reyes, A., Walker, S. (2005). Evolution of a submarine magmatic-hydrothermal system: Brothers volcano, southern Kermadec arc, New Zealand. Economic Geology, 100: 1097-1133.

de Ronde, C. E., Massoth, G. J., Butterfield, D. A., Christenson, B. W., Ishibashi, J., Ditchburn, R. G., and Takai, K. (2011). Submarine hydrothermal activity and gold-rich mineralization at Brothers Volcano, Kermadec Arc, New Zealand. Mineralium Deposita, 46: 541-584.

Derry, L. A., Brasier, M. D., Corfield, R. E. A., Rozanov, A. Y., and Zhuravlev, A. Y. (1994). Sr and C isotopes in Lower Cambrian carbonates from the Siberian craton: a paleoenvironmental record during the ‘Cambrian explosion’. Earth and Planetary Science Letters, 128: 671-681.

Derry, L. A., Keto, L. S., Jacobsen, S. B., Knoll, A. H., and Swett, K. (1989). Sr isotopic variations in Upper Proterozoic carbonates from Svalbard and East Greenland. Geochimica et Cosmochimica Acta, 53: 2331-2339.

Diamond, L. W. (2003). Introduction to gas-bearing, aqueous fluid inclusions. Fluid Inclusions: Analysis and Interpretation, 32, 101-158.

Drummond, S., and Ohmoto, H. (1985). Chemical evolution and mineral deposition in boiling hydrothermal systems. Economic Geology, 80: 126-147.

Duan, Z., Møller, N., and Weare, J. H. (1995). Equation of state for the NaCl-H_2O-CO_2 system: prediction of phase equilibria and volumetric properties. Geochimica et Cosmochimica Acta, 59: 2869-2882.

Dunning, G. R., Kean, B. F., Thurlow, J. G., and Swinden, H. S. (1987). Geochronology of the Buchans, Roberts Arm, and Victoria Lake groups and Mansfield Cove Complex, Newfoundland. Canadian Journal of Earth Sciences, 24: 1175-1184.

Dunning, G. R., O'Brien, S. J., Colman-Sadd, S. P., Blackwood, R. F., Dickson, W. L., O'Neill, P. P., and Krogh, T. E. (1990). Silurian orogeny in the Newfoundland Appalachians. The Journal of Geology: 895-913.

Dunning, G. R., Swinden, H. S., Kean, B. F., Evans, D. T. W., and Jenner, G. A. (1991). A Cambrian island arc in Iapetus: geochronology and geochemistry of the Lake Ambrose volcanic belt, Newfoundland Appalachians. Geological Magazine, 128: 1-17.

Eldridge, C. S., Barton Jr, P. B., and Ohmoto, H. (1983). Mineral textures and their bearing on formation of the Kuroko orebodies. Economic Geology, Monograph, 5: 241-281.

Elsgaard, L., Isaksen, M. F., Jørgensen, B. B., Alayse, A. M., and Jannasch, H. W. (1994). Microbial sulfate reduction in deep-sea sediments at the Guaymas Basin hydrothermal vent area: influence of temperature and substrates. Geochimica et Cosmochimica Acta, 58: 3335-3343.

Etoh, J., Izawa, E., Watanabe, K., Taguchi, S., and Sekine, R. (2002). Bladed quartz and its relationship to gold mineralization in the Hishikari low-sulfidation epithermal gold deposit, Japan. Economic Geology, 97: 1841-1851.

Evans, D. T. W. (1993a). Gold mineralization of the eastern Dunnage Zone, central Newfoundland. Newfoundland Department of Mines, Mineral Development Division, Report, 93-1: 339-349.

Evans, D.T.W., (1993b). The Midas Pond gold prospect, Victoria Lake Group: geology, alteration and mineralization. Unpublished M.Sc. thesis. Memorial University of Newfoundland.

Evans, D. T. W., and Kean, B. (2002). The Victoria Lake supergroup, central Newfoundland-its definition, setting and volcanogenic massive sulfide mineralization. Newfoundland and Labrador Department of Mines and Energy, Geological Survey, Open File NFLD/2790, p. 68.

Evans, D. T. W., Kean, B., and Dunning, G. (1990). Geological studies, Victoria Lake Group, central Newfoundland. Current Research. Newfoundland Department of Mines and Energy, Geological Survey Branch, Report, 90-91.

Evans, D. T. W., and Wilson, M. R. (1994). Epigenetic gold occurrences in the eastern Dunnage Zone, Newfoundland: preliminary stable isotope results. Current Research. Newfoundland Department of Mines and Energy, Geological Survey, Report, 94-1.

Farrell, C. W., and Holland, H. D. (1983). Strontium isotope geochemistry of the Kuroko deposits. Economic Geology, Monograph, 5: 302-319.

Farrell, C., Holland, H., and Petersen, U. (1978). The isotopic composition of strontium in barites and anhydrites from Kuroko deposits. Mining Geology 28: 281-291.

Faure, G. (1986). Principles of isotope geochemistry. 2nd ed. Wiley, New York, 589 pp.

Fouquet, Y., Von Stackelberg, U., Charlou, J. L., Donval, J. P., Erzinger, J., Foucher, J. P., ... and Whitechurch, H. (1991). Hydrothermal activity and metallogenesis in the Lau back-arc basin. Nature, 349: 778-781.

Franklin, J. M., Gibson, H. L., Jonasson, I. R., and Galley, A. G. (2005). Volcanogenic massive sulfide deposits. Economic Geology 100th Anniversary Volume, 98: 523-560.

Franklin, J., Hannington, M., Jonasson, I., and Barrie, C. (1998). Arc-related volcanogenic massive sulfide deposits: Proceedings of short course on metallogeny of volcanic arcs, January 24-25, Vancouver: British Columbia Geological Survey Open-File, p.8.

Franklin, J. M., Lydon, J. W., and Sangster, D. F. (1981). Volcanic-associated massive sulfide deposits. Economic Geology, 75: 485-627.

Fraser, D., Giroux, G.H., Copeland, D.A., Devine, C.A. (2012). NI-43-101 technical report and mineral resource estimate on the Lemarchant deposit, South Tally Pond VMS project, central Newfoundland, Canada. Paragon Minerals Corporation.

Galley, A. G. (1993). Characteristics of semi-conformable alteration zones associated with volcanogenic massive sulphide districts. Journal of Geochemical Exploration, 48 : 175-200.

Galley, A. G. (2003). Composite synvolcanic intrusions associated with Precambrian VMS-related hydrothermal systems. Mineralium Deposita, 38: 443-473.

Galley, A. G., Hannington, M., and Jonasson, I. (2007). Volcanogenic massive sulfide deposits. Mineral Deposits of Canada: A Synthesis of Major Deposit-Types, District Metallogeny, the Evolution of Geological Provinces, and Exploration Methods: Geological Association of Canada, Mineral Deposits Division, Special Publication, 5: 141-161.

Gamo, T., Okamura, K., Charlou, J., Urabe, T., Auzende, J., Ishibashi, J., . . . Chiba, H. (1997). Acidic and sulfate-rich hydrothermal fluids from the Manus back-arc Basin, Papua New Guinea. Geology, 25: 139-142.

German, C., and Von Damm, K. (2006). Hydrothermal processes. The Oceans and Marine Geochemistry. Treatise on Geochemistry Series, Vol.6, Elsevier: 181-222.

Gibson, H. L. (2005). Volcano-hosted ore deposits. In: Marti, J. and Emst, G.J. (eds) Volcanoes and the environment. Cambridge: Cambridge University Press: 333-386.

Gibson, H.L., Morton, R.L., Hudak, G.J. (1999), Submarine volcanic processes, deposits, and environments favorable for the location of volcanic-associated massive sulphide deposits. In: Barrie, C.T., Hannington, M.D. (Eds.), Volcanic-associated massive sulphide deposits: Progress and examples in modern and ancient settings. Reviews in Economic Geology 8: 13–51.

Gill. S. (2015). Mineralogy, metal zoning, and genesis of the Cambrian Zn-Pb-Cu-Ag-Au Lemarchant volcanogenic massive sulfide deposit. Masters thesis, Memorial University of Newfoundland.

Gill, S.B. and Piercey, S. J. (2014). Preliminary observations on styles of mineralization and sulfide-mineral zonation in the Cambrian Zn-Pb-Cu-Ag-Au Lemarchant volcanogenic massive-sulfide deposit, Newfoundland and Labrador; Geological Survey of Canada, Current Research 2014-5, p. 17.

Gill, S.B., Piercey, S.J., and Devine, C.A. (2013). Preliminary mineralogy of barite associated sulphide mineralization in the Ordovician Zn-Pb-Cu-Ag-Au Lemarchant volcanogenic massive sulphide deposit, Newfoundland and Labrador. Geological Survey of Canada, Current Research, Report 2013–17, 15 p.

Gill, S.B., Piercey, S.J., and Layton-Matthews, D. (2017). Mineralogy and Metal Zoning of the Cambrian Zn-Pb-Cu-Ag-Au Lemarchant Volcanogenic Massive Sulfide (VMS) Deposit, Newfoundland. The Canadian Mineralogist; 54: 1307-1344.

Gill, S., Piercey, S., Layton-Matthews, D., Layne, G., and Piercey, G. (2015). Mineralogical, sulphur, and lead isotopic study of the Lemarchant Zn-Pb-Cu-Ag-Au-VMS deposit: Implications for precious-metal enrichment processes in the VMS environment. Targeted Geoscience Initiative, 4, 183-195.

Gemmell, J. B., and Large, R. R. (1992). Stringer system and alteration zones underlying the Hellyer volcanogenic massive sulfide deposit, Tasmania, Australia. Economic Geology, 87: 620-649.

Goldberg, E.D. and Arrhenius, G. (1958) Chemistry of pelagic sediments. Geochim. Cosmochim. Acta, 13: 153–212.

Goldfarb, M., Converse, D., Holland, H., and Edmond, J. (1983). The genesis of hot spring deposits on the East Pacific Rise, 21 N. Economic Geology, Monograph, 5, 184-197.

Goldfarb, R. J., Groves, D. I., and Gardoll, S. (2001). Orogenic gold and geologic time: a global synthesis. Ore geology reviews, 18: 1-75.

Goldstein, S. J., and Jacobsen, S. B. (1988). Nd and Sr isotopic systematics of river water suspended material: implications for crustal evolution. Earth and Planetary Science Letters, 87: 249-265.

Goodfellow, W. D., Peter, J. M., Winchester, J. A., and van Staal, C. R. (2003). Ambient marine environment and sediment provenance during formation of massive sulfide deposits in the Bathurst Mining Camp: importance of reduced bottom waters to sulfide precipitation and preservation. Economic Geology, Monograph, 11: 129-156.

Gurvich, E. G. (2006). Metalliferous sediments of the World Ocean-fundamental theory of deep sea hydrothermal sedimentation. Berlin-Heidelberg, Springer: 1-416.

Griffith, E. M., and Paytan, A. (2012). Barite in the ocean–occurrence, geochemistry and palaeoceanographic applications. Sedimentology, 59: 1817-1835.

Griffith, E. M., Schauble, E. A., Bullen, T. D., and Paytan, A. (2008). Characterization of calcium isotopes in natural and synthetic barite. Geochimica et Cosmochimica Acta, 72: 5641-5658.

Groves, D.I., Goldfarb, R.J., Gebre-Mariam, M., Hagemann, S.G., and Robert, E. (1998). Orogenic gold deposits - a proposed classification in the context of their crustal distribution and relationship to other gold deposit types. Ore Geology Reviews, 13: 7-27.

Habicht, K. S., and Canfield, D. E. (2001). Isotope fractionation by sulfate-reducing natural populations and the isotopic composition of sulfide in marine sediments. Geology, 29: 555-558.

Halbach, P., Nakamura, K. I., Wahsner, M., Lange, J., Sakai, H., Käselitz, L., ... and Seifert, R. (1989). Probable modern analogue of Kuroko-type massive sulphide deposits in the Okinawa Trough back-arc basin. Nature, 338: 496-499.

Hannington, M.D. (2014). Volcanogenic massive sulfide deposits, In H.D.H.K. Turekian, ed., Treatise on geochemistry, 2nd ed.: Oxford, Elsevier: 463-488.

Hannington M.D., de Ronde C.E.J., and Petersen, S. (2005). Sea-floor tectonics and submarine hydrothermal systems. In: Hedenquist, J.W., Thompson, J.F.H., Goldfarb, R.J., and Richards, J.P. (eds.) 100th Anniversary Volume of Economic Geology: 111–142.

Hannington, M. D., Galley, A. G., Herzig, P. M., and Petersen, S. (1998). Comparison of the Tag mound and stockwork complex with Cyprus-type massive sulfide deposits. Paper presented at the Proceedings of the Ocean Drilling Program, Scientific Results, 158: 389-415.

Hannington, M., Herzig, P., Scott, S., Thompson, G., and Rona, P. (1991). Comparative mineralogy and geochemistry of gold-bearing sulfide deposits on the mid-ocean ridges. Marine Geology, 101: 217-248.

Hannington, M. D., and Gorton, M. (1991). Analysis of sulfides for gold and associated trace metals by direct neutron activation with a Low-Flux reactor. Geostandards Newsletter, 15: 145-154.

Hannington, M., Jonasson, I., Herzig, P., and Petersen, S. (1995a). Physical and chemical processes of seafloor mineralization at the mid-ocean ridges. Seafloor hydrothermal systems: Physical, chemical, biological, and geological interactions, Monograph 11: 115-157.

Hannington, M. D., Larocque, A. C., Petersen, S., and Rona, P. A. (1995b). The occurrence of gold in sulfide deposits of the TAG hydrothermal field, Mid-Atlantic Ridge. The Canadian Mineralogist, 33: 1285-1310.

Hannington, M. D, Peter, J., and Scott, S. (1986). Gold in sea-floor polymetallic sulfide deposits. Economic Geology, 81: 1867-1883.

Hannington, M. D., Poulsen, K. H., and Thomsen, J. F. (1999). Volcanogenic gold in the massive sulfide environment. Reviews in Economic Geology, 8: 325-356.

Hannington, M. D., and Scott, S. D. (1988). Mineralogy and geochemistry of a hydrothermal silica-sulfide-sulfate spire in the caldera of Axial Seamount, Juan de Fuca Ridge. The Canadian Mineralogist, 26: 603-625.

Hannington, M. D., and Scott, S. D. (1989). Sulfidation equilibria as guides to gold mineralization in volcanogenic massive sulfides; evidence from sulfide mineralogy and the composition of sphalerite. Economic Geology, 84: 1978-1995.

Hanor, J. S. (2000). Barite–celestine geochemistry and environments of formation. Reviews in Mineralogy and Geochemistry, 40: 193-275.

Hart, T. R., Gibson, H. L., and Lesher, C. M. (2004). Trace element geochemistry and petrogenesis of felsic volcanic rocks associated with volcanogenic massive Cu-Zn-Pb sulfide deposits. Economic Geology, 99: 1003-1013.

Haymon, R. M. (1983). Growth history of hydrothermal black smoker chimneys. Nature, 301: 695-698.

Haymon, R. M., and Kastner, M. (1981). Hot spring deposits on the East Pacific Rise 21°N: Preliminary description of mineralogy and genesis. Earth and Planetary Science Letters, 53: 363-381.

Hedenquist, J. W., Arribas, A., and Gonzalez-Urien, E. (2000). Exploration for epithermal gold deposits. Reviews in Economic Geology, 13: 245-277.

Hedenquist, J. W., Arribas, A., and Reynolds, T. J. (1998). Evolution of an intrusion-centered hydrothermal system; Far Southeast-Lepanto porphyry and epithermal Cu-Au deposits, Philippines. Economic Geology, 93: 373-404.

Hein, J. R., de Ronde, C. E., Koski, R. A., Ditchburn, R. G., Mizell, K., Tamura, Y., et al. (2014). Layered hydrothermal barite-sulfide mound field, East Diamante caldera, Mariana volcanic arc. Economic Geology, 109: 2179-2206.

Hein, J. R., Zierenberg, R. A., Maynard, J. B., and Hannington, M. D. (2007). Barite-forming environments along a rifted continental margin, Southern California Borderland. Deep Sea Research Part II: Topical Studies in Oceanography, 54: 1327-1349.

Hekinian, R., Francheteau, J., and Ballard, R. (1985). Morphology and evolution of hydrothermal deposits at the axis of the East Pacific Rise. Oceanologica Acta, 8: 147-155.

Hekinian, R., and Fouquet, Y. (1985). Volcanism and metallogenesis of axial and off-axial structures on the East Pacific Rise near 13 degrees N. Economic Geology, 80: 221-249.

Herzig, P. M., and Hannington, M. D. (1995). Polymetallic massive sulfides at the modern seafloor. A review. Ore Geology Reviews, 10: 95-115.

Herzig, P. M., Hannington, M., and Arribas Jr, A. (1998). Sulfur isotopic composition of hydrothermal precipitates from the Lau back-arc: Implications for magmatic contributions to seafloor hydrothermal systems. Mineralium Deposita, 33: 226-237.

Herzig, P. M., Hannington, M. D., Fouquet, Y., von Stackelberg, U., and Petersen, S. (1993). Gold-rich polymetallic sulfides from the Lau back arc and implications for the geochemistry of gold in sea-floor hydrothermal systems of the southwest Pacific. Economic Geology, 88: 2182-2209.

Hibbard, J. P. (2004). The Appalachian Orogen—An essay by James P. Hibbard. Van der Pluijm, B. A., and Marshak, S., Earth structure: An introduction to structural geology and tectonics (2nd edition): New York, WW Norton, 582-592.

Hibbard, J. P., van Staal, C. R., and Rankin, D. W. (2010). Comparative analysis of the geological evolution of the northern and southern Appalachian Orogen: Late Ordovician-Permian. Geological Society of America Memoirs, 206: 51-69.

Hill, A. P. (1996). Structure, Volcanic Setting, Hydrothermal Alteration and Genesis of the Thalanga Massive Sulphide Deposit. PhD thesis, University of Tasmania, Tasmania.

Hinchey, J. G. (2008). Volcanogenic massive sulphides of the northern Tulks volcanic belt, central Newfoundland: Preliminary findings, overview of deposit reclassifications and mineralizing environments. Newfoundland and Labrador Department of Natural Resources, Geological Survey, Report, 08-1: 151-172.

Hinchey, J. G. (2014). The Long Lake group: Preliminary U-Pb geochronology and lithogeochemistry, and implications for tectonostratigraphic architecture and VMS mineralization. Current Research. Newfoundland and Labrador Department of Natural Resources, Report, 14-1: 15-44.

Hinchey, J. G, and McNicoll, V. (2009). Tectonostratigraphic architecture and VMS mineralization of the southern Tulks volcanic belt: New insights from U–Pb geochronology and lithogeochemistry. Newfoundland and Labrador Department of Natural Resources, Geological Survey, Report, 09-1: 13-42.

Hippler, D., Schmitt, A. D., Gussone, N., Heuser, A., Stille, P., Eisenhauer, A., and Nägler, T. F. (2003). Calcium isotopic composition of various reference materials and seawater. Geostandards and Geoanalytical Research, 27: 13-19.

Holland, H. D., and Malinin, S. D. (1979). The solubility and occurrence of non-ore minerals. In: H. L. Barnes (Editor), Geochemistry of Hydrothermal Ore Deposits, 2nd ed. Wiley, New York, NY, pp. 461-508.

Horikoshi, E., and Shikazano, N., (1978). Sub-types and their characteristics of Kuroko-type deposits. Mining Geology, 28: 267-276.

Huston, D. L. (1999). Stable isotopes and their significance for understanding the genesis of volcanic-hosted massive sulfide deposits: A review. Reviews in Economic Geology, 8: 157-179.

Huston, D. L., Bottrill, R. S., Creelman, R. A., Zaw, K., Ramsden, T. R., Rand, S. W., ... and Large, R. R. (1992). Geologic and geochemical controls on the mineralogy and grain size of gold-bearing phases, eastern Australian volcanic-hosted massive sulfide deposits. Economic Geology, 87: 542-563.

Huston, D. L., and Large, R. R. (1989). A chemical model for the concentration of gold in volcanogenic massive sulfide deposits. Ore Geology Reviews, 4: 171-200.

Huston, D. L., Pehrsson, S., Eglington, B. M., and Zaw, K. (2010). The geology and metallogeny of volcanic-hosted massive sulfide deposits: Variations through geologic time and with tectonic setting. Economic Geology, 105: 571-591.

Huston, D. L., Relvas, J. M., Gemmell, J. B., and Drieberg, S. (2011). The role of granites in volcanic-hosted massive sulphide ore-forming systems: an assessment of magmatic–hydrothermal contributions. Mineralium Deposita, 46: 473-507.

Ishibashi, J. I., and Urabe, T. (1995). Hydrothermal activity related to arc- back-arc magmatism in the western Pacific. In Backarc Basins, Springer US. pp. 451-495.

Jamieson, J. W., Hannington, M. D., Tivey, M. K., Hansteen, T., Williamson, N. M. B., Stewart, M., Fietzke, J., Butterfield, D., Frische, M., Allen, L., Cousens, B., and Langer, J. (2016). Precipitation and growth of barite within hydrothermal vent deposits from the Endeavour Segment, Juan de Fuca Ridge. Geochimica et Cosmochimica Acta, 173: 64-85.

Janecky, D. R., and Shanks III, W. C. (1988). Computational modeling of chemical and sulfur isotopic reaction processes in seafloor hydrothermal systems: chimneys, massive sulfides, and subjacent alterations zones. The Canadian Mineralogist, 26: 805-825.

Jochum, K. P., Nohl, U., Herwig, K., Lammel, E., Stoll, B., and Hofmann, A. W. (2005). GeoReM: a new geochemical database for reference materials and isotopic standards. Geostandards and Geoanalytical Research, 29: 333-338.

Jones, F., Oliviera, A., Parkinson, G. M., Rohl, A. L., Stanley, A., and Upson, T. (2004). The effect of calcium ions on the precipitation of barium sulphate 1: calcium ions in the absence of organic additives. Journal of Crystal Growth, 262: 572-580.

Kalogeropoulos, S. I., and Scott, S. D. (1983). Mineralogy and geochemistry of tuffaceous exhalites (Tetsusekiei) of the Fukazawa mine, Hokuroku district, Japan. Economic Geology, Monograph, 5: 412-432.

Kalogeropoulos, S. I., and Scott, S. D. (1989). Mineralogy and geochemistry of an Archean tuffaceous exhalite: The main contact tuff, Millenbach mine area, Noranda, Quebec. Canadian Journal of Earth Sciences, 26: 88-105.

Kean, B.F. (1977). Geology of the Victoria Lake area (12-A/06), Newfoundland: Newfoundland and Labrador Department of Mines and Energy, Mineral Development Division, Report N. 77-4, 11.

Kean, B. F., and Evans, D. T. W. (1986). Metallogeny of the Tulks Hill volcanics, Victoria Lake Group, central Newfoundland. Government of Newfoundland and Labrador Report, 86-1.

Kowalik, J., Rye, R. O., and Sawkins, F. J. (1981). Stable isotope study of the Buchans, Newfoundland, polymetallic sulphide deposits. Geological Association of Canada, Special Paper, 22: 229-254.

Koski, R. A., Jonasson, I. R., Kadko, D. C., Smith, V. K., and Wong, F. L. (1994). Compositions, growth mechanisms, and temporal relations of hydrothermal sulfide-sulfate-silica chimneys at the northern Cleft Segment, Juan de Fuca Ridge. Journal of Geophysical Research: Solid Earth, 99: 4813-4832.

Kramers, J. D., and Tolstikhin, I. N. (1997). Two terrestrial lead isotope paradoxes, forward transport modelling, core formation and the history of the continental crust. Chemical Geology, 139: 75-110.

Kusakabe, M., and Chiba, H. (1983). Oxygen and sulfur isotope composition of barite and anhydrite from the Fukazawa deposit, Japan. Economic Geology Monograph 5: 292-301.

Large, R. R. (1977). Chemical evolution and zonation of massive sulfide deposits in volcanic terrains. Economic Geology, 72: 549-572.

Large, R.R. (1992). Australian volcanic-hosted massive sulfide deposits: Features, styles, and genetic models. Economic Geology, 87: 549–572.

Large, R.R., Huston, D.L., McGoldrick, P. J., and Ruxton, P. A. (1989). Gold distribution and genesis in Australian volcanogenic massive sulfide deposits and their significance for gold transport models. Economic Geology Monologue, 6: 520-536.

Large, R. R., Allen, R. L., Blake, M. D., and Herrmann, W. (2001). Hydrothermal Alteration and Volatile Element Halos for the Rosebery K Lens Volcanic-Hosted Massive Sulfide Deposit, Western Tasmania. Economic Geology, 96: 1055-1072.

Leistel, J., Marcoux, E., Thiéblemont, D., Quesada, C., Sánchez, A., Almodóvar, G., Pascual, E., and Sev, R. (1998). The volcanic-hosted massive sulfide deposits of the Iberian Pyrite Belt. Review and preface to the thematic issue. Mineralium Deposita, 33: 2-30.

Liaghat, S., and MacLean, W. (1992). The Key Tuffite, Matagami mining district; origin of the tuff components and mass changes. Exploration and Mining Geology, 1: 197-207.

Ligi, M., Cocchi, L., Bortoluzzi, G., D'Oriano, F., Muccini, F., Tontini, F. C., ... & Carmisciano, C. (2014). Mapping of seafloor hydrothermally altered rocks using geophysical methods: Marsili and Palinuro seamounts, southern Tyrrhenian Sea. Economic Geology, 109: 2103-2117.

Lode, S., Piercey, S. J., and Devine, C. A. (2015). Geology, mineralogy, and lithogeochemistry of metalliferous mudstones associated with the Lemarchant volcanogenic massive sulfide deposit, Tally Pond group, central Newfoundland. Economic Geology, 110: 1835-1859.

Lode, S., Piercey, S. J., Layne, G. D., Piercey, G., and Cloutier, J. (2016). Multiple sulphur and lead sources recorded in hydrothermal exhalites associated with the Lemarchant volcanogenic massive sulphide deposit, central Newfoundland, Canada. Mineralium Deposita: 1-24.

Lüders, V., Pracejus, B., and Halbach, P. (2001). Fluid inclusion and sulfur isotope studies in probable modern analogue Kuroko-type ores from the JADE hydrothermal field (Central Okinawa Trough, Japan). Chemical Geology, 173: 45-58.

Lydon, J.W. (1984). Volcanogenic massive sulfide deposits Part I: A descriptive model. Geoscience Canada, 11: 195–202.

Lydon J.W. (1988). Volcanogenic massive sulfide deposits Part 2: Genetic Models. Geoscience Canada, 15: 43–65.

MacLachlan, K., and Dunning, G. (1998a). U-Pb ages and tectono-magmatic evolution of Middle Ordovician volcanic rocks of the Wild Bight Group, Newfoundland Appalachians. Canadian Journal of Earth Sciences, 35: 998-1017.

MacLachlan, K., and Dunning, G. (1998b). U-Pb ages and tectonomagmatic relationships of Early Ordovician low-ti tholeiites, boninites and related plutonic rocks in central Newfoundland, Canada. Contributions to Mineralogy and Petrology, 133: 235-258.

Marchev, P., Downes, H., Thirlwall, M. F., and Moritz, R. (2002). Small-scale variations of $^{87}Sr/^{86}Sr$ isotope composition of barite in the Madjarovo low-sulphidation epithermal system, SE Bulgaria: implications for sources of Sr, fluid fluxes and pathways of the ore-forming fluids. Mineralium Deposita, 37: 669-677.

McArthur, J., Howarth, R., and Bailey, T. (2001). Strontium isotope stratigraphy: LOWESS version 3: Best fit to the marine Sr-isotope curve for 0–509 Ma and accompanying look-up table for deriving numerical age. The Journal of Geology, 109: 155-170.

McCuaig, T. C., and Kerrich, R. (1998). P-T-t-deformation-fluid characteristics of lode gold deposits: evidence from alteration systematics. Ore Geology Reviews, 12: 381-453.

McNicoll, V., Squires, G., Kerr, A. and Moore, P. (2010). The Duck Pond and Boundary Cu-Zn deposits, Newfoundland: new insights into the ages of host rocks and the timing of VHMS mineralization. Canadian Journal of Earth Sciences, 47: 1481-1506.

McPhie, J., Doyle, M., Allen, R. L. (1993). Volcanic textures: A Guide to the Interpretation of Textures in Volcanic Rocks. Hobart, Australia. Center for Ore Deposit and Exploration Studies, University of Tasmania, p. 198.

Mercier-Langevin, P., Hannington, M. D., Dubé, B., and Bécu, V. (2011). The gold content of volcanogenic massive sulfide deposits. Mineralium Deposita, 46: 509-539.

Mills R., Teagle D. and Tivey M. (1998) Fluid mixing and anhydrite precipitation within the TAG mound. In Proceedings of the Ocean Drilling Program, Scientific Results, 158 (eds. P. Herzig, S. Humphris, D. Miller and R. Zierenberg). Ocean Drilling Program, College Station, TX, pp. 119–127.

Monecke, T., Petersen, S., and Hannington, M.D. (2014). Constraints on water depth of massive sulfide formation: Evidence from modern seafloor hydrothermal systems in arc-related settings. Economic Geology, 109: 2079-2101.

Monnin, C., and Cividini, D. (2006). The saturation state of the world's ocean with respect to (Ba, Sr)SO_4 solid solutions. Geochimica Et Cosmochimica Acta, 70: 3290-3298.

Montañez, I. P., Banner, J. L., Osleger, D. A., Borg, L. E., and Bosserman, P. J. (1996). Integrated Sr isotope variations and sea-level history of Middle to Upper Cambrian platform carbonates: Implications for the evolution of Cambrian seawater $^{87}Sr/^{86}Sr$. Geology, 24: 917-920.

Moss, R., Scott, S. D., and Binns, R. A. (2001). Gold content of eastern Manus basin volcanic rocks: implications for enrichment in associated hydrothermal precipitates. Economic Geology, 96: 91-107.

Murchey, B. L., Madrid, R. J., and Poole, F. G. (1987). Paleozoic bedded barite associated with chert in western North America. Siliceous Sedimentary Rock-Hosted Ores and Petroleum. J.R. Hein (Ed.) Van Nostrand: 269-283.

Nance, R. D., Murphy, J. B., Strachan, R. A., Keppie, J. D., Gutiérrez-Alonso, G., Fernández-Suárez, J., and Pisarevsky, S. A. (2008). Neoproterozoic-Early Palaeozoic tectonostratigraphy and palaeogeography of the peri-Gondwanan terranes: Amazonian v. west African connections. Geological Society, London, Special Publications, 297: 345-383.

Neuman, R. B. (1984). Geology and paleobiology of islands in the Ordovician Iapetus ocean: Review and implications. Geological Society of America Bulletin, 95: 1188-1201.

Ohmoto, H. (1996). Formation of volcanogenic massive sulfide deposits: the Kuroko perspective. Ore geology reviews, 10: 135-177.

Ohmoto, H., and Goldhaber, M. B. (1997). Sulfur and carbon isotopes. Geochemistry of hydrothermal ore deposits, 3: 517-611.

Ohmoto, H., Mizukami, M., Drummond, S. E., Eldridge, C. S., Pisutha-Arnond, V., and Lenagh, T. C. (1983). Chemical processes of Kuroko formation. Economic Geology Monographs, 5: 570-604.

Ohmoto, H., and Rye, R.O. (1979) Isotopes of sulfur and carbon. In: H.L. Barnes (Editor). Geochemistry of Hydrothermal Ore Deposits, 2nd e. Wiley, New York: 509-567.

Paytan, A., Kastner, M., Martin, E. E., Macdougall, J. D., and Herbert, T. (1993). Marine barite as a monitor of seawater strontium isotope composition. Nature, 366: 445-449.

Paytan, A., Mearon, S., Cobb, K., and Kastner, M. (2002). Origin of marine barite deposits: Sr and S isotope characterization. Geology, 30: 747-750.

Pearce, J. A. (1996). A user's guide to basalt discrimination diagrams. Trace element geochemistry of volcanic rocks: applications for massive sulphide exploration. Geological Association of Canada, Short Course Notes, 12: 113.

Peter, J., and Lentz, D. (2003). Ancient iron formations: Their genesis and use in the exploration for stratiform base metal sulfide deposits, with examples from the Bathurst mining camp. Geotext, 4: 145-176.

Petersen, S., Monecke, T., Westhues, A., Hannington, M. D., Gemmell, J. B., Sharpe, R., ... & Gibson, H. (2014). Drilling shallow-water massive sulfides at the Palinuro volcanic complex, Aeolian island arc, Italy. Economic Geology, 109: 2129-2158.

Piercey, S. J. (2010). An overview of petrochemistry in the regional exploration for volcanogenic massive sulphide (VMS) deposits. Geochemistry: Exploration, Environment, Analysis, 10: 119-136.

Piercey, S. J. (2011). The setting, style, and role of magmatism in the formation of volcanogenic massive sulfide deposits. Mineralium Deposita, 46: 449-471.

Piercey, S.J. and Hinchey, J. G. (2012). Volcanogenic massive sulfide (VMS) deposits of the Central Mineral Belt, Newfoundland. Geological Association of Canada Mineralogical Association of Canada Joint Annual Meeting, Field Trip Guidebook B4. Newfoundland and Labrador Department of Natural Resources, Geological Survey, Open File NFLD/3173, 56 pages.

Piercey, S. J., Squires, G. C., and Brace, T. D. (2014). Lithostratigraphic, hydrothermal, and tectonic setting of the Boundary volcanogenic massive sulfide deposit, Newfoundland Appalachians, Canada: formation by subseafloor replacement in a Cambrian rifted arc. Economic Geology, 109: 661-687.

Pisutha-Arnond, V., and Ohmoto. J. (1983). Thermal History, and chemical and isotopic compositions of the ore-forming fluids responsible for the Kuroko massive sulfide deposits in the Hokuroko District of Japan. Economic Geology, 5: 523-558.

Pollock, J., (2004). Geology and paleotectonic history of the Tally Pond Group, Dunnage zone, Newfoundland Appalachians: an integrated geochemical, geochronological, metallogenic and isotopic study of Cambrian island arc along the Peri-Gondwanan margin of Iapetus. MSc. Thesis, Memorial University, St. John's, Newfoundland, p. 420.

Pollock, J., and Wilton, D. (2001). Metallogenic studies of the Tally Pond group, Victoria Lake group: Trace element geochemistry and lead isotope data from the Exploits subzone, Newfoundland. Newfoundland and Labrador Department of Natural Resources, Geological Survey, Report, 2001-01, p. 247-266.

Pollock, J.C., Wilton, D.H.C., van Staal, C.R., and Tubrett, M.N. (2002). Laser ablation ICP-MS geochronology and provenance of detrital zircons from the Rogerson Lake Conglomerate, Botwood Belt, Newfoundland. *In* Current Research. Newfoundland Department of Mines and Energy, Geological Survey Branch, Report 02-1, p. 169-183.

Poulsen, K. H., & Hannington, M. D. (1996). Volcanic-associated massive sulphide gold. Geology of Canadian Mineral Deposit Types, Geological Survey of Canada, Geology of Canada, 8: 183-196.

Ramezani, J., Dunning, G. R., and Wilson, M. R. (2000). Geologic setting, geochemistry of alteration, and U-Pb age of hydrothermal zircon from the Silurian Stog'er Tight gold prospect, Newfoundland Appalachians, Canada. Exploration and Mining Geology, 9: 171-188.

Robb, L. (2005). Introduction to ore-forming processes. Blackwell Publishing company.

Reeves, E. P., Seewald, J. S., Saccocia, P., Bach, W., Craddock, P. R., Shanks, W. C., . . . Rosner, M. (2011). Geochemistry of hydrothermal fluids from the PACMANUS, northeast Pual and Vienna Woods hydrothermal fields, Manus Basin, Papua New Guinea. Geochimica Et Cosmochimica Acta, 75: 1088-1123.

Riverin, G., and Hodgson, C. J. (1980). Wall-rock alteration at the Millenbach Cu-Zn mine, Noranda, Quebec. Economic Geology, 75: 424-444.

Roedder, E. (1984). Fluid inclusions. Mineralogical Society of America. Reviews in Mineralogy, 12. p. 644.

Roedder, E., and Coombs, D. S. (1967). Immiscibility in granitic melts, indicated by fluid inclusions in ejected granitic blocks from Ascension Island. Journal of Petrology, 8: 417-451.

Rogers, N., and van Staal, C. (2002). Toward a Victoria Lake supergroup: A provisional stratigraphic revision of the Red Indian to Victoria Lakes area, central Newfoundland. Newfoundland and Labrador Department of Natural Resources, Geological Survey, Report, 02-01: 185-195.

Rogers, N., van Staal, C., McNicoll, V., Pollock, J., Zagorevski, A., and Whalen, J. (2006). Neoproterozoic and Cambrian arc magmatism along the eastern margin of the Victoria Lake supergroup: A remnant of Ganderian basement in central Newfoundland? Precambrian Research, 147: 320-341.

Rogers, N., van Staal, C., Zagorevski, A., Skulski, T., Piercey, S., and McNicoll, V. (2007). Timing and tectonic setting of volcanogenic massive sulfide bearing terranes within the Central Mobile Belt of the Canadian Appalachians. Paper presented at the Proceedings of Exploration, 7: 1199-1205.

Rye, R. O. (1993). The evolution of magmatic fluids in the epithermal environment; the stable isotope perspective. Economic Geology, 88: 733-752.

Sabine, P. A., Young, B. R. (1954). Cell size and composition of the baryte-celestine isomorphous series. Acta Crystallogr 7: 630 (abstract).

Safina, N. P., Melekestseva, I. Y., Nimis, P., Ankusheva, N. N., Yuminov, A. M., Kotlyarov, V. A., and Sadykov, S. A. (2016). Barite from the Saf'yanovka VMS deposit (central Urals) and Semenov-1 and Semenov-3 hydrothermal sulfide fields (Mid-Atlantic Ridge): A comparative analysis of formation conditions. Mineralium Deposita, 51: 491-507.

Sakai, H., Des Marais, D. J., Ueda, A., and Moore, J. G. (1984). Concentrations and isotope ratios of carbon, nitrogen and sulfur in ocean-floor basalts. Geochimica et Cosmochimica Acta, 48: 2433-2441.

Sakai, H., Gamo, T., Kim, E., Shitashima, K., Yanagisawa, F., Tsutsumi, M., . . . Tanaka, T. (1990). Unique chemistry of the hydrothermal solution in the Mid-Okinawa Trough backarc basin. Geophysical Research Letters, 17: 2133-2136.

Salters, V. J., and Stracke, A. (2004). Composition of the depleted mantle. Geochemistry, Geophysics, Geosystems, 5, Q05B07, doi:10.1029/2003GC000597

Sangster, D. (1968). Relative sulfur isotope abundances of ancient seas and strata-bound sulfide deposits. Paper presented at the Proceedings of the Geological Association of Canada, 19: p. 79.

Sasaki, N., and Minato, H. (1983). Effect of the degree of supersaturation upon apparent partition coefficients of lead and strontium ions between $BaSO_4$ and aqueous solution. Mineralogical Journal, 1: 365-381.

Sato, T. (1977). Kuroko deposits: Their geology, geochemistry and origin. Geological Society, London, Special Publications, 7: 153-161.

Scotney, P. M., Roberts, S., Herrington, R. J., Boyce, A. J., and Burgess, R. (2005). The development of volcanic hosted massive sulfide and barite–gold orebodies on Wetar Island, Indonesia. Mineralium Deposita, 40: 76-99.

Scott, S. (1980). Geology and structural control of Kuroko-type massive sulphide deposits. Geological Association of Canada, Special Paper, 20: 705-721.

Scott, S. D., and Barnes, H. L. (1971). Sphalerite geothermometry and geobarometry. Economic Geology, 66: 653-669.

Seal, R. R. II (2006). Sulfur isotope geochemistry of sulfide minerals. Reviews in mineralogy and geochemistry, 61: 633-677.

Seal, R. R., Alpers, C. N., and Rye, R. O. (2000). Stable isotope systematics of sulfate minerals. Reviews in Mineralogy and Geochemistry, 40: 541-602.

Seal II, R. R., Ayuso, R. A., Foley, N. K., and Clark, S. H. (2001). Sulfur and lead isotope geochemistry of hypogene mineralization at the Barite Hill gold deposit, Carolina Slate Belt, southeastern United States: A window into and through regional metamorphism. Mineralium Deposita, 36: 137-148.

Seal, R.R. II, and Wandless, G.A. (2003). Sulfur isotope evidence for sea-floor mineralizing processes at the Bald Mountain and Mount Chase massive sulfide deposits, northern Maine. Economic Geology Monograph, 11: 567-587.

Seward, T. M. (1973). Thio complexes of gold and the transport of gold in hydrothermal ore solutions. Geochimica et Cosmochimica Acta, 37: 379-399.

Seward, T. (1984). The transport and deposition of gold in hydrothermal systems. Paper presented at the Gold, 8: 165-181.

Seyfried, W. E., & Ding, K. (1995). Phase equilibria in subseafloor hydrothermal systems: A review of the role of redox, temperature, pH and dissolved Cl on the chemistry of hot spring fluids at mid-ocean ridges. Seafloor Hydrothermal Systems: Physical, Chemical, Biological, and Geological Interactions. Geophysical Monograph, 91: 248-272.

Shanks, W. C. (2001). Stable isotopes in seafloor hydrothermal systems: vent fluids, hydrothermal deposits, hydrothermal alteration, and microbial processes. Reviews in Mineralogy and Geochemistry, 43: 469-525.

Sharpe, R. (1991). The Hellyer baritic and siliceous caps: Unpublished B.Sc. dissertation, Honors thesis, University of Tasmania, Australia.

Shepherd, T. J., Rankin, A. H., and Alderton, D. (1985). A practical guide to fluid inclusion studies. Blackie, Glasgow, p. 239.

Sherlock, R., Roth, T., Spooner, E., and Bray, C. (1999). Origin of the Eskay Creek precious metal-rich volcanogenic massive sulfide deposit; fluid inclusion and stable isotope evidence. Economic Geology, 94: 803-824.

Shikazono, N., Kawabe, H., and Ogawa, Y. (2012). Interpretation of mineral zoning in submarine hydrothermal ore deposits in terms of coupled fluid flow-precipitation kinetics model. Resource Geology, 62: 352-368.

Sillitoe, R. H., Hannington, M. D., and Thompson, J. F. (1996). High sulfidation deposits in the volcanogenic massive sulfide environment. Economic Geology, 91: 204-212.

Sillitoe, R. H. (1994). Indonesian mineral deposits—introductory comments, comparisons and speculations. Journal of Geochemical Exploration, 50: 1-11.

Simmons, S.F., and Christenson, B.W. (1994), Origins of calcite in boiling geothermal system. American Journal of Science, 294: 361–400.

Simmons, S. F., White, N. C., and John, D. A. (2005). Geological characteristics of epithermal precious and base metal deposits. Economic Geology One Hundredth Anniversary Volume: 1905-2005: 485-522.

Singer, D. A. (1995). World class base and precious metal deposits; a quantitative analysis. Economic Geology, 90: 88-104.

Solomon, M., Eastoe, C. J., Walshe, J. L., & Green, G. R. (1988). Mineral deposits and sulfur isotope abundances in the Mount Read Volcanics between Que River and Mount Darwin, Tasmania. Economic Geology, 83: 1307-1328.

Spiess, F., Macdonald, K. C., Atwater, T., Bal, R., Francheteau, J., Guerrero, J., Juteau, M. K. (1980). East Pacific Rise: Hot spring and geophysical experiment. Science, 207: p. 28.

Spooner, E. T. and Fyfe, W. S. (1973). Sub-seafloor metamorphism of F/S “Meteor” near 40°N. Earth and Planetary Science Letters 23: 91-9.

Squires, G., Brace, T., and Hussey, A. (2001). Newfoundland’s polymetallic Duck Pond deposit: Earliest Iapetan VMS mineralization, formed within a sub-seafloor, carbonate-rich alteration system. Paper presented at the Geology and Mineral Deposits of the Northern Dunnage Zone, Newfoundland Appalachians. Edited by D.T.W. Evans and A. Kerr. Geological Association of Canada–Mineralogical Association of Canada (GAC–MAC) Annual Meeting, St. John’s, Nfld, pp. 167-187.

Squires, G.C., and Hinchey, J.G. (2006). Geology of the Tally Pond Volcanic Belt and adjacent areas (parts of NTS 12A/09 and 12A/10. Government of Newfoundland and Labrador, Department of Natural Resources, Geological Survey, Map 2006-01, Open File 012A/1202.

Squires, G. C., and Moore, P. J. (2004). Volcanogenic massive sulfide environments of the Tally Pond volcanics and adjacent area: Geological, lithogeochemical and geochronological results. Geological Survey, Report, 04-1: 63-91.

Stanton, R. L. (1991). Understanding volcanic massive sulfides; past, present, and future: Economic Geology Monograph, 8: 82-95.

Swinden, H. S. (1988). Introduction to volcanogenic sulphide deposits in Newfoundland In: Swinden HS, Kean BF (eds) The volcanogenic sulphide districts of central Newfoundland, Geological Association of Canada: 1-26.

Swinden, H. S. (1991). Paleotectonic settings of volcanogenic massive sulphide deposits in the Dunnage Zone, Newfoundland Appalachians CIM bulletin, 84: 59-69.

Swinden, H.S., and Dunsworth, S.M., (1995). Metallogeny; Chapter 9, in Williams, H., ed., The Appalachian/Caledonian Orogen: Canada and Greenland, Geology of Canada, No. 6: Geological Survey of Canada: 681-814

Swinden, H. S., Jenner, G., Kean, B., and Evans, D. (1989). Volcanic rock geochemistry as a guide for massive sulfide exploration in central Newfoundland. Newfoundland Department of Mines and Energy, Geological Survey Branch, Report, 89: 201-219.

Swinden, H. S., and Thorpe, R. I. (1984). Variations in style of volcanism and massive sulfide deposition in Early to Middle Ordovician island-arc sequences of the Newfoundland Central Mobile Belt. Economic Geology, 79: 1596-1619.

Teichert, B. M., Gussone, N., Eisenhauer, A., and Bohrmann, G. (2005). Clathrites: archives of near-seafloor pore-fluid evolution ($\delta^{44/40}$Ca, δ^{13}C, δ^{18}O) in gas hydrate environments. Geology, 33: 213-216.

Thurlow, J. G. (2010). Great Mining Camps of Canada 3. The history and geology of the Buchans mine, Newfoundland and Labrador. Geoscience Canada, 37: 145-173.

Tufar, W. (1991). Paragenesis of complex massive sulfide ores from the Tyrrhenian Sea. Mitteilungen Der Österreichischen Geologischen Gesellschaft, 84: 265-300.

Ulrich, M. R., and Bodnar, R. J. (1988). Systematics of stretching of fluid inclusions; II, Barite at 1 atm confining pressure. Economic Geology, 83: 1037-1046.

Urabe, T. (1987). The effect of pressure on the partitioning ratios of lead and zinc between vapor and rhyolite melts. Economic Geology, 82: 1049-1052.

Urabe, T., and Sato, T. (1978). Kuroko deposits of the Kosaka mine, northeast Honshu, Japan; products of submarine hot springs on Miocene sea floor. Economic Geology, 73: 161-179.

Van den Kerkhof, A., and Thiery, R. (2001). Carbonic inclusions. Lithos, 55: 49-68.

van Staal, C. R. (1994). Brunswick subduction complex in the Canadian Appalachians: Record of the Late Ordovician to Late Silurian collision between Laurentia and the Gander margin of Avalon. Tectonics, 13: 946-962.

van Staal, C. R. (2007). Pre-Carboniferous tectonic evolution and metallogeny of the Canadian Appalachians. *Mineral Resources of Canada:* A Synthesis of Major Deposit Types, District Metallogeny, the Evolution of Geological Provinces, and Exploration Methods. Edited by W.D. Goodfellow. Geological Association of Canada, Mineral Deposits Division, Special Publication, 5: 793-818.

van Staal, C. R., and Barr, S. M. (2012). Lithospheric architecture and tectonic evolution of the Canadian Appalachians and associated Atlantic margin. Tectonic Styles in Canada: The Lithoprobe Perspective: Geological Association of Canada Special Paper, 49: 55.

van Staal, C., Dewey, J., Mac Niocaill, C., and McKerrow, W. (1998). The Cambrian-Silurian tectonic evolution of the northern Appalachians and British Caledonides: History of a complex, west and southwest Pacific-type segment of Iapetus. Geological Society, London, Special Publications, 143: 197-242.

van Staal, C. R., and Hatcher, R. D. (2010). Global setting of Ordovician orogenesis. Geological Society of America Special Papers, 466: 1-11.

van Staal, C. R., Sullivan, R. W., and Whalen, J. B. (1996). Provenance and tectonic history of the Gander zone in the Caledonian/Appalachian orogen: Implications for the origin and assembly of Avalon. Special Papers-Geological Society of America, 304: 347-368.

van Staal, C. R., Whalen, J. B., Valverde-Vaquero, P., Zagorevski, A., and Rogers, N. (2009). Pre-Carboniferous, episodic accretion-related, orogenesis along the Laurentian margin of the northern Appalachians. Geological Society, London, Special Publications, 327: 271-316.

Veizer, J. (1989). Strontium isotopes in seawater through time. Annual Review of Earth and Planetary Sciences, 17: 141.

Veizer, J., Ala, D., Azmy, K., Bruckschen, P., Buhl, D., Bruhn, F., ... and Jasper, T. (1999). $^{87}Sr/^{86}Sr$, $\delta^{13}C$ and $\delta^{18}O$ evolution of Phanerozoic seawater. Chemical geology, 161: 59-88.

Von Damm, K. L. (1990). Seafloor hydrothermal activity: black smoker chemistry and chimneys. Annual Review of Earth and Planetary Sciences, 18: 173.

Von Damm, K. L., Edmond, J. M., Grant, B., Measures, C. I., Walden, B., and Weiss, R. F. (1985). Chemistry of submarine hydrothermal solutions at 21° N, East Pacific Rise. Geochimica et Cosmochimica Acta, 49: 2197-2220.

Wagner, D. W., (1993). Volcanic stratigraphy and hydrothermal alteration associated with the Duck Pond and Boundary volcanogenic massive sulphide deposits, central Newfoundland. Unpublished dissertation. Carleton University, Ottawa.

Wallace, P. J. (2005). Volatiles in subduction zone magmas: Concentrations and fluxes based on melt inclusion and volcanic gas data. Journal of Volcanology and Geothermal Research, 140: 217-240.

Workman, R. K., and Hart, S. R. (2005). Major and trace element composition of the depleted MORB mantle (DMM). Earth and Planetary Science Letters, 231: 53-72.

Watanabe, M., and Sakai, H. (1983). Stable isotope geochemistry of sulfates from the Neogene ore deposits in the Green Tuff region, Japan. Economic Geology Monograph, 5: 282-291.

Whitford, D. J., Korsch, M. J., and Solomon, M. (1992). Strontium isotope studies of barites; implications for the origin of base metal mineralization in Tasmania. Economic Geology, 87: 953-959.

Williams, H. (1979). Appalachian orogen in Canada. Canadian Journal of Earth Sciences, 16: 792-807.

Williams, H. (1995). Geology of the Appalachian-Caledonian Orogen in Canada and Greenland. Geological Survey of Canada: Minister of Energy, Mines and Resources Canada, p. 944.

Williams, H., Colman-Sadd, S., and Swinden, H. (1988). Tectonic-stratigraphic subdivisions of central Newfoundland. Current Research, Part B. Geological Survey of Canada, Paper, 88: 91-98.

Williams-Jones, A. E., Bowell, R. J., and Migdisov, A. A. (2009). Gold in solution. Elements, 5: 281-287.

Wilson, J. T. (1966). Did the Atlantic close and then re-open? Nature, 211: 676-681.

Yang, K. H., and Scott, S. D. (1996). Possible contribution of a metal-rich magmatic fluid to a sea-floor hydrothermal system. Nature, 383: 420-423.

Yang, K., and Scott, S. D. (2002). Magmatic degassing of volatiles and ore metals into a hydrothermal system on the modern sea floor of the eastern Manus back-arc basin, western Pacific. Economic Geology, 97: 1079-1100.

Zagorevski, A., Van Staal, C., McNicoll, V., and Rogers, N. (2007). Upper Cambrian to upper Ordovician peri-Gondwanan island arc activity in the Victoria Lake supergroup, central Newfoundland: Tectonic development of the northern Ganderian margin. American Journal of Science, 307: 339-370.

Zagorevski, A., van Staal, C.R., Rogers, N., McNicoll, V., Dunning, G.R., and Pollock, J.C. (2010). Middle Cambrian to Ordovician arc-backarc development on the leading edge of Ganderia, Newfoundland Appalachians. *In* From Rodinia to Pangea: The Lithotectonic Record of the Appalachian Region. *Edited by* R.P. Tollo, M.J. Batholomew, J.P. Hibbard, and P.M. Karabinos. Geological Society of America, Memoir 206, pp.367–396.

Zaw, K., Hunns, S., Large, R., Gemmell, J., Ryan, C., and Mernagh, T. (2003). Microthermometry and chemical composition of fluid inclusions from the Mt Chalmers volcanic-hosted massive sulfide deposits, central Queensland, Australia: Implications for ore genesis. Chemical Geology, 194: 225-244.

Zhu, C. (2004). Coprecipitation in the barite isostructural family: 1. binary mixing properties. Geochimica Et Cosmochimica Acta, 68: 3327-3337.

Appendix 1: Graphic logs

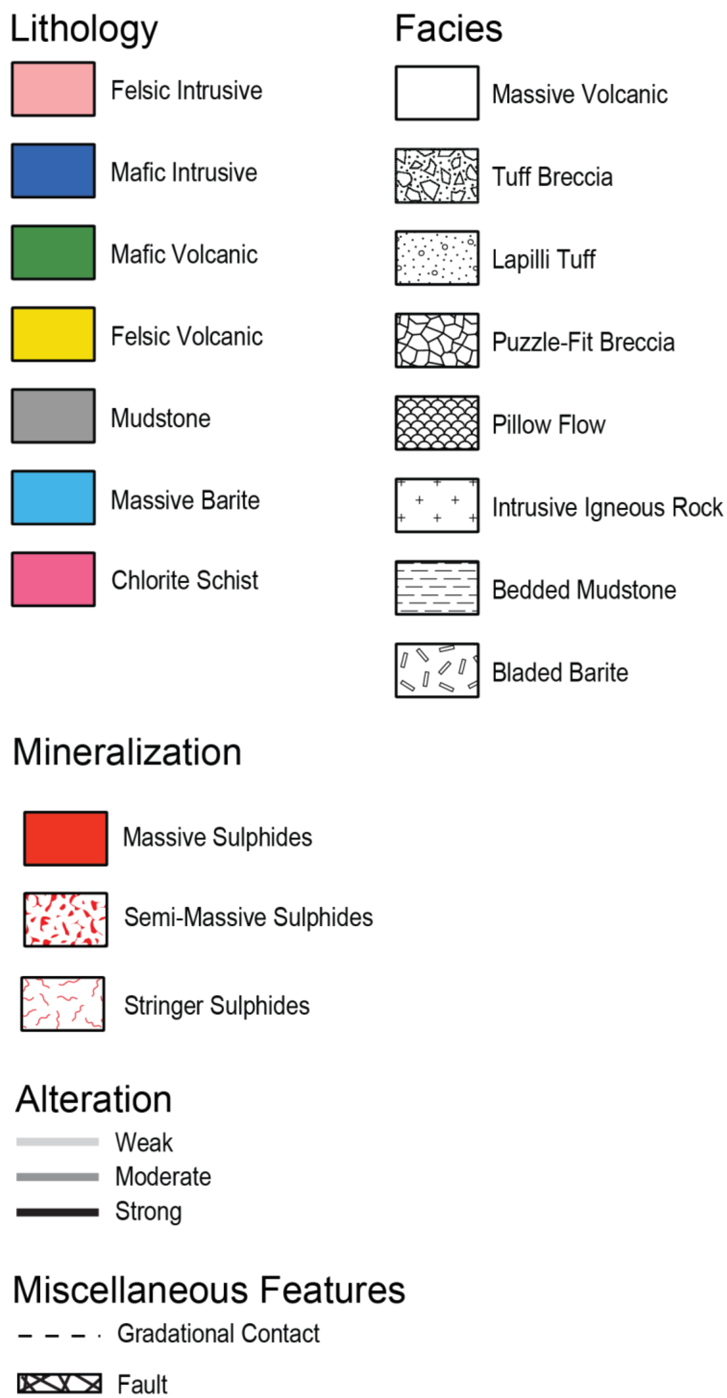

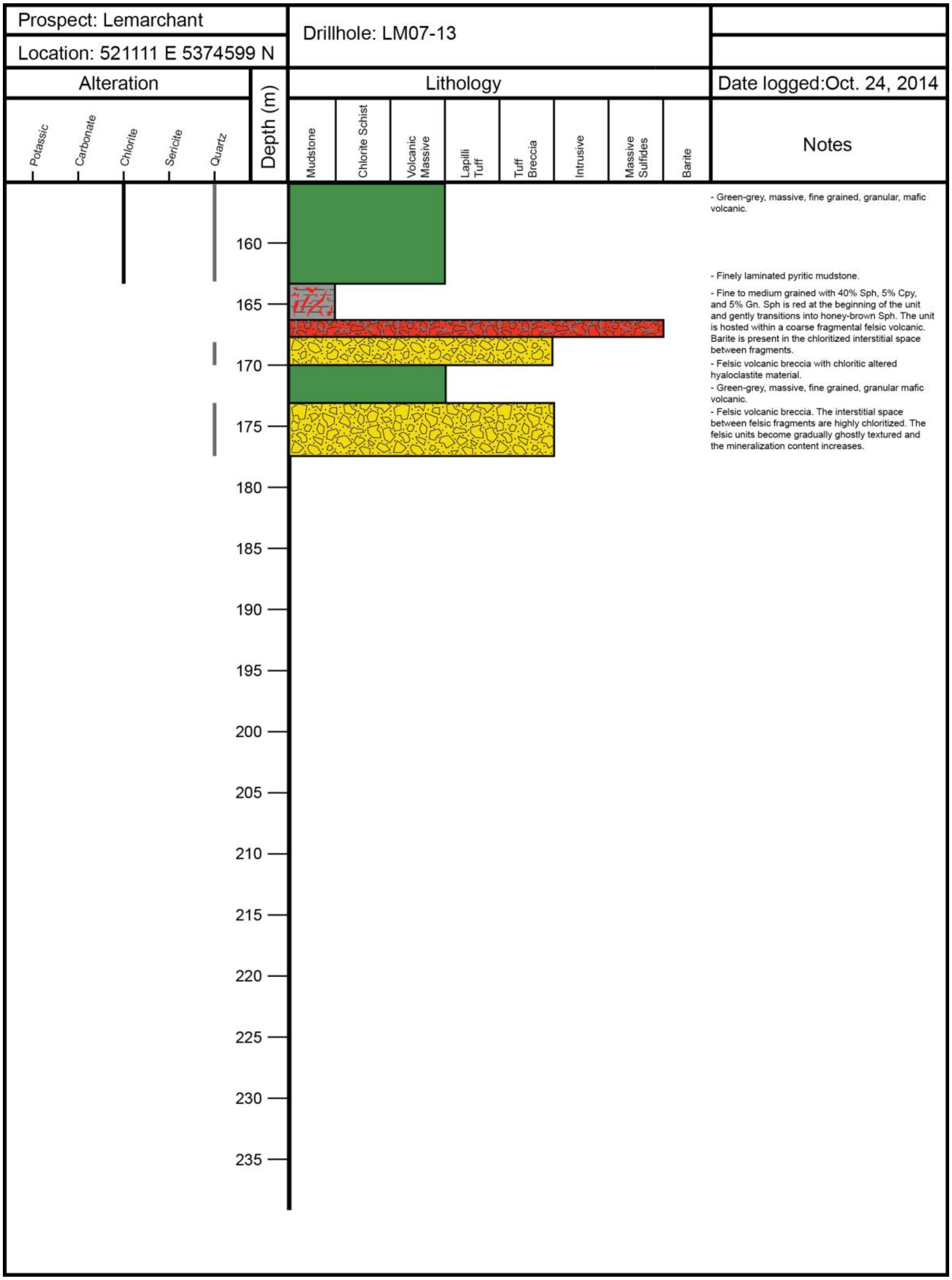

Prospect: Lemarchant
Location: 521111 E 5374599 N
Drillhole: LM07-13
Alteration
Depth (m)
Lithology
Date logged:Oct. 24, 2014
Potassic
Carbonate
Chlorite
Sericite
Quartz
Mudstone
Chlorite Schist
Volcanic Massive
Lapilli Tuff
Tuff Breccia
Intrusive
Massive Sulfides
Barite
Notes
160
165
170
175
180
185
190
195
200
205
210
215
220
225
230
235
- Green-grey, massive, fine grained, granular, mafic volcanic.
- Finely laminated pyritic mudstone.
- Fine to medium grained with 40% Sph, 5% Cpy, and 5% Gn. Sph is red at the beginning of the unit and gently transitions into honey-brown Sph. The unit is hosted within a coarse fragmental felsic volcanic. Barite is present in the chloritized interstitial space between fragments.
- Felsic volcanic breccia with chloritic altered hyaloclastite material.
- Green-grey, massive, fine grained, granular mafic volcanic.
- Felsic volcanic breccia. The interstitial space between felsic fragments are highly chloritized. The felsic units become gradually ghostly textured and the mineralization content increases.

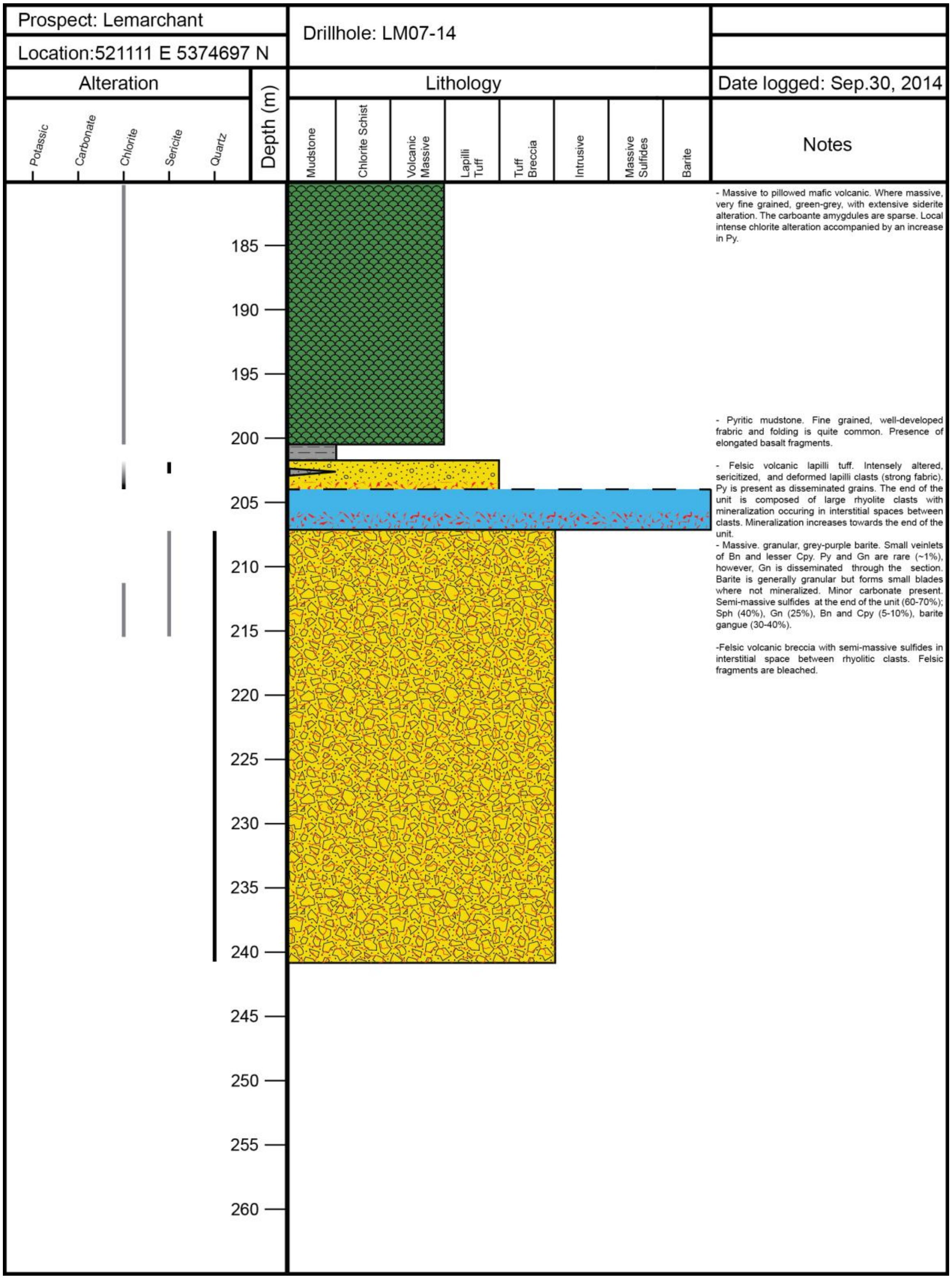

Prospect: Lemarchant
Location:521111 E 5374697 N
Drillhole: LM07-14
Alteration
Depth (m)
Lithology
Date logged: Sep.30, 2014
Potassic
Carbonate
Chlorite
Sericite
Quartz
Mudstone
Chlorite Schist
Volcanic Massive
Lapilli Tuff
Tuff Breccia
Intrusive
Massive Sulfides
Barite
Notes
185
190
195
200
205
210
215
220
225
230
235
240
245
250
255
260
- Massive to pillowed mafic volcanic. Where massive, very fine grained, green-grey, with extensive siderite alteration. The carboante amygdules are sparse. Local intense chlorite alteration accompanied by an increase in Py.
- Pyritic mudstone. Fine grained, well-developed frabric and folding is quite common. Presence of elongated basalt fragments.
- Felsic volcanic lapilli tuff. Intensely altered, sericitized, and deformed lapilli clasts (strong fabric). Py is present as disseminated grains. The end of the unit is composed of large rhyolite clasts with mineralization occuring in interstitial spaces between clasts. Mineralization increases towards the end of the unit.
- Massive. granular, grey-purple barite. Small veinlets of Bn and lesser Cpy. Py and Gn are rare (~1%), however, Gn is disseminated through the section. Barite is generally granular but forms small blades where not mineralized. Minor carbonate present. Semi-massive sulfides at the end of the unit (60-70%); Sph (40%), Gn (25%), Bn and Cpy (5-10%), barite gangue (30-40%).
-Felsic volcanic breccia with semi-massive sulfides in interstitial space between rhyolitic clasts. Felsic fragments are bleached.

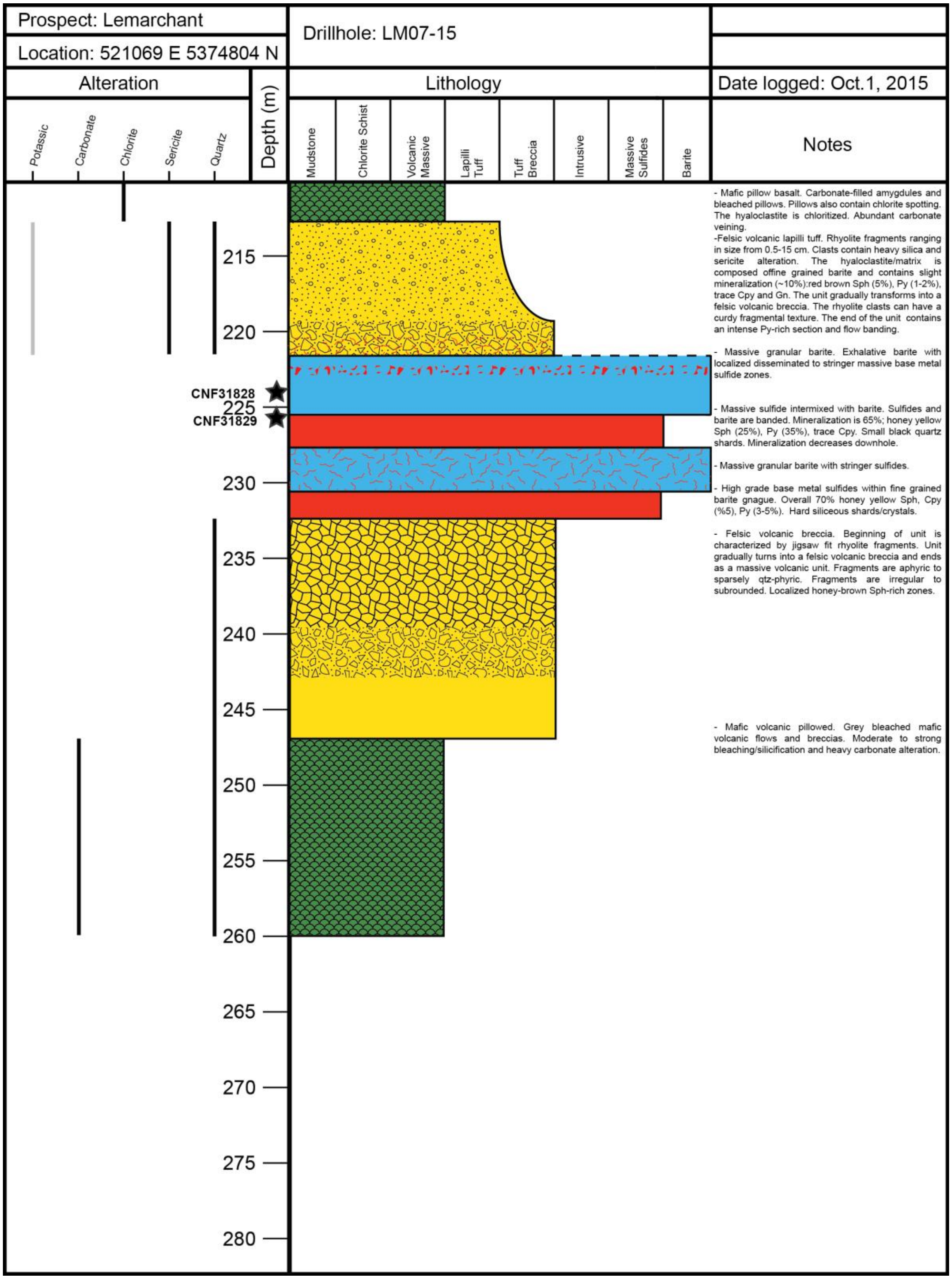

Prospect: Lemarchant
Location: 521069 E 5374804 N
Drillhole: LM07-15
Date logged: Oct.1, 2015
Alteration
Potassic
Carbonate
Chlorite
Sericite
Quartz
Depth (m)
Lithology
Mudstone
Chlorite Schist
Volcanic Massive
Lapilli Tuff
Tuff Breccia
Intrusive
Massive Sulfides
Barite
Notes
- Mafic pillow basalt. Carbonate-filled amygdules and bleached pillows. Pillows also contain chlorite spotting. The hyaloclastite is chloritized. Abundant carbonate veining.
-Felsic volcanic lapilli tuff. Rhyolite fragments ranging in size from 0.5-15 cm. Clasts contain heavy silica and sericite alteration. The hyaloclastite/matrix is composed offine grained barite and contains slight mineralization (~10%):red brown Sph (5%), Py (1-2%), trace Cpy and Gn. The unit gradually transforms into a felsic volcanic breccia. The rhyolite clasts can have a curdy fragmental texture. The end of the unit contains an intense Py-rich section and flow banding.
- Massive granular barite. Exhalative barite with localized disseminated to stringer massive base metal sulfide zones.
- Massive sulfide intermixed with barite. Sulfides and barite are banded. Mineralization is 65%; honey yellow Sph (25%), Py (35%), trace Cpy. Small black quartz shards. Mineralization decreases downhole.
- Massive granular barite with stringer sulfides.
- High grade base metal sulfides within fine grained barite gnague. Overall 70% honey yellow Sph, Cpy (%5), Py (3-5%). Hard siliceous shards/crystals.
- Felsic volcanic breccia. Beginning of unit is characterized by jigsaw fit rhyolite fragments. Unit gradually turns into a felsic volcanic breccia and ends as a massive volcanic unit. Fragments are aphyric to sparsely qtz-phyric. Fragments are irregular to subrounded. Localized honey-brown Sph-rich zones.
- Mafic volcanic pillowed. Grey bleached mafic volcanic flows and breccias. Moderate to strong bleaching/silicification and heavy carbonate alteration.
CNF31828
CNF31829
215
220
225
230
235
240
245
250
255
260
265
270
275
280

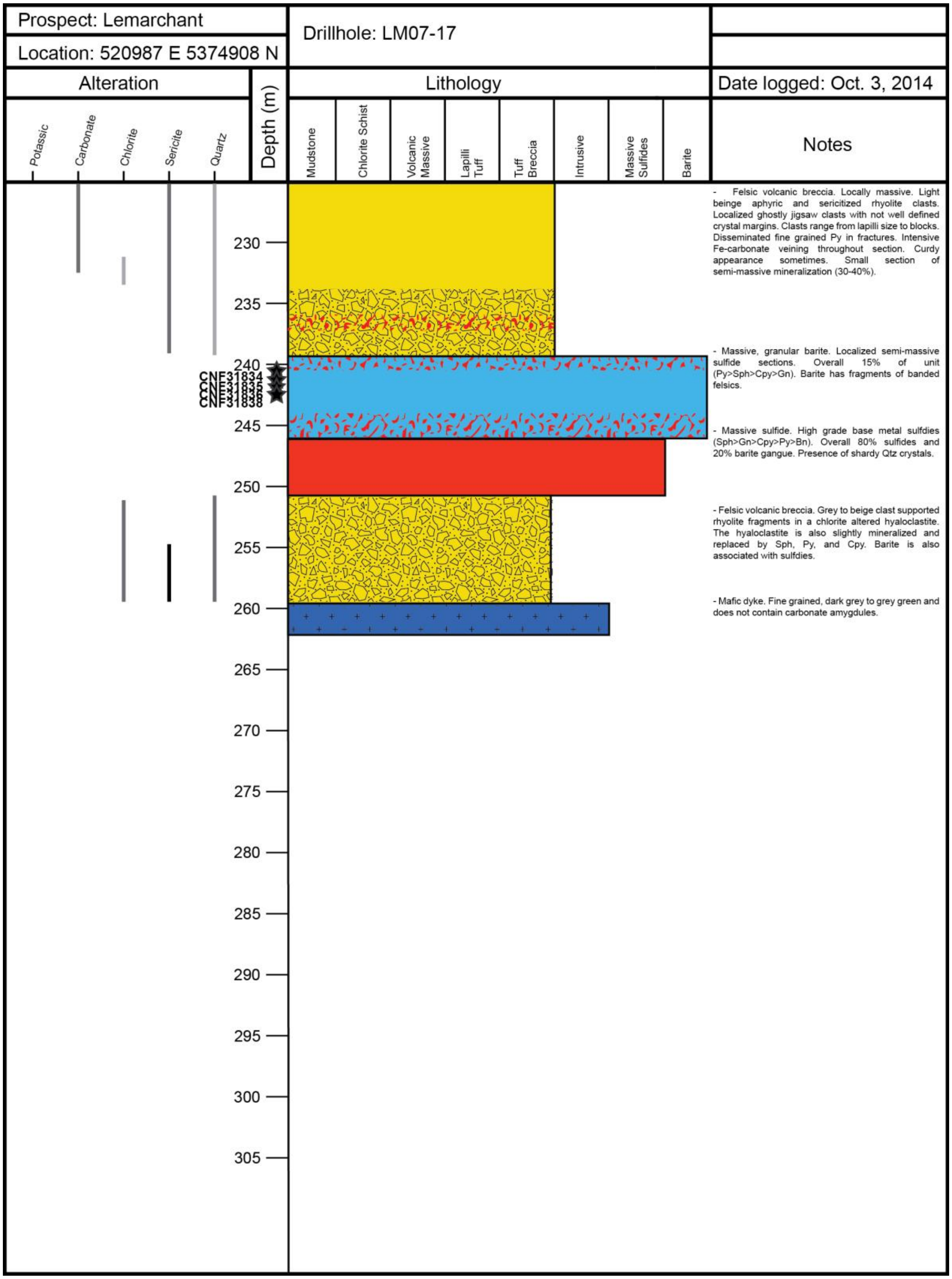

Prospect: Lemarchant
Location: 520987 E 5374908 N
Drillhole: LM07-17
Date logged: Oct. 3, 2014
Alteration
Potassic
Carbonate
Chlorite
Sericite
Quartz
Depth (m)
Lithology
Mudstone
Chlorite Schist
Volcanic Massive
Lapilli Tuff
Tuff Breccia
Intrusive
Massive Sulfides
Barite
Notes
230
235
240
245
250
255
260
265
270
275
280
285
290
295
300
305
CNF31834
CNF31835
CNF31836
CNF31838
- Felsic volcanic breccia. Locally massive. Light beinge aphyric and sericitized rhyolite clasts. Localized ghostly jigsaw clasts with not well defined crystal margins. Clasts range from lapilli size to blocks. Disseminated fine grained Py in fractures. Intensive Fe-carbonate veining throughout section. Curdy appearance sometimes. Small section of semi-massive mineralization (30-40%).
- Massive, granular barite. Localized semi-massive sulfide sections. Overall 15% of unit (Py>Sph>Cpy>Gn). Barite has fragments of banded felsics.
- Massive sulfide. High grade base metal sulfdies (Sph>Gn>Cpy>Py>Bn). Overall 80% sulfides and 20% barite gangue. Presence of shardy Qtz crystals.
- Felsic volcanic breccia. Grey to beige clast supported rhyolite fragments in a chlorite altered hyaloclastite. The hyaloclastite is also slightly mineralized and replaced by Sph, Py, and Cpy. Barite is also associated with sulfdies.
- Mafic dyke. Fine grained, dark grey to grey green and does not contain carbonate amygdules.

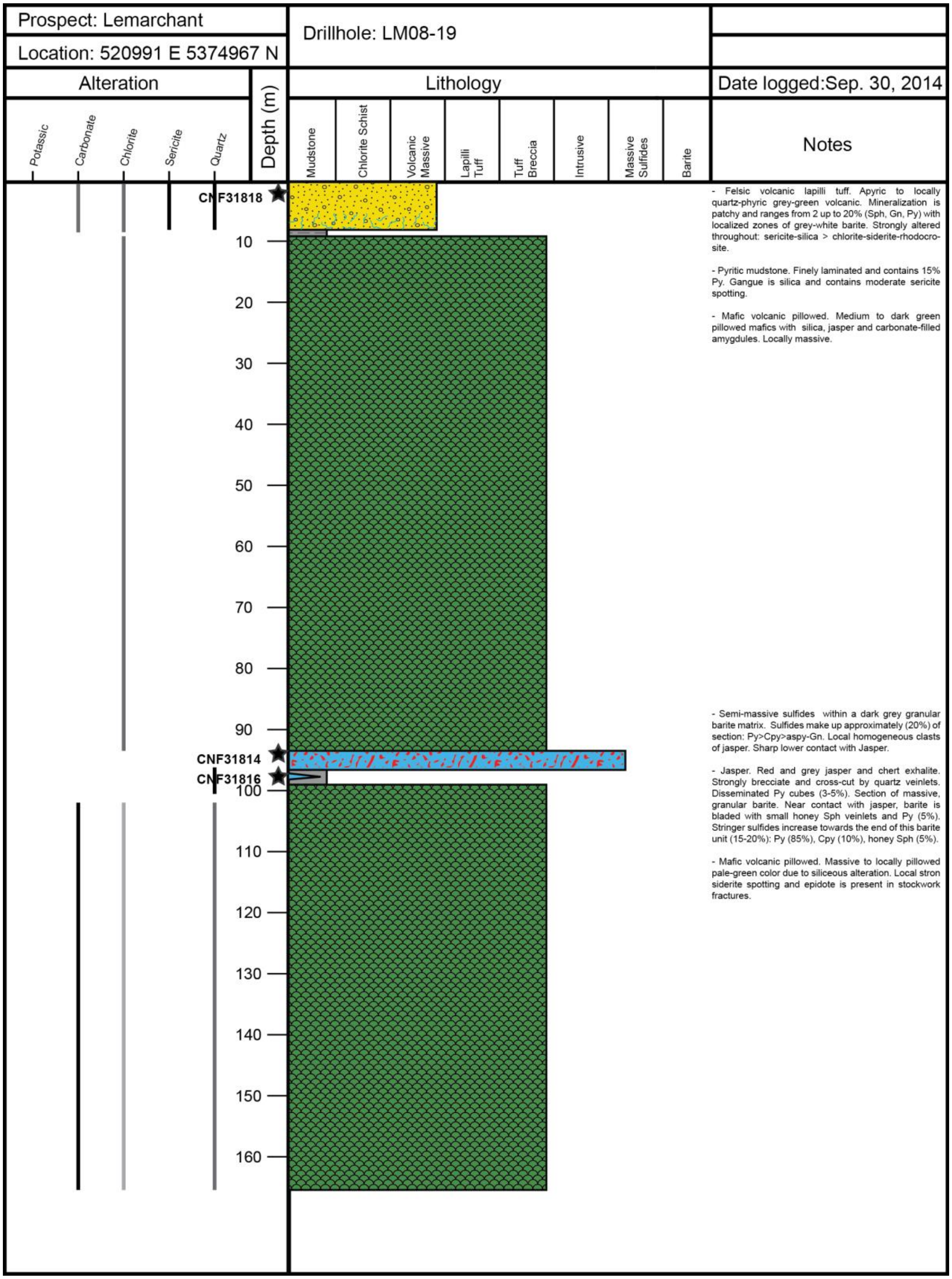

Prospect: Lemarchant
Location: 520991 E 5374967 N
Drillhole: LM08-19
Date logged:Sep. 30, 2014
Alteration
Potassic
Carbonate
Chlorite
Sericite
Quartz
Depth (m)
Lithology
Mudstone
Chlorite Schist
Volcanic Massive
Lapilli Tuff
Tuff Breccia
Intrusive
Massive Sulfides
Barite
Notes
CNF31818
CNF31814
CNF31816
10
20
30
40
50
60
70
80
90
100
110
120
130
140
150
160
- Felsic volcanic lapilli tuff. Apyric to locally quartz-phyric grey-green volcanic. Mineralization is patchy and ranges from 2 up to 20% (Sph, Gn, Py) with localized zones of grey-white barite. Strongly altered throughout: sericite-silica > chlorite-siderite-rhodocro-site.
- Pyritic mudstone. Finely laminated and contains 15% Py. Gangue is silica and contains moderate sericite spotting.
- Mafic volcanic pillowed. Medium to dark green pillowed mafics with silica, jasper and carbonate-filled amygdules. Locally massive.
- Semi-massive sulfides within a dark grey granular barite matrix. Sulfides make up approximately (20%) of section: Py>Cpy>aspy-Gn. Local homogeneous clasts of jasper. Sharp lower contact with Jasper.
- Jasper. Red and grey jasper and chert exhalite. Strongly brecciate and cross-cut by quartz veinlets. Disseminated Py cubes (3-5%). Section of massive, granular barite. Near contact with jasper, barite is bladed with small honey Sph veinlets and Py (5%). Stringer sulfides increase towards the end of this barite unit (15-20%): Py (85%), Cpy (10%), honey Sph (5%).
- Mafic volcanic pillowed. Massive to locally pillowed pale-green color due to siliceous alteration. Local stron siderite spotting and epidote is present in stockwork fractures.

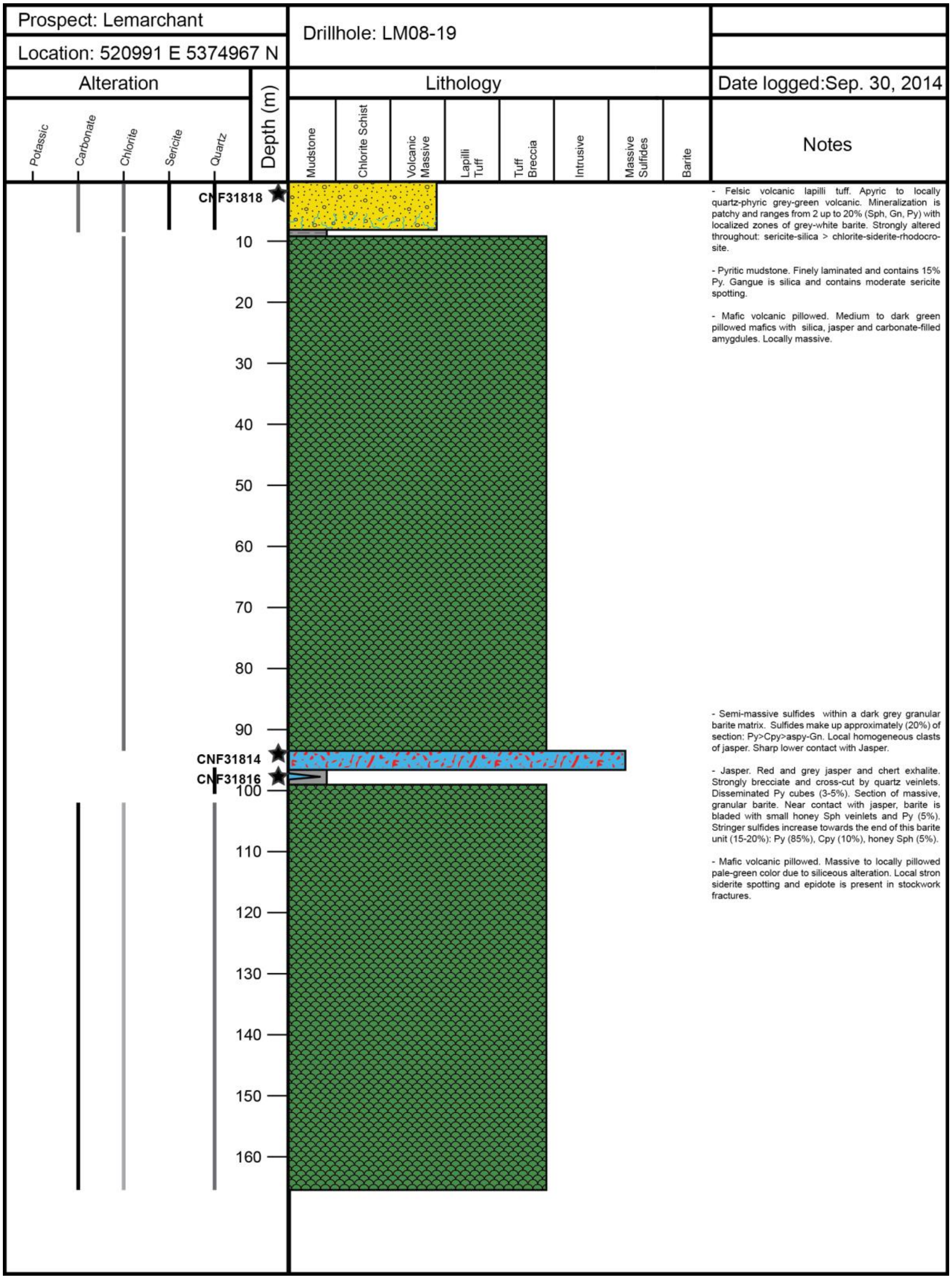

Prospect: Lemarchant
Location: 520991 E 5374967 N
Drillhole: LM08-19
Date logged:Sep. 30, 2014
Alteration
Potassic
Carbonate
Chlorite
Sericite
Quartz
Depth (m)
Lithology
Mudstone
Chlorite Schist
Volcanic Massive
Lapilli Tuff
Tuff Breccia
Intrusive
Massive Sulfides
Barite
Notes
CNF31818
10
20
30
40
50
60
70
80
90
CNF31814
CNF31816
100
110
120
130
140
150
160
- Felsic volcanic lapilli tuff. Apyric to locally quartz-phyric grey-green volcanic. Mineralization is patchy and ranges from 2 up to 20% (Sph, Gn, Py) with localized zones of grey-white barite. Strongly altered throughout: sericite-silica > chlorite-siderite-rhodocrosite.
- Pyritic mudstone. Finely laminated and contains 15% Py. Gangue is silica and contains moderate sericite spotting.
- Mafic volcanic pillowed. Medium to dark green pillowed mafics with silica, jasper and carbonate-filled amygdules. Locally massive.
- Semi-massive sulfides within a dark grey granular barite matrix. Sulfides make up approximately (20%) of section: Py>Cpy>aspy-Gn. Local homogeneous clasts of jasper. Sharp lower contact with Jasper.
- Jasper. Red and grey jasper and chert exhalite. Strongly brecciate and cross-cut by quartz veinlets. Disseminated Py cubes (3-5%). Section of massive, granular barite. Near contact with jasper, barite is bladed with small honey Sph veinlets and Py (5%). Stringer sulfides increase towards the end of this barite unit (15-20%): Py (85%), Cpy (10%), honey Sph (5%).
- Mafic volcanic pillowed. Massive to locally pillowed pale-green color due to siliceous alteration. Local stron siderite spotting and epidote is present in stockwork fractures.

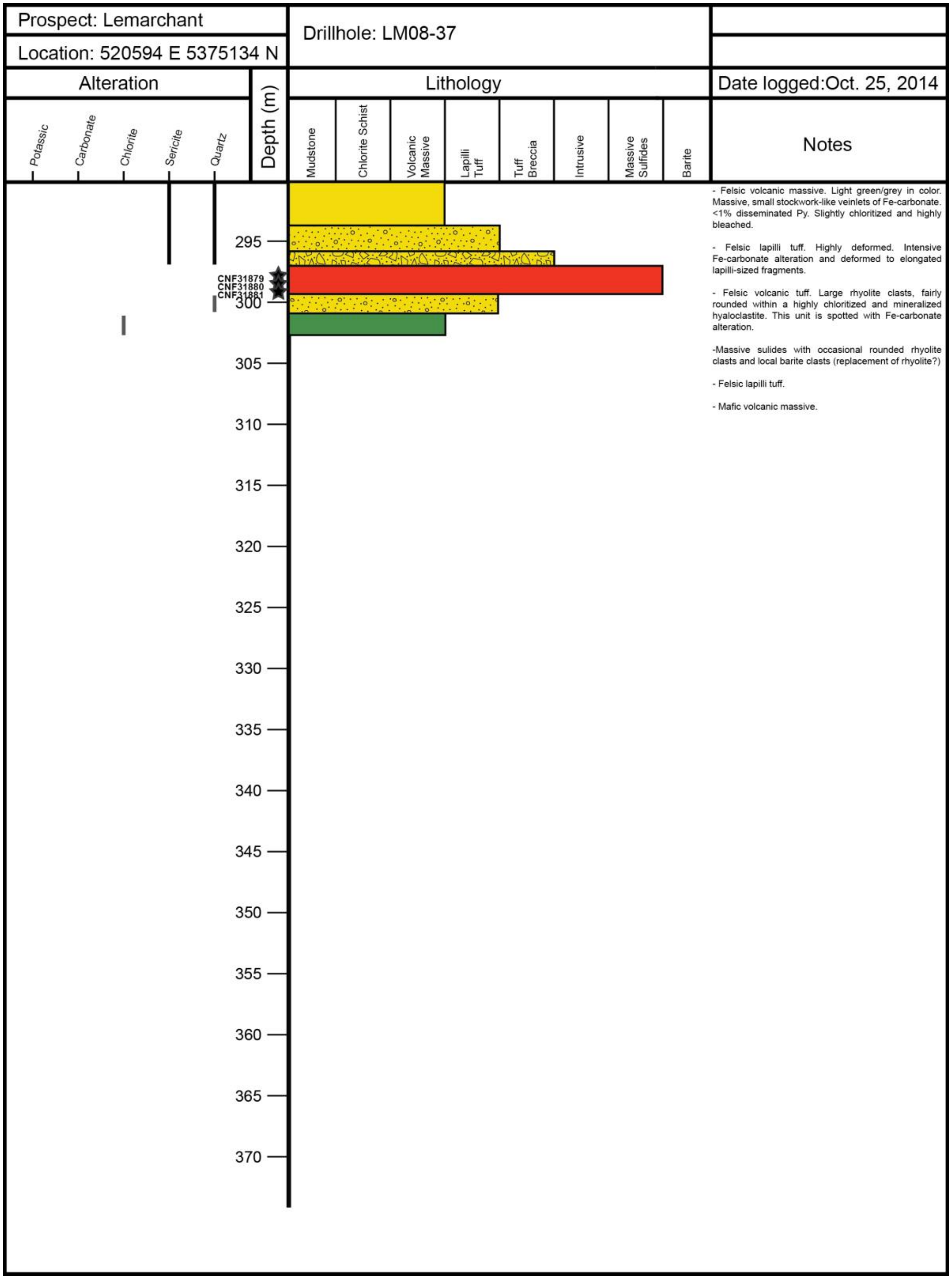

Prospect: Lemarchant
Location: 520594 E 5375134 N
Drillhole: LM08-37
Date logged:Oct. 25, 2014
Alteration
Potassic
Carbonate
Chlorite
Sericite
Quartz
Depth (m)
Lithology
Mudstone
Chlorite Schist
Volcanic Massive
Lapilli Tuff
Tuff Breccia
Intrusive
Massive Sulfides
Barite
Notes
295
CNF31879
CNF31880
CNF31881
300
305
310
315
320
325
330
335
340
345
350
355
360
365
370
- Felsic volcanic massive. Light green/grey in color. Massive, small stockwork-like veinlets of Fe-carbonate. <1% disseminated Py. Slightly chloritized and highly bleached.
- Felsic lapilli tuff. Highly deformed. Intensive Fe-carbonate alteration and deformed to elongated lapilli-sized fragments.
- Felsic volcanic tuff. Large rhyolite clasts, fairly rounded within a highly chloritized and mineralized hyaloclastite. This unit is spotted with Fe-carbonate alteration.
-Massive sulides with occasional rounded rhyolite clasts and local barite clasts (replacement of rhyolite?)
- Felsic lapilli tuff.
- Mafic volcanic massive.

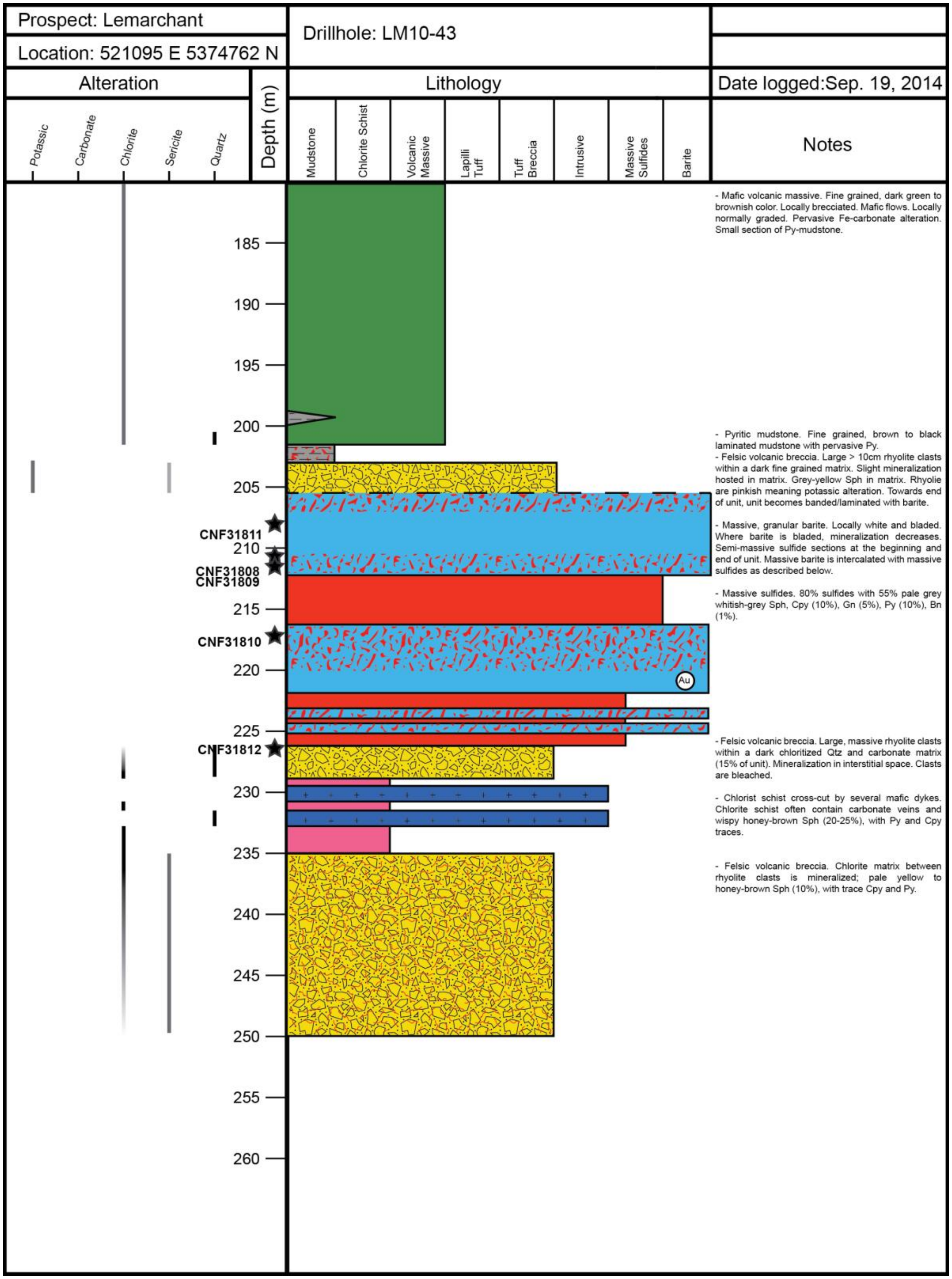

Prospect: Lemarchant
Location: 521095 E 5374762 N
Drillhole: LM10-43
Date logged:Sep. 19, 2014
Alteration
Potassic
Carbonate
Chlorite
Sericite
Quartz
Depth (m)
Lithology
Mudstone
Chlorite Schist
Volcanic Massive
Lapilli Tuff
Tuff Breccia
Intrusive
Massive Sulfides
Barite
Notes
185
190
195
200
205
210
215
220
225
230
235
240
245
250
255
260
CNF31811
CNF31808
CNF31809
CNF31810
CNF31812
Au
- Mafic volcanic massive. Fine grained, dark green to brownish color. Locally brecciated. Mafic flows. Locally normally graded. Pervasive Fe-carbonate alteration. Small section of Py-mudstone.
- Pyritic mudstone. Fine grained, brown to black laminated mudstone with pervasive Py.
- Felsic volcanic breccia. Large > 10cm rhyolite clasts within a dark fine grained matrix. Slight mineralization hosted in matrix. Grey-yellow Sph in matrix. Rhyolie are pinkish meaning potassic alteration. Towards end of unit, unit becomes banded/laminated with barite.
- Massive, granular barite. Locally white and bladed. Where barite is bladed, mineralization decreases. Semi-massive sulfide sections at the beginning and end of unit. Massive barite is intercalated with massive sulfides as described below.
- Massive sulfides. 80% sulfides with 55% pale grey whitish-grey Sph, Cpy (10%), Gn (5%), Py (10%), Bn (1%).
- Felsic volcanic breccia. Large, massive rhyolite clasts within a dark chloritized Qtz and carbonate matrix (15% of unit). Mineralization in interstitial space. Clasts are bleached.
- Chlorist schist cross-cut by several mafic dykes. Chlorite schist often contain carbonate veins and wispy honey-brown Sph (20-25%), with Py and Cpy traces.
- Felsic volcanic breccia. Chlorite matrix between rhyolite clasts is mineralized; pale yellow to honey-brown Sph (10%), with trace Cpy and Py.

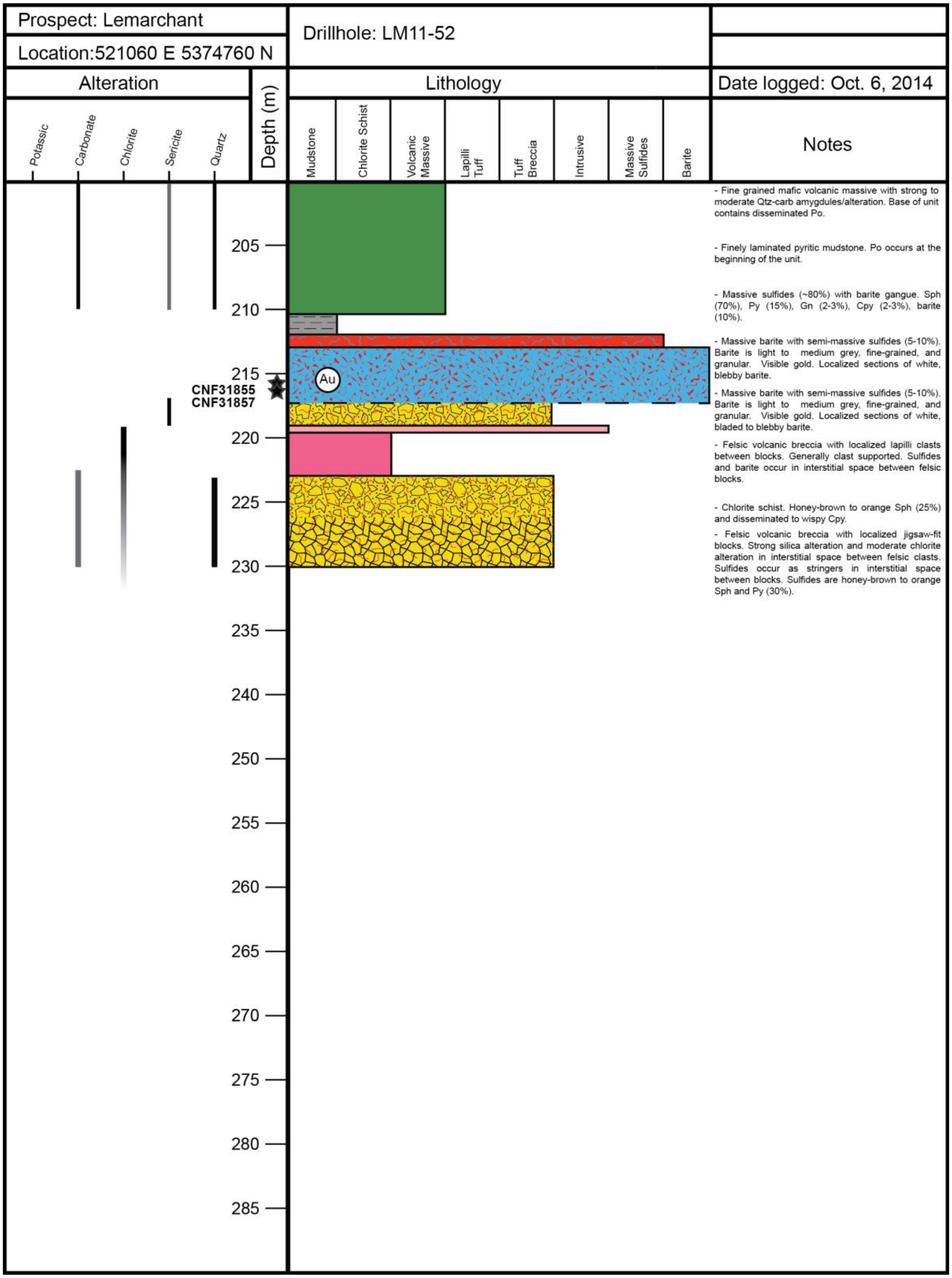
Prospect: Lemarchant
Location:521060 E 5374760 N
Drillhole: LM11-52
Alteration
Depth (m)
Lithology
Date logged: Oct. 6, 2014
Potassic
Carbonate
Chlorite
Sericite
Quartz
Mudstone
Chlorite Schist
Volcanic Massive
Lapilli Tuff
Tuff Breccia
Intrusive
Massive Sulfides
Barite
Notes
205
210
215
220
225
230
235
240
250
255
260
265
270
275
280
285
CNF31855
CNF31857
Au
- Fine grained mafic volcanic massive with strong to moderate Qtz-carb amygdules/alteration. Base of unit contains disseminated Po.
- Finely laminated pyritic mudstone. Po occurs at the beginning of the unit.
- Massive sulfides (~80%) with barite gangue. Sph (70%), Py (15%), Gn (2-3%), Cpy (2-3%), barite (10%).
- Massive barite with semi-massive sulfides (5-10%). Barite is light to medium grey, fine-grained, and granular. Visible gold. Localized sections of white, blebby barite.
- Massive barite with semi-massive sulfides (5-10%). Barite is light to medium grey, fine-grained, and granular. Visible gold. Localized sections of white, bladed to blebby barite.
- Felsic volcanic breccia with localized lapilli clasts between blocks. Generally clast supported. Sulfides and barite occur in interstitial space between felsic blocks.
- Chlorite schist. Honey-brown to orange Sph (25%) and disseminated to wispy Cpy.
- Felsic volcanic breccia with localized jigsaw-fit blocks. Strong silica alteration and moderate chlorite alteration in interstitial space between felsic clasts. Sulfides occur as stringers in interstitial space between blocks. Sulfides are honey-brown to orange Sph and Py (30%).

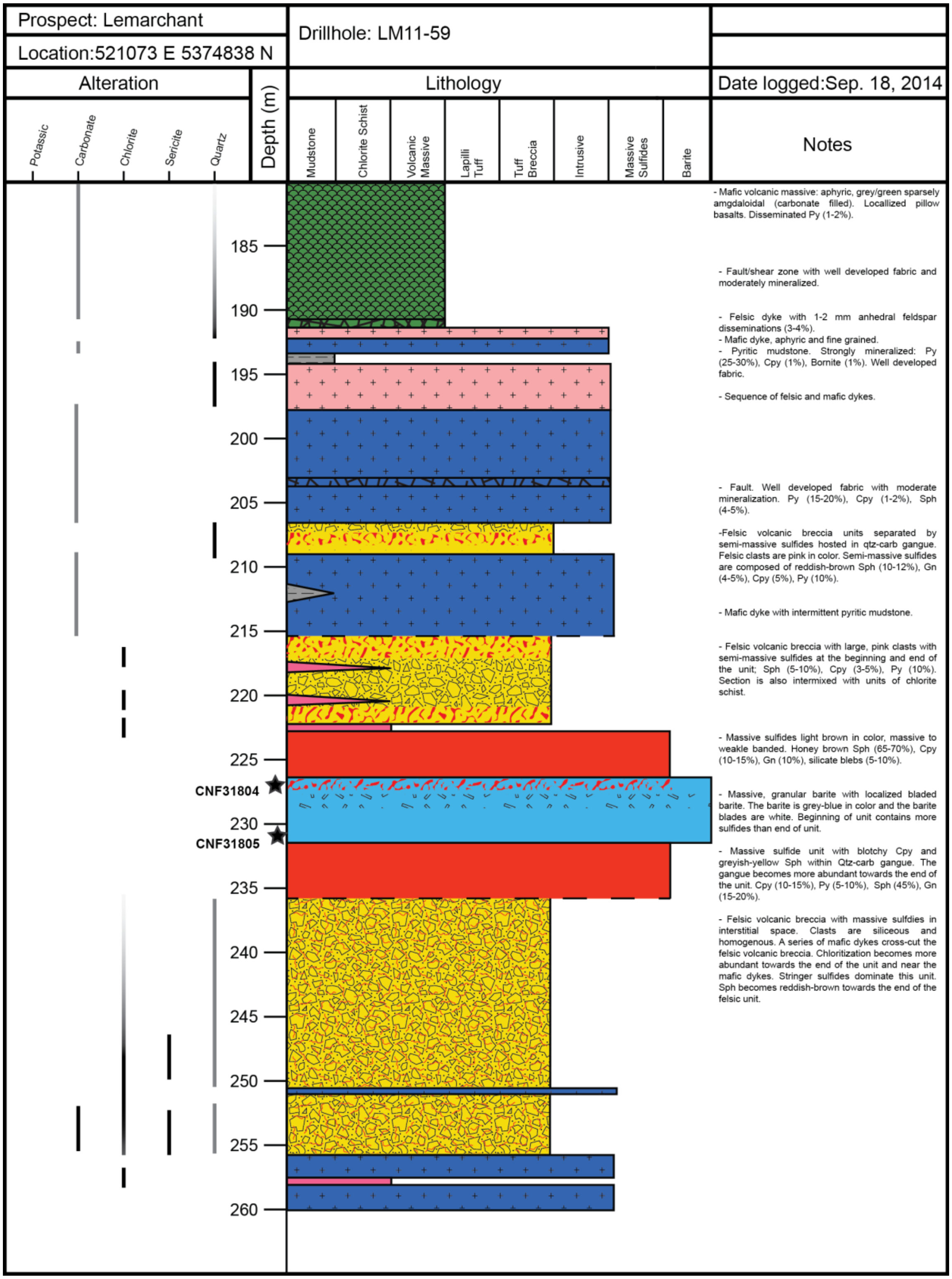

Prospect: Lemarchant
Location:521073 E 5374838 N
Drillhole: LM11-59
Alteration
Depth (m)
Lithology
Date logged:Sep. 18, 2014
Potassic
Carbonate
Chlorite
Sericite
Quartz
Mudstone
Chlorite Schist
Volcanic Massive
Lapilli Tuff
Tuff Breccia
Intrusive
Massive Sulfides
Barite
Notes
185
190
195
200
205
210
215
220
225
CNF31804
230
CNF31805
235
240
245
250
255
260
- Mafic volcanic massive: aphyric, grey/green sparsely amgdaloidal (carbonate filled). Locallized pillow basalts. Disseminated Py (1-2%).
- Fault/shear zone with well developed fabric and moderately mineralized.
- Felsic dyke with 1-2 mm anhedral feldspar disseminations (3-4%).
- Mafic dyke, aphyric and fine grained.
- Pyritic mudstone. Strongly mineralized: Py (25-30%), Cpy (1%), Bornite (1%). Well developed fabric.
- Sequence of felsic and mafic dykes.
- Fault. Well developed fabric with moderate mineralization. Py (15-20%), Cpy (1-2%), Sph (4-5%).
-Felsic volcanic breccia units separated by semi-massive sulfides hosted in qtz-carb gangue. Felsic clasts are pink in color. Semi-massive sulfides are composed of reddish-brown Sph (10-12%), Gn (4-5%), Cpy (5%), Py (10%).
- Mafic dyke with intermittent pyritic mudstone.
- Felsic volcanic breccia with large, pink clasts with semi-massive sulfides at the beginning and end of the unit; Sph (5-10%), Cpy (3-5%), Py (10%). Section is also intermixed with units of chlorite schist.
- Massive sulfides light brown in color, massive to weakle banded. Honey brown Sph (65-70%), Cpy (10-15%), Gn (10%), silicate blebs (5-10%).
- Massive, granular barite with localized bladed barite. The barite is grey-blue in color and the barite blades are white. Beginning of unit contains more sulfides than end of unit.
- Massive sulfide unit with blotchy Cpy and greyish-yellow Sph within Qtz-carb gangue. The gangue becomes more abundant towards the end of the unit. Cpy (10-15%), Py (5-10%), Sph (45%), Gn (15-20%).
- Felsic volcanic breccia with massive sulfdies in interstitial space. Clasts are siliceous and homogenous. A series of mafic dykes cross-cut the felsic volcanic breccia. Chloritization becomes more abundant towards the end of the unit and near the mafic dykes. Stringer sulfides dominate this unit. Sph becomes reddish-brown towards the end of the felsic unit.

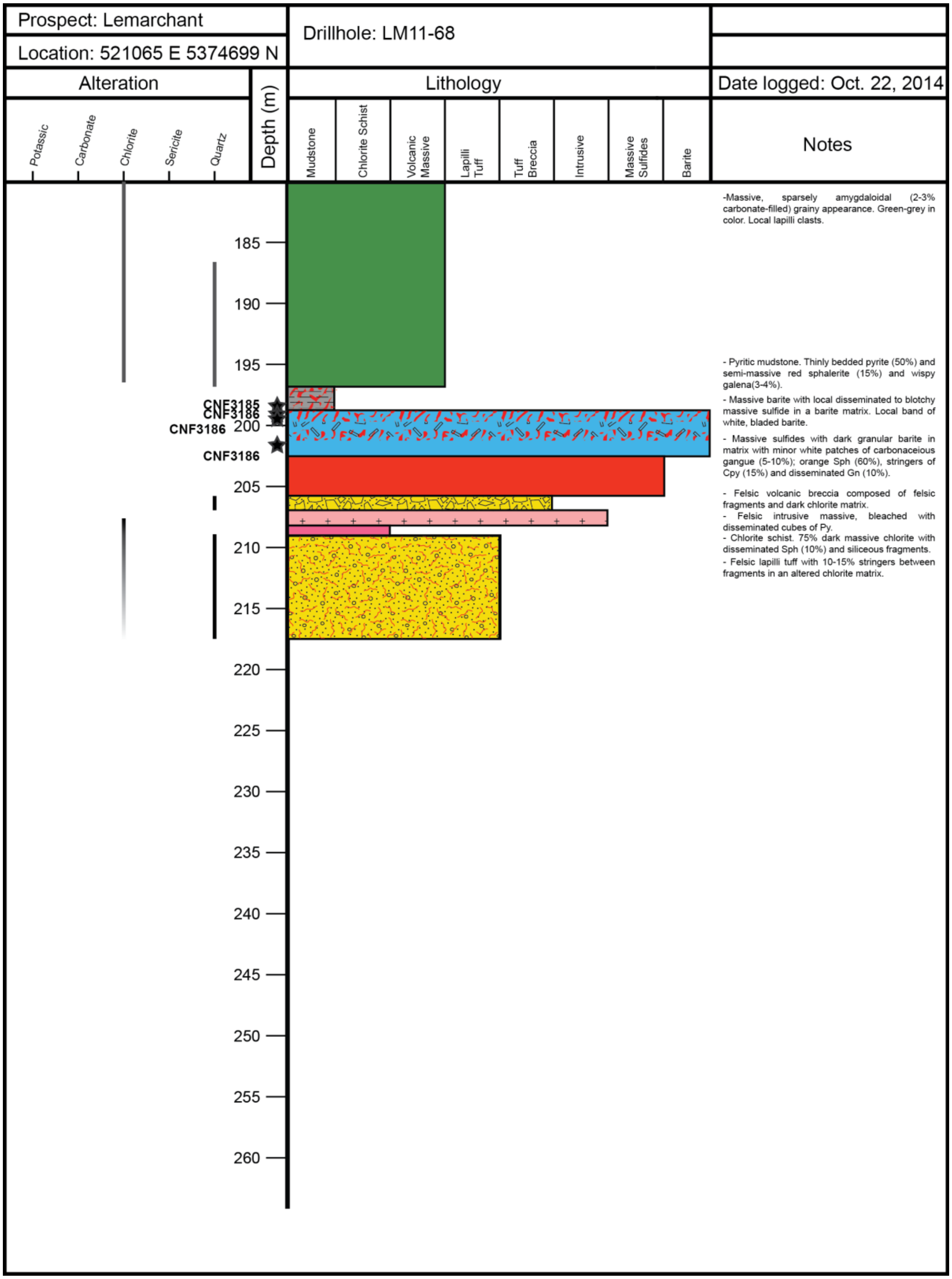

Prospect: Lemarchant
Location: 521065 E 5374699 N
Drillhole: LM11-68
Date logged: Oct. 22, 2014
Alteration
Potassic
Carbonate
Chlorite
Sericite
Quartz
Depth (m)
Lithology
Mudstone
Chlorite Schist
Volcanic Massive
Lapilli Tuff
Tuff Breccia
Intrusive
Massive Sulfides
Barite
Notes
-Massive, sparsely amygdaloidal (2-3% carbonate-filled) grainy appearance. Green-grey in color. Local lapilli clasts.
- Pyritic mudstone. Thinly bedded pyrite (50%) and semi-massive red sphalerite (15%) and wispy galena(3-4%).
- Massive barite with local disseminated to blotchy massive sulfide in a barite matrix. Local band of white, bladed barite.
- Massive sulfides with dark granular barite in matrix with minor white patches of carbonaceious gangue (5-10%); orange Sph (60%), stringers of Cpy (15%) and disseminated Gn (10%).
- Felsic volcanic breccia composed of felsic fragments and dark chlorite matrix.
- Felsic intrusive massive, bleached with disseminated cubes of Py.
- Chlorite schist. 75% dark massive chlorite with disseminated Sph (10%) and siliceous fragments.
- Felsic lapilli tuff with 10-15% stringers between fragments in an altered chlorite matrix.
CNF3185
CNF3186
CNF3186
CNF3186
185
190
195
200
205
210
215
220
225
230
235
240
245
250
255
260

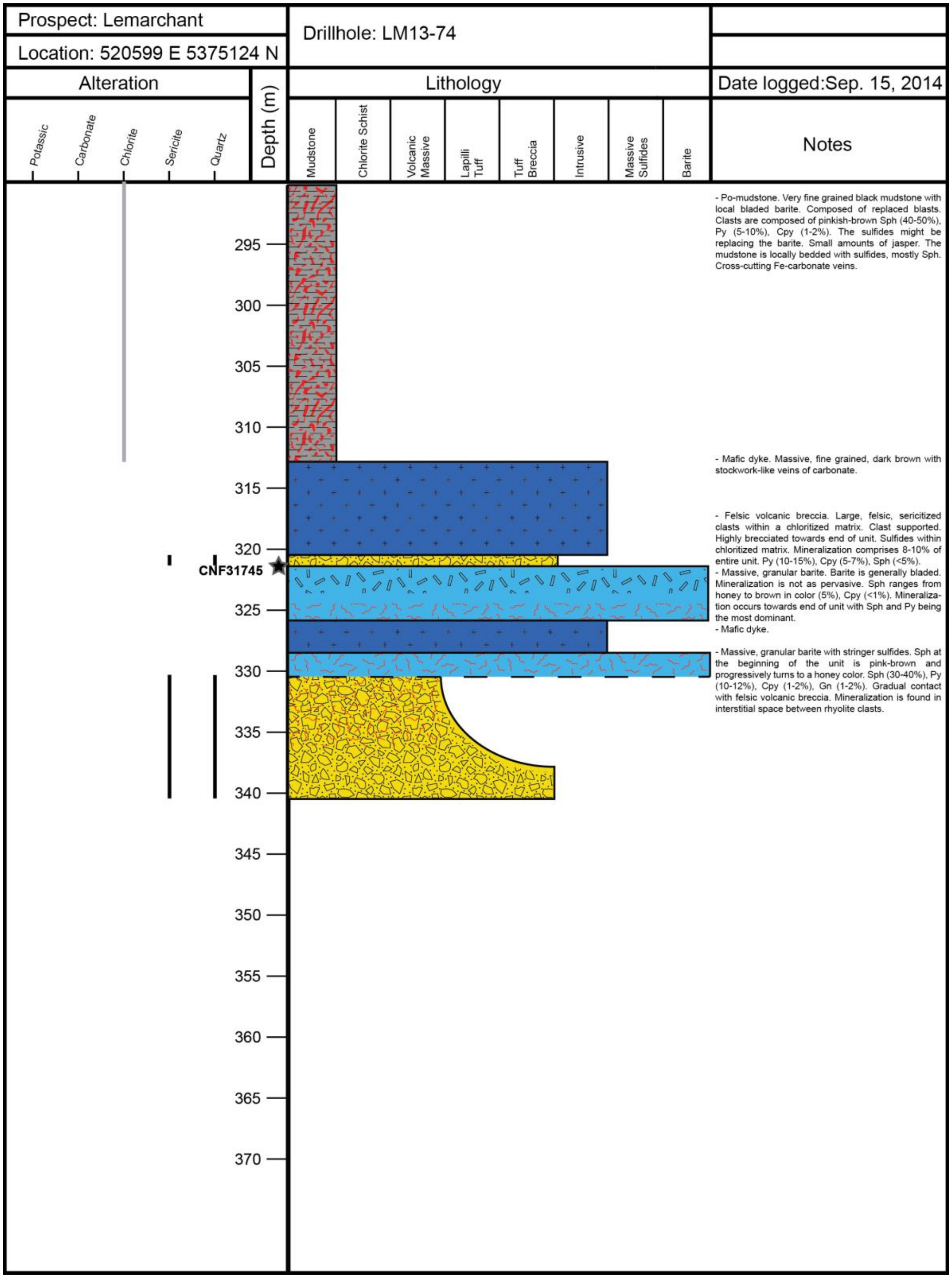

Prospect: Lemarchant
Location: 520599 E 5375124 N
Drillhole: LM13-74
Date logged:Sep. 15, 2014
Alteration
Potassic
Carbonate
Chlorite
Sericite
Quartz
Depth (m)
Lithology
Mudstone
Chlorite Schist
Volcanic Massive
Lapilli Tuff
Tuff Breccia
Intrusive
Massive Sulfides
Barite
Notes
295
300
305
310
315
320
CNF31745
325
330
335
340
345
350
355
360
365
370
- Po-mudstone. Very fine grained black mudstone with local bladed barite. Composed of replaced blasts. Clasts are composed of pinkish-brown Sph (40-50%), Py (5-10%), Cpy (1-2%). The sulfides might be replacing the barite. Small amounts of jasper. The mudstone is locally bedded with sulfides, mostly Sph. Cross-cutting Fe-carbonate veins.
- Mafic dyke. Massive, fine grained, dark brown with stockwork-like veins of carbonate.
- Felsic volcanic breccia. Large, felsic, sericitized clasts within a chloritized matrix. Clast supported. Highly brecciated towards end of unit. Sulfides within chloritized matrix. Mineralization comprises 8-10% of entire unit. Py (10-15%), Cpy (5-7%), Sph (<5%).
- Massive, granular barite. Barite is generally bladed. Mineralization is not as pervasive. Sph ranges from honey to brown in color (5%), Cpy (<1%). Mineralization occurs towards end of unit with Sph and Py being the most dominant.
- Mafic dyke.
- Massive, granular barite with stringer sulfides. Sph at the beginning of the unit is pink-brown and progressively turns to a honey color. Sph (30-40%), Py (10-12%), Cpy (1-2%), Gn (1-2%). Gradual contact with felsic volcanic breccia. Mineralization is found in interstitial space between rhyolite clasts.

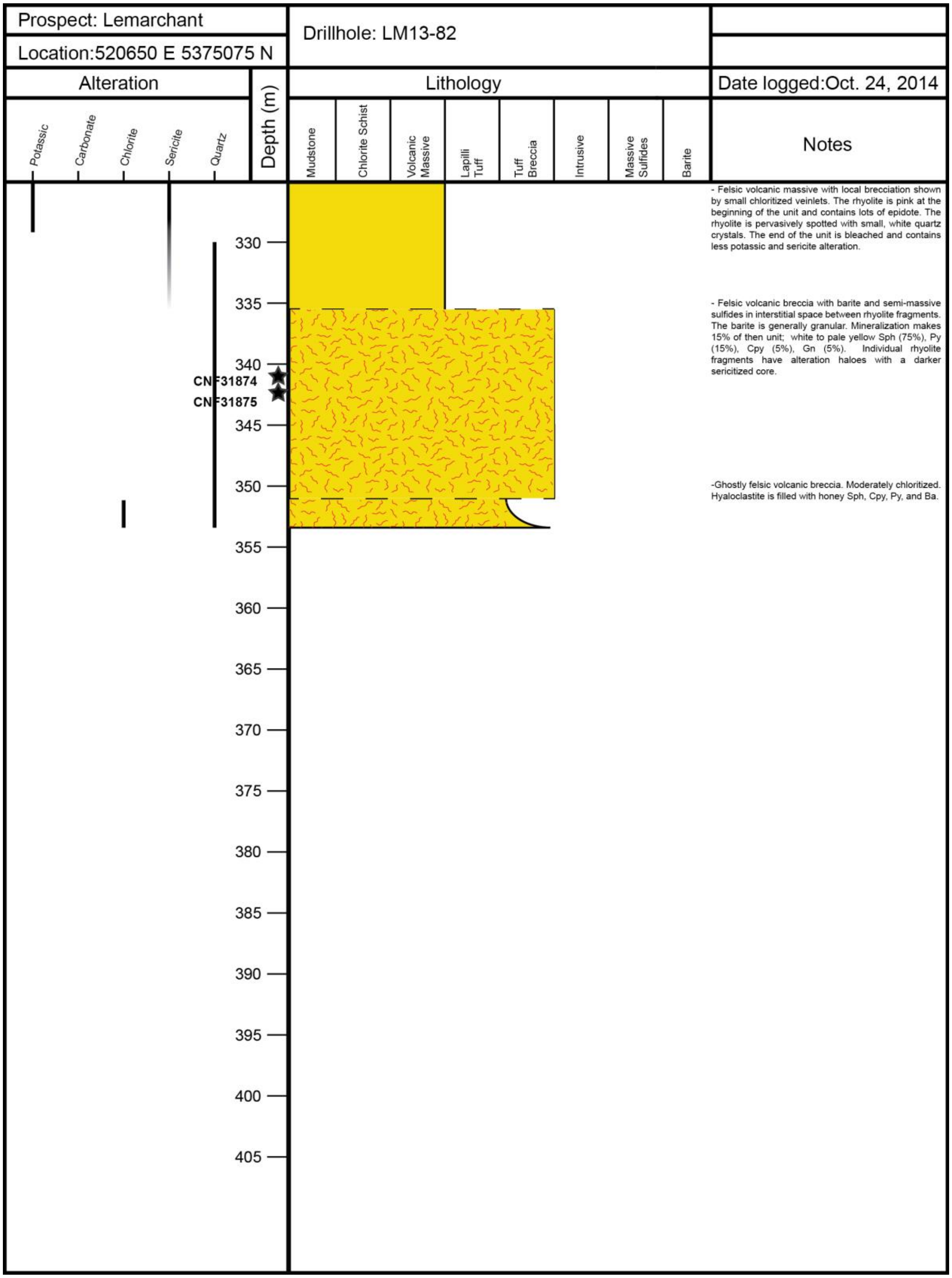

Prospect: Lemarchant
Location:520650 E 5375075 N
Drillhole: LM13-82
Date logged:Oct. 24, 2014
Alteration
Depth (m)
Lithology
Potassic
Carbonate
Chlorite
Sericite
Quartz
Mudstone
Chlorite Schist
Volcanic Massive
Lapilli Tuff
Tuff Breccia
Intrusive
Massive Sulfides
Barite
Notes
330
335
340
CNF31874
CNF31875
345
350
355
360
365
370
375
380
385
390
395
400
405
- Felsic volcanic massive with local brecciation shown by small chloritized veinlets. The rhyolite is pink at the beginning of the unit and contains lots of epidote. The rhyolite is pervasively spotted with small, white quartz crystals. The end of the unit is bleached and contains less potassic and sericite alteration.
- Felsic volcanic breccia with barite and semi-massive sulfides in interstitial space between rhyolite fragments. The barite is generally granular. Mineralization makes 15% of then unit; white to pale yellow Sph (75%), Py (15%), Cpy (5%), Gn (5%). Individual rhyolite fragments have alteration haloes with a darker sericitized core.
-Ghostly felsic volcanic breccia. Moderately chloritized. Hyaloclastite is filled with honey Sph, Cpy, Py, and Ba.

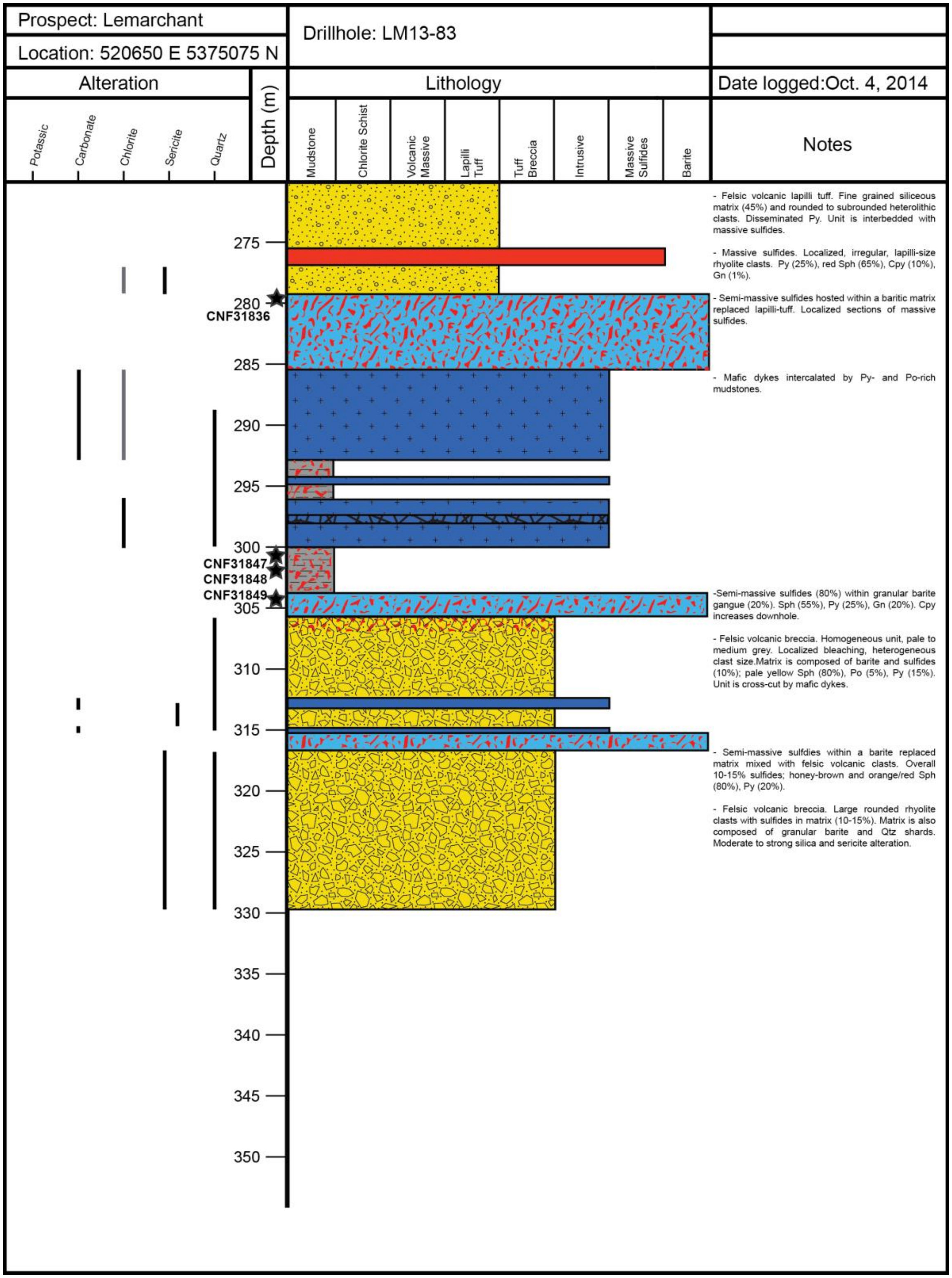

Prospect: Lemarchant
Location: 520650 E 5375075 N
Drillhole: LM13-83
Date logged:Oct. 4, 2014
Alteration
Potassic
Carbonate
Chlorite
Sericite
Quartz
Depth (m)
Lithology
Mudstone
Chlorite Schist
Volcanic Massive
Lapilli Tuff
Tuff Breccia
Intrusive
Massive Sulfides
Barite
Notes
275
280
CNF31836
285
290
295
300
CNF31847
CNF31848
CNF31849
305
310
315
320
325
330
335
340
345
350
- Felsic volcanic lapilli tuff. Fine grained siliceous matrix (45%) and rounded to subrounded heterolithic clasts. Disseminated Py. Unit is interbedded with massive sulfides.
- Massive sulfides. Localized, irregular, lapilli-size rhyolite clasts. Py (25%), red Sph (65%), Cpy (10%), Gn (1%).
- Semi-massive sulfides hosted within a baritic matrix replaced lapilli-tuff. Localized sections of massive sulfides.
- Mafic dykes intercalated by Py- and Po-rich mudstones.
-Semi-massive sulfides (80%) within granular barite gangue (20%). Sph (55%), Py (25%), Gn (20%). Cpy increases downhole.
- Felsic volcanic breccia. Homogeneous unit, pale to medium grey. Localized bleaching, heterogeneous clast size.Matrix is composed of barite and sulfides (10%); pale yellow Sph (80%), Po (5%), Py (15%). Unit is cross-cut by mafic dykes.
- Semi-massive sulfdies within a barite replaced matrix mixed with felsic volcanic clasts. Overall 10-15% sulfides; honey-brown and orange/red Sph (80%), Py (20%).
- Felsic volcanic breccia. Large rounded rhyolite clasts with sulfides in matrix (10-15%). Matrix is also composed of granular barite and Qtz shards. Moderate to strong silica and sericite alteration.

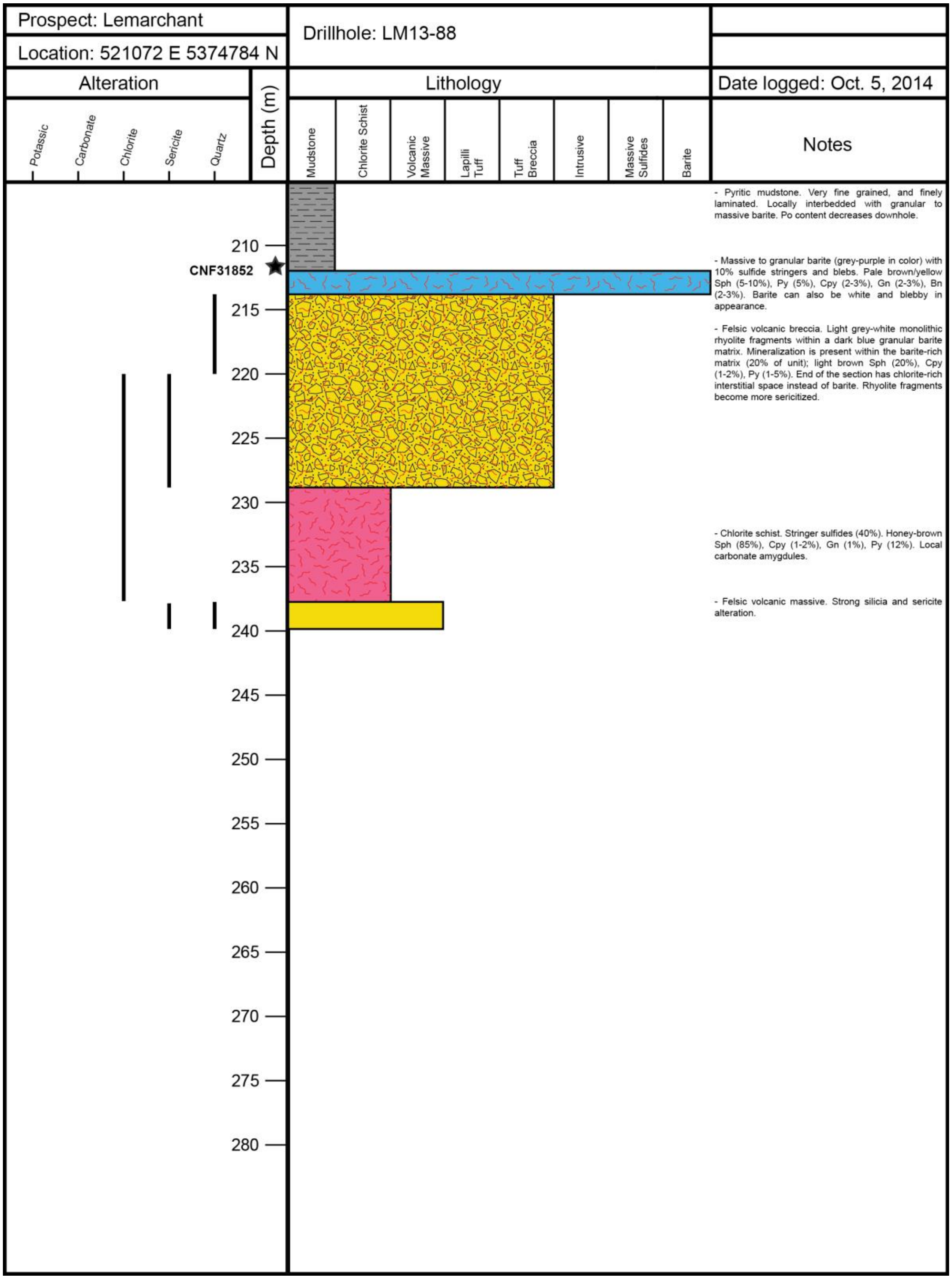

Prospect: Lemarchant
Location: 521072 E 5374784 N
Drillhole: LM13-88
Alteration
Depth (m)
Lithology
Date logged: Oct. 5, 2014
Potassic
Carbonate
Chlorite
Sericite
Quartz
Mudstone
Chlorite Schist
Volcanic Massive
Lapilli Tuff
Tuff Breccia
Intrusive
Massive Sulfides
Barite
Notes
210
CNF31852
215
220
225
230
235
240
245
250
255
260
265
270
275
280
- Pyritic mudstone. Very fine grained, and finely laminated. Locally interbedded with granular to massive barite. Po content decreases downhole.
- Massive to granular barite (grey-purple in color) with 10% sulfide stringers and blebs. Pale brown/yellow Sph (5-10%), Py (5%), Cpy (2-3%), Gn (2-3%), Bn (2-3%). Barite can also be white and blebby in appearance.
- Felsic volcanic breccia. Light grey-white monolithic rhyolite fragments within a dark blue granular barite matrix. Mineralization is present within the barite-rich matrix (20% of unit); light brown Sph (20%), Cpy (1-2%), Py (1-5%). End of the section has chlorite-rich interstitial space instead of barite. Rhyolite fragments become more sericitized.
- Chlorite schist. Stringer sulfides (40%). Honey-brown Sph (85%), Cpy (1-2%), Gn (1%), Py (12%). Local carbonate amygdules.
- Felsic volcanic massive. Strong silicia and sericite alteration.

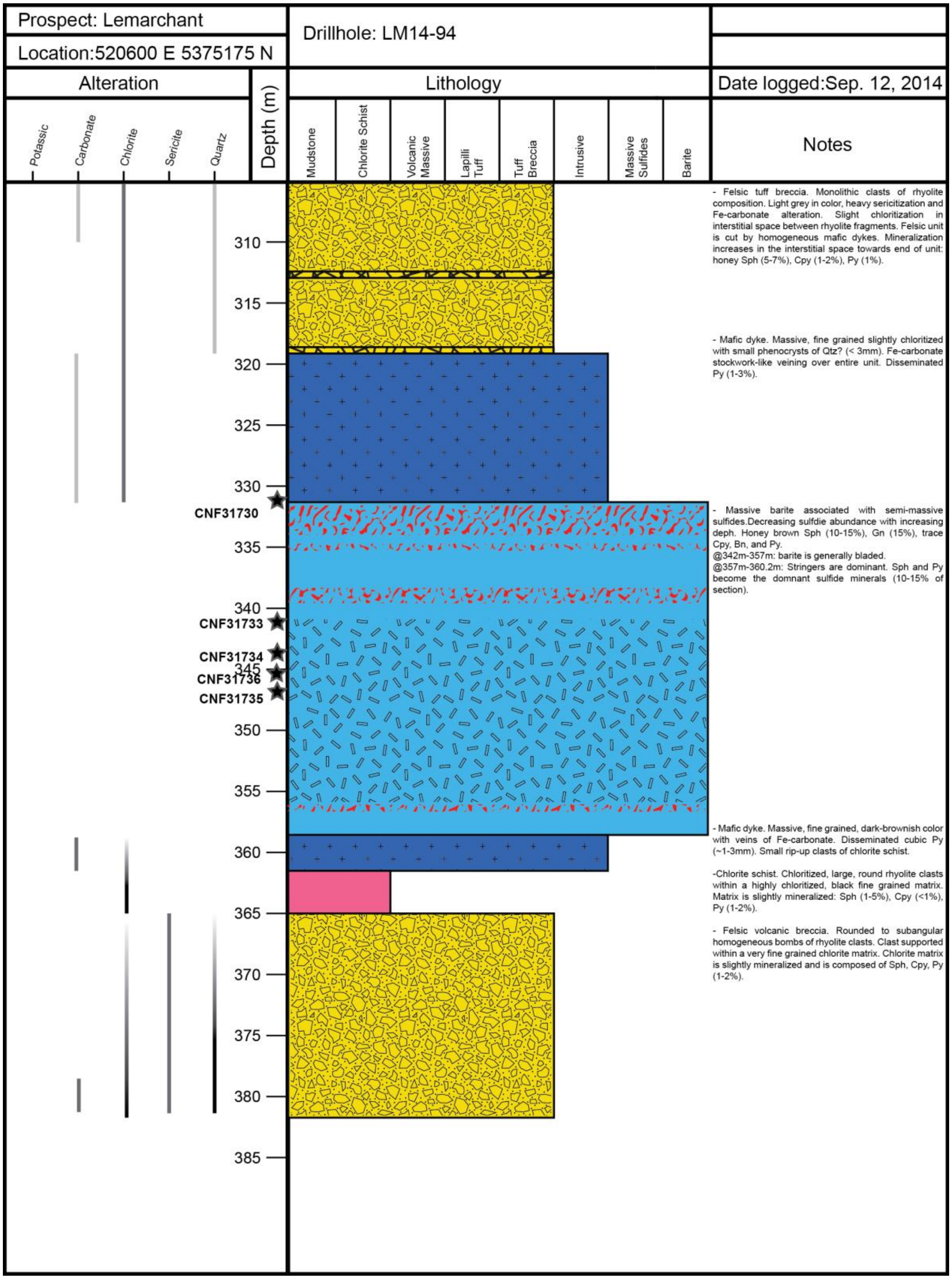

Prospect: Lemarchant
Location:520600 E 5375175 N
Drillhole: LM14-94
Date logged:Sep. 12, 2014
Alteration
Potassic
Carbonate
Chlorite
Sericite
Quartz
Depth (m)
Lithology
Mudstone
Chlorite Schist
Volcanic Massive
Lapilli Tuff
Tuff Breccia
Intrusive
Massive Sulfides
Barite
Notes
310
315
320
325
330
CNF31730
335
340
CNF31733
CNF31734
345
CNF31736
CNF31735
350
355
360
365
370
375
380
385
- Felsic tuff breccia. Monolithic clasts of rhyolite composition. Light grey in color, heavy sericitization and Fe-carbonate alteration. Slight chloritization in interstitial space between rhyolite fragments. Felsic unit is cut by homogeneous mafic dykes. Mineralization increases in the interstitial space towards end of unit: honey Sph (5-7%), Cpy (1-2%), Py (1%).
- Mafic dyke. Massive, fine grained slightly chloritized with small phenocrysts of Qtz? (< 3mm). Fe-carbonate stockwork-like veining over entire unit. Disseminated Py (1-3%).
- Massive barite associated with semi-massive sulfides.Decreasing sulfdie abundance with increasing deph. Honey brown Sph (10-15%), Gn (15%), trace Cpy, Bn, and Py.
@342m-357m: barite is generally bladed.
@357m-360.2m: Stringers are dominant. Sph and Py become the domnant sulfide minerals (10-15% of section).
- Mafic dyke. Massive, fine grained, dark-brownish color with veins of Fe-carbonate. Disseminated cubic Py (~1-3mm). Small rip-up clasts of chlorite schist.
-Chlorite schist. Chloritized, large, round rhyolite clasts within a highly chloritized, black fine grained matrix. Matrix is slightly mineralized: Sph (1-5%), Cpy (<1%), Py (1-2%).
- Felsic volcanic breccia. Rounded to subangular homogeneous bombs of rhyolite clasts. Clast supported within a very fine grained chlorite matrix. Chlorite matrix is slightly mineralized and is composed of Sph, Cpy, Py (1-2%).

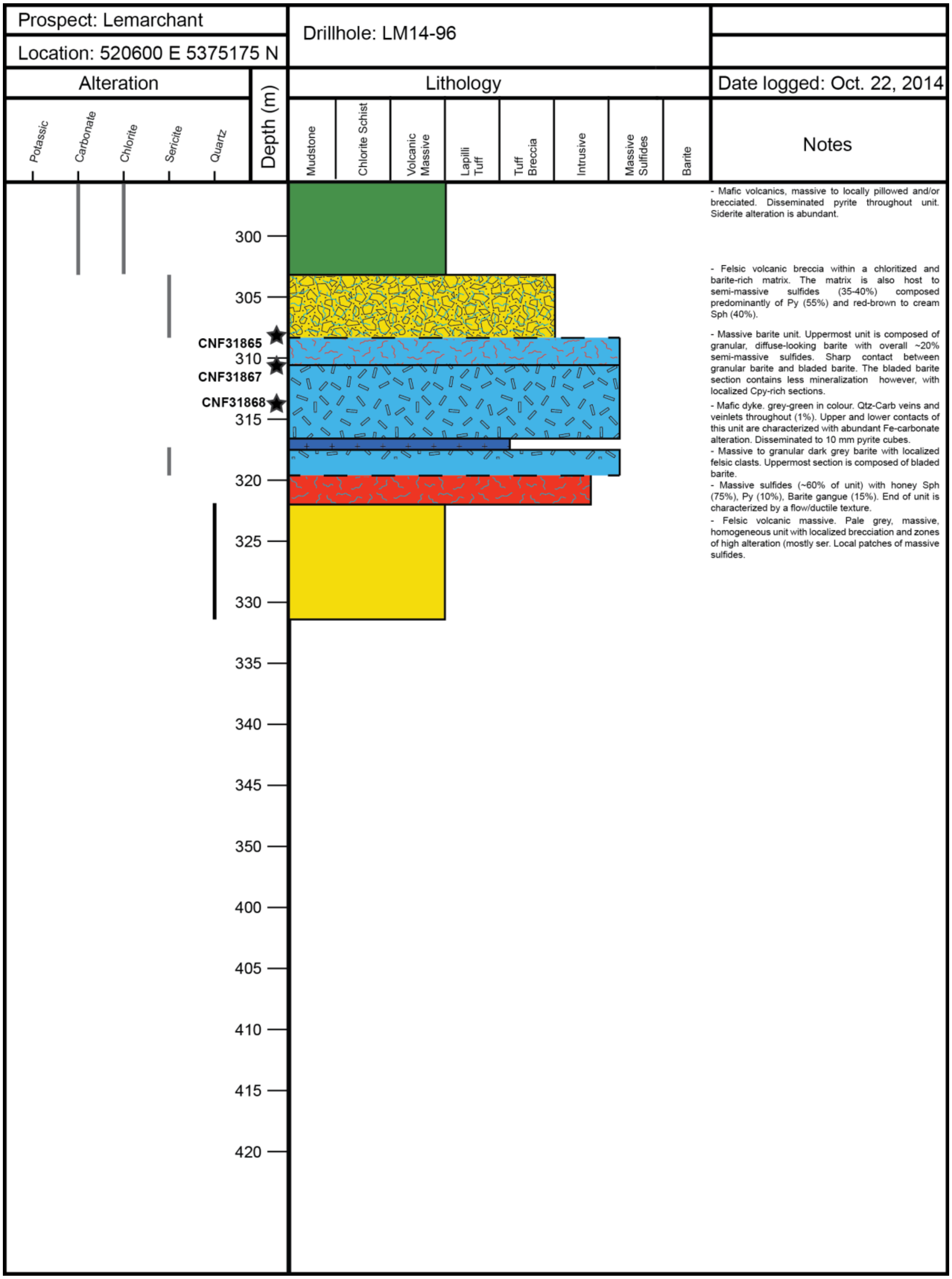
Prospect: Lemarchant
Location: 520600 E 5375175 N
Drillhole: LM14-96
Date logged: Oct. 22, 2014
Alteration
Potassic
Carbonate
Chlorite
Sericite
Quartz
Depth (m)
Lithology
Mudstone
Chlorite Schist
Volcanic Massive
Lapilli Tuff
Tuff Breccia
Intrusive
Massive Sulfides
Barite
Notes
300
305
310
315
320
325
330
335
340
345
350
400
405
410
415
420
CNF31865
CNF31867
CNF31868
- Mafic volcanics, massive to locally pillowed and/or brecciated. Disseminated pyrite throughout unit. Siderite alteration is abundant.
- Felsic volcanic breccia within a chloritized and barite-rich matrix. The matrix is also host to semi-massive sulfides (35-40%) composed predominantly of Py (55%) and red-brown to cream Sph (40%).
- Massive barite unit. Uppermost unit is composed of granular, diffuse-looking barite with overall ~20% semi-massive sulfides. Sharp contact between granular barite and bladed barite. The bladed barite section contains less mineralization however, with localized Cpy-rich sections.
- Mafic dyke. grey-green in colour. Qtz-Carb veins and veinlets throughout (1%). Upper and lower contacts of this unit are characterized with abundant Fe-carbonate alteration. Disseminated to 10 mm pyrite cubes.
- Massive to granular dark grey barite with localized felsic clasts. Uppermost section is composed of bladed barite.
- Massive sulfides (~60% of unit) with honey Sph (75%), Py (10%), Barite gangue (15%). End of unit is characterized by a flow/ductile texture.
- Felsic volcanic massive. Pale grey, massive, homogeneous unit with localized brecciation and zones of high alteration (mostly ser. Local patches of massive sulfides.

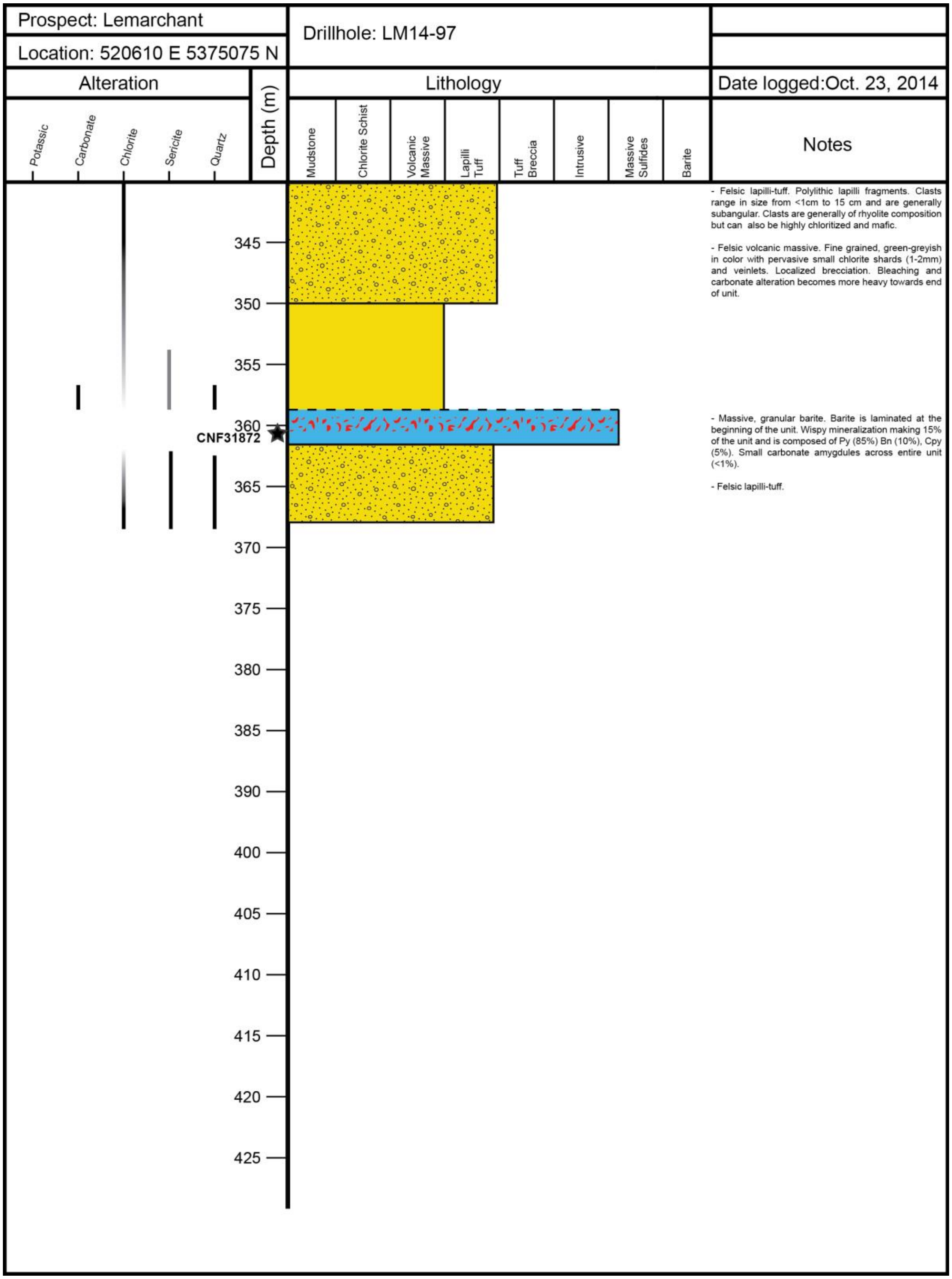

Prospect: Lemarchant
Location: 520610 E 5375075 N
Drillhole: LM14-97
Date logged:Oct. 23, 2014
Alteration
Potassic
Carbonate
Chlorite
Sericite
Quartz
Depth (m)
Lithology
Mudstone
Chlorite Schist
Volcanic Massive
Lapilli Tuff
Tuff Breccia
Intrusive
Massive Sulfides
Barite
Notes
345
350
355
360
CNF31872
365
370
375
380
385
390
400
405
410
415
420
425
- Felsic lapilli-tuff. Polylithic lapilli fragments. Clasts range in size from <1cm to 15 cm and are generally subangular. Clasts are generally of rhyolite composition but can also be highly chloritized and mafic.
- Felsic volcanic massive. Fine grained, green-greyish in color with pervasive small chlorite shards (1-2mm) and veinlets. Localized brecciation. Bleaching and carbonate alteration becomes more heavy towards end of unit.
- Massive, granular barite. Barite is laminated at the beginning of the unit. Wispy mineralization making 15% of the unit and is composed of Py (85%) Bn (10%), Cpy (5%). Small carbonate amygdules across entire unit (<1%).
- Felsic lapilli-tuff.

Appendix 2: Whole-rock lithogeochemistry results

Whole-rock major, trace, and rare earth element (REE) concentraions were determined on 10 of the 18 samples analyzed for Sr isotope geochemistry (Table A-2-2). Samples were crushed and sieved to < 80 μm and centrifuged to isolate barite. Samples were analysed by inductively coupled plasma-mass spectrometry (ICP-MS) at Activation Laboratories Inc. in Ontario, Canada, using the 4B2-Research-Lithium Metaborate/Tetraborate Fusion-ICP/MS package that involves lithium metaborate/tetraborate fusion and HNO_3 dissolution. Lithogeochemical analyses of these samples were determined prior to Sr isotope analyses in order to determine the concentrations of Sr and Rb.

Quality assurance and quality control (QA-QC) were monitored using certified reference materials at Activation Laboratories. Precision could not be calculated because reference materials were only analyzed once due to the low number of sample analyses. Accuracy is summarized for the elements of interest in table (A-2-1). Accuracy for reference materials is given as percent relative difference (% RD) and calculated using the following equation:

$$RD(\%) = 100 * \frac{\mu_i - C_i}{C_i}$$

Where μ_i = mean value of element *i* in the standard over a number of analytical runs; and C_i = certified value of *i* in the reference material. Table (A-2-1) shows that the accuracy of most elements is $-10\% \leq RD \leq 10\%$, which shows that the analyses have good accuracy. However, some elements have accuracies above ± 10% because the concentrations of these elements are close to the detection limit.

Table A-2-1. Summary of accuracy for reference materials used in this study.

Analyte Symbol	Unit Symbo	Detection Limit	Analysis Method	NIST 694 RD (%)	DNC-1 RD (%)	GBW 07113 RD (%)	LKSD-3 RD (%)	TDB-1 RD (%)	BaSO4 RD (%)	W-2a RD (%)	DTS-2b RD (%)
SiO2	%	0.01	FUS-ICP	-1.61	0.11	-2.01	-	-	-	0.82	-
Al2O3	%	0.01	FUS-ICP	6.11	-1.25	0.31	-	-	-	0.52	-
Fe2O3(T)	%	0.01	FUS-ICP	-5.06	-4.21	0.00	-	-	-	-1.40	-
MnO	%	0.001	FUS-ICP	-13.79	0.00	0.00	-	-	-	4.29	-
MgO	%	0.01	FUS-ICP	3.03	-0.10	-6.25	-	-	-	-0.78	-
CaO	%	0.01	FUS-ICP	-1.72	0.00	3.39	-	-	-	1.10	-
Na2O	%	0.01	FUS-ICP	0.00	1.06	-3.11	-	-	-	4.21	-
K2O	%	0.01	FUS-ICP	7.84	-1.71	-0.18	-	-	-	-0.96	-
TiO2	%	0.001	FUS-ICP	9.09	-2.08	-3.33	-	-	-	0.94	-
P2O5	%	0.01	FUS-ICP	0.10	0.00	-40.00	-	-	-	7.69	-
Sc	ppm	1	FUS-ICP	-	0.00	20.00	-	-	-	-2.78	-
Be	ppm	1	FUS-ICP	-	-	0.00	-	-	-	-	-
V	ppm	5	FUS-ICP	-6.21	3.38	20.00	-	-	-	5.34	-
Cr	ppm	20	FUS-MS	-	0.00	-	-	-0.40	-	-2.17	-
Co	ppm	1	FUS-MS	-	-3.51	-	-3.33	-	-	0.00	5.83
Ni	ppm	20	FUS-MS	-	1.21	-	6.38	-2.17	-	0.00	0.26
Cu	ppm	10	FUS-MS	-	10.00	-	-14.29	5.26	-	0.00	-
Zn	ppm	30	FUS-MS	-	0.00	-	-	-3.23	-	-12.50	-
Ga	ppm	1	FUS-MS	-	0.00	-	-	-	-	0.00	-
Ge	ppm	0.5	FUS-MS	-	-	-	-	-	-	40.00	-
As	ppm	5	FUS-MS	-	-	-	0.00	-	-	-	-
Rb	ppm	1	FUS-MS	-	-40.00	-	-8.97	-	-	-4.76	-
Sr	ppm	2	FUS-ICP	-	-0.69	-6.98	-	-	-	3.68	-
Y	ppm	0.5	FUS-MS	-	5.56	-	0.00	-3.61	-	-12.50	-
Zr	ppm	1	FUS-ICP	-	-2.63	-1.49	-	-	-	-5.32	-
Nb	ppm	0.2	FUS-MS	-	-63.33	-	-	-	-	-	-
Mo	ppm	2	FUS-MS	-	-	-	-	-	-	-	-
Ag	ppm	0.5	FUS-MS	-	-	-	3.70	-	-	-	-
In	ppm	0.1	FUS-MS	-	-	-	-	-	-	-	-
Sn	ppm	1	FUS-MS	-	-	-	-	-	-	-	-
Sb	ppm	0.2	FUS-MS	-	-6.25	-	-	-	-	13.92	-
Cs	ppm	0.1	FUS-MS	-	-	-	13.04	-	-	-	-
Ba	ppm	3	FUS-ICP	-	-10.17	-0.79	-	-	-1.40	-4.40	-
La	ppm	0.05	FUS-MS	-	-	-	-7.69	2.35	-	-	-
Ce	ppm	0.05	FUS-MS	-	-	-	-0.56	-0.49	-	7.39	-
Pr	ppm	0.01	FUS-MS	-	-	-	-	-	-	-	-
Nd	ppm	0.05	FUS-MS	-	3.85	-	4.77	6.52	-	3.08	-
Sm	ppm	0.01	FUS-MS	-	-	-	3.75	-	-	0.00	-
Eu	ppm	0.005	FUS-MS	-	-	-	-6.67	0.00	-	-	-
Gd	ppm	0.01	FUS-MS	-	-	-	-	-	-	-	-
Tb	ppm	0.01	FUS-MS	-	-	-	-10.00	-	-	0.00	-
Dy	ppm	0.01	FUS-MS	-	-	-	10.20	-13.00	-	-	-
Ho	ppm	0.01	FUS-MS	-	-	-	-	-	-	1.32	-
Er	ppm	0.01	FUS-MS	-	-	-	-	-	-	-	-
Tm	ppm	0.005	FUS-MS	-	-	-	-	-	-	-	-
Yb	ppm	0.01	FUS-MS	-	5.00	-	7.41	0.00	-	0.00	-
Lu	ppm	0.002	FUS-MS	-	-	-	15.00	-	-	-9.09	-
Hf	ppm	0.1	FUS-MS	-	-	-	2.08	-	-	-3.85	-
Ta	ppm	0.01	FUS-MS	-	-	-	-14.29	-	-	-	-
W	ppm	0.5	FUS-MS	-	-	-	-	-	-	-	-
Tl	ppm	0.05	FUS-MS	-	-	-	-	-	-	-65.00	-
Pb	ppm	5	FUS-MS	-	-4.76	-	-	-	-	-	-
Bi	ppm	0.1	FUS-MS	-	-	-	-	-	-	-	-
Th	ppm	0.05	FUS-MS	-	-	-	0.00	0.00	-	-8.33	-
U	ppm	0.01	FUS-MS	-	-	-	8.70	-	-	-5.66	-

Table A-2-1. *Cont.'d*

Analyte Symbol	Unit Symbo	Detection Limit	Analysis Method	SY-4	CTA-AC-1	BIR-1a	NCS DC86321	ZW-C	NCS DC7000(	OREAS 100a	OREAS 101a
				RD (%)	RD (%)	RD (%)	RD (%)	RD (%)	RD (%)	RD (%)	RD (%)
SiO2	%	0.01	FUS-ICP	0.38	-	0.92	-	-	-	-	-
Al2O3	%	0.01	FUS-ICP	-0.87	-	2.06	-	-	-	-	-
Fe2O3(T)	%	0.01	FUS-ICP	-0.32	-	-2.57	-	-	-	-	-
MnO	%	0.001	FUS-ICP	1.85	-	-2.86	-	-	-	-	-
MgO	%	0.01	FUS-ICP	-7.41	-	-1.24	-	-	-	-	-
CaO	%	0.01	FUS-ICP	0.50	-	1.80	-	-	-	-	-
Na2O	%	0.01	FUS-ICP	-2.25	-	1.65	-	-	-	-	-
K2O	%	0.01	FUS-ICP	0.00	-	-33.33	-	-	-	-	-
TiO2	%	0.001	FUS-ICP	1.05	-	0.00	-	-	-	-	-
P2O5	%	0.01	FUS-ICP	-8.40	-	-52.38	-	-	-	-	-
Sc	ppm	1	FUS-ICP	-9.09	-	0.00	-	-	-	-	-
Be	ppm	1	FUS-ICP	15.38	-	-	-	-	-	-	-
V	ppm	5	FUS-ICP	0.00	-	7.42	-	-	-	-	-
Cr	ppm	20	FUS-MS	-	-	5.41	-	-	0.00	-	-
Co	ppm	1	FUS-MS	-	-	-3.85	-	-	8.11	-6.08	-5.74
Ni	ppm	20	FUS-MS	-	-	0.00	-	-	-	-	-
Cu	ppm	10	FUS-MS	-	11.11	-	-	-	9.38	-5.33	-
Zn	ppm	30	FUS-MS	-	5.26	0.00	-	-6.67	10.00	-	-
Ga	ppm	1	FUS-MS	-	-	6.25	-	-4.04	3.03	-	-
Ge	ppm	0.5	FUS-MS	-	-	-	-	-	-0.89	-	-
As	ppm	5	FUS-MS	-	-	-	-	-	4.43	-	-
Rb	ppm	1	FUS-MS	-	-	-	-	-	3.20	-	-
Sr	ppm	2	FUS-ICP	0.92	-	-0.91	-	-	-	-	-
Y	ppm	0.5	FUS-MS	-	4.04	12.50	-0.51	-	-0.78	5.63	0.00
Zr	ppm	1	FUS-ICP	2.32	-	-16.67	-	-	-	-	-
Nb	ppm	0.2	FUS-MS	-	-	-	-	-	-	-	-
Mo	ppm	2	FUS-MS	-	-	-	-	-	-	3.73	-8.68
Ag	ppm	0.5	FUS-MS	-	-	-	-	-	-5.56	-	-
In	ppm	0.1	FUS-MS	-	-	-	-	-	-7.69	-	-
Sn	ppm	1	FUS-MS	-	-	-	-	-	-	-	-
Sb	ppm	0.2	FUS-MS	-	-	3.45	-	-	-	-	-
Cs	ppm	0.1	FUS-MS	-	-	-	-	-2.31	-	-	-
Ba	ppm	3	FUS-ICP	2.94	-	16.67	-	-	-	-	-
La	ppm	0.05	FUS-MS	-	-	-4.76	-	-	8.86	5.38	-3.06
Ce	ppm	0.05	FUS-MS	-	-	-5.26	-3.68	-	8.29	7.13	-1.15
Pr	ppm	0.01	FUS-MS	-	-	-	-	-	1.27	6.16	-2.99
Nd	ppm	0.05	FUS-MS	-	3.96	-4.00	-5.00	-	0.30	9.21	-0.25
Sm	ppm	0.01	FUS-MS	-	0.62	9.09	-	-	4.00	10.17	4.51
Eu	ppm	0.005	FUS-MS	-	7.92	-1.82	-	-	-	9.70	-0.12
Gd	ppm	0.01	FUS-MS	-	0.00	-5.00	-	-	1.35	5.93	-
Tb	ppm	0.01	FUS-MS	-	-	-	0.87	-	-3.03	7.11	-4.90
Dy	ppm	0.01	FUS-MS	-	-	0.00	7.10	-	1.45	5.17	0.60
Ho	ppm	0.01	FUS-MS	-	-	-	4.44	-	-2.22	5.41	4.49
Er	ppm	0.01	FUS-MS	-	-	-	0.42	-	-0.75	8.05	6.67
Tm	ppm	0.005	FUS-MS	-	-	-	-3.97	-	0.00	3.90	3.45
Yb	ppm	0.01	FUS-MS	-	8.77	5.88	2.97	-	6.71	4.70	8.00
Lu	ppm	0.002	FUS-MS	-	-	-13.33	8.70	-	7.50	-0.44	1.88
Hf	ppm	0.1	FUS-MS	-	-	0.00	-	-	-	-	-
Ta	ppm	0.01	FUS-MS	-	-	-	-	0.12	-	-	-
W	ppm	0.5	FUS-MS	-	-	-	-	2.81	-7.27	-	-
Tl	ppm	0.05	FUS-MS	-	-	-	-	-1.18	5.56	-	-
Pb	ppm	5	FUS-MS	-	-	66.67	-	-	-	-	-
Bi	ppm	0.1	FUS-MS	-	-	-	-	-	-	-	-
Th	ppm	0.05	FUS-MS	-	10.55	-	4.24	-	1.77	4.07	8.47
U	ppm	0.01	FUS-MS	-	9.09	-	-	-	-	5.93	0.47

Table A-2-1. *Cont.'d*

Analyte Symbol	Unit Symbo	Detection Limit	Analysis Method	OREAS 101b RD (%)	JR-1 RD (%)	BXGO-1 RD (%)	BXMG-3 RD (%)	BXSP-1 RD (%)
SiO2	%	0.01	FUS-ICP	-	-	1.59	-4.37	0.20
Al2O3	%	0.01	FUS-ICP	-	-	-0.87	0.40	1.66
Fe2O3(T)	%	0.01	FUS-ICP	-	-	-	-	-
MnO	%	0.001	FUS-ICP	-	-	-	-	-
MgO	%	0.01	FUS-ICP	-	-	-	-	-
CaO	%	0.01	FUS-ICP	-	-	-	-	-
Na2O	%	0.01	FUS-ICP	-	-	-	-	-
K2O	%	0.01	FUS-ICP	-	-	-	42.86	0.00
TiO2	%	0.001	FUS-ICP	-	-	-5.87	0.45	0.81
P2O5	%	0.01	FUS-ICP	-	-	19.05	-7.61	-16.26
Sc	ppm	1	FUS-ICP	-	-	-	-	-
Be	ppm	1	FUS-ICP	-	-	-	-	-
V	ppm	5	FUS-ICP	-	-	-	-	-
Cr	ppm	20	FUS-MS	-	-	-	-	-
Co	ppm	1	FUS-MS	-4.26	20.48	-	-	-
Ni	ppm	20	FUS-MS	-	-	-	-	-
Cu	ppm	10	FUS-MS	0.96	-	-	-	-
Zn	ppm	30	FUS-MS	-	-	-	-	-
Ga	ppm	1	FUS-MS	-	11.80	-	-	-
Ge	ppm	0.5	FUS-MS	-	-	-	-	-
As	ppm	5	FUS-MS	-	-1.84	-	-	-
Rb	ppm	1	FUS-MS	-	-9.73	-	-	-
Sr	ppm	2	FUS-ICP	-	-	-	-	-
Y	ppm	0.5	FUS-MS	-1.12	2.88	-	-	-
Zr	ppm	1	FUS-ICP	-	-	-	-	-
Nb	ppm	0.2	FUS-MS	-	-1.97	-	-	-
Mo	ppm	2	FUS-MS	0.48	-	-	-	-
Ag	ppm	0.5	FUS-MS	-	-	-	-	-
In	ppm	0.1	FUS-MS	-	-	-	-	-
Sn	ppm	1	FUS-MS	-	4.90	-	-	-
Sb	ppm	0.2	FUS-MS	-	-7.56	-	-	-
Cs	ppm	0.1	FUS-MS	-	9.13	-	-	-
Ba	ppm	3	FUS-ICP	-	-	-	-	-
La	ppm	0.05	FUS-MS	3.42	-1.52	-	-	-
Ce	ppm	0.05	FUS-MS	4.43	-1.91	-	-	-
Pr	ppm	0.01	FUS-MS	0.79	9.32	-	-	-
Nd	ppm	0.05	FUS-MS	0.00	4.72	-	-	-
Sm	ppm	0.01	FUS-MS	2.08	-0.83	-	-	-
Eu	ppm	0.005	FUS-MS	4.38	-10.00	-	-	-
Gd	ppm	0.01	FUS-MS	-	-	-	-	-
Tb	ppm	0.01	FUS-MS	0.56	0.00	-	-	-
Dy	ppm	0.01	FUS-MS	0.62	-	-	-	-
Ho	ppm	0.01	FUS-MS	0.47	-	-	-	-
Er	ppm	0.01	FUS-MS	2.67	-	-	-	-
Tm	ppm	0.005	FUS-MS	4.14	7.46	-	-	-
Yb	ppm	0.01	FUS-MS	3.41	7.03	-	-	-
Lu	ppm	0.002	FUS-MS	0.00	4.23	-	-	-
Hf	ppm	0.1	FUS-MS	-	-0.22	-	-	-
Ta	ppm	0.01	FUS-MS	-	-8.60	-	-	-
W	ppm	0.5	FUS-MS	-	-	-	-	-
Tl	ppm	0.05	FUS-MS	-	-1.28	-	-	-
Pb	ppm	5	FUS-MS	-	-1.55	-	-	-
Bi	ppm	0.1	FUS-MS	-	-28.57	-	-	-
Th	ppm	0.05	FUS-MS	-5.39	5.24	-	-	-
U	ppm	0.01	FUS-MS	-4.04	5.86	-	-	-

Table A-2-2. Whole-rock lithogeochemical data of barite samples from the Lemarchant deposit.

Sample	CNF31816	CNF31861	CNF31733	CNF31810	CNF31730	CNF31721	CNF31874	CNF31865	CNF31868	CNF31855
Drill hole	LM08-19	LM11-68	LM13-94	LM10-43	LM13-94	LM13-73	LM13-82	LM14-96	LM14-96	LM11-52
Depth (m)	98.1	199.9	341.4	218.8	326.3	332.9	340.8	309.9	314.4	216.2
Mineralized zone	24 zone	Main zone	Northwest zone	Main zone	Northwest zone	Northwest zone	Northwest zone	Northwest zone	Northwest zone	Main zone
SiO_2 *wt.%*	0.83	0.53	1.46	0.5	1.47	0.42	4.63	0.03	0.23	1.18
Al_2O_3	0.63	0.08	0.12	0.06	0.77	0.14	0.19	< 0.01	0.1	0.43
Fe_2O_3	4.28	0.44	0.28	0.87	0.41	0.23	0.51	0.06	0.12	0.28
MnO	0.034	< 0.001	< 0.001	0.059	< 0.001	0.005	< 0.001	< 0.001	< 0.001	0.003
MgO	0.28	0.08	0.08	1.87	0.14	0.12	0.02	0.03	0.02	0.17
CaO	2.51	0.13	0.14	2.82	0.18	0.2	0.06	0.06	0.03	0.31
Na_2O	0.01	< 0.01	< 0.01	< 0.01	0.02	0.03	0.04	< 0.01	< 0.01	0.05
K_2O	0.07	< 0.01	0.02	< 0.01	0.1	< 0.01	0.03	< 0.01	< 0.01	0.04
TiO_2	0.01	0.001	0.001	< 0.001	0.001	< 0.001	0.004	< 0.001	0.001	0.001
P_2O_5	0.25	0.02	0.01	0.01	0.09	0.01	< 0.01	< 0.01	< 0.01	0.08
LOI	2.81	0.7	0.68	1.72	0.86	0.83	1.62	0.23	0.15	0.91
Total	11.71	1.99	2.8	7.94	4.04	1.99	7.12	0.4	0.65	3.47
Ba *ppm*	510000	551200	548300	505200	520300	547300	521400	568600	576500	543100
Cu	430	2780	3070	7090	2790	2000	1100	1390	240	1060
Zn	190	5040	5160	> 10000	> 10000	> 10000	> 10000	5260	510	> 10000
Pb	326	8640	4670	5320	> 10000	8460	6880	2910	401	3370
Ag	0.8	16.1	13.5	1.5	8.5	4.2	< 0.5	1.1	1	2.3
Cr	< 20	< 20	< 20	< 20	< 20	< 20	< 20	< 20	< 20	< 20
Co	< 1	< 1	< 1	< 1	< 1	< 1	< 1	< 1	< 1	< 1
Ni	30	< 20	< 20	< 20	< 20	< 20	< 20	< 20	< 20	< 20
Sc	< 1	< 1	< 1	< 1	< 1	< 1	< 1	< 1	< 1	< 1
Be	< 1	< 1	< 1	< 1	< 1	< 1	< 1	< 1	< 1	< 1
V	103	10	20	6	102	15	11	< 5	19	45
Ga	3	3	3	7	10	11	6	2	2	9
Ge	< 0.5	< 0.5	14.4	1.4	4.7	3.6	< 0.5	< 0.5	< 0.5	< 0.5
As	105	378	53	47	52	30	105	13	29	22
Rb	1	< 1	< 1	< 1	2	< 1	< 1	< 1	< 1	< 1
Sr	4889	5905	9348	4034	5419	4997	3604	7438	7233	5693
Y	12.1	4.2	4.9	3.8	6.8	4.8	4	3.6	3.8	8.7
Zr	6	2	3	2	4	2	3	2	3	2
Nb	< 0.2	< 0.2	< 0.2	< 0.2	< 0.2	< 0.2	< 0.2	< 0.2	< 0.2	< 0.2
Mo	3	33	59	> 100	68	81	> 100	7	3	76
In	< 0.1	< 0.1	< 0.1	< 0.1	< 0.1	< 0.1	< 0.1	< 0.1	< 0.1	< 0.1
Sn	< 1	< 1	< 1	< 1	< 1	< 1	< 1	< 1	< 1	< 1
Sb	30.4	103	56.1	64.6	119	87.1	46.3	12.6	23.8	48.7
Cs	< 0.1	< 0.1	< 0.1	< 0.1	< 0.1	< 0.1	< 0.1	< 0.1	< 0.1	< 0.1
La	7.12	12.8	11.4	7.22	10.9	8.8	7.4	11.1	7.72	8.47
Ce	4.09	9.23	8.05	2.57	7.3	4.38	5.12	7.29	3.26	5.16
Pr	0.64	0.63	0.71	0.19	0.65	0.3	0.39	0.52	0.21	0.57
Nd	3.06	1.62	2.12	0.55	1.98	0.8	1.48	1.22	0.56	2.29
Sm	1.47	0.73	0.97	0.67	0.79	0.71	1.05	0.71	0.64	1.27
Eu	1.88	0.188	0.07	< 0.005	1.05	0.622	< 0.005	1.68	0.648	2.45
Gd	1.99	1.14	1.28	0.91	1.2	1.06	1.63	1.01	0.92	1.84
Tb	0.18	0.04	0.08	0.04	0.07	0.04	0.12	0.05	0.04	0.15
Dy	0.82	0.1	0.22	0.11	0.31	0.12	0.36	0.08	0.1	0.66
Ho	0.16	0.02	0.03	0.02	0.06	0.02	0.05	0.01	0.02	0.11
Er	0.45	0.06	0.09	0.06	0.15	0.06	0.13	0.03	0.05	0.25
Tm	0.07	0.01	0.014	0.01	0.019	0.008	0.018	< 0.005	0.007	0.032
Yb	0.41	0.07	0.08	0.07	0.12	0.06	0.11	0.04	0.05	0.18
Lu	0.053	0.011	0.014	0.01	0.021	0.01	0.019	0.007	0.009	0.026
Hf	0.3	0.3	0.3	0.2	0.2	0.3	0.2	0.2	0.2	0.3
Ta	0.27	0.31	0.32	0.28	0.29	0.33	< 0.01	0.26	0.26	0.31
W	1.9	2.1	< 0.5	0.7	0.6	0.9	< 0.5	2.4	0.8	0.8
Tl	< 0.05	< 0.05	0.29	< 0.05	< 0.05	< 0.05	< 0.05	< 0.05	< 0.05	< 0.05
Bi	< 0.1	< 0.1	< 0.1	< 0.1	< 0.1	< 0.1	< 0.1	< 0.1	< 0.1	< 0.1
Th	0.12	< 0.05	0.44	< 0.05	< 0.05	< 0.05	< 0.05	< 0.05	< 0.05	< 0.05
U	8.81	0.5	1.53	3.23	3.05	0.4	3.15	0.08	0.57	10.6

Appendix 3: Electron microprobe Results

3.1 Supplementary electron microprobe methods

Major element concentrations of individual barite crystals were determined by electron microprobe analysis (EMPA). 21 carbon-coated thin sections were analyzed for ten elements (Ba, S, Sr, Na, Si, Ca, K, Fe, Zn, Pb, F) on different barite textures using a five-spectrometer JEOL JXA-8230 electron microprobe at Memorial University of Newfoundland. The analyses were conducted at an accelerating voltage of 15 kV and intensity of 20 nA using a spot size of 1 µm. Natural and synthetic mineral phases were used as calibration standards. The following standards and lines were used: SPI synthetic compound group $BaSO_4$ (BaLα), and then the Astimex mineral suite, including: pyrite (SKα), celestite (SrKα), albite (NaKα, SiKα), bustamite (CaKα), orthoclase (KKα), almandine garnet (FeKα), willemite (ZnKα), and galena (PbKα). A summary of electron microprobe conditions are listed in the Table (A-3-1) below. Quality control was maintained by using a secondary standard (BaF_2; obtained from SPI Supplies®). The secondary standard was measured at the beginning and end of each run and the measured values were in compliance with the accepted concentrations in this standard. The analytical totals were accepted if they fell within a range of 100 ± 1.5 wt. % (*John Hanchar, pers comm*, 2016).

Table A-3-1. Summary of electron microprobe conditions for barite analyses

Element	X-ray	Crystal	Spectrometer	Accelerating voltage (kV)	Intensity (nA)	Spot size (μm)	Peak Position	Background - lower - (mm)	Background - upper- (mm)
Fe	Kα	LIFL	2	15	20	1	134.575	4	3
Ba	Lα	LIFL	2	15	20	1	192.990	3	2
Zn	Kα	LIFL	2	15	20	1	99.723	2	2
K	Kα	PETL	3	15	20	1	119.908	3	3
S	Kα	PETL	3	15	20	1	172.126	2	1.5
Sr	Lα	PETL	3	15	20	1	219.870	2.3	2
Ca	Kα	PETL	3	15	20	1	107.660	4	5.5
Pb	Mα	PETL	3	15	20	1	169.318	3.2	4.5
Na	Kα	TAP	4	15	20	1	129.536	3.8	6
Si	Kα	TAP	4	15	20	1	77.461	7	3

Chemical analyses using the electron microprobe are reported in weight percent (wt. %) of the oxides of the elements determined. Atoms per formula units (*apfu*) for each element analysed for barite was calculated based on 1 sulfur atom. An example for barite calculation is included below.

3.2 Mineral formula calculations for barite

Step 1: Analysed composition (wt. %) is determined for each element from probe analyses. Elements that are below detection limit are considered to be zero in the mineral calculation.

Step 2: Oxide molecular weight percent (wt. %) is determined for each element.

Step 3: Calculate the molecular proportion by dividing the element composition (wt. %) by the oxide molecular weight (wt. %) for each element.

Step 4: The total S in the barite unit cell is equal to 1. Therefore, the conversation factor is calculated by dividing 1 by the atomic proportion (step 3) calculated only for the element S.

Step 5: The atoms per formula unit (*apfu*) for each element was determined by multiplying the correction factor (step 4) by the molecular proportion (step 3) for each element.

Step 6: Calculated total atoms is equal to the sum of the *apfu* (step 5) of each element.

Step 7: The accepted total atoms is the ideal number of atoms (two) in the barite unit cell ($BaSO_4$). This value is important to determine barite stoichiometry.

Table A-3-2. Example mineral formula calculation for barite.

Formula	**A**	**MW**	**A/(MW)**	**C**	**C*(A/MW)**	**sum of C*(A/MW)**	
Oxide	Analysed microprobe composition (wt. %)	Molecular weight of oxide (wt. %)	Molecular proportion	Correc-tion factor	Number of cations in formula unit	Total cations	Accepted total cations in $BaSO_4$
FeO wt%	0.000	71.850	0.000	2.297	0.000	1.989	1.989
BaO wt%	64.374	153.330	0.420		0.965		
ZnO wt%	0.053	81.380	0.001		0.002		
K2O wt%	0.003	94.200	0.000		0.000		
SO3 wt%	34.848	80.060	0.435		1.000		
SrO wt%	0.706	103.620	0.007		0.016		
CaO wt%	0.006	56.080	0.000		0.000		
PbO wt%	0.046	223.200	0.000		0.000		
Na_2O wt%	0.164	61.980	0.003		0.006		
SiO2 wt%	0.000	60.080	0.000		0.000		

3.3 Mole fraction calculations

Mole fraction calculations for the solid solution between barite and celestine were calculated using the following equations:

Step 1:

	Element	Symbol	Atomic Mass	# of Atoms	Mass Percent
Barite	Barium	Ba	137.327	1	58.840*
	Oxygen	O	15.9994	4	27.421
	Sulfur	S	32.065	1	13.739
Celestine	Stronitum	Sr	87.62	1	47.703
	Oxygen	O	15.9994	4	34.842
	Sulfur	S	32.065	1	17.457

**Calculation example for mass percent of Ba:*

$$X = \frac{Ba\ (atomic\ mass)}{BaSO4\ \ (molar\ mass)}$$

$$X = \frac{137.33\ u}{233.39\ g/mol}$$

$$X = 58.84\ \%$$

Step 2:

$$X = \frac{Ba\ (measured\ wt.\%)\ **}{Ba\ (mass\ percent\ \%)}$$

** $\boldsymbol{Ba\ (wt.\%) = BaO\ (wt.\%) \times conversion\ factor}$

$\boldsymbol{Ba\ (wt.\%) = BaO\ (wt.\%) \times 0.895}$

3.4 Compiled electron microprobe analyses

Probe analysis	CNF31723_1_A	CNF31723_1_B	CNF31723_1_C	CNF31723_1_D	CNF31723_1_E	CNF31723_1_F	CNF31723_1_G	CNF31723_1_H	CNF31723_1_I	CNF31723_1_J
Drill hole	LM13-73	LM13-73	LM13-73	LM13-73	LM13-73	LM13-73	LM13-73	LM13-73	LM13-73	LM13-73
Sample	CNF31723	CNF31723	CNF31723	CNF31723	CNF31723	CNF31723	CNF31723	CNF31723	CNF31723	CNF31723
Depth (m)	346.50	346.50	346.50	346.50	346.50	346.50	346.50	346.50	346.50	346.50
Barite texture	Tabular	Tabular	Tabular	Tabular	Tabular	Tabular	Granular	Granular	Granular	Tabular
Mineral assemblage type	Type 1	Type 1	Type 1	Type 1	Type 1	Type 1	Type 1	Type 1	Type 1	Type 1
Specimen	1	2	3	4	5	6	7	8	9	10
SO_3 *wt.%*	35.05	35.19	34.95	34.94	35.14	35.57	35.18	35.24	35.02	35.45
BaO	65.06	64.01	63.41	63.55	64.91	65.61	62.91	65.17	63.32	63.97
SrO	0.34	0.60	0.64	0.72	0.44	0.26	1.42	0.78	0.42	0.83
Na_2O	0.06	0.22	0.20	0.09	0.23	0.22	0.12	0.07	0.10	0.12
CaO	0.01	-	0.01	0.00	0.03	0.00	-	-	0.02	-
K_2O	-	-	-	-	-	0.00	-	-	-	-
SiO_2	-	-	0.02	-	-	-	-	0.01	-	-
FeO	0.01	-	-	0.02	-	-	-	0.03	0.02	-
ZnO	-	0.06	-	0.02	-	0.06	0.09	0.02	0.04	0.08
PbO	-	0.02	-	0.07	0.03	-	-	-	0.04	-
Total	100.54	100.09	99.23	99.41	100.78	101.73	99.72	101.32	98.99	100.45
S *apfu*	1.00	1.00	1.00	1.00	1.00	1.00	1.00	1.00	1.00	1.00
Ba	0.97	0.95	0.95	0.95	0.96	0.96	0.93	0.97	0.94	0.94
Sr	0.01	0.01	0.01	0.02	0.01	0.01	0.03	0.02	0.01	0.02
Na	0.00	0.01	0.01	0.00	0.01	0.01	0.00	0.00	0.00	0.00
Ca	0.00	0.00	0.00	0.00	0.00	0.00	0.00	0.00	0.00	0.00
K	0.00	0.00	0.00	0.00	0.00	0.00	0.00	0.00	0.00	0.00
Si	0.00	0.00	0.00	0.00	0.00	0.00	0.00	0.00	0.00	0.00
Fe	0.00	0.00	0.00	0.00	0.00	0.00	0.00	0.00	0.00	0.00
Zn	0.00	0.00	0.00	0.00	0.00	0.00	0.00	0.00	0.00	0.00
Pb	0.00	0.00	0.00	0.00	0.00	0.00	0.00	0.00	0.00	0.00
Total	1.98	1.97	1.97	1.97	1.98	1.98	1.97	1.99	1.96	1.97
Brt	0.99	0.97	0.97	0.97	0.99	1.00	0.96	0.99	0.96	0.97
Cls	0.01	0.01	0.01	0.01	0.01	0.00	0.03	0.01	0.01	0.01

Probe analysis	CNF31723_1_K	CNF31723_2_A	CNF31723_2_B	CNF31723_2_C	CNF31723_2_D	CNF31723_2_E	CNF31723_2_F	CNF31723_2_G	CNF31723_2_H	CNF31723_2_I
Drill Hole	LM13-73	LM13-73	LM13-73	LM13-73	LM13-73	LM13-73	LM13-73	LM13-73	LM13-73	LM13-73
Sample	CNF31723	CNF31723	CNF31723	CNF31723	CNF31723	CNF31723	CNF31723	CNF31723	CNF31723	CNF31723
Depth (m)	346.50	346.50	346.50	346.50	346.50	346.50	346.50	346.50	346.50	346.50
Barite Texture	Tabular	Tabular	Tabular	Tabular	Tabular	Tabular	Granular	Granular	Granular	Granular
Mineral assemblage type	Type 1	Type 1	Type 1	Type 1	Type 1	Type 1	Type 1	Type 1	Type 1	Type 1
Specimen	11	1	2	3	4	5	6	7	8	9
SO_3 *wt.%*	35.03	35.06	35.25	35.09	35.23	35.14	35.42	35.32	35.44	35.46
BaO	64.28	63.98	64.55	64.39	64.96	64.05	63.60	63.59	63.63	64.95
SrO	0.89	0.72	0.71	0.50	0.56	0.51	0.88	0.70	0.67	0.59
Na_2O	0.07	0.14	0.14	0.18	0.10	0.10	0.14	0.13	0.17	0.14
CaO	0.01	-	-	-	0.02	0.02	-	0.01	0.02	-
K_2O	-	-	0.01	0.00	-	0.00	0.01	-	-	0.01
SiO_2	-	0.01	0.01	-	-	-	0.02	-	-	-
FeO	-	0.01	-	-	-	-	-	-	0.01	0.01
ZnO	0.05	0.05	-	-	-	0.02	-	0.06	0.04	0.01
PbO	0.06	-	-	-	-	-	0.02	0.01	0.04	-
Total	100.40	99.92	100.60	100.05	100.80	99.77	100.04	99.81	100.04	101.03
S *apfu*	1.00	1.00	1.00	1.00	1.00	1.00	1.00	1.00	1.00	1.00
Ba	0.96	0.95	0.96	0.96	0.96	0.95	0.94	0.94	0.94	0.96
Sr	0.02	0.02	0.02	0.01	0.01	0.01	0.02	0.02	0.01	0.01
Na	0.00	0.01	0.01	0.01	0.00	0.00	0.01	0.00	0.01	0.01
Ca	0.00	0.00	0.00	0.00	0.00	0.00	0.00	0.00	0.00	0.00
K	0.00	0.00	0.00	0.00	0.00	0.00	0.00	0.00	0.00	0.00
Si	0.00	0.00	0.00	0.00	0.00	0.00	0.00	0.00	0.00	0.00
Fe	0.00	0.00	0.00	0.00	0.00	0.00	0.00	0.00	0.00	0.00
Zn	0.00	0.00	0.00	0.00	0.00	0.00	0.00	0.00	0.00	0.00
Pb	0.00	0.00	0.00	0.00	0.00	0.00	0.00	0.00	0.00	0.00
Total	1.98	1.98	1.98	1.97	1.98	1.97	1.96	1.96	1.96	1.97
Brt	0.98	0.97	0.98	0.98	0.99	0.98	0.97	0.97	0.97	0.99
Cls	0.02	0.01	0.01	0.01	0.01	0.01	0.02	0.01	0.01	0.01

Probe analysis	CNF31723_2_J	CNF31723_2_K	CNF31723_2_L	CNF31723_2_M	CNF31723_2_N	CNF31723_2_O	CNF31723_2_P	CNF31723_2_Q	CNF31723_2_R	CNF31723_2_S
Drill Hole	LM13-73	LM13-73	LM13-73	LM13-73	LM13-73	LM13-73	LM13-73	LM13-73	LM13-73	LM13-73
Sample	CNF31723	CNF31723	CNF31723	CNF31723	CNF31723	CNF31723	CNF31723	CNF31723	CNF31723	CNF31723
Depth (m)	346.50	346.50	346.50	346.50	346.50	346.50	346.50	346.50	346.50	346.50
Barite Texture	Tabular	Tabular	Tabular	Tabular	Tabular	Tabular	Tabular	Granular	Granular	Granular
Mineral assemblage type	Type 1	Type 1	Type 1	Type 1	Type 1	Type 1	Type 1	Type 1	Type 1	Type 1
Specimen	10	11	12	13	14	15	16	17	18	19
SO_3 *wt.%*	35.28	34.80	35.31	35.21	33.92	35.39	34.58	35.19	35.40	35.09
BaO	64.97	64.14	64.85	64.50	63.98	64.89	64.66	63.92	63.22	64.88
SrO	0.60	0.86	0.57	0.56	0.62	0.40	0.41	0.80	0.84	0.88
Na_2O	0.10	0.14	0.20	0.14	0.09	0.12	0.13	0.13	0.09	0.04
CaO	0.02	-	0.00	-	0.03	0.01	0.01	0.01	0.01	-
K_2O	0.02	-	0.01	0.01	0.02	0.01	-	0.01	0.00	-
SiO_2	-	-	-	0.02	-	-	-	-	-	-
FeO	0.01	0.02	-	-	-	-	0.01	0.02	0.02	0.03
ZnO	0.06	0.05	0.03	-	0.03	0.02	-	-	-	0.07
PbO	0.01	-	-	-	-	-	-	-	-	-
Total	101.07	99.95	100.89	100.37	98.64	100.75	99.77	100.03	99.39	100.95
S *apfu*	1.00	1.00	1.00	1.00	1.00	1.00	1.00	1.00	1.00	1.00
Ba	0.96	0.96	0.96	0.96	0.98	0.96	0.98	0.95	0.93	0.97
Sr	0.01	0.02	0.01	0.01	0.01	0.01	0.01	0.02	0.02	0.02
Na	0.00	0.01	0.01	0.01	0.00	0.00	0.00	0.00	0.00	0.00
Ca	0.00	0.00	0.00	0.00	0.00	0.00	0.00	0.00	0.00	0.00
K	0.00	0.00	0.00	0.00	0.00	0.00	0.00	0.00	0.00	0.00
Si	0.00	0.00	0.00	0.00	0.00	0.00	0.00	0.00	0.00	0.00
Fe	0.00	0.00	0.00	0.00	0.00	0.00	0.00	0.00	0.00	0.00
Zn	0.00	0.00	0.00	0.00	0.00	0.00	0.00	0.00	0.00	0.00
Pb	0.00	0.00	0.00	0.00	0.00	0.00	0.00	0.00	0.00	0.00
Total	1.98	1.99	1.98	1.97	2.00	1.97	1.99	1.97	1.95	1.99
Brt	0.99	0.98	0.99	0.98	0.97	0.99	0.98	0.97	0.96	0.99
Cls	0.01	0.02	0.01	0.01	0.01	0.01	0.01	0.01	0.01	0.02

Probe analysis	CNF31723_3_A	CNF31723_3_B	CNF31723_3_C	CNF31723_3_D	CNF31723_3_E	CNF31723_3_G	CNF31723_3_H	CNF31723_3_I	CNF31723_3_J	CNF31723_3_K
Drill hole	LM13-73	LM13-73	LM13-73	LM13-73	LM13-73	LM13-73	LM13-73	LM13-73	LM13-73	LM13-73
Sample	CNF31723	CNF31723	CNF31723	CNF31723	CNF31723	CNF31723	CNF31723	CNF31723	CNF31723	CNF31723
Depth (m)	346.50	346.50	346.50	346.50	346.50	346.50	346.50	346.50	346.50	346.50
Barite Texture	Vein	Vein	Vein	Vein	Vein	Vein	Vein	Granular	Granular	Granular
Mineral assemblage type	Type 2A	Type 2A	Type 2A	Type 2A	Type 2A	Type 2A	Type 2A	Type 1	Type 1	Type 1
Specimen	1	2	3	4	5	6	7	8	9	10
SO_3 *wt.%*	35.02	35.29	34.73	35.09	35.60	34.87	35.25	34.85	35.29	35.09
BaO	66.28	64.35	64.08	63.60	64.07	65.21	63.34	63.93	64.62	64.80
SrO	0.66	0.78	0.93	0.73	0.70	0.71	0.71	0.71	0.67	0.71
CaO	0.00	0.01	0.01	0.00	0.00	0.01	0.00	0.01	0.00	0.01
K_2O	0.01	-	-	0.02	0.01	0.01	-	0.00	-	0.03
SiO_2	-	-	-	-	-	-	-	0.01	-	-
FeO	-	0.01	-	-	-	0.01	-	-	0.01	-
ZnO	0.08	0.07	0.02	-	-	0.03	0.04	0.04	-	0.03
PbO	0.02	-	-	-	-	-	-	-	-	-
Na_2O	0.14	0.15	0.16	0.10	0.16	0.14	0.16	0.19	0.07	0.12
Total	102.21	100.60	99.86	99.53	100.50	100.88	99.47	99.63	100.58	100.79
S *apfu*	1.00	1.00	1.00	1.00	1.00	1.00	1.00	1.00	1.00	1.00
Ba	0.99	0.95	0.96	0.95	0.94	0.98	0.94	0.96	0.96	0.96
Sr	0.01	0.02	0.02	0.02	0.02	0.02	0.02	0.02	0.01	0.02
Na	0.01	0.01	0.01	0.00	0.01	0.01	0.01	0.01	0.00	0.00
Ca	0.00	0.00	0.00	0.00	0.00	0.00	0.00	0.00	0.00	0.00
K	0.00	0.00	0.00	0.00	0.00	0.00	0.00	0.00	0.00	0.00
Si	0.00	0.00	0.00	0.00	0.00	0.00	0.00	0.00	0.00	0.00
Fe	0.00	0.00	0.00	0.00	0.00	0.00	0.00	0.00	0.00	0.00
Zn	0.00	0.00	0.00	0.00	0.00	0.00	0.00	0.00	0.00	0.00
Pb	0.00	0.00	0.00	0.00	0.00	0.00	0.00	0.00	0.00	0.00
Total	2.01	1.98	1.99	1.97	1.96	2.00	1.96	1.98	1.97	1.99
Brt	1.01	0.98	0.98	0.97	0.98	0.99	0.96	0.97	0.98	0.99
Cls	0.01	0.01	0.02	0.01	0.01	0.01	0.01	0.01	0.01	0.01

Probe analysis	CNF31723_3_L	CNF31723_3_M	CNF31723_3_O	CNF31723_3_P	CNF31723_4_A	CNF31723_4_B	CNF31723_4_C	CNF31723_4_D	CNF31723_4_E	CNF31723_4_F
Drill hole	LM13-73	LM13-73	LM13-73	LM13-73	LM13-73	LM13-73	LM13-73	LM13-73	LM13-73	LM13-73
Sample	CNF31723	CNF31723	CNF31723	CNF31723	CNF31723	CNF31723	CNF31723	CNF31723	CNF31723	CNF31723
Depth (m)	346.50	346.50	346.50	346.50	346.50	346.50	346.50	346.50	346.50	346.50
Barite Texture	Granular	Granular	Granular	Granular	Tabular	Tabular	Tabular	Tabular	Tabular	Tabular
Mineral assemblage type	Type 1	Type 1	Type 1	Type 1	Type 1	Type 1	Type 1	Type 1	Type 1	Type 1
Specimen	11	12	13	14	1	2	3	4	5	6
SO_3 *wt.%*	35.19	34.66	35.03	34.91	35.14	35.01	34.93	35.28	35.23	35.50
BaO	64.74	65.12	65.02	64.53	63.61	63.24	64.51	63.84	63.34	62.10
SrO	0.70	0.26	0.28	0.34	1.64	1.17	0.80	1.32	1.90	2.63
CaO	0.00	0.01	0.02	0.02	0.17	0.22	0.18	0.11	0.18	0.16
K_2O	-	0.00	-	0.01	0.03	-	-	0.01	-	0.08
SiO_2	-	0.02	-	-	-	0.01	-	0.01	0.01	0.01
FeO	-	0.02	0.03	0.01	0.02	0.03	-	-	-	-
ZnO	-	-	-	0.02	-	0.03	0.05	0.01	0.02	-
PbO	0.05	-	0.01	0.02	0.03	-	-	-	0.01	-
Na_2O	0.15	0.05	0.14	0.20	0.05	-	-	0.03	0.01	-
Total	100.69	100.10	100.47	100.05	100.68	99.71	100.48	100.62	100.71	100.48
S *apfu*	1.00	1.00	1.00	1.00	1.00	1.00	1.00	1.00	1.00	1.00
Ba	0.96	0.98	0.97	0.97	0.95	0.94	0.96	0.94	0.94	0.91
Sr	0.02	0.01	0.01	0.01	0.04	0.03	0.02	0.03	0.04	0.06
Na	0.01	0.00	0.01	0.01	0.01	0.01	0.01	0.00	0.01	0.01
Ca	0.00	0.00	0.00	0.00	0.00	0.00	0.00	0.00	0.00	0.00
K	0.00	0.00	0.00	0.00	0.00	0.00	0.00	0.00	0.00	0.00
Si	0.00	0.00	0.00	0.00	0.00	0.00	0.00	0.00	0.00	0.00
Fe	0.00	0.00	0.00	0.00	0.00	0.00	0.00	0.00	0.00	0.00
Zn	0.00	0.00	0.00	0.00	0.00	0.00	0.00	0.00	0.00	0.00
Pb	0.00	0.00	0.00	0.00	0.00	0.00	0.00	0.00	0.00	0.00
Total	1.98	1.99	1.98	1.98	1.99	1.98	1.99	1.98	1.99	1.98
Brt	0.99	0.99	0.99	0.98	0.97	0.96	0.98	0.97	0.96	0.95
Cls	0.01	0.00	0.00	0.01	0.03	0.02	0.01	0.02	0.03	0.05

Probe analysis	CNF31723_4_G	CNF31723_4_H	CNF31723_4_I	CNF31723_4_J	CNF31723_4_K	CNF31723_4_L	CNF31723_4_M	CNF31723_4_N	CNF31723_4_O	CNF31723_4_P
Drill hole	LM13-73	LM13-73	LM13-73	LM13-73	LM13-73	LM13-73	LM13-73	LM13-73	LM13-73	LM13-73
Sample	CNF31723	CNF31723	CNF31723	CNF31723	CNF31723	CNF31723	CNF31723	CNF31723	CNF31723	CNF31723
Depth (m)	346.50	346.50	346.50	346.50	346.50	346.50	346.50	346.50	346.50	346.50
Barite Texture	Tabular	Tabular	Granular	Granular	Granular	Granular	Granular	Granular	Granular	Granular
Mineral assemblage type	Type 1	Type 1	Type 1	Type 1	Type 1	Type 1	Type 1	Type 1	Type 1	Type 1
Specimen	7	8	9	10	11	12	13	14	15	16
SO_3 *wt.%*	35.26	34.75	35.53	35.26	35.52	34.99	35.66	34.80	35.15	34.77
BaO	64.04	62.89	64.12	64.35	64.60	63.95	64.62	64.64	66.90	63.53
SrO	0.91	1.29	1.35	0.55	0.87	0.88	0.94	0.42	0.34	0.76
CaO	0.18	0.08	0.28	0.12	0.22	0.21	0.23	0.20	0.17	0.17
K_2O	0.00	0.01	-	-	-	0.01	0.01	0.03	0.00	0.02
SiO_2	-	0.01	-	0.01	-	0.00	0.02	-	-	0.00
FeO	-	-	-	-	-	0.04	-	-	0.01	0.03
ZnO	0.02	0.03	0.01	0.02	-	-	-	-	-	-
PbO	-	-	0.02	-	-	-	-	-	0.04	-
Na_2O	-	0.02	-	-	-	-	0.02	-	-	0.02
Total	100.40	99.07	101.32	100.31	101.21	100.09	101.50	100.08	102.62	99.30
S *apfu*	1.00	1.00	1.00	1.00	1.00	1.00	1.00	1.00	1.00	1.00
Ba	0.95	0.94	0.94	0.95	0.95	0.95	0.95	0.97	0.99	0.95
Sr	0.02	0.03	0.03	0.01	0.02	0.02	0.02	0.01	0.01	0.02
Na	0.01	0.00	0.01	0.00	0.01	0.01	0.01	0.01	0.01	0.01
Ca	0.00	0.00	0.00	0.00	0.00	0.00	0.00	0.00	0.00	0.00
K	0.00	0.00	0.00	0.00	0.00	0.00	0.00	0.00	0.00	0.00
Si	0.00	0.00	0.00	0.00	0.00	0.00	0.00	0.00	0.00	0.00
Fe	0.00	0.00	0.00	0.00	0.00	0.00	0.00	0.00	0.00	0.00
Zn	0.00	0.00	0.00	0.00	0.00	0.00	0.00	0.00	0.00	0.00
Pb	0.00	0.00	0.00	0.00	0.00	0.00	0.00	0.00	0.00	0.00
Total	1.97	1.98	1.98	1.97	1.97	1.98	1.97	1.98	2.01	1.98
Brt	0.97	0.96	0.98	0.98	0.98	0.97	0.98	0.98	1.02	0.97
Cls	0.02	0.02	0.02	0.01	0.02	0.02	0.02	0.01	0.01	0.01

Probe analysis	CNF31723_4_Q	CNF31723_4_R	CNF31723_4_S	CNF31723_4_T	CNF31723_4_U	CNF31730_1_A	CNF31730_1_B	CNF31730_1_C	CNF31730_1_D	CNF31730_1_E
Drill hole	LM13-73	LM13-73	LM13-73	LM13-73	LM13-73	LM13-94	LM13-94	LM13-94	LM13-94	LM13-94
Sample	CNF31723	CNF31723	CNF31723	CNF31723	CNF31723	CNF31730	CNF31730	CNF31730	CNF31730	CNF31730
Depth (m)	346.50	346.50	346.50	346.50	346.50	332.30	332.30	332.30	332.30	332.30
Barite Texture	Granular	Granular	Granular	Granular	Granular	Granular	Granular	Granular	Granular	Plumerose
Mineral assemblage type	Type 1	Type 1	Type 1	Type 1	Type 1	Type 1	Type 1	Type 1	Type 1	Type 1
Specimen	17	18	19	20	21	1	2	3	4	5
SO_3 *wt.%*	35.49	35.06	35.32	35.64	34.94	35.10	35.57	35.27	35.67	35.29
BaO	63.88	64.98	64.37	64.03	65.33	63.74	62.94	65.26	62.67	64.00
SrO	0.77	0.41	0.36	0.77	0.83	0.85	1.25	0.42	1.70	1.16
CaO	0.13	0.08	0.11	0.08	0.21	0.05	0.17	0.09	0.14	0.11
K_2O	0.00	-	0.00	-	0.02	0.02	0.03	-	0.03	0.00
SiO_2	0.01	0.02	-	0.00	0.00	0.01	-	0.01	-	0.00
FeO	-	-	-	0.01	-	-	0.02	-	-	-
ZnO	-	-	0.01	0.01	-	-	-	-	-	0.04
PbO	0.04	0.03	0.05	-	-	-	0.05	-	-	-
Na_2O	-	0.01	-	0.01	0.01	0.04	-	0.05	-	0.01
Total	100.31	100.59	100.23	100.55	101.34	99.82	100.04	101.10	100.21	100.62
S *apfu*	1.00	1.00	1.00	1.00	1.00	1.00	1.00	1.00	1.00	1.00
Ba	0.94	0.97	0.95	0.94	0.98	0.95	0.92	0.97	0.92	0.95
Sr	0.02	0.01	0.01	0.02	0.02	0.02	0.03	0.01	0.04	0.03
Na	0.00	0.00	0.00	0.00	0.01	0.00	0.01	0.00	0.01	0.00
Ca	0.00	0.00	0.00	0.00	0.00	0.00	0.00	0.00	0.00	0.00
K	0.00	0.00	0.00	0.00	0.00	0.00	0.00	0.00	0.00	0.00
Si	0.00	0.00	0.00	0.00	0.00	0.00	0.00	0.00	0.00	0.00
Fe	0.00	0.00	0.00	0.00	0.00	0.00	0.00	0.00	0.00	0.00
Zn	0.00	0.00	0.00	0.00	0.00	0.00	0.00	0.00	0.00	0.00
Pb	0.00	0.00	0.00	0.00	0.00	0.00	0.00	0.00	0.00	0.00
Total	1.96	1.98	1.96	1.96	2.00	1.97	1.96	1.97	1.96	1.98
Brt	0.97	0.99	0.98	0.97	0.99	0.97	0.96	0.99	0.95	0.97
Cls	0.01	0.01	0.01	0.01	0.01	0.02	0.02	0.01	0.03	0.02

Probe analysis	CNF31730_1_F	CNF31730_1_G	CNF31730_1_H	CNF31730_1_I	CNF31730_1_J	CNF31730_1_K	CNF31730_1_L	CNF31730_1_M	CNF31730_1_N	CNF31730_1_O
Drill hole	LM13-94	LM13-94	LM13-94	LM13-94	LM13-94	LM13-94	LM13-94	LM13-94	LM13-94	LM13-94
Sample	CNF31730	CNF31730	CNF31730	CNF31730	CNF31730	CNF31730	CNF31730	CNF31730	CNF31730	CNF31730
Depth (m)	332.30	332.30	332.30	332.30	332.30	332.30	332.30	332.30	332.30	332.30
Barite texture	Plumerose	Plumerose	Plumerose	Plumerose	Plumerose	Plumerose	Plumerose	Plumerose	Plumerose	Plumerose
Mineral assemblage type	Type 1	Type 1	Type 1	Type 1	Type 1	Type 1	Type 1	Type 1	Type 1	Type 1
Specimen	6	7	8	9	10	11	12	13	14	15
SO_3 *wt.%*	35.08	35.21	34.82	35.18	34.81	35.15	34.39	35.22	35.37	35.03
BaO	62.69	64.55	64.08	63.85	64.14	64.71	64.01	64.79	62.72	65.24
SrO	1.54	0.71	0.36	1.16	0.97	1.09	0.77	0.59	1.87	0.59
Na_2O	0.07	0.11	0.08	0.06	0.14	0.14	0.12	0.18	0.16	0.17
CaO	0.01	-	0.01	-	0.02	0.02	0.73	-	0.00	-
K_2O	-	-	-	-	-	0.02	-	-	-	0.00
SiO_2	-	-	-	-	-	-	-	-	-	0.02
FeO	-	0.05	0.03	-	-	-	0.01	-	-	-
ZnO	-	0.06	-	0.02	-	0.05	-	-	0.02	-
PbO	-	-	-	-	-	0.04	-	-	0.04	0.02
Total	99.38	100.70	99.38	100.27	100.09	101.22	100.03	100.78	100.18	101.08
S *apfu*	1.00	1.00	1.00	1.00	1.00	1.00	1.00	1.00	1.00	1.00
Ba	0.93	0.96	0.96	0.95	0.96	0.96	0.97	0.96	0.93	0.97
Sr	0.03	0.02	0.01	0.03	0.02	0.02	0.02	0.01	0.04	0.01
Na	0.00	0.00	0.00	0.00	0.01	0.01	0.00	0.01	0.01	0.01
Ca	0.00	0.00	0.00	0.00	0.00	0.00	0.03	0.00	0.00	0.00
K	0.00	0.00	0.00	0.00	0.00	0.00	0.00	0.00	0.00	0.00
Si	0.00	0.00	0.00	0.00	0.00	0.00	0.00	0.00	0.00	0.00
Fe	0.00	0.00	0.00	0.00	0.00	0.00	0.00	0.00	0.00	0.00
Zn	0.00	0.00	0.00	0.00	0.00	0.00	0.00	0.00	0.00	0.00
Pb	0.00	0.00	0.00	0.00	0.00	0.00	0.00	0.00	0.00	0.00
Total	1.97	1.98	1.97	1.98	1.99	1.99	2.02	1.98	1.97	1.99
Brt	0.95	0.98	0.98	0.97	0.98	0.99	0.97	0.99	0.95	0.99
Cls	0.03	0.01	0.01	0.02	0.02	0.02	0.01	0.01	0.03	0.01

Probe analysis	CNF31730_1_Q	CNF31730_1_R	CNF31730_1_S	CNF31730_1_T	CNF31730_1_U	CNF31730_2_A	CNF31730_2_B	CNF31730_2_C	CNF31730_2_D	CNF31730_2_E
Drill hole	LM13-94	LM13-94	LM13-94	LM13-94	LM13-94	LM13-94	LM13-94	LM13-94	LM13-94	LM13-94
Sample	CNF31730	CNF31730	CNF31730	CNF31730	CNF31730	CNF31730	CNF31730	CNF31730	CNF31730	CNF31730
Depth (m)	332.30	332.30	332.30	332.30	332.30	332.30	332.30	332.30	332.30	332.30
Barite texture	Plumerose	Plumerose	Plumerose	Plumerose	Plumerose	Granular	Granular	Granular	Granular	Granular
Mineral assemblage type	Type 1	Type 1	Type 1	Type 1	Type 1	Type 1	Type 1	Type 1	Type 1	Type 1
Specimen	16	17	18	19	20	1	2	3	4	5
SO_3 *wt.%*	35.60	35.14	35.10	35.42	35.38	34.85	35.24	34.87	35.18	35.53
BaO	62.79	64.59	64.62	62.63	64.41	64.37	64.90	64.99	65.33	64.24
SrO	2.01	0.85	0.75	1.78	1.44	0.71	0.67	0.66	0.21	0.63
Na_2O	0.14	0.12	0.18	0.17	0.15	0.16	0.19	0.15	0.07	0.14
CaO	0.02	0.01	0.01	0.00	0.02	0.01	-	0.00	0.00	0.01
K_2O	-	0.00	-	0.01	0.00	0.00	-	0.00	0.00	-
SiO_2	-	-	-	0.01	0.01	-	-	-	-	-
FeO	-	-	0.01	-	-	-	-	-	-	0.02
ZnO	-	-	-	-	0.04	0.05	0.11	0.09	0.02	0.02
PbO	-	-	-	0.03	-	0.05	-	-	-	-
Total	100.55	100.71	100.68	100.06	101.46	100.20	101.12	100.76	100.82	100.59
S *apfu*	1.00	1.00	1.00	1.00	1.00	1.00	1.00	1.00	1.00	1.00
Ba	0.92	0.96	0.96	0.92	0.95	0.96	0.96	0.97	0.97	0.94
Sr	0.04	0.02	0.02	0.04	0.03	0.02	0.01	0.01	0.00	0.01
Na	0.01	0.00	0.01	0.01	0.01	0.01	0.01	0.01	0.00	0.01
Ca	0.00	0.00	0.00	0.00	0.00	0.00	0.00	0.00	0.00	0.00
K	0.00	0.00	0.00	0.00	0.00	0.00	0.00	0.00	0.00	0.00
Si	0.00	0.00	0.00	0.00	0.00	0.00	0.00	0.00	0.00	0.00
Fe	0.00	0.00	0.00	0.00	0.00	0.00	0.00	0.00	0.00	0.00
Zn	0.00	0.00	0.00	0.00	0.00	0.00	0.00	0.00	0.00	0.00
Pb	0.00	0.00	0.00	0.00	0.00	0.00	0.00	0.00	0.00	0.00
Total	1.97	1.98	1.98	1.97	1.99	1.98	1.98	2.00	1.97	1.96
Brt	0.96	0.98	0.98	0.95	0.98	0.98	0.99	0.99	0.99	0.98
Cls	0.04	0.02	0.01	0.03	0.03	0.01	0.01	0.01	0.00	0.01

Probe analysis	CNF31730_2_F	CNF31730_3_A	CNF31730_5_B	CNF31730_3_C	CNF31730_3_D	CNF31730_3_E	CNF31730_3_F	CNF31730_3_G	CNF31730_3_H	CNF31730_3_I
Drill hole	LM13-94	LM13-94	LM13-94	LM13-94	LM13-94	LM13-94	LM13-94	LM13-94	LM13-94	LM13-94
Sample	CNF31730	CNF31730	CNF31730	CNF31730	CNF31730	CNF31730	CNF31730	CNF31730	CNF31730	CNF31730
Depth (m)	332.30	332.30	332.30	332.30	332.30	332.30	332.30	332.30	332.30	332.30
Barite texture	Granular	Tabular	Tabular	Tabular	Tabular	Tabular	Tabular	Tabular	Tabular	Tabular
Mineral assemblage type	Type 1	Type 1	Type 1	Type 1	Type 1	Type 1	Type 1	Type 1	Type 1	Type 1
Specimen	6	1	2	3	4	5	6	7	8	9
SO_3 *wt.%*	35.00	35.25	35.29	34.92	35.28	35.52	35.15	35.47	35.42	35.03
BaO	63.72	62.73	63.02	63.52	63.94	63.23	63.88	63.86	63.55	62.46
SrO	0.58	1.45	1.41	0.81	1.76	1.88	0.70	1.91	0.63	0.95
Na_2O	0.12	0.06	0.16	0.20	0.14	0.26	0.19	0.14	0.13	0.08
CaO	-	0.01	-	0.01	0.04	0.03	-	0.04	0.01	0.01
K_2O	0.01	0.01	-	0.01	0.01	-	0.00	-	-	-
SiO_2	-	-	-	-	-	-	-	0.05	-	-
FeO	-	0.04	-	0.03	0.02	-	-	-	-	-
ZnO	-	-	-	-	-	-	0.05	-	0.02	-
PbO	0.04	-	-	-	-	-	-	-	-	-
Total	99.47	99.53	99.88	99.50	101.18	100.93	99.97	101.46	99.76	98.52
S *apfu*	1.00	1.00	1.00	1.00	1.00	1.00	1.00	1.00	1.00	1.00
Ba	0.95	0.94	0.93	0.95	0.95	0.93	0.94	0.94	0.94	0.93
Sr	0.01	0.02	0.03	0.02	0.04	0.04	0.02	0.04	0.01	0.02
Na	0.00	0.01	0.01	0.01	0.01	0.01	0.01	0.01	0.00	0.00
Ca	0.00	0.00	0.00	0.00	0.00	0.00	0.00	0.00	0.00	0.00
K	0.00	0.00	0.00	0.00	0.00	0.00	0.00	0.00	0.00	0.00
Si	0.00	0.00	0.00	0.00	0.00	0.00	0.00	0.00	0.00	0.00
Fe	0.00	0.00	0.00	0.00	0.00	0.00	0.00	0.00	0.00	0.00
Zn	0.00	0.00	0.00	0.00	0.00	0.00	0.00	0.00	0.00	0.00
Pb	0.00	0.00	0.00	0.00	0.00	0.00	0.00	0.00	0.00	0.00
Total	1.97	1.97	1.97	1.97	1.99	1.98	1.97	1.99	1.95	1.95
Brt	0.97	0.95	0.96	0.97	0.97	0.96	0.97	0.97	0.97	0.95
Cls	0.01	0.02	0.02	0.01	0.03	0.03	0.01	0.03	0.01	0.01

Probe analysis	CNF31730_3_J	CNF31730_3_K	CNF31730_3_L	CNF31730_3_M	CNF31733_1_A	CNF31733_1_B	CNF31733_1_C	CNF31733_1_D	CNF31733_1_E	CNF31733_1_F
Drill hole	LM13-94	LM13-94	LM13-94	LM13-94	LM13-94	LM13-94	LM13-94	LM13-94	LM13-94	LM13-94
Sample	CNF31730	CNF31730	CNF31730	CNF31730	CNF31733	CNf31733	CNF31733	CNF31733	CNF31733	CNF31733
Depth (m)	332.30	332.30	332.30	332.30	341.40	341.40	341.40	341.40	341.40	341.40
Barite texture	Tabular	Tabular	Tabular	Tabular	Tabular	Tabular	Tabular	Tabular	Tabular	Tabular
Mineral assemblage type	Type 1	Type 1	Type 1	Type 1	Type 2B ± 2A	Type 2B ± 2A	Type 2B ± 2A	Type 2B ± 2A	Type 2B ± 2A	Type 2B ± 2A
Specimen	10	11	12	13	1	2	3	4	5	6
SO_3 *wt.%*	35.68	35.35	35.48	35.17	35.34	35.26	35.25	35.08	35.55	35.03
BaO	64.34	63.83	63.90	62.58	63.46	61.92	62.19	63.00	61.79	63.50
SrO	1.14	1.80	1.88	2.11	1.85	2.51	2.31	1.80	2.78	1.02
Na_2O	0.16	0.04	0.12	0.07	0.15	0.14	0.12	0.18	0.20	0.10
CaO	0.02	0.08	0.01	0.01	0.04	0.01	0.00	-	0.03	-
K_2O	0.01	0.01	0.01	-	-	-	-	-	0.02	0.02
SiO_2	-	-	-	-	-	0.02	-	-	-	-
FeO	0.01	0.02	0.02	-	-	0.02	-	0.02	-	-
ZnO	-	0.03	-	-	0.03	0.05	0.01	0.04	-	-
PbO	-	-	-	-	-	0.02	-	-	-	-
Total	101.35	101.14	101.42	99.96	100.87	99.96	99.88	100.13	100.37	99.66
S *apfu*	1.00	1.00	1.00	1.00	1.00	1.00	1.00	1.00	1.00	1.00
Ba	0.94	0.94	0.94	0.93	0.94	0.92	0.92	0.94	0.91	0.95
Sr	0.02	0.02	0.04	0.05	0.04	0.06	0.05	0.04	0.06	0.02
Na	0.01	0.01	0.00	0.00	0.01	0.01	0.00	0.01	0.01	0.00
Ca	0.00	0.00	0.00	0.00	0.00	0.00	0.00	0.00	0.00	0.00
K	0.00	0.00	0.00	0.00	0.00	0.00	0.00	0.00	0.00	0.00
Si	0.00	0.00	0.00	0.00	0.00	0.00	0.00	0.00	0.00	0.00
Fe	0.00	0.00	0.00	0.00	0.00	0.00	0.00	0.00	0.00	0.00
Zn	0.00	0.00	0.00	0.00	0.00	0.00	0.00	0.00	0.00	0.00
Pb	0.00	0.00	0.00	0.00	0.00	0.00	0.00	0.00	0.00	0.00
Total	1.97	1.97	1.98	1.98	1.98	1.98	1.97	1.98	1.98	1.97
Brt	0.98	0.97	0.97	0.95	0.97	0.94	0.95	0.96	0.94	0.97
Cls	0.02	0.03	0.03	0.03	0.03	0.04	0.04	0.03	0.04	0.02

Probe analysis	CNF31733_1_G	CNF31733_1_H	CNF31733_1_I	CNF31733_1_J	CNF31733_1_K	CNF31733_1_L	CNF31733_1_M	CNF31733_1_N	CNF31733_1_O	CNF31733_3_A
Drill hole	LM13-94	LM13-94	LM13-94	LM13-94	LM13-94	LM13-94	LM13-94	LM13-94	LM13-94	LM13-94
Sample	CNF31733	CNF31733	CNF31733	CNF31733	CNF31733	CNF31733	CNF31733	CNF31733	CNF31733	CNF31733
Depth (m)	341.40	341.40	341.40	341.40	341.40	341.40	341.40	341.40	341.40	341.40
Barite texture	Tabular	Tabular	Tabular	Tabular	Tabular	Granular	Granular	Granular	Granular	Tabular
Mineral assemblage type	Type 2B ± 2A	Type 2B ± 2A	Type 2B ± 2A	Type 2B ± 2A	Type 2B ± 2A	Type 2B ± 2A	Type 2B ± 2A	Type 2B ± 2A	Type 2B ± 2A	Type 2B ± 2A
Specimen	7	8	9	10	11	12	13	14	15	1
SO_3 *wt.%*	35.06	35.17	34.97	34.92	35.60	35.01	35.08	35.20	35.00	35.25
BaO	64.74	64.23	63.19	64.53	64.40	65.05	64.42	63.81	63.13	63.82
SrO	0.80	1.46	1.53	0.99	1.04	0.74	0.86	1.53	1.31	1.12
Na_2O	0.12	0.14	0.18	0.21	0.14	0.07	0.15	0.07	0.13	0.09
CaO	-	-	0.02	-	-	-	0.00	-	0.01	-
K_2O	0.00	0.01	-	-	-	-	0.00	0.02	0.01	-
SiO_2	-	-	-	-	-	-	0.01	-	-	-
FeO	-	0.03	-	-	-	0.02	0.03	-	0.02	-
ZnO	0.11	-	0.04	0.01	0.05	-	-	0.03	-	0.05
PbO	0.02	-	-	-	-	0.01	-	-	-	-
Total	100.85	101.02	99.92	100.66	101.23	100.90	100.56	100.65	99.61	100.33
S *apfu*	1.00	1.00	1.00	1.00	1.00	1.00	1.00	1.00	1.00	1.00
Ba	0.96	0.95	0.94	0.96	0.94	0.97	0.96	0.95	0.94	0.95
Sr	0.02	0.03	0.03	0.02	0.02	0.02	0.02	0.03	0.03	0.02
Na	0.00	0.00	0.01	0.01	0.01	0.00	0.01	0.00	0.00	0.00
Ca	0.00	0.00	0.00	0.00	0.00	0.00	0.00	0.00	0.00	0.00
K	0.00	0.00	0.00	0.00	0.00	0.00	0.00	0.00	0.00	0.00
Si	0.00	0.00	0.00	0.00	0.00	0.00	0.00	0.00	0.00	0.00
Fe	0.00	0.00	0.00	0.00	0.00	0.00	0.00	0.00	0.00	0.00
Zn	0.00	0.00	0.00	0.00	0.00	0.00	0.00	0.00	0.00	0.00
Pb	0.00	0.00	0.00	0.00	0.00	0.00	0.00	0.00	0.00	0.00
Total	1.99	1.99	1.98	1.99	1.97	1.99	1.98	1.98	1.97	1.97
Brt	0.99	0.98	0.96	0.98	0.98	0.99	0.98	0.97	0.96	0.97
Cls	0.01	0.02	0.02	0.02	0.02	0.01	0.01	0.02	0.02	0.02

Probe analysis	CNF31733_3_B	CNF31733_3_C	CNF31733_3_D	CNF31733_3_E	CNF31733_3_F	CNF31733_3_G	CNF31733_3_H	CNF31733_3_I	CNF31733_3_J	CNF31733_3_K
Drill hole	LM13-94	LM13-94	LM13-94	LM13-94	LM13-94	LM13-94	LM13-94	LM13-94	LM13-94	LM13-94
Sample	CNf31733	CNF31733	CNF31733	CNF31733	CNF31733	CNF31733	CNF31733	CNF31733	CNF31733	CNF31733
Depth (m)	341.40	341.40	341.40	341.40	341.40	341.40	341.40	341.40	341.40	341.40
Barite Texture	Tabular	Tabular	Tabular	Tabular	Tabular	Tabular	Tabular	Tabular	Tabular	Tabular
Mineral assemblage type	Type 2B ± 2A	Type 2B ± 2A	Type 2B ± 2A	Type 2B ± 2A	Type 2B ± 2A	Type 2B ± 2A	Type 2B ± 2A	Type 2B ± 2A	Type 2B ± 2A	Type 2B ± 2A
Specimen	2	3	4	5	6	7	8	9	10	11
SO_3 *wt.%*	34.99	35.20	35.49	35.03	35.14	35.34	35.07	35.09	34.84	34.84
BaO	64.05	64.36	64.90	63.89	65.12	63.93	64.81	63.99	63.94	64.10
SrO	1.07	0.93	1.69	1.23	1.10	1.00	1.00	1.36	1.23	1.05
CaO	0.16	0.20	0.18	0.15	0.09	0.07	0.21	0.06	0.21	0.15
K_2O	0.01	0.01	-	-	0.01	0.01	0.01	0.01	0.02	-
SiO_2	-	0.02	-	-	0.01	0.00	0.01	0.01	-	0.01
FeO	-	-	-	0.03	0.01	-	-	-	-	0.03
ZnO	-	0.01	0.03	0.04	-	-	-	-	0.01	0.04
PbO	-	-	-	-	0.01	-	-	0.02	-	0.01
Na_2O	-	-	-	-	-	-	-	-	-	-
Total	100.28	100.72	102.29	100.37	101.48	100.36	101.11	100.54	100.26	100.25
S *apfu*	1.00	1.00	1.00	1.00	1.00	1.00	1.00	1.00	1.00	1.00
Ba	0.96	0.95	0.95	0.95	0.97	0.94	0.96	0.95	0.96	0.96
Sr	0.02	0.02	0.04	0.03	0.02	0.02	0.02	0.03	0.03	0.02
Na	0.01	0.01	0.01	0.01	0.00	0.00	0.01	0.00	0.01	0.01
Ca	0.00	0.00	0.00	0.00	0.00	0.00	0.00	0.00	0.00	0.00
K	0.00	0.00	0.00	0.00	0.00	0.00	0.00	0.00	0.00	0.00
Si	0.00	0.00	0.00	0.00	0.00	0.00	0.00	0.00	0.00	0.00
Fe	0.00	0.00	0.00	0.00	0.00	0.00	0.00	0.00	0.00	0.00
Zn	0.00	0.00	0.00	0.00	0.00	0.00	0.00	0.00	0.00	0.00
Pb	0.00	0.00	0.00	0.00	0.00	0.00	0.00	0.00	0.00	0.00
Total	1.98	1.98	2.00	1.99	2.00	1.97	1.99	1.98	1.99	1.99
Brt	0.97	0.98	0.99	0.97	0.99	0.97	0.99	0.97	0.97	0.98
Cls	0.02	0.01	0.03	0.02	0.02	0.02	0.02	0.02	0.02	0.02

Probe analysis	CNF31733_3_L	CNF31733_3_M	CNF31733_2_A	CNF31733_2_B	CNF31733_2_C	CNF31733_2_D	CNF31733_2_E	CNF31733_2_F	CNF31733_2_G	CNF31733_2_H
Drill hole	LM13-94	LM13-94	LM13-94	LM13-94	LM13-94	LM13-94	LM13-94	LM13-94	LM13-94	LM13-94
Sample	CNF31733	CNF31733	CNF31733	CNf31733	CNF31733	CNF31733	CNF31733	CNF31733	CNF31733	CNF31733
Depth (m)	341.40	341.40	341.40	341.40	341.40	341.40	341.40	341.40	341.40	341.40
Barite Texture	Granular	Granular	Granular	Granular	Granular	Granular	Granular	Granular	Granular	Granular
Mineral assemblage type	Type 2B ± 2A	Type 2B ± 2A	Type 2B ± 2A	Type 2B ± 2A	Type 2B ± 2A	Type 2B ± 2A	Type 2B ± 2A	Type 2B ± 2A	Type 2B ± 2A	Type 2B ± 2A
Specimen	12	13	1	2	3	4	5	6	7	8
SO_3 *wt.%*	35.16	35.05	34.92	34.36	35.16	35.35	35.11	35.21	34.91	34.77
BaO	65.10	63.97	64.37	64.32	64.35	64.04	65.05	64.75	63.07	63.50
SrO	1.19	1.00	0.55	0.44	0.98	1.18	0.56	0.58	0.99	1.65
CaO	0.10	0.15	0.11	0.19	0.10	0.11	0.17	0.21	0.09	0.19
K_2O	-	0.01	-	0.00	-	-	-	-	-	-
SiO_2	0.02	-	-	0.01	-	-	-	-	0.00	-
FeO	0.02	-	-	0.01	-	0.01	-	-	0.03	-
ZnO	-	-	0.01	-	-	-	-	0.04	-	0.01
PbO	-	0.08	-	-	0.15	-	0.07	0.08	0.01	-
Na_2O	-	-	-	0.07	-	-	-	0.03	0.14	0.07
Total	101.58	100.26	99.96	99.40	100.74	100.69	100.97	100.89	99.24	100.19
S *apfu*	1.00	1.00	1.00	1.00	1.00	1.00	1.00	1.00	1.00	1.00
Ba	0.97	0.95	0.96	0.98	0.96	0.95	0.97	0.96	0.94	0.95
Sr	0.03	0.02	0.01	0.01	0.02	0.03	0.01	0.01	0.02	0.04
Na	0.00	0.01	0.00	0.01	0.00	0.00	0.01	0.01	0.00	0.01
Ca	0.00	0.00	0.00	0.00	0.00	0.00	0.00	0.00	0.00	0.00
K	0.00	0.00	0.00	0.00	0.00	0.00	0.00	0.00	0.00	0.00
Si	0.00	0.00	0.00	0.00	0.00	0.00	0.00	0.00	0.00	0.00
Fe	0.00	0.00	0.00	0.00	0.00	0.00	0.00	0.00	0.00	0.00
Zn	0.00	0.00	0.00	0.00	0.00	0.00	0.00	0.00	0.00	0.00
Pb	0.00	0.00	0.00	0.00	0.00	0.00	0.00	0.00	0.00	0.00
Total	2.00	1.98	1.98	1.99	1.98	1.97	1.99	1.98	1.97	2.00
Brt	0.99	0.97	0.98	0.98	0.98	0.97	0.99	0.99	0.96	0.97
Cls	0.02	0.02	0.01	0.01	0.01	0.02	0.01	0.01	0.02	0.03

Probe analysis	CNF31733_2_I	CNF31733_2_J	CNF31733_2_K	CNF31735_1_A	CNF31735_1_B	CNF31735_1_C	CNF31735_1_D	CNF31735_1_E	CNF31735_1_F	CNF31735_1_G
Drill hole	LM13-94	LM13-94	LM13-94	LM13-94	LM13-94	LM13-94	LM13-94	LM13-94	LM13-94	LM13-94
Sample	CNF31733	CNF31733	CNF31733	CNF31735	CNF31735	CNF31735	CNF31735	CNF31735	CNF31735	CNF31735
Depth (m)	341.40	341.40	341.40	346.20	346.20	346.20	346.20	346.20	346.20	346.20
Barite texture	Granular	Granular	Granular	Tabular	Tabular	Tabular	Tabular	Tabular	Tabular	Tabular
Mineral assemblage type	Type 2B ± 2A	Type 2B ± 2A	Type 2B ± 2A	Type 1 ±2B	Type 1 ±2B	Type 1 ±2B	Type 1 ±2B	Type 1 ±2B	Type 1 ±2B	Type 1 ±2B
Specimen	9	10	11	1	2	3	4	5	6	7
SO_3 *wt.%*	34.97	34.91	34.50	35.19	35.06	35.61	35.21	36.05	35.17	35.41
BaO	64.51	63.41	64.49	61.97	63.00	63.68	63.48	61.83	62.45	63.07
SrO	0.83	1.48	0.64	2.11	2.03	2.54	1.53	2.65	1.75	2.10
Na_2O	0.04	0.07	0.10	0.12	0.13	0.19	0.07	0.09	0.20	0.11
CaO	0.01	0.02	-	0.10	0.10	0.06	-	0.14	0.03	0.01
K_2O	-	0.00	-	-	-	0.01	-	-	0.01	-
SiO_2	-	0.01	0.03	-	-	-	-	0.02	0.01	0.04
FeO	0.01	-	0.04	0.02	-	-	-	-	-	0.02
ZnO	-	0.08	-	0.04	-	-	0.04	-	0.04	-
PbO	-	-	-	-	-	-	-	-	0.04	-
Total	100.37	99.97	99.79	99.55	100.31	102.09	100.34	100.77	99.70	100.76
S *apfu*	1.00	1.00	1.00	1.00	1.00	1.00	1.00	1.00	1.00	1.00
Ba	0.96	0.95	0.98	0.92	0.94	0.93	0.94	0.90	0.93	0.93
Sr	0.02	0.03	0.01	0.05	0.04	0.06	0.03	0.06	0.04	0.05
Na	0.00	0.00	0.00	0.00	0.00	0.01	0.00	0.00	0.01	0.00
Ca	0.00	0.00	0.00	0.00	0.00	0.00	0.00	0.01	0.00	0.00
K	0.00	0.00	0.00	0.00	0.00	0.00	0.00	0.00	0.00	0.00
Si	0.00	0.00	0.00	0.00	0.00	0.00	0.00	0.00	0.00	0.00
Fe	0.00	0.00	0.00	0.00	0.00	0.00	0.00	0.00	0.00	0.00
Zn	0.00	0.00	0.00	0.00	0.00	0.00	0.00	0.00	0.00	0.00
Pb	0.00	0.00	0.00	0.00	0.00	0.00	0.00	0.00	0.00	0.00
Total	1.98	1.99	1.99	1.98	1.99	2.00	1.97	1.96	1.98	1.98
Brt	0.98	0.97	0.98	0.94	0.96	0.97	0.97	0.94	0.95	0.96
Cls	0.01	0.02	0.01	0.03	0.03	0.04	0.02	0.04	0.03	0.03

Probe analysis	CNF31735_1_H	CNF31735_1_I	CNF31735_1_J	CNF31735_1_K	CNF31735_1_L	CNF31735_1_M	CNF31735_1_O	CNF31735_1_P	CNF31735_1_Q	CNF31735_1_R
Drill hole	LM13-94	LM13-94	LM13-94	LM13-94	LM13-94	LM13-94	LM13-94	LM13-94	LM13-94	LM13-94
Sample	CNF31735	CNF31735	CNF31735	CNF31735	CNF31735	CNF31735	CNF31735	CNF31735	CNF31735	CNF31735
Depth (m)	346.20	346.20	346.20	346.20	346.20	346.20	346.20	346.20	346.20	346.20
Barite texture	Tabular	Tabular	Tabular	Tabular	Tabular	Granular	Granular	Granular	Granular	Granular
Mineral assemblage type	Type 1 ±2B	Type 1 ±2B	Type 1 ±2B	Type 1 ±2B	Type 1 ±2B	Type 1 ±2B	Type 1 ±2B	Type 1 ±2B	Type 1 ±2B	Type 1 ±2B
Specimen	8	9	10	11	12	13	14	15	16	17
SO_3 *wt.%*	35.10	35.11	35.19	35.44	34.89	35.17	35.02	34.96	34.91	35.06
BaO	64.55	64.00	63.00	61.02	61.91	63.22	63.46	64.45	65.50	64.66
SrO	1.35	0.68	1.67	2.67	1.88	1.16	1.49	0.99	1.08	1.24
Na_2O	0.12	0.14	0.04	0.14	0.19	0.16	0.21	0.12	0.22	0.20
CaO	0.01	0.01	0.01	0.02	0.01	0.02	0.01	0.02	0.02	-
K_2O	0.00	0.01	-	-	-	0.01	-	-	0.01	0.00
SiO_2	-	-	-	-	-	-	-	-	-	-
FeO	-	0.03	0.02	-	-	-	-	-	-	-
ZnO	0.01	-	-	-	-	-	0.03	0.02	0.05	-
PbO	-	-	0.03	0.01	-	-	0.04	-	-	-
Total	101.16	99.98	99.95	99.30	98.89	99.74	100.26	100.55	101.80	101.16
S *apfu*	1.00	1.00	1.00	1.00	1.00	1.00	1.00	1.00	1.00	1.00
Ba	0.96	0.95	0.93	0.90	0.93	0.94	0.95	0.96	0.98	0.96
Sr	0.03	0.02	0.04	0.06	0.04	0.03	0.03	0.02	0.02	0.03
Na	0.00	0.01	0.00	0.01	0.01	0.01	0.01	0.00	0.01	0.01
Ca	0.00	0.00	0.00	0.00	0.00	0.00	0.00	0.00	0.00	0.00
K	0.00	0.00	0.00	0.00	0.00	0.00	0.00	0.00	0.00	0.00
Si	0.00	0.00	0.00	0.00	0.00	0.00	0.00	0.00	0.00	0.00
Fe	0.00	0.00	0.00	0.00	0.00	0.00	0.00	0.00	0.00	0.00
Zn	0.00	0.00	0.00	0.00	0.00	0.00	0.00	0.00	0.00	0.00
Pb	0.00	0.00	0.00	0.00	0.00	0.00	0.00	0.00	0.00	0.00
Total	1.99	1.97	1.97	1.96	1.97	1.97	1.99	1.99	2.01	1.99
Brt	0.98	0.97	0.96	0.93	0.94	0.96	0.97	0.98	1.00	0.98
Cls	0.02	0.01	0.03	0.04	0.03	0.02	0.02	0.02	0.02	0.02

Probe analysis	CNF31809_1_A	CNF31809_1_B	CNF31809_1_C	CNF31809_1_D	CNF31809_1_E	CNF31809_1_F	CNF31809_1_G	CNF31809_1_H	CNF31809_2_A	CNF31809_2_B
Drill hole	LM10-43	LM10-43	LM10-43	LM10-43	LM10-43	LM10-43	LM10-43	LM10-43	LM10-43	LM10-43
Sample	CNF31809	CNF31809	CNF31809	CNF31809	CNF31809	CNF31809	CNF31809	CNF31809	CNF31809	CNF31809
Depth (m)	213.70	213.70	213.70	213.70	213.70	213.70	213.70	213.70	213.70	213.70
Barite texture	Granular	Granular	Granular	Granular	Granular	Tabular	Tabular	Tabular	Tabular	Tabular
Mineral assemblage type	Type 1 ±2A	Type 1 ±2A	Type 1 ±2A	Type 1 ±2A	Type 1 ±2A	Type 1 ±2A	Type 1 ±2A	Type 1 ±2A	Type 1 ±2A	Type 1 ±2A
Specimen	1	2	3	4	5	6	7	8	1	2
SO_3 *wt.%*	35.14	35.25	34.79	35.04	34.84	35.06	34.98	34.84	34.56	34.96
BaO	65.22	64.64	65.52	64.63	64.65	63.83	64.32	65.75	65.18	63.90
SrO	0.80	0.84	0.81	0.74	0.86	1.22	0.60	0.52	0.39	1.56
Na_2O	0.10	0.17	0.13	0.08	0.14	0.23	0.21	0.11	0.13	0.16
CaO	0.01	0.02	0.01	0.01	0.00	0.03	0.00	0.02	0.01	0.03
K_2O	0.01	-	-	-	-	0.01	-	0.01	-	0.02
SiO_2	-	0.02	-	-	-	-	-	0.01	-	-
FeO	-	-	-	0.04	-	-	-	0.01	0.02	-
ZnO	-	0.04	-	-	0.02	-	0.04	-	-	-
PbO	-	-	-	-	-	0.04	-	0.01	-	-
Total	101.28	100.99	101.26	100.55	100.51	100.42	100.15	101.28	100.30	100.61
S *apfu*	1.00	1.00	1.00	1.00	1.00	1.00	1.00	1.00	1.00	1.00
Ba	0.97	0.96	0.98	0.96	0.97	0.95	0.96	0.99	0.98	0.95
Sr	0.02	0.02	0.02	0.02	0.02	0.03	0.01	0.01	0.01	0.03
Na	0.00	0.01	0.00	0.00	0.01	0.01	0.01	0.00	0.01	0.01
Ca	0.00	0.00	0.00	0.00	0.00	0.00	0.00	0.00	0.00	0.00
K	0.00	0.00	0.00	0.00	0.00	0.00	0.00	0.00	0.00	0.00
Si	0.00	0.00	0.00	0.00	0.00	0.00	0.00	0.00	0.00	0.00
Fe	0.00	0.00	0.00	0.00	0.00	0.00	0.00	0.00	0.00	0.00
Zn	0.00	0.00	0.00	0.00	0.00	0.00	0.00	0.00	0.00	0.00
Pb	0.00	0.00	0.00	0.00	0.00	0.00	0.00	0.00	0.00	0.00
Total	1.99	1.98	2.01	1.98	1.99	1.99	1.98	2.00	2.00	1.99
Brt	0.99	0.98	1.00	0.98	0.98	0.97	0.98	1.00	0.99	0.97
Cls	0.01	0.01	0.01	0.01	0.01	0.02	0.01	0.01	0.01	0.02

Probe analysis	CNF31809_2_C	CNF31809_2_D	CNF31809_2_E	CNF31809_2_F	CNF31809_2_G	CNF31809_2_H	CNF31809_2_I	CNF31809_2_J	CNF31809_3_A	CNF31809_3_B
Drill hole	LM10-43	LM10-43	LM10-43	LM10-43	LM10-43	LM10-43	LM10-43	LM10-43	LM10-43	LM10-43
Sample	CNF31809	CNF31809	CNF31809	CNF31809	CNF31809	CNF31809	CNF31809	CNF31809	CNF31809	CNF31809
Depth (m)	213.70	213.70	213.70	213.70	213.70	213.70	213.70	213.70	213.70	213.70
Barite texture	Tabular	Tabular	Tabular	Tabular	Tabular	Tabular	Tabular	Tabular	Tabular	Tabular
Mineral assemblage type	Type 1 ±2A	Type 1 ±2A	Type 1 ±2A	Type 1 ±2A	Type 1 ±2A	Type 1 ±2A	Type 1 ±2A	Type 1 ±2A	Type 1 ±2A	Type 1 ±2A
Specimen	3	4	5	6	7	8	9	10	1	2
SO_3 *wt.%*	34.68	35.05	34.94	34.93	34.80	35.13	34.96	34.56	34.84	34.69
BaO	64.23	63.88	63.36	64.67	64.36	64.49	64.19	64.56	63.48	64.72
SrO	1.00	1.23	0.90	0.78	0.96	0.74	0.78	0.88	1.70	0.64
Na_2O	0.06	0.13	0.17	0.27	0.16	0.26	0.07	0.05	0.03	0.21
CaO	0.01	0.02	-	-	0.02	-	0.03	0.03	0.02	0.02
K_2O	-	-	0.00	0.01	-	-	-	0.01	0.01	0.01
SiO_2	-	-	-	-	0.04	0.02	-	-	-	0.05
FeO	0.01	-	0.03	0.02	-	0.01	-	0.02	-	-
ZnO	-	-	-	-	0.07	-	-	-	-	-
PbO	-	0.06	-	0.04	0.02	0.02	0.02	-	-	0.01
Total	100.00	100.37	99.41	100.72	100.44	100.66	100.04	100.11	100.07	100.34
S *apfu*	1.00	1.00	1.00	1.00	1.00	1.00	1.00	1.00	1.00	1.00
Ba	0.97	0.95	0.95	0.97	0.97	0.96	0.96	0.98	0.95	0.97
Sr	0.02	0.03	0.02	0.02	0.02	0.02	0.02	0.02	0.04	0.01
Na	0.00	0.00	0.01	0.01	0.01	0.01	0.00	0.00	0.00	0.01
Ca	0.00	0.00	0.00	0.00	0.00	0.00	0.00	0.00	0.00	0.00
K	0.00	0.00	0.00	0.00	0.00	0.00	0.00	0.00	0.00	0.00
Si	0.00	0.00	0.00	0.00	0.00	0.00	0.00	0.00	0.00	0.00
Fe	0.00	0.00	0.00	0.00	0.00	0.00	0.00	0.00	0.00	0.00
Zn	0.00	0.00	0.00	0.00	0.00	0.00	0.00	0.00	0.00	0.00
Pb	0.00	0.00	0.00	0.00	0.00	0.00	0.00	0.00	0.00	0.00
Total	1.99	1.98	1.97	1.99	2.00	1.98	1.98	2.00	1.99	2.00
Brt	0.98	0.97	0.96	0.98	0.98	0.98	0.98	0.98	0.97	0.99
Cls	0.02	0.02	0.01	0.01	0.01	0.01	0.01	0.01	0.03	0.01

Probe analysis	CNF31809_3_C	CNF31809_3_D	CNF31809_3_E	CNF31809_3_F	CNF31809_3_G	CNF31809_3_H	CNF31809_3_I	CNF31809_3_J	CNF31809_3_K	CNF31809_3_L
Drill hole	LM10-43	LM10-43	LM10-43	LM10-43	LM10-43	LM10-43	LM10-43	LM10-43	LM10-43	LM10-43
Sample	CNF31809	CNF31809	CNF31809	CNF31809	CNF31809	CNF31809	CNF31809	CNF31809	CNF31809	CNF31809
Depth (m)	213.70	213.70	213.70	213.70	213.70	213.70	213.70	213.70	213.70	213.70
Barite texture	Tabular	Tabular	Tabular	Tabular	Tabular	Tabular	Tabular	Tabular	Tabular	Tabular
Mineral assemblage type	Type 1 ±2A	Type 1 ±2A	Type 1 ±2A	Type 1 ±2A	Type 1 ±2A	Type 1 ±2A	Type 1 ±2A	Type 1 ±2A	Type 1 ±2A	Type 1 ±2A
Specimen	3	4	5	6	7	8	9	10	11	12
SO_3 *wt.%*	34.74	34.80	34.56	35.07	35.01	34.52	34.53	34.94	34.38	34.86
BaO	63.90	64.72	65.15	64.54	65.88	65.73	64.86	64.29	64.94	64.80
SrO	1.47	0.51	0.59	0.58	0.49	0.42	0.54	0.44	0.71	0.96
Na_2O	0.08	0.23	0.15	0.12	0.11	0.14	0.22	0.17	0.15	0.14
CaO	0.03	-	0.01	-	0.01	-	-	0.00	-	-
K_2O	-	-	-	0.02	-	0.00	-	-	-	-
SiO_2	-	-	-	-	-	-	-	-	-	-
FeO	-	-	-	-	0.02	-	-	-	-	0.04
ZnO	0.07	-	-	0.03	0.06	-	-	0.06	-	-
PbO	0.05	0.03	-	-	-	-	-	0.03	0.03	-
Total	100.35	100.29	100.46	100.36	101.58	100.81	100.14	99.92	100.22	100.80
S *apfu*	1.00	1.00	1.00	1.00	1.00	1.00	1.00	1.00	1.00	1.00
Ba	0.96	0.97	0.98	0.96	0.98	0.99	0.98	0.96	0.99	0.97
Sr	0.03	0.01	0.01	0.01	0.01	0.01	0.01	0.01	0.02	0.02
Na	0.00	0.01	0.01	0.00	0.00	0.01	0.01	0.01	0.01	0.01
Ca	0.00	0.00	0.00	0.00	0.00	0.00	0.00	0.00	0.00	0.00
K	0.00	0.00	0.00	0.00	0.00	0.00	0.00	0.00	0.00	0.00
Si	0.00	0.00	0.00	0.00	0.00	0.00	0.00	0.00	0.00	0.00
Fe	0.00	0.00	0.00	0.00	0.00	0.00	0.00	0.00	0.00	0.00
Zn	0.00	0.00	0.00	0.00	0.00	0.00	0.00	0.00	0.00	0.00
Pb	0.00	0.00	0.00	0.00	0.00	0.00	0.00	0.00	0.00	0.00
Total	2.00	1.99	2.00	1.98	2.00	2.01	2.00	1.98	2.01	1.99
Brt	0.97	0.99	0.99	0.98	1.00	1.00	0.99	0.98	0.99	0.99
Cls	0.02	0.01	0.01	0.01	0.01	0.01	0.01	0.01	0.01	0.01

Probe analysis	CNF31812_1_A	CNF31812_1_B	CNF31812_1_C	CNF31812_1_D	CNF31812_1_E	CNF31812_1_F	CNF31812_1_G	CNF31812_1_H	CNF31812_1_I	CNF31812_2_A
Drill hole	LM10-43	LM10-43	LM10-43	LM10-43	LM10-43	LM10-43	LM10-43	LM10-43	LM10-43	LM10-43
Sample	CNF31812	CNF31812	CNF31812	CNF31812	CNF31812	CNF31812	CNF31812	CNF31812	CNF31812	CNF31812
Depth (m)	226.10	226.10	226.10	226.10	226.10	226.10	226.10	226.10	226.10	226.10
Barite texture	Granular	Granular	Granular	Granular	Granular	Granular	Granular	Granular	Granular	Granular
Mineral assemblage type	Type 1	Type 1	Type 1	Type 1	Type 1	Type 1	Type 1	Type 1	Type 1	Type 2A
Specimen	1	2	3	4	5	6	7	8	9	1
SO_3 *wt.%*	35.70	35.17	34.64	34.90	34.74	34.69	34.49	34.91	34.60	35.06
BaO	62.65	63.79	64.92	62.61	64.26	63.04	64.96	65.51	64.28	63.80
SrO	2.89	1.10	0.79	2.09	1.13	2.10	1.12	0.42	1.37	1.14
Na_2O	0.11	0.12	0.16	0.13	0.19	0.12	0.17	0.12	0.19	0.14
CaO	-	0.00	0.02	0.03	0.01	-	-	-	-	0.00
K_2O	0.00	0.01	0.02	-	0.02	0.00	-	-	-	0.00
SiO_2	-	-	-	-	-	-	-	-	0.07	-
FeO	-	-	-	-	-	0.01	0.01	-	-	0.03
ZnO	-	0.02	-	-	0.07	-	0.03	0.06	0.10	0.06
PbO	-	-	-	-	-	-	0.01	-	-	0.01
Total	101.35	100.21	100.53	99.76	100.42	99.97	100.80	101.02	100.61	100.25
S *apfu*	1.00	1.00	1.00	1.00	1.00	1.00	1.00	1.00	1.00	1.00
Ba	0.92	0.95	0.98	0.94	0.97	0.95	0.98	0.98	0.97	0.95
Sr	0.06	0.02	0.02	0.05	0.03	0.05	0.03	0.01	0.03	0.03
Na	0.00	0.00	0.01	0.00	0.01	0.00	0.01	0.00	0.01	0.01
Ca	0.00	0.00	0.00	0.00	0.00	0.00	0.00	0.00	0.00	0.00
K	0.00	0.00	0.00	0.00	0.00	0.00	0.00	0.00	0.00	0.00
Si	0.00	0.00	0.00	0.00	0.00	0.00	0.00	0.00	0.00	0.00
Fe	0.00	0.00	0.00	0.00	0.00	0.00	0.00	0.00	0.00	0.00
Zn	0.00	0.00	0.00	0.00	0.00	0.00	0.00	0.00	0.00	0.00
Pb	0.00	0.00	0.00	0.00	0.00	0.00	0.00	0.00	0.00	0.00
Total	1.98	1.97	2.00	1.98	2.00	2.00	2.01	1.99	2.01	1.98
Brt	0.95	0.97	0.99	0.95	0.98	0.96	0.99	1.00	0.98	0.97
Cls	0.04	0.02	0.01	0.03	0.02	0.03	0.02	0.01	0.02	0.02

Probe analysis	CNF31812_2_B	CNF31812_2_C	CNF31812_2_D	CNF31812_2_E	CNF31812_2_F	CNF31812_2_G	CNF31812_2_H	CNF31812_2_I	CNF31812_2_J	CNF31812_2_K
Drill hole	LM10-43	LM10-43	LM10-43	LM10-43	LM10-43	LM10-43	LM10-43	LM10-43	LM10-44	LM10-45
Sample	CNF31812	CNF31812	CNF31812	CNF31812	CNF31812	CNF31812	CNF31812	CNF31812	CNF31813	CNF31814
Depth (m)	226.10	226.10	226.10	226.10	226.10	226.10	226.10	226.10	227.10	228.10
Barite texture	Granular	Granular	Granular	Granular	Tabular	Tabular	Tabular	Tabular	Tabular	Tabular
Mineral assemblage type	Type 2A	Type 2A	Type 2A	Type 2A	Type 2A	Type 2A	Type 2A	Type 2A	Type 2A	Type 2A
Specimen	2	3	4	5	6	7	8	9	10	11
SO_3 *wt.%*	34.72	34.75	34.89	34.89	34.89	34.88	34.79	34.61	34.70	35.08
BaO	65.50	64.85	64.07	64.84	63.71	64.60	64.65	65.39	64.44	64.35
SrO	0.57	0.64	1.15	0.23	1.03	0.76	0.66	0.53	0.67	0.52
Na_2O	0.24	0.18	0.09	0.14	0.08	0.08	0.10	0.13	0.21	0.23
CaO	0.01	0.02	-	0.01	0.01	0.00	0.02	0.00	-	0.02
K_2O	-	-	-	-	0.01	0.01	0.00	0.01	0.00	0.01
SiO_2	-	0.05	0.01	-	-	-	-	0.04	-	-
FeO	-	0.01	-	-	-	-	-	-	-	-
ZnO	-	-	0.02	-	0.04	0.04	0.02	-	0.10	-
PbO	-	-	0.03	-	0.03	-	-	-	0.05	-
Total	101.04	100.51	100.26	100.11	99.80	100.39	100.23	100.72	100.17	100.20
S *apfu*	1.00	1.00	1.00	1.00	1.00	1.00	1.00	1.00	1.00	1.00
Ba	0.99	0.97	0.96	0.97	0.95	0.97	0.97	0.99	0.97	0.96
Sr	0.01	0.01	0.03	0.01	0.02	0.02	0.01	0.01	0.01	0.01
Na	0.01	0.01	0.00	0.01	0.00	0.00	0.00	0.00	0.01	0.01
Ca	0.00	0.00	0.00	0.00	0.00	0.00	0.00	0.00	0.00	0.00
K	0.00	0.00	0.00	0.00	0.00	0.00	0.00	0.00	0.00	0.00
Si	0.00	0.00	0.00	0.00	0.00	0.00	0.00	0.00	0.00	0.00
Fe	0.00	0.00	0.00	0.00	0.00	0.00	0.00	0.00	0.00	0.00
Zn	0.00	0.00	0.00	0.00	0.00	0.00	0.00	0.00	0.00	0.00
Pb	0.00	0.00	0.00	0.00	0.00	0.00	0.00	0.00	0.00	0.00
Total	2.00	2.00	1.99	1.98	1.98	1.99	1.99	2.00	1.99	1.98
Brt	1.00	0.99	0.98	0.99	0.97	0.98	0.98	1.00	0.98	0.98
Cls	0.01	0.01	0.02	0.00	0.02	0.01	0.01	0.01	0.01	0.01

Probe analysis	CNF31812_2_L	CNF31812_2_M	CNF31812_2_N	CNF31812_2_O	CNF31812_2_P	CNF31812_2_Q	CNF31812_2_R	CNF31812_2_S	CNF31812_2_T	CNF31812_2_U
Drill hole	LM10-46	LM10-47	LM10-48	LM10-49	LM10-50	LM10-51	LM10-52	LM10-53	LM10-54	LM10-55
Sample	CNF31815	CNF31816	CNF31817	CNF31818	CNF31819	CNF31820	CNF31821	CNF31822	CNF31823	CNF31824
Depth (m)	229.10	230.10	231.10	232.10	233.10	234.10	235.10	236.10	237.10	238.10
Barite texture	Tabular	Tabular	Tabular	Tabular	Tabular	Tabular	Tabular	Tabular	Tabular	Tabular
Mineral assemblage type	Type 2A	Type 2A	Type 2A	Type 2A	Type 2A	Type 2A	Type 2A	Type 2A	Type 2A	Type 2A
Specimen	12	13	14	15	16	17	18	19	20	21
SO_3 *wt.%*	34.84	34.99	35.17	34.65	35.09	34.87	34.77	34.70	34.84	34.14
BaO	64.91	64.61	63.99	63.88	64.35	64.68	64.08	62.64	63.32	63.48
SrO	0.95	0.65	0.52	1.26	1.60	0.63	1.04	1.72	0.93	0.25
Na_2O	0.10	0.12	0.11	0.15	0.16	0.20	0.13	0.15	0.17	0.22
CaO	0.02	0.01	-	0.01	-	0.01	0.16	-	0.01	-
K_2O	-	0.01	0.01	0.00	0.01	-	0.00	0.01	-	0.01
SiO_2	-	0.01	0.01	-	-	-	-	-	-	-
FeO	-	-	0.03	-	0.01	-	-	-	0.04	0.02
ZnO	-	-	0.08	0.01	-	0.06	-	0.10	0.07	-
PbO	0.05	-	-	-	-	-	-	-	-	-
Total	100.86	100.39	99.92	99.96	101.21	100.45	100.20	99.31	99.37	98.12
S *apfu*	1.00	1.00	1.00	1.00	1.00	1.00	1.00	1.00	1.00	1.00
Ba	0.97	0.96	0.95	0.96	0.96	0.97	0.96	0.94	0.95	0.88
Sr	0.02	0.01	0.01	0.03	0.04	0.01	0.02	0.04	0.02	0.10
Na	0.00	0.00	0.00	0.01	0.01	0.01	0.00	0.01	0.01	0.01
Ca	0.00	0.00	0.00	0.00	0.00	0.00	0.01	0.00	0.00	0.00
K	0.00	0.00	0.00	0.00	0.00	0.00	0.00	0.00	0.00	0.00
Si	0.00	0.00	0.00	0.00	0.00	0.00	0.00	0.00	0.00	0.00
Fe	0.00	0.00	0.00	0.00	0.00	0.00	0.00	0.00	0.00	0.00
Zn	0.00	0.00	0.00	0.00	0.00	0.00	0.00	0.00	0.00	0.00
Pb	0.00	0.00	0.00	0.00	0.00	0.00	0.00	0.00	0.00	0.00
Total	2.00	1.98	1.97	1.99	2.00	1.99	2.00	1.99	1.98	1.99
Brt	0.99	0.98	0.97	0.97	0.98	0.98	0.98	0.95	0.96	0.97
Cls	0.01	0.01	0.01	0.02	0.02	0.01	0.02	0.03	0.01	0.00

Probe analysis	CNF31812_2_V	CNF31812_2_W	CNF31812_2_X	CNF31816_1_A	CNF31816_1_B	CNF31816_1_C	CNF31816_1_D	CNF31816_1_E	CNF31816_1_F	CNF31816_1_G
Drill hole	LM10-56	LM10-57	LM10-58	LM10-43	LM10-43	LM10-43	LM10-43	LM10-43	LM10-43	LM10-43
Sample	CNF31825	CNF31826	CNF31827	CNF31812	CNF31812	CNF31812	CNF31812	CNF31812	CNF31812	CNF31812
Depth (m)	239.10	240.10	241.10	226.10	226.10	226.10	226.10	226.10	226.10	226.10
Barite texture	Tabular	Tabular	Tabular	Tabular	Tabular	Tabular	Tabular	Tabular	Tabular	Tabular
Mineral assemblage type	Type 2A	Type 2A	Type 2A	Type 1	Type 1	Type 1	Type 1	Type 1	Type 1	Type 1
Specimen	22	23	24	1	2	3	4	5	6	7
SO_3 *wt.%*	35.55	35.20	34.44	34.32	34.90	34.98	34.81	34.85	34.99	34.36
BaO	59.66	60.30	63.95	65.31	64.49	65.42	64.37	63.54	64.37	64.98
SrO	4.78	4.39	0.69	0.52	1.02	0.70	1.06	0.49	0.75	1.03
Na_2O	0.14	0.13	0.14	0.13	0.17	0.04	0.10	0.15	0.06	0.08
CaO	-	-	-	0.00	0.02	0.01	0.01	0.01	0.00	0.01
K_2O	0.01	-	0.00	0.02	0.01	-	-	-	0.02	-
SiO_2	-	-	-	-	-	-	-	-	-	-
FeO	-	-	0.03	-	-	-	0.03	0.04	-	-
ZnO	0.05	-	-	-	-	-	-	0.04	-	-
PbO	0.03	0.03	-	-	-	0.03	-	0.01	0.01	0.02
Total	100.20	100.04	99.26	100.30	100.62	101.18	100.38	99.12	100.20	100.47
S *apfu*	1.00	1.00	1.00	1.00	1.00	1.00	1.00	1.00	1.00	1.00
Ba	0.89	0.97	0.96	0.99	0.96	0.98	0.97	0.95	0.96	0.99
Sr	0.10	0.02	0.03	0.01	0.02	0.02	0.02	0.01	0.02	0.02
Na	0.00	0.01	0.01	0.00	0.01	0.00	0.00	0.01	0.00	0.00
Ca	0.00	0.00	0.00	0.00	0.00	0.00	0.00	0.00	0.00	0.00
K	0.00	0.00	0.00	0.00	0.00	0.00	0.00	0.00	0.00	0.00
Si	0.00	0.00	0.00	0.00	0.00	0.00	0.00	0.00	0.00	0.00
Fe	0.00	0.00	0.00	0.00	0.00	0.00	0.00	0.00	0.00	0.00
Zn	0.00	0.00	0.00	0.00	0.00	0.00	0.00	0.00	0.00	0.00
Pb	0.00	0.00	0.00	0.00	0.00	0.00	0.00	0.00	0.00	0.00
Total	1.99	1.99	1.99	2.01	1.99	1.99	1.99	1.97	1.98	2.01
Brt	0.91	0.92	0.97	0.99	0.98	1.00	0.98	0.97	0.98	0.99
Cls	0.07	0.07	0.01	0.01	0.02	0.01	0.02	0.01	0.01	0.02

Probe analysis	CNF31816_1_H	CNF31816_1_I	CNF31816_1_J	CNF31816_1_K	CNF31816_1_L	CNF31816_1_M	CNF31816_1_N	CNF31816_1_O	CNF31816_1_P	CNF31847_1_A
Drill hole	LM10-43	LM10-43	LM10-44	LM10-45	LM10-46	LM10-47	LM10-48	LM10-49	LM10-50	LM13-83
Sample	CNF31812	CNF31812	CNF31813	CNF31814	CNF31815	CNF31816	CNF31817	CNF31818	CNF31819	CNF31847
Depth (m)	226.10	226.10	227.10	228.10	229.10	230.10	231.10	232.10	233.10	300.20
Barite texture	Granular	Granular	Granular	Granular	Granular	Granular	Granular	Granular	Granular	Interstitial
Mineral assemblage type	Type 1	Type 1	Type 1	Type 1	Type 1	Type 1	Type 1	Type 1	Type 1	Type 3
Specimen	8	9	10	11	12	13	14	15	16	1
SO_3 *wt.%*	34.45	34.17	34.86	34.39	34.40	34.56	34.98	34.24	34.81	34.78
BaO	64.50	64.59	65.28	64.77	65.15	64.51	63.93	65.09	65.45	64.46
SrO	0.72	0.42	0.80	0.73	0.62	0.60	0.69	0.44	0.58	0.02
Na_2O	0.09	0.19	0.07	0.13	0.21	0.13	0.17	0.17	0.09	0.18
CaO	0.01	-	0.02	0.04	0.02	0.01	0.02	0.01	0.02	0.02
K_2O	0.02	-	-	-	0.01	-	0.01	-	-	-
SiO_2	-	-	-	-	-	-	-	-	0.04	-
FeO	-	0.02	0.04	-	-	-	0.02	-	0.01	0.02
ZnO	-	0.03	-	-	-	-	-	-	0.02	-
PbO	0.05	-	-	0.06	-	0.06	-	-	-	-
Total	99.83	99.42	101.07	100.11	100.41	99.87	99.81	99.96	101.02	99.47
S *apfu*	1.00	1.00	1.00	1.00	1.00	1.00	1.00	1.00	1.00	1.00
Ba	0.98	0.99	0.98	0.98	0.99	0.97	0.95	0.99	0.98	0.97
Sr	0.02	0.01	0.02	0.02	0.01	0.01	0.02	0.01	0.01	0.00
Na	0.00	0.01	0.00	0.00	0.01	0.00	0.01	0.01	0.00	0.01
Ca	0.00	0.00	0.00	0.00	0.00	0.00	0.00	0.00	0.00	0.00
K	0.00	0.00	0.00	0.00	0.00	0.00	0.00	0.00	0.00	0.00
Si	0.00	0.00	0.00	0.00	0.00	0.00	0.00	0.00	0.00	0.00
Fe	0.00	0.00	0.00	0.00	0.00	0.00	0.00	0.00	0.00	0.00
Zn	0.00	0.00	0.00	0.00	0.00	0.00	0.00	0.00	0.00	0.00
Pb	0.00	0.00	0.00	0.00	0.00	0.00	0.00	0.00	0.00	0.00
Total	2.00	2.00	2.00	2.00	2.01	1.99	1.97	2.01	2.00	1.97
Brt	0.98	0.98	0.99	0.99	0.99	0.98	0.97	0.99	1.00	0.98
Cls	0.01	0.01	0.01	0.01	0.01	0.01	0.01	0.01	0.01	0.01

Probe analysis	CNF31847_1_B	CNF31847_1_C	CNF31847_1_D	CNF31847_1_E	CNF31847_1_F	CNF31847_2_A	CNF31847_2_B	CNF31847_2_C	CNF31855_1_A	CNF31855_1_B
Drill hole	LM13-83	LM13-83	LM13-83	LM13-83	LM13-83	LM13-83	LM13-83	LM13-83	LM11-52	LM11-52
Sample	CNF31847	CNF31847	CNF31847	CNF31847	CNF31847	CNF31847	CNF31847	CNF31847	CNF31855	CNF31855
Depth (m)	300.20	300.20	300.20	300.20	300.20	300.20	300.20	300.20	216.20	216.20
Barite texture	Interstitial	Interstitial	Interstitial	Interstitial	Interstitial	Interstitial	Interstitial	Interstitial	Tabular	Tabular
Mineral assemblage type	Type 3	Type 3	Type 3	Type 3	Type 3	Type 3	Type 3	Type 3	Type 1 ± 2A	Type 1 ± 2A
Specimen	2	3	4	5	6	7	8	9	1	2
SO_3 *wt.%*	34.84	34.19	34.28	34.45	34.34	34.38	33.80	34.11	34.63	34.19
BaO	65.08	65.09	64.99	65.94	65.12	64.61	66.45	65.88	63.69	65.21
SrO	0.08	0.05	-	0.17	-	-	-	-	1.52	0.53
Na_2O	0.11	0.10	0.12	0.10	0.15	0.14	0.12	0.12	0.08	0.18
CaO	0.05	0.02	0.03	0.02	0.03	0.01	0.00	-0.02	0.02	0.00
K_2O	-	0.01	-	-	-	-	0.01	0.04	0.01	-
SiO_2	0.03	0.02	0.02	-	-	0.02	-	-	-	-
FeO	0.01	-	-	-	-	-	0.01	0.05	-	-
ZnO	-	0.01	0.02	-	0.04	0.01	0.04	-	0.06	-
PbO	0.06	-	-	0.01	0.04	0.02	-	0.01	-	-
Total	100.26	99.49	99.46	100.68	99.71	99.20	100.43	100.19	100.00	100.10
S *apfu*	1.00	1.00	1.00	1.00	1.00	1.00	1.00	1.00	1.00	1.00
Ba	0.98	0.99	0.99	1.00	0.99	0.98	1.03	1.01	0.96	1.00
Sr	0.00	0.00	0.00	0.00	0.00	0.00	0.00	0.00	0.03	0.01
Na	0.00	0.00	0.00	0.00	0.01	0.01	0.00	0.00	0.00	0.01
Ca	0.00	0.00	0.00	0.00	0.00	0.00	0.00	0.00	0.00	0.00
K	0.00	0.00	0.00	0.00	0.00	0.00	0.00	0.00	0.00	0.00
Si	0.00	0.00	0.00	0.00	0.00	0.00	0.00	0.00	0.00	0.00
Fe	0.00	0.00	0.00	0.00	0.00	0.00	0.00	0.00	0.00	0.00
Zn	0.00	0.00	0.00	0.00	0.00	0.00	0.00	0.00	0.00	0.00
Pb	0.00	0.00	0.00	0.00	0.00	0.00	0.00	0.00	0.00	0.00
Total	1.99	2.00	2.00	2.01	2.00	1.99	2.03	2.01	2.00	2.01
Brt	0.99	0.99	0.99	1.00	0.99	0.98	1.01	1.00	0.97	0.99
Cls	0.01	0.01	0.01	0.01	0.01	0.01	0.01	0.01	0.02	0.01

Probe analysis	CNF31855_1_C	CNF31855_1_D	CNF31855_1_E	CNF31855_1_F	CNF31855_1_G	CNF31855_1_H	CNF31855_1_I	CNF31855_1_J	CNF31855_1_K	CNF31855_1_L
Drill hole	LM11-52	LM11-52	LM11-52	LM11-52	LM11-52	LM11-52	LM11-52	LM11-52	LM11-52	LM11-52
Sample	CNF31855	CNF31855	CNF31855	CNF31855	CNF31855	CNF31855	CNF31855	CNF31855	CNF31855	CNF31855
Depth (m)	216.20	216.20	216.20	216.20	216.20	216.20	216.20	216.20	216.20	216.20
Barite texture	Tabular	Tabular	Tabular	Tabular	Tabular	Tabular	Tabular	Granular	Granular	Granular
Mineral assemblage type	Type 1 ± 2A	Type 1 ± 2A	Type 1 ± 2A	Type 1 ± 2A	Type 1 ± 2A	Type 1 ± 2A	Type 1 ± 2A	Type 1 ± 2A	Type 1 ± 2A	Type 1 ± 2A
Specimen	3	4	5	6	7	8	9	10	11	12
SO_3 *wt.%*	34.11	34.11	34.37	34.64	34.41	34.40	34.82	33.91	34.20	34.31
BaO	64.69	63.65	61.66	64.47	63.95	63.83	62.72	64.49	65.11	64.52
SrO	1.45	2.17	2.62	1.24	2.47	1.69	2.92	0.50	0.55	1.18
Na_2O	0.08	0.10	0.14	0.11	0.14	0.11	0.21	0.13	0.12	0.23
CaO	0.02	0.02	0.03	0.03	0.02	0.01	0.06	0.01	0.00	0.01
K_2O	-	-	-	-	-	-	-	-	0.01	-
SiO_2	-	-	-	-	-	-	-	-	-	-
FeO	-	-	-	0.01	-	0.03	-	-	-	-
ZnO	-	-	0.03	0.03	-	-	-	0.03	-	0.05
PbO	0.03	0.04	-	-	0.00	-	0.01	-	-	-
Total	100.38	100.09	98.85	100.51	100.99	100.08	100.75	99.07	99.98	100.30
S *apfu*	1.00	1.00	1.00	1.00	1.00	1.00	1.00	1.00	1.00	1.00
Ba	0.99	0.97	0.94	0.97	0.97	0.97	0.94	0.99	0.99	0.98
Sr	0.03	0.05	0.06	0.03	0.06	0.04	0.06	0.01	0.01	0.03
Na	0.00	0.00	0.01	0.00	0.01	0.00	0.01	0.00	0.00	0.01
Ca	0.00	0.00	0.00	0.00	0.00	0.00	0.00	0.00	0.00	0.00
K	0.00	0.00	0.00	0.00	0.00	0.00	0.00	0.00	0.00	0.00
Si	0.00	0.00	0.00	0.00	0.00	0.00	0.00	0.00	0.00	0.00
Fe	0.00	0.00	0.00	0.00	0.00	0.00	0.00	0.00	0.00	0.00
Zn	0.00	0.00	0.00	0.00	0.00	0.00	0.00	0.00	0.00	0.00
Pb	0.00	0.00	0.00	0.00	0.00	0.00	0.00	0.00	0.00	0.00
Total	2.02	2.02	2.00	2.01	2.02	2.01	2.01	2.01	2.01	2.02
Brt	0.98	0.97	0.94	0.98	0.97	0.97	0.95	0.98	0.99	0.98
Cls	0.02	0.03	0.04	0.02	0.04	0.03	0.04	0.01	0.01	0.02

Probe analysis	CNF31860_1_A	CNF31860_1_B	CNF31860_1_C	CNF31860_1_D	CNF31860_1_E	CNF31860_1_F	CNF31860_1_G	CNF31860_1_H	CNF31860_1_I	CNF31860_1_J
Drill hole	LM11-68	LM11-68	LM11-68	LM11-68	LM11-68	LM11-68	LM11-68	LM11-68	LM11-68	LM11-68
Sample	CNF31860	CNF31860	CNF31860	CNF31860	CNF31860	CNF31860	CNF31860	CNF31860	CNF31860	CNF31860
Depth (m)	197.95	197.95	197.95	197.95	197.95	197.95	197.95	197.95	197.95	197.95
Barite texture	Tabular	Tabular	Tabular	Tabular	Granular	Granular	Granular	Tabular	Tabular	Granular
Mineral assemblage type	Type 1 ± 2B ± 2A	Type 1 ± 2B ± 2A	Type 1 ± 2B ± 2A	Type 1 ± 2B ± 2A	Type 1 ± 2B ± 2A	Type 1 ± 2B ± 2A	Type 1 ± 2B ± 2A	Type 1 ± 2B ± 2A	Type 1 ± 2B ± 2A	Type 1 ± 2B ± 2A
Specimen	1	2	3	4	5	6	7	8	9	10
SO_3 *wt.%*	34.77	34.98	35.00	35.07	34.94	34.98	34.52	34.91	35.61	34.57
BaO	62.87	61.49	62.65	62.69	63.52	64.24	65.77	63.48	63.61	65.31
SrO	2.28	3.15	2.51	2.49	1.22	0.63	0.87	2.16	2.34	1.05
Na_2O	0.10	0.19	-	0.10	0.10	0.14	0.17	0.22	0.17	0.08
CaO	-	0.22	0.17	0.15	0.01	0.01	-	0.09	0.14	-
K_2O	0.00	0.01	-	-	0.01	0.00	-	0.01	-	-
SiO_2	-	0.02	-	-	0.03	0.01	-	-	-	-
FeO	-	0.01	0.01	-	-	0.02	0.01	-	0.01	-
ZnO	0.00	0.04	-	-	0.06	-	0.01	-	0.06	0.04
PbO	0.05	-	-	-	0.01	-	0.05	0.06	0.01	-
Total	100.07	100.12	100.35	100.50	99.90	100.02	101.41	100.93	101.95	101.04
S *apfu*	1.00	1.00	1.00	1.00	1.00	1.00	1.00	1.00	1.00	1.00
Ba	0.94	0.92	0.93	0.93	0.95	0.96	0.99	0.95	0.93	0.99
Sr	0.05	0.07	0.06	0.05	0.03	0.01	0.02	0.05	0.05	0.02
Na	0.00	0.01	0.00	0.00	0.00	0.01	0.01	0.01	0.01	0.00
Ca	0.00	0.01	0.01	0.01	0.00	0.00	0.00	0.00	0.01	0.00
K	0.00	0.00	0.00	0.00	0.00	0.00	0.00	0.00	0.00	0.00
Si	0.00	0.00	0.00	0.00	0.00	0.00	0.00	0.00	0.00	0.00
Fe	0.00	0.00	0.00	0.00	0.00	0.00	0.00	0.00	0.00	0.00
Zn	0.00	0.00	0.00	0.00	0.00	0.00	0.00	0.00	0.00	0.00
Pb	0.00	0.00	0.00	0.00	0.00	0.00	0.00	0.00	0.00	0.00
Total										
Brt	0.96	0.94	0.95	0.95	0.97	0.98	1.00	0.97	0.97	0.99
Cls	0.03	0.05	0.04	0.04	0.02	0.01	0.01	0.03	0.04	0.02

Probe analysis	CNF31860_1_K	CNF31860_1_L	CNF31860_1_M	CNF31860_1_N	CNF31860_1_O	CNF31860_1_P	CNF31860_2_A	CNF31860_2_B	CNF31860_2_C	CNF31860_2_D
Drill hole	LM11-68	LM11-68	LM11-68	LM11-68	LM11-68	LM11-68	LM11-68	LM11-68	LM11-68	LM11-68
Sample	CNF31860	CNF31860	CNF31860	CNF31860	CNF31860	CNF31860	CNF31860	CNF31860	CNF31860	CNF31860
Depth (m)	197.95	197.95	197.95	197.95	197.95	197.95	197.95	197.95	197.95	197.95
Barite texture	Granular	Granular	Granular	Tabular	Tabular	Tabular	Bladed	Bladed	Bladed	Granular
Mineral assemblage type	Type 1 ± 2B ± 2A	Type 1 ± 2B ± 2A	Type 1 ± 2B ± 2A	Type 1 ± 2B ± 2A	Type 1 ± 2B ± 2A	Type 1 ± 2B ± 2A	Type 1 ± 2B ± 2A	Type 1 ± 2B ± 2A	Type 1 ± 2B ± 2A	Type 1 ± 2B ± 2A
Specimen	11	12	13	14	15	16	1	2	3	4
SO_3 *wt.%*	34.89	34.80	34.89	34.78	34.24	34.01	34.30	34.47	34.42	34.50
BaO	64.31	63.77	64.80	65.69	63.44	67.97	65.24	63.51	64.92	64.69
SrO	0.60	0.91	0.81	0.18	2.00	0.17	0.67	1.27	0.18	0.84
Na_2O	0.15	0.14	0.04	0.17	0.16	0.16	0.19	0.13	0.15	0.11
CaO	0.00	0.00	0.01	0.01	0.02	-	0.01	0.02	0.01	-
K_2O	0.00	-	0.01	-	-	-	-	-	0.02	0.01
SiO_2	-	-	-	-	0.01	-	-	-	-	-
FeO	-	-	-	-	-	-	0.04	0.01	-	-
ZnO	-	0.10	0.05	0.02	B-	-	-	0.06	-	-
PbO	-	-	-	-	-	-	-	-	-	0.10
Total	99.97	99.72	100.59	100.85	99.87	102.30	100.44	99.46	99.70	100.25
S *apfu*	1.00	1.00	1.00	1.00	1.00	1.00	1.00	1.00	1.00	1.00
Ba	0.96	0.96	0.97	0.99	0.97	1.04	0.99	0.96	0.98	0.98
Sr	0.01	0.02	0.02	0.00	0.05	0.00	0.02	0.03	0.00	0.02
Na	0.01	0.01	0.00	0.01	0.01	0.01	0.01	0.00	0.01	0.00
Ca	0.00	0.00	0.00	0.00	0.00	0.00	0.00	0.00	0.00	0.00
K	0.00	0.00	0.00	0.00	0.00	0.00	0.00	0.00	0.00	0.00
Si	0.00	0.00	0.00	0.00	0.00	0.00	0.00	0.00	0.00	0.00
Fe	0.00	0.00	0.00	0.00	0.00	0.00	0.00	0.00	0.00	0.00
Zn	0.00	0.00	0.00	0.00	0.00	0.00	0.00	0.00	0.00	0.00
Pb	0.00	0.00	0.00	0.00	0.00	0.00	0.00	0.00	0.00	0.00
Total							2.02	2.00	1.99	2.00
Brt	0.98	0.97	0.99	1.00	0.97	1.03	0.99	0.97	0.99	0.98
Cls	0.01	0.01	0.01	0.00	0.03	0.00	0.01	0.02	0.00	0.01

Probe analysis	CNF31860_2_E	CNF31860_2_F	CNF31860_2_G	CNF31860_2_H	CNF31860_2_J	CNF31860_2_I	CNF31860_2_K	CNF31860_2_L	CNF31860_2_M	CNF31860_2_N
Drill hole	LM11-68	LM11-68	LM11-68	LM11-68	LM11-68	LM11-68	LM11-68	LM11-68	LM11-68	LM11-68
Sample	CNF31860	CNF31860	CNF31860	CNF31860	CNF31860	CNF31860	CNF31860	CNF31860	CNF31860	CNF31860
Depth (m)	197.95	197.95	197.95	197.95	197.95	197.95	197.95	197.95	197.95	197.95
Barite texture	Granular	Granular	Granular	Granular	Granular	Granular	Bladed	Bladed	Bladed	Granular
Mineral assemblage type	Type 1 ± 2B ± 2A	Type 1 ± 2B ± 2A	Type 1 ± 2B ± 2A	Type 1 ± 2B ± 2A	Type 1 ± 2B ± 2A	Type 1 ± 2B ± 2A	Type 1 ± 2B ± 2A	Type 1 ± 2B ± 2A	Type 1 ± 2B ± 2A	Type 1 ± 2B ± 2A
Specimen	5	6	7	8	9	10	11	12	13	14
SO_3 *wt.%*	35.19	34.94	34.99	34.38	34.51	34.72	34.60	34.80	34.12	33.50
BaO	65.70	65.74	65.15	66.21	64.34	64.95	65.43	63.86	65.88	67.75
SrO	0.75	0.81	0.85	0.71	0.93	0.74	0.78	1.73	0.42	0.53
Na_2O	0.12	0.10	0.09	0.15	0.06	0.16	0.06	0.14	0.22	0.11
CaO	0.01	0.01	0.01	-	-	-	0.01	0.03	0.01	0.01
K_2O	0.00	0.01	-	-	-	-	-	-	-	-
SiO_2	-	-	0.08	0.02	0.02	-	-	0.02	-	-
FeO	0.03	-	-	-	0.03	-	-	0.01	0.01	-
ZnO	0.07	-	-	0.06	0.11	0.13	0.05	-	-	0.02
PbO	-	-	-	-	-	0.02	-	0.01	-	0.12
Total	101.88	101.61	101.18	101.54	100.00	100.70	100.92	100.61	100.66	102.03
S *apfu*	1.00	1.00	1.00	1.00	1.00	1.00	1.00	1.00	1.00	1.00
Ba	0.97	0.98	0.97	1.01	0.97	0.98	0.99	0.96	1.01	1.06
Sr	0.02	0.02	0.02	0.02	0.02	0.02	0.02	0.04	0.01	0.01
Na	0.00	0.00	0.00	0.01	0.00	0.01	0.00	0.01	0.01	0.00
Ca	0.00	0.00	0.00	0.00	0.00	0.00	0.00	0.00	0.00	0.00
K	0.00	0.00	0.00	0.00	0.00	0.00	0.00	0.00	0.00	0.00
Si	0.00	0.00	0.00	0.00	0.00	0.00	0.00	0.00	0.00	0.00
Fe	0.00	0.00	0.00	0.00	0.00	0.00	0.00	0.00	0.00	0.00
Zn	0.00	0.00	0.00	0.00	0.00	0.00	0.00	0.00	0.00	0.00
Pb	0.00	0.00	0.00	0.00	0.00	0.00	0.00	0.00	0.00	0.00
Total	2.00	2.00	1.99	2.03	2.00	2.00	2.00	2.00	2.02	2.07
Brt	1.00	1.00	0.99	1.01	0.98	0.99	1.00	0.97	1.00	1.03
Cls	0.01	0.01	0.01	0.01	0.01	0.01	0.01	0.03	0.01	0.01

Probe analysis	CNF31860_2_O	CNF31860_2_P	CNF31860_2_Q	CNF31860_2_R	CNF31860_2_S	CNF31860_2_T	CNF31860_2_U	CNF31860_2_V	CNF31860_3_A	CNF31860_3_B
Drill hole	LM11-68	LM11-68	LM11-68	LM11-68	LM11-68	LM11-68	LM11-68	LM11-68	LM11-68	LM11-68
Sample	CNF31860	CNF31860	CNF31861	CNF31862	CNF31863	CNF31864	CNF31865	CNF31866	CNF31847	CNF31847
Depth (m)	197.95	197.95	197.95	197.95	197.95	197.95	197.95	197.95	197.95	197.95
Barite texture	Granular	Granular	Granular	Granular	Granular	Granular	Granular	Granular	Granular	Granular
Mineral assemblage type	Type 1 ± 2B ± 2A	Type 1 ± 2B ± 2A	Type 1 ± 2B ± 2A	Type 1 ± 2B ± 2A	Type 1 ± 2B ± 2A	Type 1 ± 2B ± 2A	Type 1 ± 2B ± 2A	Type 1 ± 2B ± 2A	Type 1 ± 2B ± 2A	Type 1 ± 2B ± 2A
Specimen	15	16	17	18	19	20	21	22	1	2
SO_3 *wt.%*	34.18	34.58	34.47	34.45	34.59	34.73	34.74	34.60	34.33	34.20
BaO	65.20	64.00	64.78	65.35	64.20	66.10	65.35	64.20	65.36	64.96
SrO	0.88	0.94	1.46	0.82	2.09	0.30	1.29	1.01	0.50	0.82
Na_2O	0.07	0.14	0.08	0.06	0.18	0.14	0.09	0.15	0.16	0.14
CaO	0.02	0.01	0.00	0.01	-	0.00	0.01	0.01	-	0.01
K_2O	-	0.01	-	-	-	-	0.00	0.01	-	-
SiO_2	0.05	-	-	-	-	-	-	0.04	-	-
FeO	-	-	0.02	-	-	0.01	-	-	-	-
ZnO	-	0.14	0.04	-	-	0.05	0.17	0.02	-	-
PbO	-	-	-	-	-	0.05	-	0.02	-	-
Total	100.40	99.82	100.85	100.69	101.06	101.39	101.66	100.05	100.34	100.13
S *apfu*	1.00	1.00	1.00	1.00	1.00	1.00	1.00	1.00	1.00	1.00
Ba	1.00	0.97	0.98	0.99	0.97	0.99	0.98	0.97	0.99	0.99
Sr	0.02	0.02	0.03	0.02	0.05	0.01	0.03	0.02	0.01	0.02
Na	0.00	0.01	0.00	0.00	0.01	0.01	0.00	0.01	0.01	0.01
Ca	0.00	0.00	0.00	0.00	0.00	0.00	0.00	0.00	0.00	0.00
K	0.00	0.00	0.00	0.00	0.00	0.00	0.00	0.00	0.00	0.00
Si	0.00	0.00	0.00	0.00	0.00	0.00	0.00	0.00	0.00	0.00
Fe	0.00	0.00	0.00	0.00	0.00	0.00	0.00	0.00	0.00	0.00
Zn	0.00	0.00	0.00	0.00	0.00	0.00	0.00	0.00	0.00	0.00
Pb	0.00	0.00	0.00	0.00	0.00	0.00	0.00	0.00	0.00	0.00
Total	2.02	1.99	2.02	2.01	2.02	2.01	2.02	2.00	2.01	2.01
Brt	0.99	0.97	0.99	0.99	0.98	1.01	0.99	0.98	0.99	0.99
Cls	0.01	0.01	0.02	0.01	0.03	0.00	0.02	0.02	0.01	0.01

Probe analysis	CNF31860_3_C	CNF31860_3_D	CNF31860_3_E	CNF31860_3_F	CNF31860_3_G	CNF31860_3_H	CNF31860_3_I	CNF31861_2_A	CNF31861_2_B	CNF31861_2_C
Drill hole	LM11-68	LM11-68	LM11-68	LM11-68	LM11-68	LM11-68	LM11-68	LM11-68	LM11-68	LM11-68
Sample	CNF31847	CNF31847	CNF31847	CNF31847	CNF31847	CNF31847	CNF31847	CNF31861	CNF31861	CNF31861
Depth (m)	197.95	197.95	197.95	197.95	197.95	197.95	197.95	200.00	200.00	200.00
Barite texture	Granular	Granular	Granular	Granular	Granular	Granular	Granular	Bladed/tabular	Bladed/tabular	Bladed/tabular
Mineral assemblage type	Type 1 ± 2B ± 2A	Type 1 ± 2B ± 2A	Type 1 ± 2B ± 2A	Type 1 ± 2B ± 2A	Type 1 ± 2B ± 2A	Type 1 ± 2B ± 2A	Type 1 ± 2B ± 2A	Type 1 ± 2A ± 2B	Type 1 ± 2A ± 2B	Type 1 ± 2A ± 2B
Specimen	3	4	5	6	7	8	9	1	2	3
SO_3 *wt.%*	34.12	34.21	34.79	34.45	34.16	34.55	33.98	35.59	34.55	34.72
BaO	65.10	64.27	63.89	65.15	65.62	65.75	64.61	62.25	62.96	61.76
SrO	0.59	0.85	0.99	0.85	0.36	0.51	0.66	3.74	2.44	2.79
Na_2O	0.16	0.15	0.12	0.13	0.06	0.23	0.14	0.20	0.06	0.21
CaO	0.01	0.00	0.00	-	0.01	0.01	-	0.01	0.08	0.03
K_2O	-	-	-	0.01	-	-	-	0.01	0.01	-
SiO_2	-	0.03	-	-	-	0.01	0.04	-	-	-
FeO	-	0.02	-	0.03	0.01	0.05	0.01	-	0.01	-
ZnO	-	0.06	0.05	-	0.03	0.05	-	-	-	-
PbO	0.01	-	-	-	-	-	-	-	-	-
Total	99.99	99.59	99.86	100.62	100.26	101.16	99.43	101.79	100.11	99.51
S *apfu*	1.00	1.00	1.00	1.00	1.00	1.00	1.00	1.00	1.00	1.00
Ba	1.00	0.98	0.96	0.99	1.00	0.99	0.99	0.91	0.95	0.93
Sr	0.01	0.02	0.02	0.02	0.01	0.01	0.01	0.08	0.05	0.06
Na	0.01	0.01	0.00	0.00	0.00	0.01	0.01	0.01	0.00	0.01
Ca	0.00	0.00	0.00	0.00	0.00	0.00	0.00	0.00	0.00	0.00
K	0.00	0.00	0.00	0.00	0.00	0.00	0.00	0.00	0.00	0.00
Si	0.00	0.00	0.00	0.00	0.00	0.00	0.00	0.00	0.00	0.00
Fe	0.00	0.00	0.00	0.00	0.00	0.00	0.00	0.00	0.00	0.00
Zn	0.00	0.00	0.00	0.00	0.00	0.00	0.00	0.00	0.00	0.00
Pb	0.00	0.00	0.00	0.00	0.00	0.00	0.00	0.00	0.00	0.00
Total	2.01	2.01	1.99	2.01	2.01	2.02	2.01	2.00	2.01	2.00
Brt	0.99	0.98	0.97	0.99	1.00	1.00	0.98	0.95	0.96	0.94
Cls	0.01	0.01	0.02	0.01	0.01	0.01	0.01	0.06	0.04	0.04

Probe analysis	CNF31861_2_D	CNF31861_2_E	CNF31861_2_F	CNF31861_2_G	CNF31861_2_H	CNF31861_2_I	CNF31861_2_J	CNF31861_2_K	CNF31861_2_L	CNF31861_2_M
Drill hole	LM11-68	LM11-68	LM11-68	LM11-68	LM11-68	LM11-68	LM11-68	LM11-68	LM11-68	LM11-68
Sample	CNF31861	CNF31861	CNF31861	CNF31861	CNF31861	CNF31861	CNF31861	CNF31861	CNF31861	CNF31861
Depth (m)	200.00	200.00	200.00	200.00	200.00	200.00	200.00	200.00	200.00	200.00
Barite texture	Bladed/tabular	Bladed/tabular	Bladed/tabular	Granular	Granular	Granular	Granular	Granular	Granular	Granular
Mineral assemblage type	Type 1 ± 2A ± 2B	Type 1 ± 2A ± 2B	Type 1 ± 2A ± 2B	Type 1 ± 2A ± 2B	Type 1 ± 2A ± 2B	Type 1 ± 2A ± 2B	Type 1 ± 2A ± 2B	Type 1 ± 2A ± 2B	Type 1 ± 2A ± 2B	Type 1 ± 2A ± 2B
Specimen	4	5	6	7	8	9	10	11	12	13
SO_3 *wt.%*	34.79	34.84	35.35	34.23	34.33	34.10	34.28	34.42	34.79	34.62
BaO	62.56	62.87	62.38	65.16	64.41	64.83	65.76	64.77	64.54	64.61
SrO	2.76	2.42	2.95	0.75	0.92	0.95	0.30	0.66	0.81	0.46
Na_2O	0.15	0.08	0.11	0.09	0.16	0.14	0.18	0.22	0.12	0.08
CaO	0.17	0.12	0.09	0.01	-	0.02	0.00	0.01	0.01	-
K_2O	0.01	0.00	0.00	0.01	-	0.00	0.00	0.01	-	0.02
SiO_2	-	-	-	0.01	-	-	0.03	-	0.04	-
FeO	-	0.01	-	-	-	-	-	-	-	0.04
ZnO	0.07	-	0.04	0.01	0.09	-	0.02	-	-	0.05
PbO	-	-	0.01	0.02	-	-	-	-	0.03	-
Total	100.52	100.36	100.94	100.31	99.90	100.04	100.56	100.08	100.35	99.88
S *apfu*	1.00	1.00	1.00	1.00	1.00	1.00	1.00	1.00	1.00	1.00
Ba	0.94	0.94	0.92	0.99	0.98	0.99	1.00	0.98	0.97	0.97
Sr	0.06	0.05	0.06	0.02	0.02	0.02	0.01	0.01	0.02	0.01
Na	0.01	0.00	0.00	0.00	0.01	0.01	0.01	0.01	0.00	0.00
Ca	0.01	0.01	0.00	0.00	0.00	0.00	0.00	0.00	0.00	0.00
K	0.00	0.00	0.00	0.00	0.00	0.00	0.00	0.00	0.00	0.00
Si	0.00	0.00	0.00	0.00	0.00	0.00	0.00	0.00	0.00	0.00
Fe	0.00	0.00	0.00	0.00	0.00	0.00	0.00	0.00	0.00	0.00
Zn	0.00	0.00	0.00	0.00	0.00	0.00	0.00	0.00	0.00	0.00
Pb	0.00	0.00	0.00	0.00	0.00	0.00	0.00	0.00	0.00	0.00
Total	2.01	2.00	1.99	2.02	2.01	2.02	2.02	2.00	1.99	1.99
Brt	0.95	0.96	0.95	0.99	0.98	0.99	1.00	0.99	0.98	0.98
Cls	0.04	0.04	0.04	0.01	0.01	0.01	0.00	0.01	0.01	0.01

Probe analysis	CNF31861_2_N	CNF31861_2_O	CNF31861_2_P	CNF31861_2_Q	CNF31861_2_R	CNF31861_2_S	CNF31865_1_A	CNF31865_1_B	CNF31865_1_C	CNF31865_1_D
Drill hole	LM11-68	LM11-68	LM11-68	LM11-68	LM11-68	LM11-68	LM14-96	LM14-96	LM14-96	LM14-96
Sample	CNF31861	CNF31861	CNF31861	CNF31861	CNF31861	CNF31861	CNF31865	CNF31865	CNF31865	CNF31865
Depth (m)	200.00	200.00	200.00	200.00	200.00	200.00	309.90	309.90	309.90	309.90
Barite texture	Granular	Granular	Granular	Tabular	Tabular	Tabular	Tabular	Tabular	Tabular	Tabular
Mineral assemblage type	Type 1 ± 2A ± 2B	Type 1 ± 2A ± 2B	Type 1 ± 2A ± 2B	Type 1 ± 2A ± 2B	Type 1 ± 2A ± 2B	Type 1 ± 2A ± 2B	Type 1 ± 2A	Type 1 ± 2A	Type 1 ± 2A	Type 1 ± 2A
Specimen	14	15	16	17	18	19	1	2	3	4
SO_3 *wt.%*	34.73	34.49	34.60	34.50	34.05	34.33	34.24	34.24	34.50	34.11
BaO	63.20	65.86	64.46	63.08	64.45	64.80	65.73	64.38	64.42	64.46
SrO	1.11	0.76	0.69	2.24	1.10	0.36	0.26	0.86	1.22	1.03
Na_2O	0.13	0.11	0.18	0.18	0.19	0.21	0.06	0.18	0.08	0.07
CaO	0.04	-	0.00	0.07	0.01	-	0.01	0.01	-	0.04
K_2O	0.01	-	0.02	0.02	0.01	0.02	-	-	0.00	-
SiO_2	-	0.01	-	0.05	-	-	0.01	-	0.02	0.04
FeO	0.01	-	-	-	0.02	0.01	-	0.02	-	-
ZnO	0.05	-	-	0.07	-	0.02	-	-	-	-
PbO	-	0.01	0.02	0.06	-	-	0.04	-	0.01	-
Total	99.27	101.25	99.97	100.28	99.82	99.74	100.35	99.69	100.25	99.77
S *apfu*	1.00	1.00	1.00	1.00	1.00	1.00	1.00	1.00	1.00	1.00
Ba	0.95	1.00	0.97	0.95	0.99	0.99	1.00	0.98	0.98	0.99
Sr	0.02	0.02	0.02	0.05	0.02	0.01	0.01	0.02	0.03	0.02
Na	0.00	0.00	0.01	0.01	0.01	0.01	0.00	0.01	0.00	0.00
Ca	0.00	0.00	0.00	0.00	0.00	0.00	0.00	0.00	0.00	0.00
K	0.00	0.00	0.00	0.00	0.00	0.00	0.00	0.00	0.00	0.00
Si	0.00	0.00	0.00	0.00	0.00	0.00	0.00	0.00	0.00	0.00
Fe	0.00	0.00	0.00	0.00	0.00	0.00	0.00	0.00	0.00	0.00
Zn	0.00	0.00	0.00	0.00	0.00	0.00	0.00	0.00	0.00	0.00
Pb	0.00	0.00	0.00	0.00	0.00	0.00	0.00	0.00	0.00	0.00
Total	1.98	2.02	1.99	2.02	2.02	2.00	2.01	2.01	2.01	2.01
Brt	0.96	1.00	0.98	0.96	0.98	0.99	1.00	0.98	0.98	0.98
Cls	0.02	0.01	0.01	0.03	0.02	0.01	0.00	0.01	0.02	0.02

Probe analysis	CNF31865_1_E	CNF31865_1_F	CNF31865_1_G	CNF31865_1_H	CNF31865_1_I	CNF31865_1_J	CNF31865_1_K	CNF31865_1_L	CNF31865_1_M	CNF31865_1_N
Drill hole	LM14-96	LM14-96	LM14-96	LM14-96	LM14-96	LM14-96	LM14-96	LM14-96	LM14-96	LM14-96
Sample	CNF31865	CNF31865	CNF31865	CNF31865	CNF31865	CNF31865	CNF31865	CNF31865	CNF31865	CNF31865
Depth (m)	309.90	309.90	309.90	309.90	309.90	309.90	309.90	309.90	309.90	309.90
Barite texture	Tabular	Tabular	Tabular	Tabular	Tabular	Granular	Granular	Granular	Granular	Granular
Mineral assemblage type	Type 1 ± 2A	Type 1 ± 2A	Type 1 ± 2A	Type 1 ± 2A	Type 1 ± 2A	Type 1 ± 2A	Type 1 ± 2A	Type 1 ± 2A	Type 1 ± 2A	Type 1 ± 2A
Specimen	5	6	7	8	9	10	11	12	13	14
SO_3 *wt.%*	33.94	34.69	35.36	34.37	34.54	34.02	33.84	34.25	34.05	34.18
BaO	63.87	64.05	62.05	63.09	63.00	64.50	64.67	64.54	64.94	64.35
SrO	1.68	1.31	2.76	1.84	1.46	1.15	1.00	1.16	1.06	1.10
Na_2O	0.13	0.07	0.19	0.15	0.14	0.08	0.04	0.08	0.03	0.10
CaO	-	0.02	0.01	0.01	0.05	0.01	-	-	0.01	0.01
K_2O	-	-	-	-	0.02	-	0.01	0.00	0.01	0.02
SiO_2	-	-	-	0.02	-	-	0.02	0.05	-	-
FeO	0.03	-	-	0.02	0.01	-	-	-	0.02	0.02
ZnO	0.08	-	-	-	-	-	0.04	0.02	-	-
PbO	-	-	0.06	0.03	-	-	-	-	0.01	-
Total	99.72	100.14	100.43	99.53	99.22	99.76	99.62	100.10	100.13	99.78
S *apfu*	1.00	1.00	1.00	1.00	1.00	1.00	1.00	1.00	1.00	1.00
Ba	0.98	0.96	0.92	0.96	0.95	0.99	1.00	0.98	1.00	0.98
Sr	0.04	0.03	0.06	0.04	0.03	0.03	0.02	0.03	0.02	0.02
Na	0.00	0.00	0.01	0.01	0.01	0.00	0.00	0.00	0.00	0.00
Ca	0.00	0.00	0.00	0.00	0.00	0.00	0.00	0.00	0.00	0.00
K	0.00	0.00	0.00	0.00	0.00	0.00	0.00	0.00	0.00	0.00
Si	0.00	0.00	0.00	0.00	0.00	0.00	0.00	0.00	0.00	0.00
Fe	0.00	0.00	0.00	0.00	0.00	0.00	0.00	0.00	0.00	0.00
Zn	0.00	0.00	0.00	0.00	0.00	0.00	0.00	0.00	0.00	0.00
Pb	0.00	0.00	0.00	0.00	0.00	0.00	0.00	0.00	0.00	0.00
Total	2.03	1.99	1.98	2.01	1.99	2.02	2.02	2.01	2.02	2.01
Brt	0.97	0.97	0.94	0.96	0.96	0.98	0.98	0.98	0.99	0.98
Cls	0.03	0.02	0.04	0.03	0.02	0.02	0.02	0.02	0.02	0.02

Probe analysis	CNF31865_1_O	CNF31865_1_P	CNF31865_1_Q	CNF31865_1_R	CNF31865_2_A	CNF31865_2_B	CNF31865_2_C	CNF31865_2_D	CNF31865_2_E	CNF31865_2_F
Drill hole	LM14-96	LM14-96	LM14-96	LM14-96	LM14-96	LM14-96	LM14-96	LM14-96	LM14-96	LM14-96
Sample	CNF31865	CNF31865	CNF31865	CNF31865	CNF31865	CNF31865	CNF31865	CNF31865	CNF31865	CNF31865
Depth (m)	309.90	309.90	309.90	309.90	309.90	309.90	309.90	309.90	309.90	309.90
Barite texture	Granular	Granular	Granular	Granular	Granular	Granular	Granular	Granular	Granular	Granular
Mineral assemblage type	Type 1 ± 2A	Type 1 ± 2A	Type 1 ± 2A	Type 1 ± 2A	Type 1 ± 2B	Type 1 ± 2B	Type 1 ± 2B	Type 1 ± 2B	Type 1 ± 2B	Type 1 ± 2B
Specimen	15	16	17	18	1	2	3	4	5	6
SO_3 *wt.%*	34.13	34.33	34.49	34.46	34.27	34.28	34.05	33.99	34.24	34.04
BaO	65.25	65.41	65.08	64.56	64.94	66.21	65.75	64.07	66.34	66.08
SrO	1.00	1.05	0.92	1.27	0.83	0.19	0.90	0.95	0.43	0.40
Na_2O	0.12	0.17	0.14	0.12	0.18	0.18	0.10	0.22	0.08	0.16
CaO	0.01	0.02	-	0.00	-	0.01	-	0.02	0.01	0.02
K_2O	-	0.01	0.01	-	0.01	0.00	-	-	-	-
SiO_2	-	-	-	-	0.03	-	-	-	0.01	-
FeO	-	-	-	-	-	-	0.01	-	-	0.03
ZnO	-	0.05	0.02	0.05	-	-	-	-	0.05	0.07
PbO	-	0.03	0.01	-	-	0.05	-	0.01	-	-
Total	100.52	101.06	100.68	100.46	100.25	100.93	100.81	99.27	101.17	100.79
S *apfu*	1.00	1.00	1.00	1.00	1.00	1.00	1.00	1.00	1.00	1.00
Ba	1.00	0.99	0.99	0.98	0.99	1.01	1.01	0.98	1.01	1.01
Sr	0.02	0.02	0.02	0.03	0.02	0.00	0.02	0.02	0.01	0.01
Na	0.00	0.01	0.01	0.00	0.01	0.01	0.00	0.01	0.00	0.01
Ca	0.00	0.00	0.00	0.00	0.00	0.00	0.00	0.00	0.00	0.00
K	0.00	0.00	0.00	0.00	0.00	0.00	0.00	0.00	0.00	0.00
Si	0.00	0.00	0.00	0.00	0.00	0.00	0.00	0.00	0.00	0.00
Fe	0.00	0.00	0.00	0.00	0.00	0.00	0.00	0.00	0.00	0.00
Zn	0.00	0.00	0.00	0.00	0.00	0.00	0.00	0.00	0.00	0.00
Pb	0.00	0.00	0.00	0.00	0.00	0.00	0.00	0.00	0.00	0.00
Total	2.02	2.03	2.01	2.01	2.01	2.02	2.03	2.01	2.03	2.03
Brt	0.99	1.00	0.99	0.98	0.99	1.01	1.00	0.98	1.01	1.01
Cls	0.02	0.02	0.01	0.02	0.01	0.00	0.01	0.01	0.01	0.01

Probe analysis	CNF31865_2_G	CNF31865_2_H	CNF31865_2_I	CNF31865_2_J	CNF31865_2_K	CNF31865_2_L	CNF31865_2_M	CNF31865_2_N	CNF31865_2_O	CNF31865_2_P
Drill hole	LM14-96	LM14-96	LM14-96	LM14-96	LM14-96	LM14-96	LM14-96	LM14-96	LM14-96	LM14-96
Sample	CNF31865	CNF31865	CNF31865	CNF31865	CNF31865	CNF31865	CNF31865	CNF31865	CNF31865	CNF31865
Depth (m)	309.90	309.90	309.90	309.90	309.90	309.90	309.90	309.90	309.90	309.90
Barite texture	Tabular	Bladed	Bladed	Bladed	Bladed	Bladed	Granular	Granular	Granular	Granular
Mineral assemblage type	Type 1 ± 2B	Type 1 ± 2B	Type 1 ± 2B	Type 1 ± 2B	Type 1 ± 2B	Type 1 ± 2B	Type 1 ± 2B	Type 1 ± 2B	Type 1 ± 2B	Type 1 ± 2B
Specimen	7	8	9	10	11	12	13	14	15	16
SO_3 *wt.%*	33.87	34.21	34.67	33.72	34.35	34.23	34.22	34.09	33.91	34.22
BaO	63.61	63.73	64.34	65.26	65.10	65.95	64.68	64.66	64.93	65.33
SrO	1.96	1.77	1.23	0.64	1.08	0.15	0.92	0.83	0.63	0.90
Na_2O	0.15	0.16	0.12	0.22	0.24	0.16	0.13	0.15	0.07	0.04
CaO	0.01	0.02	0.00	0.01	0.02	-	-	-	0.01	0.02
K_2O	0.01	0.01	-	0.01	-	0.01	0.01	-	0.00	-
SiO_2	-	0.02	-	-	0.01	-	-	-	0.04	-
FeO	-	-	-	-	0.01	0.01	-	0.01	-	-
ZnO	0.09	-	0.02	0.03	-	-	0.05	-	0.02	-
PbO	0.04	-	-	0.03	0.04	-	0.03	-	-	0.02
Total	99.74	99.93	100.37	99.93	100.84	100.52	100.04	99.75	99.61	100.53
S *apfu*	1.00	1.00	1.00	1.00	1.00	1.00	1.00	1.00	1.00	1.00
Ba	0.98	0.97	0.97	1.01	0.99	1.01	0.99	0.99	1.00	1.00
Sr	0.04	0.04	0.03	0.01	0.02	0.00	0.02	0.02	0.01	0.02
Na	0.01	0.01	0.00	0.01	0.01	0.01	0.00	0.01	0.00	0.00
Ca	0.00	0.00	0.00	0.00	0.00	0.00	0.00	0.00	0.00	0.00
K	0.00	0.00	0.00	0.00	0.00	0.00	0.00	0.00	0.00	0.00
Si	0.00	0.00	0.00	0.00	0.00	0.00	0.00	0.00	0.00	0.00
Fe	0.00	0.00	0.00	0.00	0.00	0.00	0.00	0.00	0.00	0.00
Zn	0.00	0.00	0.00	0.00	0.00	0.00	0.00	0.00	0.00	0.00
Pb	0.00	0.00	0.00	0.00	0.00	0.00	0.00	0.00	0.00	0.00
Total	2.03	2.02	2.00	2.03	2.02	2.01	2.01	2.01	2.02	2.02
Brt	0.97	0.97	0.98	0.99	0.99	1.00	0.98	0.98	0.99	0.99
Cls	0.03	0.03	0.02	0.01	0.02	0.00	0.01	0.01	0.01	0.01

Probe analysis	CNF31865_2_Q	CNF31865_2_R	CNF31874_1_A	CNF31874_1_B	CNF31874_1_C	CNF31874_1_D	CNF31874_1_E	CNF31874_1_F	CNF31874_1_G	CNF31875_1_A
Drill hole	LM14-97	LM14-98	LM13-82	LM13-82	LM13-82	LM13-82	LM13-82	LM13-82	LM13-82	LM13-82
Sample	CNF31866	CNF31867	CNF31874	CNF31874	CNF31874	CNF31874	CNF31874	CNF31874	CNF31874	CNF31875
Depth (m)	309.90	309.90	340.80	340.80	340.80	340.80	340.80	340.80	340.80	342.40
Barite texture	Granular	Granular	Bladed	Bladed	Bladed	Bladed	Bladed	Bladed	Bladed	Granular
Mineral assemblage type	Type 1 ± 2B	Type 1 ± 2B	Type 1 ± 2B	Type 1 ± 2B	Type 1 ± 2B	Type 1 ± 2B	Type 1 ± 2B	Type 1 ± 2B	Type 1 ± 2B	Type 1
Specimen	17	18	1	2	3	4	5	6	7	1
SO_3 *wt.%*	34.07	34.70	34.77	34.95	35.01	35.64	35.27	34.35	34.89	34.71
BaO	64.61	64.46	65.25	65.32	65.72	65.01	64.69	65.11	65.62	65.73
SrO	0.87	0.87	0.34	0.34	0.39	0.60	0.45	0.38	0.53	0.65
Na_2O	0.15	0.13	0.26	0.09	0.09	0.15	0.17	0.04	0.07	0.13
CaO	0.01	0.03	0.00	0.01	0.01	0.07	-0.01	-0.01	0.00	-
K_2O	0.00	-	-	-	0.01	0.01	-	0.00	0.00	-
SiO_2	-	-	0.05	0.03	-	0.02	-	-	0.04	0.01
FeO	-	0.02	-	0.02	-	-	-	0.01	-	-
ZnO	-	-	0.10	0.02	-	-	-	-	-	0.03
PbO	-	-	-	-	-	-	-	-	-	0.03
Total	99.71	100.21	100.77	100.79	101.23	101.50	100.57	99.89	101.16	101.28
S *apfu*	1.00	1.00	1.00	1.00	1.00	1.00	1.00	1.00	1.00	1.00
Ba	0.99	0.97	0.98	0.98	0.98	0.95	0.96	0.99	0.98	0.99
Sr	0.02	0.02	0.01	0.01	0.01	0.01	0.01	0.01	0.01	0.01
Na	0.01	0.00	0.01	0.00	0.00	0.01	0.01	0.00	0.00	0.00
Ca	0.00	0.00	0.00	0.00	0.00	0.00	0.00	0.00	0.00	0.00
K	0.00	0.00	0.00	0.00	0.00	0.00	0.00	0.00	0.00	0.00
Si	0.00	0.00	0.00	0.00	0.00	0.00	0.00	0.00	0.00	0.00
Fe	0.00	0.00	0.00	0.00	0.00	0.00	0.00	0.00	0.00	0.00
Zn	0.00	0.00	0.00	0.00	0.00	0.00	0.00	0.00	0.00	0.00
Pb	0.00	0.00	0.00	0.00	0.00	0.00	0.00	0.00	0.00	0.00
Total	2.01	1.99	2.00	1.99	1.99	1.97	1.97	2.00	2.00	2.01
Brt	0.98	0.98	0.99	0.99	1.00	0.99	0.98	0.99	1.00	1.00
Cls	0.01	0.01	0.01	0.01	0.01	0.01	0.01	0.01	0.01	0.01

Probe analysis	CNF31875_1_B	CNF31875_1_C	CNF31875_1_D	CNF31875_1_E	CNF31875_1_F	CNF31875_1_G	CNF31875_1_H	CNF31875_1_I	CNF31875_1_J	CNF31875_1_K
Drill hole	LM13-82	LM13-82	LM13-82	LM13-82	LM13-82	LM13-82	LM13-82	LM13-82	LM13-82	LM13-82
Sample	CNF31875	CNF31875	CNF31875	CNF31875	CNF31875	CNF31875	CNF31875	CNF31875	CNF31875	CNF31875
Depth (m)	342.40	342.40	342.40	342.40	342.40	342.40	342.40	342.40	342.40	342.40
Barite texture	Granular	Granular	Tabular	Tabular	Tabular	Tabular	Tabular	Tabular	Tabular	Tabular
Mineral assemblage type	Type 1	Type 1	Type 1	Type 1	Type 1	Type 1	Type 1	Type 1	Type 1	Type 1
Specimen	2	3	4	5	6	7	8	9	10	11
SO_3 *wt.%*	34.35	34.68	34.64	34.77	34.30	34.72	34.78	34.96	34.49	34.90
BaO	66.03	63.95	65.76	64.61	63.90	64.75	66.20	64.67	65.15	64.51
SrO	0.39	0.47	0.46	0.80	0.49	0.38	0.31	0.67	0.24	0.50
Na_2O	0.19	0.23	0.25	0.02	0.20	0.21	0.17	0.10	0.19	0.20
CaO	0.02	0.02	0.02	0.01	-	0.01	-	0.01	0.01	0.01
K_2O	0.01	0.01	0.02	0.00	0.01	-	-	-	0.00	-
SiO_2	-	0.02	-	-	0.01	0.04	-	-	-	-
FeO	-	0.01	-	-	-	-	-	0.02	-	-
ZnO	-	-	0.05	0.08	-	0.03	-	0.03	0.02	-
PbO	-	0.01	-	0.03	-	-	0.01	-	-	-
Total	101.00	99.41	101.20	100.34	98.91	100.14	101.46	100.46	100.10	100.11
S *apfu*	1.00	1.00	1.00	1.00	1.00	1.00	1.00	1.00	1.00	1.00
Ba	1.00	0.96	0.99	0.97	0.97	0.97	0.99	0.97	0.99	0.97
Sr	0.01	0.01	0.01	0.02	0.01	0.01	0.01	0.01	0.01	0.01
Na	0.01	0.01	0.01	0.00	0.01	0.01	0.01	0.00	0.01	0.01
Ca	0.00	0.00	0.00	0.00	0.00	0.00	0.00	0.00	0.00	0.00
K	0.00	0.00	0.00	0.00	0.00	0.00	0.00	0.00	0.00	0.00
Si	0.00	0.00	0.00	0.00	0.00	0.00	0.00	0.00	0.00	0.00
Fe	0.00	0.00	0.00	0.00	0.00	0.00	0.00	0.00	0.00	0.00
Zn	0.00	0.00	0.00	0.00	0.00	0.00	0.00	0.00	0.00	0.00
Pb	0.00	0.00	0.00	0.00	0.00	0.00	0.00	0.00	0.00	0.00
Total	2.02	1.98	2.01	1.99	1.99	1.99	2.00	1.99	2.00	1.98
Brt	1.01	0.97	1.00	0.98	0.97	0.99	1.01	0.98	0.99	0.98
Cls	0.01	0.01	0.01	0.01	0.01	0.01	0.00	0.01	0.00	0.01

Probe analysis	CNF31875_1_L	CNF31875_1_M	CNF31875_1_N	CNF31875_1_O	CNF31875_1_P	CNF31875_1_Q	CNF31875_1_R	CNF31877_1_A	CNF31877_1_B	CNF31877_1_C
Drill hole	LM13-82	LM13-82	LM13-82	LM13-82	LM13-82	LM13-82	LM13-82	LM11-66	LM11-66	LM11-66
Sample	CNF31875	CNF31875	CNF31875	CNF31875	CNF31875	CNF31875	CNF31875	CNF31877	CNF31877	CNF31877
Depth (m)	342.40	342.40	342.40	342.40	342.40	342.40	342.40	164.40	164.40	164.40
Barite texture	Tabular	Granular	Granular	Granular	Granular	Granular	Granular	Vein	Vein	Vein
Mineral assemblage type	Type 1	Type 1	Type 1	Type 1	Type 1	Type 1	Type 1	Type 4	Type 4	Type 4
Specimen	12	13	14	15	16	17	18	1	2	3
SO_3 *wt.%*	34.56	34.23	34.80	34.87	34.74	35.18	34.77	35.14	35.26	35.08
BaO	65.31	63.95	64.30	65.00	64.37	65.28	64.91	65.51	64.35	64.92
SrO	0.45	0.33	0.63	0.04	0.42	0.35	0.36	0.57	0.68	0.67
Na_2O	0.20	0.08	0.20	0.09	0.18	0.11	0.17	0.04	0.10	0.21
CaO	-	0.01	0.01	0.02	-	0.02	0.02	0.01	-	0.01
K_2O	0.01	-	-	-	-	-	-	0.01	-	-
SiO_2	-	-	0.05	-	-	-	0.04	0.02	-	-
FeO	-	0.03	-	-	-	0.01	-	0.04	0.05	-
ZnO	-	-	0.01	-	-	0.04	-	0.06	0.05	-
PbO	-	0.03	-	-	-	-	0.06	0.06	-	-
Total	100.53	98.66	100.01	100.01	99.71	100.99	100.32	101.46	100.48	100.88
S *apfu*	1.00	1.00	1.00	1.00	1.00	1.00	1.00	1.00	1.00	1.00
Ba	0.99	0.98	0.96	0.97	0.97	0.97	0.97	0.97	0.95	0.97
Sr	0.01	0.01	0.01	0.00	0.01	0.01	0.01	0.01	0.01	0.01
Na	0.01	0.00	0.01	0.00	0.01	0.00	0.01	0.00	0.00	0.01
Ca	0.00	0.00	0.00	0.00	0.00	0.00	0.00	0.00	0.00	0.00
K	0.00	0.00	0.00	0.00	0.00	0.00	0.00	0.00	0.00	0.00
Si	0.00	0.00	0.00	0.00	0.00	0.00	0.00	0.00	0.00	0.00
Fe	0.00	0.00	0.00	0.00	0.00	0.00	0.00	0.00	0.00	0.00
Zn	0.00	0.00	0.00	0.00	0.00	0.00	0.00	0.00	0.00	0.00
Pb	0.00	0.00	0.00	0.00	0.00	0.00	0.00	0.00	0.00	0.00
Total	2.00	1.98	1.99	1.98	1.98	1.98	1.99	1.99	1.97	1.99
Brt	0.99	0.97	0.98	0.99	0.98	0.99	0.99	1.00	0.98	0.99
Cls	0.01	0.01	0.01	0.00	0.01	0.01	0.01	0.01	0.01	0.01

Probe analysis	CNF31877_1_D	CNF31877_1_E	CNF31877_2_A	CNF31877_2_B	CNF31877_2_C	CNF31877_2_D	CNF31877_2_E	CNF31810_1_A	CNF31810_1_B	CNF31810_1_C
Drill hole	LM11-66	LM11-66	LM11-66	LM11-66	LM11-66	LM11-66	LM11-66	LM10-43	LM10-43	LM10-43
Sample	CNF31877	CNF31877	CNF31877	CNF31877	CNF31877	CNF31877	CNF31877	CNF31810	CNF31810	CNF31810
Depth (m)	164.40	164.40	164.40	164.40	164.40	164.40	164.40	218.75	218.75	218.75
Barite texture	Vein	Vein	Interstitial	Interstitial	Interstitial	Interstitial	Interstitial	Bladed	Bladed	Bladed
Mineral assemblage type	Type 4	Type 4	Type 4	Type 4	Type 4	Type 4	Type 4	Type 1 ±2B	Type 1 ±2B	Type 1 ±2B
Specimen	4	5	1	2	3	4	5	1	2	3
SO_3 *wt.%*	34.83	34.57	34.55	34.97	34.93	34.41	34.75	34.72	34.95	34.85
BaO	65.58	65.21	65.47	64.49	65.46	65.76	65.01	65.72	63.81	63.79
SrO	0.41	0.41	0.29	0.28	0.34	0.13	0.13	0.54	0.62	1.18
Na_2O	0.13	0.17	0.12	0.24	0.17	0.10	0.04	0.22	0.39	0.30
CaO	0.01	0.01	0.00	0.00	-	0.01	0.01	0.00	0.03	0.03
K_2O	-	-	0.01	-	-	-	-	0.02	0.01	0.01
SiO_2	0.02	0.02	0.01	0.03	-	-	0.02	-	-	0.01
FeO	-	0.02	-	-	0.02	0.01	-	-	0.01	0.01
ZnO	-	0.04	0.06	0.04	0.04	-	0.03	-	0.10	-
PbO	-	0.03	-	0.05	-	0.06	-	-	0.02	0.01
Total	100.98	100.48	100.50	100.11	100.96	100.47	100.00	101.23	99.94	100.19
S *apfu*	1.00	1.00	1.00	1.00	1.00	1.00	1.00	1.00	1.00	1.00
Ba	0.98	0.98	0.97	0.95	0.97	0.98	0.98	0.99	0.95	0.96
Sr	0.01	0.01	0.01	0.01	0.01	0.00	0.00	0.01	0.01	0.03
Na	0.00	0.01	0.00	0.01	0.01	0.00	0.00	0.01	0.01	0.01
Ca	0.00	0.00	0.00	0.00	0.00	0.00	0.00	0.00	0.00	0.00
K	0.00	0.00	0.00	0.00	0.00	0.00	0.00	0.00	0.00	0.00
Si	0.00	0.00	0.00	0.00	0.00	0.00	0.00	0.00	0.00	0.00
Fe	0.00	0.00	0.00	0.00	0.00	0.00	0.00	0.00	0.00	0.00
Zn	0.00	0.00	0.00	0.00	0.00	0.00	0.00	0.00	0.00	0.00
Pb	0.00	0.00	0.00	0.00	0.00	0.00	0.00	0.00	0.00	0.00
Total	2.00	2.00	1.99	1.97	1.98	1.99	1.99	2.01	1.99	2.00
Brt	1.00	0.99	1.00	0.98	1.00	1.00	0.99	1.00	0.97	0.97
Cls	0.01	0.01	0.00	0.00	0.01	0.00	0.00	0.01	0.01	0.02

Probe analysis	CNF31810_1_D	CNF31810_1_E	CNF31810_1_F	CNF31810_1_G	CNF31810_1_H	CNF31810_1_I	CNF31810_1_J	CNF31810_1_K	CNF31810_1_L	CNF31810_1_M
Drill hole	LM10-43	LM10-43	LM10-43	LM10-43	LM10-43	LM10-43	LM10-43	LM10-43	LM10-43	LM10-43
Sample	CNF31810	CNF31810	CNF31810	CNF31810	CNF31810	CNF31810	CNF31810	CNF31810	CNF31810	CNF31810
Depth (m)	218.75	218.75	218.75	218.75	218.75	218.75	218.75	218.75	218.75	218.75
Barite texture	Bladed	Bladed	Bladed	Bladed	Bladed	Bladed	Bladed	Bladed	Bladed	Bladed
Mineral assemblage type	Type 1 ±2B	Type 1 ±2B	Type 1 ±2B	Type 1 ±2B	Type 1 ±2B	Type 1 ±2B	Type 1 ±2B	Type 1 ±2B	Type 1 ±2B	Type 1 ±2B
Specimen	4	5	6	7	8	9	10	11	12	13
SO_3 *wt.%*	34.95	34.63	34.80	34.46	34.40	35.16	34.52	34.55	34.91	34.44
BaO	65.29	65.26	64.49	65.24	64.33	64.51	64.88	63.68	65.55	63.56
SrO	0.81	0.57	0.49	0.47	0.51	0.81	0.67	0.71	0.84	0.77
Na_2O	0.27	0.42	0.34	0.33	0.24	0.44	0.40	0.36	0.34	0.40
CaO	0.01	0.02	0.13	0.03	0.10	0.01	0.02	0.01	0.02	0.02
K_2O	0.01	-	0.01	0.01	0.02	0.02	-	0.01	-	0.02
SiO_2	0.02	0.05	-	-	0.01	-	0.09	0.02	0.04	-
FeO	0.02	-	-	0.04	-	0.01	-	-	-	0.01
ZnO	0.02	-	-	0.01	0.05	0.04	0.02	-	-	0.05
PbO	-	-	-	0.01	-	-	-	-	0.02	0.01
Total	101.40	100.95	100.26	100.60	99.66	100.99	100.60	99.32	101.72	99.28
S *apfu*	1.00	1.00	1.00	1.00	1.00	1.00	1.00	1.00	1.00	1.00
Ba	0.98	0.98	0.97	0.99	0.98	0.96	0.98	0.96	0.98	0.96
Sr	0.02	0.01	0.01	0.01	0.01	0.02	0.01	0.02	0.02	0.02
Na	0.01	0.02	0.01	0.01	0.01	0.02	0.02	0.01	0.01	0.02
Ca	0.00	0.00	0.01	0.00	0.00	0.00	0.00	0.00	0.00	0.00
K	0.00	0.00	0.00	0.00	0.00	0.00	0.00	0.00	0.00	0.00
Si	0.00	0.00	0.00	0.00	0.00	0.00	0.00	0.00	0.00	0.00
Fe	0.00	0.00	0.00	0.00	0.00	0.00	0.00	0.00	0.00	0.00
Zn	0.00	0.00	0.00	0.00	0.00	0.00	0.00	0.00	0.00	0.00
Pb	0.00	0.00	0.00	0.00	0.00	0.00	0.00	0.00	0.00	0.00
Total	2.01	2.01	2.00	2.01	2.00	1.99	2.02	1.99	2.01	2.00
Brt	0.99	0.99	0.98	0.99	0.98	0.98	0.99	0.97	1.00	0.97
Cls	0.01	0.01	0.01	0.01	0.01	0.01	0.01	0.01	0.01	0.01

Probe analysis	CNF31810_2_A	CNF31810_2_B	CNF31810_2_C	CNF31810_2_D	CNF31810_2_E	CNF31810_2_F	CNF31810_2_G	CNF31810_2_H	CNF31810_2_I	CNF31810_2_J
Drill hole	LM10-43	LM10-43	LM10-43	LM10-43	LM10-43	LM10-43	LM10-43	LM10-43	LM10-43	LM10-43
Sample	CNF31810	CNF31810	CNF31810	CNF31810	CNF31810	CNF31810	CNF31810	CNF31810	CNF31810	CNF31810
Depth (m)	218.75	218.75	218.75	218.75	218.75	218.75	218.75	218.75	218.75	218.75
Barite texture	Bladed	Bladed	Bladed	Bladed	Bladed	Bladed	Bladed	Bladed	Bladed	Bladed
Mineral assemblage type	Type 1 ±2B	Type 1 ±2B	Type 1 ±2B	Type 1 ±2B	Type 1 ±2B	Type 1 ±2B	Type 1 ±2B	Type 1 ±2B	Type 1 ±2B	Type 1 ±2B
Specimen	1	2	3	4	5	6	7	8	9	10
SO_3 *wt.%*	34.94	34.83	34.38	34.61	34.59	34.53	34.64	33.77	34.61	34.95
BaO	65.24	64.29	65.35	65.52	65.60	65.58	64.96	65.54	65.10	65.54
SrO	0.37	0.40	0.35	0.27	0.21	0.31	0.37	0.52	0.45	0.78
Na_2O	0.31	0.32	0.35	0.41	0.19	0.32	0.58	0.50	0.43	0.29
CaO	0.06	0.03	0.02	0.01	0.03	0.02	0.05	0.05	0.06	0.07
K_2O	0.00	0.00	0.01	0.02	0.01	-	-	0.01	0.02	0.00
SiO_2	-	0.08	0.01	0.03	-	0.01	-	0.03	-	-
FeO	0.02	-	-	0.03	0.03	-	0.01	-	-	-
ZnO	-	0.01	-	-	0.02	-	-	0.01	0.01	0.02
PbO	-	-	-	-	-	-	0.04	0.02	0.01	0.01
Total	100.95	99.95	100.46	100.89	100.69	100.77	100.66	100.43	100.69	101.67
S *apfu*	1.00	1.00	1.00	1.00	1.00	1.00	1.00	1.00	1.00	1.00
Ba	0.97	0.96	0.99	0.99	0.99	0.99	0.98	1.01	0.98	0.98
Sr	0.01	0.01	0.01	0.01	0.00	0.01	0.01	0.01	0.01	0.02
Na	0.01	0.01	0.01	0.02	0.01	0.01	0.02	0.02	0.02	0.01
Ca	0.00	0.00	0.00	0.00	0.00	0.00	0.00	0.00	0.00	0.00
K	0.00	0.00	0.00	0.00	0.00	0.00	0.00	0.00	0.00	0.00
Si	0.00	0.00	0.00	0.00	0.00	0.00	0.00	0.00	0.00	0.00
Fe	0.00	0.00	0.00	0.00	0.00	0.00	0.00	0.00	0.00	0.00
Zn	0.00	0.00	0.00	0.00	0.00	0.00	0.00	0.00	0.00	0.00
Pb	0.00	0.00	0.00	0.00	0.00	0.00	0.00	0.00	0.00	0.00
Total	2.00	1.99	2.01	2.01	2.00	2.01	2.01	2.05	2.01	2.01
Brt	0.99	0.98	0.99	1.00	1.00	1.00	0.99	1.00	0.99	1.00
Cls	0.01	0.01	0.01	0.00	0.00	0.00	0.01	0.01	0.01	0.01

Probe analysis	CNF31810_2_K	CNF31810_2_L	CNF31810_2_M	CNF31810_2_N	CNF31810_2_O	CNF31811_1_A	CNF31811_1_B	CNF31811_1_C	CNF31811_1_D	CNF31811_1_E
Drill hole	LM10-43	LM10-43	LM10-43	LM10-43	LM10-43	LM10-43	LM10-43	LM10-43	LM10-43	LM10-43
Sample	CNF31810	CNF31810	CNF31810	CNF31810	CNF31810	CNF31811	CNF31811	CNF31811	CNF31811	CNF31811
Depth (m)	218.75	218.75	218.75	218.75	218.75	209.85	209.85	209.85	209.85	209.85
Barite texture	Bladed	Bladed	Bladed	Bladed	Bladed	Bladed	Bladed	Bladed	Bladed	Bladed
Mineral assemblage type	Type 1 ±2B	Type 1 ±2B	Type 1 ±2B	Type 1 ±2B	Type 1 ±2B	Type 1 ±2B	Type 1 ±2B	Type 1 ±2B	Type 1 ±2B	Type 1 ±2B
Specimen	11	12	13	14	15	1	2	3	4	5
SO_3 *wt.%*	34.24	34.66	34.92	34.57	34.18	34.64	34.59	34.42	34.65	34.28
BaO	64.26	64.83	65.43	64.96	65.38	64.40	65.31	64.24	63.95	64.95
SrO	0.46	0.39	0.31	0.60	0.43	0.94	0.62	1.25	1.33	0.82
Na_2O	0.67	0.32	0.20	0.29	0.43	0.22	0.27	0.23	0.27	0.17
CaO	0.04	0.05	0.02	0.03	0.03	0.03	0.01	0.10	0.07	0.03
K_2O	0.02	0.01	0.02	0.01	0.01	-	-	0.01	-	0.01
SiO_2	-	-	0.02	-	0.02	-	-	-	-	-
FeO	0.03	0.06	-	0.02	-	-	-	0.03	-	0.01
ZnO	0.00	-	0.04	-	-	0.04	-	-	-	-
PbO	-	-	-	-	0.00	-	0.05	-	-	0.02
Total	99.72	100.30	100.95	100.47	100.48	100.27	100.85	100.29	100.27	100.28
S *apfu*	1.00	1.00	1.00	1.00	1.00	1.00	1.00	1.00	1.00	1.00
Ba	0.98	0.98	0.98	0.98	1.00	0.97	0.99	0.97	0.96	0.99
Sr	0.01	0.01	0.01	0.01	0.01	0.02	0.01	0.03	0.03	0.02
Na	0.03	0.01	0.01	0.01	0.02	0.01	0.01	0.01	0.01	0.01
Ca	0.00	0.00	0.00	0.00	0.00	0.00	0.00	0.00	0.00	0.00
K	0.00	0.00	0.00	0.00	0.00	0.00	0.00	0.00	0.00	0.00
Si	0.00	0.00	0.00	0.00	0.00	0.00	0.00	0.00	0.00	0.00
Fe	0.00	0.00	0.00	0.00	0.00	0.00	0.00	0.00	0.00	0.00
Zn	0.00	0.00	0.00	0.00	0.00	0.00	0.00	0.00	0.00	0.00
Pb	0.00	0.00	0.00	0.00	0.00	0.00	0.00	0.00	0.00	0.00
Total	2.02	2.00	1.99	2.01	2.02	2.00	2.01	2.01	2.00	2.02
Brt	0.98	0.99	1.00	0.99	1.00	0.98	0.99	0.98	0.97	0.99
Cls	0.01	0.01	0.00	0.01	0.01	0.01	0.01	0.02	0.02	0.01

Probe analysis	CNF31811_1_F	CNF31811_1_G	CNF31811_1_H	CNF31811_1_I	CNF31811_1_J	CNF31811_1_K	CNF31811_1_L	CNF31811_1_M	CNF31811_1_N	CNF31811_1_O
Drill hole	LM10-43	LM10-43	LM10-43	LM10-43	LM10-43	LM10-43	LM10-43	LM10-43	LM10-43	LM10-43
Sample	CNF31811	CNF31811	CNF31811	CNF31811	CNF31811	CNF31811	CNF31811	CNF31811	CNF31811	CNF31811
Depth (m)	209.85	209.85	209.85	209.85	209.85	209.85	209.85	209.85	209.85	209.85
Barite texture	Bladed	Bladed	Bladed	Bladed	Bladed	Bladed	Bladed	Bladed	Bladed	Bladed
Mineral assemblage type	Type 1 ±2B	Type 1 ±2B	Type 1 ±2B	Type 1 ±2B	Type 1 ±2B	Type 1 ±2B	Type 1 ±2B	Type 1 ±2B	Type 1 ±2B	Type 1 ±2B
Specimen	6	7	8	9	10	11	12	13	14	15
SO_3 *wt.%*	34.58	34.39	34.72	34.06	34.50	34.55	34.29	34.09	34.52	34.53
BaO	65.35	65.01	64.05	65.46	65.29	66.83	66.12	65.14	64.55	66.01
SrO	0.70	0.35	1.18	0.64	1.00	0.60	0.57	0.80	1.23	1.05
Na_2O	0.23	0.28	0.29	0.22	0.19	0.14	0.30	0.31	0.24	0.27
CaO	0.07	0.01	0.11	0.01	0.06	0.02	0.04	0.02	0.04	0.08
K_2O	-	0.00	0.03	0.01	0.01	0.01	0.02	-	0.01	0.01
SiO_2	-	0.01	0.01	-	-	-	0.04	-	-	-
FeO	0.03	-	-	-	-	-	-	-	0.02	-
ZnO	0.09	-	-	0.03	-	-	0.04	0.02	-	-
PbO	-	-	-	-	-	0.02	-	-	-	-
Total	101.04	100.05	100.39	100.45	101.06	102.17	101.42	100.37	100.60	101.96
S *apfu*	1.00	1.00	1.00	1.00	1.00	1.00	1.00	1.00	1.00	1.00
Ba	0.99	0.99	0.96	1.00	0.99	1.01	1.01	1.00	0.98	1.00
Sr	0.02	0.01	0.03	0.01	0.02	0.01	0.01	0.02	0.03	0.02
Na	0.01	0.01	0.01	0.01	0.01	0.01	0.01	0.01	0.01	0.01
Ca	0.00	0.00	0.00	0.00	0.00	0.00	0.00	0.00	0.00	0.00
K	0.00	0.00	0.00	0.00	0.00	0.00	0.00	0.00	0.00	0.00
Si	0.00	0.00	0.00	0.00	0.00	0.00	0.00	0.00	0.00	0.00
Fe	0.00	0.00	0.00	0.00	0.00	0.00	0.00	0.00	0.00	0.00
Zn	0.00	0.00	0.00	0.00	0.00	0.00	0.00	0.00	0.00	0.00
Pb	0.00	0.00	0.00	0.00	0.00	0.00	0.00	0.00	0.00	0.00
Total	2.02	2.00	2.00	2.03	2.02	2.03	2.04	2.03	2.01	2.03
Brt	0.99	0.99	0.97	1.00	0.99	1.02	1.01	0.99	0.98	1.00
Cls	0.01	0.01	0.02	0.01	0.02	0.01	0.01	0.01	0.02	0.02

Probe analysis	CNF31811_1_P	CNF31811_2_A	CNF31811_2_B	CNF31811_2_C	CNF31811_2_D	CNF31811_2_E	CNF31811_2_F	CNF31811_2_G	CNF31811_2_H	CNF31811_2_I
Drill hole	LM10-43	LM10-43	LM10-43	LM10-43	LM10-43	LM10-43	LM10-43	LM10-43	LM10-44	LM10-45
Sample	CNF31811	CNF31811	CNF31811	CNF31811	CNF31811	CNF31811	CNF31811	CNF31811	CNF31811	CNF31811
Depth (m)	209.85	209.85	209.85	209.85	209.85	209.85	209.85	209.85	209.85	209.85
Barite texture	Bladed	Tabular	Tabular	Tabular	Tabular	Tabular	Tabular	Tabular	Tabular	Tabular
Mineral assemblage type	Type 1 ±2B	Type 1 ±2B	Type 1 ±2B	Type 1 ±2B	Type 1 ±2B	Type 1 ±2B	Type 1 ±2B	Type 1 ±2B	Type 1 ±2B	Type 1 ±2B
Specimen	16	1	2	3	4	5	6	7	8	9
SO_3 *wt.%*	34.77	35.05	34.14	34.49	34.55	33.89	34.62	34.19	34.12	34.44
BaO	64.08	64.73	65.01	65.02	65.23	66.43	66.07	64.40	64.28	65.41
SrO	1.24	1.05	0.17	0.70	1.11	0.68	0.56	0.87	0.80	1.03
Na_2O	0.22	0.13	0.26	0.32	0.10	0.27	0.26	0.36	0.27	0.31
CaO	0.07	0.05	0.07	0.05	0.02	0.04	0.08	0.05	0.04	0.03
K_2O	0.00	0.01	0.01	0.02	0.02	0.00	0.01	0.02	0.01	0.01
SiO_2	-	-	-	-	-	-	-	-	-	-
FeO	-	-	0.01	-	-	0.03	0.01	-	-	-
ZnO	0.07	-	0.04	0.04	0.03	-	0.01	0.05	-	-
PbO	-	-	-	-	-	0.03	0.04	-	-	-
Total	100.44	101.02	99.72	100.65	101.05	101.37	101.66	99.95	99.51	101.23
S *apfu*	1.00	1.00	1.00	1.00	1.00	1.00	1.00	1.00	1.00	1.00
Ba	0.96	0.96	0.99	0.98	0.99	1.02	1.00	0.98	0.98	0.99
Sr	0.03	0.02	0.00	0.02	0.02	0.02	0.01	0.02	0.02	0.02
Na	0.01	0.00	0.01	0.01	0.00	0.01	0.01	0.01	0.01	0.01
Ca	0.00	0.00	0.00	0.00	0.00	0.00	0.00	0.00	0.00	0.00
K	0.00	0.00	0.00	0.00	0.00	0.00	0.00	0.00	0.00	0.00
Si	0.00	0.00	0.00	0.00	0.00	0.00	0.00	0.00	0.00	0.00
Fe	0.00	0.00	0.00	0.00	0.00	0.00	0.00	0.00	0.00	0.00
Zn	0.00	0.00	0.00	0.00	0.00	0.00	0.00	0.00	0.00	0.00
Pb	0.00	0.00	0.00	0.00	0.00	0.00	0.00	0.00	0.00	0.00
Total	2.00	1.99	2.01	2.01	2.01	2.05	2.02	2.02	2.01	2.02
Brt	0.98	0.99	0.99	0.99	0.99	1.01	1.01	0.98	0.98	1.00
Cls	0.02	0.02	0.00	0.01	0.02	0.01	0.01	0.01	0.01	0.02

Probe analysis	CNF31818_1_A	CNF31818_1_B	CNF31818_1_C	CNF31818_1_D	CNF31818_1_E	CNF31818_1_F	CNF31818_1_G	CNF31818_1_H	CNF31818_1_I	CNF31721_1_A
Drill hole	LM08-19	LM08-19	LM08-19	LM08-19	LM08-19	LM08-19	LM08-19	LM08-19	LM08-19	LM13-73
Sample	CNF31811	CNF31811	CNF31811	CNF31811	CNF31811	CNF31811	CNF31811	CNF31811	CNF31811	CNF31721
Depth (m)	6.50	6.50	6.50	6.50	6.50	6.50	6.50	6.50	6.50	6.50
Barite texture	Bladed	Bladed	Bladed	Bladed	Bladed	Bladed	Bladed	Bladed	Bladed	Tabular
Mineral assemblage type	Type 1 ±2B	Type 1 ±2B	Type 1 ±2B	Type 1 ±2B	Type 1 ±2B	Type 1 ±2B	Type 1 ±2B	Type 1 ±2B	Type 1 ±2B	Type 1 ± 2A
Specimen	1	2	3	4	5	6	7	8	9	1
SO_3 *wt.%*	34.42	33.88	34.24	34.85	34.24	34.49	34.04	34.52	33.78	35.02
BaO	65.22	65.76	64.45	65.18	64.83	64.56	63.70	66.17	65.23	65.15
SrO	0.60	0.74	1.17	0.88	0.53	0.79	1.41	0.45	0.74	1.23
Na_2O	0.28	0.31	0.37	0.35	0.24	0.25	0.16	0.34	0.34	0.29
CaO	-	-	0.01	0.01	0.01	0.02	-	0.02	0.00	0.00
K_2O	0.60	0.74	1.17	0.88	0.53	0.79	1.41	0.45	0.74	0.00
SiO_2	0.01	-	0.01	0.02	0.01	0.01	0.01	0.00	-	-
FeO	0.01	-	-	0.01	-	-	-	0.04	0.01	-
ZnO	0.06	0.02	0.04	-	-	-	-	0.05	-	0.06
PbO	-	0.01	-	0.01	-	-	-	0.01	0.04	-
Total	101.20	101.45	101.46	102.21	100.40	100.91	100.73	102.06	100.88	101.76
S *apfu*	1.00	1.00	1.00	1.00	1.00	1.00	1.00	1.00	1.00	1.00
Ba	0.99	1.01	0.98	0.98	0.99	0.98	0.98	1.00	1.01	0.97
Sr	0.01	0.02	0.03	0.02	0.01	0.02	0.03	0.01	0.02	0.03
Na	0.01	0.01	0.01	0.01	0.01	0.01	0.01	0.01	0.01	0.01
Ca	0.00	0.00	0.00	0.00	0.00	0.00	0.00	0.00	0.00	0.00
K	0.00	0.00	0.00	0.00	0.00	0.00	0.00	0.00	0.00	0.00
Si	0.00	0.00	0.00	0.00	0.00	0.00	0.00	0.00	0.00	0.00
Fe	0.00	0.00	0.00	0.00	0.00	0.00	0.00	0.00	0.00	0.00
Zn	0.00	0.00	0.00	0.00	0.00	0.00	0.00	0.00	0.00	0.00
Pb	0.00	0.00	0.00	0.00	0.00	0.00	0.00	0.00	0.00	0.00
Total	2.02	2.04	2.03	2.01	2.01	2.01	2.01	2.03	2.04	2.01
Brt	0.99	1.00	0.98	0.99	0.99	0.98	0.97	1.01	0.99	0.99
Cls	0.01	0.01	0.02	0.01	0.01	0.01	0.02	0.01	0.01	0.02

Probe analysis	CNF31721_2_A	CNF31721_2_B	CNF31721_2_C	CNF31721_2_D	CNF31721_2_E	CNF31721_2_F	CNF31721_2_G	CNF31721_2_H	CNF31868_1_A	CNF31868_1_B
Drill hole	LM13-73	LM13-73	LM13-73	LM13-73	LM13-73	LM13-73	LM13-73	LM13-73	LM14-96	LM14-96
Sample	CNF31721	CNF31721	CNF31721	CNF31721	CNF31721	CNF31721	CNF31721	CNF31721	CNF31868	CNF31868
Depth (m)	6.50	6.50	6.50	6.50	6.50	6.50	6.50	6.50	314.40	314.40
Barite texture	Granular	Granular	Granular	Granular	Granular	Granular	Granular	Granular	Bladed/Tabular	Bladed/Tabular
Mineral assemblage type	Type 1 ± 2A	Type 1 ± 2A	Type 1 ± 2A	Type 1 ± 2A	Type 1 ± 2A	Type 1 ± 2A	Type 1 ± 2A	Type 1 ± 2A	Type 1 ± 2A ± 2B	Type 1 ± 2A ± 2B
Specimen	1	2	3	4	5	6	7	8	1	2
SO_3 *wt.%*	34.53	35.02	34.39	34.69	34.57	35.16	34.48	34.67	34.92	34.88
BaO	65.01	65.77	65.93	65.92	65.31	65.71	66.67	65.20	63.66	64.81
SrO	0.78	0.88	0.61	0.88	0.79	0.86	0.61	0.81	1.87	1.58
Na_2O	0.24	0.12	0.15	0.15	0.26	0.25	0.12	0.14	0.23	0.16
CaO	0.02	0.03	0.02	0.04	0.05	0.01	0.03	0.01	0.04	0.02
K_2O	-	0.01	0.01	0.02	-	-	0.01	0.02	0.00	-
SiO_2	-	-	-	-	-	0.02	-	0.05	0.06	-
FeO	0.01	0.01	-	0.03	0.02	0.05	-	0.01	-	-
ZnO	-	-	-	-	-	0.04	0.06	-	-	-
PbO	0.02	-	-	-	0.01	0.02	0.01	-	-	-
Total	100.61	101.85	101.12	101.72	101.01	102.11	101.99	100.91	100.78	101.45
S *apfu*	1.00	1.00	1.00	1.00	1.00	1.00	1.00	1.00	1.00	1.00
Ba	0.98	0.98	1.00	0.99	0.99	0.98	1.01	0.98	0.95	0.97
Sr	0.02	0.02	0.01	0.02	0.02	0.02	0.01	0.02	0.04	0.04
Na	0.01	0.00	0.01	0.01	0.01	0.01	0.00	0.01	0.01	0.01
Ca	0.00	0.00	0.00	0.00	0.00	0.00	0.00	0.00	0.00	0.00
K	0.00	0.00	0.00	0.00	0.00	0.00	0.00	0.00	0.00	0.00
Si	0.00	0.00	0.00	0.00	0.00	0.00	0.00	0.00	0.00	0.00
Fe	0.00	0.00	0.00	0.00	0.00	0.00	0.00	0.00	0.00	0.00
Zn	0.00	0.00	0.00	0.00	0.00	0.00	0.00	0.00	0.00	0.00
Pb	0.00	0.00	0.00	0.00	0.00	0.00	0.00	0.00	0.00	0.00
Total	2.01	2.01	2.02	2.02	2.02	2.01	2.03	2.01	2.00	2.01
Brt	0.99	1.00	1.00	1.00	0.99	1.00	1.01	0.99	0.97	0.99
Cls	0.01	0.01	0.01	0.01	0.01	0.01	0.01	0.01	0.03	0.02

Probe analysis	CNF31868_1_C	CNF31868_1_D	CNF31868_1_E	CNF31868_1_F	CNF31868_1_G	CNF31868_1_H	CNF31868_1_I	CNF31868_1_J	CNF31868_1_K	CNF31868_1_L
Drill hole	LM14-96	LM14-96	LM14-96	LM14-96	LM14-96	LM14-96	LM14-96	LM14-96	LM14-96	LM14-96
Sample	CNF31868	CNF31868	CNF31868	CNF31868	CNF31868	CNF31868	CNF31868	CNF31868	CNF31868	CNF31868
Depth (m)	314.40	314.40	314.40	314.40	314.40	314.40	314.40	314.40	314.40	314.40
Barite texture	Bladed/Tabular	Bladed/Tabular	Granular	Granular	Granular	Granular	Granular	Granular	Bladed/Tabular	Bladed/Tabular
Mineral assemblage type	Type 1 ± 2A ± 2B	Type 1 ± 2A ± 2B	Type 1 ± 2A ± 2B	Type 1 ± 2A ± 2B	Type 1 ± 2A ± 2B	Type 1 ± 2A ± 2B	Type 1 ± 2A ± 2B	Type 1 ± 2A ± 2B	Type 1 ± 2A ± 2B	Type 1 ± 2A ± 2B
Specimen	3	4	5	6	7	8	9	10	11	12
SO_3 *wt.%*	34.71	34.59	34.42	34.33	34.83	34.97	34.19	34.92	34.64	34.80
BaO	64.80	64.07	64.63	65.84	64.37	64.88	65.52	64.33	63.64	64.71
SrO	1.09	1.76	0.73	0.12	0.77	0.81	0.41	0.79	1.72	1.77
Na_2O	0.09	0.06	0.14	0.16	0.13	0.08	0.22	0.17	-	0.12
CaO	0.02	0.03	0.01	0.01	0.01	-	-	0.01	0.06	0.05
K_2O	0.00	0.00	-	0.00	0.01	-	-	0.01	-	0.01
SiO_2	0.03	0.03	-	0.04	0.01	0.09	0.01	-	-	-
FeO	-	0.01	-	-	0.03	-	-	-	-	-
ZnO	-	-	0.06	0.02	-	0.16	-	0.08	-	-
PbO	0.06	-	-	0.01	0.05	-	-	0.01	0.03	-
Total	100.80	100.56	100.00	100.53	100.20	100.99	100.35	100.31	100.09	101.45
S *apfu*	1.00	1.00	1.00	1.00	1.00	1.00	1.00	1.00	1.00	1.00
Ba	0.97	0.97	0.98	1.00	0.96	0.97	1.00	0.96	0.96	0.97
Sr	0.02	0.04	0.02	0.00	0.02	0.02	0.01	0.02	0.04	0.04
Na	0.00	0.00	0.01	0.01	0.00	0.00	0.01	0.01	0.00	0.00
Ca	0.00	0.00	0.00	0.00	0.00	0.00	0.00	0.00	0.00	0.00
K	0.00	0.00	0.00	0.00	0.00	0.00	0.00	0.00	0.00	0.00
Si	0.00	0.00	0.00	0.00	0.00	0.00	0.00	0.00	0.00	0.00
Fe	0.00	0.00	0.00	0.00	0.00	0.00	0.00	0.00	0.00	0.00
Zn	0.00	0.00	0.00	0.00	0.00	0.00	0.00	0.00	0.00	0.00
Pb	0.00	0.00	0.00	0.00	0.00	0.00	0.00	0.00	0.00	0.00
Total	2.00	2.01	2.00	2.01	1.99	2.00	2.02	1.99	2.00	2.01
Brt	0.99	0.98	0.98	1.00	0.98	0.99	1.00	0.98	0.97	0.99
Cls	0.02	0.03	0.01	0.00	0.01	0.01	0.01	0.01	0.03	0.03

Probe analysis	CNF31868_1_M	CNF31868_1_N	CNF31868_1_O	CNF31868_1_P	CNF31868_1_Q	CNF31879_A	CNF31879_B	CNF31879_C	CNF31879_D	CNF31879_E
Drill hole	LM14-96	LM14-96	LM14-96	LM14-96	LM14-96	LM08-37	LM08-37	LM08-37	LM08-37	LM08-37
Sample	CNF31868	CNF31868	CNF31868	CNF31868	CNF31868	CNF31879	CNF31879	CNF31879	CNF31879	CNF31879
Depth (m)	314.40	314.40	314.40	314.40	314.40	297.90	297.90	297.90	297.90	297.90
Barite texture	Bladed/Tabular	Bladed/Tabular	Bladed/Tabular	Bladed/Tabular	Bladed/Tabular	Tabular	Tabular	Tabular	Tabular	Tabular
Mineral assemblage type	Type 1 ± 2A ± 2B	Type 1 ± 2A ± 2B	Type 1 ± 2A ± 2B	Type 1 ± 2A ± 2B	Type 1 ± 2A ± 2B	Type 1 , 3 ±2A	Type 1 , 3 ±2A	Type 1 , 3 ±2A	Type 1 , 3 ±2A	Type 1 , 3 ±2A
Specimen	13	14	15	16	17	1	2	3	4	5
SO_3 *wt.%*	35.04	34.62	34.74	34.49	34.73	34.32	34.55	34.86	34.55	34.67
BaO	65.50	65.70	65.51	64.87	66.22	63.50	64.75	63.78	65.27	64.75
SrO	0.94	0.67	0.61	0.99	0.79	1.08	0.43	1.10	1.20	1.17
Na_2O	0.13	0.11	0.16	0.15	0.15	0.13	0.20	0.07	0.21	0.18
CaO	0.01	0.00	-	0.01	0.01	0.02	0.01	0.02	0.03	0.02
K_2O	0.01	-	0.01	-	-	-	-	-	0.01	0.01
SiO_2	-	-	-	-	-	-	0.04	-	-	-
FeO	0.01	-	0.03	0.02	-	-	0.05	-	-	0.04
ZnO	-	0.03	-	0.08	0.02	-	-	-	-	0.07
PbO	0.04	0.04	-	-	0.01	0.03	0.05	0.01	0.03	-
Total	101.68	101.18	101.06	100.61	101.93	99.08	100.09	99.85	101.30	100.90
S *apfu*	1.00	1.00	1.00	1.00	1.00	1.00	1.00	1.00	1.00	1.00
Ba	0.98	0.99	0.98	0.98	1.00	0.97	0.98	0.96	0.99	0.98
Sr	0.02	0.01	0.01	0.02	0.02	0.02	0.01	0.02	0.03	0.03
Na	0.00	0.00	0.01	0.01	0.01	0.01	0.01	0.00	0.01	0.01
Ca	0.00	0.00	0.00	0.00	0.00	0.00	0.00	0.00	0.00	0.00
K	0.00	0.00	0.00	0.00	0.00	0.00	0.00	0.00	0.00	0.00
Si	0.00	0.00	0.00	0.00	0.00	0.00	0.00	0.00	0.00	0.00
Fe	0.00	0.00	0.00	0.00	0.00	0.00	0.00	0.00	0.00	0.00
Zn	0.00	0.00	0.00	0.00	0.00	0.00	0.00	0.00	0.00	0.00
Pb	0.00	0.00	0.00	0.00	0.00	0.00	0.00	0.00	0.00	0.00
Total	2.00	2.01	2.00	2.01	2.02	1.99	2.00	1.98	2.02	2.01
Brt	1.00	1.00	1.00	0.99	1.01	0.97	0.99	0.97	0.99	0.99
Cls	0.01	0.01	0.01	0.02	0.01	0.02	0.01	0.02	0.02	0.02

Probe analysis	CNF31879_F	CNF31879_G	CNF31879_2_A	CNF31879_2_B	CNF31879_2_C	CNF31879_2_D	CNF31879_2_E	CNF31879_2_F	CNF31879_2_G	CNF31879_2_H
Drill hole	LM08-37	LM08-37	LM08-37	LM08-37	LM08-37	LM08-37	LM08-37	LM08-37	LM08-37	LM08-37
Sample	CNF31879	CNF31879	CNF31879	CNF31879	CNF31879	CNF31879	CNF31879	CNF31879	CNF31879	CNF31879
Depth (m)	297.90	297.90	297.90	297.90	297.90	297.90	297.90	297.90	297.90	297.90
Barite texture	Tabular	Tabular	Tabular	Tabular	Tabular	Tabular	Tabular	Tabular	Tabular	Tabular
Mineral assemblage type	Type 1 , 3 ±2A	Type 1 , 3 ±2A	Type 1 , 3 ±2A	Type 1 , 3 ±2A	Type 1 , 3 ±2A	Type 1 , 3 ±2A	Type 1 , 3 ±2A	Type 1 , 3 ±2A	Type 1 , 3 ±2A	Type 1 , 3 ±2A
Specimen	6	7	1	2	3	4	5	6	7	8
SO_3 *wt.%*	34.81	34.84	34.22	34.30	34.76	34.60	34.69	34.49	34.00	34.88
BaO	64.87	63.84	65.17	66.20	65.63	66.04	64.62	65.42	65.75	64.48
SrO	1.20	1.24	0.26	0.49	0.39	0.35	1.19	0.47	0.24	2.51
Na_2O	0.12	0.18	0.13	0.24	0.22	0.18	0.15	0.29	0.18	0.18
CaO	0.02	0.01	0.00	0.00	0.01	-	0.02	0.01	-	0.06
K_2O	-	0.01	-	0.00	-	-	0.02	-	-	0.02
SiO_2	-	0.04	0.05	-	0.04	0.01	-	-	-	-
FeO	-	-	-	-	-	-	-	-	0.04	-
ZnO	-	-	0.08	-	-	0.06	-	-	-	-
PbO	-	0.04	-	0.02	0.01	0.04	-	-	-	0.01
Total	101.03	100.21	99.92	101.26	101.06	101.28	100.68	100.68	100.21	102.13
S *apfu*	1.00	1.00	1.00	1.00	1.00	1.00	1.00	1.00	1.00	1.00
Ba	0.97	0.96	0.99	1.01	0.99	1.00	0.97	0.99	1.01	0.97
Sr	0.03	0.03	0.01	0.01	0.01	0.01	0.03	0.01	0.01	0.06
Na	0.00	0.01	0.01	0.01	0.01	0.01	0.01	0.01	0.01	0.01
Ca	0.00	0.00	0.00	0.00	0.00	0.00	0.00	0.00	0.00	0.00
K	0.00	0.00	0.00	0.00	0.00	0.00	0.00	0.00	0.00	0.00
Si	0.00	0.00	0.00	0.00	0.00	0.00	0.00	0.00	0.00	0.00
Fe	0.00	0.00	0.00	0.00	0.00	0.00	0.00	0.00	0.00	0.00
Zn	0.00	0.00	0.00	0.00	0.00	0.00	0.00	0.00	0.00	0.00
Pb	0.00	0.00	0.00	0.00	0.00	0.00	0.00	0.00	0.00	0.00
Total	2.00	1.99	2.01	2.03	2.00	2.01	2.00	2.01	2.02	2.03
Brt	0.99	0.97	0.99	1.01	1.00	1.01	0.98	1.00	1.00	0.98
Cls	0.02	0.02	0.00	0.01	0.01	0.01	0.02	0.01	0.00	0.04

Probe analysis	CNF31879_2_I	CNF31879_2_J	CNF31879_2_K	CNF31879_2_L	CNF31879_2_M
Drill hole	LM08-37	LM08-37	LM08-37	LM08-37	LM08-37
Sample	CNF31879	CNF31879	CNF31879	CNF31879	CNF31879
Depth (m)	297.90	297.90	297.90	297.90	297.90
Barite texture	Tabular	Tabular	Tabular	Tabular	Tabular
Mineral assemblage type	Type 1 , 3 ±2A	Type 1 , 3 ±2A	Type 1 , 3 ±2A	Type 1 , 3 ±2A	Type 1 , 3 ±2A
Specimen	9	10	11	12	13
SO_3 *wt.%*	34.43	34.53	34.74	34.32	34.76
BaO	65.51	64.56	64.39	64.30	64.14
SrO	0.76	1.49	0.92	0.82	0.96
Na_2O	0.18	0.20	0.15	0.11	0.17
CaO	0.01	-	0.01	0.02	0.01
K_2O	-	-	0.00	-	0.01
SiO_2	-	0.01	-	0.04	-
FeO	-	0.03	-	-	-
ZnO	-	0.04	-	0.09	-
PbO	-	0.02	-	-	-
Total	100.89	100.89	100.22	99.71	100.05
S *apfu*	1.00	1.00	1.00	1.00	1.00
Ba	0.99	0.98	0.97	0.98	0.96
Sr	0.02	0.03	0.02	0.02	0.02
Na	0.01	0.01	0.01	0.00	0.01
Ca	0.00	0.00	0.00	0.00	0.00
K	0.00	0.00	0.00	0.00	0.00
Si	0.00	0.00	0.00	0.00	0.00
Fe	0.00	0.00	0.00	0.00	0.00
Zn	0.00	0.00	0.00	0.00	0.00
Pb	0.00	0.00	0.00	0.00	0.00
Total	2.01	2.02	1.99	2.01	1.99
Brt	1.00	0.98	0.98	0.98	0.98
Cls	0.01	0.02	0.01	0.01	0.01

Appendix 4: Laser ablation ICP-MS

4.1 Supplementary laser ablation methods

4.1.1 Quadrupole ICP-MS

Trace element analyses were conducted with a ThermoFisher^{TM} X-series 2 quadrupole ICP-MS coupled to an ESI^{TM} NWR-193nm Excimer laser system at Queen's Facility for Isotope Research (QFIR) on 14 of the 21 samples analyzed by EMPA. Thin section samples containing different barite textures and standards were affixed in the laser chamber using mounting putty. Barite crystals were ablated at 100% power using a repetition rate of 20 Hz and focused laser beam of 50 µm. Between each sample analysis, gas blanks were analysed for 30s. The ablation speed was 5µm/s with a fluence of approximately 5 J/cm^2. Analytical parameters are summarised in Table A-4-1. Samples were ablated using a line pattern. USGS glass standards (GSC-1G, GSD-1G, and GSE-1G) were used as external calibration at the beginning and end of every run. The K-0253 standard glass was used as a reference material for Ba at the beginning and end of each run and the BHVO-2G standard was used as an unknown once every ten sample analysis to monitor instrument drift, correct for changes in element ionization, and assess data quality. Quantitative results were obtained through calibration and normalisation of each analysis to Sr contents of the barites as determined by electron microprobe analysis.

4.1.2 High resolution ICP-MS

In order to eliminate or reduce the effect of interferences due to mass overlap, trace element concentrations were collected with a Finnigan MAT Element ICP-MS and Thermo Scientfic 2 XR high-resolution instrument coupled to an ESI^{TM} NWR-193nm Excimer laser system at QFIR. High resolution ICP-MS was used preceding quadrupole ICP-MS analyses. Laser parameters for HR-ICP-MS analyses are identical to those for quadrupole-ICP-MS (Table A-4-1). The ablated material was carried into the high-resolution mass spectrometer using ultra-high purity helium at a daily optimized flow rate of approximately 1 L/min. The sample gas flow rate (~0.9 L/min) was optimized daily for sensitivity and for the reduction of oxide generation. Similar to quadrupole ICP-MS analysis, a standard bracketing approach was used to monitor instrument drift and correct for changes in element ionization. USGS glass standards (GSC-1G, GSD-1G, and GSE-1G) as well as the NIST 612 glass and NIST 610 standard glass were used for external calibration at the beginning and end of every run and (BHVO-2G) was analysed as an unknown every ~10 samples.

Measured isotopes on the HR-ICP-MS were: ^{134}Ba, ^{135}Ba, ^{138}Ba, ^{139}La, ^{140}Ce, ^{141}Pr, ^{143}Nd, ^{145}Nd, ^{147}Sm, ^{149}Sm, ^{151}Eu, ^{153}Eu, ^{155}Gd, ^{157}Gd, ^{159}Tb, ^{161}Dy, ^{163}Dy, ^{165}Ho, ^{166}Er, ^{167}Er, ^{169}Tm, ^{172}Yb, ^{173}Yb, ^{175}Lu, ^{197}Au, and ^{209}Bi.

Table A-4-1. Instrument parameters for quadrupole ICP-MS and high resolution ICP-MS.

Quadrupole-ICP-MS		**High-resolution-ICP-MS**	
Model	Xseries 2 ICP-MS	Model	ThermoFisher Element 2 XR high-resolution instrument ICP-MS
Type	Magnetic sector field	Type	
Forward power		Forward power	
Scan mode		Scan mode	E-scan
Cooling gas		Cooling gas	
Auxiliary gas flow rate		Auxiliary gas flow rate (Ar)	0.75 L/min
Sample gas flow rate		Sample gas flow rate (Ar)	0.9 L/min
Carrier gas		Carrier gas (ultra-high purity He)	1 L/min
Calibration standards	NIST612 glass	Acquisition time	1 min and 16sec
	NIST610 glass	Calibration standards	NIST612 glass
	BHVO-2G		NIST610 glass
	GSC-1G		BHVO-2G
	GSD-1G		GSC-1G
	GSE-1G		GSD-1G
Reference material	K-0253 glass		GSE-1G
		Reference material	K-0253 glass
New Wave Research Excimer, 193 nm laser		**New Wave Research Excimer, 193 nm laser**	
Power	100%	Power	100%
Spot size	50 µm	Spot size	50 µm
Repetition rate	20 Hz	Repetition rate	20 Hz
Ablation speed	5 µm/s	Ablation speed	5 µm/s
Laser fluence	~5 J/cm2	Laser fluence	~5 J/cm2

4.2 QA-QC Quadrupole ICP-MS

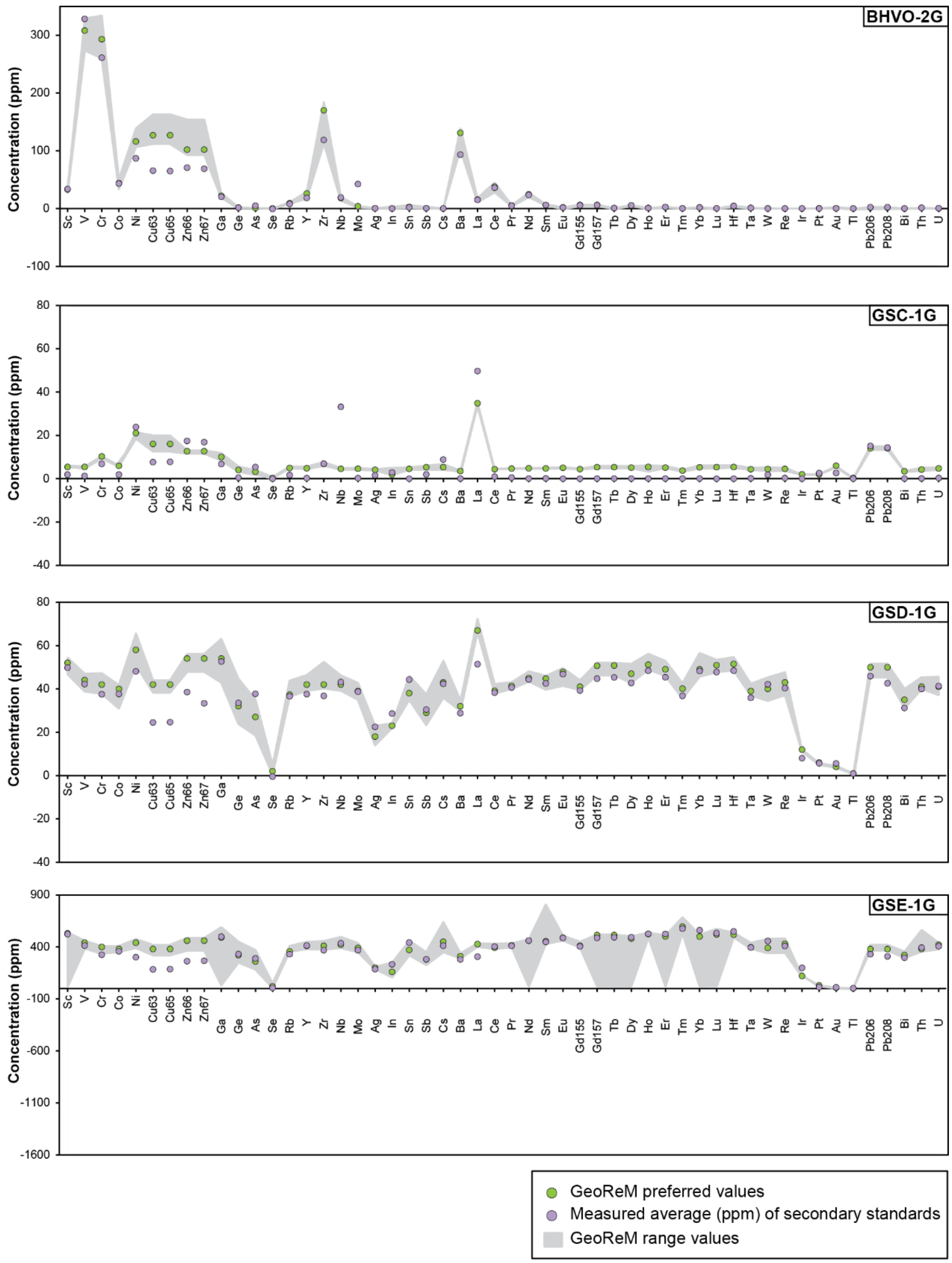

Figure A-4-1. Plots of measured average concentrations (ppm) of secondary standards compared to GeoReM preferred values using NIST-612 as a calibration standard. Quantitative results were obtained through calibration and normalisation of each analysis to Sr contents of the barites determined by electron-probe analysis.

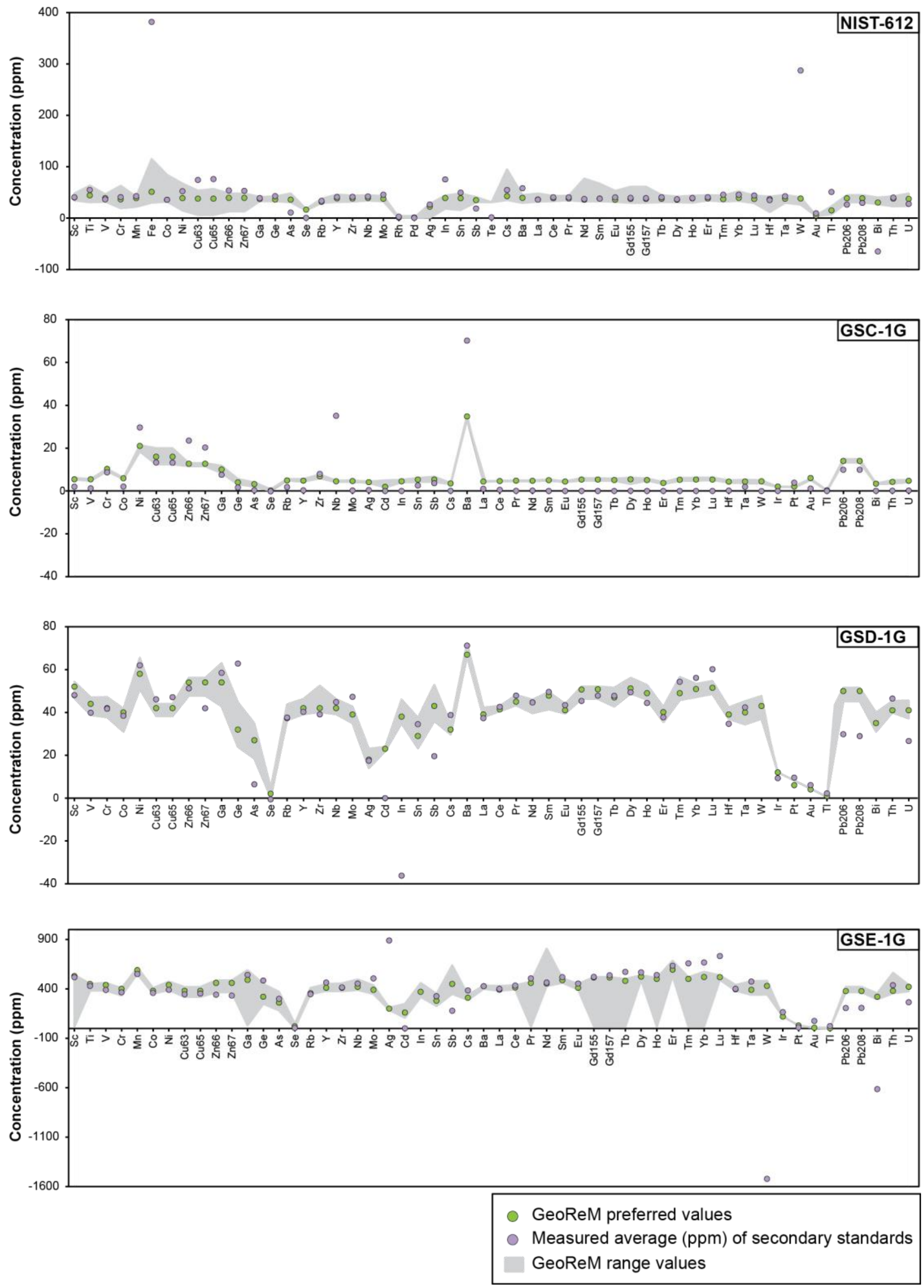

Figure A-4-2. Plots of measured average concentrations (ppm) of secondary standards compared to GeoReM preferred values using BHVO-2G as a calibration standard. Quantitative results were obtained through calibration and normalisation of each analysis to Sr contents of the barites determined by electron-probe analysis.

4.3 Compiled laser ablation inductively coupled plasma quadrupole mass spectrometer (LA-ICP-QMS) analyses

Sample/spot analysis #	Drill Hole	Mineralized zone	Barite texture	Mineral Assemblage Type	Sc	Ti	V	Cr	Mn	Fe	Co	Ni	Cu63	Cu65	Zn66	Zn67	Ga
					ppm	ppm	ppm	ppm	ppm	ppm	ppm	ppm	ppm	ppm	ppm	ppm	ppm
CNF31875-1	LM13-82	Northwest zone	bladed/tabular	Type 1	-	-	-	158.67	134.87	11503.33	-	-	166.60	182.47	912.33	30940.00	0.75
CNF31875-2	LM13-82	Northwest zone	interstitial	Type 1	-	90.60	-	-	-	-	-	-	-	201.33	-	16106.67	-
CNF31875-3	LM13-82	Northwest zone	bladed/tabular	Type 1	-	-	-	-	-	-	-	-	-	-	252.00	14868.00	-
CNF31875-4	LM13-82	Northwest zone	bladed/tabular	Type 1	-	-	-	-	108.80	-	-	-	-	-	430.67	18586.67	-
CNF31875-5	LM13-82	Northwest zone	interstitial	Type 1	-	-	-	-	-	-	3.80	-	-	-	-	11730.00	-
CNF31875-6	LM13-82	Northwest zone	interstitial	Type 1	-	-	-	-	-	1808.00	-	-	161.97	252.37	71.57	17703.33	-
CNF31875-7	LM13-82	Northwest zone	interstitial	Type 1	-	41.43	-	-	-	2335.33	-	-	-	-	86.63	9040.00	-
CNF31875-8	LM13-82	Northwest zone	bladed/tabular	Type 1	-	-	-	-	-	-	-	-	-	-	91.23	9004.33	-
CNF31875-9	LM13-82	Northwest zone	bladed/tabular	Type 1	14.68	150.73	-	61.88	-	-	-	-	87.27	154.70	158.67	9401.00	-
CNF31874-1	LM13-82	Northwest zone	bladed/tabular	Type 1 ± 2B	-	-	-	-	-	-	-	-	-	66.23	294.34	7012.29	-
CNF31874-2	LM13-82	Northwest zone	bladed/tabular	Type 1 ± 2B	-	-	-	-	-	1991.14	-	-	-	-	90.90	3246.43	-
CNF31874-3	LM13-82	Northwest zone	bladed/tabular	Type 1 ± 2B	-	-	-	-	38.96	3116.57	-	-	160.16	95.23	229.41	6709.29	-
CNF31874-4	LM13-82	Northwest zone	bladed/tabular	Type 1 ± 2B	-	-	-	69.26	-	-	-	-	380.91	203.44	129.86	7185.43	-
CNF31874-5	LM13-82	Northwest zone	granular	Type 1 ± 2B	-	-	-	-	-	-	-	-	-	-	268.37	8657.14	-
CNF31874-6	LM13-82	Northwest zone	granular	Type 1 ± 2B	-	-	-	-	-	-	-	-	-	-	65.36	9090.00	-
CNF31874-7	LM13-82	Northwest zone	granular	Type 1 ± 2B	-	-	-	78.78	-	-	0.82	-	-	-	-	11254.29	-
CNF31874-8	LM13-82	Northwest zone	bladed/tabular	Type 1 ± 2B	-	3.90	-	-	30.30	5194.29	0.82	-	-	168.81	735.86	346285.71	-
CNF31874-9	LM13-82	Northwest zone	bladed/tabular	Type 1 ± 2B	-	-	-	-	-	-	10.82	-	-	-	103.89	26837.14	0.43
CNF31874-10	LM13-82	Northwest zone	granular	Type 1 ± 2B	-	-	-	-	-	-	-	-	-	-	562.71	8657.14	-
CNF31874-11	LM13-82	Northwest zone	granular	Type 1 ± 2B	-	-	-	-	43.29	-	-	-	-	-	277.03	12552.86	-
CNF31874-12	LM13-82	Northwest zone	bladed	Type 1 ± 2B	-	0.71	-	-	-	-	0.18	-	-	103.43	146.23	13196.67	-
CNF31874-13	LM13-82	Northwest zone	bladed	Type 1 ± 2B	-	-	-	75.37	-	-	-	-	-	301.47	545.30	16846.67	0.19
CNF31874-14	LM13-82	Northwest zone	bladed	Type 1 ± 2B	-	-	-	-	-	2810.67	-	-	-	126.93	684.53	17226.67	1.90
CNF31874-15	LM13-82	Northwest zone	tabular	Type 1 ± 2A	-	-	-	61.36	25.96	-	-	42.48	87.32	63.72	158.12	19588.00	-
CNF31874-16	LM13-82	Northwest zone	tabular	Type 1 ± 2A	12.04	63.72	-	51.92	42.48	1699.20	5.19	-	-	136.88	172.28	25724.00	-
CNF31874-17	LM13-82	Northwest zone	tabular	Type 1 ± 2A	11.46	-	3.22	-	-	-	3.02	-	-	110.55	168.84	6411.90	-
CNF31874-18	LM13-82	Northwest zone	tabular	Type 1 ± 2A	-	-	12.83	-	-	-	12.02	-	-	175.00	-	36166.67	-
CNF31874-19	LM13-82	Northwest zone	tabular	Type 1 ± 2A	-	-	-	-	-	-	2.47	-	-	-	64.58	6247.50	-
CNF31735-1	LM13-94	Northwest zone	tabular	Type 1 ± 2B	7.88	22.81	-	33.17	-	704.93	1.87	-	622.00	93.30	99.52	7878.67	0.68
CNF31735-2	LM13-94	Northwest zone	tabular	Type 1 ± 2B	-	-	-	84.93	26.69	2426.67	-	109.20	-	-	81.29	4853.33	-
CNF31735-3	LM13-94	Northwest zone	tabular	Type 1 ± 2B	-	9.54	0.73	21.77	31.10	207.33	-	10.37	49.76	124.40	321.37	7671.33	2.07
CNF31735-4	LM13-94	Northwest zone	tabular	Type 1 ± 2B	-	-	-	32.00	-	-	-	-	-	-	253.77	2206.67	-
CNF31735-5	LM13-94	Northwest zone	tabular	Type 1 ± 2B	-	-	-	37.56	27.67	1581.33	5.93	49.42	47.44	156.16	256.97	13441.33	5.14
CNF31735-6	LM13-94	Northwest zone	tabular	Type 1 ± 2B	-	5.29	-	36.67	12.66	-	-	28.35	96.39	139.86	253.26	8505.00	-
CNF31735-7	LM13-94	Northwest zone	tabular	Type 1 ± 2B	-	23.72	-	35.58	35.58	-	0.26	-	43.49	90.93	154.18	20952.67	-
CNF31735-8	LM13-94	Northwest zone	tabular	Type 1 ± 2B	-	44.05	2.62	19.27	26.16	5093.67	3.58	46.81	48.18	170.71	256.06	11288.67	-
CNF31735-9	LM13-94	Northwest zone	tabular	Type 1 ± 2B	-	-	-	303.33	88.57	-	-	-	218.40	110.41	218.40	19413.33	-
CNF31809-1	LM10-43	Main zone	bladed/tabular	Type 1 ± 2A	-	167.20	18.48	-	70.40	4664.00	-	-	1144.00	1152.80	3432.00	12936.00	6.25
CNF31809-2	LM10-43	Main zone	bladed/tabular	Type 1 ± 2A	-	246.40	7.57	26.40	84.48	5368.00	-	-	2147.20	2173.60	1504.80	7392.00	3.43
CNF31809-3	LM10-43	Main zone	bladed/tabular	Type 1 ± 2A	-	413.60	15.84	30.80	148.72	24640.00	-	-	14960.00	25520.00	3872.00	13552.00	20.24
CNF31809-4	LM10-43	Main zone	granular	Type 1 ± 2A	32.00	-	18.40	80.00	72.80	5840.00	-	-	2080.00	2112.00	2800.00	9680.00	-
CNF31809-5	LM10-43	Main zone	granular	Type 1 ± 2A	-	172.80	14.40	54.40	83.20	8880.00	0.15	-	3280.00	3120.00	2352.00	14320.00	6.24
CNF31809-6	LM10-43	Main zone	granular	Type 1 ± 2A	-	240.00	26.40	63.20	54.40	7520.00	4.80	-	1000.00	2080.00	1760.00	5920.00	-
CNF31809-7	LM10-43	Main zone	granular	Type 1 ± 2A	-	290.57	20.21	59.38	180.66	17307.67	8.09	202.13	4800.67	4800.67	3385.73	20718.67	-
CNF31809-8	LM10-43	Main zone	bladed/tabular	Type 1 ± 2A	-	355.30	21.95	94.05	217.36	10554.50	-	131.67	4598.00	4075.50	4807.00	18287.50	15.68
CNF31809-9	LM10-43	Main zone	bladed/tabular	Type 1 ± 2A	13.59	543.40	11.81	-	111.82	7942.00	-	-	4284.50	3448.50	4389.00	11704.00	5.75
CNF31809-10	LM10-43	Main zone	bladed/tabular	Type 1 ± 2A	-	700.15	28.22	128.54	248.71	12435.50	-	101.37	4535.30	4807.00	5538.50	23930.50	5.64
CNF31809-11	LM10-43	Main zone	bladed/tabular	Type 1 ± 2A	-	163.80	25.48	79.17	177.45	10647.00	7.28	-	3913.00	4459.00	4550.00	21021.00	7.28
CNF31809-12	LM10-43	Main zone	bladed/tabular	Type 1 ± 2A	-	336.70	20.93	86.45	150.15	9919.00	1.55	209.30	3276.00	2884.70	4277.00	23114.00	4.00
CNF31809-13	LM10-43	Main zone	bladed/tabular	Type 1 ± 2A	-	455.00	17.29	34.58	161.07	11011.00	-	95.55	3913.00	4368.00	4277.00	12649.00	6.83
CNF31809-14	LM10-43	Main zone	granular	Type 1 ± 2A	-	175.45	17.55	582.18	183.43	7815.50	-	-	2001.73	2791.25	1754.50	11962.50	1.28
CNF31809-15	LM10-43	Main zone	granular	Type 1 ± 2A	-	685.85	-	55.83	152.32	9490.25	-	-	1595.00	1929.95	1834.25	18342.50	-
CNF31809-16	LM10-43	Main zone	bladed/tabular	Type 1 ± 2A	-	199.75	10.20	-	59.78	4360.67	-	-	1533.27	1652.83	1617.67	10057.67	1.76

Sample/spot analysis #	Drill Hole	Mineralized zone	Barite texture	Mineral Assemblage Type	Ge ppm	As ppm	Se ppm	Rb ppm	Y ppm	Zr ppm	Nb ppm	Mo ppm	Ru ppm	Rh ppm	Pd ppm	Ag ppm	In ppm
CNF31875-1	LM13-82	Northwest zone	bladed/tabular	Type 1	-	-	55.53	-	21.02	6.35	21.82	-	-	-	-	9.52	7.14
CNF31875-2	LM13-82	Northwest zone	interstitial	Type 1	-	20.13	44.80	-	7.05	-	-	-	-	-	-	-	-
CNF31875-3	LM13-82	Northwest zone	bladed/tabular	Type 1	-	-	30.24	-	12.10	-	0.76	-	-	-	-	-	-
CNF31875-4	LM13-82	Northwest zone	bladed/tabular	Type 1	-	-	70.72	-	2.45	-	0.45	-	-	-	-	-	-
CNF31875-5	LM13-82	Northwest zone	interstitial	Type 1	-	-	17.25	-	6.56	-	0.90	-	-	-	-	-	-
CNF31875-6	LM13-82	Northwest zone	interstitial	Type 1	-	-	22.60	14.31	24.11	-	13.18	-	-	-	-	-	-
CNF31875-7	LM13-82	Northwest zone	interstitial	Type 1	-	-	18.83	-	3.16	-	0.90	0.34	-	-	-	-	-
CNF31875-8	LM13-82	Northwest zone	bladed/tabular	Type 1	-	-	6.74	-	2.02	-	3.97	-	-	-	-	-	-
CNF31875-9	LM13-82	Northwest zone	bladed/tabular	Type 1	-	-	23.80	3.17	14.28	1.35	2181.67	0.44	-	-	-	-	-
CNF31874-1	LM13-82	Northwest zone	bladed/tabular	Type 1 ± 2B	-	-	12.99	-	4.50	-	-	-	-	-	-	10.39	-
CNF31874-2	LM13-82	Northwest zone	bladed/tabular	Type 1 ± 2B	-	-	-	-	2.29	-	0.19	-	-	-	-	1.82	-
CNF31874-3	LM13-82	Northwest zone	bladed/tabular	Type 1 ± 2B	-	-	-	-	5.19	0.10	-	-	-	-	-	-	-
CNF31874-4	LM13-82	Northwest zone	bladed/tabular	Type 1 ± 2B	-	-	0.43	-	5.63	-	-	0.39	-	-	-	-	-
CNF31874-5	LM13-82	Northwest zone	granular	Type 1 ± 2B	-	-	-	-	3.07	-	-	-	-	-	-	3.03	-
CNF31874-6	LM13-82	Northwest zone	granular	Type 1 ± 2B	-	17.31	-	-	8.66	-	-	-	-	-	-	-	-
CNF31874-7	LM13-82	Northwest zone	granular	Type 1 ± 2B	-	-	-	-	1.39	-	-	-	-	-	-	-	-
CNF31874-8	LM13-82	Northwest zone	bladed/tabular	Type 1 ± 2B	-	95.23	21.64	-	22.51	-	0.61	-	-	-	-	-	-
CNF31874-9	LM13-82	Northwest zone	bladed/tabular	Type 1 ± 2B	-	73.59	-	-	5.19	-	-	-	-	-	-	9.96	-
CNF31874-10	LM13-82	Northwest zone	granular	Type 1 ± 2B	-	82.24	-	-	4.42	-	-	7.36	-	-	-	-	3.03
CNF31874-11	LM13-82	Northwest zone	granular	Type 1 ± 2B	-	-	-	11.25	7.79	-	-	-	-	-	-	-	-
CNF31874-12	LM13-82	Northwest zone	bladed	Type 1 ± 2B	-	35.67	-	-	8.92	-	-	-	-	-	-	-	-
CNF31874-13	LM13-82	Northwest zone	bladed	Type 1 ± 2B	-	35.47	-	-	3.46	-	0.21	1.68	-	-	-	11.08	-
CNF31874-14	LM13-82	Northwest zone	bladed	Type 1 ± 2B	-	-	-	-	8.30	-	-	-	-	-	3.63	15.87	-
CNF31874-15	LM13-82	Northwest zone	tabular	Type 1 ± 2A	-	-	-	1.18	8.73	-	-	-	-	-	-	89.68	-
CNF31874-16	LM13-82	Northwest zone	tabular	Type 1 ± 2A	-	94.40	-	-	9.44	-	-	-	-	-	-	-	-
CNF31874-17	LM13-82	Northwest zone	tabular	Type 1 ± 2A	16.08	-	-	3.22	5.83	-	-	-	-	-	-	30.15	-
CNF31874-18	LM13-82	Northwest zone	tabular	Type 1 ± 2A	14.00	-	-	6.65	3.62	-	-	-	-	-	-	-	-
CNF31874-19	LM13-82	Northwest zone	tabular	Type 1 ± 2A	-	-	4.20	-	4.62	-	-	-	-	-	-	-	-
CNF31735-1	LM13-94	Northwest zone	tabular	Type 1 ± 2B	-	311.00	82.93	-	4.98	-	-	-	-	-	-	51.83	-
CNF31735-2	LM13-94	Northwest zone	tabular	Type 1 ± 2B	-	-	266.93	-	1.94	-	-	-	-	-	-	-	-
CNF31735-3	LM13-94	Northwest zone	tabular	Type 1 ± 2B	-	-	275.75	-	9.54	-	-	-	-	-	-	559.80	-
CNF31735-4	LM13-94	Northwest zone	tabular	Type 1 ± 2B	-	33.10	165.50	2.10	5.52	0.55	-	-	-	-	-	-	-
CNF31735-5	LM13-94	Northwest zone	tabular	Type 1 ± 2B	-	-	51.39	4.55	9.88	-	-	-	-	-	-	73.14	-
CNF31735-6	LM13-94	Northwest zone	tabular	Type 1 ± 2B	-	-	41.58	-	5.67	-	-	-	-	-	-	37.80	-
CNF31735-7	LM13-94	Northwest zone	tabular	Type 1 ± 2B	-	-	116.62	1.78	12.45	-	-	-	-	-	-	21.74	-
CNF31735-8	LM13-94	Northwest zone	tabular	Type 1 ± 2B	-	-	-	-	9.50	-	0.14	-	-	-	-	137.67	-
CNF31735-9	LM13-94	Northwest zone	tabular	Type 1 ± 2B	-	-	-	-	4.37	-	-	-	-	-	-	24.27	-
CNF31809-1	LM10-43	Main zone	bladed/tabular	Type 1 ± 2A	-	26.40	4.40	4.93	7.48	-	50.16	220.00	-	-	-	563.20	-
CNF31809-2	LM10-43	Main zone	bladed/tabular	Type 1 ± 2A	-	-	40.48	-	8.18	4.75	51.92	51.04	-	-	-	519.20	-
CNF31809-3	LM10-43	Main zone	bladed/tabular	Type 1 ± 2A	6.78	-	-	6.51	13.38	24.64	84.48	145.20	-	-	-	721.60	-
CNF31809-4	LM10-43	Main zone	granular	Type 1 ± 2A	-	208.00	88.00	-	2.64	9.60	44.00	120.00	-	-	-	200.00	-
CNF31809-5	LM10-43	Main zone	granular	Type 1 ± 2A	-	-	85.60	5.52	9.92	1.44	68.00	81.60	-	-	-	448.00	-
CNF31809-6	LM10-43	Main zone	granular	Type 1 ± 2A	-	160.00	-	-	4.08	4.85	36.80	104.00	-	-	-	360.00	-
CNF31809-7	LM10-43	Main zone	granular	Type 1 ± 2A	18.95	-	-	-	10.49	3.16	74.54	94.75	-	-	-	593.77	-
CNF31809-8	LM10-43	Main zone	bladed/tabular	Type 1 ± 2A	14.84	188.10	58.52	7.00	11.91	13.59	98.23	127.49	-	-	-	815.10	-
CNF31809-9	LM10-43	Main zone	bladed/tabular	Type 1 ± 2A	-	-	128.54	-	6.79	2.09	136.90	177.65	-	-	-	992.75	-
CNF31809-10	LM10-43	Main zone	bladed/tabular	Type 1 ± 2A	-	20.90	58.52	11.18	17.77	14.73	183.92	125.40	-	-	-	1065.90	-
CNF31809-11	LM10-43	Main zone	bladed/tabular	Type 1 ± 2A	30.03	36.40	-	-	12.74	12.74	92.82	245.70	-	-	-	737.10	-
CNF31809-12	LM10-43	Main zone	bladed/tabular	Type 1 ± 2A	-	27.30	81.90	-	11.19	-	94.64	75.53	-	-	-	600.60	-
CNF31809-13	LM10-43	Main zone	bladed/tabular	Type 1 ± 2A	10.92	-	11.83	-	14.38	7.92	130.13	144.69	-	-	-	1164.80	-
CNF31809-14	LM10-43	Main zone	granular	Type 1 ± 2A	-	-	-	-	0.96	-	51.84	47.05	-	-	-	215.33	-
CNF31809-15	LM10-43	Main zone	granular	Type 1 ± 2A	19.14	3.19	-	-	6.06	4.79	55.83	55.83	-	-	-	2631.75	-
CNF31809-16	LM10-43	Main zone	bladed/tabular	Type 1 ± 2A	-	98.47	70.33	-	10.90	0.42	54.86	62.60	-	-	-	1026.87	-

Sample/spot analysis #	Drill Hole	Mineralized zone	Barite texture	Mineral Assemblage Type	Sn ppm	Sb ppm	Te ppm	Cs ppm	La ppm	Ce ppm	Pr ppm	Nd ppm	Sm ppm	Eu ppm	Gd155 ppm	Gd157 ppm	Tb ppm
CNF31875-1	LM13-82	Northwest zone	bladed/tabular	Type 1	238.00	-	-	-	7.93	1.15	-	-	-	17.45	785.40	-	-
CNF31875-2	LM13-82	Northwest zone	interstitial	Type 1	10.07	-	-	-	2.72	0.49	-	-	-	20.13	362.40	0.50	-
CNF31875-3	LM13-82	Northwest zone	bladed/tabular	Type 1	30.87	-	-	0.09	7.43	2.46	-	-	-	21.42	409.50	-	-
CNF31875-4	LM13-82	Northwest zone	bladed/tabular	Type 1	3.08	0.07	-	-	5.53	1.50	0.12	-	-	8.61	453.33	-	-
CNF31875-5	LM13-82	Northwest zone	interstitial	Type 1	37.95	-	-	-	-	-	-	-	-	7.59	552.00	-	-
CNF31875-6	LM13-82	Northwest zone	interstitial	Type 1	-	2.22	-	-	2.18	2.64	-	-	-	6.40	286.27	-	-
CNF31875-7	LM13-82	Northwest zone	interstitial	Type 1	11.30	-	-	-	1.13	0.09	-	-	-	6.63	177.03	-	-
CNF31875-8	LM13-82	Northwest zone	bladed/tabular	Type 1	18.64	-	-	-	4.40	0.99	-	-	-	7.14	531.53	0.20	-
CNF31875-9	LM13-82	Northwest zone	bladed/tabular	Type 1	52.36	-	-	-	37.68	18.64	2.82	5.55	6.35	9.12	448.23	10.31	0.91
CNF31874-1	LM13-82	Northwest zone	bladed/tabular	Type 1 ± 2B	9.09	-	-	-	25.54	12.99	0.07	-	0.95	5.84	142.84	-	-
CNF31874-2	LM13-82	Northwest zone	bladed/tabular	Type 1 ± 2B	-	-	-	-	2.64	1.30	0.10	-	-	1.34	220.76	-	-
CNF31874-3	LM13-82	Northwest zone	bladed/tabular	Type 1 ± 2B	18.61	-	-	-	16.02	6.62	-	-	-	6.49	298.67	-	-
CNF31874-4	LM13-82	Northwest zone	bladed/tabular	Type 1 ± 2B	73.59	-	-	-	38.96	17.75	-	-	-	21.21	389.57	-	-
CNF31874-5	LM13-82	Northwest zone	granular	Type 1 ± 2B	15.15	-	-	-	5.02	2.90	-	-	-	6.06	125.53	2.16	-
CNF31874-6	LM13-82	Northwest zone	granular	Type 1 ± 2B	-	-	-	-	8.66	0.48	-	-	-	2.60	350.61	-	-
CNF31874-7	LM13-82	Northwest zone	granular	Type 1 ± 2B	-	-	-	-	12.55	1.30	-	-	-	4.76	389.57	-	-
CNF31874-8	LM13-82	Northwest zone	bladed/tabular	Type 1 ± 2B	0.56	1.00	-	-	3.03	2.38	-	-	-	6.49	290.01	-	-
CNF31874-9	LM13-82	Northwest zone	bladed/tabular	Type 1 ± 2B	23.37	0.35	-	-	2.81	4.67	-	-	-	3.55	333.30	-	-
CNF31874-10	LM13-82	Northwest zone	granular	Type 1 ± 2B	7.79	-	-	-	952.29	1.69	-	-	-	3.03	151.50	-	-
CNF31874-11	LM13-82	Northwest zone	granular	Type 1 ± 2B	-	-	-	-	99.56	-	-	-	-	5.89	562.71	-	-
CNF31874-12	LM13-82	Northwest zone	bladed	Type 1 ± 2B	3.57	-	-	32.10	1.53	1.32	-	-	-	5.49	345.97	-	-
CNF31874-13	LM13-82	Northwest zone	bladed	Type 1 ± 2B	-	-	-	-	9.75	1.55	-	-	-	7.09	341.37	-	-
CNF31874-14	LM13-82	Northwest zone	bladed	Type 1 ± 2B	-	0.32	-	-	2.86	0.21	-	-	-	14.05	358.13	-	-
CNF31874-15	LM13-82	Northwest zone	tabular	Type 1 ± 2A	11.56	8.02	-	-	12.51	5.66	-	1.09	0.71	7.32	346.92	-	-
CNF31874-16	LM13-82	Northwest zone	tabular	Type 1 ± 2A	5.43	-	-	-	13.69	3.54	-	1.89	-	13.45	637.20	-	-
CNF31874-17	LM13-82	Northwest zone	tabular	Type 1 ± 2A	4.42	1.01	-	-	22.91	12.26	0.16	-	-	8.64	416.07	0.36	-
CNF31874-18	LM13-82	Northwest zone	tabular	Type 1 ± 2A	-	-	-	-	793.33	3.38	0.34	-	-	11.55	735.00	-	-
CNF31874-19	LM13-82	Northwest zone	tabular	Type 1 ± 2A	12.08	-	-	-	1.58	0.26	-	-	0.18	4.15	64.58	-	-
CNF31735-1	LM13-94	Northwest zone	tabular	Type 1 ± 2B	5.18	-	-	0.48	14.31	8.71	0.03	-	-	7.05	400.15	0.54	-
CNF31735-2	LM13-94	Northwest zone	tabular	Type 1 ± 2B	-	-	-	-	0.50	5.10	-	-	-	1.33	109.20	-	-
CNF31735-3	LM13-94	Northwest zone	tabular	Type 1 ± 2B	3.73	2.49	-	-	10.37	7.67	0.06	0.25	-	8.71	184.53	1.22	-
CNF31735-4	LM13-94	Northwest zone	tabular	Type 1 ± 2B	8.50	-	-	-	2.87	-	-	-	-	10.37	81.65	-	-
CNF31735-5	LM13-94	Northwest zone	tabular	Type 1 ± 2B	9.49	-	-	-	46.45	27.87	3.95	21.74	-	16.21	608.81	0.24	-
CNF31735-6	LM13-94	Northwest zone	tabular	Type 1 ± 2B	10.21	0.08	-	-	23.81	5.67	-	0.72	-	11.53	304.29	-	-
CNF31735-7	LM13-94	Northwest zone	tabular	Type 1 ± 2B	6.13	-	-	-	39.53	26.88	3.16	4.94	1.19	22.14	513.93	-	-
CNF31735-8	LM13-94	Northwest zone	tabular	Type 1 ± 2B	24.78	-	-	0.10	11.01	3.58	0.05	-	-	12.53	523.13	-	-
CNF31735-9	LM13-94	Northwest zone	tabular	Type 1 ± 2B	2.91	0.24	-	-	3.03	-	-	-	-	4.00	679.47	-	-
CNF31809-1	LM10-43	Main zone	bladed/tabular	Type 1 ± 2A	13.20	1.67	-	-	8.45	5.63	0.55	4.14	-	5.46	334.40	1.23	-
CNF31809-2	LM10-43	Main zone	bladed/tabular	Type 1 ± 2A	8.10	-	-	-	29.04	12.06	0.49	1.14	-	13.90	205.04	-	-
CNF31809-3	LM10-43	Main zone	bladed/tabular	Type 1 ± 2A	-	3.34	-	-	10.91	14.17	1.41	5.02	2.02	7.74	197.12	0.15	-
CNF31809-4	LM10-43	Main zone	granular	Type 1 ± 2A	-	0.80	-	-	6.24	2.64	0.28	-	-	8.24	148.00	1.12	-
CNF31809-5	LM10-43	Main zone	granular	Type 1 ± 2A	4.96	1.02	-	0.37	6.56	15.20	0.32	1.68	-	8.32	252.00	-	-
CNF31809-6	LM10-43	Main zone	granular	Type 1 ± 2A	-	-	-	1.44	48.00	10.40	1.20	-	-	5.92	272.00	-	-
CNF31809-7	LM10-43	Main zone	granular	Type 1 ± 2A	17.94	3.16	6.32	-	17.69	8.34	1.77	-	1.26	11.75	429.53	-	-
CNF31809-8	LM10-43	Main zone	bladed/tabular	Type 1 ± 2A	14.63	4.18	-	0.33	17.45	19.86	0.34	2.61	0.94	6.69	229.90	-	-
CNF31809-9	LM10-43	Main zone	bladed/tabular	Type 1 ± 2A	11.39	3.87	-	0.44	22.99	8.99	0.95	5.23	-	5.96	218.41	0.94	-
CNF31809-10	LM10-43	Main zone	bladed/tabular	Type 1 ± 2A	2.72	4.08	-	0.22	6.37	12.75	0.38	-	0.38	12.33	355.30	5.02	0.50
CNF31809-11	LM10-43	Main zone	bladed/tabular	Type 1 ± 2A	-	3.00	-	-	11.10	8.46	2.18	-	-	12.19	455.00	-	-
CNF31809-12	LM10-43	Main zone	bladed/tabular	Type 1 ± 2A	-	-	-	-	8.46	14.47	2.18	-	-	7.46	336.70	-	-
CNF31809-13	LM10-43	Main zone	bladed/tabular	Type 1 ± 2A	6.55	1.78	-	-	17.29	16.11	1.14	7.01	3.37	5.64	210.21	0.91	0.40
CNF31809-14	LM10-43	Main zone	granular	Type 1 ± 2A	-	-	-	-	0.48	1.04	-	-	-	4.07	103.68	-	-
CNF31809-15	LM10-43	Main zone	granular	Type 1 ± 2A	-	2.95	-	-	7.98	7.26	-	-	17.55	8.45	287.10	-	-
CNF31809-16	LM10-43	Main zone	bladed/tabular	Type 1 ± 2A	-	0.65	-	-	4.85	4.92	0.77	4.36	7.74	9.85	330.57	1.69	0.05

Sample/spot analysis #	Drill Hole	Mineralized zone	Barite texture	Mineral Assemblage Type	Dy ppm	Ho ppm	Er ppm	Tm ppm	Yb ppm	Lu ppm	Hf ppm	Ta ppm	W ppm	Re ppm	Os ppm	Au ppm	Hg ppm
CNF31875-1	LM13-82	Northwest zone	bladed/tabular	Type 1	-	-	-	-	-	-	-	0.48	1.94	-	-	-	43.63
CNF31875-2	LM13-82	Northwest zone	interstitial	Type 1	-	-	-	-	-	-	-	-	6.54	-	-	13.09	171.13
CNF31875-3	LM13-82	Northwest zone	bladed/tabular	Type 1	0.63	-	-	-	-	-	-	3.09	20.16	-	-	-	157.50
CNF31875-4	LM13-82	Northwest zone	bladed/tabular	Type 1	0.07	-	-	-	-	-	-	1.41	5.26	-	-	3.63	145.07
CNF31875-5	LM13-82	Northwest zone	interstitial	Type 1	-	-	-	-	-	-	-	-	-	-	-	-	144.90
CNF31875-6	LM13-82	Northwest zone	interstitial	Type 1	-	-	-	-	-	-	-	-	27.50	-	-	6.40	86.63
CNF31875-7	LM13-82	Northwest zone	interstitial	Type 1	-	-	-	-	-	-	-	-	3.77	-	-	9.79	139.37
CNF31875-8	LM13-82	Northwest zone	bladed/tabular	Type 1	-	-	-	-	-	-	-	0.10	-	-	-	1.90	162.63
CNF31875-9	LM13-82	Northwest zone	bladed/tabular	Type 1	-	-	-	-	-	-	-	1.23	50.77	-	-	16.66	11.90
CNF31874-1	LM13-82	Northwest zone	bladed/tabular	Type 1 ± 2B	-	-	-	-	-	-	-	0.01	0.15	-	-	-	129.86
CNF31874-2	LM13-82	Northwest zone	bladed/tabular	Type 1 ± 2B	-	-	-	-	-	-	-	-	-	-	-	-	160.16
CNF31874-3	LM13-82	Northwest zone	bladed/tabular	Type 1 ± 2B	-	-	-	-	-	-	-	0.17	186.13	-	-	-	60.60
CNF31874-4	LM13-82	Northwest zone	bladed/tabular	Type 1 ± 2B	-	-	-	-	-	-	-	-	-	-	-	-	56.27
CNF31874-5	LM13-82	Northwest zone	granular	Type 1 ± 2B	-	-	-	-	-	-	-	0.43	-	-	-	5.19	95.23
CNF31874-6	LM13-82	Northwest zone	granular	Type 1 ± 2B	-	-	-	-	0.26	-	-	-	3.59	-	-	-	69.26
CNF31874-7	LM13-82	Northwest zone	granular	Type 1 ± 2B	-	-	-	-	-	-	-	-	-	-	-	-	34.63
CNF31874-8	LM13-82	Northwest zone	bladed/tabular	Type 1 ± 2B	-	-	-	-	-	-	-	0.10	-	-	-	-	43.29
CNF31874-9	LM13-82	Northwest zone	bladed/tabular	Type 1 ± 2B	-	-	-	-	-	-	-	-	8.66	-	-	-	112.54
CNF31874-10	LM13-82	Northwest zone	granular	Type 1 ± 2B	-	-	-	-	-	-	-	-	1.47	-	-	-	116.87
CNF31874-11	LM13-82	Northwest zone	granular	Type 1 ± 2B	-	-	-	-	-	-	-	-	0.69	-	-	-	17.31
CNF31874-12	LM13-82	Northwest zone	bladed	Type 1 ± 2B	-	-	-	-	-	-	-	-	2.57	-	-	-	292.47
CNF31874-13	LM13-82	Northwest zone	bladed	Type 1 ± 2B	-	0.07	-	-	-	-	-	2.22	19.51	-	-	1.91	150.73
CNF31874-14	LM13-82	Northwest zone	bladed	Type 1 ± 2B	-	-	-	-	-	-	-	0.05	2.72	0.02	-	14.05	194.93
CNF31874-15	LM13-82	Northwest zone	tabular	Type 1 ± 2A	-	-	-	-	-	-	-	-	-	-	-	-	637.20
CNF31874-16	LM13-82	Northwest zone	tabular	Type 1 ± 2A	-	-	-	-	-	-	-	-	-	0.03	-	-	165.20
CNF31874-17	LM13-82	Northwest zone	tabular	Type 1 ± 2A	-	-	-	-	-	-	-	-	-	-	-	-	140.70
CNF31874-18	LM13-82	Northwest zone	tabular	Type 1 ± 2A	-	-	-	-	-	-	-	-	-	-	-	-	58.33
CNF31874-19	LM13-82	Northwest zone	tabular	Type 1 ± 2A	-	-	-	-	-	-	-	0.05	-	-	-	-	210.00
CNF31735-1	LM13-94	Northwest zone	tabular	Type 1 ± 2B	-	-	-	-	-	-	-	-	-	-	-	8.92	331.73
CNF31735-2	LM13-94	Northwest zone	tabular	Type 1 ± 2B	-	-	-	-	-	-	-	-	-	-	-	-	121.33
CNF31735-3	LM13-94	Northwest zone	tabular	Type 1 ± 2B	-	-	-	-	-	-	-	0.03	-	0.01	-	-	1057.40
CNF31735-4	LM13-94	Northwest zone	tabular	Type 1 ± 2B	-	-	-	-	-	-	-	-	-	-	-	-	342.03
CNF31735-5	LM13-94	Northwest zone	tabular	Type 1 ± 2B	0.43	0.05	-	-	-	-	-	0.06	-	-	-	-	474.40
CNF31735-6	LM13-94	Northwest zone	tabular	Type 1 ± 2B	-	-	-	-	-	-	-	-	-	-	-	-	699.30
CNF31735-7	LM13-94	Northwest zone	tabular	Type 1 ± 2B	-	-	0.51	-	-	-	-	-	-	-	-	-	395.33
CNF31735-8	LM13-94	Northwest zone	tabular	Type 1 ± 2B	-	-	-	-	-	-	-	0.21	-	-	-	-	509.37
CNF31735-9	LM13-94	Northwest zone	tabular	Type 1 ± 2B	-	-	-	-	-	-	-	-	-	0.01	-	-	145.60
CNF31809-1	LM10-43	Main zone	bladed/tabular	Type 1 ± 2A	-	-	-	-	-	-	-	0.22	0.44	-	-	10.56	1100.00
CNF31809-2	LM10-43	Main zone	bladed/tabular	Type 1 ± 2A	2.46	-	-	-	-	-	-	0.14	0.61	-	-	53.68	721.60
CNF31809-3	LM10-43	Main zone	bladed/tabular	Type 1 ± 2A	-	0.02	-	-	-	-	-	-	1.23	-	-	6.16	730.40
CNF31809-4	LM10-43	Main zone	granular	Type 1 ± 2A	-	-	-	-	-	-	-	0.30	1.84	-	-	-	360.00
CNF31809-5	LM10-43	Main zone	granular	Type 1 ± 2A	-	-	-	-	-	-	-	-	0.80	-	-	-	552.00
CNF31809-6	LM10-43	Main zone	granular	Type 1 ± 2A	-	-	-	-	-	-	-	-	-	-	40.00	-	328.00
CNF31809-7	LM10-43	Main zone	granular	Type 1 ± 2A	-	-	-	-	-	-	-	-	2.91	-	-	31.58	1288.60
CNF31809-8	LM10-43	Main zone	bladed/tabular	Type 1 ± 2A	-	-	-	-	-	-	-	0.31	3.34	-	-	3.45	752.40
CNF31809-9	LM10-43	Main zone	bladed/tabular	Type 1 ± 2A	0.39	-	-	-	-	-	-	0.17	-	-	-	3.97	668.80
CNF31809-10	LM10-43	Main zone	bladed/tabular	Type 1 ± 2A	-	0.19	-	-	-	0.63	-	0.17	10.03	-	-	3.97	543.40
CNF31809-11	LM10-43	Main zone	bladed/tabular	Type 1 ± 2A	-	-	-	-	-	-	-	-	-	-	-	-	464.10
CNF31809-12	LM10-43	Main zone	bladed/tabular	Type 1 ± 2A	-	-	-	-	-	-	0.64	-	-	-	-	-	573.30
CNF31809-13	LM10-43	Main zone	bladed/tabular	Type 1 ± 2A	-	-	-	-	-	-	-	0.10	4.46	-	-	22.75	1046.50
CNF31809-14	LM10-43	Main zone	granular	Type 1 ± 2A	-	-	-	-	-	-	-	-	-	-	-	-	175.45
CNF31809-15	LM10-43	Main zone	granular	Type 1 ± 2A	-	-	-	-	-	-	-	-	-	-	-	-	638.00
CNF31809-16	LM10-43	Main zone	bladed/tabular	Type 1 ± 2A	-	-	-	-	-	-	-	0.24	2.60	-	-	70.33	787.73

Sample/spot analysis #	Drill Hole	Mineralized zone	Barite texture	Mineral Assemblage Type	Tl ppm	Pb206 ppm	Pb208 ppm	Bi ppm	Th ppm	U ppm
CNF31875-1	LM13-82	Northwest zone	bladed/tabular	Type 1	5.16	4085.67	3927.00	-	0.44	1.07
CNF31875-2	LM13-82	Northwest zone	interstitial	Type 1	-	34.73	19.63	0.04	-	-
CNF31875-3	LM13-82	Northwest zone	bladed/tabular	Type 1	-	22.05	49.77	0.02	-	-
CNF31875-4	LM13-82	Northwest zone	bladed/tabular	Type 1	-	10.88	16.32	-	-	-
CNF31875-5	LM13-82	Northwest zone	interstitial	Type 1	-	72.45	75.90	0.08	-	-
CNF31875-6	LM13-82	Northwest zone	interstitial	Type 1	-	226.00	248.60	0.68	0.68	2.83
CNF31875-7	LM13-82	Northwest zone	interstitial	Type 1	24.11	1054.67	1280.67	-	-	-
CNF31875-8	LM13-82	Northwest zone	bladed/tabular	Type 1	3.97	6.27	9.72	-	0.14	-
CNF31875-9	LM13-82	Northwest zone	bladed/tabular	Type 1	-	84.49	85.68	-	34.91	6.74
CNF31874-1	LM13-82	Northwest zone	bladed/tabular	Type 1 ± 2B	-	290.01	389.57	-	0.09	-
CNF31874-2	LM13-82	Northwest zone	bladed/tabular	Type 1 ± 2B	-	84.41	115.14	1.21	-	-
CNF31874-3	LM13-82	Northwest zone	bladed/tabular	Type 1 ± 2B	12.99	87.00	129.86	25.97	-	-
CNF31874-4	LM13-82	Northwest zone	bladed/tabular	Type 1 ± 2B	16.45	212.10	238.07	-	-	-
CNF31874-5	LM13-82	Northwest zone	granular	Type 1 ± 2B	-	89.60	118.17	-	-	-
CNF31874-6	LM13-82	Northwest zone	granular	Type 1 ± 2B	4.33	121.20	91.77	-	-	-
CNF31874-7	LM13-82	Northwest zone	granular	Type 1 ± 2B	19.48	125.53	337.63	-	-	-
CNF31874-8	LM13-82	Northwest zone	bladed/tabular	Type 1 ± 2B	-	51.94	82.24	-	0.26	0.25
CNF31874-9	LM13-82	Northwest zone	bladed/tabular	Type 1 ± 2B	1.95	367.93	307.33	-	-	-
CNF31874-10	LM13-82	Northwest zone	granular	Type 1 ± 2B	14.28	30.30	44.58	-	-	-
CNF31874-11	LM13-82	Northwest zone	granular	Type 1 ± 2B	-	90.90	125.53	-	-	-
CNF31874-12	LM13-82	Northwest zone	bladed	Type 1 ± 2B	-	121.27	146.23	-	-	-
CNF31874-13	LM13-82	Northwest zone	bladed	Type 1 ± 2B	-	487.67	372.40	-	-	-
CNF31874-14	LM13-82	Northwest zone	bladed	Type 1 ± 2B	-	308.27	262.93	2.45	-	6.48
CNF31874-15	LM13-82	Northwest zone	tabular	Type 1 ± 2A	-	165.20	188.80	-	-	0.45
CNF31874-16	LM13-82	Northwest zone	tabular	Type 1 ± 2A	-	193.52	103.84	-	-	0.57
CNF31874-17	LM13-82	Northwest zone	tabular	Type 1 ± 2A	-	88.44	74.37	-	-	0.18
CNF31874-18	LM13-82	Northwest zone	tabular	Type 1 ± 2A	-	47.83	31.97	-	-	-
CNF31874-19	LM13-82	Northwest zone	tabular	Type 1 ± 2A	19.43	16.80	19.43	-	-	-
CNF31735-1	LM13-94	Northwest zone	tabular	Type 1 ± 2B	24.88	55.98	55.98	0.09	-	0.11
CNF31735-2	LM13-94	Northwest zone	tabular	Type 1 ± 2B	-	10.31	11.53	-	-	7.28
CNF31735-3	LM13-94	Northwest zone	tabular	Type 1 ± 2B	-	62.20	74.64	-	0.17	0.06
CNF31735-4	LM13-94	Northwest zone	tabular	Type 1 ± 2B	30.89	176.53	136.81	-	-	-
CNF31735-5	LM13-94	Northwest zone	tabular	Type 1 ± 2B	-	274.76	203.60	-	-	0.26
CNF31735-6	LM13-94	Northwest zone	tabular	Type 1 ± 2B	109.62	262.71	472.50	-	-	-
CNF31735-7	LM13-94	Northwest zone	tabular	Type 1 ± 2B	-	36.17	36.17	-	-	0.04
CNF31735-8	LM13-94	Northwest zone	tabular	Type 1 ± 2B	12.39	468.07	660.80	0.02	-	-
CNF31735-9	LM13-94	Northwest zone	tabular	Type 1 ± 2B	30.33	473.20	339.73	-	-	-
CNF31809-1	LM10-43	Main zone	bladed/tabular	Type 1 ± 2A	10.56	1144.00	1029.60	-	1.85	0.88
CNF31809-2	LM10-43	Main zone	bladed/tabular	Type 1 ± 2A	7.04	1425.60	1416.80	0.05	1.31	0.48
CNF31809-3	LM10-43	Main zone	bladed/tabular	Type 1 ± 2A	51.92	2596.00	2411.20	-	2.29	-
CNF31809-4	LM10-43	Main zone	granular	Type 1 ± 2A	29.60	2480.00	2240.00	-	3.28	-
CNF31809-5	LM10-43	Main zone	granular	Type 1 ± 2A	25.60	2576.00	2328.00	-	0.50	1.09
CNF31809-6	LM10-43	Main zone	granular	Type 1 ± 2A	104.00	1136.00	936.00	0.55	1.04	0.56
CNF31809-7	LM10-43	Main zone	granular	Type 1 ± 2A	78.33	2791.97	2299.27	0.09	3.16	0.88
CNF31809-8	LM10-43	Main zone	bladed/tabular	Type 1 ± 2A	34.49	4618.90	3793.35	-	3.14	2.05
CNF31809-9	LM10-43	Main zone	bladed/tabular	Type 1 ± 2A	42.85	3657.50	2905.10	-	3.24	3.14
CNF31809-10	LM10-43	Main zone	bladed/tabular	Type 1 ± 2A	45.98	5956.50	4274.05	-	7.94	0.90
CNF31809-11	LM10-43	Main zone	bladed/tabular	Type 1 ± 2A	49.14	3549.00	3913.00	-	1.00	6.64
CNF31809-12	LM10-43	Main zone	bladed/tabular	Type 1 ± 2A	7.28	3185.00	2730.00	-	4.73	-
CNF31809-13	LM10-43	Main zone	bladed/tabular	Type 1 ± 2A	57.33	2356.90	2375.10	-	0.78	0.31
CNF31809-14	LM10-43	Main zone	granular	Type 1 ± 2A	-	957.00	980.93	-	0.77	-
CNF31809-15	LM10-43	Main zone	granular	Type 1 ± 2A	-	924.30	901.18	-	-	0.40
CNF31809-16	LM10-43	Main zone	bladed/tabular	Type 1 ± 2A	30.24	759.60	914.33	-	1.90	-

Sample/spot analysis #	Drill Hole	Mineralized zone	Barite texture	Mineral Assemblage Type	Sc ppm	Ti ppm	V ppm	Cr ppm	Mn ppm	Fe ppm	Co ppm	Ni ppm	Cu63 ppm	Cu65 ppm	Zn66 ppm	Zn67 ppm	Ga ppm
CNF31809-17	LM10-43	Main zone	bladed/tabular	Type 1 ± 2A	-	260.23	4.92	-	42.90	2954.00	-	-	886.20	1097.20	1434.80	8721.33	3.73
CNF31809-18	LM10-43	Main zone	bladed/tabular	Type 1 ± 2A	-	225.07	11.04	18.29	88.62	4782.67	0.07	-	1301.17	1315.23	1688.00	7666.33	3.80
CNF31809-19	LM10-43	Main zone	bladed/tabular	Type 1 ± 2A	-	127.27	9.96	-	58.10	3154.00	-	-	702.73	885.33	807.87	8687.33	5.53
CNF31809-20	LM10-43	Main zone	bladed/tabular	Type 1 ± 2A	-	77.20	3.09	-	30.88	2316.00	-	-	868.50	530.75	559.70	4535.50	1.88
CNF31809-21	LM10-43	Main zone	bladed/tabular	Type 1 ± 2A	-	33.48	-	-	15.98	583.20	-	-	294.84	320.76	712.80	9612.00	-
CNF31809-22	LM10-43	Main zone	bladed/tabular	Type 1 ± 2A	-	79.92	7.34	-	47.52	2181.60	-	-	572.40	583.20	1231.20	5832.00	-
CNF31812-1	LM10-43	Main zone	granular	Type 1	-	7.45	-	-	-	2482.67	-	-	886.67	922.13	744.80	12945.33	4.79
CNF31812-2	LM10-43	Main zone	granular	Type 1	-	-	-	15.96	13.30	1986.13	1.95	-	117.04	205.71	485.89	10640.00	-
CNF31812-3	LM10-43	Main zone	granular	Type 1	-	-	3.88	20.37	-	6111.00	-	-	203.70	155.20	1455.00	3686.00	-
CNF31812-4	LM10-43	Main zone	granular	Type 1	-	-	-	83.35	17.73	-	2.66	40.79	301.47	656.13	815.73	49653.33	-
CNF31812-5	LM10-43	Main zone	granular	Type 1	-	-	-	-	-	-	0.82	39.01	514.27	620.67	1276.80	16137.33	-
CNF31812-6	LM10-43	Main zone	granular	Type 1	-	-	7.45	-	26.60	1596.00	-	-	296.15	532.00	4628.40	33338.67	7.09
CNF31812-7	LM10-43	Main zone	granular	Type 1	6.37	15.93	-	22.78	31.87	-	-	239.00	382.40	525.80	3186.67	17526.67	11.15
CNF31812-8	LM10-43	Main zone	granular	Type 1	-	-	5.10	-	30.27	-	-	54.17	254.93	366.47	2613.07	43020.00	-
CNF31812-9	LM10-43	Main zone	bladed	Type 2A	13.30	-	-	50.14	25.07	-	-	-	61.04	180.94	195.11	38150.00	-
CNF31812-10	LM10-43	Main zone	bladed	Type 2A	-	-	-	29.97	-	-	-	51.84	37.26	82.62	70.47	11178.00	-
CNF31812-11	LM10-43	Main zone	bladed	Type 2A	-	-	-	50.14	-	1308.00	-	-	28.34	87.20	175.49	18857.00	-
CNF31812-12	LM10-43	Main zone	bladed	Type 2A	-	1.09	-	63.22	-	1526.00	-	-	53.41	164.59	188.57	27795.00	-
CNF31812-13	LM10-43	Main zone	bladed	Type 2A	-	-	-	-	-	-	-	-	48.33	128.57	160.47	21653.33	-
CNF31812-14	LM10-43	Main zone	bladed	Type 2A	-	-	-	-	-	-	0.50	-	-	120.55	228.27	19260.00	-
CNF31812-15	LM10-43	Main zone	bladed	Type 2A	-	-	-	-	-	-	2.42	-	46.40	101.50	309.33	17400.00	-
CNF31812-16	LM10-43	Main zone	granular	Type 2A	-	-	-	29.77	-	-	-	-	53.27	84.60	188.00	25066.67	0.78
CNF31812-17	LM10-43	Main zone	granular	Type 2A	-	-	-	-	-	-	-	-	49.35	195.83	113.58	16371.67	-
CNF31812-18	LM10-43	Main zone	granular	Type 2A	-	-	-	-	-	-	-	-	-	134.67	168.33	20200.00	-
CNF31816-1	LM08-19	Main zone	bladed/tabular	Type 1	-	-	-	35.84	-	-	-	67.95	32.85	194.13	94.08	11872.00	-
CNF31816-2	LM08-19	Main zone	bladed/tabular	Type 1	-	-	-	-	-	-	-	-	-	164.27	120.96	23146.67	-
CNF31816-3	LM08-19	Main zone	bladed/tabular	Type 1	-	-	-	-	22.40	896.00	-	-	-	70.19	99.31	16128.00	-
CNF31816-4	LM08-19	Main zone	bladed/tabular	Type 1	-	-	-	29.51	-	-	0.08	-	31.02	75.67	47.67	7718.00	-
CNF31816-5	LM08-19	Main zone	granular	Type 1	-	-	-	-	-	-	-	-	-	159.60	76.38	19380.00	-
CNF31816-6	LM08-19	Main zone	granular	Type 1	-	-	-	-	-	-	-	-	-	151.80	165.60	22770.00	-
CNF31816-7	LM08-19	Main zone	granular	Type 1	-	-	-	-	-	-	-	-	-	-	105.41	13903.33	-
CNF31816-8	LM08-19	Main zone	granular	Type 1	-	-	-	20.05	-	1487.33	-	-	-	-	142.27	11381.33	-
CNF31847-1	LM13-83	Northwest zone	interstitial	Type 3	-	-	-	-	-	-	-	-	-	-	-	14000.00	-
CNF31847-2	LM13-83	Northwest zone	interstitial	Type 3	-	-	-	-	-	-	-	-	-	-	-	17500.00	-
CNF31847-3	LM13-83	Northwest zone	interstitial	Type 3	-	-	-	-	-	-	-	-	-	-	425.00	70000.00	-
CNF31847-4	LM13-83	Northwest zone	interstitial	Type 3	-	-	-	-	-	-	3	-	-	-	350.00	12000.00	-
CNF31847-5	LM13-83	Northwest zone	interstitial	Type 3	-	-	-	-	-	-	-	-	-	-	-	20230.00	-
CNF31847-6	LM13-83	Northwest zone	interstitial	Type 3	-	77.35	-	-	-	-	-	-	-	-	348.50	34000.00	-
CNF31847-7	LM13-83	Northwest zone	interstitial	Type 3	-	-	-	-	-	-	-	-	-	-	663.00	26350.00	-
CNF31860-1	LM11-68	Main zone	tabular	Type 1 ± 2B ± 2A	-	31.45	2.41	52.73	14.060	703.00	-	-	94.35	229.40	223.85	28305.00	0.09
CNF31860-2	LM11-68	Main zone	tabular	Type 1 ± 2B ± 2A	-	-	-	49.40	21.645	962.00	-	-	170.20	277.50	220.15	26825.00	-
CNF31860-3	LM11-68	Main zone	tabular	Type 1 ± 2B ± 2A	-	75.85	-	36.82	19.980	1184.00	-	-	129.50	188.70	162.80	22570.00	0.76
CNF31860-4	LM11-68	Main zone	tabular	Type 1 ± 2B ± 2A	-	88.80	-	47.73	11.655	851.00	2.41	-	192.40	271.95	201.65	23310.00	-
CNF31860-5	LM11-68	Main zone	tabular	Type 1 ± 2B ± 2A	8.51	133.20	5.92	70.30	57.165	4292.00	-	-	449.55	580.90	331.15	30710.00	3.15
CNF31860-6	LM11-68	Main zone	tabular	Type 1 ± 2B ± 2A	-	444.00	-	105.45	101.750	5180.00	6.48	-	479.15	765.90	429.20	39035.00	-
CNF31860-7	LM11-68	Main zone	tabular	Type 1 ± 2B ± 2A	10.92	194.25	10.36	85.10	54.945	3533.50	-	75.85	429.20	586.45	283.05	29600.00	0.78
CNF31860-8	LM11-68	Main zone	tabular	Type 1 ± 2B ± 2A	19.80	303.40	6.85	88.80	81.400	4310.50	-	-	1850.00	3145.00	283.05	29230.00	2.22
CNF31860-9	LM11-68	Main zone	tabular	Type 1 ± 2B ± 2A	11.47	242.35	7.59	61.05	49.025	1258.00	2.78	-	493.95	560.55	629.00	30710.00	2.28
CNF31860-10	LM11-68	Main zone	tabular	Type 1 ± 2B ± 2A	-	222.00	11.47	83.07	78.440	3663.00	-	-	468.05	484.70	334.85	33300.00	-
CNF31860-11	LM11-68	Main zone	tabular	Type 1 ± 2B ± 2A	-	11.75	-	39.17	32.900	1410.00	-	-	151.97	166.07	98.70	15353.33	-
CNF31860-12	LM11-68	Main zone	granular	Type 1 ± 2B ± 2A	-	-	-	20.85	-	-	-	-	36.27	88.85	47.15	7344.00	-
CNF31860-13	LM11-68	Main zone	granular	Type 1 ± 2B ± 2A	-	-	-	20.49	-	471.47	-	-	37.17	66.19	35.36	9973.33	-
CNF31860-14	LM11-68	Main zone	tabular	Type 1 ± 2B ± 2A	3.71	24.88	-	42.08	-	-	-	-	134.98	187.91	105.87	11274.80	0.45

Sample/spot analysis #	Drill Hole	Mineralized zone	Barite texture	Mineral Assemblage Type	Ge ppm	As ppm	Se ppm	Rb ppm	Y ppm	Zr ppm	Nb ppm	Mo ppm	Ru ppm	Rh ppm	Pd ppm	Ag ppm	In ppm
CNF31809-17	LM10-43	Main zone	bladed/tabular	Type 1 ± 2A	-	77.37	-	2.25	8.58	1.13	42.90	56.27	-	-	4.22	738.50	-
CNF31809-18	LM10-43	Main zone	bladed/tabular	Type 1 ± 2A	-	119.57	-	0.98	18.99	0.32	76.66	50.64	-	-	4.92	640.03	-
CNF31809-19	LM10-43	Main zone	bladed/tabular	Type 1 ± 2A	-	99.60	58.10	-	9.68	0.11	39.29	58.10	-	-	-	641.87	-
CNF31809-20	LM10-43	Main zone	bladed/tabular	Type 1 ± 2A	-	-	26.06	-	4.00	0.72	36.67	28.47	-	-	-	246.08	-
CNF31809-21	LM10-43	Main zone	bladed/tabular	Type 1 ± 2A	-	54.00	216.00	-	9.07	0.12	18.58	13.82	-	-	7.56	820.80	-
CNF31809-22	LM10-43	Main zone	bladed/tabular	Type 1 ± 2A	-	97.20	97.20	1.34	5.94	0.24	27.43	48.60	-	12.96	-	1436.40	-
CNF31812-1	LM10-43	Main zone	granular	Type 1	-	-	177.33	-	9.58	-	-	-	-	-	-	248.27	-
CNF31812-2	LM10-43	Main zone	granular	Type 1	-	131.23	177.33	2.13	2.41	-	-	-	-	-	-	333.39	-
CNF31812-3	LM10-43	Main zone	granular	Type 1	-	48.50	-	2.04	-	-	-	-	-	-	-	611.10	-
CNF31812-4	LM10-43	Main zone	granular	Type 1	-	-	319.20	-	23.05	-	-	-	-	-	-	54.97	-
CNF31812-5	LM10-43	Main zone	granular	Type 1	-	19.51	212.80	-	3.37	0.34	15.96	3.19	-	-	-	602.93	-
CNF31812-6	LM10-43	Main zone	granular	Type 1	-	3.55	-	-	11.35	-	-	-	-	-	-	283.73	-
CNF31812-7	LM10-43	Main zone	granular	Type 1	-	-	15.93	1.59	8.29	-	-	-	-	-	11.15	149.77	0.18
CNF31812-8	LM10-43	Main zone	granular	Type 1	9.56	3.19	-	1.75	5.58	1.59	-	-	-	-	-	-	-
CNF31812-9	LM10-43	Main zone	bladed	Type 2A	-	-	37.06	-	17.33	-	-	-	-	-	-	0.11	-
CNF31812-10	LM10-43	Main zone	bladed	Type 2A	-	9.72	-	-	3.97	-	-	0.28	-	-	-	14.58	-
CNF31812-11	LM10-43	Main zone	bladed	Type 2A	-	45.78	-	-	6.87	-	-	-	-	-	-	-	-
CNF31812-12	LM10-43	Main zone	bladed	Type 2A	-	55.59	-	-	15.91	0.45	-	-	-	-	-	44.69	-
CNF31812-13	LM10-43	Main zone	bladed	Type 2A	-	53.17	-	-	8.60	-	-	-	-	-	-	21.27	-
CNF31812-14	LM10-43	Main zone	bladed	Type 2A	-	-	17.12	-	8.35	-	-	-	-	-	-	13.55	-
CNF31812-15	LM10-43	Main zone	bladed	Type 2A	-	-	-	-	7.35	-	-	1.35	-	-	-	56.07	-
CNF31812-16	LM10-43	Main zone	granular	Type 2A	-	36.82	19.58	-	7.13	-	-	-	-	-	-	18.80	-
CNF31812-17	LM10-43	Main zone	granular	Type 2A	-	55.62	-	0.63	4.00	-	-	-	-	-	-	3.92	-
CNF31812-18	LM10-43	Main zone	granular	Type 2A	-	54.54	-	4.98	8.89	-	-	-	-	-	-	-	0.22
CNF31816-1	LM08-19	Main zone	bladed/tabular	Type 1	-	14.93	14.93	-	7.24	0.40	1.19	-	-	-	-	-	-
CNF31816-2	LM08-19	Main zone	bladed/tabular	Type 1	-	14.93	-	-	9.41	-	-	-	-	-	-	21.65	-
CNF31816-3	LM08-19	Main zone	bladed/tabular	Type 1	-	-	-	-	6.87	-	0.23	-	-	-	-	7.47	-
CNF31816-4	LM08-19	Main zone	bladed/tabular	Type 1	-	121.82	-	-	1.82	-	-	-	-	-	-	7.57	-
CNF31816-5	LM08-19	Main zone	granular	Type 1	-	16.53	-	-	7.07	-	-	-	-	-	-	2.85	-
CNF31816-6	LM08-19	Main zone	granular	Type 1	-	-	13.80	13.80	11.04	-	-	-	-	-	-	-	-
CNF31816-7	LM08-19	Main zone	granular	Type 1	-	-	-	-	13.58	-	-	-	-	-	-	-	-
CNF31816-8	LM08-19	Main zone	granular	Type 1	10.35	43.33	-	-	10.73	0.19	-	-	-	-	-	-	-
CNF31847-1	LM13-83	Northwest zone	interstitial	Type 3	-	-	-	-	12.50	-	-	-	-	-	-	-	-
CNF31847-2	LM13-83	Northwest zone	interstitial	Type 3	-	7.50	0.45	-	24.50	-	4.00	-	-	-	-	-	-
CNF31847-3	LM13-83	Northwest zone	interstitial	Type 3	-	-	4.00	-	16.00	-	-	3	-	-	-	-	-
CNF31847-4	LM13-83	Northwest zone	interstitial	Type 3	-	-	-	-	4.70	-	1.80	-	-	-	-	1.25	-
CNF31847-5	LM13-83	Northwest zone	interstitial	Type 3	-	-	-	-	9.52	0.27	-	-	-	-	-	-	-
CNF31847-6	LM13-83	Northwest zone	interstitial	Type 3	6.80	-	2.89	-	29.75	0.68	-	-	-	-	-	-	-
CNF31847-7	LM13-83	Northwest zone	interstitial	Type 3	-	5.95	1.96	-	22.10	0.77	-	3.23	-	-	-	-	-
CNF31860-1	LM11-68	Main zone	tabular	Type 1 ± 2B ± 2A	-	207.20	-	-	15.36	2.15	0.03	-	-	-	-	24.05	-
CNF31860-2	LM11-68	Main zone	tabular	Type 1 ± 2B ± 2A	-	196.10	-	5.00	10.92	7.22	-	0.06	-	-	-	-	-
CNF31860-3	LM11-68	Main zone	tabular	Type 1 ± 2B ± 2A	-	-	-	3.52	12.58	8.14	0.15	-	-	-	-	3.15	0.15
CNF31860-4	LM11-68	Main zone	tabular	Type 1 ± 2B ± 2A	-	148.00	-	-	9.99	3.27	-	2.41	-	-	-	14.99	-
CNF31860-5	LM11-68	Main zone	tabular	Type 1 ± 2B ± 2A	-	142.45	22.20	16.10	16.47	39.41	0.50	-	-	-	-	79.55	-
CNF31860-6	LM11-68	Main zone	tabular	Type 1 ± 2B ± 2A	-	96.20	42.55	29.23	20.17	85.10	0.74	5.92	-	-	-	111.00	-
CNF31860-7	LM11-68	Main zone	tabular	Type 1 ± 2B ± 2A	-	103.60	-	11.84	12.58	36.26	1.46	-	-	-	-	209.05	-
CNF31860-8	LM11-68	Main zone	tabular	Type 1 ± 2B ± 2A	-	149.85	40.70	31.27	22.39	71.78	0.65	6.48	-	-	5.37	1091.50	-
CNF31860-9	LM11-68	Main zone	tabular	Type 1 ± 2B ± 2A	-	44.40	-	23.13	19.80	44.40	0.06	-	-	-	-	290.45	-
CNF31860-10	LM11-68	Main zone	tabular	Type 1 ± 2B ± 2A	-	-	-	20.54	21.09	47.73	1.26	0.44	-	-	-	412.55	-
CNF31860-11	LM11-68	Main zone	tabular	Type 1 ± 2B ± 2A	-	30.55	16.45	-	4.47	2.35	-	0.20	-	-	-	101.05	-
CNF31860-12	LM11-68	Main zone	granular	Type 1 ± 2B ± 2A	-	76.16	-	-	2.18	0.55	-	-	-	-	-	-	-
CNF31860-13	LM11-68	Main zone	granular	Type 1 ± 2B ± 2A	-	72.53	51.68	-	4.53	-	0.06	-	-	-	-	-	0.15
CNF31860-14	LM11-68	Main zone	tabular	Type 1 ± 2B ± 2A	-	140.27	87.34	-	6.14	2.96	0.19	-	-	-	-	-	-

Sample/spot analysis #	Drill Hole	Mineralized zone	Barite texture	Mineral Assemblage Type	Sn ppm	Sb ppm	Te ppm	Cs ppm	La ppm	Ce ppm	Pr ppm	Nd ppm	Sm ppm	Eu ppm	Gd155 ppm	Gd157 ppm	Tb ppm
CNF31809-17	LM10-43	Main zone	bladed/tabular	Type 1 ± 2A	-	0.37	-	0.20	26.73	20.40	2.39	4.64	-	6.89	268.67	0.98	-
CNF31809-18	LM10-43	Main zone	bladed/tabular	Type 1 ± 2A	-	0.37	-	0.08	43.61	81.59	6.19	35.87	9.85	18.43	260.94	18.99	0.84
CNF31809-19	LM10-43	Main zone	bladed/tabular	Type 1 ± 2A	-	0.22	-	-	5.15	7.08	0.22	1.22	0.21	5.92	293.27	0.61	0.01
CNF31809-20	LM10-43	Main zone	bladed/tabular	Type 1 ± 2A	-	-	-	-	3.67	6.03	0.03	0.13	-	4.87	173.70	0.21	-
CNF31809-21	LM10-43	Main zone	bladed/tabular	Type 1 ± 2A	-	-	-	-	14.36	12.53	1.08	1.73	3.13	10.15	328.32	0.81	0.10
CNF31809-22	LM10-43	Main zone	bladed/tabular	Type 1 ± 2A	-	0.48	-	-	6.70	5.94	0.42	2.38	0.76	7.56	231.12	0.57	0.07
CNF31812-1	LM10-43	Main zone	granular	Type 1	9.93	1.77	-	-	8.69	3.72	-	-	-	35.11	939.87	-	-
CNF31812-2	LM10-43	Main zone	granular	Type 1	21.28	-	-	-	9.75	6.03	0.55	1.60	-	12.06	496.53	0.69	-
CNF31812-3	LM10-43	Main zone	granular	Type 1	-	-	-	-	6.40	0.64	0.28	-	-	2.62	174.60	-	0.05
CNF31812-4	LM10-43	Main zone	granular	Type 1	12.41	-	-	-	4.26	-	-	-	-	12.24	975.33	-	-
CNF31812-5	LM10-43	Main zone	granular	Type 1	9.40	-	-	-	11.17	1.95	0.25	-	-	27.13	221.67	-	-
CNF31812-6	LM10-43	Main zone	granular	Type 1	18.27	-	-	1.01	22.34	2.48	0.14	-	-	35.47	691.60	-	-
CNF31812-7	LM10-43	Main zone	granular	Type 1	7.33	0.08	-	0.11	16.25	10.52	0.76	2.55	-	35.05	462.07	2.07	-
CNF31812-8	LM10-43	Main zone	granular	Type 1	7.17	4.62	-	-	10.36	4.94	-	-	-	22.78	637.33	-	-
CNF31812-9	LM10-43	Main zone	bladed	Type 2A	-	-	-	-	14.82	12.97	0.09	0.44	-	25.07	970.10	0.43	-
CNF31812-10	LM10-43	Main zone	bladed	Type 2A	4.21	-	-	-	7.61	3.81	0.18	-	-	6.24	136.89	0.29	-
CNF31812-11	LM10-43	Main zone	bladed	Type 2A	-	-	-	-	16.35	6.21	0.11	0.41	-	16.24	501.40	-	-
CNF31812-12	LM10-43	Main zone	bladed	Type 2A	-	-	-	1.85	3.92	2.51	-	-	-	31.61	752.10	-	-
CNF31812-13	LM10-43	Main zone	bladed	Type 2A	3.48	1.35	-	-	14.98	3.58	0.08	-	-	14.31	512.33	-	-
CNF31812-14	LM10-43	Main zone	bladed	Type 2A	-	-	-	0.15	5.42	0.60	0.04	0.22	-	9.34	535.00	0.34	-
CNF31812-15	LM10-43	Main zone	bladed	Type 2A	-	-	-	0.68	14.98	3.58	-	-	-	26.29	908.67	-	-
CNF31812-16	LM10-43	Main zone	granular	Type 2A	-	-	-	-	14.88	0.35	-	-	0.24	8.70	438.67	-	-
CNF31812-17	LM10-43	Main zone	granular	Type 2A	-	-	-	-	6.82	-	-	-	-	14.88	376.00	-	-
CNF31812-18	LM10-43	Main zone	granular	Type 2A	-	-	-	0.19	8.28	0.35	-	-	-	13.60	430.93	-	-
CNF31816-1	LM08-19	Main zone	bladed/tabular	Type 1	-	-	-	-	13.44	-	-	-	-	7.91	350.93	-	-
CNF31816-2	LM08-19	Main zone	bladed/tabular	Type 1	-	-	-	-	3.51	0.11	-	-	-	17.62	530.13	-	-
CNF31816-3	LM08-19	Main zone	bladed/tabular	Type 1	-	1.19	-	-	19.41	1.05	0.04	0.12	-	20.46	395.73	-	-
CNF31816-4	LM08-19	Main zone	bladed/tabular	Type 1	-	-	-	-	2.57	-	-	-	-	9.08	287.53	-	-
CNF31816-5	LM08-19	Main zone	granular	Type 1	9.69	-	-	-	2.74	0.03	-	-	-	21.66	364.80	0.68	-
CNF31816-6	LM08-19	Main zone	granular	Type 1	-	-	-	-	5.38	0.18	-	-	-	17.25	848.70	-	-
CNF31816-7	LM08-19	Main zone	granular	Type 1	-	-	-	-	5.04	0.36	-	-	-	12.29	575.53	0.31	-
CNF31816-8	LM08-19	Main zone	granular	Type 1	-	0.20	-	-	6.47	0.09	-	-	-	14.23	420.33	-	-
CNF31847-1	LM13-83	Northwest zone	interstitial	Type 3	-	-	-	-	2.30	0.04	-	-	-	5.35	260.00	-	-
CNF31847-2	LM13-83	Northwest zone	interstitial	Type 3	5.00	-	-	-	1.40	-	-	0.5	-	7.75	225.00	-	-
CNF31847-3	LM13-83	Northwest zone	interstitial	Type 3	-	-	-	-	2.65	1.65	-	-	-	0.55	800.00	-	-
CNF31847-4	LM13-83	Northwest zone	interstitial	Type 3	-	-	-	-	1.30	2.05	-	-	-	5.35	310.00	-	-
CNF31847-5	LM13-83	Northwest zone	interstitial	Type 3	-	-	-	0.18	0.99	-	0.06	-	-	13.35	251.60	-	-
CNF31847-6	LM13-83	Northwest zone	interstitial	Type 3	-	-	-	-	6.04	-	-	-	-	26.35	425.00	-	-
CNF31847-7	LM13-83	Northwest zone	interstitial	Type 3	-	-	-	1.36	4.59	1.45	-	-	-	25.50	637.50	-	-
CNF31860-1	LM11-68	Main zone	tabular	Type 1 ± 2B ± 2A	37.56	-	-	0.39	10.73	5.92	0.19	0.19	0.04	13.69	484.70	0.44	-
CNF31860-2	LM11-68	Main zone	tabular	Type 1 ± 2B ± 2A	27.75	0.59	-	-	37.00	31.45	2.59	5.18	0.61	11.84	377.40	1.28	-
CNF31860-3	LM11-68	Main zone	tabular	Type 1 ± 2B ± 2A	23.87	-	-	0.83	22.20	33.30	1.35	4.44	0.76	14.80	338.55	1.26	0.01
CNF31860-4	LM11-68	Main zone	tabular	Type 1 ± 2B ± 2A	38.11	0.33	-	-	10.73	7.59	0.50	1.13	0.20	10.73	294.15	-	-
CNF31860-5	LM11-68	Main zone	tabular	Type 1 ± 2B ± 2A	69.93	3.70	-	-	22.76	29.60	1.11	2.74	-	14.43	423.65	0.72	-
CNF31860-6	LM11-68	Main zone	tabular	Type 1 ± 2B ± 2A	94.35	4.63	-	3.15	61.42	57.54	4.44	8.70	-	21.46	553.15	1.41	-
CNF31860-7	LM11-68	Main zone	tabular	Type 1 ± 2B ± 2A	83.25	4.07	-	-	40.89	34.23	2.20	4.63	-	14.43	473.60	2.31	0.01
CNF31860-8	LM11-68	Main zone	tabular	Type 1 ± 2B ± 2A	107.30	-	-	-	34.60	38.11	2.31	9.44	-	14.80	381.10	-	-
CNF31860-9	LM11-68	Main zone	tabular	Type 1 ± 2B ± 2A	87.69	5.74	-	-	30.53	34.04	2.42	5.00	-	12.21	440.30	-	-
CNF31860-10	LM11-68	Main zone	tabular	Type 1 ± 2B ± 2A	68.27	8.51	-	-	37.56	37.19	3.07	4.81	0.89	15.73	464.35	0.20	-
CNF31860-11	LM11-68	Main zone	tabular	Type 1 ± 2B ± 2A	19.58	3.13	-	-	26.63	21.07	1.72	1.80	-	9.09	221.68	-	-
CNF31860-12	LM11-68	Main zone	granular	Type 1 ± 2B ± 2A	1.18	-	-	-	1.90	0.19	0.02	0.09	0.06	5.89	93.39	1.36	-
CNF31860-13	LM11-68	Main zone	granular	Type 1 ± 2B ± 2A	6.35	0.46	-	-	1.54	0.80	-	-	-	4.62	152.32	-	-
CNF31860-14	LM11-68	Main zone	tabular	Type 1 ± 2B ± 2A	11.91	0.95	-	-	32.02	30.97	1.85	4.76	-	8.15	254.08	0.24	-

Sample/spot analysis #	Drill Hole	Mineralized zone	Barite texture	Mineral Assemblage Type	Dy ppm	Ho ppm	Er ppm	Tm ppm	Yb ppm	Lu ppm	Hf ppm	Ta ppm	W ppm	Re ppm	Os ppm	Au ppm	Hg ppm
CNF31809-17	LM10-43	Main zone	bladed/tabular	Type 1 ± 2A	-	0.03	-	-	-	-	-	0.08	1.55	-	-	43.61	935.43
CNF31809-18	LM10-43	Main zone	bladed/tabular	Type 1 ± 2A	4.22	0.35	1.62	0.03	-	-	-	-	0.77	-	-	33.06	801.80
CNF31809-19	LM10-43	Main zone	bladed/tabular	Type 1 ± 2A	0.06	0.04	0.08	-	-	0.01	-	0.14	0.89	-	-	37.63	442.67
CNF31809-20	LM10-43	Main zone	bladed/tabular	Type 1 ± 2A	0.29	-	-	-	-	-	-	0.01	0.43	-	-	9.17	381.18
CNF31809-21	LM10-43	Main zone	bladed/tabular	Type 1 ± 2A	0.06	-	-	-	-	-	-	-	0.14	-	-	158.76	1090.80
CNF31809-22	LM10-43	Main zone	bladed/tabular	Type 1 ± 2A	0.56	0.03	0.06	-	-	-	-	-	1.94	-	-	7.56	680.40
CNF31812-1	LM10-43	Main zone	granular	Type 1	-	-	-	-	-	-	-	0.12	2.48	-	-	-	1010.80
CNF31812-2	LM10-43	Main zone	granular	Type 1	-	-	-	-	-	-	-	0.27	0.16	-	-	72.71	744.80
CNF31812-3	LM10-43	Main zone	granular	Type 1	-	-	-	-	-	-	-	-	-	-	-	-	485.00
CNF31812-4	LM10-43	Main zone	granular	Type 1	-	-	-	-	-	-	-	-	-	-	-	-	230.53
CNF31812-5	LM10-43	Main zone	granular	Type 1	-	-	-	-	-	-	-	-	-	-	-	-	939.87
CNF31812-6	LM10-43	Main zone	granular	Type 1	-	-	-	-	-	-	-	-	-	-	-	-	1418.67
CNF31812-7	LM10-43	Main zone	granular	Type 1	-	-	-	-	-	-	-	-	-	-	-	-	828.53
CNF31812-8	LM10-43	Main zone	granular	Type 1	-	-	-	-	-	-	-	-	-	0.01	-	-	701.07
CNF31812-9	LM10-43	Main zone	bladed	Type 2A	-	-	-	-	-	-	-	-	-	-	-	23.98	414.20
CNF31812-10	LM10-43	Main zone	bladed	Type 2A	-	-	-	-	-	-	-	-	0.14	0.01	-	-	113.40
CNF31812-11	LM10-43	Main zone	bladed	Type 2A	-	-	-	-	-	-	-	-	-	-	-	44.69	98.10
CNF31812-12	LM10-43	Main zone	bladed	Type 2A	-	-	-	-	-	-	-	-	-	-	-	7.74	305.20
CNF31812-13	LM10-43	Main zone	bladed	Type 2A	-	-	-	-	-	-	-	-	-	-	-	25.13	126.63
CNF31812-14	LM10-43	Main zone	bladed	Type 2A	-	-	-	-	-	-	-	-	-	-	-	8.56	114.13
CNF31812-15	LM10-43	Main zone	bladed	Type 2A	-	-	-	-	-	-	-	-	-	-	-	-	193.33
CNF31812-16	LM10-43	Main zone	granular	Type 2A	-	-	-	-	-	-	-	-	-	-	-	6.27	313.33
CNF31812-17	LM10-43	Main zone	granular	Type 2A	-	-	-	-	-	-	-	-	-	-	-	-	188.00
CNF31812-18	LM10-43	Main zone	granular	Type 2A	-	-	-	-	0.25	-	-	-	-	-	-	-	121.20
CNF31816-1	LM08-19	Main zone	bladed/tabular	Type 1	-	-	-	-	-	-	-	3.14	-	-	-	-	44.80
CNF31816-2	LM08-19	Main zone	bladed/tabular	Type 1	-	-	-	-	-	-	-	1.27	0.52	-	-	-	171.73
CNF31816-3	LM08-19	Main zone	bladed/tabular	Type 1	-	-	-	-	-	-	-	1.27	6.94	-	-	-	104.53
CNF31816-4	LM08-19	Main zone	bladed/tabular	Type 1	-	-	-	-	-	-	-	-	-	0.00	-	3.41	45.40
CNF31816-5	LM08-19	Main zone	granular	Type 1	-	-	-	-	-	-	-	-	-	-	-	-	74.10
CNF31816-6	LM08-19	Main zone	granular	Type 1	-	-	-	-	-	-	-	-	-	-	-	-	138.00
CNF31816-7	LM08-19	Main zone	granular	Type 1	-	-	-	-	-	-	-	-	-	-	-	-	109.93
CNF31816-8	LM08-19	Main zone	granular	Type 1	-	-	-	-	-	-	-	0.02	-	-	-	-	168.13
CNF31847-1	LM13-83	Northwest zone	interstitial	Type 3	-	-	-	-	-	-	-	-	-	-	-	7.00	38.50
CNF31847-2	LM13-83	Northwest zone	interstitial	Type 3	-	-	-	-	-	-	-	-	-	-	-	1.65	22.50
CNF31847-3	LM13-83	Northwest zone	interstitial	Type 3	-	-	-	-	-	-	-	0.75	-	-	-	0.30	23.00
CNF31847-4	LM13-83	Northwest zone	interstitial	Type 3	-	-	-	-	-	-	-	-	0.50	-	-	-	18.50
CNF31847-5	LM13-83	Northwest zone	interstitial	Type 3	-	-	-	-	-	-	-	-	-	-	-	1.62	46.75
CNF31847-6	LM13-83	Northwest zone	interstitial	Type 3	-	-	-	-	-	-	-	-	-	-	-	4.08	31.45
CNF31847-7	LM13-83	Northwest zone	interstitial	Type 3	-	-	-	-	-	-	-	-	4.25	-	-	-	10.71
CNF31860-1	LM11-68	Main zone	tabular	Type 1 ± 2B ± 2A	-	-	-	-	-	-	-	-	0.52	-	-	86.95	1202.50
CNF31860-2	LM11-68	Main zone	tabular	Type 1 ± 2B ± 2A	0.22	0.01	0.02	-	-	-	-	-	-	-	-	70.30	1063.75
CNF31860-3	LM11-68	Main zone	tabular	Type 1 ± 2B ± 2A	-	-	-	-	-	-	-	0.02	-	-	-	103.60	851.00
CNF31860-4	LM11-68	Main zone	tabular	Type 1 ± 2B ± 2A	-	-	-	-	-	-	-	0.06	0.31	-	-	51.80	597.55
CNF31860-5	LM11-68	Main zone	tabular	Type 1 ± 2B ± 2A	0.13	-	-	-	-	-	0.41	0.15	2.00	-	-	59.20	593.85
CNF31860-6	LM11-68	Main zone	tabular	Type 1 ± 2B ± 2A	-	0.01	-	-	-	-	0.57	0.09	0.59	-	-	30.90	388.50
CNF31860-7	LM11-68	Main zone	tabular	Type 1 ± 2B ± 2A	0.13	-	0.07	-	-	-	0.09	0.05	1.48	-	-	49.95	584.60
CNF31860-8	LM11-68	Main zone	tabular	Type 1 ± 2B ± 2A	-	0.04	-	-	-	0.05	0.07	0.20	1.67	-	-	59.20	529.10
CNF31860-9	LM11-68	Main zone	tabular	Type 1 ± 2B ± 2A	-	-	0.09	-	-	-	0.30	0.50	2.22	-	-	53.65	608.65
CNF31860-10	LM11-68	Main zone	tabular	Type 1 ± 2B ± 2A	2.04	0.07	-	-	-	-	2.31	0.26	1.57	-	-	66.60	645.65
CNF31860-11	LM11-68	Main zone	tabular	Type 1 ± 2B ± 2A	-	-	-	-	-	-	-	-	-	-	-	16.45	32.90
CNF31860-12	LM11-68	Main zone	granular	Type 1 ± 2B ± 2A	-	-	-	-	-	-	-	-	0.25	-	-	9.07	235.73
CNF31860-13	LM11-68	Main zone	granular	Type 1 ± 2B ± 2A	-	-	-	-	-	-	-	-	-	-	-	8.16	217.60
CNF31860-14	LM11-68	Main zone	tabular	Type 1 ± 2B ± 2A	-	-	-	-	-	-	-	0.12	-	-	-	23.03	444.64

Sample/spot analysis #	Drill Hole	Mineralized zone	Barite texture	Mineral Assemblage Type	Tl ppm	Pb206 ppm	Pb208 ppm	Bi ppm	Th ppm	U ppm
CNF31809-17	LM10-43	Main zone	bladed/tabular	Type 1 ± 2A	58.38	443.10	485.30	0.01	0.99	-
CNF31809-18	LM10-43	Main zone	bladed/tabular	Type 1 ± 2A	54.16	569.70	668.17	-	2.46	1.62
CNF31809-19	LM10-43	Main zone	bladed/tabular	Type 1 ± 2A	2.77	354.13	426.07	-	0.35	0.27
CNF31809-20	LM10-43	Main zone	bladed/tabular	Type 1 ± 2A	-	164.05	188.18	-	1.16	-
CNF31809-21	LM10-43	Main zone	bladed/tabular	Type 1 ± 2A	30.24	116.64	140.40	0.00	0.39	-
CNF31809-22	LM10-43	Main zone	bladed/tabular	Type 1 ± 2A	116.64	842.40	712.80	-	0.84	-
CNF31812-1	LM10-43	Main zone	granular	Type 1	26.60	-	305.01	-	-	-
CNF31812-2	LM10-43	Main zone	granular	Type 1	-	-	85.12	-	-	-
CNF31812-3	LM10-43	Main zone	granular	Type 1	39.77	-	242.50	-	-	-
CNF31812-4	LM10-43	Main zone	granular	Type 1	101.08	-	549.73	-	-	-
CNF31812-5	LM10-43	Main zone	granular	Type 1	109.95	-	407.87	-	-	-
CNF31812-6	LM10-43	Main zone	granular	Type 1	143.64	-	461.07	-	-	-
CNF31812-7	LM10-43	Main zone	granular	Type 1	25.49	-	194.39	-	-	0.76
CNF31812-8	LM10-43	Main zone	granular	Type 1	9.56	-	143.40	-	-	-
CNF31812-9	LM10-43	Main zone	bladed	Type 2A	49.05	-	78.48	-	-	-
CNF31812-10	LM10-43	Main zone	bladed	Type 2A	-	-	35.64	-	-	-
CNF31812-11	LM10-43	Main zone	bladed	Type 2A	-	-	66.49	-	-	-
CNF31812-12	LM10-43	Main zone	bladed	Type 2A	35.97	-	54.50	-	-	0.57
CNF31812-13	LM10-43	Main zone	bladed	Type 2A	-	-	50.27	-	-	-
CNF31812-14	LM10-43	Main zone	bladed	Type 2A	-	-	79.18	-	-	-
CNF31812-15	LM10-43	Main zone	bladed	Type 2A	31.90	-	124.70	-	-	-
CNF31812-16	LM10-43	Main zone	granular	Type 2A	21.93	-	55.62	-	-	0.15
CNF31812-17	LM10-43	Main zone	granular	Type 2A	-	-	86.17	-	-	-
CNF31812-18	LM10-43	Main zone	granular	Type 2A	-	-	56.56	-	-	0.67
CNF31816-1	LM08-19	Main zone	bladed/tabular	Type 1	-	-	17.32	-	-	-
CNF31816-2	LM08-19	Main zone	bladed/tabular	Type 1	-	-	16.35	-	-	-
CNF31816-3	LM08-19	Main zone	bladed/tabular	Type 1	-	-	23.89	-	-	-
CNF31816-4	LM08-19	Main zone	bladed/tabular	Type 1	-	-	5.90	-	-	-
CNF31816-5	LM08-19	Main zone	granular	Type 1	-	-	33.63	-	-	0.59
CNF31816-6	LM08-19	Main zone	granular	Type 1	-	-	22.08	-	-	-
CNF31816-7	LM08-19	Main zone	granular	Type 1	-	-	174.60	-	-	-
CNF31816-8	LM08-19	Main zone	granular	Type 1	-	-	13.90	-	-	-
CNF31847-1	LM13-83	Northwest zone	interstitial	Type 3	-	3.25	-	-	-	-
CNF31847-2	LM13-83	Northwest zone	interstitial	Type 3	-	-	36.50	-	-	-
CNF31847-3	LM13-83	Northwest zone	interstitial	Type 3	-	-	195.00	-	-	-
CNF31847-4	LM13-83	Northwest zone	interstitial	Type 3	-	36.50	16.50	-	-	-
CNF31847-5	LM13-83	Northwest zone	interstitial	Type 3	-	20.40	19.55	-	-	-
CNF31847-6	LM13-83	Northwest zone	interstitial	Type 3	-	-	102.00	-	0.57	0.77
CNF31847-7	LM13-83	Northwest zone	interstitial	Type 3	-	-	-	-	-	-
CNF31860-1	LM11-68	Main zone	tabular	Type 1 ± 2B ± 2A	-	146.15	159.10	-	-	-
CNF31860-2	LM11-68	Main zone	tabular	Type 1 ± 2B ± 2A	19.80	120.25	114.70	-	-	0.65
CNF31860-3	LM11-68	Main zone	tabular	Type 1 ± 2B ± 2A	14.43	75.85	85.10	-	0.01	-
CNF31860-4	LM11-68	Main zone	tabular	Type 1 ± 2B ± 2A	26.83	94.35	105.45	-	-	-
CNF31860-5	LM11-68	Main zone	tabular	Type 1 ± 2B ± 2A	-	1461.50	1258.00	-	0.35	2.05
CNF31860-6	LM11-68	Main zone	tabular	Type 1 ± 2B ± 2A	-	1905.50	1387.50	-	1.17	-
CNF31860-7	LM11-68	Main zone	tabular	Type 1 ± 2B ± 2A	11.47	1794.50	2016.50	-	0.50	-
CNF31860-8	LM11-68	Main zone	tabular	Type 1 ± 2B ± 2A	-	2035.00	2072.00	-	1.76	1.63
CNF31860-9	LM11-68	Main zone	tabular	Type 1 ± 2B ± 2A	-	1942.50	2275.50	-	0.61	1.37
CNF31860-10	LM11-68	Main zone	tabular	Type 1 ± 2B ± 2A	19.61	3385.50	3903.50	-	1.04	-
CNF31860-11	LM11-68	Main zone	tabular	Type 1 ± 2B ± 2A	-	423.00	477.83	-	-	-
CNF31860-12	LM11-68	Main zone	granular	Type 1 ± 2B ± 2A	9.07	25.39	30.83	-	-	-
CNF31860-13	LM11-68	Main zone	granular	Type 1 ± 2B ± 2A	-	17.23	16.32	-	0.03	0.23
CNF31860-14	LM11-68	Main zone	tabular	Type 1 ± 2B ± 2A	-	108.51	116.45	-	0.04	0.34

Sample/spot analysis #	Drill Hole	Mineralized zone	Barite texture	Mineral Assemblage Type	Sc ppm	Ti ppm	V ppm	Cr ppm	Mn ppm	Fe ppm	Co ppm	Ni ppm	Cu63 ppm	Cu65 ppm	Zn66 ppm	Zn67 ppm	Ga ppm
CNF31860-15	LM11-68	Main zone	tabular	Type 1 ± 2B ± 2A	4.08	46.18	3.04	60.85	-	461.83	-	40.75	206.47	350.45	190.17	22548.33	0.24
CNF31860-16	LM11-68	Main zone	bladed	Type 1 ± 2B ± 2A	-	-	6.59	20.67	-	1201.67	2.13	-	3158.67	3090.00	1229.13	13802.00	4.94
CNF31860-17	LM11-68	Main zone	bladed	Type 1 ± 2B ± 2A	-	-	6.18	18.88	7.62	-	1.45	-	2025.67	2568.13	899.53	14076.67	4.05
CNF31860-18	LM11-68	Main zone	bladed	Type 1 ± 2B ± 2A	-	14.15	22.66	21.15	14.97	515.00	-	-	3776.67	3570.67	2060.00	16686.00	5.42
CNF31860-19	LM11-68	Main zone	bladed	Type 1 ± 2B ± 2A	-	8.72	8.45	8.31	7.42	7278.67	-	-	2526.93	2293.47	5150.00	16548.67	6.52
CNF31860-20	LM11-68	Main zone	bladed	Type 1 ± 2B ± 2A	-	-	44.63	22.80	-	878.93	-	-	666.07	727.87	645.47	14214.00	10.51
CNF31860-21	LM11-68	Main zone	bladed	Type 1 ± 2B ± 2A	-	31.59	57.68	14.42	-	2128.67	-	-	824.00	631.73	1442.00	14008.00	12.63
CNF31860-22	LM11-68	Main zone	bladed	Type 1 ± 2B ± 2A	-	-	37.77	19.16	7.14	2472.00	-	-	1442.00	1469.47	734.73	12566.00	11.33
CNF31860-23	LM11-68	Main zone	bladed	Type 1 ± 2B ± 2A	-	75.47	17.42	49.34	83.21	4257.00	-	45.47	3579.75	2805.75	71595.00	55147.50	51.28
CNF31860-24	LM11-68	Main zone	bladed	Type 1 ± 2B ± 2A	-	241.88	14.71	82.24	251.55	3483.00	-	-	3192.75	2902.50	183825.00	217687.50	143.19
CNF31860-25	LM11-68	Main zone	bladed	Type 1 ± 2B ± 2A	-	270.90	36.77	59.02	233.17	2534.85	-	-	2215.58	2341.35	76432.50	125775.00	270.90
CNF31860-26	LM11-68	Main zone	bladed	Type 1 ± 2B ± 2A	-	202.21	55.15	79.34	219.62	4547.25	-	-	4102.20	4276.35	152865.00	328950.00	267.03
CNF31860-27	LM11-68	Main zone	granular	Type 1 ± 2B ± 2A	-	38.16	3.50	86.66	17.49	2226.00	-	270.30	413.40	532.65	2385.00	21465.00	-
CNF31860-28	LM11-68	Main zone	granular	Type 1 ± 2B ± 2A	-	-	-	-	-	-	-	-	33.11	52.84	33.74	10887.00	-
CNF31860-29	LM11-68	Main zone	granular	Type 1 ± 2B ± 2A	-	7.13	-	-	-	-	-	-	28.01	43.93	22.28	4711.33	-
CNF31860-30	LM11-68	Main zone	granular	Type 1 ± 2B ± 2A	-	29.33	-	-	5.28	-	-	-	35.20	66.00	68.93	9020.00	-
CNF31860-31	LM11-68	Main zone	granular	Type 1 ± 2B ± 2A	-	16.87	3.37	-	13.93	-	-	-	91.67	74.07	43.27	9533.33	1.39
CNF31860-32	LM11-68	Main zone	granular	Type 1 ± 2B ± 2A	-	34.07	-	12.37	4.30	-	-	-	80.70	128.22	46.63	10670.33	-
CNF31860-33	LM11-68	Main zone	bladed	Type 1 ± 2B ± 2A	-	18.54	12.57	13.05	-	1414.53	-	-	3433.33	3708.00	3570.67	17372.67	5.63
CNF31860-34	LM11-68	Main zone	bladed	Type 1 ± 2B ± 2A	-	18.54	24.72	20.60	-	1222.27	-	-	3982.67	3502.00	954.47	10849.33	6.59
CNF31860-35	LM11-68	Main zone	bladed	Type 1 ± 2B ± 2A	4.53	-	9.68	35.02	14.63	652.33	-	-	3845.33	4326.00	2678.00	12909.33	9.27
CNF31860-36	LM11-68	Main zone	bladed	Type 1 ± 2B ± 2A	-	26.78	15.11	17.03	8.86	858.33	-	-	1153.60	1249.73	3364.67	12772.00	8.31
CNF31860-37	LM11-68	Main zone	bladed	Type 1 ± 2B ± 2A	-	24.72	21.97	24.86	24.03	1325.27	-	-	1400.80	2334.67	4394.67	13733.33	12.50
CNF31860-38	LM11-68	Main zone	bladed	Type 1 ± 2B ± 2A	-	30.90	10.78	19.02	18.54	659.20	-	-	2430.80	3158.67	6248.67	14488.67	6.25
CNF31860-39	LM11-68	Main zone	bladed	Type 1 ± 2B ± 2A	-	8.10	11.06	15.59	9.54	487.53	-	-	2472.00	2403.33	1448.87	8858.00	2.20
CNF31861-1	LM11-68	Main zone	granular	Type 1 ± 2B ± 2A	-	41.05	-	24.45	9.61	1222.67	-	33.19	142.35	137.99	288.20	6637.33	-
CNF31861-2	LM11-68	Main zone	granular	Type 1 ± 2B ± 2A	-	-	-	19.21	17.47	882.07	-	-	73.36	136.24	89.08	17816.00	0.26
CNF31861-3	LM11-68	Main zone	granular	Type 1 ± 2B ± 2A	-	27.14	-	16.52	14.75	708.00	-	-	59.59	159.30	112.10	14750.00	0.94
CNF31861-4	LM11-68	Main zone	granular	Type 1 ± 2B ± 2A	-	76.47	-	120.87	56.73	3330.00	-	-	900.33	986.67	2466.67	39836.67	0.49
CNF31861-5	LM11-68	Main zone	granular	Type 1 ± 2B ± 2A	-	-	53.03	197.33	93.73	209666.67	-	-	234333.33	185000.00	4316.67	45633.33	185.00
CNF31861-6	LM11-68	Main zone	granular	Type 1 ± 2B ± 2A	-	83.87	49.33	80.17	55.50	44400.00	-	-	72766.67	108533.33	2836.67	32190.00	22.20
CNF31861-7	LM11-68	Main zone	granular	Type 1 ± 2B ± 2A	-	177.60	135.67	136.90	112.23	11593.33	-	-	20966.67	19733.33	119633.33	172666.67	101.13
CNF31861-8	LM11-68	Main zone	granular	Type 1 ± 2B ± 2A	-	98.67	43.17	249.13	629.00	4686.67	-	-	9003.33	7276.67	505666.67	555000.00	260.23
CNF31861-9	LM11-68	Main zone	bladed	Type 1 ± 2B ± 2A	3.42	108.30	3.14	104.60	61.85	9405.00	-	-	381.90	675.45	5130.00	47880.00	7.70
CNF31861-10	LM11-68	Main zone	bladed	Type 1 ± 2B ± 2A	-	270.75	8.27	148.20	87.50	7695.00	-	-	399.00	504.45	282.15	33060.00	-
CNF31861-11	LM11-68	Main zone	bladed	Type 1 ± 2B ± 2A	51.30	524.40	22.52	168.15	182.40	25650.00	-	51.30	1140.00	1111.50	11685.00	48165.00	25.65
CNF31861-12	LM11-68	Main zone	bladed	Type 1 ± 2B ± 2A	13.97	513.00	23.09	136.80	205.20	9690.00	-	111.15	912.00	1026.00	39900.00	68400.00	39.90
CNF31861-13	LM11-68	Main zone	bladed	Type 1 ± 2B ± 2A	-	327.75	14.25	128.25	136.80	5187.00	2.02	-	558.60	1140.00	31350.00	71250.00	31.92
CNF31861-14	LM11-68	Main zone	bladed	Type 1 ± 2B ± 2A	17.67	359.10	17.10	216.60	173.85	8350.50	4.96	-	595.65	627.00	869.25	41040.00	1.43
CNF31861-15	LM11-68	Main zone	bladed	Type 1 ± 2B ± 2A	-	165.30	9.41	293.55	79.80	6583.50	5.13	-	510.15	615.60	957.60	37050.00	3.05
CNF31861-16	LM11-68	Main zone	bladed	Type 1 ± 2B ± 2A	-	165.30	13.11	99.18	72.68	4560.00	2.22	-	290.70	532.95	4275.00	28500.00	6.56
CNF31861-17	LM11-68	Main zone	bladed	Type 1 ± 2B ± 2A	-	114.00	5.73	47.88	58.14	1710.00	-	19.95	199.50	322.05	6840.00	25080.00	8.27
CNF31861-18	LM11-68	Main zone	bladed	Type 1 ± 2B ± 2A	-	128.25	5.42	48.74	66.12	3135.00	-	-	270.75	316.35	3990.00	24795.00	10.26
CNF31861-19	LM11-68	Main zone	bladed	Type 1 ± 2B ± 2A	-	77.52	6.10	55.58	353.40	4132.50	0.77	-	746.70	664.05	513000.00	570000.00	210.90
CNF31861-20	LM11-68	Main zone	bladed	Type 1 ± 2B ± 2A	-	82.65	4.05	38.76	69.54	3505.50	-	48.45	322.05	333.45	4759.50	23085.00	6.70
CNF31861-21	LM11-68	Main zone	bladed	Type 1 ± 2B ± 2A	-	105.45	6.27	72.68	125.40	4959.00	1.82	-	473.10	524.40	1624.50	20235.00	2.51
CNF31861-22	LM11-68	Main zone	bladed	Type 1 ± 2B ± 2A	-	142.50	3.42	87.50	139.65	4075.50	2.85	23.66	672.60	1738.50	732.45	19665.00	2.05
CNF31861-23	LM11-68	Main zone	bladed	Type 1 ± 2B ± 2A	5.70	165.30	13.40	60.99	193.80	4446.00	0.94	42.75	587.10	695.40	997.50	25650.00	2.25
CNF31865-1	LM14-96	Northwest zone	bladed	Type 1 ± 2B	28.11	81.01	26.45	-	94.24	1653.33	1.98	-	198.40	248.00	89.28	14053.33	0.23
CNF31865-2	LM14-96	Northwest zone	bladed	Type 1 ± 2B	-	292.97	20.57	61.09	73.55	3428.33	-	-	99.73	155.83	511.13	14523.67	13.09
CNF31865-3	LM14-96	Northwest zone	granular	Type 1 ± 2B	-	104.72	-	19.36	34.11	1586.67	2.46	-	65.05	92.03	148.35	12376.00	0.87
CNF31865-4	LM14-96	Northwest zone	granular	Type 1 ± 2B	-	-	8.81	72.19	65.85	1586.67	-	-	115.03	120.59	285.60	22530.67	-
CNF31865-5	LM14-96	Northwest zone	granular	Type 1 ± 2B	-	33.32	3.09	13.25	31.73	1071.00	1.27	-	36.49	81.71	112.65	8330.00	-

Sample/spot analysis #	Drill Hole	Mineralized zone	Barite texture	Mineral Assemblage Type	Ge ppm	As ppm	Se ppm	Rb ppm	Y ppm	Zr ppm	Nb ppm	Mo ppm	Ru ppm	Rh ppm	Pd ppm	Ag ppm	In ppm
CNF31860-15	LM11-68	Main zone	tabular	Type 1 ± 2B ± 2A	-	62.48	-	-	16.30	4.29	0.06	-	-	-	-	16.57	-
CNF31860-16	LM11-68	Main zone	bladed	Type 1 ± 2B ± 2A	2.40	741.60	-	-	7.07	0.27	-	13.39	-	1.65	-	14076.67	-
CNF31860-17	LM11-68	Main zone	bladed	Type 1 ± 2B ± 2A	2.68	1366.47	24.72	-	6.94	0.48	0.02	7.42	-	12.22	-	14488.67	-
CNF31860-18	LM11-68	Main zone	bladed	Type 1 ± 2B ± 2A	-	1689.20	4.12	2.13	5.91	0.27	-	9.82	-	10.16	3.23	28840.00	0.01
CNF31860-19	LM11-68	Main zone	bladed	Type 1 ± 2B ± 2A	0.41	1654.87	-	1.39	5.38	0.07	-	15.24	-	26.78	3.64	40513.33	0.01
CNF31860-20	LM11-68	Main zone	bladed	Type 1 ± 2B ± 2A	-	192.27	-	4.39	6.39	-	0.07	18.33	-	0.62	-	3982.67	0.02
CNF31860-21	LM11-68	Main zone	bladed	Type 1 ± 2B ± 2A	-	219.73	6.87	4.94	4.81	0.24	-	23.35	-	-	-	4532.00	0.01
CNF31860-22	LM11-68	Main zone	bladed	Type 1 ± 2B ± 2A	-	405.13	-	-	5.49	0.65	0.03	26.09	-	1.30	1.92	7347.33	0.02
CNF31860-23	LM11-68	Main zone	bladed	Type 1 ± 2B ± 2A	-	302.83	18.38	-	13.25	1.01	1.02	764.33	-	4.16	-	2534.85	0.04
CNF31860-24	LM11-68	Main zone	bladed	Type 1 ± 2B ± 2A	-	145.13	-	-	9.09	2.90	-	1557.68	-	-	-	1064.25	0.22
CNF31860-25	LM11-68	Main zone	bladed	Type 1 ± 2B ± 2A	-	164.48	-	10.06	13.64	1.64	0.99	8707.50	-	-	-	1528.65	0.14
CNF31860-26	LM11-68	Main zone	bladed	Type 1 ± 2B ± 2A	-	109.33	12.58	7.55	9.68	2.52	-	12384.00	-	2.71	-	2979.90	0.30
CNF31860-27	LM11-68	Main zone	granular	Type 1 ± 2B ± 2A	-	15.90	-	-	5.25	0.59	-	2.39	-	-	-	19.88	-
CNF31860-28	LM11-68	Main zone	granular	Type 1 ± 2B ± 2A	-	108.23	31.83	-	4.27	-	-	-	-	5.09	-	-	-
CNF31860-29	LM11-68	Main zone	granular	Type 1 ± 2B ± 2A	-	-	-	-	2.74	0.37	-	-	-	-	-	-	-
CNF31860-30	LM11-68	Main zone	granular	Type 1 ± 2B ± 2A	-	-	-	0.93	4.40	5.28	-	-	-	-	-	-	-
CNF31860-31	LM11-68	Main zone	granular	Type 1 ± 2B ± 2A	-	-	-	2.71	5.43	4.62	-	-	-	-	-	-	-
CNF31860-32	LM11-68	Main zone	granular	Type 1 ± 2B ± 2A	-	152.43	73.53	4.04	4.75	6.28	0.09	-	-	-	-	-	-
CNF31860-33	LM11-68	Main zone	bladed	Type 1 ± 2B ± 2A	-	1359.60	18.54	-	5.56	0.21	0.01	17.37	-	28.84	-	37766.67	0.02
CNF31860-34	LM11-68	Main zone	bladed	Type 1 ± 2B ± 2A	-	1242.87	6.18	1.65	6.87	0.25	0.12	10.99	-	9.34	-	25406.67	-
CNF31860-35	LM11-68	Main zone	bladed	Type 1 ± 2B ± 2A	-	1689.20	-	-	7.35	0.53	0.02	30.90	-	4.33	-	26093.33	-
CNF31860-36	LM11-68	Main zone	bladed	Type 1 ± 2B ± 2A	-	405.13	29.53	-	5.22	0.31	-	31.59	-	6.59	-	9201.33	-
CNF31860-37	LM11-68	Main zone	bladed	Type 1 ± 2B ± 2A	3.57	542.47	4.81	2.33	4.74	0.25	0.08	16.34	-	9.82	-	8583.33	0.00
CNF31860-38	LM11-68	Main zone	bladed	Type 1 ± 2B ± 2A	-	508.13	8.24	-	6.04	0.46	-	31.59	-	13.05	-	14557.33	-
CNF31860-39	LM11-68	Main zone	bladed	Type 1 ± 2B ± 2A	-	927.00	18.54	-	4.26	0.19	0.01	19.30	-	4.33	0.62	17441.33	0.02
CNF31861-1	LM11-68	Main zone	granular	Type 1 ± 2B ± 2A	-	-	87.33	2.27	5.50	0.96	-	-	-	-	13.10	47.16	-
CNF31861-2	LM11-68	Main zone	granular	Type 1 ± 2B ± 2A	-	-	26.20	3.23	7.07	2.36	0.03	-	-	-	-	-	-
CNF31861-3	LM11-68	Main zone	granular	Type 1 ± 2B ± 2A	-	-	64.90	-	4.84	1.00	-	2.48	-	-	-	306.80	-
CNF31861-4	LM11-68	Main zone	granular	Type 1 ± 2B ± 2A	-	72.77	134.43	-	14.55	0.62	-	14.68	-	-	-	1048.33	-
CNF31861-5	LM11-68	Main zone	granular	Type 1 ± 2B ± 2A	64.13	-	-	49.33	17.14	18.50	-	2096.67	-	-	-	826.33	-
CNF31861-6	LM11-68	Main zone	granular	Type 1 ± 2B ± 2A	-	1726.67	-	8.26	12.83	6.54	-	333.00	-	2.34	-	48100.00	-
CNF31861-7	LM11-68	Main zone	granular	Type 1 ± 2B ± 2A	-	592.00	41.93	6.17	19.36	8.76	-	308.33	-	-	-	2910.67	-
CNF31861-8	LM11-68	Main zone	granular	Type 1 ± 2B ± 2A	-	185.00	59.20	-	39.47	5.18	0.14	1714.33	-	4.44	-	5056.67	0.10
CNF31861-9	LM11-68	Main zone	bladed	Type 1 ± 2B ± 2A	15.39	453.15	14.25	9.41	24.80	23.37	0.05	10.55	-	-	-	76.95	-
CNF31861-10	LM11-68	Main zone	bladed	Type 1 ± 2B ± 2A	9.41	259.35	28.50	33.06	27.65	61.28	0.12	1.17	-	-	-	29.07	-
CNF31861-11	LM11-68	Main zone	bladed	Type 1 ± 2B ± 2A	21.95	-	-	62.99	29.07	216.60	1.45	9.98	-	-	-	370.50	0.14
CNF31861-12	LM11-68	Main zone	bladed	Type 1 ± 2B ± 2A	12.83	28.50	59.85	52.73	20.81	168.15	3.14	68.40	-	7.98	-	655.50	-
CNF31861-13	LM11-68	Main zone	bladed	Type 1 ± 2B ± 2A	7.98	28.50	51.30	30.21	19.95	90.92	0.71	19.10	-	-	-	712.50	0.04
CNF31861-14	LM11-68	Main zone	bladed	Type 1 ± 2B ± 2A	20.24	65.55	82.65	41.33	25.37	114.29	1.54	6.27	-	-	-	88.35	0.06
CNF31861-15	LM11-68	Main zone	bladed	Type 1 ± 2B ± 2A	-	14.25	139.65	14.54	19.10	53.87	0.23	2.94	-	-	-	96.90	0.05
CNF31861-16	LM11-68	Main zone	bladed	Type 1 ± 2B ± 2A	-	273.60	182.40	18.24	15.68	69.54	0.40	1.71	-	51.30	-	196.65	-
CNF31861-17	LM11-68	Main zone	bladed	Type 1 ± 2B ± 2A	-	208.05	42.75	11.97	12.83	39.62	0.37	59.85	-	-	-	222.30	-
CNF31861-18	LM11-68	Main zone	bladed	Type 1 ± 2B ± 2A	-	196.65	-	15.68	11.23	34.49	0.46	29.36	-	-	-	208.05	-
CNF31861-19	LM11-68	Main zone	bladed	Type 1 ± 2B ± 2A	3.42	276.45	-	14.54	8.72	33.92	0.18	29.36	-	7.98	-	940.50	0.05
CNF31861-20	LM11-68	Main zone	bladed	Type 1 ± 2B ± 2A	4.56	173.85	-	10.12	12.08	31.35	0.19	21.95	-	-	-	208.05	0.04
CNF31861-21	LM11-68	Main zone	bladed	Type 1 ± 2B ± 2A	-	302.10	-	25.94	13.65	70.40	0.11	9.41	-	22.80	-	1539.00	-
CNF31861-22	LM11-68	Main zone	bladed	Type 1 ± 2B ± 2A	9.69	695.40	5.70	18.24	14.42	56.15	0.40	2.57	-	-	13.40	2337.00	0.03
CNF31861-23	LM11-68	Main zone	bladed	Type 1 ± 2B ± 2A	8.55	370.50	131.10	21.95	20.24	83.51	0.35	2.34	-	59.85	-	1624.50	-
CNF31865-1	LM14-96	Northwest zone	bladed	Type 1 ± 2B	-	-	67.79	17.03	14.38	46.29	-	-	-	-	-	173.60	-
CNF31865-2	LM14-96	Northwest zone	bladed	Type 1 ± 2B	-	68.57	-	24.93	19.95	92.25	1.25	-	-	-	-	75.42	-
CNF31865-3	LM14-96	Northwest zone	granular	Type 1 ± 2B	-	-	-	20.23	8.09	49.19	-	11.11	-	-	-	39.67	-
CNF31865-4	LM14-96	Northwest zone	granular	Type 1 ± 2B	-	63.47	-	19.52	18.88	61.88	-	-	-	-	-	7.14	-
CNF31865-5	LM14-96	Northwest zone	granular	Type 1 ± 2B	-	-	-	9.12	4.13	44.43	0.18	-	-	-	-	11.11	-

Sample/spot analysis #	Drill Hole	Mineralized zone	Barite texture	Mineral Assemblage Type	Sn ppm	Sb ppm	Te ppm	Cs ppm	La ppm	Ce ppm	Pr ppm	Nd ppm	Sm ppm	Eu ppm	Gd155 ppm	Gd157 ppm	Tb ppm
CNF31860-15	LM11-68	Main zone	tabular	Type 1 ± 2B ± 2A	20.65	-	-	0.11	27.71	24.72	0.54	0.41	0.04	11.14	369.47	-	-
CNF31860-16	LM11-68	Main zone	bladed	Type 1 ± 2B ± 2A	10.23	309.00	-	-	11.60	12.22	0.78	1.46	0.05	4.05	149.01	0.10	-
CNF31860-17	LM11-68	Main zone	bladed	Type 1 ± 2B ± 2A	5.63	446.33	-	-	13.60	15.93	0.82	1.92	0.04	4.94	161.37	0.52	-
CNF31860-18	LM11-68	Main zone	bladed	Type 1 ± 2B ± 2A	5.63	666.07	-	-	11.33	9.89	0.54	1.65	0.03	4.55	179.91	0.26	0.01
CNF31860-19	LM11-68	Main zone	bladed	Type 1 ± 2B ± 2A	3.23	384.53	-	0.04	6.25	5.01	0.27	0.78	0.05	4.52	149.01	0.04	-
CNF31860-20	LM11-68	Main zone	bladed	Type 1 ± 2B ± 2A	11.26	178.53	-	-	5.22	3.71	0.05	0.02	-	4.46	159.31	-	-
CNF31860-21	LM11-68	Main zone	bladed	Type 1 ± 2B ± 2A	5.01	127.72	-	0.20	7.07	3.36	0.16	-	0.10	4.53	146.26	0.26	0.01
CNF31860-22	LM11-68	Main zone	bladed	Type 1 ± 2B ± 2A	5.36	157.25	-	-	5.49	2.95	0.34	0.36	0.04	4.05	157.25	0.01	-
CNF31860-23	LM11-68	Main zone	bladed	Type 1 ± 2B ± 2A	33.19	47.41	-	-	5.13	1.86	0.04	0.13	0.03	6.97	220.59	0.15	-
CNF31860-24	LM11-68	Main zone	bladed	Type 1 ± 2B ± 2A	67.73	17.80	-	-	5.22	2.32	0.35	-	0.09	5.90	251.55	0.29	-
CNF31860-25	LM11-68	Main zone	bladed	Type 1 ± 2B ± 2A	94.82	15.87	-	-	6.68	2.71	0.05	0.14	-	10.74	270.90	0.35	-
CNF31860-26	LM11-68	Main zone	bladed	Type 1 ± 2B ± 2A	76.43	30.86	-	-	6.58	3.68	0.11	-	0.04	9.29	279.61	0.04	-
CNF31860-27	LM11-68	Main zone	granular	Type 1 ± 2B ± 2A	81.09	0.76	-	-	4.61	0.09	-	-	-	4.05	273.48	-	-
CNF31860-28	LM11-68	Main zone	granular	Type 1 ± 2B ± 2A	-	-	-	-	0.85	0.05	-	-	-	1.66	104.41	-	-
CNF31860-29	LM11-68	Main zone	granular	Type 1 ± 2B ± 2A	0.39	-	-	0.01	8.28	8.72	0.73	1.34	0.39	2.05	72.58	-	0.04
CNF31860-30	LM11-68	Main zone	granular	Type 1 ± 2B ± 2A	-	-	-	-	8.07	2.93	0.03	-	-	5.35	140.07	0.10	-
CNF31860-31	LM11-68	Main zone	granular	Type 1 ± 2B ± 2A	1.03	-	-	-	13.93	1.98	0.54	1.47	-	5.13	135.67	-	-
CNF31860-32	LM11-68	Main zone	granular	Type 1 ± 2B ± 2A	4.12	-	-	-	11.57	5.92	0.30	0.66	-	6.55	186.51	-	-
CNF31860-33	LM11-68	Main zone	bladed	Type 1 ± 2B ± 2A	5.97	487.53	-	-	8.24	8.24	0.46	0.64	0.04	5.36	149.01	0.08	-
CNF31860-34	LM11-68	Main zone	bladed	Type 1 ± 2B ± 2A	7.21	672.93	-	-	11.12	9.06	0.46	0.90	0.12	5.36	170.98	0.26	-
CNF31860-35	LM11-68	Main zone	bladed	Type 1 ± 2B ± 2A	12.02	741.60	-	-	12.77	10.85	0.80	0.55	0.23	5.97	163.43	0.27	0.21
CNF31860-36	LM11-68	Main zone	bladed	Type 1 ± 2B ± 2A	4.67	164.80	-	-	4.26	2.41	0.19	0.12	0.15	4.20	119.48	0.09	-
CNF31860-37	LM11-68	Main zone	bladed	Type 1 ± 2B ± 2A	5.08	195.70	-	-	6.11	3.71	0.36	0.34	-	4.60	138.71	0.12	0.00
CNF31860-38	LM11-68	Main zone	bladed	Type 1 ± 2B ± 2A	4.46	453.20	-	-	5.42	3.98	0.16	0.92	0.15	4.26	131.15	0.17	0.01
CNF31860-39	LM11-68	Main zone	bladed	Type 1 ± 2B ± 2A	3.98	329.60	-	-	5.29	4.60	0.30	0.69	0.07	4.05	109.87	-	0.01
CNF31861-1	LM11-68	Main zone	granular	Type 1 ± 2B ± 2A	9.34	1.14	-	-	0.60	2.36	-	-	-	4.02	145.85	-	-
CNF31861-2	LM11-68	Main zone	granular	Type 1 ± 2B ± 2A	10.74	-	-	-	1.14	0.30	0.11	-	-	4.10	183.40	0.21	-
CNF31861-3	LM11-68	Main zone	granular	Type 1 ± 2B ± 2A	5.55	10.62	-	-	1.24	0.77	-	-	-	4.96	159.30	-	-
CNF31861-4	LM11-68	Main zone	granular	Type 1 ± 2B ± 2A	10.85	2.96	-	-	13.81	1.73	0.06	-	-	8.39	404.53	-	-
CNF31861-5	LM11-68	Main zone	granular	Type 1 ± 2B ± 2A	54.27	8.14	-	-	12.83	4.32	0.09	-	0.36	17.76	444.00	-	-
CNF31861-6	LM11-68	Main zone	granular	Type 1 ± 2B ± 2A	15.05	135.67	-	-	11.72	3.70	-	-	-	10.36	334.23	-	-
CNF31861-7	LM11-68	Main zone	granular	Type 1 ± 2B ± 2A	25.90	17.76	-	-	125.80	160.33	10.11	27.13	10.85	29.60	392.20	11.84	0.20
CNF31861-8	LM11-68	Main zone	granular	Type 1 ± 2B ± 2A	12.70	11.59	-	-	183.77	196.10	13.44	28.37	8.88	28.74	518.00	6.66	0.16
CNF31861-9	LM11-68	Main zone	bladed	Type 1 ± 2B ± 2A	27.65	19.10	-	-	17.39	18.53	1.14	2.85	0.10	17.10	453.15	-	-
CNF31861-10	LM11-68	Main zone	bladed	Type 1 ± 2B ± 2A	52.16	4.73	-	-	19.38	16.53	1.31	3.14	0.43	17.39	484.50	-	-
CNF31861-11	LM11-68	Main zone	bladed	Type 1 ± 2B ± 2A	133.95	13.97	-	-	29.07	31.92	4.02	16.25	-	10.03	473.10	0.09	-
CNF31861-12	LM11-68	Main zone	bladed	Type 1 ± 2B ± 2A	75.81	21.09	-	1.03	37.05	28.50	2.11	5.42	0.77	16.53	467.40	0.29	0.48
CNF31861-13	LM11-68	Main zone	bladed	Type 1 ± 2B ± 2A	49.59	4.76	-	0.74	11.80	19.10	1.14	2.48	-	11.63	381.90	0.06	-
CNF31861-14	LM11-68	Main zone	bladed	Type 1 ± 2B ± 2A	85.50	6.56	-	1.34	17.39	25.65	1.00	5.70	-	19.10	467.40	0.14	-
CNF31861-15	LM11-68	Main zone	bladed	Type 1 ± 2B ± 2A	62.70	1.08	-	1.40	10.40	13.40	1.17	1.77	-	16.82	473.10	1.05	-
CNF31861-16	LM11-68	Main zone	bladed	Type 1 ± 2B ± 2A	32.21	7.41	-	-	15.68	21.38	1.51	2.65	0.16	10.09	265.05	0.46	-
CNF31861-17	LM11-68	Main zone	bladed	Type 1 ± 2B ± 2A	18.24	6.70	-	-	17.96	19.95	1.45	6.36	0.43	6.84	236.55	0.66	0.02
CNF31861-18	LM11-68	Main zone	bladed	Type 1 ± 2B ± 2A	29.36	1.91	-	-	12.94	15.56	0.86	3.08	0.37	8.29	216.60	1.03	0.03
CNF31861-19	LM11-68	Main zone	bladed	Type 1 ± 2B ± 2A	17.10	3.96	-	0.18	13.79	18.24	3.16	3.51	0.26	7.10	225.15	-	0.06
CNF31861-20	LM11-68	Main zone	bladed	Type 1 ± 2B ± 2A	16.53	6.84	-	0.23	11.20	12.77	0.94	1.94	0.54	7.78	239.40	0.74	-
CNF31861-21	LM11-68	Main zone	bladed	Type 1 ± 2B ± 2A	30.50	68.40	-	-	16.53	24.23	1.00	4.42	-	10.17	282.15	0.16	0.01
CNF31861-22	LM11-68	Main zone	bladed	Type 1 ± 2B ± 2A	23.37	427.50	-	-	51.30	34.49	3.33	5.70	1.74	12.26	250.80	1.28	0.10
CNF31861-23	LM11-68	Main zone	bladed	Type 1 ± 2B ± 2A	31.92	108.30	-	-	21.09	28.22	2.02	6.01	0.77	11.97	324.90	0.06	0.10
CNF31865-1	LM14-96	Northwest zone	bladed	Type 1 ± 2B	11.24	-	-	-	4.46	9.26	-	0.33	-	5.29	231.47	-	-
CNF31865-2	LM14-96	Northwest zone	bladed	Type 1 ± 2B	19.32	16.83	-	1.31	13.65	18.70	1.06	0.69	-	11.41	243.10	-	-
CNF31865-3	LM14-96	Northwest zone	granular	Type 1 ± 2B	6.58	-	-	-	8.17	7.06	0.94	3.57	-	7.77	134.07	-	-
CNF31865-4	LM14-96	Northwest zone	granular	Type 1 ± 2B	13.41	-	-	0.71	10.71	10.47	1.19	7.38	0.21	8.89	349.07	0.48	-
CNF31865-5	LM14-96	Northwest zone	granular	Type 1 ± 2B	6.03	-	-	-	2.78	6.27	0.95	1.90	-	3.17	103.13	-	0.05

Sample/spot analysis #	Drill Hole	Mineralized zone	Barite texture	Mineral Assemblage Type	Dy ppm	Ho ppm	Er ppm	Tm ppm	Yb ppm	Lu ppm	Hf ppm	Ta ppm	W ppm	Re ppm	Os ppm	Au ppm	Hg ppm
CNF31860-15	LM11-68	Main zone	tabular	Type 1 ± 2B ± 2A	-	0.07	-	-	-	-	-	0.41	0.82	-	-	16.57	570.50
CNF31860-16	LM11-68	Main zone	bladed	Type 1 ± 2B ± 2A	-	-	0.01	-	0.05	-	-	0.12	0.16	-	-	412.00	521.87
CNF31860-17	LM11-68	Main zone	bladed	Type 1 ± 2B ± 2A	-	0.02	-	-	-	-	-	0.05	0.10	-	-	161.37	508.13
CNF31860-18	LM11-68	Main zone	bladed	Type 1 ± 2B ± 2A	0.01	-	-	-	-	-	-	0.06	0.01	-	-	142.83	563.07
CNF31860-19	LM11-68	Main zone	bladed	Type 1 ± 2B ± 2A	0.01	-	-	-	0.00	-	-	0.07	0.13	-	-	322.73	782.80
CNF31860-20	LM11-68	Main zone	bladed	Type 1 ± 2B ± 2A	-	0.00	-	-	-	-	-	0.06	0.04	-	-	56.99	377.67
CNF31860-21	LM11-68	Main zone	bladed	Type 1 ± 2B ± 2A	-	-	-	-	-	-	-	0.15	0.19	-	-	41.89	377.67
CNF31860-22	LM11-68	Main zone	bladed	Type 1 ± 2B ± 2A	0.03	0.00	-	-	-	-	-	0.06	0.34	-	-	226.60	288.40
CNF31860-23	LM11-68	Main zone	bladed	Type 1 ± 2B ± 2A	0.02	0.02	0.03	-	-	-	-	0.04	1.46	-	-	62.89	1064.25
CNF31860-24	LM11-68	Main zone	bladed	Type 1 ± 2B ± 2A	-	-	-	0.00	-	-	-	0.17	1.94	-	-	17.22	2360.70
CNF31860-25	LM11-68	Main zone	bladed	Type 1 ± 2B ± 2A	-	-	-	-	-	-	-	0.20	7.64	-	-	41.60	2912.18
CNF31860-26	LM11-68	Main zone	bladed	Type 1 ± 2B ± 2A	-	-	-	-	0.09	-	-	0.03	4.64	-	-	87.08	3183.08
CNF31860-27	LM11-68	Main zone	granular	Type 1 ± 2B ± 2A	-	-	-	-	-	-	-	-	-	-	-	-	71.55
CNF31860-28	LM11-68	Main zone	granular	Type 1 ± 2B ± 2A	-	-	-	-	-	-	-	-	-	-	-	5.09	44.57
CNF31860-29	LM11-68	Main zone	granular	Type 1 ± 2B ± 2A	-	-	-	-	-	-	-	0.03	-	-	-	3.18	148.98
CNF31860-30	LM11-68	Main zone	granular	Type 1 ± 2B ± 2A	-	-	-	-	-	-	-	-	-	-	-	-	139.33
CNF31860-31	LM11-68	Main zone	granular	Type 1 ± 2B ± 2A	0.17	-	-	-	-	-	-	-	-	-	-	-	51.33
CNF31860-32	LM11-68	Main zone	granular	Type 1 ± 2B ± 2A	-	-	-	-	-	-	-	-	-	-	-	-	161.40
CNF31860-33	LM11-68	Main zone	bladed	Type 1 ± 2B ± 2A	0.02	-	-	-	-	-	-	0.01	0.07	-	-	391.40	348.83
CNF31860-34	LM11-68	Main zone	bladed	Type 1 ± 2B ± 2A	0.02	0.00	-	-	-	-	-	0.02	0.20	-	-	260.93	193.64
CNF31860-35	LM11-68	Main zone	bladed	Type 1 ± 2B ± 2A	0.06	0.04	0.06	-	-	-	-	0.47	0.45	-	-	274.67	282.22
CNF31860-36	LM11-68	Main zone	bladed	Type 1 ± 2B ± 2A	-	-	-	-	-	-	0.02	0.02	0.02	-	-	59.05	309.00
CNF31860-37	LM11-68	Main zone	bladed	Type 1 ± 2B ± 2A	0.01	-	-	0.00	-	-	-	0.30	0.21	-	-	92.70	302.13
CNF31860-38	LM11-68	Main zone	bladed	Type 1 ± 2B ± 2A	0.04	-	-	-	-	-	0.01	0.19	0.29	-	-	54.25	274.67
CNF31860-39	LM11-68	Main zone	bladed	Type 1 ± 2B ± 2A	-	0.00	-	-	-	-	-	0.04	0.16	-	-	81.03	274.67
CNF31861-1	LM11-68	Main zone	granular	Type 1 ± 2B ± 2A	-	-	-	-	-	-	-	-	-	-	-	-	157.20
CNF31861-2	LM11-68	Main zone	granular	Type 1 ± 2B ± 2A	-	-	-	-	-	-	-	-	0.61	-	-	-	234.93
CNF31861-3	LM11-68	Main zone	granular	Type 1 ± 2B ± 2A	-	-	-	-	-	-	-	-	4.72	-	-	17.70	200.60
CNF31861-4	LM11-68	Main zone	granular	Type 1 ± 2B ± 2A	-	-	-	-	-	-	-	-	7.28	-	-	19.73	62.90
CNF31861-5	LM11-68	Main zone	granular	Type 1 ± 2B ± 2A	0.26	-	0.14	-	0.48	0.06	-	1.85	2.71	-	-	14.80	370.00
CNF31861-6	LM11-68	Main zone	granular	Type 1 ± 2B ± 2A	-	-	-	-	-	-	-	0.31	-	-	-	4.69	225.70
CNF31861-7	LM11-68	Main zone	granular	Type 1 ± 2B ± 2A	1.11	-	0.28	-	-	-	-	0.63	2.59	-	-	11.22	949.67
CNF31861-8	LM11-68	Main zone	granular	Type 1 ± 2B ± 2A	3.70	0.21	0.99	0.14	0.16	0.03	-	0.39	6.04	-	-	18.62	5180.00
CNF31861-9	LM11-68	Main zone	bladed	Type 1 ± 2B ± 2A	-	-	-	-	-	-	-	0.35	19.67	-	-	32.49	1231.20
CNF31861-10	LM11-68	Main zone	bladed	Type 1 ± 2B ± 2A	0.37	-	-	-	-	-	0.26	0.77	12.83	-	-	-	712.50
CNF31861-11	LM11-68	Main zone	bladed	Type 1 ± 2B ± 2A	-	0.01	-	-	-	0.05	0.60	2.62	29.07	-	-	39.62	675.45
CNF31861-12	LM11-68	Main zone	bladed	Type 1 ± 2B ± 2A	-	0.14	1.00	-	-	-	1.31	0.63	14.54	-	-	24.80	632.70
CNF31861-13	LM11-68	Main zone	bladed	Type 1 ± 2B ± 2A	-	-	-	-	0.06	-	1.17	3.51	32.21	-	-	37.62	684.00
CNF31861-14	LM11-68	Main zone	bladed	Type 1 ± 2B ± 2A	0.13	-	-	-	-	-	1.20	2.28	13.68	-	-	28.50	330.60
CNF31861-15	LM11-68	Main zone	bladed	Type 1 ± 2B ± 2A	-	-	0.17	-	-	-	0.48	9.69	68.40	-	-	39.90	367.65
CNF31861-16	LM11-68	Main zone	bladed	Type 1 ± 2B ± 2A	0.37	-	0.14	-	0.05	0.03	0.66	1.31	27.36	-	-	29.93	800.85
CNF31861-17	LM11-68	Main zone	bladed	Type 1 ± 2B ± 2A	0.09	0.01	0.04	-	-	-	0.51	1.03	30.50	-	-	-	852.15
CNF31861-18	LM11-68	Main zone	bladed	Type 1 ± 2B ± 2A	0.01	-	0.13	0.01	-	-	0.43	0.53	18.24	-	-	32.78	760.95
CNF31861-19	LM11-68	Main zone	bladed	Type 1 ± 2B ± 2A	0.16	-	0.01	-	0.11	-	0.40	0.23	57.00	-	-	-	3277.50
CNF31861-20	LM11-68	Main zone	bladed	Type 1 ± 2B ± 2A	0.03	0.01	-	-	-	0.05	0.68	0.27	-	-	-	29.36	681.15
CNF31861-21	LM11-68	Main zone	bladed	Type 1 ± 2B ± 2A	0.22	0.07	-	-	0.04	-	0.91	0.57	-	-	-	35.06	396.15
CNF31861-22	LM11-68	Main zone	bladed	Type 1 ± 2B ± 2A	0.48	0.01	0.24	0.04	0.01	-	0.83	0.60	-	-	-	47.03	418.95
CNF31861-23	LM11-68	Main zone	bladed	Type 1 ± 2B ± 2A	0.01	-	0.02	0.01	-	0.00	0.94	0.14	-	-	-	29.36	353.40
CNF31865-1	LM14-96	Northwest zone	bladed	Type 1 ± 2B	-	-	-	-	-	-	-	-	-	-	-	7.94	224.85
CNF31865-2	LM14-96	Northwest zone	bladed	Type 1 ± 2B	-	-	-	-	-	-	0.69	-	-	-	-	-	84.15
CNF31865-3	LM14-96	Northwest zone	granular	Type 1 ± 2B	-	-	-	-	-	-	1.51	-	-	-	-	-	86.47
CNF31865-4	LM14-96	Northwest zone	granular	Type 1 ± 2B	-	-	-	-	-	-	0.23	-	0.40	-	-	12.69	190.40
CNF31865-5	LM14-96	Northwest zone	granular	Type 1 ± 2B	-	-	-	-	-	-	-	-	-	-	-	-	134.87

Sample/spot analysis #	Drill Hole	Mineralized zone	Barite texture	Mineral Assemblage Type	Tl ppm	Pb206 ppm	Pb208 ppm	Bi ppm	Th ppm	U ppm
CNF31860-15	LM11-68	Main zone	tabular	Type 1 ± 2B ± 2A	11.68	49.17	69.00	-	0.01	-
CNF31860-16	LM11-68	Main zone	bladed	Type 1 ± 2B ± 2A	49.44	5150.00	5424.67	-	-	-
CNF31860-17	LM11-68	Main zone	bladed	Type 1 ± 2B ± 2A	39.83	5150.00	5493.33	-	-	0.14
CNF31860-18	LM11-68	Main zone	bladed	Type 1 ± 2B ± 2A	70.04	11330.00	9956.67	-	0.01	-
CNF31860-19	LM11-68	Main zone	bladed	Type 1 ± 2B ± 2A	67.29	8858.00	7965.33	-	0.00	0.26
CNF31860-20	LM11-68	Main zone	bladed	Type 1 ± 2B ± 2A	51.50	2884.00	3158.67	-	-	-
CNF31860-21	LM11-68	Main zone	bladed	Type 1 ± 2B ± 2A	76.91	3021.33	2952.67	-	-	-
CNF31860-22	LM11-68	Main zone	bladed	Type 1 ± 2B ± 2A	41.89	5768.00	4944.00	-	0.00	-
CNF31860-23	LM11-68	Main zone	bladed	Type 1 ± 2B ± 2A	62.89	6772.50	6385.50	-	0.07	1.51
CNF31860-24	LM11-68	Main zone	bladed	Type 1 ± 2B ± 2A	63.86	5901.75	5708.25	-	-	2.35
CNF31860-25	LM11-68	Main zone	bladed	Type 1 ± 2B ± 2A	209.95	10642.50	10352.25	-	-	3.10
CNF31860-26	LM11-68	Main zone	bladed	Type 1 ± 2B ± 2A	333.79	11126.25	10352.25	0.14	-	3.08
CNF31860-27	LM11-68	Main zone	granular	Type 1 ± 2B ± 2A	17.49	429.30	453.15	0.19	0.11	-
CNF31860-28	LM11-68	Main zone	granular	Type 1 ± 2B ± 2A	-	9.49	9.87	-	-	-
CNF31860-29	LM11-68	Main zone	granular	Type 1 ± 2B ± 2A	-	8.47	8.79	-	0.02	-
CNF31860-30	LM11-68	Main zone	granular	Type 1 ± 2B ± 2A	-	6.09	4.91	-	-	-
CNF31860-31	LM11-68	Main zone	granular	Type 1 ± 2B ± 2A	-	18.33	12.91	-	-	-
CNF31860-32	LM11-68	Main zone	granular	Type 1 ± 2B ± 2A	-	9.33	11.12	-	0.09	-
CNF31860-33	LM11-68	Main zone	bladed	Type 1 ± 2B ± 2A	30.21	14282.67	13390.00	-	-	-
CNF31860-34	LM11-68	Main zone	bladed	Type 1 ± 2B ± 2A	65.92	18402.67	11261.33	0.08	-	-
CNF31860-35	LM11-68	Main zone	bladed	Type 1 ± 2B ± 2A	28.84	11810.67	10849.33	0.17	0.02	-
CNF31860-36	LM11-68	Main zone	bladed	Type 1 ± 2B ± 2A	35.02	8720.67	8308.67	-	-	-
CNF31860-37	LM11-68	Main zone	bladed	Type 1 ± 2B ± 2A	33.65	6248.67	6317.33	0.88	-	0.65
CNF31860-38	LM11-68	Main zone	bladed	Type 1 ± 2B ± 2A	32.27	11673.33	9613.33	-	-	0.36
CNF31860-39	LM11-68	Main zone	bladed	Type 1 ± 2B ± 2A	23.35	7278.67	8789.33	0.04	-	-
CNF31861-1	LM11-68	Main zone	granular	Type 1 ± 2B ± 2A	-	2532.67	3056.67	-	-	-
CNF31861-2	LM11-68	Main zone	granular	Type 1 ± 2B ± 2A	-	36.68	41.92	-	-	-
CNF31861-3	LM11-68	Main zone	granular	Type 1 ± 2B ± 2A	-	194.70	218.30	-	-	-
CNF31861-4	LM11-68	Main zone	granular	Type 1 ± 2B ± 2A	10.98	3946.67	3206.67	-	-	-
CNF31861-5	LM11-68	Main zone	granular	Type 1 ± 2B ± 2A	39.47	2368.00	1689.67	-	-	25.90
CNF31861-6	LM11-68	Main zone	granular	Type 1 ± 2B ± 2A	25.90	7646.67	5673.33	-	-	6.04
CNF31861-7	LM11-68	Main zone	granular	Type 1 ± 2B ± 2A	32.07	5673.33	4440.00	0.65	0.48	6.17
CNF31861-8	LM11-68	Main zone	granular	Type 1 ± 2B ± 2A	69.07	118400.00	76466.67	-	-	50.57
CNF31861-9	LM11-68	Main zone	bladed	Type 1 ± 2B ± 2A	-	296.40	353.40	-	0.01	0.37
CNF31861-10	LM11-68	Main zone	bladed	Type 1 ± 2B ± 2A	-	336.30	361.95	-	0.32	0.37
CNF31861-11	LM11-68	Main zone	bladed	Type 1 ± 2B ± 2A	24.23	481.65	504.45	-	3.59	1.82
CNF31861-12	LM11-68	Main zone	bladed	Type 1 ± 2B ± 2A	-	94050.00	119700.00	-	1.54	-
CNF31861-13	LM11-68	Main zone	bladed	Type 1 ± 2B ± 2A	10.83	6555.00	18240.00	-	1.45	0.31
CNF31861-14	LM11-68	Main zone	bladed	Type 1 ± 2B ± 2A	-	1268.25	1482.00	-	1.34	-
CNF31861-15	LM11-68	Main zone	bladed	Type 1 ± 2B ± 2A	-	1068.75	1014.60	-	0.71	2.45
CNF31861-16	LM11-68	Main zone	bladed	Type 1 ± 2B ± 2A	32.78	13680.00	12540.00	-	0.71	1.28
CNF31861-17	LM11-68	Main zone	bladed	Type 1 ± 2B ± 2A	-	1510.50	1254.00	-	0.48	0.80
CNF31861-18	LM11-68	Main zone	bladed	Type 1 ± 2B ± 2A	-	564.30	552.90	-	0.54	0.57
CNF31861-19	LM11-68	Main zone	bladed	Type 1 ± 2B ± 2A	19.10	3705.00	4275.00	-	0.86	1.31
CNF31861-20	LM11-68	Main zone	bladed	Type 1 ± 2B ± 2A	-	10545.00	7980.00	-	0.52	0.91
CNF31861-21	LM11-68	Main zone	bladed	Type 1 ± 2B ± 2A	-	65550.00	51300.00	0.23	1.08	1.43
CNF31861-22	LM11-68	Main zone	bladed	Type 1 ± 2B ± 2A	13.40	13110.00	11970.00	-	0.34	0.97
CNF31861-23	LM11-68	Main zone	bladed	Type 1 ± 2B ± 2A	-	125400.00	114000.00	0.12	0.91	0.26
CNF31865-1	LM14-96	Northwest zone	bladed	Type 1 ± 2B	-	211.63	175.25	-	0.43	-
CNF31865-2	LM14-96	Northwest zone	bladed	Type 1 ± 2B	12.47	6046.33	8602.00	-	0.19	-
CNF31865-3	LM14-96	Northwest zone	granular	Type 1 ± 2B	-	144.39	129.31	-	1.09	1.19
CNF31865-4	LM14-96	Northwest zone	granular	Type 1 ± 2B	-	173.74	148.35	-	2.14	0.54
CNF31865-5	LM14-96	Northwest zone	granular	Type 1 ± 2B	-	46.01	62.67	-	0.10	-

Sample/spot analysis #	Drill Hole	Mineralized zone	Barite texture	Mineral Assemblage Type	Sc ppm	Ti ppm	V ppm	Cr ppm	Mn ppm	Fe ppm	Co ppm	Ni ppm	Cu63 ppm	Cu65 ppm	Zn66 ppm	Zn67 ppm	Ga ppm
CNF31865-6	LM14-96	Northwest zone	granular	Type 1 ± 2B	-	83.60	4.75	27.28	40.48	-	-	-	38.72	112.64	85.36	8272.00	2.82
CNF31865-7	LM14-96	Northwest zone	granular	Type 1 ± 2B	-	50.16	-	76.56	23.76	-	-	-	140.80	228.80	82.72	12672.00	1.32
CNF31865-8	LM14-96	Northwest zone	granular	Type 1 ± 2B	-	35.60	59.33	17.21	-	-	-	89.00	-	-	213.60	28480.00	2.97
CNF31865-9	LM14-96	Northwest zone	granular	Type 1 ± 2B	-	81.29	332.27	32.63	35.01	1827.47	1.84	-	75.35	142.99	121.63	8959.33	51.03
CNF31865-10	LM14-96	Northwest zone	granular	Type 1 ± 2B	-	-	-	71.20	-	2610.67	-	231.40	53.40	-	166.13	6170.67	2.43
CNF31865-11	LM14-96	Northwest zone	granular	Type 1 ± 2B	-	-	67.05	59.33	59.33	-	7.12	-	112.73	224.87	4509.33	34413.33	22546.67
CNF31865-12	LM14-96	Northwest zone	granular	Type 1 ± 2A	-	46.35	1.54	-	15.69	184.33	-	-	42.13	80.05	48.45	8637.33	-
CNF31865-13	LM14-96	Northwest zone	granular	Type 1 ± 2A	-	195.29	4.19	-	67.30	1997.03	-	-	87.16	133.50	110.33	11585.00	5.30
CNF31865-14	LM14-96	Northwest zone	granular	Type 1 ± 2A	-	87.43	2.32	-	22.86	779.47	0.72	-	31.07	68.47	284.40	7794.67	1.79
CNF31865-15	LM14-96	Northwest zone	granular	Type 1 ± 2A	2.59	79.92	3.78	9.83	34.56	842.40	-	-	68.04	96.12	74.52	10584.00	0.83
CNF31865-16	LM14-96	Northwest zone	granular	Type 1 ± 2A	-	72.36	3.24	11.99	29.16	907.20	-	-	43.20	145.80	74.52	8532.00	0.29
CNF31865-17	LM14-96	Northwest zone	granular	Type 1 ± 2A	-	88.56	3.13	8.64	22.68	658.80	-	-	32.40	73.44	65.88	9288.00	1.51
CNF31865-18	LM14-96	Northwest zone	granular	Type 1 ± 2A	-	49.58	2.47	3.08	16.08	348.40	0.43	-	35.38	111.22	80.40	10452.00	0.36
CNF31865-19	LM14-96	Northwest zone	granular	Type 1 ± 2A	-	22.07	1.26	-	10.45	343.20	-	-	37.44	53.82	43.68	5803.20	0.24

Sample/spot analysis #	Drill Hole	Mineralized zone	Barite texture	Mineral Assemblage Type	Ge ppm	As ppm	Se ppm	Rb ppm	Y ppm	Zr ppm	Nb ppm	Mo ppm	Ru ppm	Rh ppm	Pd ppm	Ag ppm	In ppm
CNF31865-6	LM14-96	Northwest zone	granular	Type 1 ± 2B	-	4.40	34.32	6.69	6.16	31.68	0.70	-	-	-	-	18.48	-
CNF31865-7	LM14-96	Northwest zone	granular	Type 1 ± 2B	-	26.40	35.20	7.13	12.06	15.84	-	6.16	-	-	-	-	-
CNF31865-8	LM14-96	Northwest zone	granular	Type 1 ± 2B	-	-	47.47	-	1.84	-	-	-	-	-	-	-	-
CNF31865-9	LM14-96	Northwest zone	granular	Type 1 ± 2B	1.60	29.67	-	31.45	6.70	37.97	0.77	0.65	-	-	-	18.99	0.04
CNF31865-10	LM14-96	Northwest zone	granular	Type 1 ± 2B	15.43	-	-	7.71	18.39	11.27	-	4.75	-	-	14.83	14.83	-
CNF31865-11	LM14-96	Northwest zone	granular	Type 1 ± 2B	-	31.45	94.93	17.21	35.60	-	2.55	-	-	-	-	89.00	-
CNF31865-12	LM14-96	Northwest zone	granular	Type 1 ± 2A	-	263.33	-	7.27	6.74	26.33	0.34	0.47	-	-	-	-	-
CNF31865-13	LM14-96	Northwest zone	granular	Type 1 ± 2A	-	33.10	-	36.41	11.81	120.26	1.66	-	-	-	-	-	-
CNF31865-14	LM14-96	Northwest zone	granular	Type 1 ± 2A	2.11	305.47	3.16	13.59	5.06	42.13	0.17	0.53	-	-	-	-	-
CNF31865-15	LM14-96	Northwest zone	granular	Type 1 ± 2A	2.16	85.32	-	12.96	10.69	42.12	2.05	-	-	-	-	-	-
CNF31865-16	LM14-96	Northwest zone	granular	Type 1 ± 2A	-	-	-	11.66	7.13	44.28	0.10	-	-	-	-	-	-
CNF31865-17	LM14-96	Northwest zone	granular	Type 1 ± 2A	-	313.20	-	13.50	5.40	37.80	0.42	-	-	-	5.40	-	-
CNF31865-18	LM14-96	Northwest zone	granular	Type 1 ± 2A	-	348.40	-	8.84	7.24	24.66	0.31	-	-	-	16.08	9.38	0.03
CNF31865-19	LM14-96	Northwest zone	granular	Type 1 ± 2A	-	116.22	35.88	6.16	4.91	12.56	0.35	-	-	-	-	-	0.01

Sample/spot analysis #	Drill Hole	Mineralized zone	Barite texture	Mineral Assemblage Type	Sn	Sb	Te	Cs	La	Ce	Pr	Nd	Sm	Eu	Gd155	Gd157	Tb
					ppm	ppm	ppm	ppm	ppm	ppm	ppm	ppm	ppm	ppm	ppm	ppm	ppm
CNF31865-6	LM14-96	Northwest zone	granular	Type 1 ± 2B	8.80	-	-	-	8.80	9.68	-	0.79	0.70	6.16	141.68	-	-
CNF31865-7	LM14-96	Northwest zone	granular	Type 1 ± 2B	3.34	1.32	-	-	2.46	5.46	-	-	-	6.25	242.00	-	-
CNF31865-8	LM14-96	Northwest zone	granular	Type 1 ± 2B	94.93	-	-	-	10.09	0.42	-	-	-	2.79	47.47	-	-
CNF31865-9	LM14-96	Northwest zone	granular	Type 1 ± 2B	5.87	0.49	-	1.25	6.35	5.64	0.11	1.01	0.36	3.20	125.19	0.09	-
CNF31865-10	LM14-96	Northwest zone	granular	Type 1 ± 2B	-	-	-	2.14	5.93	1.66	-	-	-	1.19	219.53	-	-
CNF31865-11	LM14-96	Northwest zone	granular	Type 1 ± 2B	12.46	-	-	4.75	1.66	-	-	-	-	16.02	236.74	-	-
CNF31865-12	LM14-96	Northwest zone	granular	Type 1 ± 2A	4.00	-	-	-	2.79	4.11	0.93	0.87	1.13	4.22	127.45	0.16	-
CNF31865-13	LM14-96	Northwest zone	granular	Type 1 ± 2A	24.49	0.28	-	-	11.25	23.61	1.35	5.63	1.21	3.20	157.78	0.38	-
CNF31865-14	LM14-96	Northwest zone	granular	Type 1 ± 2A	7.90	-	-	-	4.74	7.90	0.75	2.95	0.53	3.90	100.07	1.05	-
CNF31865-15	LM14-96	Northwest zone	granular	Type 1 ± 2A	8.96	0.05	-	0.26	8.53	9.61	0.69	3.56	0.41	6.91	136.08	0.26	-
CNF31865-16	LM14-96	Northwest zone	granular	Type 1 ± 2A	6.59	-	-	0.40	4.97	5.62	0.75	1.40	1.40	4.10	136.08	-	-
CNF31865-17	LM14-96	Northwest zone	granular	Type 1 ± 2A	8.42	0.04	-	0.19	3.10	6.91	0.49	2.38	-	5.72	127.44	0.14	-
CNF31865-18	LM14-96	Northwest zone	granular	Type 1 ± 2A	5.36	-	-	0.15	14.34	12.19	1.11	3.26	0.16	5.31	143.38	0.59	0.01
CNF31865-19	LM14-96	Northwest zone	granular	Type 1 ± 2A	2.03	0.01	-	-	8.03	6.79	0.61	1.61	0.02	2.88	85.80	0.12	0.00

Sample/spot analysis #	Drill Hole	Mineralized zone	Barite texture	Mineral Assemblage Type	Dy	Ho	Er	Tm	Yb	Lu	Hf	Ta	W	Re	Os	Au	Hg
					ppm	ppm	ppm	ppm	ppm	ppm	ppm	ppm	ppm	ppm	ppm	ppm	ppm
CNF31865-6	LM14-96	Northwest zone	granular	Type 1 ± 2B	-	-	-	-	-	-	-	-	0.10	-	-	-	91.52
CNF31865-7	LM14-96	Northwest zone	granular	Type 1 ± 2B	-	-	-	-	-	-	-	-	-	-	-	-	148.72
CNF31865-8	LM14-96	Northwest zone	granular	Type 1 ± 2B	-	-	-	-	-	-	-	-	8.31	-	-	-	11.87
CNF31865-9	LM14-96	Northwest zone	granular	Type 1 ± 2B	0.02	-	0.05	-	-	-	0.95	-	0.36	-	-	4.39	86.63
CNF31865-10	LM14-96	Northwest zone	granular	Type 1 ± 2B	-	-	-	-	-	-	-	-	-	-	-	-	90.19
CNF31865-11	LM14-96	Northwest zone	granular	Type 1 ± 2B	-	-	-	-	-	-	-	4.75	-	-	-	-	213.60
CNF31865-12	LM14-96	Northwest zone	granular	Type 1 ± 2A	-	-	0.13	-	-	-	0.51	-	-	-	-	-	-
CNF31865-13	LM14-96	Northwest zone	granular	Type 1 ± 2A	0.26	0.02	-	0.08	0.39	-	2.32	-	-	-	-	-	26.48
CNF31865-14	LM14-96	Northwest zone	granular	Type 1 ± 2A	-	-	-	-	-	-	0.36	-	-	-	-	-	129.56
CNF31865-15	LM14-96	Northwest zone	granular	Type 1 ± 2A	0.10	-	-	-	0.12	0.01	0.58	0.02	-	-	-	-	27.00
CNF31865-16	LM14-96	Northwest zone	granular	Type 1 ± 2A	-	-	-	-	-	-	0.58	-	-	-	-	-	91.80
CNF31865-17	LM14-96	Northwest zone	granular	Type 1 ± 2A	-	0.01	0.19	-	0.13	-	0.82	-	-	-	-	-	102.60
CNF31865-18	LM14-96	Northwest zone	granular	Type 1 ± 2A	0.23	0.04	-	-	-	-	0.47	-	-	-	-	-	213.06
CNF31865-19	LM14-96	Northwest zone	granular	Type 1 ± 2A	-	0.00	0.02	-	-	-	0.24	0.04	-	-	-	-	72.54

Sample/spot analysis #	Drill Hole	Mineralized zone	Barite texture	Mineral Assemblage Type	Tl ppm	Pb206 ppm	Pb208 ppm	Bi ppm	Th ppm	U ppm
CNF31865-6	LM14-96	Northwest zone	granular	Type 1 ± 2B	-	167.20	176.00	-	0.28	0.59
CNF31865-7	LM14-96	Northwest zone	granular	Type 1 ± 2B	7.04	82.72	92.40	-	-	-
CNF31865-8	LM14-96	Northwest zone	granular	Type 1 ± 2B	593.33	15.43	23.14	-	-	3.56
CNF31865-9	LM14-96	Northwest zone	granular	Type 1 ± 2B	63.49	296.67	308.53	-	0.72	1.35
CNF31865-10	LM14-96	Northwest zone	granular	Type 1 ± 2B	-	136.47	78.32	-	-	-
CNF31865-11	LM14-96	Northwest zone	granular	Type 1 ± 2B	-	148.93	178.00	-	-	-
CNF31865-12	LM14-96	Northwest zone	granular	Type 1 ± 2A	-	14.64	10.43	-	0.23	0.18
CNF31865-13	LM14-96	Northwest zone	granular	Type 1 ± 2A	-	190.88	159.98	-	1.58	0.71
CNF31865-14	LM14-96	Northwest zone	granular	Type 1 ± 2A	-	421.33	389.73	-	1.17	-
CNF31865-15	LM14-96	Northwest zone	granular	Type 1 ± 2A	-	43.20	46.44	-	0.80	0.22
CNF31865-16	LM14-96	Northwest zone	granular	Type 1 ± 2A	-	45.36	83.16	0.14	0.27	0.48
CNF31865-17	LM14-96	Northwest zone	granular	Type 1 ± 2A	-	22.14	18.36	-	0.59	0.29
CNF31865-18	LM14-96	Northwest zone	granular	Type 1 ± 2A	-	23.72	18.22	0.05	0.42	0.31
CNF31865-19	LM14-96	Northwest zone	granular	Type 1 ± 2A	-	13.49	7.57	-	0.17	0.08

4.3 Compiled high resolution ICP-MS analyses

Table A-4-2. Compiled results of HR-ICP-MS analyses of different barite textures from the Lemarchant deposit.

Sample	CNF31723	CNF31723	CNF31723	CNF31723	CNF31723	CNF31723	CNF31723	CNF31723	CNF31723	CNF31723
Barite Texture	Bladed/Tabular	Bladed/Tabular	Tabular	Granular	Tabular	Tabular	Granular	Vein	Vein	Granular
Spot analysis	1	2	3	4	5	6	7	8	9	10
Ba^{134}	101.65	45278.79	-	-	-	-	-	-	-	-
Ba^{135}	127.79	44823.94	-	-	-	-	-	-	57978.74	46206.19
Ba^{138}	125.43	-	120116.50	-	123559.26	139596.80	-	-	69619.34	37912.89
La^{139}	15.35	0.14	0.55	-	-	-	-	-	-	-
Ce^{140}	32.74	-	-	-	-	-	-	-	-	-
Pr^{141}	4.57	-	-	-	-	-	-	-	-	-
Nd^{143}	20.83	-	-	-	-	-	-	-	-	-
Nd^{145}	23.43	-	-	-	-	-	-	-	-	-
Sm^{147}	-	-	-	-	-	-	-	-	-	-
Sm^{149}	-	-	-	-	-	-	-	-	-	-
Eu^{151}	-	-	-	-	-	-	-	-	-	-
Eu^{153}	-	-	-	-	-	-	-	-	-	-
Gd^{155}	-	-	-	-	-	-	-	-	-	-
Gd^{157}	-	-	-	-	-	-	-	-	-	-
Tb^{159}	-	-	-	-	-	-	-	-	-	-
Dy^{161}	-	-	-	-	-	-	-	-	-	-
Dy^{163}	-	-	-	-	-	-	-	-	-	-
Ho^{165}	-	-	-	-	-	-	-	-	-	-
Er^{166}	-	-	-	-	-	-	-	-	-	-
Er^{167}	-	-	-	-	-	-	-	-	-	-
Tm^{169}	-	-	-	-	-	-	-	-	-	-
Yb^{172}	-	-	-	-	-	-	-	-	-	-
Yb^{173}	-	-	-	-	-	-	-	-	-	-
Lu^{175}	-	-	-	-	-	-	-	-	-	-
Au^{197}	-	2.64	-	-	-	-	-	-	-	-
Bi^{209}	-	-	0.03	-	-	-	-	-	-	-

Table A-4-3. *Cont.'d.*

Sample	CNF31723	CNF31723	CNF31723	CNF31723	CNF31723	CNF31723	CNF31723	CNF31730	CNF31730	CNF31730
Barite Texture	Granular	Vein	Tabular	Tabular	Granular	Granular	Granular	Plumose	Plumose	Bladed/Tabular
Spot analysis	11	12	13	14	15	16	17	1	2	3
Ba^{134}	-	-	-	-	104575.65	-	-	-	92737.77	155317.66
Ba^{135}	-	-	-	-	104841.16	-	-	-	-	-
Ba^{138}	119.82	-	-	284324.02	130924.24	-	-	-	-	-
La^{139}	-	-	-	331.18	-	-	-	-	-	-
Ce^{140}	-	-	-	311.75	-	-	-	-	-	-
Pr^{141}	-	-	-	17.22	-	-	-	-	-	-
Nd^{143}	22.02	-	-	-	-	-	-	-	-	-
Nd^{145}	-	-	-	-	-	-	-	-	-	-
Sm^{147}	-	-	-	-	-	-	-	-	-	-
Sm^{149}	5.12	-	-	-	-	-	-	-	-	-
Eu^{151}	1.67	-	-	-	-	-	-	-	-	-
Eu^{153}	-	-	-	-	-	-	-	-	-	-
Gd^{155}	-	0.16	-	-	-	1.52	-	-	-	-
Gd^{157}	-	-	-	-	-	-	-	-	-	-
Tb^{159}	-	-	-	-	-	-	-	-	-	-
Dy^{161}	-	-	-	-	0.61	-	-	-	-	-
Dy^{163}	4.99	-	-	-	-	-	-	-	-	-
Ho^{165}	-	-	-	-	-	-	-	-	-	-
Er^{166}	2.92	-	-	-	-	-	-	-	-	-
Er^{167}	-	-	-	-	-	-	-	-	-	-
Tm^{169}	-	-	-	-	-	-	-	-	-	-
Yb^{172}	-	-	-	-	-	-	-	-	-	-
Yb^{173}	-	-	-	-	-	-	-	-	-	-
Lu^{175}	0.20	-	-	-	-	-	-	-	-	-
Au^{197}	-	-	-	-	-	-	-	-	69.42	-
Bi^{209}	0.03	-	0.02	-	0.01	-	-	51.16	-	-

Table A-4-3. *Cont.'d.*

Sample	CNF31730	CNF31730	CNF31733	CNF31733	CNF31733	CNF31733	CNF31733	CNF31733	CNF31733	CNF31733
Barite Texture	Bladed/Tabular	Bladed/Tabular	Bladed/Tabular	Bladed/Tabular	Bladed/Tabular	Granular	Bladed/Tabular	Bladed/Tabular	Bladed/Tabular	Granular
Spot analysis	4	5	1	2	3	4	5	6	7	8
Ba^{134}	-	-	139074.24	100061.20	161867.69	-	-	-	60351.74	-
Ba^{135}	-	-	-	-	228961.31	-	-	91403.21	63544.29	-
Ba^{138}	-	88533.12	-	-	196846.00	-	-	-	-	-
La^{139}	-	-	-	-	26.41	-	-	-	-	-
Ce^{140}	-	-	-	-	-	-	-	-	-	-
Pr^{141}	-	-	-	-	-	-	-	-	-	-
Nd^{143}	-	-	-	-	-	-	-	-	-	-
Nd^{145}	-	-	-	-	-	-	-	-	-	-
Sm^{147}	-	-	-	-	-	-	-	-	-	-
Sm^{149}	-	-	-	-	8.33	-	-	-	-	-
Eu^{151}	-	-	-	-	-	-	-	-	-	-
Eu^{153}	-	-	-	-	-	-	-	-	-	-
Gd^{155}	-	-	-	-	-	-	16.46	-	-	20.29
Gd^{157}	-	-	-	-	-	-	-	-	-	-
Tb^{159}	-	-	-	-	-	10.38	-	-	-	-
Dy^{161}	-	-	-	-	6.90	-	-	-	-	-
Dy^{163}	-	-	-	-	-	-	-	-	-	-
Ho^{165}	-	-	-	-	-	-	-	-	-	-
Er^{166}	-	-	-	-	-	-	-	-	-	-
Er^{167}	-	-	-	-	-	-	-	-	-	-
Tm^{169}	-	-	-	-	-	-	-	-	-	-
Yb^{172}	-	-	-	-	-	-	-	-	-	-
Yb^{173}	-	-	-	-	-	-	-	-	-	-
Lu^{175}	-	-	-	-	-	-	-	-	-	-
Au^{197}	-	-	-	-	-	-	-	-	-	-
Bi^{209}	152.36	-	721.84	-	-	-	-	-	-	-

Table A-4-3. *Cont.'d.*

Sample	CNF31733	CNF31860	CNF31860	CNF31860	CNF31860	CNF31860	CNF31860	CNF31860	CNF31860	CNF31860
Barite Texture	Granular	Granular	Granular	Granular	Granular	Granular	Granular	Bladed/Tabular	Bladed/Tabular	Bladed/Tabular
Spot analysis	9	1	2	3	4	5	6	7	8	9
Ba^{134}	119118.96	-	-	537404.03	383317.44	-	296426.79	79792.00	-	-
Ba^{135}	110005.43	-	-	506247.76	323252.61	-	238995.96	89586.91	98863.87	184196.73
Ba^{138}	122054.08	-	-	440479.97	-	552762.26	231687.29	111521.26	98829.29	177204.78
La^{139}	-	-	-	147.11	-	-	15.73	-	-	-
Ce^{140}	-	-	-	18.79	5.96	-	-	-	-	-
Pr^{141}	-	-	1.49	-	-	-	-	-	-	-
Nd^{143}	-	-	-	-	-	-	-	-	-	-
Nd^{145}	-	-	-	-	-	-	-	-	-	-
Sm^{147}	-	-	-	-	-	-	0.98	-	-	-
Sm^{149}	-	-	-	-	-	-	-	-	-	-
Eu^{151}	-	-	-	-	-	-	-	-	-	-
Eu^{153}	-	-	-	-	-	-	-	-	-	-
Gd^{155}	-	-	-	-	-	-	-	-	-	-
Gd^{157}	-	-	-	-	1.38	-	-	-	-	-
Tb^{159}	-	-	-	-	-	-	-	-	-	-
Dy^{161}	-	-	-	-	-	-	-	-	-	-
Dy^{163}	-	-	-	-	-	-	-	-	-	-
Ho^{165}	-	-	-	-	-	-	-	-	-	-
Er^{166}	-	-	-	-	-	-	-	-	-	-
Er^{167}	-	-	-	-	-	-	11.83	-	-	-
Tm^{169}	-	-	-	-	-	-	14.54	-	-	-
Yb^{172}	-	-	-	-	-	-	-	-	-	-
Yb^{173}	-	-	-	-	-	-	-	-	-	-
Lu^{175}	-	-	-	-	-	-	-	-	-	-
Au^{197}	-	-	-	-	-	-	131.84	-	-	-
Bi^{209}	-	-	-	-	-	-	-	-	-	-

Table A-4-2. *Cont.'d.*

Sample	CNF31860	CNF31860	CNF31860	CNF31860	CNF31860	CNF31860	CNF31860	CNF31860	CNF31860	CNF31860
Barite Texture	Bladed/Tabular	Granular	Granular	Granular	Granular	Granular	Bladed/Tabular	Bladed/Tabular	Bladed/Tabular	Granular
Spot analysis	10	11	12	13	14	15	16	17	18	19
Ba^{134}	96842.91	-	192918.74	-	-	-	398597.17	121356.48	-	177049.88
Ba^{135}	103171.42	125407.87	-	-	-	-	314597.52	82399.51	-	-
Ba^{138}	133935.10	-	130570.97	-	79041.82	-	-	72965.43	-	-
La^{139}	6.91	-	2.94	-	-	-	26.50	-	84.12	-
Ce^{140}	-	-	1.53	-	-	-	4.02	-	-	-
Pr^{141}	-	-	-	-	-	-	-	-	-	-
Nd^{143}	-	-	-	-	-	-	-	-	8.60	-
Nd^{145}	-	-	-	-	-	-	-	-	-	-
Sm^{147}	-	-	-	-	-	-	-	-	-	-
Sm^{149}	-	-	-	-	-	-	-	-	-	-
Eu^{151}	-	-	-	-	-	-	-	-	-	-
Eu^{153}	-	-	-	-	-	-	-	-	-	-
Gd^{155}	-	-	-	-	-	-	-	-	-	-
Gd^{157}	-	-	-	-	-	-	-	-	-	-
Tb^{159}	-	-	-	-	-	-	-	-	-	-
Dy^{161}	-	-	-	-	-	-	-	-	-	-
Dy^{163}	-	-	-	-	-	-	-	-	-	-
Ho^{165}	-	-	-	-	-	-	-	-	-	-
Er^{166}	-	-	-	-	-	-	-	-	-	-
Er^{167}	-	-	-	-	-	-	-	-	-	-
Tm^{169}	-	-	-	-	-	50.33	74.94	-	-	-
Yb^{172}	-	-	-	-	-	-	-	-	-	-
Yb^{173}	-	-	-	-	-	-	-	-	-	-
Lu^{175}	-	-	-	-	-	-	-	-	-	-
Au^{197}	-	-	803.82	709.06	-	-	-	-	-	-
Bi^{209}	-	-	-	213.48	-	-	261.05	-	450.31	-

Table A-4-2. *Cont.'d.*

Sample	CNF31860	CNF31860	CNF31860	CNF31860	CNF31860	CNF31861	CNF31861	CNF31861	CNF31861	CNF31861	CNF31861
Barite Texture	Bladed/Tabular	Bladed/Tabular	Bladed/Tabular	Granular	Granular	Granular	Granular	Granular	Granular	Bladed/Tabular	Bladed/Tabular
Spot analysis	20	21	22	23	24	1	2	3	4	5	6
Ba^{134}	134990.66	-	-	-	224105.56	95927.96	-	-	67212.05	-	-
Ba^{135}	146364.08	231909.42	-	-	331403.47	81262.01	222195.45	-	46901.18	135220.24	-
Ba^{138}	218986.83	247182.38	-	102519.39	298365.53	82969.81	137754.69	-	41592.25	146523.69	-
La^{139}	-	-	-	3.81	-	-	-	-	1.55	-	-
Ce^{140}	2.66	-	-	-	-	-	0.69	-	-	-	-
Pr^{141}	-	-	-	-	-	2.34	-	-	-	-	-
Nd^{143}	-	-	-	-	-	-	-	-	-	5.70	-
Nd^{145}	-	-	-	-	-	-	-	-	-	-	-
Sm^{147}	-	-	-	-	-	-	-	-	-	-	-
Sm^{149}	-	-	-	-	-	-	-	-	-	-	-
Eu^{151}	-	-	-	-	-	-	-	-	-	-	-
Eu^{153}	-	-	-	-	-	-	-	-	-	-	-
Gd^{155}	-	-	-	-	-	-	-	-	-	-	-
Gd^{157}	-	-	-	-	-	-	-	-	-	-	-
Tb^{159}	-	-	-	-	-	-	-	-	-	-	-
Dy^{161}	-	-	-	-	-	-	-	-	-	-	-
Dy^{163}	-	-	-	-	-	-	-	-	-	-	-
Ho^{165}	-	-	-	-	-	-	-	-	-	-	-
Er^{166}	-	-	-	-	-	-	-	-	-	-	-
Er^{167}	-	-	-	-	-	-	-	-	-	-	-
Tm^{169}	-	-	-	-	-	-	-	-	-	-	-
Yb^{172}	-	-	-	-	-	-	-	-	-	-	-
Yb^{173}	-	-	-	-	-	-	-	-	-	-	-
Lu^{175}	-	-	-	-	-	-	-	-	-	-	-
Au^{197}	-	-	-	-	-	-	-	-	-	-	-
Bi^{209}	-	-	-	-	-	-	-	-	65.15	-	-

Table A-4-2. *Cont.'d.*

Sample	CNF31861	CNF31861	CNF31861	CNF31861	CNF31865	CNF31865	CNF31865	CNF31865	CNF31865	CNF31865	CNF31865	CNF31865
Barite Texture	Bladed/Tabular	Bladed/Tabular	Granular	Granular	Granular	Granular	Granular	Granular	Bladed/Tabular	Bladed/Tabular	Bladed/Tabular	Bladed/Tabular
Spot analysis	7	8	9	10	1	2	3	4	5	6	7	8
Ba^{134}	-	-	-	78676.81	803251.93	-	-	-	-	-	321744.06	117776.86
Ba^{135}	123393.44	153816.65	104324.44	97368.41	622643.56	-	-	-	-	262114.08	271051.35	114784.35
Ba^{138}	-	134497.51	97859.13	-	-	-	170490.47	-	-	318912.33	-	138532.04
La^{139}	-	-	2.81	-	-	19.36	22.89	-	-	-	-	16.84
Ce^{140}	-	-	-	-	6.14	-	12.51	-	-	-	-	-
Pr^{141}	-	-	-	-	10.83	4.48	6.66	-	-	-	-	8.02
Nd^{143}	-	-	-	-	-	-	-	-	-	-	-	-
Nd^{145}	6.07	-	-	-	4.31	-	-	-	-	-	-	-
Sm^{147}	-	-	-	-	-	-	4.69	-	-	26.39	-	-
Sm^{149}	-	-	-	-	-	-	-	-	-	-	-	-
Eu^{151}	-	-	-	-	85.44	-	31.65	-	-	-	-	5.34
Eu^{153}	-	-	-	-	101.07	-	-	-	-	-	-	-
Gd^{155}	-	-	-	-	-	-	-	-	-	17.62	-	5.21
Gd^{157}	-	-	-	-	-	-	-	-	-	-	-	-
Tb^{159}	-	-	-	-	-	-	-	-	-	-	-	-
Dy^{161}	-	4.74	-	-	-	-	-	-	-	-	-	-
Dy^{163}	-	-	-	-	-	-	-	-	-	1.27	-	-
Ho^{165}	-	-	-	-	-	-	-	-	-	-	-	-
Er^{166}	-	-	-	-	-	-	-	-	-	-	-	-
Er^{167}	-	-	-	-	-	-	-	-	-	-	-	-
Tm^{169}	-	-	-	-	-	-	-	-	-	-	-	-
Yb^{172}	-	-	-	-	-	-	-	-	-	-	-	-
Yb^{173}	-	-	-	-	-	-	-	-	-	-	-	-
Lu^{175}	-	-	-	-	-	-	-	-	-	-	-	-
Au^{197}	-	-	-	-	19.97	-	-	-	-	-	-	-
Bi^{209}	-	-	-	-	-	-	-	-	-	-	-	-

Table A-4-2. *Cont.'d.*

Sample	CNF31865	CNF31865	CNF31865	CNF31865	CNF31865	CNF31812	CNF31812	CNF31812	CNF31812	CNF31812	CNF31812	CNF31812
Barite Texture	Granular	Granular	Granular	Granular	Granular	Granular	Granular	Granular	Granular	Bladed/Tabular	Bladed/Tabular	Bladed/Tabular
Spot analysis	9	10	11	12	13	1	2	3	4	5	6	7
Ba^{134}	-	-	-	-	-	-	-	76729.32	-	-	-	69367.31
Ba^{135}	-	-	-	49154.19	-	110803.83	-	83065.02	-	75484.47	129220.23	63724.37
Ba^{138}	63581.57	95760.18	57492.84	47297.29	65516.19	114961.85	100518.13	86439.27	-	-	180197.92	-
La^{139}	-	-	11.71	-	-	-	-	-	-	-	-	-
Ce^{140}	-	-	-	-	-	-	-	-	-	-	-	-
Pr^{141}	-	-	7.51	-	-	-	-	-	-	-	-	1.49
Nd^{143}	-	-	-	-	-	-	-	-	-	-	-	-
Nd^{145}	-	-	-	-	-	-	-	-	-	-	-	-
Sm^{147}	-	-	-	-	-	-	-	-	-	-	-	-
Sm^{149}	-	-	-	-	-	-	-	-	-	-	-	-
Eu^{151}	-	-	-	-	-	-	-	-	-	-	-	-
Eu^{153}	-	-	-	-	-	-	-	-	-	-	-	-
Gd^{155}	17.24	-	-	-	-	-	-	-	-	-	-	-
Gd^{157}	-	-	-	-	-	-	-	-	-	-	-	-
Tb^{159}	-	-	-	-	-	-	-	-	-	-	-	-
Dy^{161}	-	-	-	-	-	-	-	-	-	-	-	-
Dy^{163}	-	-	-	-	-	-	-	-	-	-	-	-
Ho^{165}	-	-	-	-	-	-	-	-	-	-	-	-
Er^{166}	-	-	-	-	-	-	-	-	-	-	-	-
Er^{167}	-	-	-	-	-	-	-	-	-	-	-	-
Tm^{169}	-	-	-	-	-	-	-	-	-	-	-	-
Yb^{172}	-	-	-	-	-	-	-	-	-	-	-	-
Yb^{173}	-	-	-	-	-	-	-	-	-	-	-	-
Lu^{175}	-	-	-	-	-	-	-	-	-	-	-	-
Au^{197}	-	-	-	-	-	-	-	-	-	-	-	-
Bi^{209}	-	-	-	-	-	-	-	349.33	-	-	-	-

Table A-4-2. *Cont.'d.*

Sample	CNF31812	CNF31812	CNF31812	CNF31812	CNF31812
Barite Texture	Bladed/Tabular	Bladed/Tabular	Bladed/Tabular	Bladed/Tabular	Bladed/Tabular
Spot analysis	8	9	10	11	12
Ba^{134}	-	-	-	-	-
Ba^{135}	89692.75	136250.54	-	102722.80	-
Ba^{138}	141300.01	-	-	-	136037.68
La^{139}	-	-	-	-	-
Ce^{140}	-	-	-	-	-
Pr^{141}	-	-	-	-	-
Nd^{143}	-	-	-	-	-
Nd^{145}	-	-	-	-	-
Sm^{147}	-	-	-	-	-
Sm^{149}	-	-	-	-	-
Eu^{151}	-	-	-	-	-
Eu^{153}	-	-	-	-	-
Gd^{155}	-	-	-	-	-
Gd^{157}	-	-	-	-	-
Tb^{159}	-	-	-	-	-
Dy^{161}	-	-	-	-	-
Dy^{163}	-	-	-	-	-
Ho^{165}	-	-	-	-	-
Er^{166}	-	-	-	-	-
Er^{167}	-	-	-	-	-
Tm^{169}	-	-	-	-	-
Yb^{172}	-	-	-	-	-
Yb^{173}	-	-	-	-	-
Lu^{175}	-	-	-	-	-
Au^{197}	-	-	-	-	-
Bi^{209}	-	-	-	-	-

Appendix 5: Stable isotope analysis

5.1 Supplementary sulfur-isotope methods

A total of 28 core samples from the massive sulfide/barite lenses were selected for sulfur-isotope analysis. In this study, three types of textures were analyzed. These are: (1) granular purple-grey barite (n=6), (2) bladed white barite (n=20), and (3) clasts composed of barite (n=2). Core samples from both the Main and the Northwest zones were selected in order to study the spatial variation of sulfur-isotopes in the deposit. In some cases, multiple core samples from the same drill hole were selected with the purpose of determining sulfur isotope variations with depth. Petrographic examination aided in the selection of the samples.

For each core sample, the sulfate was drilled out with the aid of a hand-held micro-drill. The micro-drill was cleaned between each sample in order to eliminate sample contamination. For each analysis, approximately 0.35 mg of drilled mineral separates was used for sulfur-isotope analysis. Sulfur-isotope analyses were performed at Memorial University of Newfoundland on a Finnigan MAT252 isotope ratio mass spectrometer (IRMS). Stable isotope results are reported in standard (δ) notation as per mil (‰) relative to the Vienna Canyon Diablo Troilite (V-CDT).

5.2 Compiled sulfur-isotope analyses

Table A-5-1. Compiled sulfur isotope ($\delta^{34}S$ ‰ V-CDT) analyses of barite.

Drill Hole	Sample	Depth (m)	Mineralized zone	Texture	$\delta^{34}S$ (‰ V-CDT)
LM13-73	CNF31715	315.45	Northwest zone	Massive/granular	27.84
LM13-73	CNF31721	332.95	Northwest zone	Massive/granular	27.00
LM13-73	CNF31723	346.49	Northwest zone	Massive/granular	24.70
LM13-94	CNF31730	332.26	Northwest zone	Massive/granular	27.09
LM11-68	CNF31861	199.90	Main Zone	Massive/granular	27.44
LM13-73	CNF31721	332.96	Northwest zone	Bladed	27.82
LM13-73	CNF31723	346.49	Northwest zone	Bladed	28.12
LM13-97	CNF31733	341.40	Northwest zone	Bladed	26.70
LM10-43	CNF31809	213.68	Main Zone	Bladed	27.86
LM10-43	CNF31810	218.75	Main Zone	Bladed	27.56
LM10-43	CNF31811	209.85	Main Zone	Bladed	26.05
LM10-43	CNF31811	209.85	Main Zone	Bladed	26.90
LLM10-43	CNF31812	226.10	Main Zone	Bladed	26.58
LM10-43	CNF31812	226.10	Main Zone	Bladed	26.50
LM10-43	CNF31812	226.10	Main Zone	Bladed	26.13
LM07-15	CNF31829	226.81	Main Zone	Bladed	27.78
LM11-68	CNF31860	197.95	Main Zone	Bladed	28.67
LM11-52	CNF31855	216.21	Main Zone	Bladed	27.30
LM08-19	CNF31816	98.10	24 Zone	Bladed	27.27
LM14-96	CNF31865	309.88	Northwest zone	Bladed	25.72
LM14-96	CNF31868	314.30	Northwest zone	Bladed	27.00
LM13-82	CNF31874	340.83	Northwest zone	Bladed	27.90
LM13-82	CNF31874	340.83	Northwest zone	Bladed	27.19
LM11-68	CNF31861	199.90	Main Zone	Bladed	27.02
LM11-68	CNF31861	199.90	Main Zone	Bladed	26.72
LM08-37	CNF31879	297.90	Northwest zone	Clast	26.33

Appendix 6: Whole-rock strontium isotope geochemistry

6.1 Supplementary strontium-isotope methods

Whole-rock strontium isotope ($^{87}Sr/^{86}Sr$) compositions were acquired from ten of the 18 samples used for sulfur isotope analysis with a Finningan MAT 262V thermal ionization mass spectrometer (TIMS) in dynamic mode. Instrumental mass fractionation of Sr isotopes were corrected using a Raleigh law relative to $^{88}Sr/^{86}Sr = 8.375209$. The reported $^{87}Sr/^{86}Sr$ ratios were corrected for the deviation from repeated duplicates of NBS 987 standard ($^{87}Sr/^{86}Sr = 0.710240$, Veizer et al., 1999[1]). Replicates of the standard give an average of $^{87}Sr/^{86}Sr = 0.710245 \pm 11$ (n=23). Samples were selected based on the spatial distribution across the deposit. The core samples containing barite were crushed and sieved to < 80μm and then centrifuged to isolate the barite.

6.1.1 Leaching

Approximately 50 mg of the crushed barite samples were placed in 15 mL beakers. Enough 7N HNO_3 was added to the beakers to cover each sample. The uncovered beakers were then placed on a hot plate at 100°C for a couple of hours. Generally, if the samples contained sulfides, a rigorous reaction would take place. In our case, no chemical reactions were visually observed suggesting that there were no sulfides present in the samples. The beakers were taken off the hot plate after a couple of hours and left covered for two days to allow the samples to settle at the bottom of the beakers. The acid was pipetted from each beaker and the process was repeated a second and third time. The beakers were again left

[1] Veizer, J., Ala, D., Azmy, K., Bruckschen, P., Buhl, D., Bruhn, F., ... & Jasper, T. (1999). $^{87}Sr/^{86}Sr$, $\delta^{13}C$ and $\delta^{18}O$ evolution of Phanerozoic seawater. Chemical geology, 161: 59-88.

on a hot plate at 100°C for a few hours to make sure that everything was dissolved. After a couple of hours, the acid was pipetted from the beakers and the samples were left on the hot plate for a couple more hours to make sure that the barite samples were dry and no more HNO_3 remained. Each sample was then immersed in 6N HCl^- and covered and subsequently placed on hot plates at 100°C for three days. The 6N HCl^- was then pipetted from the beakers and the barite samples were left to dry down overnight. Finally, approximately 1.5 mL of 2.5N HCl^- was added to each beaker and the samples were left covered for two days.

6.1.2 Sr columns

After leaching procedures, the samples were run through cation exchange columns in order to isolate the strontium from the barite. The type of resin used is AG-50W-X8. The resin volume is 3.5 mL with a mesh size of 200-400. The barite samples were centrifuged in the 1.5 mL of 2.5N HCl^- from the last step of the leaching process. Precisely 0.5 ml of the barite samples were pipetted from the centrifuge beakers into the columns. It is important to make sure that no solid material must be loaded into the columns. The columns used are commercially-built, ~12-mL borosilicate glass columns with built-in frits. The columns were washed with approximately 7 mL of 2.5N HCl^- after the initial 0.5 mL of 2.5N HCl^- had passed through the columns. At this stage, the next element to pass through the resin is strontium. Therefore, the acid containing the strontium was collected in clean 7 mL savillex beakers placed beneath the columns. The acid that had been collected up to that point was discarded. 2 mL of 6N HCl^- was run though the columns and collected in the beakers. The snap caps were placed on a hot plate overnight and the residue left after drying was used for the $^{87}Sr/^{86}Sr$ analyses on the mass spectrometer.

6.2 Compiled strontium isotope analyses

Table A-6-1. Compiled strontium isotope analyses ($^{87}Sr/^{86}Sr$) and whole-rock Sr and Rb concentrations (ppm) of barite.

Sample Nº	Drill Hole	Depth (m)	$^{87}Sr/^{86}Sr \pm 2\sigma$	Sr (ppm)	Rb (ppm)
CNF31816	LM08-19	98.10	0.707510 ± 0.000016	4889	1
CNF31861	LM11-68	199.90	0.707320 ± 0.000010	5905	< 1
CNF31733	LM13-94	341.40	0.707053 ± 0.000010	9348	< 1
CNF31810	LM10-43	218.75	0.707049 ± 0.000010	4034	< 1
CNF31730	LM13-94	332.25	0.707283 ± 0.000010	5419	2
CNF31721	LM13-73	332.95	0.706993 ± 0.000010	4997	< 1
CNF31874	LM13-82	340.80	0.707172 ± 0.000024	3604	< 1
CNF31865	LM14-96	309.90	0.706905 ± 0.000010	7438	< 1
CNF31868	LM14-96	314.30	0.707031 ± 0.000010	7233	< 1
CNF31855	LM11-52	216.20	0.707305 ± 0.000010	5693	< 1

6.3 Rb-Sr source tracing calculations

We can measure the Sr isotopic composition of rocks at the present day. However, if a rock formed at time *t* in the past, these modern values do not reflect the isotopic composition of the rock at time *t*. Hence, we must recalculate to obtain the initial $^{87}Sr/^{86}Sr$ ratio of the rock at time *t* in the past.

We have determined that the $^{87}Sr/^{86}$ composition of our barite is primary since barite is highly depleted in Rb, which eliminates any need to apply a correction for addition of radiogenic ^{87}Sr from Rb. Thus, barite preserves the original $^{87}Sr/^{86}Sr$ ratio of the fluid from which it was precipitated. However, to determine the sources(s) of Sr in our barite, we must determine the endmember $^{87}Sr/^{86}Sr$ composition of upper crust and depleted mantle at time *t* (i.e. 510 Ma) since there is no available Sr isotopic data in the region. This is done to account for the ^{87}Sr that has formed since time *t* due to ^{87}Rb breakdown. To calculate the original ratios, we can use the following equation using the present-day average $^{87}Sr/^{86}Sr$ isotopic compositions of both the upper crust and the depleted mantle at t = 510 Ma (age of formation of the Lemarchant deposit and Tally Pond group):

$$\left(\frac{^{87}Sr}{^{86}Sr}\right)_o = \left(\frac{^{87}Sr}{^{86}Sr}\right) - \left(\frac{^{87}Rb}{^{86}Sr}\right)\left(e^{\lambda t} - 1\right) \qquad (1)$$

where $(^{87}Sr/^{86}Sr)_o$ is the initial ratios at time *t*, $(^{87}Sr/^{86}Sr)$ are average present-day values for both endmember sources (i.e. upper crust and depleted mantle), $(^{87}Rb/^{86}Sr)$ are present-day values for both endmember sources (see calculations below), λ is the decay constant for the

Rb-Sr systems (1.39×10^{-11} yr^{-1}), and t is time in years (≈510 Ma). However, we need to calculate the ($^{87}Rb/^{86}Sr$) of our present-day rock using the following equation:

$$\left(\frac{^{87}Rb}{^{86}Sr}\right) = \left(\frac{Rb}{Sr}\right) \left(\frac{Ab^{87}Rb \times WSr}{Ab^{86}Sr \times WRb}\right) \qquad (2)$$

where ($^{87}Rb/^{86}Sr$) are calculated present-day ratios, (Rb/Sr) is the ratio of concentrations of these elements (ppm) for both present-day upper crust and depleted mantle, $Ab^{87}Rb$ and $Ab^{86}Sr$ are the isotopic abundances, and WSr and WRb are the respective atomic weights. The following tables (Tables A-6-2 and A-6-3) are a summary of calculations for determining the $^{87}Rb/^{86}Sr$ values for both reservoirs.

Table A-6-2. Summary of calculations for determining approximate $^{87}Rb/^{86}Sr$ ratio for Cambrian upper crust.

Isotope abundance ratios			
	Abundance ratios	***Comment(s)***	
$^{87}Sr/^{88}Sr$	0.0854904	($^{86}Sr/^{88}Sr \times {}^{87}Sr/^{86}Sr$)	
$^{86}Sr/^{88}Sr$	0.1194	fixed	
$^{84}Sr/^{88}Sr$	0.00675	fixed	
$^{88}Sr/^{88}Sr$	1	fixed	
Sum	1.2116404		
Mass			
	Abundance*	***Amu***	***Abundance × Mass***
^{87}Sr	0.07055757	86.9088	6.13207357
^{86}Sr	0.09854409	85.9092	8.46584389
^{84}Sr	0.00557096	83.9134	0.46747818
^{88}Sr	0.82532738	87.9056	72.5508988
Sum	1		87.6162944 (Atomic Weight)
		Comment(s)	
$^{87}Sr/^{86}Sr$**	0.7160		
Rb/Sr***	0.27	Rb (ppm) = 95 Sr (ppm) = 337	
λ	1.42×10^{-11} yr^{-1}		
Atomic Wt. Rb	85.46776		
Abn ^{87}Rb	0.278500		
Atomic Wt. Sr	87.61629		
Abn ^{86}Sr	0.098544		
Abn^{87}Rb×Sr (weight)	24.40113		
Abn^{86}Sr×Rb (weight)	8.422342		
$^{87}Rb/^{86}Sr$ =	0.781531178		
$^{87}Sr/^{86}Sr$ @ t=510Ma Using equation (1)	**≈0.7103**		

*Calculated by dividing the abundance ratios by the sum of abundance ratios.

**$^{87}Sr/^{86}Sr$ composition of upper crust from Goldstein and Jacobsen (1988).[2]

*** Average Rb and Sr concentration of upper crust from Goldstein and Jacobsen (1988).

[2] Goldstein, S. J., & Jacobsen, S. B. (1988). Nd and Sr isotopic systematics of river water suspended material: implications for crustal evolution. Earth and Planetary Science Letters, 87: 249-265.

Table A-6-3. Summary of calculations for determining approximate $^{87}Rb/^{86}Sr$ ratio for Cambrian depleted mantle.

Isotope abundance ratios			
	Abundance ratios	***Comment(s)***	
$^{87}Sr/^{88}Sr$	0.08389044	($^{86}Sr/^{88}Sr \times {}^{87}Sr/^{86}Sr$)	
$^{86}Sr/^{88}Sr$	0.1194	fixed	
$^{84}Sr/^{88}Sr$	0.00675	fixed	
$^{88}Sr/^{88}Sr$	1	fixed	
Sum	1.2116404		
Mass			
	Abundance*	***Amu***	***Abundance × Mass***
^{87}Sr	0.06932863	86.9088	6.02526761
^{86}Sr	0.09867439	85.9092	8.47703774
^{84}Sr	0.00557833	83.9134	0.4680963
^{88}Sr	0.82641866	87.9056	72.6468282
Sum	1		87.6172299 (Atomic Weight)
		Comment(s)	
$^{87}Sr/^{86}Sr$**	0.7026		
Rb/Sr***	0.0032		
λ	1.42×10^{-11} yr^{-1}		
Atomic Wt. Rb	85.46776		
Abn ^{87}Rb	0.278500		
Atomic Wt. Sr	87.61629		
Abn ^{86}Sr	0.098544		
Abn^{87}Rb×Sr (weight)	24.40113		
Abn^{86}Sr×Rb (weight)	8.433478		
$^{87}Rb/^{86}Sr$ =	**0.009499**		
$^{87}Sr/^{86}Sr$ @ t=510Ma Using equation (1)	**≈0.7025**		

*Calculated by dividing the abundance ratios by the sum of abundance ratios.
**$^{87}Sr/^{86}Sr$ composition of depleted mantle from Salters et al. (2004).[3]
*** Average Rb and Sr concentration of depleted mantle from Workman and Hart (2005).[4]

[3] Salters, V. J., & Stracke, A. (2004). Composition of the depleted mantle. Geochemistry, Geophysics, Geosystems, 5, Q05B07, doi:10.1029/2003GC000597

[4] Workman, R. K., & Hart, S. R. (2005). Major and trace element composition of the depleted MORB mantle (DMM). Earth and Planetary Science Letters, 231: 53-72.

Appendix 7: Fluid inclusion microthermometry

7.1 Supplementary fluid inclusion microthermometry methods

Four samples were analyzed for fluid inclusion microthermometry. The selected samples covered both the Main zone and Northwest zone of the Lemarchant deposit. All of the studied fluid inclusions are in bladed barite hosted within the massive sulfide lenses due to their pristine fluid inclusions assemblages (FIAs) and their abundance. Samples were prepared as ~60 µm doubly-polished thin sections mounted with acetone-soluble glue (cyanoacrylate). Prior to microthermometric measurements, a detailed petrographic examination of the samples was completed in order to determine FIAs and the types of fluid inclusions in each FIA were noted. Samples were examined using a petrographic microscope, starting at low magnification to document their distribution, size, and origin and then proceeding to higher magnification to identify phase relations in fluid inclusions. The polished thick sections were removed from the glass backing prior to heating and freezing experiments by immersing the samples overnight in acetone. The general method for heating/freezing experiments is described elsewhere (e.g. Roedder, (1984)[5], Shepherd et al., (1985)[6]). Measurements were completed at Memorial University of Newfoundland using a Linkam THMSG600 heating freezing stage mounted on an Olympus BX51 microscope equipped for use with reflected, transmitted, and infrared light. Fluid inclusion images were captured using an Olympus BX51 camera. The accuracy and precision of measurements was insured by calibration against the triple point of CO_2 (-56.6 ± 0.1 °C),

[5] Roedder, E. (1984). Fluid inclusions. Mineralogical Society of America. Reviews in Mineralogy, 12. p. 644.
[6] Shepherd, T. J., Rankin, A. H., & Alderton, D. (1985). A practical guide to fluid inclusion studies. Blackie, Glasgow, p. 239.

the freezing point of water (0.0 ± 0.1 °C), and the critical point of water (374.6 ± 0.5 °C) using SYNFLINC® synthetic fluid inclusions. Barite is particularly susceptible to leakage and necking-down processes. Therefore, fluid inclusions near cracks or showing necking-down or leakage were not analyzed.

Salinities were calculated using the *Q2* program within the software package CLATHRATES (Bakker et al., 1996[7]; Bakker, 1997[8], 1998[9]). Salinities were calculated for all inclusions that contain a coexisting liquid a vapor gas phase (CO_2) using the temperature of clathrate melting.

Pressure (bars) for fluid inclusion assemblages was calculated using the *Q2* program within the software package Loner15 and were calculated from homogenization temperatures of aqueous carbonic inclusions (Bakker, 1997; Bakker, 2003; Bakker and Brown, 2003).

Isochores for type-I fluid inclusion assemblages were calculated using the FLUIDS software package using the equation of state by Anderko and Pitzer (1993) and Duan et al. (1995). Bulk fluid compositions calculated from the Loner15 software and homogenization temperatures of the FIA were used to calculate the isochores on a P-T diagram for the different fluid inclusion type-I assemblages.

[7] Bakker, R. J., Dubessy, J., & Cathelineau, M. (1996). Improvements in clathrate modelling: I. the H_2O-CO_2 system with various salts. Geochimica Et Cosmochimica Acta, 60*:* 1657-1681.

[8] Bakker, R. J. (1997). Clathrates: Computer programs to calculate fluid inclusion V-X properties using clathrate melting temperatures. Computers & Geosciences, 23: 1-18.

[9] Bakker, R. (1998). Improvements in clathrate modelling II: The H_2O-CO_2-CH_4-N_2-C_2H_6 fluid system. Geological Society, London, Special Publications, 137: 75-105.

7.2 Compiled fluid inclusion microthermometry analyses

Table A-7-1. Results of fluid inclusion microthermometry and salinity calculations for different fluid inclusion assemblages in bladed barite from the Lemarchant deposit.

Sample/assemblage	Assemblage	Type	Degree of Fill (F)	First melting temperature (T_{mCO2})	Final melting temperature ($T_{m\ ice\ clathrate}$ °C)	Final melting temperature ($T_{m\ ice}$ °C)	Temperature of homogenization (T_{hCO2})	Final homogenization temperature (T_h °C)	Salinity (wt. %)*
CNF31723 (vein)									
1	1	I	0.75	-56.1	8.90	-	-	248.1	1.8
2	1	I	0.75	-56.1	9.10	-	-	248.1	1.4
3	1	I	0.75	-	9.10	-	-	248.1	1.4
4	1	I	0.75	-	9.10	-	-	246	1.4
5	1	I	0.80	-56.0	7.80	-	-	246	3.9
6	1	I	0.80	-56.0	9.70	-	-	247.8	0.2
7	1	III	0.99	-56.0	-		-	-	
8	1	III	0.99	-	7.80		-	-	3.9
1	2	I	0.75	-56.0	9.70	-	-	236	0.2
2	2	I	0.75	-	-	-	-	236	
3	2	I	0.75	-	-	-	-	-	
4	2	I	0.75	-56.0	-	-	-	-	
CNF31723 (bladed barite)									
1	1	II	0.95	-	-	-	-	decrepitated	
2	1	II	0.95	-	-	-0.3	-	decrepitated	
3	1	II	0.95	-	-	1	-	198.3	
4	1	II	0.95	-	10.5	-	-	decrepitated	0.0
5	1	II	0.95	-	9.3	-	-	-	1.0
6	1	II	0.95	-	-	-	-	-	
1	2	II	0.75	-	-	-3.2	-	-	
2	2	II	0.75	-	-	-	-	214.4	
3	2	II	0.75	-	-	-2.9	-	216.2	
CNF31874 (bladed barite)									
1	1	II	0.75	-59.2	9.5	-4	-		0.6
2	1	II	0.95	-	9.5	-	27.7-29	211.7	0.6
3	1	III	1	-	7.1	-	-	-	5.2
4	1	II	0.75	-		-3.5	-	-	
5	1	II	0.9	-		-3	-	-	
6	1	II	0.95	-		-	-	-	
7	1	II	0.95	-		-	-	-	
8	1	II	0.95	-			-	-	
9	1	II	0.95	-			-	-	
10	1	II	0.95	-			-	-	
1	2	I	0.75	-56.3	-4.7	-4.7	31	-	
2	2	I	0.5	-56.3	-	-	-	decrepitated	
3	2	I	0.75	-56.3	-	-	-	261.3	
4	2	III	1	-	10.3	-	-	decrepitated	~0.0
5	2	I	0.75	-	-	-	-	256	
6	2	I	0.75	-	-	-	-	-	
7	2	I	0.75	-	9.9	-	-	276	~0.0
8	2	I	0.75	-	9.9	-	-	decrepitated	~0.0
9	2	I	0.75	-	9.9	-	-	decrepitated	~0.0
10	2	I	0.75	-	-	-	-	decrepitated	

*Salinities (wt.%) were calculated using the Q2 program within the software CLATHRATES.

Table A-7-1. *Cont.'d*

Sample/assemblage	Assemblage	Type	Degree of Fill (F)	First melting temperature (T_{mCO2})	Final melting temperature ($T_{m\ ice\ clathrate}$ °C)	Final melting temperature ($T_{m\ ice}$ °C)	Temperature of homogenization (T_{hCO2})	Final homogenization temperature (T_h °C)	Salinity (wt. %)*
CNF31865 (bladed barite)									
1	1	I	0.75	-56.50	-	-	30.8	-	
2	1	I	0.75	-	9.5	-	-	-	0.6
3	1	I	0.95	-	7.6	-	-	-	4.2
4	1	I	0.75	-	-	-	-	-	
5	1	I	-	-	-	-	-	-	
6	1	I	-	-	-	-	-	-	
7	1	I	-	-	-	-	-	-	
8	1	I	0.75	-	9.5	-	-	-	
9	1	I	0.95	-	9.1	-	30.2	-	0.6
10	1	I	0.75	-	-	-	-	228	1.4
11	1	I	0.75	-	-	-	-	250	
12	1	I	0.75	-	-	-	-	250	
13	1	I	0.75	-	-	-	-	255	
1	2	I	0.75	-56.2	-	-	30.4	-	
2	2	I	0.75	-	-	-	30.4	-	
3	2	I	0.75	-	-	-	-	-	
4	2	I	0.95	-	9.4	-	-	-	
5	2	I	0.75	-	9.7	-	-	-	0.8
6	2	I	0.75	-	-	-	-	-	0.2
8	2	II	0.9	-	-	-	-	-	
9	2	II	0.95	-	-	-	-	-	
10	2	II	0.95	-	-	-	-	-	
11	2	II	0.75	-	-	-	-	-	
12	2	II	0.75	-	-	-	-	245	
CNF31860 (bladed barite)									
1	1	I	0.75	-	9.8	-	30.8	-	
2	1	I	0.75	-57.1	9.8	-	-	-	0.0
3	1	I	0.9	-	-	-	-	191	0.0
4	1	I	0.75	-	-	-	-	245.3	
5	1	I	0.9	-	-	-	-	245.3	

*Salinities (wt.%) were calculated using the Q2 program within the software CLATHRATES.

Table A-7-2. Pressure trapping conditions (bars) of type-I fluid inclusion assemblages in bladed barite from the Lemarchant deposit.

Sample/inclusion #	xH_2O	xCO_2	xNa	xCl	Density (cc/mol)	Pressure (bars)*	Depth (km)
CNF31723 (vein)	-	-	-	-	-	-	-
CNF31723 (bladed barite)	-	-	-	-	-	-	-
CNF31874 (bladed barite)	0.87	0.13	0.00	0.00	23.99	1759.27	6.64
	0.88	0.12	0.00	0.00	24.17	1711.21	6.46
CNF31865 (bladed barite)	0.89	0.10	0.00	0.00	23.06	1955.96	7.38
CNF31860 (bladed barite)	0.92	0.08	0.00	0.00	22.14	2006.94	7.58

*Pressures (bars) were calculated using the *Q2* program within the software *Loner15*.

Table A-7-3. Isochores calculations for fluid inclusion assemblages using the FLUIDS software package.

Sample-FIA	T (K)	T (°C)	P (MPa)	P (bar)	V (cc/mol)
CN31860 (bladed barite)	518.45	245.3	199.394	1993.94	22.13695
	536.185	263.035	215.3159	2153.159	22.13695
	553.92	280.77	232.6022	2326.022	22.13695
	571.655	298.505	251.1901	2511.901	22.13695
	589.39	316.24	271.2364	2712.364	22.13695
	607.125	333.975	292.1241	2921.241	22.13695
	624.86	351.71	313.7434	3137.434	22.13695
	642.595	369.445	336.0055	3360.055	22.13695
	660.33	387.18	358.8719	3588.719	22.13695
	678.065	404.915	382.3384	3823.384	22.13695
	695.8	422.65	406.4043	4064.043	22.13695
	713.535	440.385	431.0473	4310.473	22.13695
	731.27	458.12	456.2235	4562.235	22.13695
	749.005	475.855	481.8846	4818.846	22.13695
	766.74	493.59	507.9909	5079.909	22.13695
	784.475	511.325	537.7285	5377.285	22.13695
	802.21	529.06	566.8001	5668.001	22.13695
	819.945	546.795	596.1055	5961.055	22.13695
	837.68	564.53	625.6365	6256.365	22.13695
	855.415	582.265	655.3854	6553.854	22.13695
	873.15	600	685.3446	6853.446	22.13695
CNF31865 (bladed barite)	523.15	250	192.1437	1921.437	23.05778
	540.65	267.5	204.0378	2040.377	23.05778
	558.15	285	217.8611	2178.611	23.05778
	575.65	302.5	233.679	2336.79	23.05778
	593.15	320	251.4288	2514.288	23.05778
	610.65	337.5	270.0537	2700.537	23.05778
	628.15	355	289.3194	2893.194	23.05778
	645.65	372.5	309.082	3090.82	23.05778
	663.15	390	329.3203	3293.203	23.05778
	680.65	407.5	350.0868	3500.868	23.05778
	698.15	425	371.4291	3714.291	23.05778
	715.65	442.5	393.3363	3933.363	23.05778
	733.15	460	415.7474	4157.474	23.05778
	750.65	477.5	438.5917	4385.917	23.05778
	768.15	495	461.8174	4618.174	23.05778
	785.65	512.5	489.0386	4890.386	23.05778
	803.15	530	515.2491	5152.491	23.05778
	820.65	547.5	541.6381	5416.381	23.05778
	838.15	565	568.2071	5682.071	23.05778
	855.65	582.5	594.9578	5949.578	23.05778
	873.15	600	621.8911	6218.911	23.05778

Table A-7-3. *Cont'd.*

Sample-FIA	T (K)	T (°C)	P (MPa)	P (bar)	V (cc/mol)
CNF3174 (bladed barite)	484.15	211	166.368	1663.68	23.99464
	503.6	230.45	175.2174	1752.174	23.99464
	523.05	249.9	186.26	1862.6	23.99464
	542.5	269.35	199.175	1991.75	23.99464
	561.95	288.8	213.8848	2138.848	23.99464
	581.4	308.25	230.4216	2304.216	23.99464
	600.85	327.7	248.3555	2483.555	23.99464
	620.3	347.15	267.1637	2671.637	23.99464
	639.75	366.6	286.6399	2866.399	23.99464
	659.2	386.05	306.7074	3067.074	23.99464
	678.65	405.5	327.3822	3273.822	23.99464
	698.1	424.95	348.6954	3486.954	23.99464
	717.55	444.4	370.6309	3706.309	23.99464
	737	463.85	393.1274	3931.274	23.99464
	756.45	483.3	416.1174	4161.174	23.99464
	775.9	502.75	442.0185	4420.185	23.99464
	795.35	522.2	468.7052	4687.052	23.99464
	814.8	541.65	495.5877	4955.877	23.99464
	834.25	561.1	522.6632	5226.632	23.99464
	853.7	580.55	549.9302	5499.302	23.99464
	873.15	600	577.3868	5773.868	23.99464
CNF31874-2 (bladed barite)	533.15	260	170.7434	1707.434	24.17278
	550.15	277	183.8008	1838.008	24.17278
	567.15	294	197.7261	1977.261	24.17278
	584.15	311	212.5115	2125.115	24.17278
	601.15	328	227.9946	2279.946	24.17278
	618.15	345	244.0671	2440.671	24.17278
	635.15	362	260.6662	2606.662	24.17278
	652.15	379	277.7528	2777.528	24.17278
	669.15	396	295.3073	2953.073	24.17278
	686.15	413	313.3185	3133.185	24.17278
	703.15	430	331.7719	3317.719	24.17278
	720.15	447	350.6446	3506.446	24.17278
	737.15	464	369.9082	3699.082	24.17278
	754.15	481	389.5353	3895.353	24.17278
	771.15	498	409.5026	4095.026	24.17278
	788.15	515	433.8067	4338.067	24.17278
	805.15	532	456.6325	4566.325	24.17278
	822.15	549	479.6091	4796.091	24.17278
	839.15	566	502.7307	5027.307	24.17278
	856.15	583	525.9917	5259.917	24.17278
	873.15	600	549.3867	5493.867	24.17278

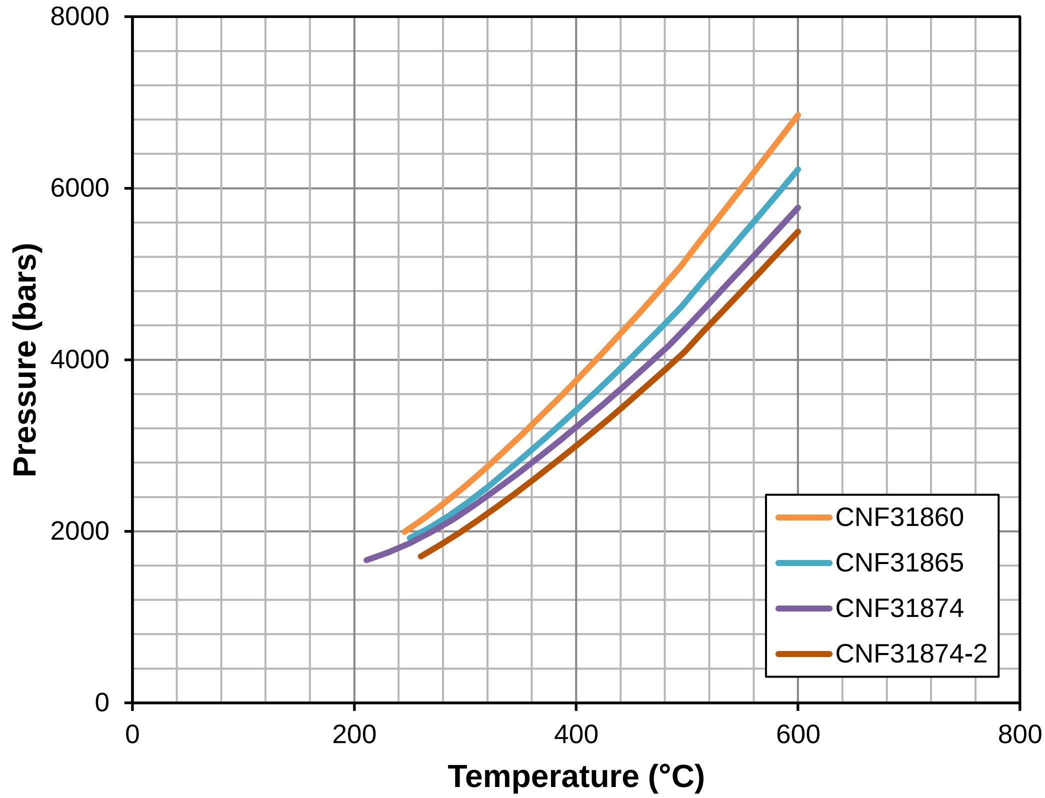

Figure A-7-1. Graphical representation of isochores of type I fluid inclusions in bladed barite from the Lemarchant deposit.